



# Dynamic soil-structure interaction of pile foundations : experimental and numerical study

Jesús Pérez-Herreros

## ► To cite this version:

Jesús Pérez-Herreros. Dynamic soil-structure interaction of pile foundations : experimental and numerical study. Civil Engineering. École centrale de Nantes, 2020. English. NNT : 2020ECDN0002 . tel-02972312

**HAL Id: tel-02972312**

**<https://theses.hal.science/tel-02972312>**

Submitted on 20 Oct 2020

**HAL** is a multi-disciplinary open access archive for the deposit and dissemination of scientific research documents, whether they are published or not. The documents may come from teaching and research institutions in France or abroad, or from public or private research centers.

L'archive ouverte pluridisciplinaire **HAL**, est destinée au dépôt et à la diffusion de documents scientifiques de niveau recherche, publiés ou non, émanant des établissements d'enseignement et de recherche français ou étrangers, des laboratoires publics ou privés.

# THESE DE DOCTORAT DE

L'ÉCOLE CENTRALE DE NANTES

ECOLE DOCTORALE N° 602

*Sciences pour l'Ingénieur*

Spécialité : Génie Civil

Par

**Jesús PÉREZ-HERREROS**

**Dynamic soil-structure interaction of pile foundations:  
experimental and numerical study**

Thèse présentée et soutenue à Paris, le 27 février 2020

Unité de recherche : UMR 6183, Institut de Recherche en Génie Civil et Mécanique (GeM)

## Rapporteurs avant soutenance :

Ioannis ANASTASOPOULOS

Claudio TAMAGNINI

Professeur, ETH Zurich

Professeur, Università degli Studi di Perugia

## Composition du Jury :

Président :

Stéphane GRANGE

Professeur, INSA de Lyon

Examineurs :

Stéphane GRANGE

Professeur, INSA de Lyon

Alain PECKER

Professeur, Ecole des Ponts ParisTech

Jean-François SEMBLAT

Professeur, ENSTA

Dir. de thèse :

Panagiotis KOTRONIS

Professeur, Ecole Centrale de Nantes

Co-dir. de thèse :

Sandra ESCOFFIER

Chargée de recherche, Université Gustave Eiffel

## Invité

Fahd CUIRA

Directeur scientifique, Terrasol (groupe Setec)





*Dedicated to my parents*



# Acknowledgments

This work would have not been possible without the contribution of many people who, in one way or another, have shared with me their time, their knowledge, their good humor and many other things that have made this adventure a more bearable path.

First and foremost, I would like to express my most sincere gratitude to my supervisors, for their patience and support during difficult times. Their skills and experience have been invaluable to me. It has been a great pleasure for me to work with them during these years.

I thank Dr. Sandra Escoffier. Her energy, her goodwill and the rigor of her work method were an inspiration during all my work. She sat with me for hours at a time going over the details of upcoming tests, verifying the results of previous tests and thinking about new ways to improve this work. Her great support, help and ideas have been indispensable for the success of the experimental work that has been conducted.

I thank my thesis director, Prof. Panagiotis Kotronis for the numerous exchanges we had, for his advice and his availability. I am also grateful for all the innovative ideas and interesting topics that we could discuss during this work. Thank you for trusting me and allowing me to freely explore many different ideas during this research.

I would also like to thank Mr. Fahd Caira for his contributions throughout this work. His advice and remarks prompted me not to forget the practical side of every development. I look forward to continuing our collaboration dealing with new challenges and projects in earthquake engineering.

I am grateful to Profs. Ioannis Anastasopoulos, Claudio Tamagnini, Alain Pecker, Stéphane Grange and Jean-François Semblat for accepting to be members of the jury. It was an honor to be assessed by such a group of experts. Your work has been a constant reference and source of inspiration during this thesis. Special thanks are due to both reviewers, Profs. Ioannis Anastasopoulos and Claudio Tamagnini for their valuable comments and suggestions on various aspects of this dissertation.

A special thought is for Prof. Alain Pecker. I would like to thank him for having introduced me to the field of soil and structure dynamics at Ecole des Ponts et Chaussées almost 10 years ago. His inspiring lectures, his enthusiastic teaching and his fruitful career are a source of inspiration to my work. Our discussions over the past few years are precious to me and I am delighted to be able to continue collaborating with him.

I am indebted to the technical staff of the centrifuge laboratory: Messrs. Patrick Gaudicheau, Philippe Audrain, Alain Neel and Stéphane Lerat. The success of the experimental work conducted in this PhD would have not been possible without their efforts and help.

These acknowledgments would be incomplete if I did not remember all my friends and colleagues (from Université Gustave Eiffel laboratory, Ecole Centrale de Nantes and Terrasol) who accompanied me during the thesis. They are so many that I would need several pages to name them all! I want to thank them for their support, their good advice and their good sense of humor. This journey would not have been the same without them!

This work could not have been carried out without the financial support provided by Terrasol and Setec TPI. Their support and continuous investment in R&D is greatly acknowledged.

Special thanks go to my parents, my brother and my family, who have always been there despite the distance that separates us. I thank them for encouraging me to persevere in my work and to support me during difficult times.

Finally, I would like to thank my girlfriend Emma for her patience and help in the last years. Without her support the thesis would have been much harder to finish.

Jesús PÉREZ HERREROS

# Abstract

The dynamic response of a structure supported by pile foundations is a complex Soil-Structure Interaction (SSI) problem. Under earthquake loading, the piles are subjected to loadings due to the deformation imposed by the soil (kinematic interaction) and to the inertial forces transmitted by the superstructure (inertial interaction).

The design of deep foundations under seismic loadings is often carried out by means of conservative methods that aim to assure zero damage of the foundation. Most of these methods consider the behavior of the foundation as linear elastic. As a result, the capability of the foundation to dissipate energy during seismic loading due to nonlinear mechanisms is neglected. This approach was justified in the past due to the lack of information about the nonlinear behavior of foundations and the absence of adapted numerical tools. Such limitations are becoming more and more obsolete, as a relevant number of experimental and numerical results are now available as well as new design methods [169].

In this Ph.D, the behavior of single piles and pile groups under seismic loading is studied using both experiments and finite element calculations. Dynamic centrifuge tests are carried out with a multilayered soil profile, several foundation configurations and a series of earthquakes and sinusoidal base shakings.

Nonlinear finite element calculations are also performed and compared to experimental results to investigate the ability of current computational models to satisfactorily reproduce the nonlinear response of foundations.

A novel macroelement for pile group foundations under seismic loading is developed and numerically validated. It allows taking into account the group effects and their variation with the loading frequency (pile-soil-pile interaction) as well as the nonlinearity developed in the system. Finally, the macroelement model for pile groups is used to perform an Incremental Dynamic Analysis (IDA) of the main pylon of a cable-stayed bridge.

**Keywords:** Soil-Structure Interaction; pile-group foundation; seismic loading; macroelement; centrifuge modelling



# Résumé

La réponse dynamique d'une structure supportée par des fondations profondes constitue un problème complexe d'Interaction Sol-Structure (ISS). Sous chargement sismique, les pieux sont soumis à la sollicitation imposée par le sol (interaction cinématique) et aux forces d'inertie transmises par la superstructure (interaction inertielle).

Le dimensionnement des fondations profondes soumises à des sollicitations sismiques est souvent réalisé au moyen de méthodes conservatrices visant à assurer que les fondations ne soient pas endommagées. La plupart de ces méthodes considèrent le comportement de la fondation élastique linéaire et par conséquent la capacité de la fondation à dissiper de l'énergie du fait des mécanismes non-linéaires est négligée. Cette approche était justifiée dans le passé en raison du manque d'informations sur le comportement non-linéaire des fondations et de l'absence d'outils numériques adaptés. De telles limitations deviennent de plus en plus obsolètes, puisqu'un nombre pertinent de résultats expérimentaux et numériques sont maintenant disponibles, ainsi que de nouvelles méthodes de conception [169].

Dans cette thèse, le comportement des pieux isolés et des groupes de pieux sous chargement sismique est étudié avec une approche couplant l'expérimental et le numérique. Des essais dynamiques en centrifugeuse sont effectués avec un sol stratifié, plusieurs configurations de fondations et une série de séismes et sollicitations sinusoïdales.

Des calculs non-linéaires aux éléments finis sont également effectués et comparés aux résultats expérimentaux afin d'étudier la capacité des modèles numériques à reproduire de manière satisfaisante la réponse non-linéaire des fondations.

Un nouveau macroélément pour les groupes de pieux sous chargement sismique est proposé et validé numériquement. Le macroélément permet de prendre en compte les effets de groupe et leur variation avec la fréquence de sollicitation (interaction pieu-sol-pieu) ainsi que la non-linéarité développée dans le système. Le nouveau macroélément est enfin utilisé pour effectuer une analyse dynamique incrémentale (IDA) du pylône centrale d'un pont à haubans.

**Mots clés:** Interaction Sol-Structure; groupe de pieux; chargement sismique; macroélément; essais en centrifugeuse





# Table of contents

<b>Acknowledgments</b>	<b>v</b>
<b>Abstract</b>	<b>vii</b>
<b>Résumé</b>	<b>ix</b>
<b>Table of contents</b>	<b>xi</b>
<b>List of figures</b>	<b>xv</b>
<b>List of tables</b>	<b>xxv</b>
<b>Notations</b>	<b>xxvii</b>
<b>1 Introduction and problem statement</b>	<b>1</b>
1.1 General context . . . . .	1
1.2 Scientific context and motivation . . . . .	2
1.3 Document outline . . . . .	3
<b>2 Literature review</b>	<b>5</b>
2.1 Introduction . . . . .	5
2.2 Dynamic Soil-Structure Interaction . . . . .	5
2.3 Post-earthquake observations of the performances of piled foundations . . . . .	7
2.3.1 Summary of post-earthquake observations of pile foundations . . . . .	14
2.4 Experimental studies on the behavior of piles in clay and stratified soil profiles under seismic loading . . . . .	16
2.4.1 Dynamic centrifuge tests . . . . .	16
2.4.2 Shaking table tests . . . . .	21
2.4.3 Full scale in-situ tests . . . . .	21
2.5 Numerical methods for dynamic soil-structure interaction analysis of piled foundations . . . . .	22
2.5.1 Direct method . . . . .	22
2.5.2 Substructuring (superposition theorem) . . . . .	23
2.5.3 Winkler-type models . . . . .	24
2.5.4 Macroelement model . . . . .	25
2.6 Seismic behavior of deep foundations . . . . .	27
2.6.1 Dynamic response of a single pile . . . . .	28
2.6.2 Dynamic response of a group of piles . . . . .	40
2.6.3 Non-linearity . . . . .	47
2.6.4 Summary . . . . .	48
2.7 Analytical study of dynamic soil-structure interaction effects . . . . .	48
2.8 Summary . . . . .	57

<b>3</b>	<b>Experimental work</b>	<b>59</b>
3.1	Introduction . . . . .	59
3.2	Dynamic centrifuge experimental set-up and program . . . . .	59
3.2.1	Centrifuge tests set-up . . . . .	59
3.2.2	Characteristics of the soils used in the tests . . . . .	61
3.2.3	Soil profile . . . . .	62
3.2.4	Instrumentation . . . . .	65
3.2.5	Properties of the single pile cap, the pile group cap and the superstructures . . . . .	66
3.2.6	Installation of single piles and pile groups . . . . .	68
3.2.7	Input signals . . . . .	70
3.3	Repeatability of the tests . . . . .	72
3.3.1	CPT profile . . . . .	72
3.3.2	Shear wave velocity profile . . . . .	74
3.3.3	Water content profile . . . . .	75
3.3.4	Quality of the input signal . . . . .	76
3.4	Free-field site response . . . . .	78
3.4.1	Soil response . . . . .	78
3.4.2	Frequency analysis . . . . .	82
3.4.3	Boundary effects . . . . .	85
3.5	Definitions and calculation of certain results . . . . .	86
3.5.1	Identification of the piles used in the tests . . . . .	86
3.5.2	Dynamic, total and residual bending moment . . . . .	87
3.5.3	Bending moment at the pile tip . . . . .	87
3.5.4	Horizontal displacement (translation) and rotation (rocking) of the pile cap . . . . .	87
3.5.5	Horizontal force and overturning moment at the base of the structure . . . . .	88
3.6	Performance of single piles under seismic loading . . . . .	90
3.6.1	Frequency analysis . . . . .	90
3.6.2	Pile head response . . . . .	91
3.6.3	Maximum bending moments . . . . .	92
3.6.4	Evolution of bending moments with time and frequency content . . . . .	98
3.7	Performance of pile groups under seismic loading . . . . .	100
3.7.1	Frequency analysis . . . . .	100
3.7.2	Response of the pile cap . . . . .	101
3.7.3	Shear force and overturning moment at the base of the superstructure . . . . .	104
3.7.4	Maximum bending moments . . . . .	105
3.7.5	Evolution of bending moment with time . . . . .	110
3.8	Summary . . . . .	113
<b>4</b>	<b>Numerical work</b>	<b>115</b>
4.1	Introduction . . . . .	115
4.2	Nonlinear soil response . . . . .	115
4.2.1	Behaviour of soils under cyclic and dynamic loading . . . . .	115
4.2.2	Dynamic properties of Hostun HN31 sand and Speswhite kaolinite . . . . .	120
4.3	Hypoplastic constitutive laws . . . . .	121
4.3.1	Introduction . . . . .	121
4.3.2	Hypoplastic constitutive law for granular soils . . . . .	123
4.3.3	Hypoplastic constitutive law for cohesive soils . . . . .	125
4.3.4	Cyclic loading (integrular strain) . . . . .	127
4.3.5	Calibration of hypoplastic parameters for HN31 sand . . . . .	128
4.3.6	Calibration of hypoplastic parameters for Speswhite kaolin clay . . . . .	130
4.4	Free field ground response . . . . .	132
4.4.1	Soil profile used in dynamic centrifuge tests . . . . .	133
4.4.2	Response at very low amplitude strains (elastic response) . . . . .	134
4.4.3	Response under weak seismic motions . . . . .	134
4.4.4	Response under strong seismic motions . . . . .	136

4.5	Dynamic soil-structure interaction . . . . .	136
4.5.1	Finite element model . . . . .	136
4.5.2	Results . . . . .	140
4.6	Summary . . . . .	142
<b>5</b>	<b>Macroelement</b> . . . . .	<b>145</b>
5.1	Introduction . . . . .	145
5.2	Macroelement model for pile groups . . . . .	145
5.2.1	1 <sup>st</sup> level: single pile macroelement model . . . . .	146
5.2.2	2 <sup>nd</sup> level: static pile group macroelement model . . . . .	151
5.2.3	3 <sup>rd</sup> level: dynamic pile group macroelement model . . . . .	157
5.3	Validation of the pile group macroelement . . . . .	160
5.3.1	Calibration . . . . .	160
5.3.2	Validation on a SSI nonlinear seismic problem . . . . .	166
5.4	Additional notes . . . . .	167
5.4.1	Response of a single pile . . . . .	167
5.4.2	Failure surface . . . . .	168
5.4.3	Group effects . . . . .	168
5.4.4	Flexible pile cap . . . . .	169
5.4.5	Radiation damping . . . . .	170
<b>6</b>	<b>Application to a real project</b> . . . . .	<b>173</b>
6.1	Introduction . . . . .	173
6.2	The Atlantic Bridge (Panama) . . . . .	173
6.2.1	Model used in the present study . . . . .	174
6.2.2	Foundation . . . . .	175
6.2.3	Modal analysis . . . . .	175
6.2.4	Calibration of pile group macroelement parameters . . . . .	178
6.3	Incremental dynamic analysis (IDA) . . . . .	180
6.3.1	Seismic loading . . . . .	180
6.3.2	Intensity measure and engineering demand parameters . . . . .	181
6.3.3	Results: IDA curves and impact of SSI on the response . . . . .	183
6.4	Additional comments . . . . .	184
6.5	Summary . . . . .	187
<b>7</b>	<b>Conclusions and perspectives</b> . . . . .	<b>189</b>
7.1	Conclusions . . . . .	189
7.2	Perspectives . . . . .	191
7.2.1	Experimental part . . . . .	191
7.2.2	Numerical part . . . . .	191
7.2.3	Macroelement . . . . .	191
	<b>Bibliography</b> . . . . .	<b>193</b>
<b>A</b>	<b>Centrifuge modeling</b> . . . . .	<b>207</b>
A.1	Principles . . . . .	207
A.2	Difficulties and/or limitations of dynamic centrifuge tests . . . . .	208
<b>B</b>	<b>Experimental program and base shaking signals</b> . . . . .	<b>211</b>
B.1	List of experiments . . . . .	211
B.1.1	List of experiments by chronological order . . . . .	211
B.1.2	Details of experiments . . . . .	211
B.2	Characteristics of the selected inputs . . . . .	217
B.3	Representation of inputs in time and frequency domain . . . . .	218

<b>C</b>	<b>Instrumentation and equipments</b>	<b>223</b>
C.1	Structures . . . . .	223
C.1.1	Single pile cap . . . . .	223
C.1.2	Pile group cap . . . . .	224
C.1.3	Short building . . . . .	224
C.1.4	Tall building . . . . .	225
C.2	Instrumented piles . . . . .	226
<b>D</b>	<b>Study of repeatability of experiments</b>	<b>227</b>
D.1	CPT profiles . . . . .	227
D.2	Ground motion parameters . . . . .	227
<b>E</b>	<b>Numerical resolution of the seismic SSI problem</b>	<b>229</b>
E.1	Finite Element Development and Analysis Environment (FEDAE) . . . . .	229
E.2	Transient dynamic analysis of a nonlinear system . . . . .	230
E.2.1	The Newmark method . . . . .	231
E.2.2	Newmark integration algorithm for a nonlinear system . . . . .	231
<b>F</b>	<b>SSI in current engineering design practice</b>	<b>235</b>
F.1	SSI in current design practice . . . . .	235
F.2	Dynamic impedance functions of the pile group used in experimental tests . . . . .	236

# List of figures

1.1	Earthquake statistics (data from [196, 181]) . . . . .	1
1.2	Global seismic hazard map (modified from [74]) . . . . .	2
2.1	Illustration of the soil-structure interaction problem . . . . .	5
2.2	Illustration of (a) kinematic and (b) inertial interaction phenomena . . . . .	6
2.3	NHK building, 1964 Niigata earthquake: (a) piles damaged by lateral spreading of the foundation soil and (b) correlation of pile damage and site conditions (after Hamada [82]) . . . . .	8
2.4	11-storey apartment: (a) plan and section of the building, (b) instrumentation plan and (c) shear wave velocity profile (modified after Ohta <i>et al.</i> [164]) . . . . .	9
2.5	10-storey pile supported building founded on soft soils, 1985 Mexico City earthquake: (a) section of the building and soil profile and (b) overturned structure (after Meymand [143], original from Mendoza and Auvinet (1988)) . . . . .	9
2.6	Collapsed Highway 1 bridge across the Struve Slough, 1989 Loma Prieta earthquake: (a) general view and (b) gap opening around piles (after Seed <i>et al.</i> [192]) . . . . .	10
2.7	Ervic building: (a) schematic view of the building and location of measurement devices and (b) soil profile (after Nikolaou <i>et al.</i> [156]) . . . . .	10
2.8	Obha Ohashi bridge case study: (a) plan and longitudinal section, (b) cross-section of pier 6 and (c) soil profile with shear wave velocity versus depth (after Ohira <i>et al.</i> [163] and Gazetas <i>et al.</i> [63]) . . . . .	11
2.9	Hanshin Expressway bridge case history, 1995 Kobe earthquake: (a) overview of the collapsed section and (b) geometric characteristics and piled foundation (after Mylonakis <i>et al.</i> [151]) . . . . .	12
2.10	Kandla Port and Customs office tower case study, 2001 Gujarat earthquake: plausible settlement mechanism of failure, assuming there is no structural failure of piles (after Dash <i>et al.</i> [46]) . . . . .	13
2.11	Konan High School case study, 2003 Tokachi-Oki earthquake: (a) soil profile, (b) shear wave velocity profile and (c) bending moment profile (after Koyamada <i>et al.</i> [109]) . . . . .	14
2.12	Potential failure modes of pile group foundations subjected to seismic loading (modified after Meymand [143], Tokimatsu <i>et al.</i> [207] and Dash <i>et al.</i> [46]) . . . . .	15
2.13	Dynamic centrifuge tests on a two storey structure founded on two pile group foundations in a silty clay soil profile, Anandarajah <i>et al.</i> [5] . . . . .	16
2.14	Dynamic centrifuge tests on a single pile in a normally consolidated San Francisco Bay Mud, Wang <i>et al.</i> [223] . . . . .	17
2.15	Dynamic centrifuge tests, soil-pile-structure interaction in dense sand and soft clay (Csp4 container layout), Wilson [228] . . . . .	18
2.16	Dynamic centrifuge tests, centrifuge model and instrumentation layout of a 2x2 pile-raft system in soft clay, Banerjee <i>et al.</i> [11] . . . . .	18
2.17	Dynamic centrifuge tests, schematic layout of the centrifuge test model containing a 4x3 pile-raft system embedded in soft clay, Zhang <i>et al.</i> [238] . . . . .	19
2.18	Dynamic centrifuge tests, cross sections and plan view of pile groups in soft clay to investigate the effects of ground improvements, Taghavi <i>et al.</i> [198] . . . . .	20

2.19	Shaking table tests, full scale container mounted on the shaking table to study the seismic interaction of soft clay-pile-superstructure, Meymand [143] . . . . .	21
2.20	Kausel superposition theorem for a SSI problem of a structure supported by deep foundations. The global SSI problem (a) is decomposed in three steps: (b1) kinematic interaction, (b2) dynamic impedances and (b3) dynamic response of structure taken into account SSI (modified from Kausel <i>et al.</i> [99]) . . . . .	23
2.21	Winkler-type models: (a) concept, (b1) rheological models for the axial response (top) and lateral (down) of a unit segment of a single pile (Nogami and Konagai [158, 159]), (b2) rheological model with Coulomb friction elements (Matlock <i>et al.</i> [136]) and (b3) phenomenological model (Gerolymos and Gazetas [71, 70]) . . . . .	24
2.22	Macroelement concept for deep foundations (2D): (a) near field and far field are integrated in the formulation of the macroelement, and (b) only the near field is managed by the macroelement . . . . .	25
2.23	The single vertical pile macroelement proposed by Correia [38]: (a) nonlinear elastic model to take into account soil-pile separation, (b) boundary surface plastic model, (c) radiation damping . . . . .	26
2.24	Loading and failure surfaces of the hypoplastic macroelement model for a single pile proposed by Li [117] and Li <i>et al.</i> [122, 123] . . . . .	27
2.25	Frequency-dependent and intensity-dependent macroelement approach proposed by Lesgidis <i>et al.</i> [116] . . . . .	27
2.26	Behavior of rigid and flexible piles under pile-head horizontal loading (after Meymand [143], original from Kulhawy and Chen (1995)) . . . . .	28
2.27	Behavior of rigid and flexible piles under kinematic loading (modified from Correia [38], original from Kramer (2007)) . . . . .	29
2.28	Kinematic interaction factors, $I_u$ , of free-head end-bearing piles in terms of the dimensionless frequency parameters $F_A$ , $F_B$ and $F_C$ (after Gazetas [61]) . . . . .	31
2.29	Influence of pile fixity on the kinematic displacement factor of a floating single pile embedded in: (a) homogeneous; and (b) inhomogeneous soil profile (after Fan <i>et al.</i> [59]) . . . . .	32
2.30	Influence of the stiffness contrast on the kinematic displacement factor of a fixed-head single pile embedded in a two-layered soil profile (modified from Gazetas <i>et al.</i> [67], original data from Kaynia and Kausel (1992)) . . . . .	32
2.31	Kinematic interaction factors for single piles under SH shear waves acting with different angles of incidence $\theta$ : (a) horizontal translation and (b) rocking (after Kaynia and Novak [102]) . . . . .	33
2.32	Influence of Rayleigh waves on the axial response of single piles, vertical displacements and axial strains: (a-b) $a_0 = 0.2$ and (c-d) $a_0 = 0.4$ (modified after Makris [128]) . . . . .	34
2.33	Kinematic bending strains along a single pile embedded in a homogeneous soil profile (case A1) and a two-layer soil profile (case A2, with $V_1/V_2 = 0.5$ and $\rho_1/\rho_2 = 0.8$ ) and excited by harmonic SH seismic waves (modified after Nikolaou <i>et al.</i> [156]) . . . . .	35
2.34	Definition of pile-head impedances . . . . .	36
2.35	Dynamic stiffness coefficients and damping ratios for flexible piles embedded in a parabolic modulus soil profile (after Gazetas [61]) . . . . .	37
2.36	Dynamic stiffness coefficients and damping ratios for flexible piles embedded in a constant modulus soil profile (after Gazetas [61]) . . . . .	38
2.37	Components of pile group response under lateral loading and overturning moment (after Meymand [143], original from O'Neill and Dunnavant (1985)) . . . . .	40
2.38	Kinematic interaction factors for horizontal displacement and rotation of the pile cap of several 4x4 pile groups with different pile spacings and embedded in a homogeneous halfspace (after Kaynia and Kausel [101]) . . . . .	42
2.39	Kinematic interaction factors for horizontal displacement and rotation of the pile cap of several pile groups (2x2, 3x3 and 4x4) embedded in a homogeneous halfspace (after Kaynia and Kausel [101]) . . . . .	42

2.40	Horizontal displacement kinematic interaction factors for (a) a single free-head pile and (b) a 3x3 hinged-head pile group, under SH shear waves acting with different angles of incidence $\theta$ (after Kaynia and Novak [102])	43
2.41	Dynamic stiffnesses of a 4x4 pile group embedded in a homogeneous halfspace (after Kaynia and Kausel [101])	45
2.42	Dynamic stiffnesses of several pile groups with $s/d = 5$ embedded in a homogeneous halfspace (after Kaynia and Kausel [101])	46
2.43	Response of a single pile embedded in a cohesionless (a) and a cohesive (b) soil, and subjected to lateral cyclic loading (after Gerolymos and Gazetas [71], original from Kishida [105])	47
2.44	Analytical model for the study of SSI	49
2.45	Definition of equivalent model accounting for foundation response in SSI analysis	50
2.46	Equivalent damping ratio of the soil-structure system	52
2.47	Influence of soil-structure interaction as a function of exciting frequency: structural distortion $u$ and displacement of the mass relative to free field ( $u_0 + h\theta + u$ )	53
2.48	Numerical application to study the impact of SSI in the response of a structure supported by a pile group	54
2.49	Dynamic stiffnesses and damping ratios of the 4x4 pile group of floating piles in a homogeneous halfspace given in Fig. 2.48	55
2.50	Effective horizontal dynamic stiffness and damping ratio of the foundation for different slenderness ratios $\bar{h}$	55
2.51	Study of the influence of inertial SSI in the case of a structure founded on a 4x4 pile group in terms of the properties of equivalent 1-dof system varying mass ratio $\bar{m}$ for three different exciting frequencies: (a-b) $a_0 = 0.05$ , (c-d) $a_0 = 0.3$ and (e-f) $a_0 = 0.5$	56
2.52	Impact of coupling terms in the effective horizontal dynamic stiffness and damping ratio of the foundation	57
3.1	Model configurations used in the dynamic centrifuge tests	60
3.2	Grain size distribution of Hostun HN31 sand (data from [15, 8])	62
3.3	Theoretical profiles of soil density, effective stress and overconsolidation ratio for the soil profile used in the centrifuge tests	63
3.4	Preparation steps of a clay layer: (a) installation of the clay slurry in the ESB container, (b) application of preloading pressure using a hydraulic cylinder and (c) installation of sensors prior to the installation of a new clay layer	64
3.5	Experimental layout of C06 dynamic test	65
3.6	Detail of spacings, gap, mass at the top of the single pile (C06 test), pile group cap and distribution of piles in pile group (C07 and C08 tests)	67
3.7	Assembly of piles and pile group cap	67
3.8	Superstructures used in the experiments	68
3.9	Cap-superstructure equivalent 2DOF models	69
3.10	Pile installation at 1g: (a) single pile and (b) pile group	70
3.11	Time and frequency representations of the real earthquake ground motions and of the 1Hz sine base shakings	71
3.12	CPT tests at arrival to 50g	73
3.13	Comparison of undrained shear stress profile to theoretical estimation of maximum shear stress and maximum acceleration at the soil surface depending on the localization of the shear failure in the clay layer	74
3.14	Small-strain shear wave velocity estimated from bender element measurements compared to the Hardin & Drnevich [85] empirical formulation	75
3.15	Water content profile	76
3.16	Repeatability of the input signal: (a) time and (b) frequency representations of the acceleration measured on the table for Landers 0.3g PGA earthquake input	77
3.17	Time representation of the horizontal acceleration measured at different depths during the C05 test, during (a) 0.05g and (b) 0.3g PGA Landers earthquake motions	79



3.18	(a) Acceleration response spectra (damping 5%) at the bottom (dotted line) and the top (solid line) of the soil column for every test and base shaking, (b) mean and standard deviation of response spectra from different tests for each base shaking . . .	80
3.19	Amplification factors for the soil column using acceleration response spectra (5% damping) given in Figure 3.18 at the bottom and at the top of the soil column . .	80
3.20	Average peak ground acceleration recorded at the bottom and at the top of the soil profile: (a) under seismic excitations and (b) sinusoidal base shakings . . . . .	81
3.21	Average peak ground displacement at the bottom and at the top of the soil profile: (a) under seismic excitations and (b) sinusoidal base shakings . . . . .	81
3.22	Time-frequency transfer function between the base and the top of the clay layer recorded during the 0.05g PGA earthquake motions in C08 test: (a) Northridge and (b) Landers . . . . .	83
3.23	Time-frequency transfer function between the base and the top of the clay layer recorded during the 0.3g PGA earthquake motions in C08 test: (a) Northridge and (b) Landers . . . . .	84
3.24	Comparison of the records at the soil ( $z = 6.25\text{ m}$ ) and at the corresponding container ring during the 0.3g PGA Northridge earthquake motion: (a) acceleration time history and (b) displacement time history (doubled integrated from acceleration records) . . . . .	86
3.25	Identification and location of the piles used in the dynamic centrifuge tests with a pile group (C07 and C08): (a) lateral and (b) top view . . . . .	86
3.26	Definition of several bending moment values . . . . .	87
3.27	Illustration of the instrumentation of the pile cap and of the superstructure: (a) single pile tests (C04, C05 and C06) and (b) pile group tests (C07 and C08) . . .	88
3.28	Schema of forces at the interface between the structure and the soil . . . . .	89
3.29	Time-frequency transfer function between the soil surface ( $z = 1\text{ m}$ ) and the pile cap in C06 test under Landers 0.3g seismic motion . . . . .	90
3.30	Frequency response of the pile cap in C06 test . . . . .	91
3.31	Normalized maximum acceleration of the pile head/cap: (a) under seismic excitations and (b) sinusoidal base shakings . . . . .	91
3.32	Measured maximum bending moments: (a-e) results from C04 test, (f-j) from C05 and (k-o) from C06 test . . . . .	93
3.33	Maximum bending moment value recorded in the pile: (a) under seismic excitations and (b) sinusoidal base shakings . . . . .	94
3.34	Depth of recorded maximum bending moment: (a) under seismic excitations and (b) sinusoidal base shakings . . . . .	94
3.35	Maximum bending moment recorded near the pile tip: (a) under seismic excitations and (b) sinusoidal base shakings . . . . .	95
3.36	Maximum residual bending moment increment in C04 and C05 tests: (a) under seismic excitations and (b) sinusoidal base shakings . . . . .	95
3.37	Evolution of accumulated residual bending moment during all 14 base shakings: (a) C04 test and (b) C05 test . . . . .	96
3.38	Maximum accumulated residual bending moment in C04 and C05 tests: (a) under seismic excitations and (b) sinusoidal base shakings . . . . .	96
3.39	Comparison of maximum bending moments results from single pile tests without mass at the pile head (C04 and C05) and with a lumped mass at the pile head (C06): under (a) Landers 0.05g earthquake motion, (b) Northridge 0.3g earthquake motion, (c) 3.2 Hz 0.1g sinusoidal base shaking and (d) 1.8 Hz 0.3g sine . . . . .	98
3.40	Time evolution and frequency analysis of the normalized bending moment in the instrumented pile used in C06 test (single pile with a mass at the pile head) under Landers 0.3g seismic motion. The accelerations recorded in the dense sand layer under the pile (at a depth of 19.55 m) and the pile cap are also presented . . . . .	99
3.41	Time-frequency transfer function between the soil surface ( $z = 1\text{ m}$ ) and the mass at the top of the structure in C08 test under Northridge 0.3g earthquake motion .	100

3.42	Frequency response of (a) the pile cap and (b) the top mass of the short structure in C07 test	100
3.43	Frequency response of (a) the pile cap and (b) the top mass of the tall structure in C08 test	101
3.44	Normalized maximum acceleration of the pile cap: (a) under seismic excitations and (b) sinusoidal base shakings	102
3.45	Normalized maximum displacement difference between the pile cap and the soil surface: (a) under seismic excitations and (b) sinusoidal base shakings	103
3.46	Normalized maximum rotation of the pile cap: (a) under seismic excitations and (b) sinusoidal base shakings	103
3.47	Normalized maximum base shear force: (a) under seismic excitations and (b) sinusoidal base shakings	104
3.48	Normalized maximum overturning moment: (a) under seismic excitations and (b) sinusoidal base shakings	105
3.49	Measured maximum bending moments in the central pile of the pile group: (a-e) pile group a short superstructure (C07 test) and (f-j) pile group with a tall superstructure (C08 test)	106
3.50	Maximum bending moment measured in central pile (IP2) in both pile group tests: (a) under seismic excitations and (b) sinusoidal base shakings	106
3.51	Comparison of maximum bending moment envelopes of the three instrumented piles in the pile group: for the short superstructure configuration (C07 test) under (a) Northridge 0.3g earthquake motion and (b) 1 Hz 0.1g sine input and for the tall superstructure configuration (C08 test) under (c) Northridge 0.3g earthquake motion and (d) 1 Hz 0.1g sine input	107
3.52	Maximum bending moment recorded near the pile tip of the central pile (IP2): (a) under seismic excitations and (b) sinusoidal base shakings	107
3.53	Maximum residual bending moment increment in C07 and C08 tests: (a) under seismic excitations and (b) sinusoidal base shakings	108
3.54	Evolution of the accumulated residual bending moment during all 14 base shakings: (a) C07 test and (b) C08 test	108
3.55	Maximum accumulated residual bending moment in C07 and C08 tests: (a) under seismic excitations and (b) sinusoidal base shakings	108
3.56	Comparison of maximum bending moments results from a single pile test (C04) and pile group tests (C07 and C08): under (a) Landers 0.05g earthquake motion, (b) Northridge 0.3g earthquake motion, (c) 1 Hz 0.1g sinusoidal base shaking and (d) 1.8 Hz 0.3g sine	109
3.57	Time evolution of the normalized bending moment and envelope of the maximum bending moment in two of the instrumented piles (IP2 and IP3) in short superstructure configuration (C07 test) under Northridge 0.3g earthquake. The accelerations recorded in the dense sand layer under the pile group (at a depth of 19.55 m), the pile cap and the superstructure are also presented	111
3.58	Time evolution of the normalized bending moment and envelope of the maximum bending moment in two of the instrumented piles (IP2 and IP3) in tall superstructure configuration (C08 test) under Northridge 0.3g earthquake. The accelerations recorded in the dense sand layer under the pile group (at a depth of 18.05 m), the pile cap and the superstructure are also presented	111
3.59	Time evolution of the normalized bending moment and envelope of the maximum bending moment in two of the instrumented piles (IP2 and IP3) short superstructure configuration (C07 test) under Sine 1 Hz 0.1g base shaking. The accelerations recorded in the dense sand layer under the pile group (at a depth of 19.55 m), the pile cap and the superstructure are also presented	112

3.60	Time evolution of the normalized bending moment and envelope of the maximum bending moment in two of the instrumented piles (IP2 and IP3) in tall superstructure configuration (C08 test) under Sine 1 Hz 0.1g base shaking. The accelerations recorded in the dense sand layer under the pile group (at a depth of 18.05 m), the pile cap and the superstructure are also presented . . . . .	112
3.61	Maximum bending moment envelopes at different time periods for (a) short superstructure (C07 test) and (b) tall superstructure (C08 test) configurations under Sine 1 Hz 0.1g base shaking . . . . .	113
4.1	Mohr-Coulomb criterion for (a) drained conditions and (b) undrained conditions . . . . .	116
4.2	Idealized cyclic loading sequence (after [166]) . . . . .	117
4.3	Cyclic behaviour of soil. Definition of (a) secant shear modulus and (b) hysteretic damping of a cycle using stress-strain curves (modified from [166, 64, 65]) . . . . .	118
4.4	Soil cyclic response and corresponding shear modulus and hysteretic damping with strain (modified from [64, 65]) . . . . .	119
4.5	Threshold values for cyclic shear strains: volumetric threshold shear strain, $\gamma_{tv}$ , and linear cyclic threshold shear strain, $\gamma_{tl}$ (after [220]) . . . . .	120
4.6	Secant shear modulus reduction and damping ratio curves for Hostun HN31 sand (data from [171, 211, 153]) . . . . .	120
4.7	Secant shear modulus reduction and damping ratio curves for Speswhite kaolinite (data from [10, 224, 225]) . . . . .	121
4.8	Hypoplastic constitutive law for granular materials: (a) pressure-dependent limiting void ratios (after Herle and Gudehus [86]), (b) influence of the parameter $\alpha$ and (c) of the parameter $\beta$ on the stress-strain curve from triaxial test simulations . . . . .	125
4.9	Hypoplastic constitutive law for cohesive materials: (a) definition of parameters $N$ , $\lambda^*$ and $\kappa^*$ (after Mašin [133]) and (b) influence of the parameter $\nu_{pp}$ on the stress-strain curve from an undrained triaxial test simulation . . . . .	127
4.10	Excessive stress (a) and strain (b) accumulation during stress and strain cycles, respectively (after Niemunis and Herle [154]) . . . . .	127
4.11	Drained triaxial compression tests on HN31 sand, simulation (solid curves) vs. experiments (dashed curves) [15] . . . . .	129
4.12	Secant shear modulus reduction and damping curves for Hostun HN31, comparison between the experimental and the numerical results with the hypoplastic constitutive law . . . . .	130
4.13	Undrained triaxial cyclic tests on HN31 sand, simulation using the hypoplastic model vs. experiments from [15] . . . . .	131
4.14	Undrained triaxial compression tests on Speswhite kaolinite ( $OCR = 1$ ), simulation (solid curves) vs. experiments (dashed curves) [149] . . . . .	131
4.15	Cyclic direct simple shear test on Speswhite kaolinite ( $\sigma'_c = 220 \text{ kPa}$ , $e = 1.26$ , $OCR = 1$ , $w = 47.5\%$ , $\gamma_c = 0.5\%$ , $f = 0.001 \text{ Hz}$ ), simulation vs. experiments [147] . . . . .	132
4.16	Secant shear modulus reduction and damping curves for Speswhite kaolin, comparison between the experimental and the numerical results with the hypoplastic constitutive law . . . . .	132
4.17	(a) Soil density, (b) effective stress and (c) overconsolidation ratio profiles for the soil profile used in dynamic centrifuge tests . . . . .	133
4.18	(a) Maximum shear modulus, (b) Poisson ratio and (c) shear wave velocity profiles for the soil profile used in dynamic centrifuge tests . . . . .	133
4.19	Eigenfrequencies, effective mass ratio and modal deformation shapes of the elastic soil profile corresponding to very low amplitude strains . . . . .	134
4.20	Secant shear modulus reduction and damping ratio curves used for Hostun HN31 sand and Speswhite kaolinite in the 1D wave propagation analysis . . . . .	135
4.21	Strain-compatible soil profiles under low intensity seismic motions (PGA 0.05g) . . . . .	135
4.22	Eigenfrequencies, effective mass ratio and modal deformation shapes of the strain-compatible equivalent linear soil profiles under low intensity seismic motions (PGA 0.05g) . . . . .	135

4.23	Free-field ground response under low intensity earthquake motion (Northridge 0.05g), acceleration time-history (left) and response spectra at 5% damping (right) at different depths of the soil profile, experimental records vs. numerical simulations (the equivalent linear model (FEM elastic) and the hypoplastic constitutive law (FEM hypoplastic))	137
4.24	Strain-compatible soil profiles under strong intensity seismic motions (PGA 0.3g)	138
4.25	Eigenfrequencies, effective mass ratio and modal deformation shapes of the strain-compatible equivalent linear soil profiles under strong intensity seismic motions (PGA 0.3g)	138
4.26	Free-field ground response under strong earthquake motion (Northridge 0.3g), acceleration time-history (left) and response spectra at 5% damping (right) at different depths of the soil profile, experimental records vs. numerical simulations (the equivalent linear model (FEM elastic) and the hypoplastic constitutive law (FEM hypoplastic))	139
4.27	Finite element mesh for (a) single pile tests (C04, C05 and C06) and (b) pile group tests (C07 and C08) (only the mesh corresponding to the soil and the piles is shown)	140
4.28	Comparison of maximum bending moment profiles of a single pile (C05 test), experimental vs numerical results: (a) Northridge 0.05g and (b) Northridge 0.3g earthquake	140
4.29	Comparison of maximum bending moment profiles of a single pile with a mass at its head (C06 test), experimental vs numerical results: (a) Northridge 0.05g and (b) Northridge 0.3g earthquake	141
4.30	Comparison of maximum bending moment profiles of the central pile in the pile group with a short superstructure (C07 test), experimental vs numerical results: (a) Northridge 0.05g and (b) Northridge 0.3g earthquake	141
4.31	Comparison of maximum bending moment profiles of the central pile in the pile group with a tall superstructure (C08 test), experimental vs numerical results: (a) Northridge 0.05g and (b) Northridge 0.3g earthquake	141
4.32	Time evolution of the normalized bending moment and the envelope of the maximum bending moment in the center pile of the pile group with a tall superstructure (C08 test) subjected to a Sine 1 Hz 0.1g loading. Accelerations in the dense sand layer under the pile group, at the pile cap and at the top of the superstructure are also presented. Numerical (finite element model with the hypoplastic constitutive laws) vs. experimental results	143
5.1	Modular macroelement concept for a pile group	146
5.2	Notation adopted for (a) forces and (b) displacement components at pile head in local coordinate system and the corresponding values, respectively (c) and (d), in global coordinate system (only the 2D case is illustrated)	147
5.3	Failure surface of a single vertical pile (after [121, 117, 122, 123])	148
5.4	Direction of plastic flow $\mathbf{m}(\mathbf{t})$	149
5.5	Static condensation of the pile group foundation system	151
5.6	Resolution scheme for the pile group macroelement at each Newton-Raphson iteration (without static or dynamic group effects)	152
5.7	Single pile response under (a) lateral loading and (b) moment	154
5.8	Example of numerical calculation procedure of static interaction factors, for different values of pile spacing $s$ and angle $\theta$ between the loading direction and the plane defined by the axis of both piles	155
5.9	Configurations of the pile group macroelement for the resolution of static and dynamic problems	157
5.10	Example of LPM models: (a) five-parameter discrete model proposed by De Barros and Luco [47] and (b) generalized Type II model with gyromass elements proposed by Saitoh [185]	158

5.11	Introduction of frequency effects and radiation damping in the pile-group macroelement: (a) elastic frequency-dependent rheological model proposed by Saitoh [185] (b) frequency-dependent pile-group macroelement model by combination of the static pile group macroelement with a LPM model . . . . .	158
5.12	Components of the rheological model used in the dynamic pile group macroelement and their influence on the impedance function . . . . .	158
5.13	Case study for the calibration and the validation of the pile group macroelement (configuration 2a): a 2x2 pile group in a constant modulus soil profile . . . . .	161
5.14	Calculation of the pile-head elastic stiffness matrix terms . . . . .	161
5.15	Calculation of the bearing capacity of the single pile . . . . .	162
5.16	Monotonic lateral loading of a single pile: elastic FEM vs nonlinear FEM vs single pile macroelement results . . . . .	162
5.17	Lateral cyclic loading of a single pile: elastic FEM vs nonlinear FEM vs single pile macroelement results . . . . .	163
5.18	Monotonic lateral loading of the 2x2 pile group: elastic FEM vs nonlinear FEM vs static pile group macroelement . . . . .	164
5.19	Lateral cyclic loading of the 2x2 pile group: elastic FEM vs nonlinear FEM vs static pile group macroelement results . . . . .	164
5.20	Lateral translation dynamic impedance function of the 2x2 pile group: numerical results using the boundary element approach and the software SASSI [126, 165] vs. the rigorous solution given by Kaynia [103] vs. the response given by the LPM Type II model proposed by Saitoh [185] . . . . .	165
5.21	Lateral response of the 2x2 pile group under dynamic loading: (a) 1 Hz sine and (b) 5 Hz sine loadings: elastic FEM vs nonlinear FEM vs dynamic pile group macroelement . . . . .	165
5.22	SSI nonlinear seismic problem: (a) cross section view and (b) plan view of the foundation . . . . .	166
5.23	Acceleration and displacement of the superstructure: nonlinear FEM vs. pile group macroelement . . . . .	166
5.24	Simple parametric study: (a) nonlinear SSI seismic problem, (b) lateral displacement of the superstructure (maximum and residual values) and (c) maximum rocking moment. Results from linear and nonlinear FEM and dynamic pile group macroelement models . . . . .	167
5.25	Modular approach using Winkler-type models as the constitutive model of the pile group macroelement . . . . .	168
5.26	Application of the modular macroelement concept for a pile group in the case of a flexible pile cap . . . . .	170
6.1	Elevation view of the Atlantic Bridge (also known as the third bridge over the Panama Canal), a cable-stayed bridge with a main span of 530 meters (note that the foundation configuration and the soil profile used in this study differ from those in the real project) . . . . .	173
6.2	Front view of the main pylon considered in this study: (a) schematic view and (b) finite element model of the structure . . . . .	174
6.3	Foundation detail: (a) plan view and (b) cross section view of the foundation and the soil profile (note that the foundation configuration and the soil profile used in this study differ from those in the real project) . . . . .	175
6.4	Dynamic impedances at the center of the pile group . . . . .	176
6.5	First vibration modes of the structure on fixed-base conditions with an effective mass ratio higher than 5% . . . . .	177
6.6	First vibration modes of the structure considering SSI and with an effective mass ratio higher than 5% . . . . .	177
6.7	Evolution of the cumulative effective modal mass ratio with frequency . . . . .	178
6.8	Real earthquake records used for analysis of the bridge pylon (data from the PEER Strong Motion Database [32]) . . . . .	181

6.9	IDA curves: maximum absolute acceleration at the pile cap and at the top of the pylon . . . . .	183
6.10	IDA curves: maximum base shear and moment . . . . .	184
6.11	IDA curves: maximum and residual relative displacement (with respect to free-field displacement) at the pile cap and at the top of the pylon, and maximum and residual rotation of the pile cap . . . . .	185
6.12	Impact of SSI in terms of maximum absolute acceleration at the pile cap and at the pylon top . . . . .	186
6.13	Impact of SSI in terms of maximum base shear and moment . . . . .	186
6.14	Impact of SSI in terms of maximum displacement at the pylon top . . . . .	186
A.1	Scaling factors use scheme . . . . .	208
B.1	Experimental layout - C01 test . . . . .	212
B.2	Experimental layout - C02 test . . . . .	213
B.3	Experimental layout - C03 test . . . . .	213
B.4	Experimental layout - C04 test . . . . .	214
B.5	Experimental layout - C05 test . . . . .	214
B.6	Experimental layout - C06 test . . . . .	215
B.7	Experimental layout - C07 test . . . . .	216
B.8	Experimental layout - C08 test . . . . .	217
B.9	Time (a) and frequency (b) representation of Northridge 0.05g earthquake . . . . .	218
B.10	Time (a) and frequency (b) representation of Landers 0.05g earthquake . . . . .	218
B.11	Time (a) and frequency (b) representation of Northridge 0.3g earthquake . . . . .	219
B.12	Time (a) and frequency (b) representation of Landers 0.3g earthquake . . . . .	219
B.13	Time (a) and frequency (b) representation of sine 1 Hz 0.1g input . . . . .	219
B.14	Time (a) and frequency (b) representation of sine 1.8 Hz 0.1g input . . . . .	220
B.15	Time (a) and frequency (b) representation of sine 2.4 Hz 0.1g input . . . . .	220
B.16	Time (a) and frequency (b) representation of sine 3.2 Hz 0.1g input . . . . .	220
B.17	Time (a) and frequency (b) representation of sine 1 Hz 0.3g input . . . . .	221
B.18	Time (a) and frequency (b) representation of sine 1.8 Hz 0.3g input . . . . .	221
B.19	Time (a) and frequency (b) representation of sine 2.4 Hz 0.3g input . . . . .	221
B.20	Time (a) and frequency (b) representation of sine 3.2 Hz 0.3g input . . . . .	222
C.1	Scheme drawing of the single pile cap (at model scale) . . . . .	223
C.2	Scheme drawing of the pile group cap (at model scale) . . . . .	224
C.3	Scheme drawing of the short building (at model scale) . . . . .	224
C.4	Scheme drawing of the tall building (at model scale) . . . . .	225
C.5	Distribution of strain gauges on instrumented piles (all dimensions are given in mm at model scale) . . . . .	226
D.1	Information about CPT measurements: elapsed time between container unloading and CPT measurement, accumulated time at 50g before CPT measurement and number of 1g-50g-1g cycles before CPT measurement . . . . .	227
E.1	FEDAE function organization . . . . .	229
E.2	Restoring force in a single degree of freedom system . . . . .	231
E.3	Modified Newton-Raphson iteration . . . . .	232
F.1	Consideration of SSI in current design of structures under earthquake loading . . . . .	235
F.2	Several possible approaches for the dynamic analysis of a structure taking into account SSI effects . . . . .	236
F.3	Dynamic stiffnesses and damping ratios for the single pile used in centrifuge tests using the equivalent linear elastic approach . . . . .	237
F.4	Dynamic stiffnesses and damping ratios of the pile group used in centrifuge tests using an equivalent linear elastic approach . . . . .	238



# List of tables

2.1	Dynamic response of single free-head flexible piles (after Gazetas [61, 68]) . . . . .	39
3.1	Experimental program . . . . .	60
3.2	Properties of Speswhite kaolin clay (Khemakhem [104]) . . . . .	61
3.3	Properties of Hostun HN31 sand (Benahmed [15]) . . . . .	62
3.4	Characteristics of Hostun sand HN31 at installation . . . . .	63
3.5	Characteristics of Speswhite kaolinite at installation . . . . .	63
3.6	Properties of the instrumented piles . . . . .	66
3.7	Characteristics of the mass at the top of the single pile . . . . .	67
3.8	Characteristics of the pile group cap . . . . .	68
3.9	Characteristics of the superstructures . . . . .	68
3.10	Characteristics of the cap-superstructure equivalent 2DOF models (at prototype scale) . . . . .	69
3.11	Characteristics of the reference input signals (prototype scale) . . . . .	72
3.12	Quantitative estimation of the input quality: average values and maximum value of relative difference of each test with respect to the average value (in brackets) . . . . .	77
4.1	Exponent $k$ (after Hardin & Drnevich [85]) . . . . .	117
4.2	Parameters of the hypoplastic model for sands [219] calibrated for Hostun sand [86] . . . . .	125
4.3	Parameters of the hypoplastic model for clay [129, 135] calibrated for Kaolin clay [130] . . . . .	127
4.4	Ranges of values of interest for the calibration of the hypoplastic constitutive laws parameters using laboratory test results for the HN31 sand and the Speswhite kaolin . . . . .	129
4.5	Best-estimate calibrated parameters of the hypoplastic model to reproduce the response of HN31 Hostun sand . . . . .	129
4.6	Best-estimate calibrated parameters of the hypoplastic model to reproduce the response of Speswhite kaolin clay . . . . .	131
5.1	Parameters of the hypoplastic macroelement for a single pile [117, 122] . . . . .	150
5.2	Calibrated parameters for the single pile macroelement . . . . .	163
5.3	Calibrated parameters of the LPM model inside the pile group macroelement to reproduce the dynamic lateral translation response of the 2x2 pile group (adapted from [185]) . . . . .	164
6.1	Calibrated parameters for the single pile hypoplastic macroelement . . . . .	179
6.2	General information and characteristics of the real earthquake records used for the analysis of the bridge pylon: component ( $\varphi$ ), average shear wave velocity in the upper 30 m of the soil profile ( $V_{s,30}$ ), moment magnitude ( $M_W$ ), closest distance to fault rupture ( $R_{rup}$ ), peak ground acceleration (PGA), peak ground velocity (PGV), Arias Intensity ( $I_A$ ) and significant duration (data from the PEER Strong Motion Database [32]) . . . . .	182
A.1	Scale factors commonly used in geotechnical centrifuge modeling . . . . .	208



B.1	List of experiments by chronological order . . . . .	211
B.2	Characteristics of the selected inputs (prototype scale): peak ground acceleration (PGA), peak ground velocity (PGV), Arias Intensity ( $I_A$ ) and significant duration . . . . .	218
C.1	Parameters of the single pile cap (at model scale) . . . . .	223
C.2	Parameters of the pile group cap (at model scale) . . . . .	224
C.3	Parameters of the short building (at model scale) . . . . .	224
C.4	Parameters of the tall building (at model scale) . . . . .	225

# Notations

Unless otherwise indicated in the text:

- Scalar magnitudes are written in plain italic:  $u$ ,  $A$ ,  $\varepsilon$ ;
- Vectors and matrices are represented with boldface symbols:  $\mathbf{v}$ ,  $\mathbf{T}$ ;
- The Euclidean norm of a vector  $\mathbf{v}$  is denoted by the operator  $\|\mathbf{v}\|$ ;
- The symbol  $\mathbf{m}^T$  indicates the transpose of a vector/matrix  $\mathbf{m}$ ;
- The time derivative of a variable  $x$  is represented by one superposed dot  $\dot{x}$ .



# Chapter 1

## Introduction and problem statement

### 1.1 General context

Earthquakes are one of the most devastating natural hazards in terms of loss of life and livelihood, with annual economic losses that are counted in billions of dollars. Figure 1.1 presents some statistics related to earthquakes between 1990 and 2018. Over this 28-year period, deaths due to earthquakes totaled about 925000 people. Monetary losses due to structural damage (or even collapse) of buildings, bridges, highways and other lifelines were also substantial. However the number of earthquakes is more or less constant from one year to another yet a very different impact is observed. The causes of fatalities and the extent of the damage depend to a great extent on the type of constructions and the density of population in the area [55].

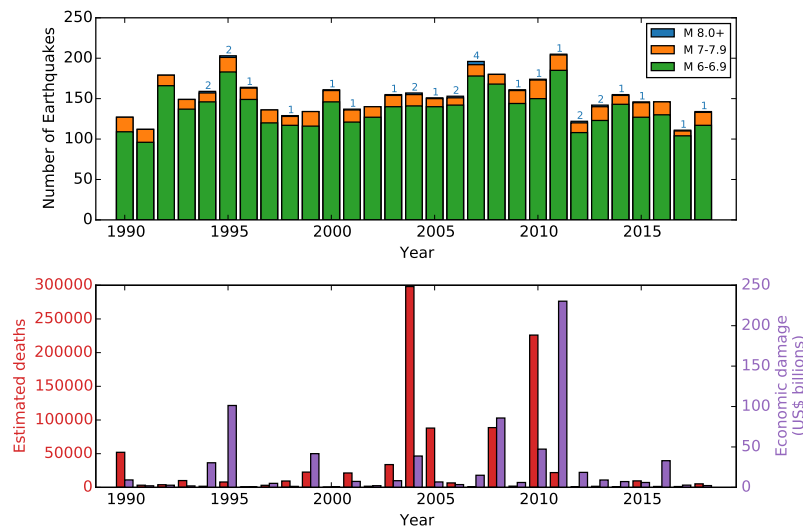


**Figure 1.1:** Earthquake statistics (data from [196, 181])

Many of the skyscrapers, bridges and several other large infrastructures (e.g., ports, harbors, water tanks, chimneys, etc.) that are being built today around the world concern countries where the seismic risk is relatively high (see Fig. 1.2) which poses several challenges when designing these structures. In addition, many major cities in those countries are built overlying soft clay (e.g., Shanghai, Bangkok, Mumbai, Kuala Lumpur, Jakarta, Singapore, etc.) which results in many important structures being supported on pile foundations to provide sufficient bearing capacity and stiffness to minimize settlements. In such situations, the response of the foundation and

the surrounding soil subjected to earthquake loading is one of the important factors affecting the integrity of infrastructures [12, 174, 175].

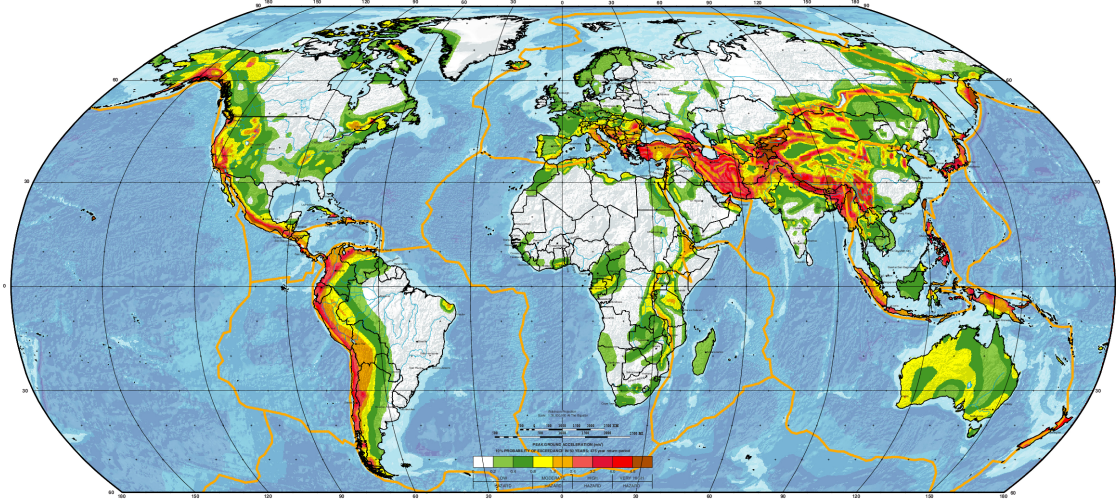


**Figure 1.2:** Global seismic hazard map (modified from [74])

Indeed, in addition to carrying the vertical compressive loads, piles must also resist to transient or cyclic lateral and uplift loads arising from earthquake, wind, wave, blast, impact or machine loading. The coincidence of major pile-supported structures sited on soft soils in areas of earthquake hazard results in significant demands on those deep foundations, with potential additional associated complex problems such as resonance between the soil and the structure, liquefaction and/or strain-softening, etc [143, 111].

The construction of new structures in earthquake prone zones present new challenges to engineers, particularly in relation to structural and geotechnical design. One of the challenges concerning piled foundations with a large number of piles is for example taking into account group interaction effects in the design. Movements of the foundation result from the superstructure loads and these movements in turn influence the behavior of the superstructure and the consequent loads transmitted to the foundation [174].

The big challenge today is to build efficiently while ensuring the safety of people and limiting economic losses. In order to avoid unnecessary overdesign, the foundation design should therefore be considered as a performance-based Soil-Structure Interaction (SSI) issue, not limited to traditional design methods [175].

## 1.2 Scientific context and motivation

The dynamic response of a structure supported by deep foundations is a complex Soil-Structure Interaction (SSI) problem that requires the use of adapted computational methods. Traditionally, the design of deep foundations under seismic loading is carried out by means of conservative methods that aim to assure zero damage of the foundation that therefore remains linear elastic. This approach was justified due to the lack of information about the dynamic non-linear behavior of foundations and the lack of adapted numerical tools. Such limitations become however more and more obsolete as an important number of experimental and numerical results are now available as well as new design methods [169]. In addition, modern design codes as the Eurocode 8 [1] recognize the effect of SSI and of the nonlinear energy dissipation that can be important in the case of strong earthquakes. Several studies on the SSI undertaken in the last two decades offer a new design philosophy of foundations under seismic loading that allows residual displacements and rotations compatible with the structure to protect the superstructure [6].

Taking into account the characteristics of the nonlinear behavior of the foundation system

requires most often the use of global models (modeling soil, foundation and the superstructure) and nonlinear dynamic transient calculations, which, despite the technological advances of the last decades, remain complex and prohibitive in terms of both calculation time and post-processing of the results. To circumvent this problem, different authors have developed the concept of the macroelement, which can be seen as a multidirectional nonlinear spring that makes possible to concentrate in a single point the overall multidirectional response of the soil and the foundation.

The macroelement concept, first introduced in foundation engineering by Nova and Montrasio [160], allows to take into account the main phenomena involved in SSI, while avoiding the complexity and the numerical cost of nonlinear finite element dynamic analysis. It is equipped with a nonlinear “constitutive law” (described in terms of generalized forces and displacements) formulated according to the theory of plasticity or hypoplasticity and making it possible to model the dynamic couplings (linear and nonlinear) in several directions between the superstructure, the soil and the foundation [42]. Taking into account these non-linearities and the coupling between degrees of freedom is the main contribution of this new approach.

The developments of this heuristic tool originally concerned shallow foundations (e.g., [160, 42, 27, 28, 78, 76, 187]) and its application for the evaluation of the seismic response of the foundation system clearly demonstrated the interest of such approach. The concept has been extended only recently to the case of deep foundations (e.g., [38, 117, 69, 122]) and is limited to the case of piles in a homogeneous soil profile.

The main objective of this Ph.D thesis is to integrate, as a part of the macroelement approach for deep foundations under seismic loading, the possibility to treat pile group foundations. In order to do so the model needs to take into account group effects and their variation with the loading frequency (pile-soil-pile interaction) as well as the nonlinearity developed in the system. This work also includes an experimental study with centrifuge seismic tests that aim to study the behavior of single piles and pile groups embedded in a multilayered soil profile and subjected to seismic loading. Experimental results are confronted to nonlinear finite element calculations in order to investigate the ability of numerical models to satisfactorily reproduce the nonlinear response of foundations. The overall objective of this research is therefore to increase the understanding of dynamic nonlinear soil-structure interaction in the case of structures supported by pile groups and to propose numerical methods adapted to the resolution of this problem.

### 1.3 Document outline

In **Chapter 2**, a brief introduction to dynamic Soil-Structure Interaction (SSI) is first given followed by case histories of post-earthquake observations in the literature concerning the performance of piled foundations. A review of previous experimental work dealing with deep foundations (single piles and pile groups) in clay and multilayered soil profiles is also done in this chapter. The numerical methods available for the study of dynamic soil-structure interaction of deep foundations are also addressed. In the continuation of the chapter a detailed survey concerning the seismic behavior of deep foundations is presented. This section resumes observations made by an important number of researchers in the SSI research field, using numerical methods but also by comparing numerical findings to real records and observations. Finally, the chapter is concluded by a simple analytical study to further illustrate the importance of SSI.

**Chapter 3** describes the experimental program that consisted in a series of dynamic centrifuge tests on single piles and pile group configurations under seismic and sinusoidal base shakings. The characteristics of the different tests are first introduced: soil profile and type of soil, applied signals, instrumentation, etc. Then, the main results are presented and analyzed, especially in terms of the evolution of the soil response with time and the bending moments in piles.

**Chapter 4** presents full nonlinear 3D finite element simulations conducted with ABAQUS software and hypoplastic constitutive laws for sand and clay. The parameters of the hypoplastic laws are calibrated using laboratory test results available in the literature. Once calibrated, the same configurations tested in the centrifuge tests are modeled. The results of the simulations are compared with the results from dynamic centrifuge tests in order to investigate the ability of the

current computational models to satisfactorily reproduce the nonlinear response of foundations.

**Chapter 5** proposes a novel macroelement for pile group foundations under seismic loading that allows taking into account the group effects and their variation with the loading frequency (pile-soil-pile interaction) as well as the nonlinearity developed in the system. The formulation is introduced and the new elements is numerically validated.

In **Chapter 6**, an Incremental Dynamic Analysis (IDA) of the pylon of a cable-stayed bridge is conducted for a set of real earthquake records. Three different support conditions are compared, namely: fixed-base approach, SSI approach using elastic stiffness matrices and nonlinear SSI approach using the proposed pile group macroelement.

**Chapter 7** summarizes the general conclusions and perspectives of this work.

# Chapter 2

## Literature review

### 2.1 Introduction

The dynamic response of a structure supported by deep foundations is a complex Soil-Structure Interaction (SSI) problem and has been an active research topic since the early 1970s. Extensive literature is available today with an uncountable number of papers concerning numerical resolution methods, post-earthquake observations and experimental tests among other topics specific to deep foundations. This chapter presents a few selected topics regarding SSI and the dynamic behavior of single piles and pile groups.

### 2.2 Dynamic Soil-Structure Interaction

The dynamic soil-structure interaction (SSI) is a phenomenon in which the movement of the soil during an earthquake is influenced by the presence of the structure and vice versa. The displacements of the soil and of the structure can no longer be considered independently. They differ from free-field and fixed-base solutions for the soil and the structure respectively. The importance of this phenomenon varies according to the nature of the soil, the characteristics of the structure and of the foundation (Fig. 2.1).

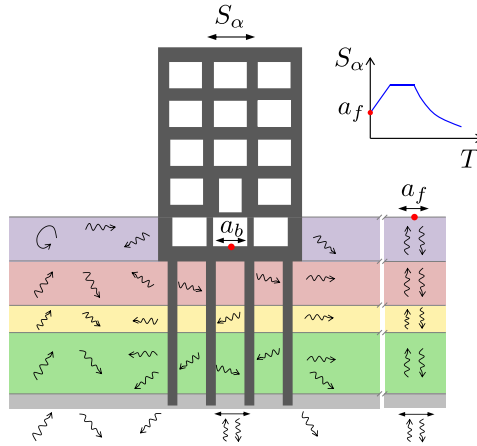


**Figure 2.1:** Illustration of the soil-structure interaction problem

A full interaction analysis takes into account several aspects, i.e., the variation of soil characteristics with depth; the non-linear behavior of the soil, the structure and the soil-structure interface; the three-dimensional nature of the problem; the complex pattern of wave propagation that generates motion and the interaction with neighboring structures (i.e., structure-soil-structure interaction) [166].



Simplifications in the resolution of an SSI problem are often adopted. They depend on the problem being addressed and the chosen calculation method. They often concern the choice of the incident wave (shear waves, pressure waves or surface waves), the schematization of the foundation soil, the use of equivalent linear elastic soil models, etc.

The movement of the foundation differs from the movement of the free field due to the differences in rigidity between the foundation and the surrounding soil. The incident wave field is reflected and diffracted by the foundation and thus the movement of the soil in the proximity of the foundation is modified (Fig. 2.2-a).

Thereby in the absence of the superstructure and foundation mass, the movement at the base of the structure differs of the free field due to the difference in stiffness between the ground and the foundation. The stiffness of the foundation doesn't allow the surrounding soil to follow the movements imposed by the soil in free-field conditions [110]. This phenomenon is known as kinematic interaction [167].

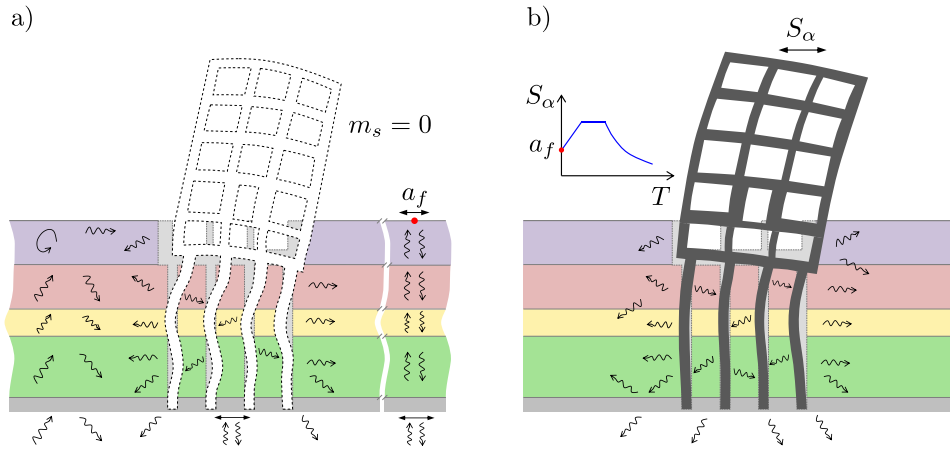


**Figure 2.2:** Illustration of (a) kinematic and (b) inertial interaction phenomena

In addition, the movement induced on the foundation develops oscillations of the superstructure and thus gives rise to inertial forces. These forces are transmitted to the foundation. As a result, the foundation and the surrounding soil will experience additional dynamic forces and displacements (Fig. 2.2-b). This phenomenon is known as inertial interaction [167].

Whenever a foundation element moves against the surrounding soil, stress waves originate at the contact surface and spread outward, carrying away some of the energy transmitted by the foundation into the soil. This results in a dissipation of energy from the system which is known as radiation (or geometric) damping. The magnitude of this damping depends mainly on the frequency of the oscillation, the geometry of the soil-foundation system, the mode of oscillation, and the stress-strain characteristics of the soil [62, 167].

Energy dissipation in the soil is also caused by the plasticity of the soil and possibly discontinuity conditions (uplift and/or sliding) at the foundation-soil interface. This type of damping is known as hysteretic damping and is fairly frequency independent [152].

It should be noted that during an earthquake, kinematic and inertial interactions are superimposed. It is often convenient to study them separately and then superimpose their results. However, this is only valid when nonlinearity is limited and the behavior of the system can be assimilated to an equivalent linear system.

A recurring question is whether soil-structure interaction (SSI) plays a beneficial or detrimental role in the response of a system. The answer depends on the response quantity under examination and on the characteristics of the ground motion and the system itself [216]. Several are the effects of SSI on the response of a system, in a general basis, lengthening of the fundamental response period of the structure-foundation system (in other words, the natural frequency of a soil-structure system is lower than the natural frequency of the structure itself) and an increase of the overall energy dissipation capacity and ductility of the system. The foundation input motion is also modified as

a result of kinematic interaction between the soil and the foundation. Finally, there is usually an increase of the overall displacement of the structure due to rigid body movements (the foundation can translate and rotate) that are superimposed to the deformations of the superstructure. Soil-structure interaction effects are significant for stiff and/or heavy structures supported on relatively soft soils. For soft and/or light structures founded on stiff soils, soil-structure interaction effects are generally small [110].

Soil-structure interaction is usually considered to have favorable effects on the seismic response of a structure. However, as pointed out by several authors (e.g., [152]), period-lengthening for structures with fixed-base periods less than the predominant period of the soil deposit can result in a resonance condition. This is particularly important in the case of soft soil profiles which are usually characterized by long fundamental response periods. The analysis of a real case history conducted by Mylonakis *et al.* [151] is a good example of detrimental influence of SSI in the response of a system.

Regarding the question of piled foundations under earthquake loading, piles are subjected to lateral loading arising from the kinematic and inertial effects imposed by the surrounding soil, as well as the dynamic response of the superstructure which they support. Soil-structure interaction of piled foundations under extreme loading conditions involve many factors, including soil and structural yielding, pile-soil gap formation, cyclic degradation of soil stiffness and strength, and radiation damping. Furthermore, nonlinearity tends to reduce radiation damping and increase material damping in both the soil and the structure [152, 2, 238].

In the following sections several topics regarding deep foundations under seismic loading are addressed. First, several post-earthquake observation cases of deep foundations in soft and stratified soil profiles are studied. Then, a review of experimental studies is done, also focused in single piles and pile groups in soft and stratified soil profiles. Numerical methods available for the study of dynamic soil-structure interaction of structures supported by deep foundations are introduced. This is followed by a review of studies of seismic behavior of deep foundations in the literature that give a complete insight of the phenomena and problems surrounding deep foundations. Finally, the impact of dynamic soil-structure interaction is highlighted using an analytical approach.

## 2.3 Post-earthquake observations of the performances of piled foundations

A significant number of cases of damage to piles and pile-supported structures during earthquakes have been reported in the literature. Due to the buried nature of deep foundations, post-earthquake observations are usually limited to the damage of the supported structures or to observations at the pile head. Most of the reported observations are therefore of qualitative type based on the visual inspection of failed structures and foundations. Few cases of instrumented structures that have undergone earthquake are available, they provide however an excellent insight of the soil-foundation-superstructure response.

In the following section several case studies, of qualitative and quantitative type, are presented. The purpose here is not to provide an exhaustive list of all the post-earthquake observations available in the literature but to review and discuss cases where the post-earthquake observations highlight the importance of Soil Structure Interaction (SSI) on the response of the foundation and the superstructure. For additional post-earthquake case histories, the reader is referred to Meymand [143], for a detailed and extensive review of historical cases of pile foundation damage essentially in Japan and in USA and to Mizuno [145] which reports 28 case histories occurred in Japan from 1923 to 1983. Regarding battered piles, an interesting review is provided by Li [117]. The author presents case studies where the contribution of the battered piles on the structural response is either detrimental or beneficial.

### NHK building, 1964 Niigata earthquake

The 1964 Niigata earthquake ( $M_w = 7.6$ ) caused widespread liquefaction related damage and numerous failures of pile-supported structures. The stratigraphy of Niigata City consists mainly

of loose sands of about 20 m to 30 m thick. The liquefaction of this formation on large thicknesses is at the origin of a significant part of the damage caused by the earthquake on the foundations and the superstructures.

An example of a damaged structure during this earthquake is the NHK 4 floor building supported on reinforced concrete piles of 0.35 m in diameter and about 11 m to 12 m in length [82].

The excavation of the foundation undertaken about 20 years after the earthquake showed damages in the piles at two different locations, close to the top of the pile and near the pile tip, where a high stiffness contrast between the layers of the soil profile was identified (Fig. 2.3). Regarding the damage located in the upper part of the pile, the most probable hypothesis is that it was mainly caused by the inertial forces transmitted to the foundation by the structure combined with the decrease in the soil lateral resistance due to liquefaction, the lateral thrust due to lateral spreading of the foundation soil and probably second-order effects.

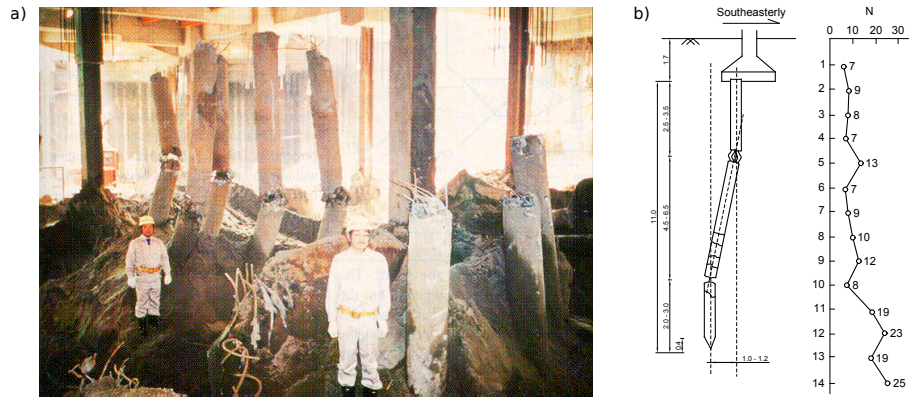


**Figure 2.3:** NHK building, 1964 Niigata earthquake: (a) piles damaged by lateral spreading of the foundation soil and (b) correlation of pile damage and site conditions (after Hamada [82])

## 11-storey apartment building

A well documented case study of SSI investigation is reported by Ohta *et al.* [164] and Gazetas [61]. The study concerns a 11-storey apartment building supported on cast-in-place concrete piles of around 1.4 m in diameter and 25 m in length. The spacing between the piles is about six diameters (8.35 m). The soil profile consists of alternating layers of sand and silt of alluvial origin overlying a dense gravelly-sand and stiff clay substratum located approximately at a depth of 25 m and that is presumed to have a depth of 170 to 200 meters. The shear wave velocity profile was measured from field tests in order to characterize the maximum shear modulus at different depths prior to the earthquake measurements (Fig. 2.4).

The structure and the soil in the proximity of the building was instrumented by means of accelerometers placed along three different vertical axes: on the building axis, on the axis 5 m away from the structure (which is considered as a "nearby-soil" axis) and on an axis 35 m away from the structure (essentially a "free-field" axis). Seven earthquakes were measured from 1975 to 1978, classified into two categories: small-magnitude, near-distant events ( $M \leq 5$  and  $R < 40$  km) and moderate to large-magnitude far-distant events ( $M \geq 5.5$  and  $R > 65$  km).

Several conclusions are drawn by the authors [164, 61]: 1) kinematic interaction filters the high frequency component of the input motion. The high frequency components are thus filtered out by the soil-structure interaction; 2) low frequency components are not affected by the pile or the structure and 3) the components in the frequency range between the fundamental frequency of the soil stratum and the fundamental frequency of the superstructure are substantially amplified due to soil-structure interaction. The foundation input motion is found to be amplified by two times that of the free-field around the characteristic response frequency of the soil profile.

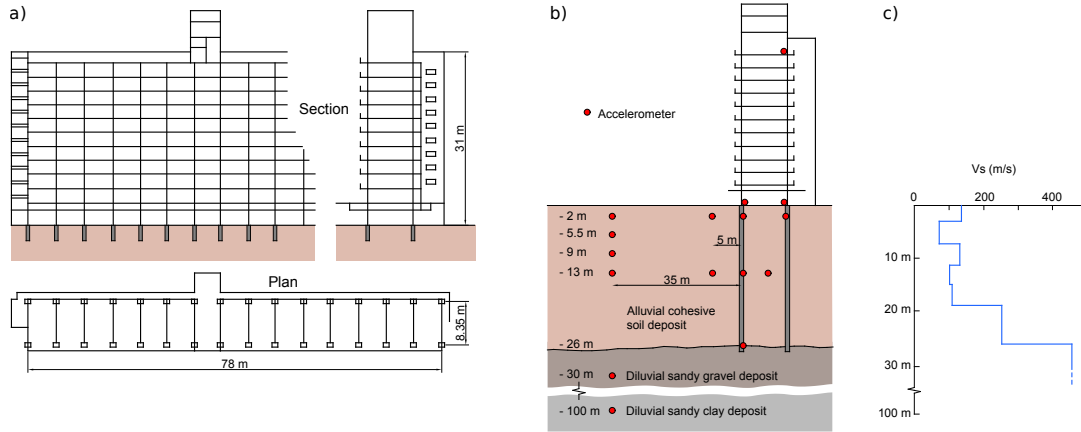


**Figure 2.4:** 11-storey apartment: (a) plan and section of the building, (b) instrumentation plan and (c) shear wave velocity profile (modified after Ohta *et al.* [164])

### Mexico City earthquake, 1985 September

The 1985 Mexico City earthquake ( $M_w = 8$ ) caused serious damage to the Greater Mexico City area and the death of at least 5000 people. The epicenter of the earthquake was located more than 350 km away but a convergence of site response factors caused massive damage on the Lake Zone of Mexico City. High frequencies were filtered out of the signal and the low frequency content was largely amplified by the deep soft clay deposits, especially at a frequency of 0.5 Hz (2 s period). In addition, the duration of ground motion in the Lake Zone was several times larger than the one recorded at the substratum outcrop (e.g., UNAM station) with durations of strong motion up to 5 minutes.

This long period signal came into resonance with many structures of intermediate height (e.g., 10 to 20 storey buildings) resulting in important damages and collapses (Fig. 2.5). The prime cause of failure of pile foundations was the excessive overturning moments and the partial loss of soil-pile adhesion due to cyclic degradation of clay. It was also found that structures supported on end bearing piles performed better than those on floating piles, suffering smaller settlement and tilting [143].

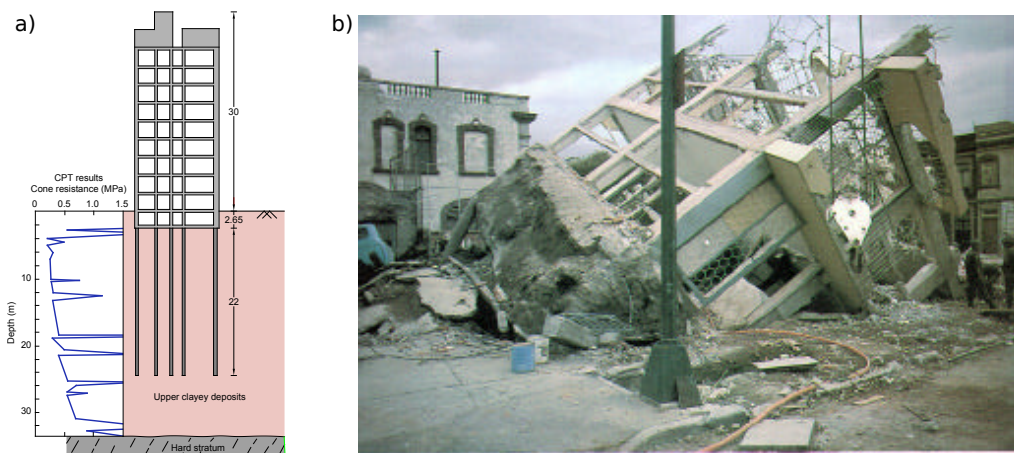


**Figure 2.5:** 10-storey pile supported building founded on soft soils, 1985 Mexico City earthquake: (a) section of the building and soil profile and (b) overturned structure (after Meymand [143], original from Mendoza and Auvinet (1988))

### Highway 1 bridge across the Struve Slough, 1989 Loma Prieta earthquake

The 1989 Loma Prieta earthquake ( $M_w = 6.9$ ) caused the failure or degradation of numerous pile-supported structures founded on soft soils [192]. One well documented example is the pile-supported Highway 1 bridge across the Struve Slough near Watsonville which collapsed and resulted in several piles punched through the roadway platform. A gap between the soil and the pile of about 30 to 45 cm was observed which indicates an inadequate lateral support (Fig. 2.6). The upper part of the soil profile consisted of soft clay and organics, with some alluvial sands present and the piles didn't show signs of settlement. The liquefaction was therefore discarded and it was concluded that the large lateral pile deflections led to flexural/shear failure at the pile head.

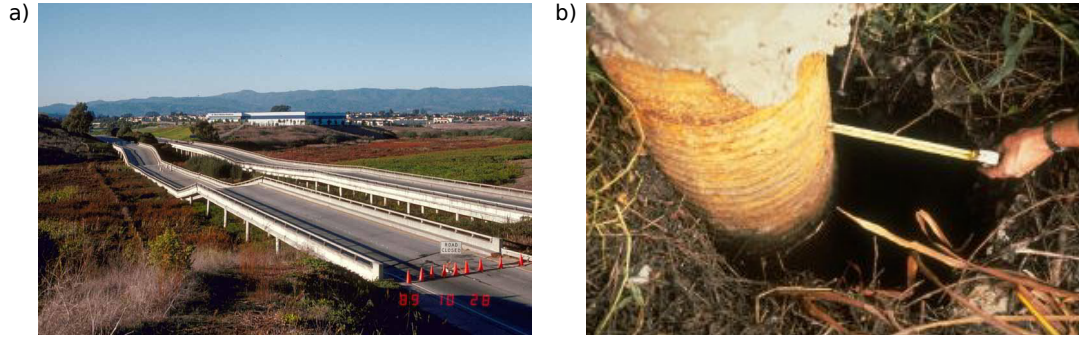


**Figure 2.6:** Collapsed Highway 1 bridge across the Struve Slough, 1989 Loma Prieta earthquake: (a) general view and (b) gap opening around piles (after Seed *et al.* [192])

### Ervc building

Nikolaou *et al.* [156] presented an interesting case study on the seismic response of the instrumented Ervc building located in Yokohama, Japan. The building is a 46.6 m high structure (with twelve floors and one basement) supported by 20 reinforced concrete piles of 35 m long and 1.7 m in diameter. The instrumentation consists of accelerometers on the building and the free-field soil as well as strain gauges on two different piles of the pile group (at the corner and near the center). The soil profile consists of about 39 m of soft saturated high-plasticity silty clay overlying stiff mudstone (Fig. 2.7).

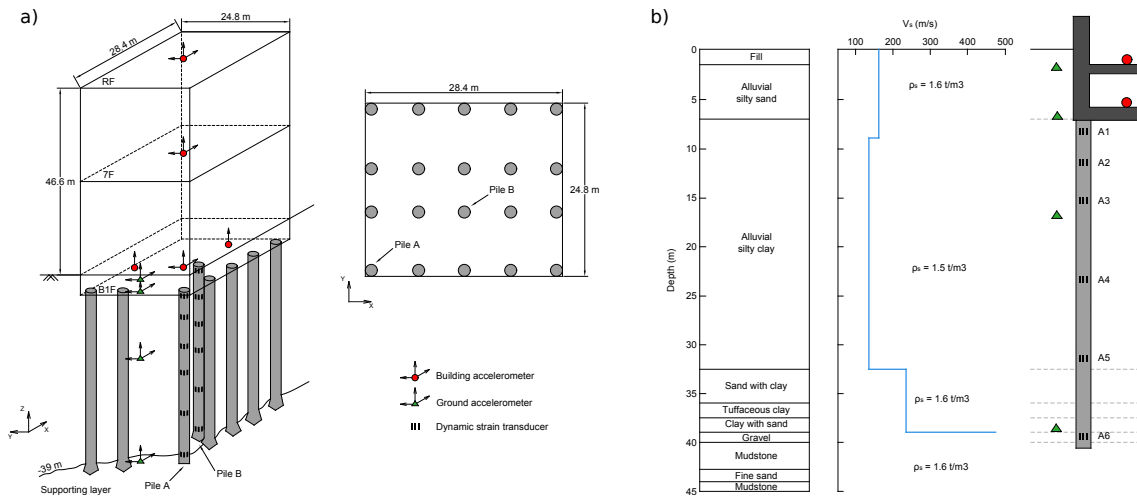


**Figure 2.7:** Ervc building: (a) schematic view of the building and location of measurement devices and (b) soil profile (after Nikolaou *et al.* [156])



The data recorded during a low intensity earthquake that took place in the Tokyo Bay area on 2 February 1992 (magnitude 5.9, focal depth 93 km, epicentral distance from the site 32 km and peak ground acceleration 0.05g) were used in the analysis. Numerical equivalent-linear simulations were also conducted by the authors. Given the low amplitude of the loading, non linear effects were found to be minor (e.g., the soil shear modulus reduction was lower than 10%).

The bending strains in both instrumented piles were found very similar and the prevailing period of the records is very close to 1 s. This highlights the importance of the soil response on the development of kinematic pile bending at depth (the fundamental period of the soil profile was estimated to be about 1 s) as opposed to loading due to structural inertia forces.

The two main conclusions of this case study are: 1) group effects are minor when only kinematic response is considered and 2) the maximum bending moment at the interface between layers with very different stiffnesses occurs at the fundamental natural period of the soil deposit.

## Obha Ohashi bridge pier foundations

Another significant case study is the Ohba-Ohashi road bridge located in Fujisawa City, near Tokyo, Japan. The bridge has a total length of 485 m and is supported by 11 piers. The bridge, the foundations and the soil in the vicinity are fairly well-instrumented with accelerometers and strain gauges.

Several authors focused their studies on the response of pier 6, adjacent to the river. The pier is supported by 64 steel pipe piles of 0.6 m in diameter and length of 22 m. Half of the piles are battered. The ends of the piles are adequately embedded in the bearing substratum. Strain gauges are installed along one vertical and one batter pile. The soil profile at the location of pier 6 consists of a 22 meters thick extremely soft alluvial strata of hummus and silty clay overlying diluvial deposits of stiff clay and sand (Fig. 2.8).

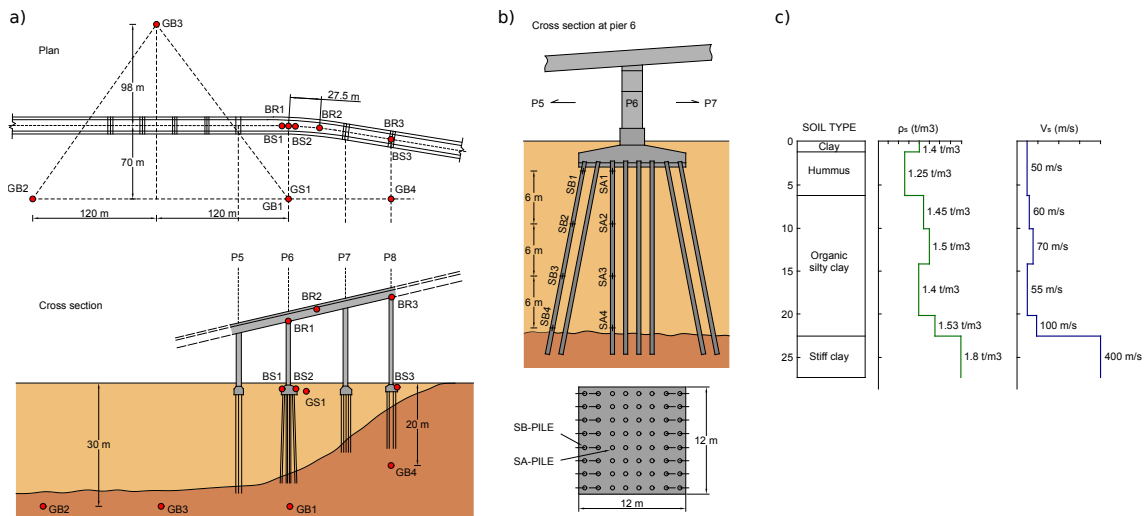


**Figure 2.8:** Obha Ohashi bridge case study: (a) plan and longitudinal section, (b) cross-section of pier 6 and (c) soil profile with shear wave velocity versus depth (after Ohira *et al.* [163] and Gazetas *et al.* [63])

A total of 14 earthquakes were recorded from April 1981 to April 1985 and analyzed by several researchers. According to Ohira *et al.* [163] and Gazetas *et al.* [63], the amplitude of the induced strains was largest at the top and at the bottom of the piles. The comparison of the power spectra of accelerations of the pier to that of the strains at the top of the piles showed a strong correlation indicating that the pile response in the upper part was dominated by inertia forces from the superstructure. Furthermore, the alternate pattern of compressive and tensile stresses at the top of the piles corresponded to the observed rocking motion of the superstructure. The large bending strains recorded near the pile tip were related to the sharp difference of stiffness between

the organic silt layer and the substratum. Such bending deformations were found not affected by the inertial load transmitted from the superstructure onto the head of the piles and were therefore results of the kinematic interaction. Finally, the analysis of the acceleration records at the pier and at the free-field surface highlighted the attenuation of the foundation input motion relative to the free-field up to a period of 1.4s, which corresponds to the fundamental natural period of the soil deposit.

### Hanshin Expressway Route 3 in Kobe, 1995 Kobe Earthquake

The 1995 Kobe earthquake ( $M_w = 6.9$ ) was the most destructive earthquake to strike Japan in over 60 years. Over 6400 people lost their lives and about one-fifth of the buildings in the worst-hit areas were completely destroyed (or rendered uninhabitable). Most of the infrastructures were degraded or severely damaged.

One of the most illustrative images of the earthquake was the collapsed section of the pile-supported Hanshin Expressway (Fig. 2.9). The bridge of about 13 meters in height consisted of 19 single circular columns of 3.1 meters in diameter. The columns were connected monolithically to the deck and founded on groups of 16 reinforced concrete piles. The piles had a length of about 15 m and a diameter of 1 m.

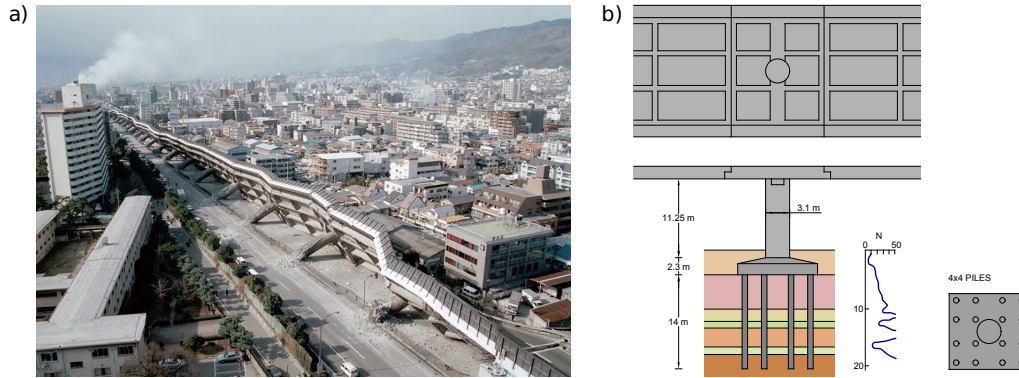


**Figure 2.9:** Hanshin Expressway bridge case history, 1995 Kobe earthquake: (a) overview of the collapsed section and (b) geometric characteristics and piled foundation (after Mylonakis *et al.* [151])

Detailed structural investigations highlighted two main factors contributing to the collapse: 1) poor reinforcement detailing and 2) the use of elastic methods for determining the design shear forces. The problem was that the concepts of ductility and capacity design were not known in the 60's, when the bridge was designed and constructed. Its structural design cannot thus be characterized as "poor" for that time. As suggested by Professor Anastasopoulos, had the transverse reinforcement been adequate, according to current code provisions, the bridge would probably survive. Mylonakis *et al.* [151] presented an analysis suggesting that local soil conditions and dynamic interaction between the foundation and the superstructure further contributed to the collapse. The authors suggested that the soil further amplified the incoming seismic waves and produced variations in the characteristics of the records depending on the differences in the local soil conditions from site to site. Given the particular stratigraphy of Kobe this resulted in significant differences in the intensity and frequency content of the seismic motion depending on the location. They also argued that the period lengthening due to the foundation flexibility probably resulted in increasing the structural forces during the earthquake, thus contributing to its failure. They numerically estimated the increase of the effective period of the bridge at about 30%.

### Kandla Port and Customs tower, 2001 Gujarat earthquake

The 2001 Gujarat earthquake ( $M_w = 7.7$ ), also known as the Bhuj earthquake, was the most damaging earthquake in India in the last 50 years. It was responsible of over 13800 deaths and the

destruction of around 40% of inhabitations.

Dash *et al.* [46] reported the failure of the foundation of the 22 m high Kandla Port and Customs tower, which leaned about 30 cm at the top. The building is supported on a piled-raft foundation with 32 short cast-in-place concrete piles of 18 m length. The soil profile at the location of the building consists of 10 m of clay overlying a 12 m deep sandy soil layer. The vertical profile slopes downwards towards the coast line and the water table is about 1.2-3 m below the ground surface (Fig. 2.10).

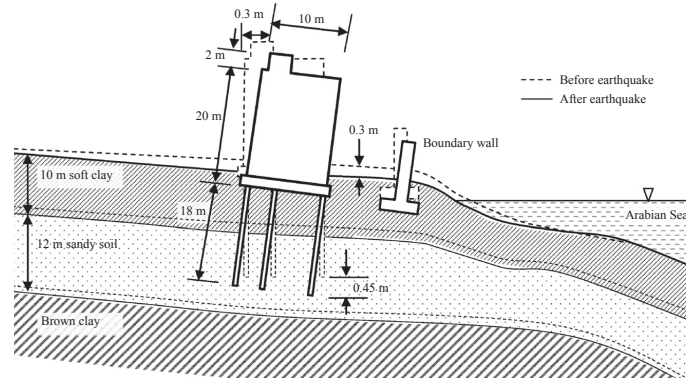


**Figure 2.10:** Kandla Port and Customs office tower case study, 2001 Gujarat earthquake: plausible settlement mechanism of failure, assuming there is no structural failure of piles (after Dash *et al.* [46])

Post-earthquake observations showed evidence of extensive liquefaction of the deep sandy soil strata below the clay layer with the presence of sand boils in the vicinity of the building. The ground around the building settled about 0.3 m. Lateral spreading was also observed, estimated about 80 to 100 cm close to the tower.

This particular case study highlights the possible interactions between lateral spreading and settlement during liquefaction. Piles passing through thick non-liquefied crust and resting on liquefiable soil may suffer excessive settlement and tilting (due to the displacements imposed by the crust on top and inertial loadings from the superstructure) rendering it unusable or expensive to rehabilitate after the earthquake. The use of piles resting on a potentially liquefiable soil layer should be avoided in practice.

### Konan High School, 2003 Tokachi-Oki earthquake

The 2003 Tokachi-Oki earthquake ( $M_w = 8.3$ ) caused extensive damage to superstructures and pile foundations in Hokkaido island (the northernmost main island of Japan). Ground failures including soil liquefaction were also reported.

One example of pile supported building that suffered severe damages is the Konan Junior High School located in Atsuma town, southeast of Sapporo city reported by Koyamada *et al.* [109]. The superstructure of the school building comprises a three-storey reinforced concrete structure. It is supported by pre-stressed high-strength concrete piles with a diameter of 40 cm and a length of 28.8 m. The soil profile consists of about 30 meters of very soft layers of peat, clay and sandy silt overlying a substratum of dense gravel (Fig. 2.11).

Strong motion stations were available in the proximity of the structure and strong motion accelerograms were recorded at the ground surface and at a depth of 153 m. The peak ground accelerations in the EW direction were 0.38 g and 0.054 g, respectively.

Field investigations on the superstructure and pile foundations performed after the earthquake showed compression failures at the pile head. The collapse of the pile foundation induced differential settlement of the superstructure resulting in a large number of shear cracks on the walls. No ground subsidence nor sand boils were observed at the site excluding thus the possibility of liquefaction.

Koyamada *et al.* [109] conducted numerical simulations to study the seismic response of the foundation and the superstructure resulting in several interesting findings: 1) displacements were



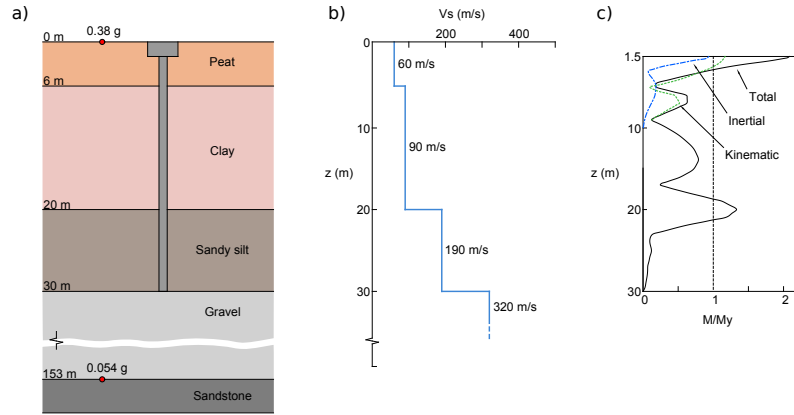


**Figure 2.11:** Konan High School case study, 2003 Tokachi-Oki earthquake: (a) soil profile, (b) shear wave velocity profile and (c) bending moment profile (after Koyamada *et al.* [109])

amplified in the upper clay layer above 20 m in depth; 2) the observed motion at the ground surface had a large component at a period of about 2 s that was mainly amplified by the soil profile above 76 m depth (for comparison, the fundamental period of the building was estimated at 0.35 s); 3) the bending moment at the pile head, which consists of both inertial and kinematic components, exceeded the ultimate bending moment and 4) the bending moment at a depth of 20 m, which consists mainly of kinematic component, also exceeded the ultimate bending moment of the pile section.

The results of this study were confirmed by an extraction survey conducted on the pile foundation. A complete crack, extending throughout the cross-section of the pile, was found at a depth of about 20 m. Furthermore, all the investigated perimeter piles were found damaged by compression failure with flexural cracks at the pile head.

This case study highlights the importance of taking into account both inertial and kinematic interaction effects in the design of piled foundations, especially when a stiffness contrast between layers is present and when the lateral resistance of the shallow soil layers is weak.

### 2.3.1 Summary of post-earthquake observations of pile foundations

The post-earthquake studies help to understand the performance and behavior of pile foundations under seismic loadings. On one hand the instrumented case studies provide information about the response of the soil-pile-superstructure system during the earthquake and more specifically:

- the high frequency content of the foundation input motion is deamplified with respect to free-field motion, especially for frequencies higher than the fundamental response frequency of the soil-pile-superstructure system;
- the components in the frequency range between the fundamental frequency of the soil substratum and the fundamental frequency of the superstructure can be substantially amplified due to SSI;
- resonance phenomena between the soil, the foundation and the superstructure may appear for particular soil conditions (site amplification);
- group effects are minor when the response of the system is mainly controlled by kinematic interaction.

On the other hand, it is observed that the failure of pile foundations is directly related to kinematic and inertial interactions. The importance of both interaction types is variable from case to case; sometimes they take place during the same earthquake causing damage at different places of the pile foundations. The most common causes for seismic damage and failure of pile foundations, as observed in the previous case studies and reported by several authors [145, 207, 143, 156], are:

- large inertial pile-head loads leading to pile structural failure by flexure and/or shear, often combined to the loss of lateral support of the soil due to liquefaction of cohesionless soils, strain softening of cohesive soils near the pile head and gap opening;
- excessive kinematic bending strains at interfaces with high stiffness contrast between soil layers;
- bearing and overturning failure of the soil-pile-structure system;
- liquefaction and lateral spreading of the surrounding soil leading to large imposed differential displacements along the pile length;
- poor design of pile to cap connections with inadequate (or inexistant) reinforcements.

Figure 2.12 summarizes the above-mentioned failure modes.

Finally, it should be noted that structures supported on end-bearing piles have performed better than those on floating piles, presenting a smaller settlement and tilting of the superstructure. Also, most of the observed damages reported in the literature [143] are due to liquefaction triggered effects and lateral spreading.

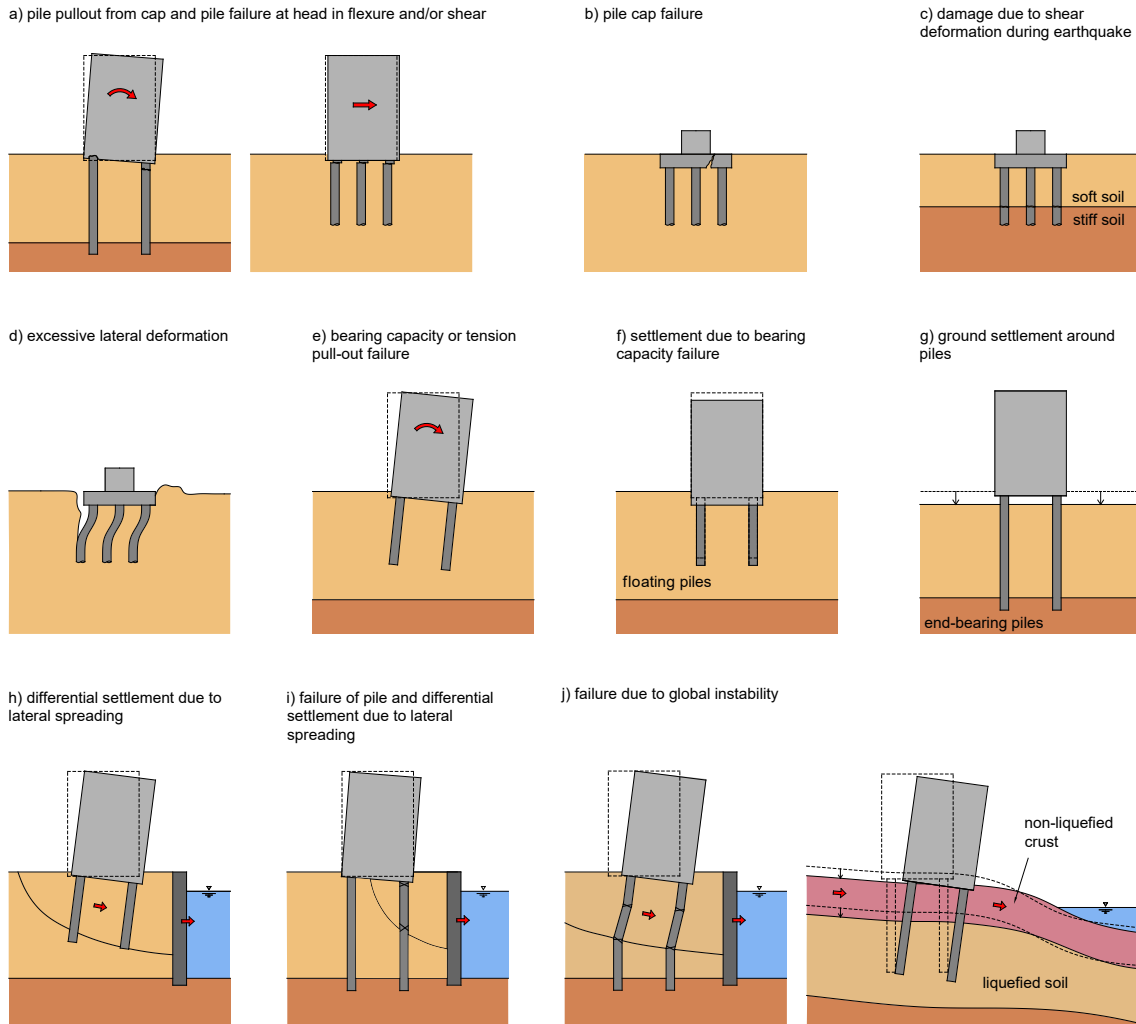


**Figure 2.12:** Potential failure modes of pile group foundations subjected to seismic loading (modified after Meymand [143], Tokimatsu *et al.* [207] and Dash *et al.* [46])

## 2.4 Experimental studies on the behavior of piles in clay and stratified soil profiles under seismic loading

Few experimental studies exist on the behavior of piles in clay and stratified soil profiles under seismic loading. Most of the existing studies deal with the behavior of pile foundations in sand, especially during liquefaction or lateral spreading (e.g., [228, 20, 43, 96, 236, 119, 120]), leaving a gap in the understanding of seismic soil-structure interaction effects of pile foundations in cohesive soils [143, 198]. The limited number of studies with cohesive and stratified soils is explained by the longer time required in the preparation and consolidation of the clay and by the increased complexity of fabrication when several soils are concerned within the same soil profile.

### 2.4.1 Dynamic centrifuge tests

In this section, a literature review is presented on experimental centrifuge studies on the dynamic response of piles in clay and stratified soil profiles. In all these studies a dynamic excitation is applied at the base (instead of loading directly the pile head) accounting thus both for kinematic and inertial effects.

In 1993, Rashidi [179, 5] performed centrifuge tests to investigate the behavior of a two storey structure founded in two 4x5 pile group foundations (Fig. 2.13). Piles were made of aluminum with a diameter and length of 30.5 cm and 9.53 m respectively in prototype scale. A pile spacing of 2.58 diameter between the pile axes was used. The soil profile consisted of a 9.53 m depth layer of Yolo Loam (silty clay) fully saturated with water. The centrifuge models were performed in a rigid rectangular container. As reported by Anandarajah *et al.* [5], the piles were installed by pushing them into the soil profile. No further details are given concerning the installation method although it can be deduced from the test layout given in Figure 2.13 that the tip of the piles was close to the bottom of the container (but not directly in contact as reported by Anandarajah *et al.*) which may have an important impact on the piles axial behavior.

Results showed that with increasing base motion amplitude, the structure residual displacement increased. The authors highlighted however that care should be taken when extending these results to real structures due to the use of a rigid container. Actually, the main hypothesis adopted in this campaign was that the distance between the structure and the rigid walls was sufficiently large to neglect the adverse effects of possible spurious wave reflections.

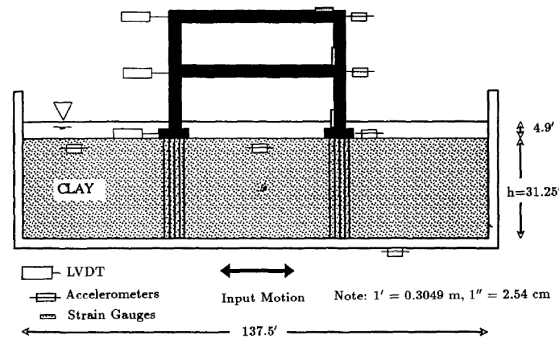


**Figure 2.13:** Dynamic centrifuge tests on a two storey structure founded on two pile group foundations in a silty clay soil profile, Anandarajah *et al.* [5]

Wang *et al.* [223] reported centrifuge seismic tests of a single pile in a normally consolidated San Francisco Bay Mud soil profile. A crust of dense sand was also used in the tests (Fig. 2.14). The clay was consolidated at 50g centrifuge acceleration prior to the application of the seismic events. The pile consisted of an aluminum tube with inner and outer diameters of 4.59 mm and 6.27 mm, respectively (0.3 m and 0.314 m at prototype scale). This corresponds to a flexural rigidity of  $7.226 \times 10^{-6} \text{ MNm}^2$  ( $EI = 45.165 \text{ MNm}^2$  at prototype scale). The pile was inserted through

the clay layer at 1g. From the test layout in Figure 2.14 it can be deduced that the pile tip was in contact with the soil container. As pointed out by the authors, the installation of the model piles at 1g does not accurately reproduce the effects of pile installation on soil behavior. A pile installed at 1g probably acts more like a drilled shaft than a driven prototype pile in terms of the lateral stress state around the pile. The superstructure was represented by a 11.5 g mass (1.44 tons at prototype scale). A hinged plate container was used to provide shear beam like boundary conditions. One interesting finding highlighted by the authors is that the measured excess pore pressures in the soil profile were generally small during the earthquake event.

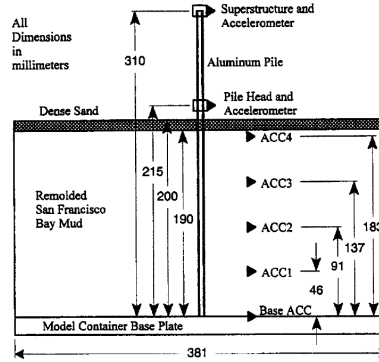


**Figure 2.14:** Dynamic centrifuge tests on a single pile in a normally consolidated San Francisco Bay Mud, Wang *et al.* [223]

Wilson [228], Boulanger *et al.* [20] and Curras *et al.* [43] reported a series of soil-pile-structure interaction tests in liquefying sand and soft clay conducted at UC Davis Centrifuge at the end of the 90s. Two tests involved a thin layer of soft clay (reconstituted Bay Mud,  $LL \approx 90$ ,  $PI \approx 40$ ) overlying a saturated dense layer of Nevada sand ( $D_r = 75 - 80\%$ ) which was air pluviated and vacuum saturated with water (Fig. 2.15). The tests were conducted at a centrifuge acceleration of 30g using a Flexible Shear Beam (FSB) container. Two different single-pile-supported structures and a structure supported by a 3x3 pile group were used. They were driven at 1g by dropping hammers from a constant height. The piles used in the tests had a flexural stiffness  $EI$  of  $417 \text{ MNm}^2$  at prototype scale which is equivalent to a 0.67 m diameter steel pile with a 19 mm wall thickness.

It is to be noted that the same soil container was used in both tests. This means that all the structures were pulled out of the soil profile and re-driven in different locations in the time between the two tests and that all the seismic loadings were applied to the same soil profile. Non-linearities were thus accumulated along the tests. The base shakings consisted of nine different earthquake motions with peak base accelerations ranging from 0.02g to 0.7g.

Residual loads and displacements in the structures after each shaking event were found to be negligible with respect to the transient loads and displacements. The ground motions recorded on the soil surface were strongly affected in both magnitude and frequency content (high frequencies were filtered by the soft clay layer). The authors reported problems with the dynamic pore pressure measurements in clay whom interpretation was complicated by a longer response time and arching effect around the transducer (as previously mentioned by Kutter *et al.* [112])

Banerjee *et al.* [10, 11, 12] performed a series of centrifuge tests to study the dynamic response of a 2x2 pile-raft system in soft kaolin clay (Malaysian kaolin clay of  $PI = 40\%$ ) (Fig. 2.16). Short-duration far-field earthquakes were used as base shakings, scaled to different peak ground accelerations of 0.022g, 0.07g and 0.1g. The tests were performed under a centrifuge acceleration of 50g using a laminar box container. The clay beds were prepared by consolidating clay slurry in the laminar box under 1g preloading following by consolidation at 50g. The soil profile corresponded to a normally consolidated clay.

Six types of model piles (with different flexural rigidities) were used, having two different diameters of 10 mm and 18 mm (0.5 m and 0.9 m at prototype scale). The minimum pile spacings were 10 and 5.1 times the diameter, respectively. The minimum distance between the piles and

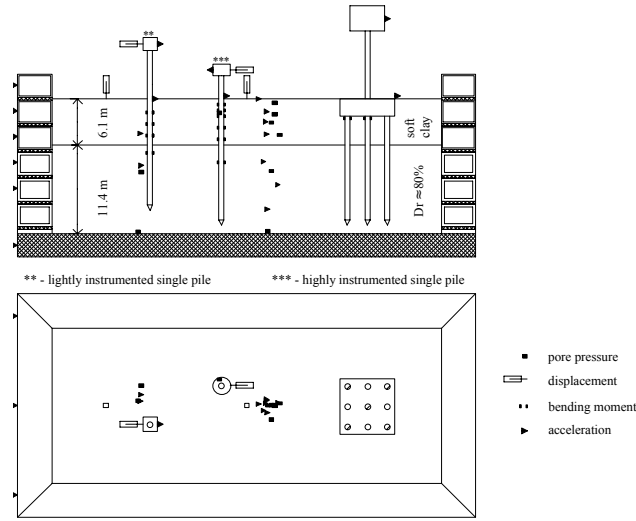


**Figure 2.15:** Dynamic centrifuge tests, soil-pile-structure interaction in dense sand and soft clay (Csp4 container layout), Wilson [228]

the inner wall of the laminar box was about 8.75 and 4.9 times the pile diameter, respectively. The authors claimed that these spacings minimize pile-soil-pile and pile-soil-wall interactions and that the piles behave thus as single piles. No experimental or numerical verifications were however conducted to confirm this hypothesis. The eventual presence of important pile group and boundary effects should be therefore considered when analyzing the results of these tests.

The piles were rigidly connected to the raft using a through-bolt system. The installation of the pile group was done by pushing it at 1g at a low penetration rate of approximately 1 cm/min. It is to be noted that in these tests, the raft was also partially embedded in the ground so that there was a direct contact between raft and soil. This should be also taken into account when analyzing the results and doing comparisons with other results in literature.

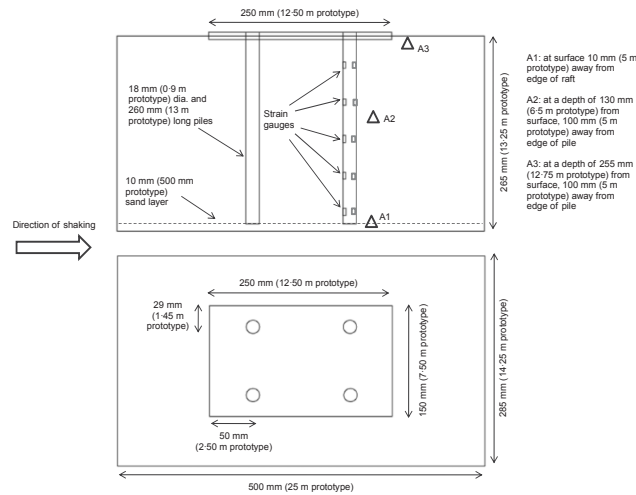


**Figure 2.16:** Dynamic centrifuge tests, centrifuge model and instrumentation layout of a 2x2 pile-raft system in soft clay, Banerjee *et al.* [11]

Results showed that the raft and the near-field ground motions differed from the response obtained in the free field tests. They appeared to be significantly influenced by the dynamic properties of the pile-raft structure as well as the stiffness degradation of the soil around the piles. Furthermore, the amplification of the ground motion increased with increasing PGA and depended

on the predominant frequency of the input motion. The maximum bending moment was recorded at the connection of the piles with the raft. The bending moment was found to increase in an almost linear way with the intensity of applied inputs. Pore pressure measurements were also conducted but resulted in no meaningful readings due to the clay arching effect around the pore pressure transducers and the very short response time, confirming thus the findings of previous studies [112, 228].

In the continuation of previous works at the centrifuge facility of the National University of Singapore, Zhang *et al.* [238] conducted a series of tests on a 4x3 pile-raft system embedded in soft kaolin clay and subjected to short and long-duration ground motions (Fig. 2.17). Each of these motions were scaled to three different peak ground accelerations of 0.01g, 0.06g and 0.13g-0.16g. The soil profile was prepared using Malaysian kaolin clay subjected to two weeks preloading under 1g followed by 20h of in-flight consolidation under 50g. The duration and the PGA of the input signal, the pile type and the raft mass influence on the pile bending moment and raft acceleration response were studied.

It was found that the maximum pile bending moment increased almost linearly with the peak ground acceleration of the base shaking, confirming the trend reported by Banerjee *et al.* [12]. It should be pointed out however that in both studies the tip of the piles rested close to the container base. This may have some influence on the lateral response of the piles close to the pile tip and certainly on the axial behavior of the piles. Numerical simulations were also carried out in order to highlight the presence of boundary effects in the centrifuge model. An increase of the raft accelerations and pile bending moments about 5-10% have been estimated.

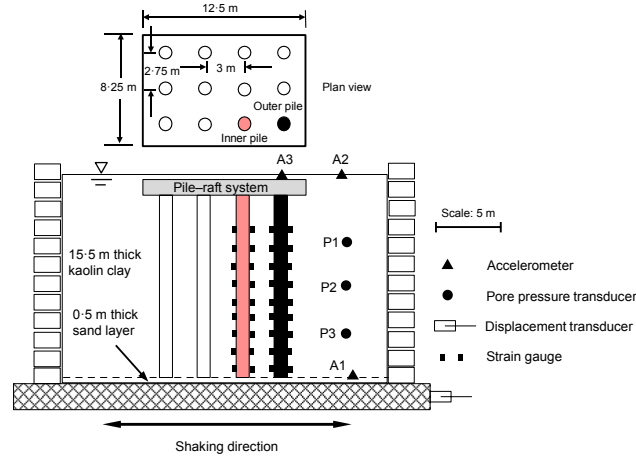


**Figure 2.17:** Dynamic centrifuge tests, schematic layout of the centrifuge test model containing a 4x3 pile-raft system embedded in soft clay, Zhang *et al.* [238]

Taghavi *et al.* [197, 198] performed a series of static and seismic centrifuge tests to investigate the effects of ground improvements on the behavior of pile groups in soft clay. The soil profile consisted of four lightly overconsolidated clay layers (mix of kaolin clay and fine sand) overlying a dense layer ( $D_r = 84\%$ ) of Nevada sand (Figure 2.18). The clay layers were lightly overconsolidated with an OCR between 1.1 and 2, except for the top layer, near the ground surface where the overconsolidation ratio reaches a value of 10. Three different configurations were tested with a 2x2 pile group and a single pile for each one of them. All piles were fabricated from hollow steel tubes, equivalent to a hollow tube of 0.29 m diameter and 0.021 m wall thickness in prototype scale. The piles were driven into the soil profile at 1g. The pile groups had a symmetrical layout with a pile spacing equal to three diameters. One of the configurations corresponded to unimproved soil and the two others to improved soil with different improvement dimensions. Tests were carried out in a Flexible Shear Beam (FSB) container under a centrifuge acceleration of 30g. Seven different earthquake events were applied with peak accelerations ranging from 0.03g to 0.66g.

Regarding acceleration responses at the ground surface, an amplification of the response in

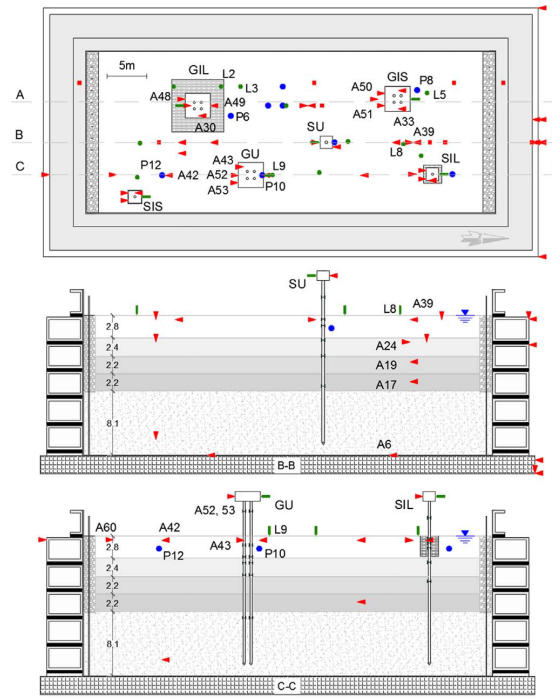


**Figure 2.18:** Dynamic centrifuge tests, cross sections and plan view of pile groups in soft clay to investigate the effects of ground improvements, Taghavi *et al.* [198]

terms of the PGA was observed during low-amplitude base shakings. In the case of high amplitude base shakings an attenuation of the response is found, indicating nonlinear behavior of the soil profile. Furthermore it was found that increasing the PGA of the base shakings increased the fundamental period of the site. Concerning the response of pile caps, it has been observed that their response was strongly affected by the frequency content of base motion and the level of shaking. One interesting observation is that the foundation level motion of the unimproved pile group was found identical to the surface free-field motion. Therefore, the kinematic and inertial interaction effects present in this particular case seem to be negligible.

Several observations can be done from the above mentioned dynamic centrifuge studies. All of them, with the exception of Rashidi's, have been conducted using flexible containers (hinged plate container [223], ESB [228, 20, 43, 197, 198] and laminar box [10, 11, 12, 238]). The installation of piles and pile groups was done at 1g for all the tests, either driving them with a hydraulic actuator at a certain driving speed or dropping hammers from a constant height. As it has been highlighted, most of the available experiments considered piles whom tip is touching or very close to the bottom of the container. Therefore, the axial behavior of the piles may not be representative of that of a real case. A complementary observation is that due to the installation of piles at 1g prior to spin-up in centrifuge, the development of a negative friction due to the relative settlement of the soil with respect to the piles may be present. This question has not been addressed in any of the aforementioned studies and may play an important role in the behavior of pile groups, specially when slender structures are studied.

Previous tests reveal the problem of pore pressure measurement in clay due to arching effect and the very short response times. Thereby small values of pore pressure build-up recorded in some tests seems questionable. Centrifuge tests highlight the effect of both magnitude and frequency of the base shaking on the soil surface acceleration and more specifically filtering of the high frequency. In addition for high amplitude of base shaking there is a deamplification phenomena and increase of the fundamental period of the site indicating nonlinear effects. Concerning the SSI it is affected by the amplitude and frequency at the base shaking and the pile group/soil configuration.



### 2.4.2 Shaking table tests

In 1998, Meymand [143, 142] conducted a series of large-scale 1g shaking table tests to study the seismic interaction of soft clay-pile-superstructure (Fig. 2.19). Single piles and piles groups were tested. The soil profile corresponded to a lightly overconsolidated soft to medium stiff clay (the soil was a mix of kaolinite, bentonite and type C fly ash) overlying a hard clay bearing layer. Sine sweeps and earthquake time histories were scaled to peak horizontal accelerations of 0.05g to 1g and applied to the model in 1D and 2D directions. The study focused on the relevance of conventional static and cyclic pile head loading tests to reproduce the seismic response, comparisons of the behavior of single piles with pile groups of various sizes, the effects of pile cap embedment and initial investigations on 2D shaking loading effects.

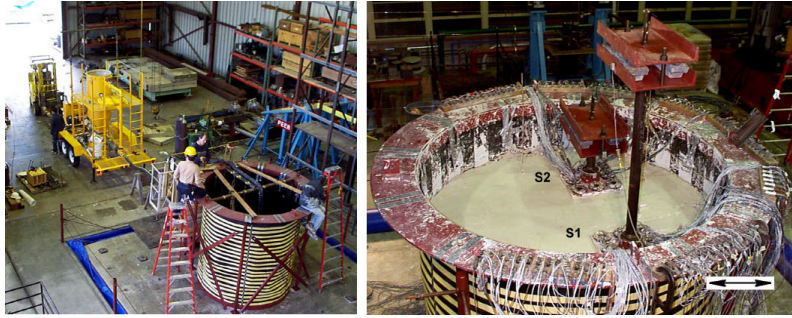


**Figure 2.19:** Shaking table tests, full scale container mounted on the shaking table to study the seismic interaction of soft clay-pile-superstructure, Meymand [143]

Inertial and kinematic interaction effects were detected in the single pile tests. The pile groups response was found to be highly frequency dependent. Wave scattering effects were observed comparing the pile cap and the free field motion illustrating the importance of considering the modified foundation input motion in a substructuring analysis. In terms of bending moment and pile displacements, a degrading behavior was observed at the near-surface pile responses, due to hysteresis and gapping. One interesting result was that a group of piles initially subjected to large deformation static lateral loadings had a lesser dynamic response than an identical group that had not been pre-loaded. This suggests that the degradation of the near-field soils accumulated in the previous loadings (i.e., static loadings but also previous dynamic events) may act like a base-isolation mechanism at the level of the foundation soil. Finally, the effect of 2D shaking were found minimal, validating for these specific cases the use of 1D shaking in the SSI analysis of simple and regular structures.

### 2.4.3 Full scale in-situ tests

Due to the high cost, very few full-scale in-situ tests have been conducted so far on piles and pile groups [117]. Except some rare cases, dynamic pile tests in the field can be classified into three categories depending on the loading type:

- vertical or lateral cyclic vibration loading at the pile head or the pile cap;
- initial lateral displacement at the pile head and resulting free vibrations;
- impact loadings.

The most important drawback of full scale in-situ tests is that in general, the loading type is not representative of those arising from seismic soil-pile interaction. Only the inertial interaction effects due to the inertial forces developed in the superstructure are thus taken into account.

A complete review on full scale in-situ tests up to 1998 was done by Meymand [143]. Several observations were found common to the different studies analyzed:

- the soil-pile dynamic response is frequency and load intensity dependent;



- the soil-pile nonlinear response induces a decrease in stiffness;
- the pile group effects depend on the loading frequency, the pile spacing and the construction site. They usually have more impact in stiffness than in damping.

Recent full scale in-situ tests conducted on single piles and pile groups in clay and multilayered soil profiles have also been reported in [183, 93, 131, 184].

## 2.5 Numerical methods for dynamic soil-structure interaction analysis of piled foundations

The dynamic response of a structure supported by deep foundations is a complex Soil-Structure Interaction (SSI) problem that requires the use of adapted computational methods. Traditionally, the design of deep foundations under seismic loading has been carried out by means of conservative methods aiming to assure zero damage of the foundation. Most of these methods consider the behavior of the foundation as linear elastic [125, 95, 161]. As a result, the capability of the foundation to dissipate energy during seismic loading due to non-linear mechanisms is neglected. This approach was justified in the past due to the lack of information about the non-linear behavior of foundations and the absence of adapted numerical tools. Such limitations are becoming more and more obsolete, as a significant number of experimental and numerical results are now available as well as new design methods [169]. Although the use of full nonlinear approaches for engineering design purposes is still exceptional, with the emergency of new design codes such as Eurocode 8 [1] which recognize the effect of SSI and of nonlinear energy dissipation (important in the case of strong earthquakes), there is a growing interest in developing new approaches to take these phenomena into account.

### 2.5.1 Direct method

In the direct method, the entire soil-foundation-structure system (Fig. 2.20-a) is modeled and analyzed in one single step [110], in the time or frequency domain. The finite element method is the most used resolution technique. When the problem is solved in the time domain it is possible to take into account nonlinear phenomena (e.g., inelastic behavior of the materials, uplift and sliding of the foundation). In the case of deep foundations, this approach allows taking into account the effect of pile-soil-pile interaction, the influence of the frequency and the intensity of the loading on the system response.

The direct method has however some disadvantages and limitations. The maximum size of the mesh elements depends on the maximum frequency of interest and the characteristics of the soil to be modeled. The use of a coarse mesh doesn't allow the correct transmission of high frequency waves. It is therefore customary to impose a mesh size not exceeding  $1/5$  to  $1/8$  of the wavelength [166]. Boundary conditions are artificially introduced via boundary elements that provide an exact solution to the problem of infinite wave propagation only in the frequency domain. In the time domain, these boundary elements represent only an approximate solution [167]. In addition, it is necessary to move the boundaries away from the model in order to attenuate the reflected waves before they impact the structure.

The complexity of the models and of the analysis of the results increases very rapidly when nonlinearities are taken into account in the structure, in the soil and in the interface between the two. Additional information is needed to calibrate the parameters of the adopted nonlinear constitutive laws. In most cases, calibration procedures are highly sensitive to input data and available information needs to be of good quality to ensure confidence in the numerical results. The resolution of nonlinear problems is undertaken using step by step iterative resolution procedures (e.g., Newton-Raphson scheme) that increase the computational cost and the necessary computational time. As a result, this type of analysis is usually reserved for specific verifications and vulnerability studies instead of current seismic design of structures.

### 2.5.2 Substructuring (superposition theorem)

For reduced levels of seismic loading, the behavior of the system can be reproduced by means of an equivalent elastic calculation. Under the linearity hypothesis, the superposition theorem is adopted to solve the interaction problem in several successive steps, each of them being simpler to solve than the global problem.

Several substructuring methods are available in the literature differing in the way the global problem is decomposed into submodels. There is a distinction between the so-called boundary methods, where the interaction between the soil and the structure is taken into account at the soil-structure interface [81, 99] and volume methods where the interaction is also considered at all nodes of the structure below the surface of the soil [126].

The Kausel superposition theorem is illustrated in Figure 2.20. This approach proposes a resolution of the SSI problem in three steps: (b1) kinematic interaction, (b2) calculation of the dynamic impedances and (b3) dynamic response of the structure taken into account SSI.

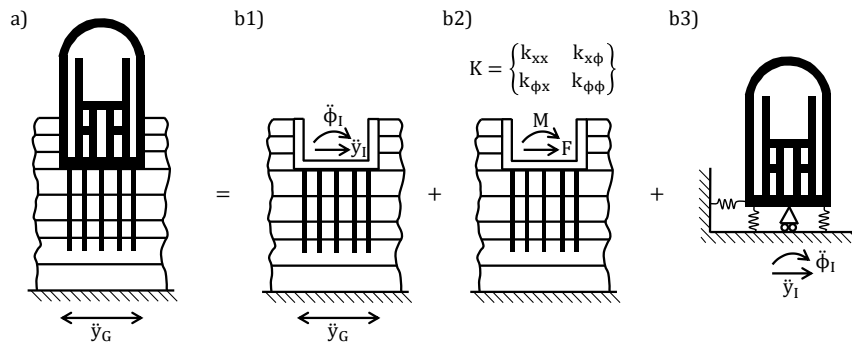


**Figure 2.20:** Kausel superposition theorem for a SSI problem of a structure supported by deep foundations. The global SSI problem (a) is decomposed in three steps: (b1) kinematic interaction, (b2) dynamic impedances and (b3) dynamic response of structure taken into account SSI (modified from Kausel *et al.* [99])

The first two steps (b1) and (b2) are usually carried out in the frequency domain. The results are used later in the dynamic resolution of the structure (b3), which is usually done in the time domain. Adding the dynamic impedances in the structure resolution model requires a transition from the frequency domain to the time domain, often carried out by means of an iterative procedure aiming to calibrate a set of constant springs and viscous dashpots at the base of the structure. Sometimes simple rheological models (also known as lumped parameter models) are adopted, consisting of constant springs, dashpots and masses. Once calibrated they are able to reproduce the frequency-dependent response of the system (see for example the monkey tail model [235]).

Substructuring becomes very interesting when it is possible to solve analytically some of the steps. In the case of deep foundations for example, several expressions of the impedance functions at the pile head exist in the literature for simple configurations [68]. Regarding kinematic interaction effects, a calculation is generally necessary (Fig. 2.20-b1). Existing parametric studies concern simple configurations (single piles, groups of simple piles, homogeneous soil profiles, etc.) and their conclusions should be used with caution [61, 59].

Substructuring presents a number of disadvantages. As in the case of direct methods, the problems related to the dependence of the mesh element size with respect to the frequencies of interest and the treatment of the boundary conditions of the model are present. In general, the nonlinear behavior of the soil is approximated using equivalent linear viscoelastic constitutive laws whose characteristics are obtained iteratively in order to be compatible with the mean strain level in the soil due to the applied loading. To this end, shear modulus and damping degradation functions that vary with the shear strain level ( $G/G_{max}(\gamma)$  and  $\beta(\gamma)$  respectively) are often used. Nevertheless, the equivalent linear methods are applicable only in the small deformation range, with shear strain values between  $10^{-6}$  and  $10^{-4}$ . Finally, one of the main limitations of this method is the impossibility to obtain irreversible displacements. For significant levels of seismic

loading the use of a nonlinear approach is mandatory (see Section 2.5.1).

### 2.5.3 Winkler-type models

Several publications discussed piled modeling using Winkler-type approaches. In what follows are presented the general aspects common to these models as well as their strengths and their disadvantages. Detailed classifications of the available methods are given in the literature [161, 31, 38].

In the Winkler-type approaches the soil-pile system is discretized in horizontal layers containing a pile segment as well as an infinite homogeneous soil layer. The response of each layer is assumed independent of the adjacent layers (Fig. 2.21-a). The existing methods vary in their complexity but all share these basic assumptions.

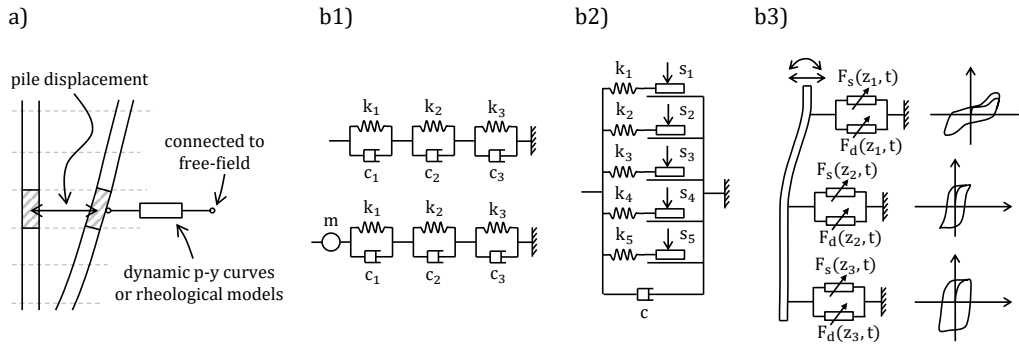


**Figure 2.21:** Winkler-type models: (a) concept, (b1) rheological models for the axial response (top) and lateral (down) of a unit segment of a single pile (Nogami and Konagai [158, 159]), (b2) rheological model with Coulomb friction elements (Matlock *et al.* [136]) and (b3) phenomenological model (Gerolymos and Gazetas [71, 70])

There are essentially two families of methods: one based on dynamic p-y curve formulations (e.g., [98]) and one that proposes the use of discrete rheological elements to represent the behavior of the soil in the near field. For low levels of loading, Nogami and Konagai [158, 159] proposed the rheological models presented in Figure 2.21-b1. For strong loadings, the behavior of the pile is controlled by the non-linear response of the surrounding soil and the associated phenomena at the soil-pile interface: gapping, sliding and friction. To circumvent this problem, several authors have incorporated in their models nonlinear springs and dampers, contact elements, Coulomb-type friction elements, etc. (Fig. 2.21-b2) or phenomenological models that are able to directly reproduce the soil-pile interaction at the interface level (Fig. 2.21-b3).

The main advantage of the Winkler-type approaches lies in their continuity with the models usually adopted for static analysis. Moreover, they are often formulated in the time domain which facilitates their use in a transient structural analysis. As the soil behavior is condensed at the interface nodes between the foundation and the soil, the numerical cost is reduced.

One drawback of the Winkler-type approach when dealing with deep foundations is that the group effect (pile-soil-pile interaction) is generally not taken into account. In addition, the interaction between the layers is neglected as well as the couplings between the different directions. Most of the models address only the problem of a single pile subjected to a dynamic loading (either applied at the pile head or as a prescribed displacement at the free-field). When the group effect is included, it is usually accounted for in a simplified form using dynamic interaction factors [101, 67].

Models of this type are very versatile but are also limited by the difficulty of linking the characteristics of discrete elements to the usual soil parameters in geotechnics. Given the large amount of available methods and assumptions at the basis of some of them (sometimes very simplifying), their use requires special care.

### 2.5.4 Macroelement model

In the macroelement approach the global behavior of the foundation and of the soil volume interacting with it is concentrated into a discrete element with nonlinear behavior that is placed at the base of the superstructure (Fig. 2.22). It has a nonlinear constitutive law, described in terms of generalized forces and displacements, establishing at the macroscopic scale the dynamic couplings (linear and nonlinear) in several directions between the superstructure, the ground and the foundation.

In the present work the macroelement definition corresponds to those models which make it possible to reproduce at the macroscopic scale the behavior of the whole soil and foundation system. Several authors in the literature have also called macroelement models discrete formulations allowing to model the behavior at the interface between several parts of the foundation and of the soil, for example the soil-pile interface (e.g., [214, 215]). Although these models could be understood as another type of macroelement (they treat their respective phenomenon on a macro scale), they do not constitute a SSI macroelement per se and can be considered as a kind of advanced Winkler-type approach (see Section 2.5.3).

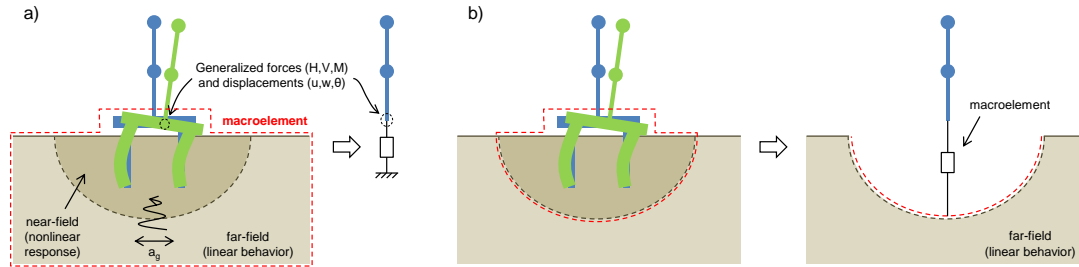


**Figure 2.22:** Macroelement concept for deep foundations (2D): (a) near field and far field are integrated in the formulation of the macroelement, and (b) only the near field is managed by the macroelement

The developments of this heuristic tool originally concerned shallow foundations (e.g., [160, 42, 27, 28, 78, 76, 187, 3]). The extension of the concept to the case of deep foundations is recent and is limited, for the moment, to the case of a single pile or a group of two piles in a simple soil profile.

Correia [38] developed a macroelement for a single vertical pile in a cohesive soil subjected to a lateral seismic loading. This model is based on a nonlinear elastic constitutive model, representing the elastic behavior with small deformations (via elastic linear impedances proposed by Gazetas [68] and adopted in EC8 [1]) with soil-pile separation (Fig. 2.23-a), coupled with a bounding surface plasticity model. The failure mechanism and the associated failure surface of the plastic model are obtained with a kinematic approach. The formulation of the loading surface in terms of plasticity makes possible to develop irreversible displacements before reaching the failure surface. Indeed, the plastic module depends at all times on the relative distance between the state of loading and the failure surface (Fig. 2.23-b).

The radiation damping is not intrinsically taken into account in this formulation but it is however possible to add viscous dampers at the head of the pile like in a conventional substructure approach (Fig. 2.23-c). Finally, the influence of the vertical load in the response is also not considered in this model.

A new macroelement for a single vertical or batter (inclined) pile foundation in sand submitted to monotonic and cyclic loading has been recently proposed by Li [117] and Li *et al.* [122, 123]. The macroelement is based on a hypoplastic constitutive law and is inspired on the macroelement proposed by Salciarini and Tamagnini [187] for shallow foundations. The response at low displacement levels or upon load reversal is controlled by the elastic stiffness calculated at the pile head. The failure surface is defined using a dimensionless formulation taking as input parameters the bearing capacity of the single pile for an horizontal loading, moment and vertical loading (Fig. 2.24). Radiation damping is not explicitly taken into account.

This model does not directly take into account the group effect and its dependence on frequency.

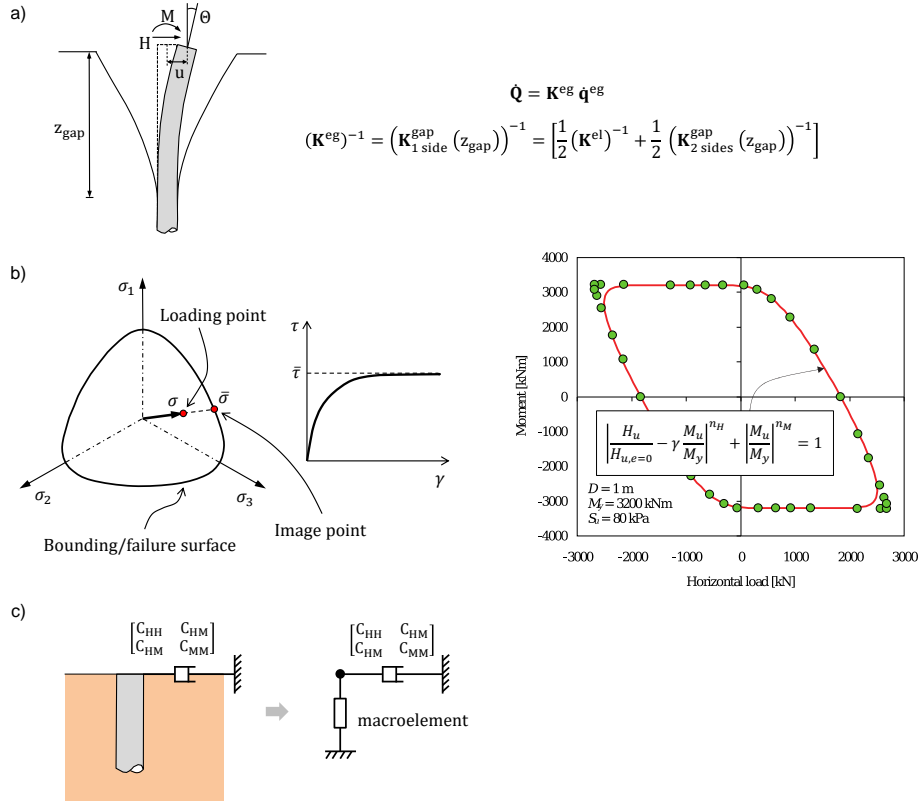


**Figure 2.23:** The single vertical pile macroelement proposed by Correia [38]: (a) nonlinear elastic model to take into account soil-pile separation, (b) boundary surface plastic model, (c) radiation damping

However the author proposes to study the case of a group of two piles by means of a constant group factor that modifies the loading and the failure surfaces. Pérez-Herreros *et al.* [176] found that for the particular case studied by Li, the group effects are found to be independent of frequency. The proposed constant factor may be understood for this particular case as a sort of static group factor. This is not the case for larger pile groups for which group effects are found to be strongly frequency dependent, even with a small number of piles [101].

Gerolymos and co-workers [69, 73] presented a macroelement to model the response of single piles and pile-groups under lateral loading. Formulated within the framework of classical elastoplasticity, this model combines a hardening rule for loading-unloading-reloading of the Bouc-Wen type coupled with an associative plastic flow rule. The calibration of the model parameters is achieved in this case through direct comparisons with 3D finite element analyses.

The macroelements for deep foundations developed to date have several limitations that do not allow to reproduce (at least in a direct way) the response of a pile group under seismic loading. Since these formulations deal with the problem of a single pile, the group effect is not taken into account rigorously. For this method to be able to make a significant contribution compared to the usual approaches it is necessary that the future developments integrate, in addition to the effects of nonlinearity and radiation, those related to the pile-soil-pile interaction and the frequency of the loading.

Lesgidis *et al.* [116] have recently developed a frequency-dependent macroelement method that is able to reproduce the dynamic properties of the system across various levels of increasing seismic intensity. The proposed macroelement can be divided in two elementary components: a frequency-independent macroelement (i.e., a standard elastoplastic or hypoplastic macroelement can be used according to the literature and depending on the problem to be solved) that manages the nonlinear pseudo-static response of the system and a frequency and intensity-dependent lumped

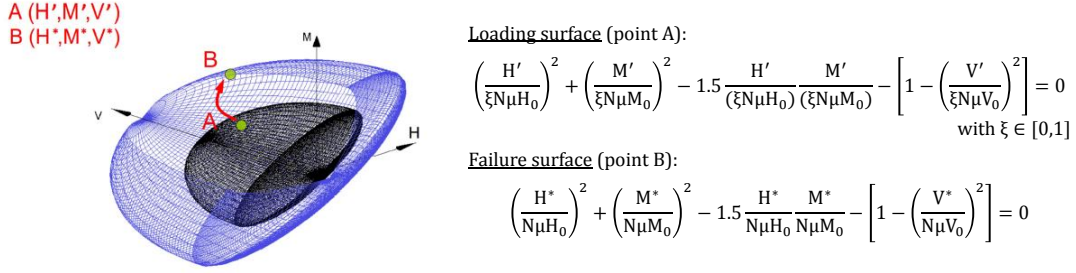


**Figure 2.24:** Loading and failure surfaces of the hypoplastic macroelement model for a single pile proposed by Li [117] and Li *et al.* [122, 123]

parameter model that is intended to capture the dynamic response of the system. The intensity-dependent lumped parameter model is equipped with nonlinear springs whose stiffness is governed by the displacement and the internal plastic variables of the macroelement base component. Both components are coupled in series (Fig. 2.25).

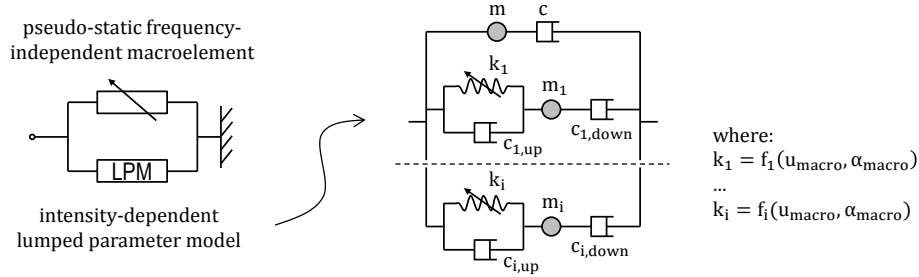


**Figure 2.25:** Frequency-dependent and intensity-dependent macroelement approach proposed by Lesgidis *et al.* [116]

The main drawback of this model is that the calibration procedure still continues to be based on a series of computationally expensive and time consuming numerical simulations (FE simulations). This may represent an important drawback in the generalization of this approach and its application in engineering practice, where equivalent linear procedures and the substructure approach with the use of dynamic impedances are often preferred.

As compared to macroscopic approaches based on continuum mechanics, the advantages of the macroelement approach lies in its remarkable computational efficiency, in the relatively simple formulation of the constitutive equations, and in the ease of numerical implementation into general purpose FE codes. One of the inherent particularities of a macroelement is that it must be constructed and calibrated for a specific foundation case study. This is one of its main limitations. However, once calibrated and the limits of the field of application well defined, it can be used intensively with a reduced computational cost as shown in Correia *et al.* [39]. Therefore, it can be concluded that this type of approach represents a suitable tool for seismic performance-based design methods.

## 2.6 Seismic behavior of deep foundations

A large number of publications have dealt with the question of the dynamic response of a single pile and a group of piles. To give a detailed account of all the existing references would be an enormous task and therefore, the objective of this chapter is limited to highlight in a brief, yet a broad way, all the salient features controlling the dynamic response of a pile and/or a group of piles under seismic loading.

The main aspects to be considered when analyzing the seismic behavior of piles are kinematic

interaction between pile and soil, inertial forces transmitted to the foundation by the superstructure and nonlinear soil behavior as a result of strong ground motions. When dealing with pile groups pile-soil-pile interaction (or group effects) is another aspect that needs to be taken into account [198].

In the following, first the response of single piles under kinematic and inertial loading is studied. Then, the case of pile groups is treated, with special attention to group effects and how they affect the response of the system. Finally, the question of non-linearity and how it modifies the response of single piles and pile groups is also regarded.

### 2.6.1 Dynamic response of a single pile

Pile response during earthquakes occurs over a broad range of frequencies with peak responses corresponding to the natural frequencies of the soil-pile-superstructure system and of the free field [53]. Several are the factors that control the overall response of the pile, specially the relative soil-pile stiffness, the boundary conditions at the pile head (fixed vs free-head piles) and at the pile tip (floating vs end-bearing piles) and the length of the pile (short vs long piles). Distinction is commonly made between "rigid" and "flexible" pile behavior [143], as illustrated in Fig. 2.26. The distinction between rigid and flexible piles is commonly made by means of the so-called parameter "active length" that is introduced hereafter. An important parameter for the dynamic response of a pile is the natural frequency of the soil profile in which the pile is embedded (i.e., natural frequency corresponding to the vertical propagation of shear waves), the characteristics of the soil profile and the frequency content of the seismic loading [59, 170, 31].

The inclination of piles plays also an important role in their response, with vertical piles performing generally better than battered ones. Although battered piles are out of the scope of the present work (and are not treated herein), it should be noted that they are often used to increase the horizontal stiffness of the group. However, the use of battered piles may not always be beneficial because the inclination of the piles restricts the pile's ability to sway and yield, resulting in greater seismic forces and possible damage to the piles and the cap. Residual bending moments due to soil settling are also an important issue that needs to be accounted for when designing battered piles.

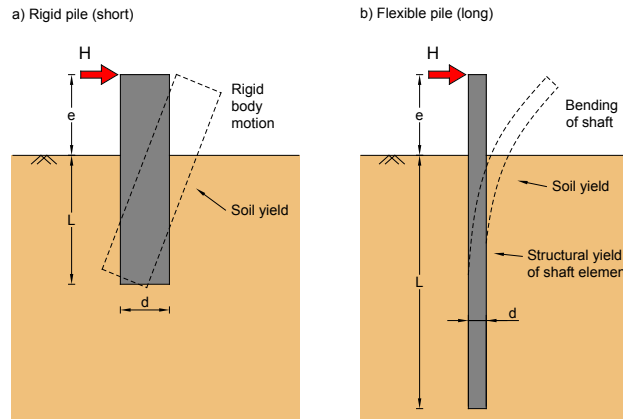


**Figure 2.26:** Behavior of rigid and flexible piles under pile-head horizontal loading (after Meymand [143], original from Kulhaw and Chen (1995))

Pile loading can result from inertial loads applied by the superstructure in the form of forces and/or moments at the pile head (inertial interaction) or as an imposed pile deflection due to ground motion (kinematic interaction) [38]. In general, the inertial forces from the superstructure dominate over kinematic interaction effects in stiff and/or non-liquefied soils. In the case of soft and/or liquefied soils as well as in laterally spreading soil, kinematic induced forces become important and play also an important role in the response of the system [208].

In addition, the deformation of a pile subjected to a lateral load at its head decreases rapidly



with depth. The deformations due to inertial effects are therefore significant only near the surface. Kinematic interactions however occur generally at greater depths, at the interface between different layers. Thus, the superposition of both phenomena can be a reasonable approximation even in the presence of nonlinear behavior [61].

### 2.6.1.1 Kinematic interaction

Pile-soil kinematic interaction has been the subject of systematic research. Even in the absence of a superstructure, piles are forced to deform along its whole length to accommodate the deformation that experiences the embedding soil under seismic loading.

Let's consider a vertical pile subjected to upward propagating seismic waves. An extremely flexible pile might simply follow the seismic motion of the ground. However, real piles are generally much more rigid than the foundation soil and thus they resist to the imposed movement, modifying nearby soil deformations (Fig. 2.27). As a result, the incident seismic waves are scattered and the seismic excitation to which the structure base is effectively subjected (pile head motion) differs from the free-field motion and may generally include rotational (in addition to translational) components. In turn, the pile experiences bending, shearing and axial stresses, which depend on its overall rigidity relative to the soil. The kinematic constraints imposed at the pile-head from the cap and the superstructure also affect the response of the system [59]. Kinematic interaction is more significant for fixed head than free-head piles [170].

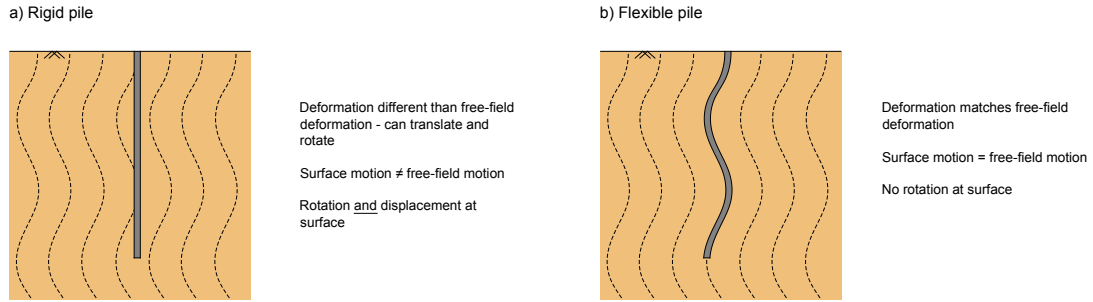


**Figure 2.27:** Behavior of rigid and flexible piles under kinematic loading (modified from Correia [38], original from Kramer (2007))

Generally it is assumed that the foundation input motion in an inertial interaction analysis is the same as the free-field one and that is not affected by the presence of the piles. This assumption is based on the idea that the dominant seismic wavelengths are much larger than the pile diameter and, given the bending flexibility of slender piles, the piles follow the horizontal motion of the ground. This simplification is acceptable for motions characterized by a predominant low frequency content, for which the scattered field is weak. However, if the motion is rich in high frequencies, the pile acts as a filter modifying the frequency content of the free-field motion as would be shown herein [146, 38, 48, 26].

To better understand the effects of kinematic soil-pile interaction on foundation input motion, kinematic interaction factors are introduced, for pile-head displacement,  $I_u$ , and rotation,  $I_\phi$ :

$$I_u = \frac{u_p}{u_f} \quad (2.1)$$

$$I_\phi = \frac{d\phi_p}{u_f} \quad (2.2)$$

Where  $u_p$  and  $\phi_p$  are the absolute values of the displacement and the rotation at the pile head,  $u_f$  the free-field displacement at the surface of the soil profile and  $d$  the pile diameter. In the absence of kinematic interaction, the displacement of the pile head is equal to the free-field surface displacement and therefore the translational kinematic interaction factor is equal to unity and that for the rotation has a zero value.



For single end-bearing piles under upward propagating shear waves, Gazetas [61] conducted an extensive parametric study and generalized the results providing kinematic interaction factors for three idealized soil profiles. Each one of the soil models is characterized by a different variation of the soil Young's modulus with depth: linear increasing modulus profile representative of uniform soft normally consolidated clay deposits; parabolic increasing modulus profile which is an appropriate idealization for uniform deposits of cohesionless soils; and a soil profile with constant modulus with depth which is typical of stiff overconsolidated clay deposits. Figure 2.28 presents the variation of  $I_u$  versus a dimensionless frequency parameter for the three idealized soil profiles.

Several interesting trends are observed in the results of this study. The displacement kinematic interaction factor is close to unity for low values of the dimensionless frequency parameter, i.e., for low frequencies or low pile-soil relative stiffness. Hence, piles essentially follow the movement of the ground and their presence has no practical effect on the foundation input motion at low frequencies. At the same time, high frequency components of the seismic loading are filtered out by the pile-soil interaction. This effect is more pronounced for high values of relative stiffness,  $E_p/E_s$ , i.e., for stiff piles or very soft soils.

The results of this study show that even relatively long piles may appreciably modify the base excitation of a supported structure. However, in the case of seismic loading essentially controlled by low frequencies the error resulting from the omission of kinematic interaction could be considered as either negligible or conservative.

The influence of pile head constraint on the response of the pile head has also been addressed in the literature [59]. The curves given in Figure 2.29 show that increasing the degree of fixity at the pile-cap level (from free-head to fixed-head piles) has an effect similar to the effect of increasing the stiffness ratio between the pile and the soil,  $E_p/E_s$ , and results in a less severe response at the pile head.

Several studies have also focused on the impact of stratified soil profiles on the response of piles (e.g., [59, 100, 67, 156]). An example of one of these studies is given in Figure 2.30. It shows the impact of the stiffness contrast between layers on the pile-head response of a fixed-head single pile embedded in a two-layered stratum. The stiffness contrast is given by means of the ratio between the shear wave velocities of both layers,  $V_a/V_b$ . As the top layer becomes relatively softer, this ratio decreases and the kinematic displacement factor starts to fluctuate with frequency. For large velocity contrast between the two layers (e.g.,  $V_a/V_b = 1/6$ ), an amplification phenomenon of the pile-head deflection with respect to free-field surface displacement is observed. This example shows the detrimental effect of a significant stiffness contrast between adjacent layers.

The characteristics of the seismic load have also an impact on the kinematic interaction of piles. Most of the studies assume vertically propagating shear waves (S-waves). This assumption is employed because of the considerable difficulties that arise in the exact prediction of the complete induced motion from a potential earthquake. Moreover, it is known that for motions close to the "epicenter", continuous transmission of upward propagating S-waves through increasingly soft soil layers gradually changes their direction of propagation of nearly vertical direction [128].

Some authors have studied the seismic response of pile foundations to excitations other than vertically propagating shear waves. To cite some examples, Kaynia and Novak [102, 162] examined the response of single piles and pile groups to incident shear and dilatational waves and to Rayleigh waves. Makris [128] was interested by the kinematic response of free-head and fixed-head piles embedded in a uniform stratum or half-space and subjected to Rayleigh waves loading.

It is interesting to analyze the results of the kinematic interaction study conducted by Kaynia and Novak [102] on floating vertical single piles under SH waves acting with different angles of incidence. Piles were embedded in a homogeneous viscoelastic halfspace. Transfer functions from this study are presented in Figure 2.31.

For low values of the dimensionless frequency,  $a_0$ , little kinematic interaction is observed (the translation interaction factors are close to unity and the rocking interaction factors are close to zero. At higher dimensionless frequencies, kinematic interaction becomes significant and is strongly dependent on the angle of incidence,  $\theta$ , with the greatest interaction effects produced by upward propagating shear waves ( $\theta = 0^\circ$ ). The same analysis is also conducted on the kinematic interaction factors for horizontal displacement and rocking response of piles under SV waves and Rayleigh waves.

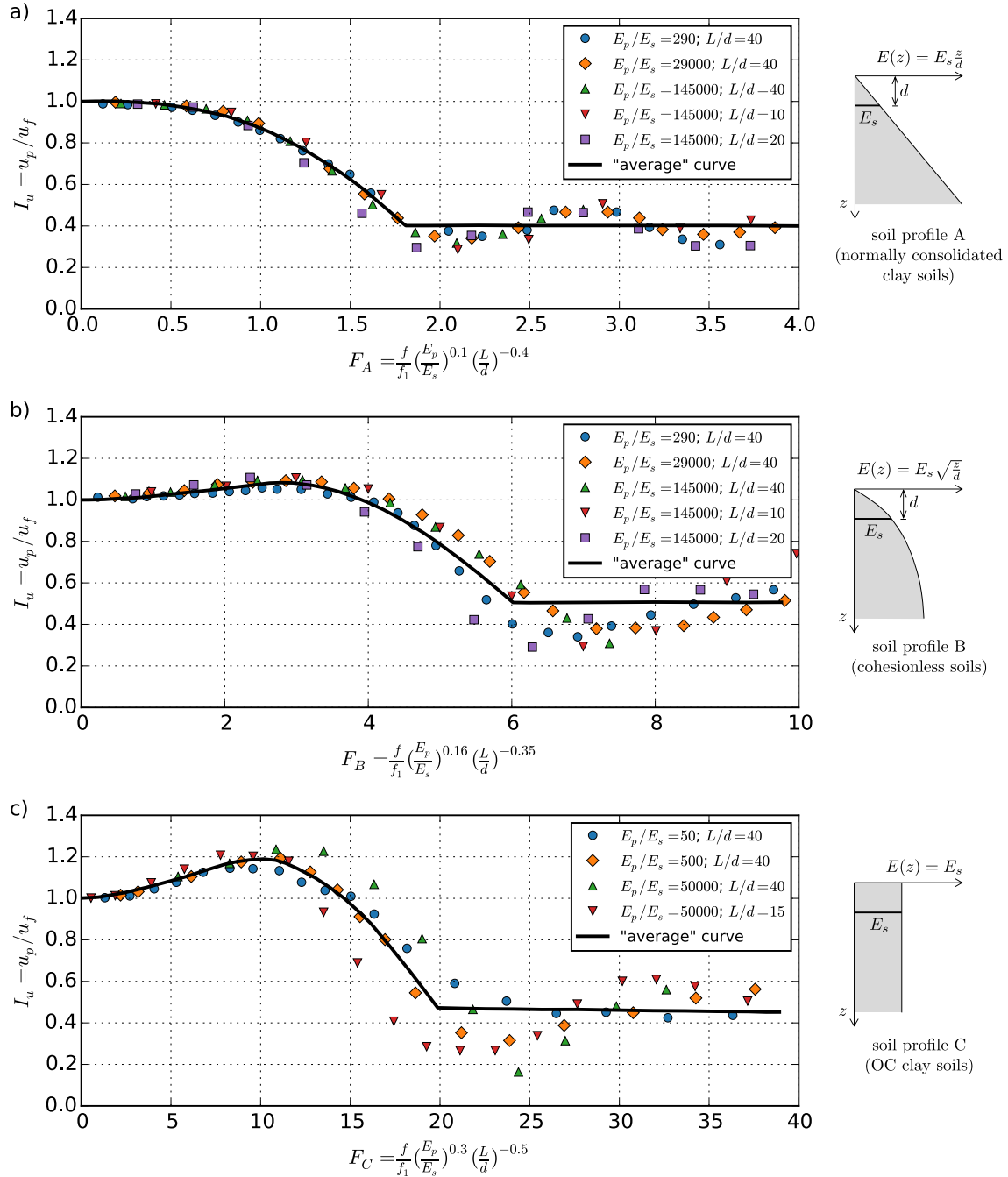


**Figure 2.28:** Kinematic interaction factors,  $I_u$ , of free-head end-bearing piles in terms of the dimensionless frequency parameters  $F_A$ ,  $F_B$  and  $F_C$  (after Gazetas [61])

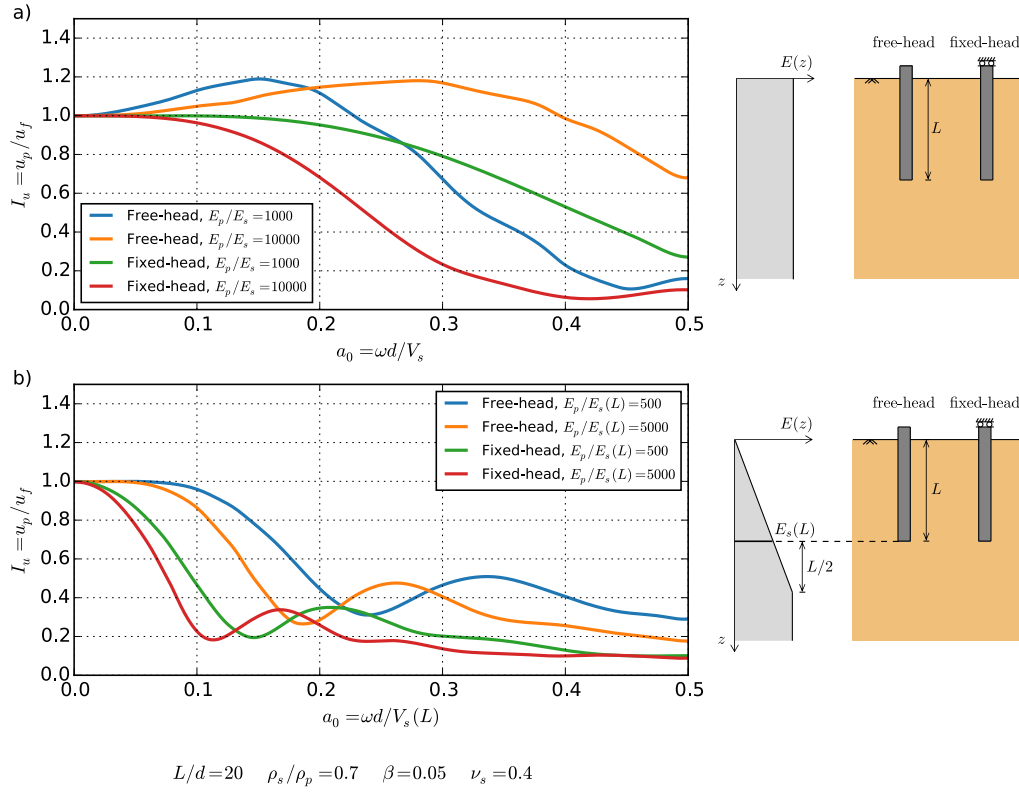


**Figure 2.29:** Influence of pile fixity on the kinematic displacement factor of a floating single pile embedded in: (a) homogeneous; and (b) inhomogeneous soil profile (after Fan *et al.* [59])

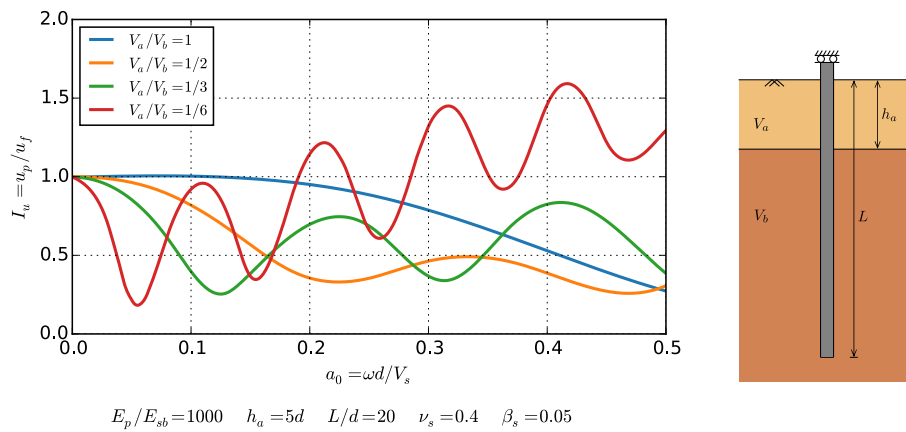


**Figure 2.30:** Influence of the stiffness contrast on the kinematic displacement factor of a fixed-head single pile embedded in a two-layered soil profile (modified from Gazetas *et al.* [67], original data from Kaynia and Kausel (1992))

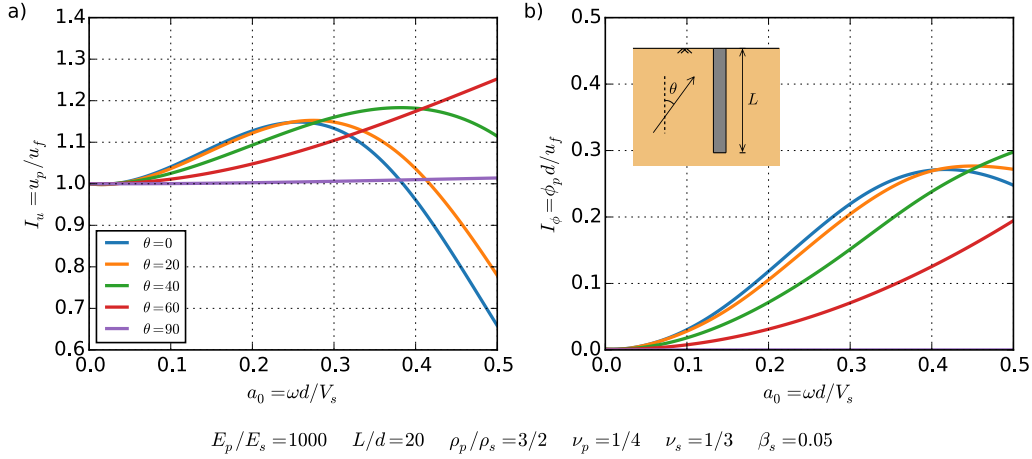


**Figure 2.31:** Kinematic interaction factors for single piles under SH shear waves acting with different angles of incidence  $\theta$ : (a) horizontal translation and (b) rocking (after Kaynia and Novak [102])

In his study, Makris [128] observed that unlike horizontal displacements, the vertical displacements of the pile during the passage of Rayleigh waves differ considerably from that of the soil displacements which suggest that soil-pile interaction might be significant for the vertical component of Rayleigh waves (Fig. 2.32). It is interesting to observe the distribution of the absolute value of the axial strain in the pile due to soil-pile interaction generated from a unit amplitude Rayleigh-wave input.

Another important topic is the account of kinematic-induced maximum bending moments in piles. Indeed, the passage of seismic waves through the soil surrounding a pile imposes lateral displacements and curvatures on the pile, thereby generating kinematic bending moments even in the absence of a superstructure. The critical region of pile distress due to kinematic loading is, in general, located at or near the interface between alternating soft and stiff soil layers and, in the case of restrained-head piles, at the pile head. The magnitude of the bending moment at such locations depends mainly on the stiffness contrast of the layers through which the pile penetrates, the relative rigidity of the pile and the excitation frequency [100, 156, 115]. This has been confirmed by observations in the field and in the laboratory showing that kinematic pile bending may be severe particularly in the case of piled foundations constructed in weak soils [132].

The mechanism behind the generation of large bending moments at the interface between layers of different stiffness is simple. Soil strains are discontinuous across such interfaces, and thereby the corresponding soil curvatures (the derivative of strain) are theoretically infinite. Curvatures in elastic piles are however finite. This is responsible of an interaction between the pile and the soil in the vicinity of the interface [156].

Several are the studies in the literature that focus in this question (e.g., [156, 50, 7]). Nikolaou *et al.* [156] considered a pile embedded in a two-layer soil deposit subjected to vertically propagating harmonic shear waves, and evaluated the maximum bending moments at the interface between the two layers based on the steady-state solution of the dynamic problem. Both free-head and fixed-head conditions at the top of the pile were studied. Figure 2.33 shows the results for an homogeneous (case A1) and a two-layered (case A2) soil profile. The bending moments are presented in terms of maximum dimensionless bending strain:

$$\varepsilon_p = \frac{dM}{2E_p I_p} \quad (2.3)$$

In addition, the transfer function relating bedrock acceleration to surface acceleration and the variation with frequency of the pile bending strain at several points of the pile for the two-layer case are also portrayed.

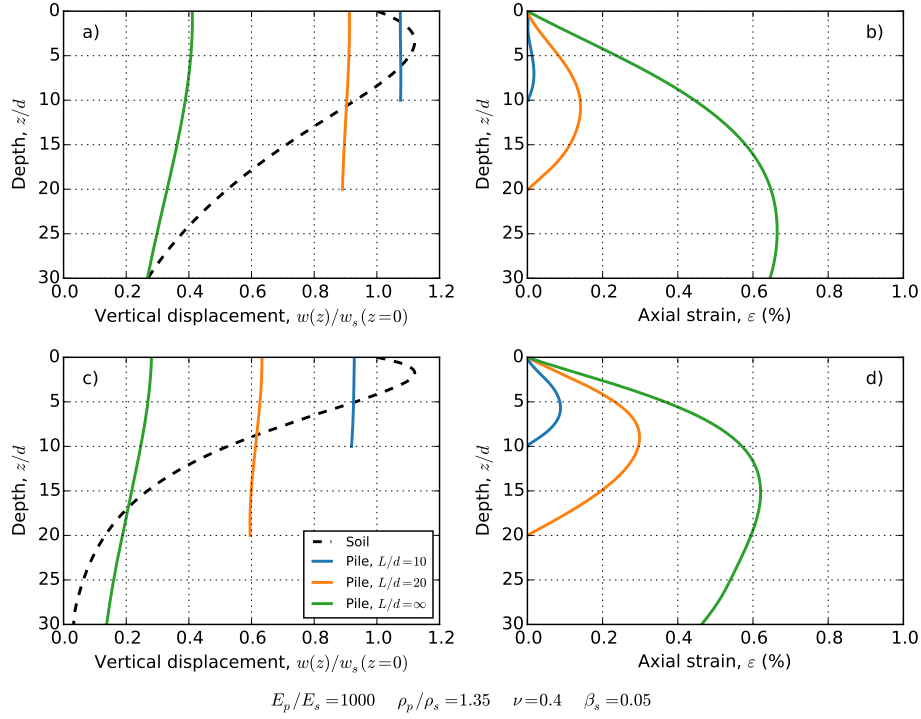


**Figure 2.32:** Influence of Rayleigh waves on the axial response of single piles, vertical displacements and axial strains: (a-b)  $a_0 = 0.2$  and (c-d)  $a_0 = 0.4$  (modified after Makris [128])

As expected, the bending moments are found to be largest either at the pile head (for fixed-head piles) or close (but not exactly) at the interface of soil layers with sharp stiffness contrast. The maximum harmonic bending moment occurs at or near the fundamental natural period of the soil profile ( $T/T_1 \approx 1$ ) for both the interface and the pile head. The variation of the bending moment with frequency is found to follow the same trend as the ratio of peak surface to bedrock acceleration. Another observation is that bending moment diagrams of free-head and fixed-head piles converged with depth and become practically identical beyond a certain distance from the surface. This depth is related to the "active pile length" parameter (which is further explained in this chapter) beyond which a head-loaded pile behaves as an infinitely long beam. These observations were consistently found for the rest of the test cases studied by the authors.

The following closed-form expression allows an approximate estimation of the maximum moment at the interface between two layers for practical applications [155, 156]:

$$M_{max}(\omega) = 0.042 \tau_c d^3 \left( \frac{L}{d} \right)^{0.3} \left( \frac{E_p}{E_1} \right)^{0.65} \left( \frac{V_{s2}}{V_{s1}} \right)^{0.5} \quad (2.4)$$

In the above expression,  $d$  is the pile diameter;  $L$  is the pile length;  $E_1$  is the Young's modulus of the upper soil layer;  $V_{s1}$  and  $V_{s2}$  are the shear wave velocities of the upper and the lower soil layers, respectively, and  $\tau_c$  is the "characteristic" shear stress, proportional to the maximum free-field surface acceleration ( $a_{max}$ ):

$$\tau_c = a_{max} \rho_s h_1 \quad (2.5)$$

where  $\rho_s$  is the soil density, and  $h_1$  the thickness of the upper soil layer. According to this equation the bending moment increases with increasing pile diameter, pile-soil stiffness ratio and stiffness ratio between layers [132].

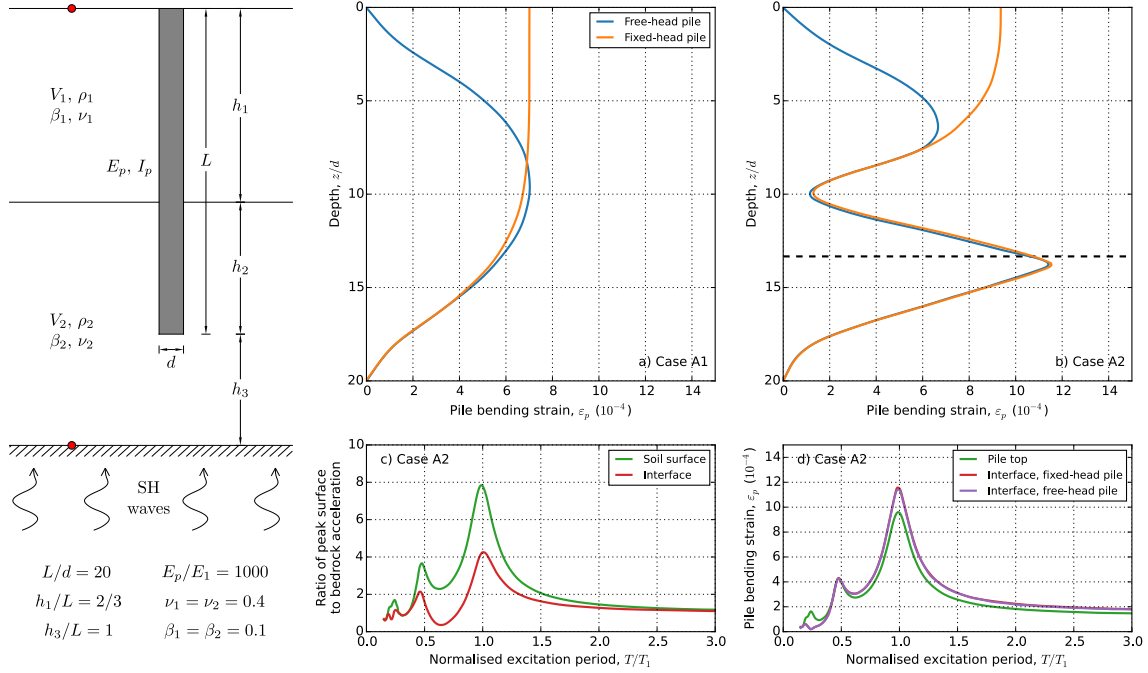


**Figure 2.33:** Kinematic bending strains along a single pile embedded in a homogeneous soil profile (case A1) and a two-layer soil profile (case A2, with  $V_1/V_2 = 0.5$  and  $\rho_1/\rho_2 = 0.8$ ) and excited by harmonic SH seismic waves (modified after Nikolaou *et al.* [156])

### 2.6.1.2 Inertial interaction

When piles vibrate under pile-head dynamic loads, they interact with the surrounding soil. This interaction affects pile stiffness which become, in general, frequency dependent. Energy dissipation is also introduced in the system. This damping is caused by the radiation of elastic stress waves in the soil medium (radiation or geometric damping) and the material hysteresis (material damping) of the soil and the pile [162].

The pile stiffnesses are, in general, not particularly sensitive to frequency, except for heavy piles or very weak soils. At frequencies less than the natural frequency of the soil profile radiation damping is absent because no progressive waves are generated in an elastic medium. Hence at low frequencies the only source of energy dissipation is the material damping [157, 62, 161, 170].

Under lateral pile-head loading, only the upper portion of a flexible pile experiences significant deformation. The length of this portion is called "active length" and is typically on the order of 10 to 20 pile diameters, depending on pile-soil stiffness contrast, soil non-homogeneity, and fixity conditions at the pile head. If the pile length exceeds the "active length" ( $L > l_a$ ) the pile is considered flexible and the actual length is an irrelevant parameter having no influence on the lateral response. Active lengths tend to be greater for dynamic loading than for static loading [61, 127, 2].

However, axially loaded piles tend to respond to much greater depths than the active length (in excess of about 50 pile diameters), and the pile tip reaction is almost always mobilized. Hence the pile tip conditions are important when piles are subjected to vertical dynamic loads. Radiation damping is generally more important for floating piles than for end-bearing piles. The vertical stiffness of the floating piles is however lower compared to the case of end-bearing piles for which the vertical reaction at the pile tip is more important [146, 2].

Much of the attention has focused on the pile complex dynamic stiffness (impedance functions) because they have a strong influence on the response of pile-supported buildings and structures. The impedance functions are defined as amplitudes of the harmonic forces (or moments) that have to be applied to the pile head in order to generate a unit amplitude harmonic displacement in a specific direction (Fig. 2.34) [161].

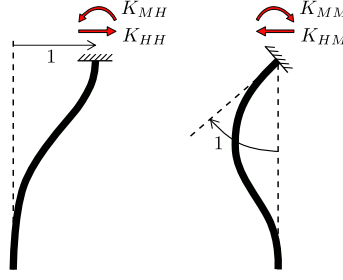


**Figure 2.34:** Definition of pile-head impedances

Dynamic impedances may be expressed as [61]:

$$\mathcal{K} = K(k + i2\xi) \quad (2.6)$$

in which  $K$  is the static stiffness (dynamic stiffness at zero frequency),  $k = k(\omega)$  is the dynamic stiffness coefficient and  $\xi = \xi(\omega)$  the "effective" damping ratio of the system. This damping ratio would normally include two parts: one, frequency-independent, which is related to hysteretic damping in the soil and another one, that increases with frequency and accounts for radiation damping in the system.

A complete study is presented by Gazetas [61] on the inertial response of single end-bearing piles embedded in a number of idealized soil deposits. Figures 2.35 and 2.36 give the variation with frequency of the dynamic stiffness coefficients and the effective damping ratios calculated for the parabolic and the constant soil profile respectively. Several values of the stiffness ratio between soil and pile,  $E_p/E_s$ , are studied. The results are plotted versus  $f/f_1$ , where  $f_1$  is the fundamental shear frequency of the soil deposit.

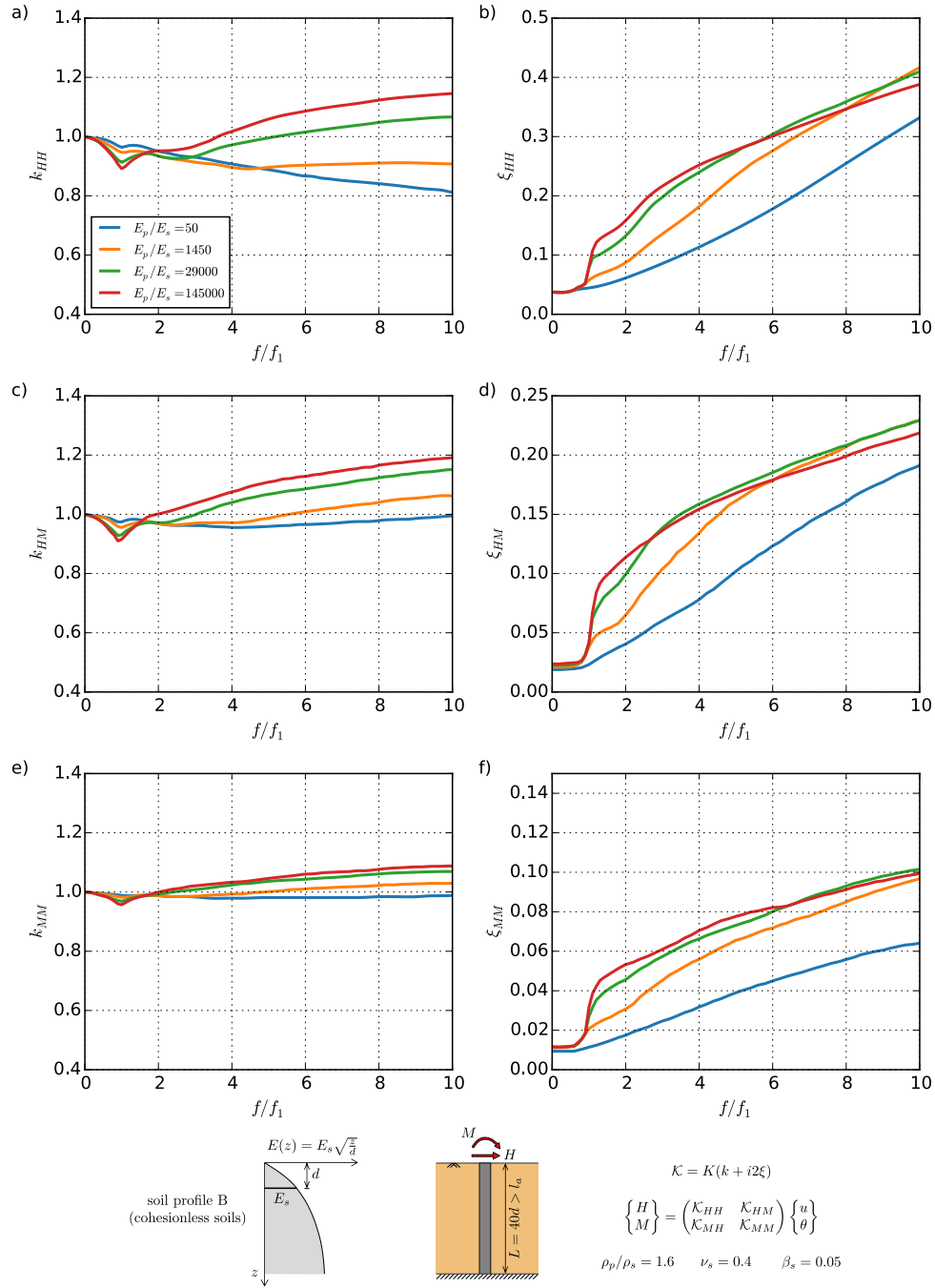
Several interesting observations can be made from these results. The dynamic stiffness coefficients are fairly insensitive to variations in frequency, except perhaps for the translational term,  $k_{HH}$ , of relatively soft piles ( $E_p/E_s \leq 1500$ ) in inhomogeneous soil profiles. Rocking coefficients,  $k_{MM}$ , are particularly insensitive to frequency regardless of soil profile. Hence, for design purposes, the pile-head static stiffness may be approximately used as dynamic ones.

Variation of the damping ratio components with frequency show an interesting trend. Below the fundamental shear frequency of the soil deposit,  $f_1$ , they have a small and frequency-independent value which corresponds to the hysteretic damping in the system (material damping of the soil and to a lesser extent in the pile). As explained before, at such low frequencies the radiation damping is absent. Once the excitation frequency exceeds  $f_1$  damping ratios start to increase with frequency due to the developing radiation damping. The effective damping ratios are found to be considerably lower for rocking than for the swaying mode of vibration. Finally, the comparison of the damping ratios obtained for different soil profiles show that soil inhomogeneity tends to reduce the radiation damping.

In a later paper, Gazetas [68] suggested simple expressions for the three lateral impedance components at the pile head of flexible piles ( $L > l_a$ ). These expressions were derived from rigorous numerical studies results as the ones presented in Figures 2.35 and 2.36. The expressions for pile-head static stiffnesses, for example, have been adapted in the Eurocode 8 - Part 5 [1], and are presented in Table 2.1.

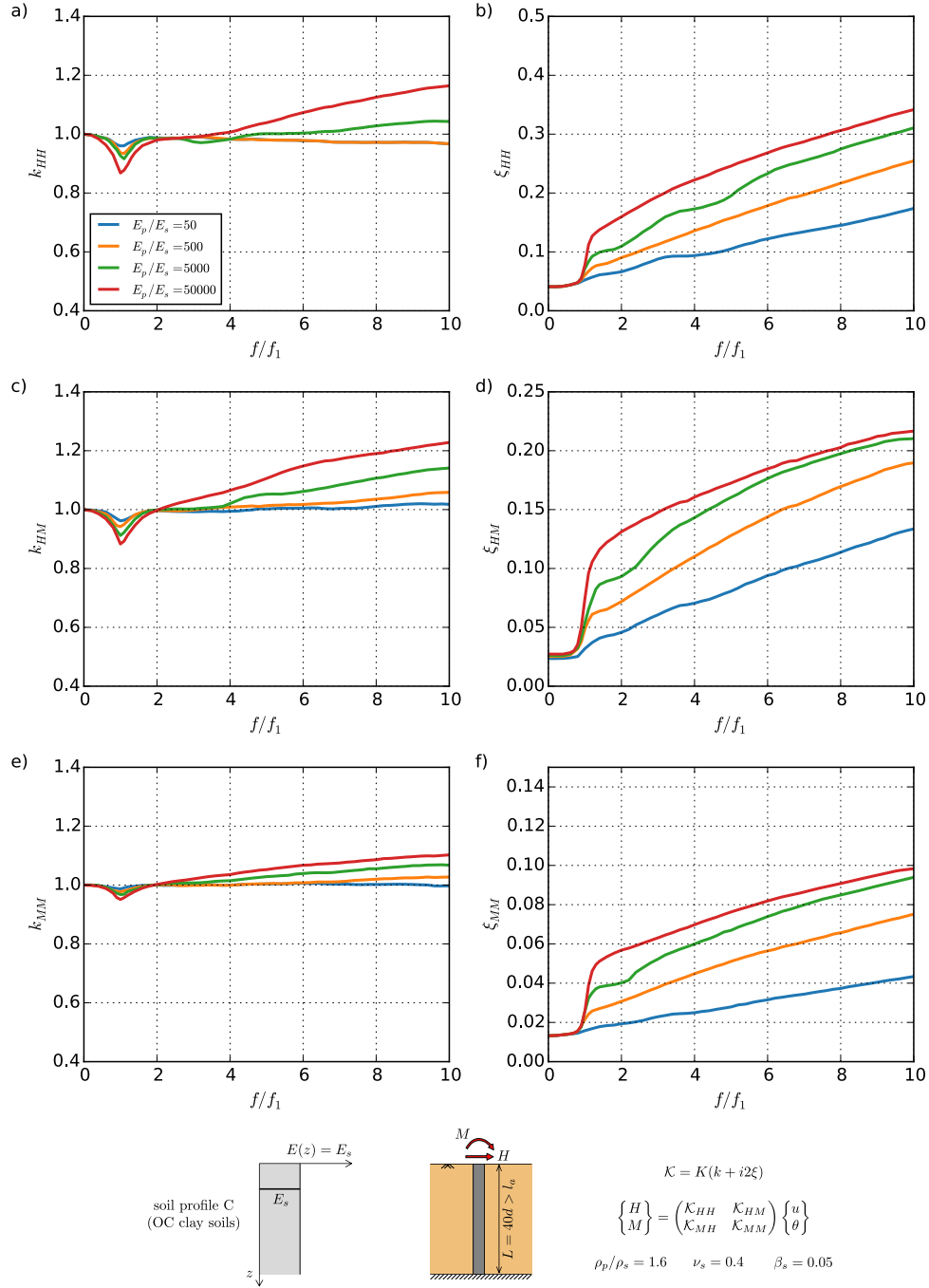
### 2.6.1.3 Combination of kinematic and inertial interaction effects

Under seismic loading, both kinematic and inertial interaction phenomena take place and contribute to the response of the system. Both type of interactions have different characteristics and influence the response differently, e.g., with pile head loading (inertial loading) the soil remains a passive resistor while in seismic events the soil is applying load to the pile (kinematic loading due to soil displacements) [228]. To better understand the response of the system, it is thus important to know if one of these interactions prevails over the other, or if they interact under certain conditions.



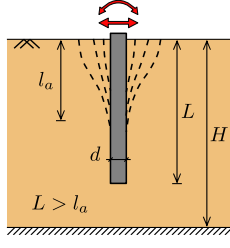
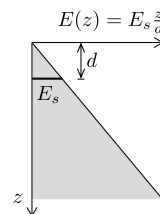
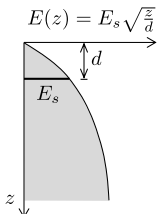
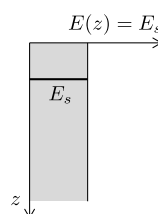
**Figure 2.35:** Dynamic stiffness coefficients and damping ratios for flexible piles embedded in a parabolic modulus soil profile (after Gazetas [61])





**Figure 2.36:** Dynamic stiffness coefficients and damping ratios for flexible piles embedded in a constant modulus soil profile (after Gazetas [61])

**Table 2.1:** Dynamic response of single free-head flexible piles (after Gazetas [61, 68])

	 soil profile A (normally consolidated clay soils)	 soil profile B (cohesionless soils)	 soil profile C (OC clay soils)
Active length	$l_a \approx 2d \left( \frac{E_p}{E_s} \right)^{0.2}$	$l_a \approx 2d \left( \frac{E_p}{E_s} \right)^{0.22}$	$l_a \approx 2d \left( \frac{E_p}{E_s} \right)^{0.25}$
Natural frequency of the soil profile	$f_1 = 0.19 \frac{V_s H}{H}$	$f_1 = 0.223 \frac{V_s H}{H}$	$f_1 = 0.25 \frac{V_s H}{H}$
2nd natural frequency of the soil profile	$\frac{f_2}{f_1} = 2.33$	$\frac{f_2}{f_1} = 2.66$	$\frac{f_2}{f_1} = 3$
Lateral pile head static stiffness			
Static lateral stiffness	$K_{HH} = 0.6dE_s \left( \frac{E_p}{E_s} \right)^{0.35}$	$K_{HH} = 0.79dE_s \left( \frac{E_p}{E_s} \right)^{0.28}$	$K_{HH} = 1.08dE_s \left( \frac{E_p}{E_s} \right)^{0.21}$
Static swaying-rocking cross-stiffness	$K_{HM} = -0.17d^2 E_s \left( \frac{E_p}{E_s} \right)^{0.6}$	$K_{HM} = -0.24d^2 E_s \left( \frac{E_p}{E_s} \right)^{0.53}$	$K_{HM} = -0.22d^2 E_s \left( \frac{E_p}{E_s} \right)^{0.5}$
Static rocking stiffness	$K_{MM} = 0.14d^3 E_s \left( \frac{E_p}{E_s} \right)^{0.8}$	$K_{MM} = 0.15d^3 E_s \left( \frac{E_p}{E_s} \right)^{0.77}$	$K_{MM} = 0.16d^3 E_s \left( \frac{E_p}{E_s} \right)^{0.75}$
Dynamic stiffness coefficients			
Dynamic lateral (swaying) stiffness coefficient	$k_{HH} \approx 1$	$k_{HH} \approx 1$	$k_{HH} \approx 1$
Dynamic swaying-rocking cross-stiffness coefficient	$k_{HM} \approx 1$	$k_{HM} \approx 1$	$k_{HM} \approx 1$
Dynamic rocking stiffness coefficient	$k_{MM} \approx 1$	$k_{MM} \approx 1$	$k_{MM} \approx 1$
Damping ratio			
$f \leq f_1$	$\xi_{HH} \approx 0.6\beta$	$\xi_{HH} \approx 0.7\beta$	$\xi_{HH} \approx 0.8\beta$
	$\xi_{HM} \approx 0.3\beta$	$\xi_{HM} \approx 0.35\beta$	$\xi_{HM} \approx 0.5\beta$
	$\xi_{MM} \approx 0.2\beta$	$\xi_{MM} \approx 0.22\beta$	$\xi_{MM} \approx 0.25\beta$
$f > f_1$	$\xi_{HH} \approx 0.6\beta + \frac{1.8fd}{V_{sd}}$	$\xi_{HH} \approx 0.7\beta + \frac{1.2fd}{V_{sd}} \left( \frac{E_p}{E_s} \right)^{0.08}$	$\xi_{HH} \approx 0.8\beta + \frac{1.1fd}{V_{sd}} \left( \frac{E_p}{E_s} \right)^{0.17}$
	$\xi_{HM} \approx 0.3\beta + \frac{fd}{V_{sd}}$	$\xi_{HM} \approx 0.6\beta + \frac{0.7fd}{V_{sd}} \left( \frac{E_p}{E_s} \right)^{0.05}$	$\xi_{HM} \approx 0.8\beta + \frac{0.85fd}{V_{sd}} \left( \frac{E_p}{E_s} \right)^{0.18}$
	$\xi_{MM} \approx 0.2\beta + \frac{0.4fd}{V_{sd}}$	$\xi_{MM} \approx 0.22\beta + \frac{0.35fd}{V_{sd}} \left( \frac{E_p}{E_s} \right)^{0.1}$	$\xi_{MM} \approx 0.35\beta + \frac{0.35fd}{V_{sd}} \left( \frac{E_p}{E_s} \right)^{0.2}$

Where  $V_{sH}$  is the shear wave velocity at depth  $z = H$ ,  $V_{sd}$  the shear wave velocity at depth  $z = d$  and  $\beta$  the material soil damping ratio.

To this regard, the numerical analysis conducted by Hussien *et al.* [92] showed that kinematic interaction can be the main contributor to seismic forces in the pile when working with relatively short/stiff piles or when the structure's natural frequency is lower than that of the soil profile. In contrast, for long/flexible piles or where structure's natural frequency is equal or greater than that of the soil profile, bending moments in a pile are found to be strongly contributed by the inertial seismic interaction.

### 2.6.2 Dynamic response of a group of piles

Piles are usually used in groups where they interact with each other because the displacement of one pile contributes to the displacement of others. This generates a phenomenon known as pile-soil-pile interaction or group effect, which exerts considerable influence on the properties and the behavior of the group. In addition, this pile-soil-pile interaction is frequency-dependent, resulting from waves that are emitted from the periphery of each pile and propagate until they encounter the neighboring piles. As a result, the seismic response of a pile group may differ substantially from the response of each individual pile taken alone [127, 162].

Under static loading, group effects are normally ignored when a large pile-to-pile spacing is used (greater than 6-8 diameters). It is important to highlight that this is no longer valid for pile groups under dynamic loading because much of the pile group interaction effects arise from wave energy reflected between neighboring piles, which does not attenuate as rapidly as static loading interactions between piles [143].

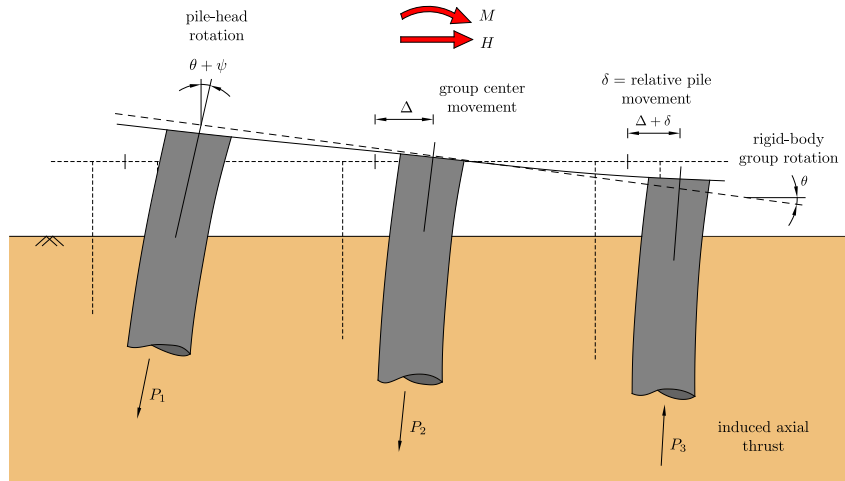


**Figure 2.37:** Components of pile group response under lateral loading and overturning moment (after Meymand [143], original from O'Neill and Dunnivant (1985))

As illustrated in Figure 2.37, several are the components that participate to the response of a pile group under lateral loading and/or overturning moment, i.e., group rotation, inducing axial tensile/compressive forces (usually most severe at outer piles); group translation and relative pile translations; individual pile head rotations at pile to cap connections; and individual pile deflections and consequent bending moments [143]. It should be noted that in the motion of pile groups, rocking and translation are coupled and that much of the rocking stiffness of the pile group develops due to the resistance of the piles to vertical movement.

#### 2.6.2.1 Kinematic interaction

As it happens with single piles, piles in a pile group are also forced to deform along their lengths to accommodate the deformation of the soil under seismic loading. The particularity in the case of pile groups is that rocking and translation motions are coupled, and the rocking movement involves also an excitation in the vertical direction of piles. Several are the studies that have treated this question (e.g., [101, 59, 102, 156]).

The effects of soil-pile-foundation kinematic interaction are usually portrayed in the form of the following two kinematic response factors, for pile-cap displacement,  $I_u$ , and rotation,  $I_\phi$ :

$$I_u = \frac{u_g}{u_f} \quad (2.7)$$

$$I_\phi = \frac{d\phi_g}{u_f} \quad (2.8)$$

Where  $u_g$  and  $\phi_g$  are the absolute values of the displacement and the rotation at the pile cap,  $u_f$  the free-field displacement at the surface of the soil and  $d$  the pile diameter. In the absence of kinematic interaction,  $I_u = 1$  and  $I_\phi = 0$ .

Kaynia and Kausel [101] studied, among other topics, the response of floating pile groups in a homogeneous half-space. In their study the pile heads were fixed to a rigid massless cap and the seismic load was applied as vertically propagating harmonic shear waves. It is interesting to observe the results, in terms of kinematic response factors, of a 4x4 pile group for different pile-to-pile spacings (Fig. 2.38) and also those obtained for a stiffer soil profile (or more flexible pile) for several pile groups (Fig. 2.39). Regarding the pile-cap displacement, it is observed that it follows globally the movement of the soil at low frequencies. However, the high frequencies are systematically filtered.

Fan *et al.* [59] conducted also a numerical study on the kinematic response of floating pile groups in several soil profiles. The results of this study give the same overall shape and trends of kinematic interaction factors for single piles and pile groups, as those previously reported in the literature (e.g., [101, 61]). In this study it was found that, under kinematic interaction, the effects of the pile group configuration, number of piles in a group, and relative spacing between piles are usually insignificant for lateral displacement in the low to intermediate range of frequencies. Hence, there is little pile-to-pile interaction in this frequency range, even for close pile spacing. However, a rocking component appears in the cap motion which needs to be accounted for when slender structures are analyzed. The amplitude of this new component is quite sensitive to pile spacing (Fig. 2.38) and pile-group configuration (Fig. 2.39). In addition, the kinematic constraints imposed at the head of the piles from the cap and the stiffness ratio between the pile and the soil are found to affect appreciably and in a similar way the seismic response of a single pile and of a pile group.

Some studies have focused on the seismic response of pile group foundations to seismic loadings other than vertically propagating shear waves, e.g., Kaynia and Novak [102, 162]. For the case of pile groups under SH shear waves acting with different angles of incidence,  $\theta$ , the authors observed that kinematic interaction is weakest for upward propagation shear waves ( $\theta = 0^\circ$ ) and strongest for  $\theta = 90^\circ$ . The influence of the angle of incidence in rocking is negligible and torsional pile group response is generated except for upward propagating shear waves. The increasing angle of incidence reduces the horizontal motion, but increases torsional group response. The authors also found that Rayleigh waves and SV waves with angles between 30 and 60 degrees produce large rocking motions in pile groups.

The results presented in Figure 2.40 allows the comparison between the horizontal displacement kinematic interaction factors obtained for a free-head single pile and for a 3x3 pile group of hinged-head piles under SH shear waves acting with different angles of incidence  $\theta$ . It should be noted that the piles in both cases have the same conditions at the pile-head. It is interesting to observe that for vertically propagating shear waves, the interaction factors are the same in both cases. When the angle of incidence  $\theta$  increases, the differences between both curves become significant, specially in the high frequency range.

The question of kinematic-induced maximum bending moments in piles in a pile group have also been addressed. Nikolaou *et al.* [156] studied the response of a pile group and found that the bending strains in the corner and center piles are very similar which suggest that group effects are only of minor importance for kinematic interaction.

From the results given in the aforementioned studies it can be concluded that kinematic interaction for a pile group under vertically propagating shear waves is similar to that for an individual pile in the group. Thus, for practical applications, the observations made for a single pile (e.g.,

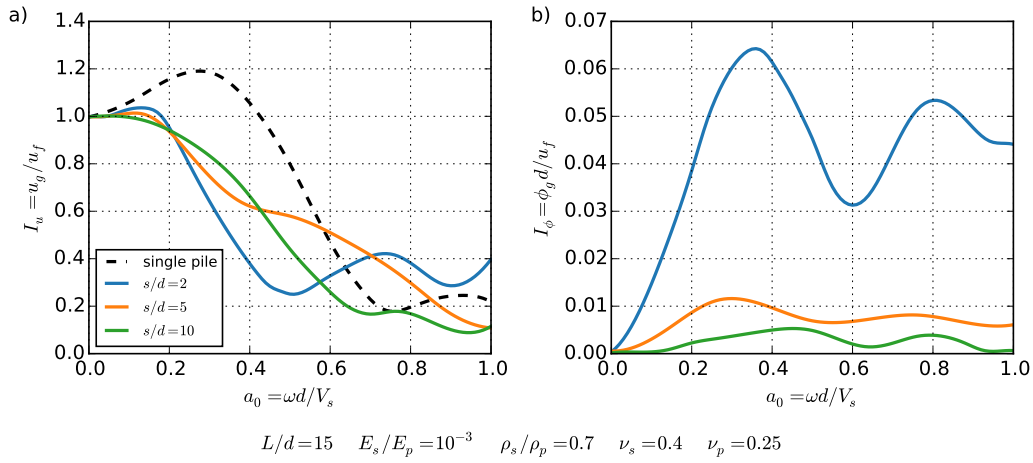


**Figure 2.38:** Kinematic interaction factors for horizontal displacement and rotation of the pile cap of several 4x4 pile groups with different pile spacings and embedded in a homogeneous halfspace (after Kaynia and Kausel [101])

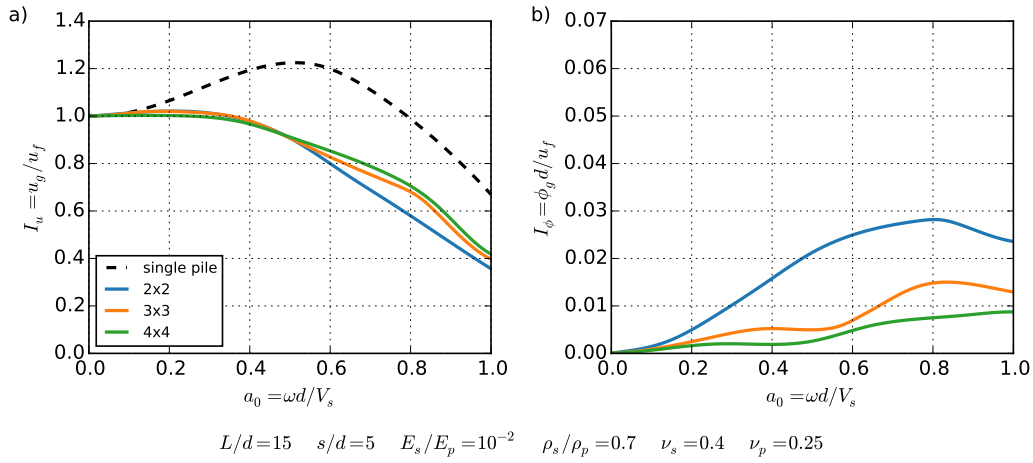


**Figure 2.39:** Kinematic interaction factors for horizontal displacement and rotation of the pile cap of several pile groups (2x2, 3x3 and 4x4) embedded in a homogeneous halfspace (after Kaynia and Kausel [101])

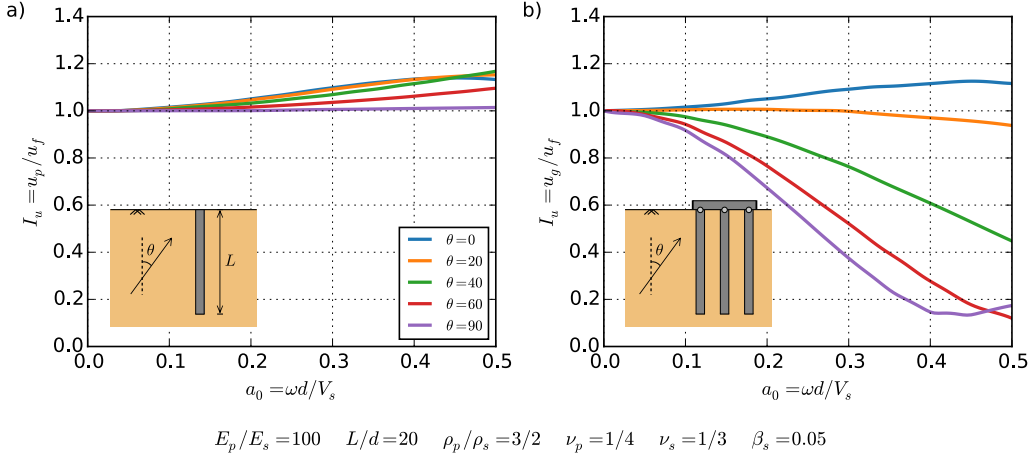


**Figure 2.40:** Horizontal displacement kinematic interaction factors for (a) a single free-head pile and (b) a 3x3 hinged-head pile group, under SH shear waves acting with different angles of incidence  $\theta$  (after Kaynia and Novak [102])

the kinematic interaction factors for a single pile by Gazetas [61], *cf.* Fig. 2.28) can be used as a reasonable approximation for the whole group [170].

Finally, it should be noted that most of the studies available in the literature treated relatively small pile groups (e.g., 4x4 pile groups). For large groups of stiff piles in soft soil kinematic interaction may be more significant with a response that may differ significantly from the free-field motion [232, 161]. Thus, when possible, a complete analysis including kinematic interaction may be desirable.

### 2.6.2.2 Inertial interaction

The dynamic impedance of a pile group cannot be determined by simply adding the impedances of the individual piles because each pile in addition to its own loading, is affected by the response of the neighboring piles transmitted through the soil in form of waves emitted from the periphery of the piles. This is called a group effect, and it can significantly affect the impedance of a pile group as well as the distribution of head loads among individual piles in the group. Group effects depend primarily on pile spacing, frequency, number and layout of the piles [161, 2, 114]. In general, pile groups are less influenced by near surface ground conditions than isolated piles, group interaction effects are stronger for softer soils and radiation damping increases with foundation size [143].

It is important to note that contribution of both lateral and axial stiffness components of each of the piles to the pile group impedance functions are equally important, given that in an inertial interaction inducing a foundation rocking response will surely mobilize the piles axial resistance [38]. Thus, by mobilizing the vertical stiffness of the piles, piles in a pile group contribute to an increase in the rocking stiffness of the foundation consequently reducing the earthquake rocking response of structures [170].

The study by Kaynia and Kausel [101] highlights the importance of the group effect in the response of the foundation. Figure 2.41 shows the normalized dynamic impedance functions (normalized to  $N$  times the static stiffness of an isolated pile) of a 4x4 floating pile group in a homogeneous half-space for three different values of spacing between piles ( $s/d = 2, 5$  and  $10$ ). In this case, the ratio between the Young modulus of the pile  $E_p$  and the soil  $E_s$  is  $E_s/E_p = 10^{-3}$ . The dynamic impedance of a single pile is also portrayed for comparison. To understand how the number of piles and the stiffness ratio between soil and piles influence the response, the authors studied also the response of several groups of piles (2x2, 3x3 and 4x4) in a stiffer soil ( $E_s/E_p = 10^{-2}$ ). The impedance functions are given in Figure 2.42.

From the results portrayed in those figures, it is obvious that the group effect plays a very important role in the response of the system. Without interaction the normalized impedance curves

for a group would be superimposed on those obtained for an isolated pile. The overall behavior of the pile group is generally controlled by the interaction effects between the piles which are due essentially to the out-of-phase vibration of the piles and are significant beyond a certain frequency. The dynamic behavior is strongly dependent on the frequency as a result of the constructive or destructive interference between the various piles in the group. Thus, both stiffness and damping are strongly frequency dependent, and they can be either reduced or increased due to pile-soil-pile interaction. Their values, as a function of frequency, may exhibit very sharp peaks which depend strongly on the size of the group and the spacing of the piles (even for relatively large pile spacings).

It is observed that the interaction effects tend to decrease for increasing values of the stiffness ratio between the soil and the pile,  $E_s/E_p$  (stiffer soil or/and more flexible piles). Furthermore, interaction effects for rotational and torsional cases are associated with the vibration of piles in phase. The radiation damping for translation modes of response (horizontal and vertical) generally increases with the size of the foundation. In addition, it is also observed in this study that pile groups are less influenced by near surface ground conditions than isolated piles.

The authors also found that for small spacings between piles and up to a certain frequency, the stiffness calculated for the pile group decreases with frequency and can become negative, which indicates that the behavior of the system is controlled by the inertial effects coming from the soil mass that is excited by the piles.

Regarding the forces at the head of the piles, perhaps the most important observation made by the authors is that the conclusions concerning the distribution of the load obtained from a static resolution cannot be directly extrapolated to the dynamic cases. Indeed, this distribution is affected by the constructive or destructive interference between the piles in the group and thus it's strongly dependent on the frequency.

Makris and Gazetas [127] showed, for the case of two vertical piles in a homogeneous soil profile, that pile-soil-pile interaction effects are far more significant for inertial interaction than for kinematic loading.

Gazetas *et al.* [67] studied the dynamic impedances of several groups of piles, with different number of piles and configurations. An interesting common feature is that pile-to-pile interaction increases as the number of piles increases but the rate at which this group effect grows decreases as the number of piles becomes large. The most important change in stiffness and damping takes place as the number of piles increases from one to two.

For the particular case of linear groups (with a 1xN piles layout), it is found that increasing the number of piles beyond two or three has only small effect on the dynamic stiffness and damping group factors. Indeed, each new pile that is introduced in the group would generate waves which would only affect the two or three nearest piles; when these waves are 180° out of phase with one of these piles, they are in phase with the next piles. As a result, the combined effect of wave interferences on impedances is quite small. In contrast, the group effects become increasingly pronounced as the number of rows in a pile group increases due to pile-to-pile interaction between piles in opposite rows.

Mylonakis and Gazetas [150] found that piles in pile groups mobilize soil reaction at greater depths than single piles.

Another interesting observation is that for large pile groups, efficiency factors (defined as the ratio of the pile group impedance to the sum of the individual static pile impedances for a given oscillation mode) at low-frequency saturate as the number of piles increases. Thus, the efficiency factors for a large number of piles group would not be significantly lower than those found for a 4x4 group [146]. Furthermore, when the number of piles in a group is very large and the pile spacing is relatively small, the interaction between two distant piles in the group will unavoidable be reduced due to scattering of waves and the corresponding shadows formed by the piles in-between [51]. Finally, group effects tend to decrease with soil inhomogeneity and nonlinearity, as the waves emitted from the periphery of the piles become less coherent [2]. Soil inhomogeneity can make the peaks of the stiffness and damping curves with frequency either more pronounced or duller, depending on conditions such as frequency and spacing [146].

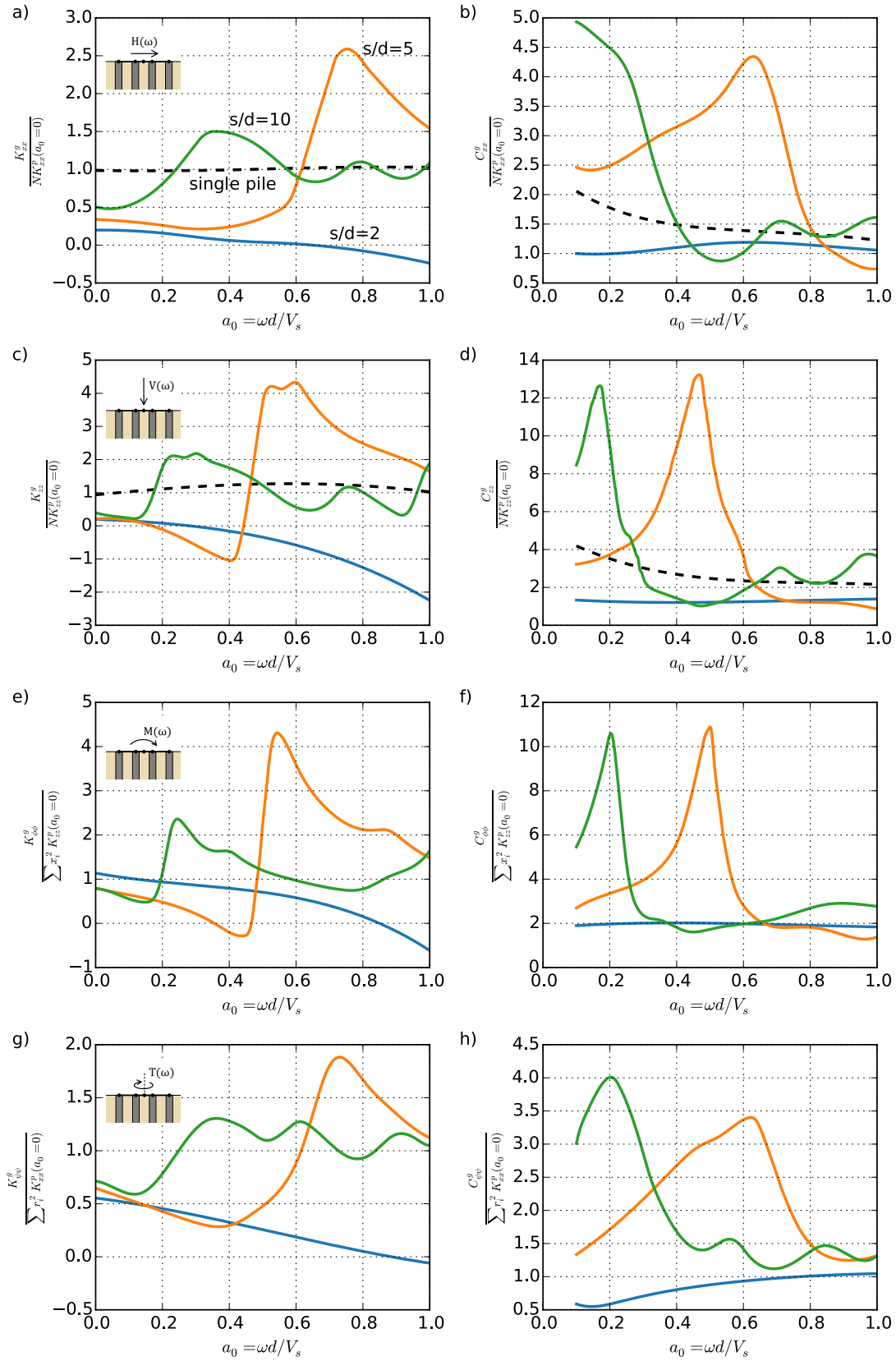


**Figure 2.41:** Dynamic stiffnesses of a 4x4 pile group embedded in a homogeneous halfspace (after Kaynia and Kausel [101])



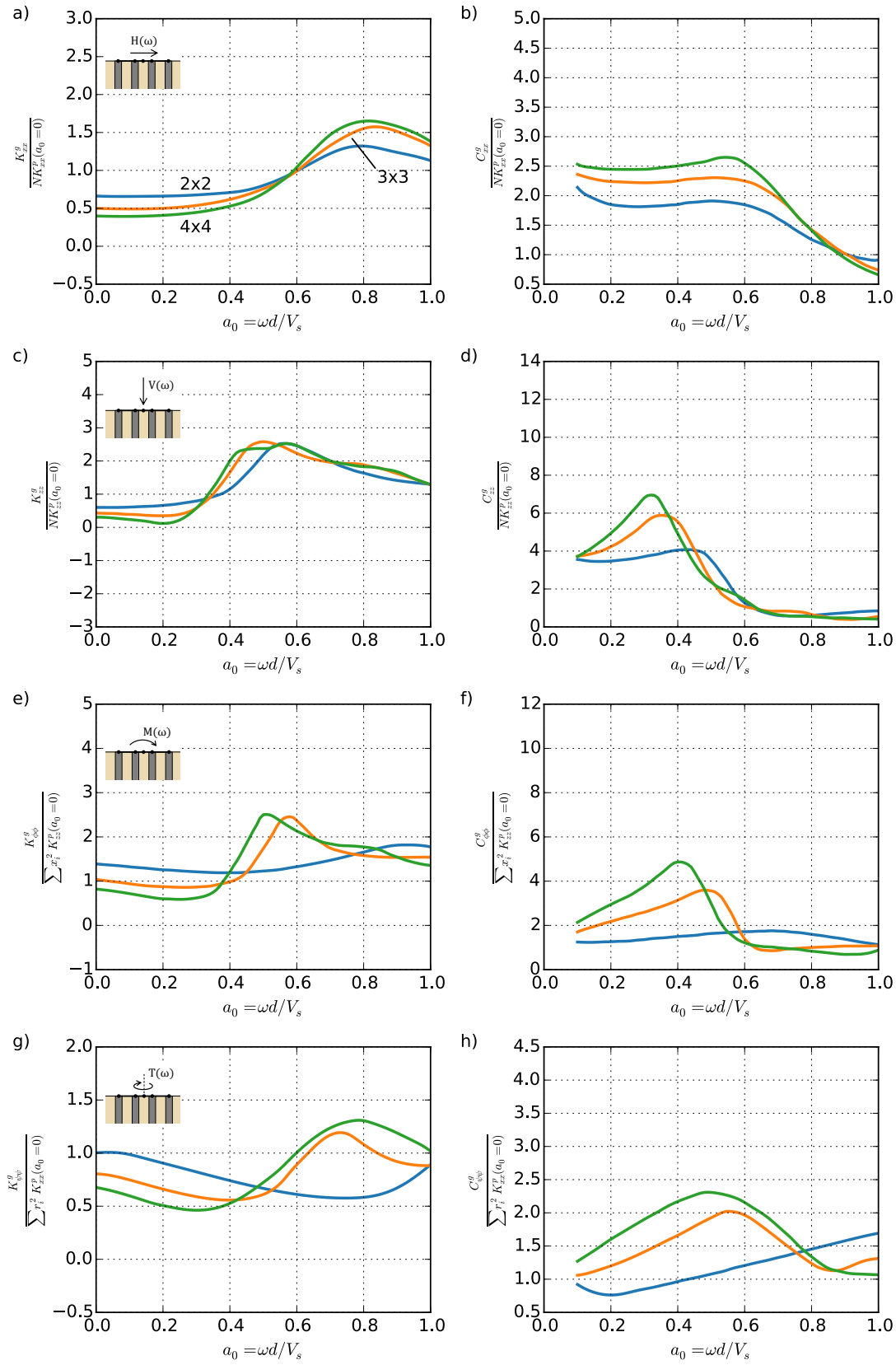


**Figure 2.42:** Dynamic stiffnesses of several pile groups with  $s/d = 5$  embedded in a homogeneous halfspace (after Kaynia and Kausel [101])

### 2.6.3 Non-linearity

Post-earthquake observations of piled foundations have shown large differences in the performance of piles depending on the soil type. In general, piles in firm soils perform better than piles in soft or liquefied soils whose behavior can variate from excellent to poor (e.g., structural damage or excessive deformations) [228].

The response of a pile under small loads is approximately elastic, which explains why most of the theoretical studies in the literature are based on the linear elasticity theory. Nonlinearity have been accounted for in those models using the so-called equivalent linear elastic method which is based on the assumption that the overall response of the system can be captured using a linear elastic modulus compatible with the level of strain that is likely to develop under seismic system. This is fairly accurate for low to medium intensity seismic loadings but is no longer valid under higher loads.

Indeed, pile foundations behave in a nonlinear fashion under large displacements, with a nonlinear relation between pile loading and deflection. The nonlinear response of the system is mainly due to several phenomena, i.e., the development of soil nonlinearity at high strain and its degradation with increasing number of cycles, pile separation (gaping), slippage and friction. The effects of these factors on the foundation generally results in the reduction of the natural frequency of the system and a change in the amount of energy that is dissipated (damping). In fact, material damping is generally increased with the developing of higher strains whereas the radiation damping can be reduced, especially when a gap appears at the top of the piles making it impossible to dissipate energy in form of waves at the interface. To summarize, the system stiffness and damping characteristics are load-level dependent [161, 53, 162, 170].

Single piles under horizontal loading are particularly sensitive to local non-linearity and pile-soil slippage near the surface. During seismic loading, gaps may open between the soil and the pile near the ground surface. In sands, the gap may fill in and be compacted during cycling. This may even conduct, under certain circumstances, to a slight increase of soil-pile lateral stiffness. In clays, the gap may stand open during cycling which would result in a reduction of soil-pile lateral stiffness. It is important to note that gaping in the case of a cohesive foundation soil not only influences the soil reaction but also affects strongly the pile-soil radiation damping under dynamic loading. Finally, it should be mentioned that if water is present and fills the gap between the soil and the pile, an additional degradation phenomenon may take place, with water alternately being drawn in and ejected from the gap during each load cycle, scouring the soil adjacent to the pile and resulting in a further reduction of stiffness [143, 71].

To illustrate the evolution of nonlinearity and its relation with the properties of the soil, it is interesting to observe the results of a two-way cyclic loading applied at the pile head (Fig. 2.43). It should be noted that cyclic loading corresponds to a repetitive loading with very low frequency so that no significant inertia forces and radiation damping arises. However the general traits of the nonlinear response can be duly observed, i.e., material degradation due to plasticity and accumulation of deformations with cycles and degradation of the response due to the evolution of gaping.

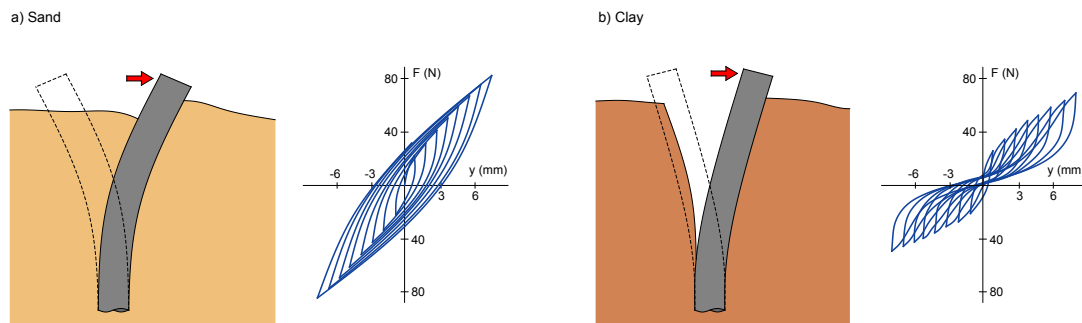


**Figure 2.43:** Response of a single pile embedded in a cohesionless (a) and a cohesive (b) soil, and subjected to lateral cyclic loading (after Gerolymos and Gazetas [71], original from Kishida [105])

An interesting point to note is that nonlinearity generally affects the inertial interaction response at a higher degree than the kinematic one. In fact, most of the soil degradation around the piles is concentrated close to the soil surface. As reported by Nikolaou *et al.* [156] the maximum kinematic induced bending moments occur at the interfaces of the layers which exhibit a stiffness contrast. These zones are usually deep enough to guarantee a higher level of soil confinement and thus a better resistance.

Under axial vibration, nonlinearity stems mainly from slippage and friction at the soil-pile interface [161, 209, 146].

Piles are often used in loose saturated sands and silts. Under seismic loading, significant pore pressure build-up can occur, even in soils with relatively high permeability, which can conduct to the liquefaction of the soil deposit. This results in the loss of much of the lateral and vertical support of the piles leading to an increase in bending moments, loss of stability and eventually, failure [132]. An interesting remark by Wilson [228] is that excess pore pressure generated by pile-head loading can dissipate to the surrounding soil, while in seismic events there will be a global as well as local pore pressure generation.

Pile group dynamic response is also a function of load level. Like for single piles, most of the analysis in the literature address small strain elastic response and only few of them focus in nonlinear response of the pile group. Pile group effects lessen with increasing soil-pile nonlinearity, which inhibits wave transmission between piles. Thus, nonlinearity under large strains reduces group interaction effects (pile-soil-pile interaction) but does not eliminate them [161, 162, 143].

If the connection between the piles and the pile cap is insufficient or it fails during a severe earthquake, the cap may experience a significant uplift, modifying the distribution of the seismic forces in the structure and increasing the loading on the piles that remain connected to the cap. Due to the overload, these piles may fail [161, 146].

#### 2.6.4 Summary

The response of a soil-pile system to dynamic loadings depends on the characteristics of the loadings and the dynamic properties of the system itself (e.g., its stiffness, mass, inelastic properties, energy dissipation (damping)).

At low level of seismic loading, kinematic interaction and radiation damping usually dominate the system response. The neglect of kinematic interaction effects on the foundation input motion generally results in an overestimate of dynamic pile cap motions transmitted to the superstructure. Indeed, soil-pile-superstructure interaction usually results in spectral deamplification of pile cap motions relative to the free-field. This deamplification typically occurs at frequencies higher than the fundamental frequency of the soil-pile-superstructure system, and varies greatly in amplitude. From the studies presented herein it can be concluded that the group effects are important for inertial interactions but negligible for kinematic ones. It is also observed that group effects (pile-soil-pile interaction) can modify in a profound way the response of the system through the different frequencies of the loading.

Under high levels of loading, inelasticity generally plays an important role on the dynamic characteristics of the system. Piles behave in a nonlinear manner because of soil nonlinearity at high strain levels, pile separation (gaping), slippage and friction. As nonlinearity develops in the system, the system period further lengthens and damping in the system is modified. The loss of much of the lateral and/or vertical support of the piles increases the impact of inertial interaction loading and can result in dramatic failure of the system.

### 2.7 Analytical study of dynamic soil-structure interaction effects

Once the dynamic response of single piles and pile groups has been addressed in the previous sub-chapters, it is convenient to analyze analytically the influence of the soil-structure interaction phenomenon on the response of a structure. Several authors have studied the impact of inertial interaction effects on the response of a structure supported by a shallow foundation (e.g., [229, 167,

79, 23]). In the following the same formalism is adapted to the particular case of deep foundations, case for which, the translations and the rotations of the pile cap are coupled.

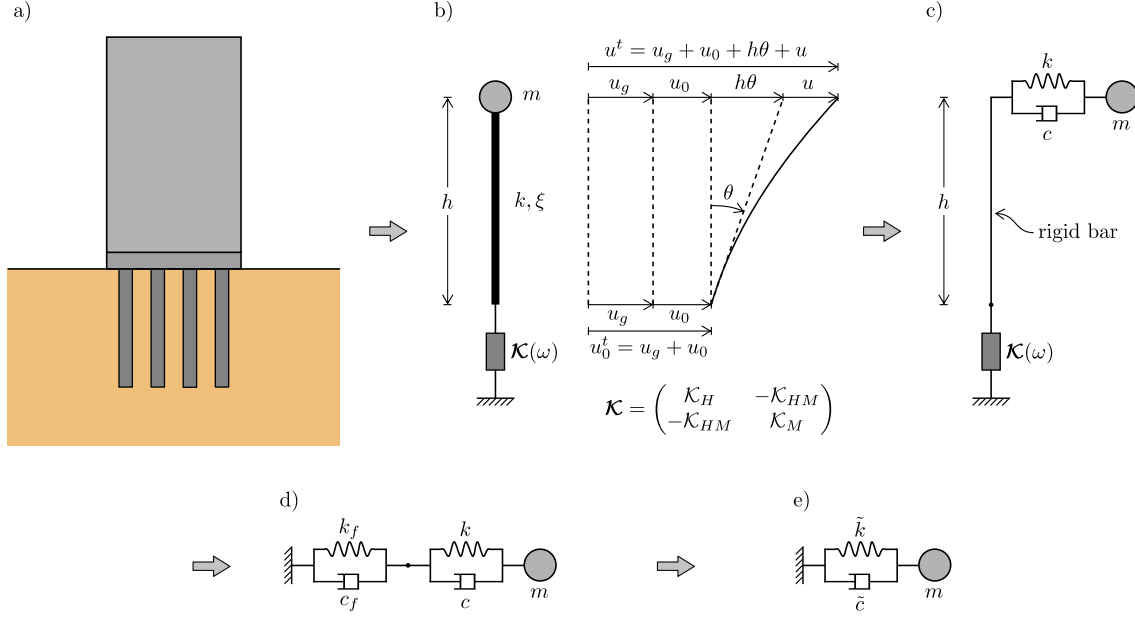


**Figure 2.44:** Analytical model for the study of SSI

Let's consider a building supported by a pile group (Fig. 2.44-a). In a first approach, the fundamental response of the structure can be modeled with an elastic Bernoulli beam of length  $h$ , with a lumped mass  $m$  attached at its top (which corresponds to the center of gravity of the structure). The structure is characterized by a lateral stiffness  $k$  and a hysteretic damping ratio  $\xi$ . The effective values  $m$ ,  $k$  and  $\xi$  are associated with the fundamental mode of vibration of the structure. The fixed-base angular frequency of the structure is denoted as  $\omega_s$ :

$$\omega_s^2 = \frac{k}{m} \quad (2.9)$$

The beam is supported by a 2x2 complex stiffness matrix  $\mathbf{K}$  characterized by the translational, the rotational and the coupling terms of the dynamic impedance functions calculated at the center of the pile cap ( $\mathcal{K}_H$ ,  $\mathcal{K}_M$ ,  $\mathcal{K}_{HM}$ ).

The degrees of freedom of the system are the following:  $u$ , horizontal displacement of the concentrated mass with respect to center of the pile cap (equal to the structural distortion);  $u_0$ , the horizontal displacement of the foundation relative to the free-field motion;  $\theta$ , the rotation of the foundation; and  $u_g$ , the free-field motion. The total displacement amplitudes at the center of gravity of the structure  $u^t$  and at the base of the structure (pile cap)  $u_0^t$  can thus be expressed as follows (with respect to the Galilean reference coordinate axis):

$$u^t = u_g + u_0 + h\theta + u \quad (2.10)$$

$$u_0^t = u_g + u_0 \quad (2.11)$$

An harmonic ground motion of amplitude  $u_g$  and angular frequency  $\omega$  is applied at the base of the system (the free-field displacement of the foundation soil).

The equivalent model can be further simplified using a spring and damper system with equivalent properties to that of the structure and an rigid beam of length  $h$  connecting the structure to the impedance matrix (Fig. 2.44-c). For the sake of simplicity, the system can be divided in two parts, one accounting for the response of the foundation alone and the other one for the response of the structure.

The response of the foundation is represented by the complex stiffness matrix and the rigid bar as depicted in Fig. 2.45. The horizontal displacement at the center of gravity of the structure due to the deformation of the foundation is given by the addition of  $u_0$  and  $h\theta$ , that is for the equivalent system defined also in the aforementioned scheme:

$$u_f = u_0 + h\theta \quad (2.12)$$

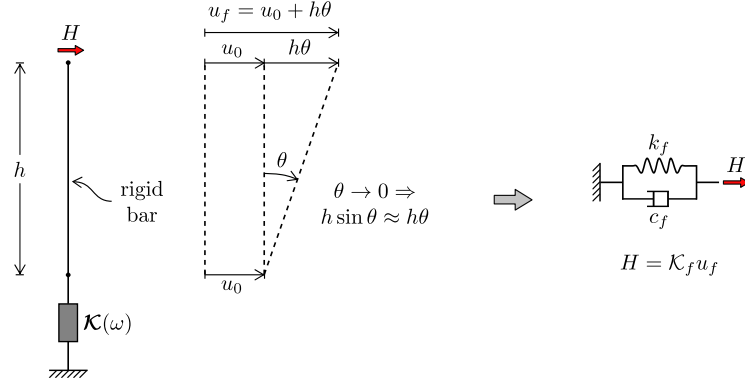


**Figure 2.45:** Definition of equivalent model accounting for foundation response in SSI analysis

Operating with the complex stiffnesses in the frequency domain, the effective complex stiffness of the foundation at the level of the center of gravity of the structure is:

$$\mathcal{K}_f = \frac{\mathcal{K}_H \mathcal{K}_M - \mathcal{K}_{HM}^2}{h^2 \mathcal{K}_H + 2h \mathcal{K}_{HM} + \mathcal{K}_M} \quad (2.13)$$

Where:

$$\begin{cases} \mathcal{K}_f = k_f(1 + i2\xi_f) \\ \mathcal{K}_H = k_H(1 + i2\xi_H) \\ \mathcal{K}_{HM} = k_{HM}(1 + i2\xi_{HM}) \\ \mathcal{K}_M = k_M(1 + i2\xi_M) \end{cases} \quad (2.14)$$

Replacing these terms in Equation (2.13):

$$\mathcal{K}_f = \frac{k_H k_M (1 + i2\xi_H)(1 + i2\xi_M) - k_{HM}^2 (1 + i2\xi_{HM})^2}{h^2 k_H (1 + i2\xi_H) + 2h k_{HM} (1 + i2\xi_{HM}) + k_M (1 + i2\xi_M)} \quad (2.15)$$

Assuming that  $\xi_H, \xi_{HM}, \xi_M \ll 1$ , we have:

$$k_f \approx \frac{k_H k_M - k_{HM}^2}{h^2 k_H + 2h k_{HM} + k_M} \quad (2.16)$$

$$\xi_f \approx \frac{k_H k_M (\xi_H + \xi_M) - 2k_{HM}^2 \xi_{HM}}{k_H k_M - k_{HM}^2} - \frac{h^2 k_H \xi_H + 2h k_{HM} \xi_{HM} + k_M \xi_M}{h^2 k_H + 2h k_{HM} + k_M} \quad (2.17)$$

Once the effective stiffness and damping ratio ( $k_f$  and  $\xi_f$ ) due to the foundation are known, it is possible to calculate the response of the full system taking into account SSI effects by combining the response of the foundation and that of the structure. The dynamic equilibrium of the mass point and the horizontal equilibrium equation of the system depicted in Fig. 2.44-d:

$$\begin{cases} -m\omega^2(u_f + u) + k(1 + i2\xi)u = m\omega^2 u_g \\ -m\omega^2(u_f + u) + k_f(1 + i2\xi_f)u_f = m\omega^2 u_g \end{cases} \quad (2.18)$$

Introducing the relations  $m\omega_s^2 = k$  and  $m\omega_f^2 = k_f$ , and removing  $u_f$  from the above system of equations:

$$\left[ \left( 1 - \frac{\omega^2}{\omega_s^2} - \frac{\omega^2}{\omega_f^2} \frac{1 + 4\xi\xi_f}{1 + 4\xi_f^2} \right) + i2 \left( \xi - \frac{\omega^2}{\omega_f^2} \frac{\xi - \xi_f}{1 + 4\xi_f^2} \right) \right] u = \frac{\omega^2}{\omega_s^2} u_g \quad (2.19)$$

To better understand the response of the soil-foundation-structure system, its response is compared to that of an equivalent 1-dof system with fundamental angular frequency  $\tilde{\omega}$  and ratio of hysteretic damping  $\tilde{\xi}$ . This equivalent system is excited at its base by an harmonic displacement  $\tilde{u}_g$  of angular frequency  $\omega$ . The equation of motion of the equivalent system is equal to:

$$\left( 1 - \frac{\omega^2}{\tilde{\omega}^2} + i2\tilde{\xi} \right) \tilde{u} = \frac{\omega^2}{\tilde{\omega}^2} \tilde{u}_g \quad (2.20)$$

The equivalent oscillator will have the same response as the initial system if the following equations are satisfied:

$$\frac{1}{\tilde{\omega}_g} = \frac{1}{\omega_s^2} + \frac{1}{\omega_f^2} \frac{1 + 4\xi\xi_f}{1 + 4\xi_f^2} \quad (2.21)$$

$$\tilde{\xi} = \xi - \frac{\omega^2}{\omega_f^2} \frac{\xi - \xi_f}{1 + 4\xi_f^2} \quad (2.22)$$

$$\tilde{u}_g = \frac{\tilde{\omega}^2}{\omega_s^2} u_g \quad (2.23)$$

Assuming that  $\xi, \xi_f \ll 1$ , and writing the equations at the fundamental frequency  $\omega = \tilde{\omega}$ , we have:

$$\frac{1}{\tilde{\omega}^2} = \frac{1}{\omega_s^2} + \frac{1}{\omega_f^2} \quad (2.24)$$

$$\tilde{\xi} = \frac{\tilde{\omega}^2}{\omega_s^2} \xi + \frac{\tilde{\omega}^2}{\omega_f^2} \xi_f \quad (2.25)$$

Several are the observations that can be made from Equations (2.23), (2.24) and (2.25). Soil-structure interaction is responsible of a decrease in the fundamental frequency with respect to that of the structure on fixed-base ( $\tilde{\omega} < \omega_s$ ), or conversely in terms of period, a period lengthening. There is, in general, an increase of the overall damping of the system compared to that of the structure alone ( $\tilde{\xi} > \xi$ ). Finally, the equivalent seismic input applied to the equivalent 1-dof system in order to have the same displacement  $u$  (equal to structural distortion) will always be smaller than that applied to the full system ( $\tilde{u}_g < u_g$ ).

The fundamental angular frequency of the soil-structure system  $\tilde{\omega}$  can be rewritten using Equation (2.24) as:

$$\tilde{\omega}^2 = \frac{\omega_s^2}{1 + \frac{k}{k_f}} \quad (2.26)$$

Given that  $\tilde{\omega}^2 = \tilde{k}/m$ , the equivalent stiffness of the soil-structure system  $\tilde{k}$  can be expressed in terms of the stiffnesses of the foundation and of the structure:

$$\tilde{k} = \frac{k}{1 + \frac{k}{k_f}} \quad (2.27)$$

Using Equations (2.24) and (2.25) the equivalent damping ratio equals:

$$\tilde{\xi} = \frac{\tilde{\omega}^2}{\omega_s^2} \xi + \left( 1 - \frac{\tilde{\omega}^2}{\omega_s^2} \right) \xi_f \quad (2.28)$$

Which allows the study of the evolution of the equivalent damping ratio of the soil-structure system according to the ratio  $\tilde{\omega}/\omega_s$  (in terms of frequencies this ratio becomes  $\tilde{f}/f_s$  or  $T_s/\tilde{T}$  when periods are used). Figure 2.46 shows this evolution for different values of the damping ratio of

the structure and of the foundation. It is observed that the equivalent damping ratio of the soil-structure system  $\tilde{\xi}$  is not necessarily bigger than that of the structure alone  $\xi$  (e.g., when the foundation damping  $\xi_f$  is lower or equal to that of the structure alone  $\xi$  (e.g., when the structure is equipped with seismic isolators or additional damping devices or when the radiation damping is absent)).

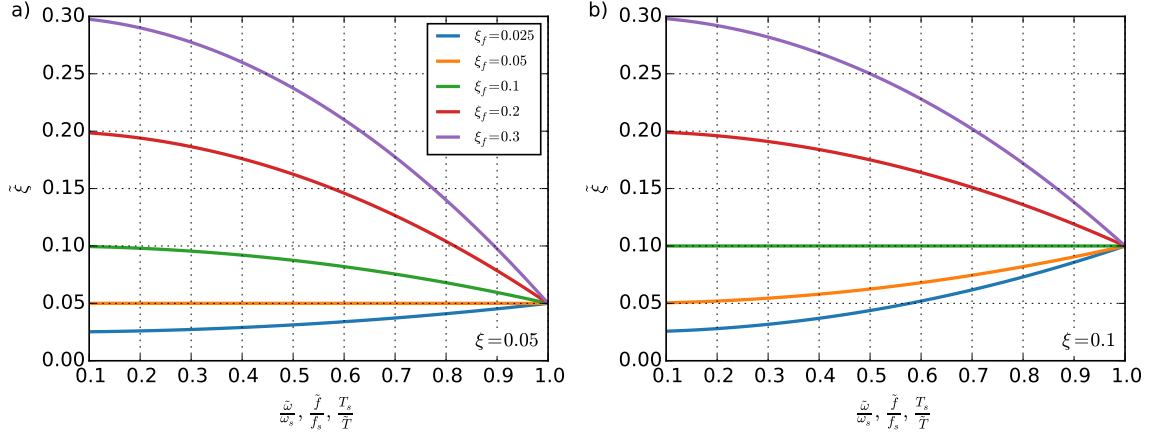


**Figure 2.46:** Equivalent damping ratio of the soil-structure system

A recurring question is how SSI effects modify the displacement response of the system. Although for the equivalent oscillator the damping ratio  $\tilde{\xi}$  is generally larger than  $\xi$  and the effective seismic input  $\tilde{u}_g$  smaller than  $u_g$ , the structural response  $u$  for a specific excitation of angular frequency  $\omega$  can be larger or smaller than that if the soil-structure interaction is neglected [229]. The same observation applies to the displacement of the mass relative to free field (in other words the addition of the foundation deformation to that of the structure). To study SSI effects on the displacements of the system it is interesting to observe the variation of the structural distortion  $u$  and the displacement of the structure mass relative to free field ( $u_0 + h\theta + u$ ) in terms of  $\omega/\omega_s$ . Given the following equations of motion:

$$\left(1 - \frac{\omega^2}{\tilde{\omega}^2} + i2\tilde{\xi}\right)u = \frac{\omega^2}{\omega_s^2}u_g \quad (2.29)$$

$$\left(1 - \frac{\omega^2}{\tilde{\omega}^2} + i2\tilde{\xi}\right)(u_0 + h\theta + u) = \frac{\omega^2}{\tilde{\omega}^2}u_g \quad (2.30)$$

The absolute values of the displacements (nondimensionalized with  $u_g$ ) are respectively:

$$\frac{|u|}{|u_g|} = \frac{\omega^2}{\omega_s^2} \frac{1}{\sqrt{\left(1 - \frac{\omega^2}{\tilde{\omega}^2}\right)^2 + \left(2\tilde{\xi}\frac{\omega}{\tilde{\omega}}\right)^2}} \quad (2.31)$$

$$\frac{|u_0 + h\theta + u|}{|u_g|} = \frac{\omega^2}{\tilde{\omega}^2} \frac{1}{\sqrt{\left(1 - \frac{\omega^2}{\tilde{\omega}^2}\right)^2 + \left(2\tilde{\xi}\frac{\omega}{\tilde{\omega}}\right)^2}} \quad (2.32)$$

Equations (2.31) and (2.32) are plotted in Figure 2.47 in terms of  $\omega/\omega_s$  for different values of  $\tilde{\omega}/\omega_s$ ,  $\xi$  and  $\xi_f$ .

Several are the observations that can be made from these curves. For the same loading at a fixed angular frequency  $\omega$ , SSI effects can increase or decrease the structural distortion  $u$  with respect to the case of the structure on fixed-base. If only the peak response is examined, which occurs at the fundamental frequency of the corresponding dynamic system (that is  $\omega = \omega_s$  for the structure on fixed-base and  $\omega = \tilde{\omega}$  when SSI is considered), then the structural distortion  $u$  for the system considering SSI effects is practically always smaller than that for the fixed-base structure [229]. An increase of damping decreases the value of the peaks but does not change the overall

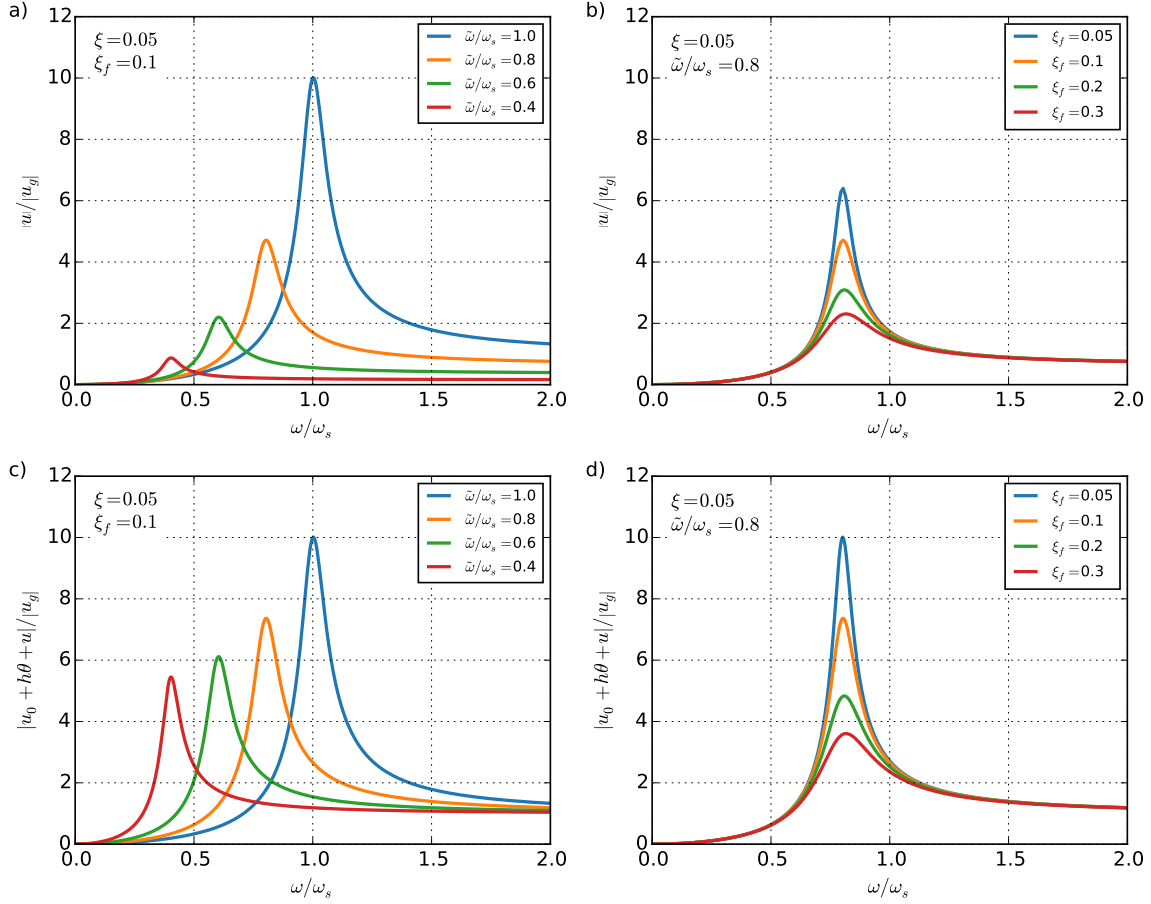


**Figure 2.47:** Influence of soil-structure interaction as a function of exciting frequency: structural distortion  $u$  and displacement of the mass relative to free field ( $u_0 + h\theta + u$ )

shape of the response. Given that the corresponding transverse-shear force in the structure equals  $ku$ , it can be concluded that, in general, taking into account SSI effects reduces transverse-shear in the structure. Regarding the question of the displacement of the mass relative to the free-field motion, the same trends are reproduced.

A final remark regarding the curves in Figure 2.47 is that they are calculated considering  $\tilde{\omega}/\omega_s$ ,  $\xi$  and  $\xi_f$  constant throughout all the range of exciting frequencies. In a real case, particularly when piled foundations are considered, the stiffness and damping values are highly frequency dependent and thus the parameters  $\tilde{\omega}/\omega_s$  and  $\xi_f$  may depend also on the exciting frequency. Structure hysteretic damping  $\xi$  on the other hand is usually considered constant.

For a specific excitation, the response of the dynamic system will depend on the properties of the structure compared to those of the soil. To continue the analysis of SSI effects it is convenient to introduce the following dimensionless parameters:

$$\bar{s} = \frac{\omega_s h}{V_s} \quad \bar{h} = \frac{h}{a} \quad \bar{m} = \frac{m}{\rho_s a^3} \quad a_0 = \frac{\omega d}{V_s} \quad (2.33)$$

Where  $\bar{s}$  is the ratio of the stiffness of the structure to that of the soil,  $V_s$  being the shear-wave velocity of the soil. The slenderness ratio  $\bar{h}$  relates a characteristic length of the rigid cap denoted  $a$  (e.g., the distance between axis for the outer piles in the group) to the height of the structure  $h$ . The mass ratio  $\bar{m}$  expresses the significance of the structural mass  $m$  to an equivalent soil mass (of mass density  $\rho_s$ ) vibrating with the foundation. Finally, to introduce the frequency of excitation  $\omega$ , the dimensionless number  $a_0$  is introduced.

To highlight the impact of SSI in the response of a structure supported by a pile group, a



numerical application is done. The dynamic impedances of the 4x4 pile group introduced in Fig. 2.48 are calculated using the boundary element method and presented in Fig. 2.49. Using Equations (2.16) and (2.17), it is straightforward to calculate the effective stiffness and damping ratio of the foundation for several slenderness ratios  $\bar{h}$  (Fig. 2.50). Finally, taking Equations (2.24) and (2.28) and the dimensionless parameters introduced before it is possible to study the evolution of the fundamental frequency and of the damping ratio for a given exciting frequency and different characteristics of the soil and of the structure (Fig. 2.51).

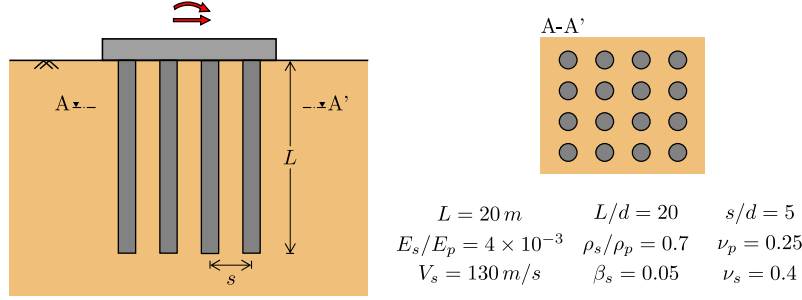


**Figure 2.48:** Numerical application to study the impact of SSI in the response of a structure supported by a pile group

As expected, decreasing the stiffness of the soil or increasing the fundamental frequency of the structure ( $\bar{s}$  increases) results in a decreasing of  $\tilde{\omega}/\omega_s$ . Augmenting the mass of the structure (increase of  $\bar{m}$ ) also leads to smaller values of  $\tilde{\omega}/\omega_s$ . Thus, soil-structure interaction effects are more important for heavy structures, slender structures and stiff structures supported on soft soils in terms of period lengthening.

The differences in terms of damping ratio between different exciting frequencies (e.g., between  $a_0 = 0.05$  and  $a_0 = 0.3$ ) highlights the importance of radiation damping in the response of the system. At low frequencies the amount of radiation damping available is lower than for other loading frequencies. This results in a different response of the system under different loading frequencies and remarks the importance of taking into account frequency effects in dynamic soil-structure interaction studies.

Another question that arises when dealing with deep foundation is whether neglecting coupling terms is acceptable or not when modeling the foundation-structure system. In order to have a better insight into this question, it is interesting to analyze for example how the effective stiffness and damping ratio of the foundation changes when coupling terms are neglected. Eliminating the coupling terms in Equations (2.16) and (2.17) results in the following expressions:

$$k_f \approx \frac{k_H k_M}{h^2 k_H + k_M} \quad (2.34)$$

$$\xi_f \approx \frac{h^2 k_H \xi_M + k_M \xi_H}{h^2 h_H + k_M} \quad (2.35)$$

Figure 2.52 presents the effective stiffness and the damping ratio of the foundation with and without using the coupling terms. It is observed that the effective stiffness of the foundation is systematically higher when coupling terms are neglected. This difference in stiffness decreases with the increase in height of the structure. Regarding the effective damping ratio, it is generally lower for the case where coupling terms are not used. A higher stiffness of the foundation may result in an underestimation of the displacement of the foundation-structure system. However, the equivalent damping of the foundation-structure system is expected to decrease (according to Equation (2.28)) which would imply higher displacements of the system. What should be retained from this analysis is that not considering coupling terms in the analysis alters the dynamic response of the foundation-structure system and that is difficult to quantify in a simple manner how this modification changes the output of the system in a beneficial or detrimental role.

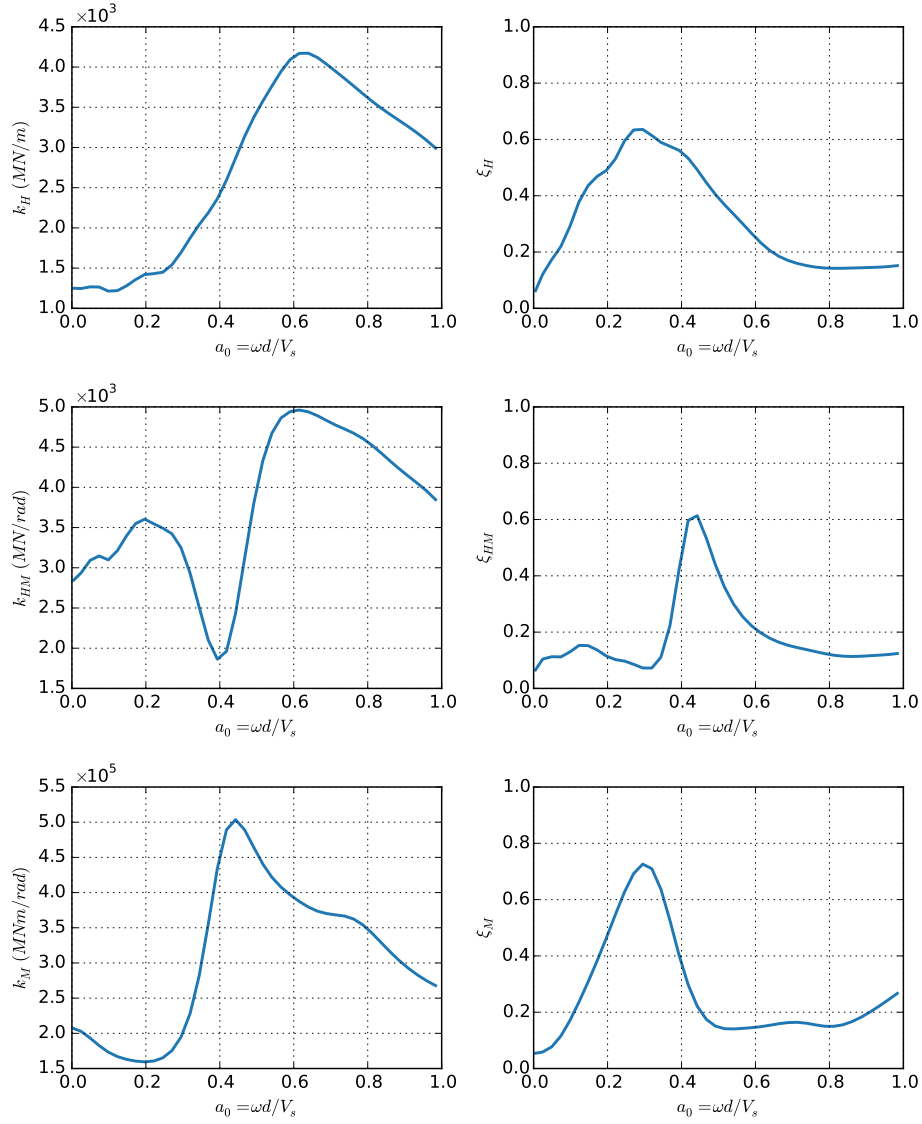


**Figure 2.49:** Dynamic stiffnesses and damping ratios of the 4x4 pile group of floating piles in a homogeneous halfspace given in Fig. 2.48

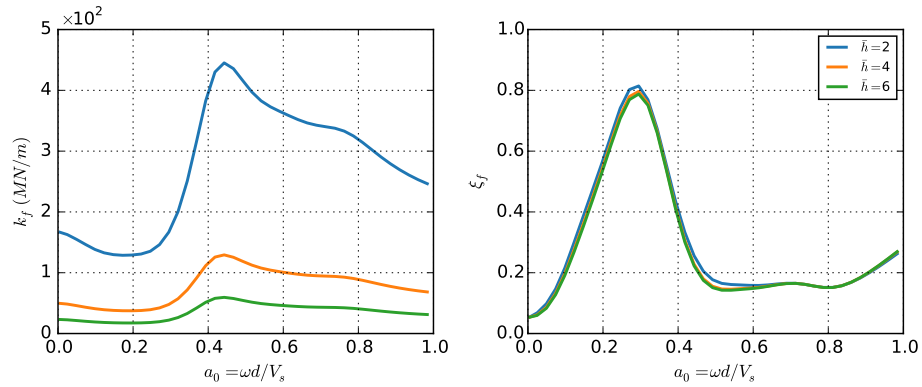


**Figure 2.50:** Effective horizontal dynamic stiffness and damping ratio of the foundation for different slenderness ratios  $\bar{h}$

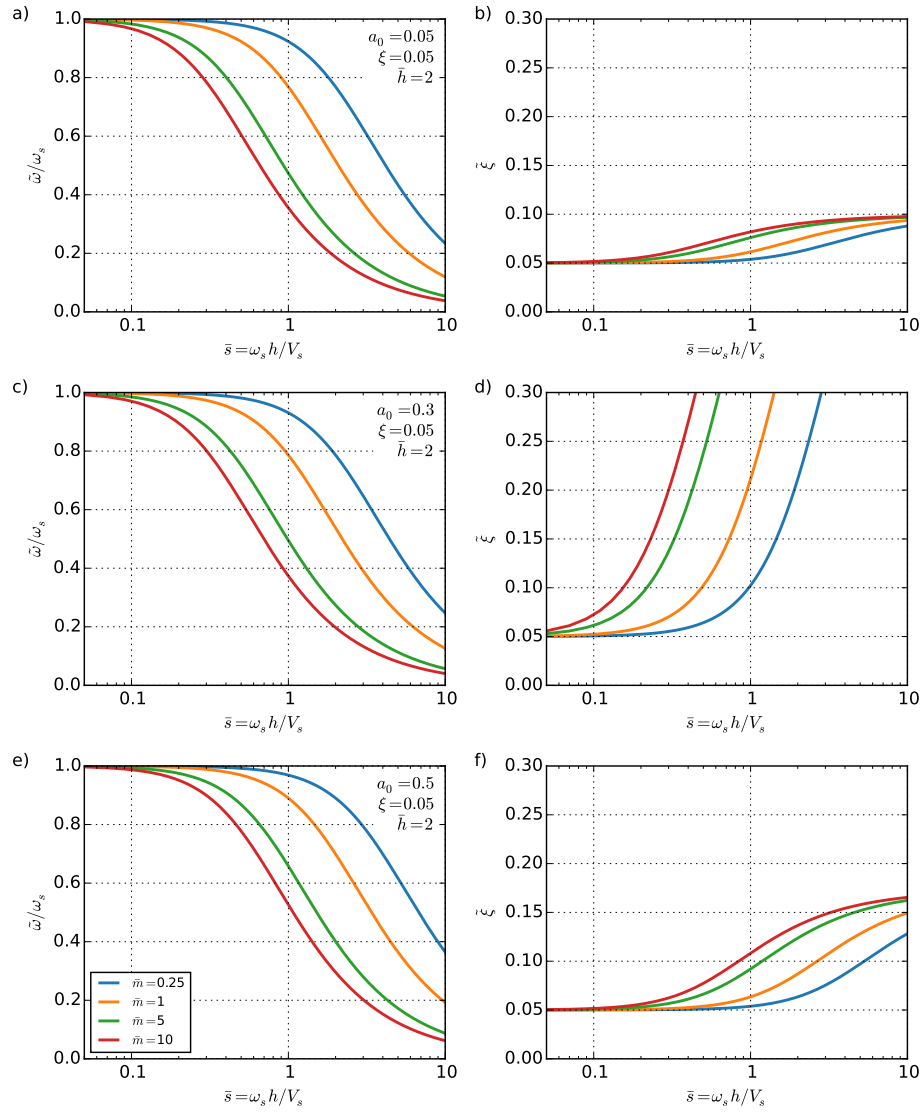


**Figure 2.51:** Study of the influence of inertial SSI in the case of a structure founded on a 4x4 pile group in terms of the properties of equivalent 1-dof system varying mass ratio  $\bar{m}$  for three different exciting frequencies: (a-b)  $a_0 = 0.05$ , (c-d)  $a_0 = 0.3$  and (e-f)  $a_0 = 0.5$

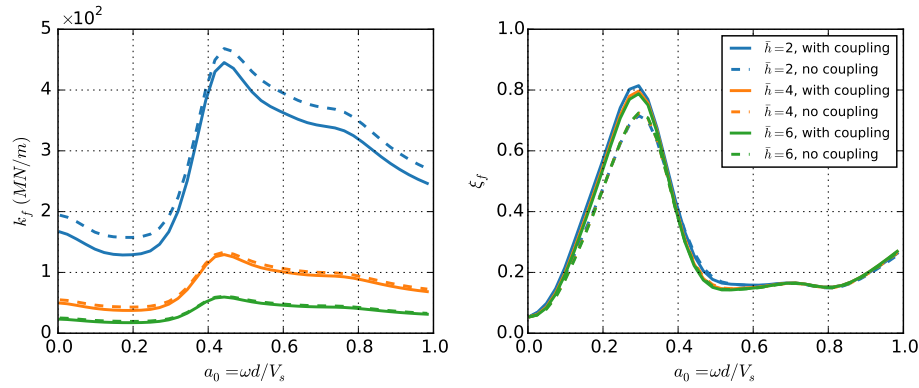


**Figure 2.52:** Impact of coupling terms in the effective horizontal dynamic stiffness and damping ratio of the foundation

It has been shown herein that the influence of the soil-foundation properties on the determination of the fundamental periods is of primary importance for the design of a structure. A shift in the fundamental period can strongly affect the global elastic response of the structure. This is particularly obvious when considering the elastic spectral response of a structure. The maximum spectral acceleration, and thus the force applied to the mass, can be reduced or increased due to this shifting in frequency [79].

## 2.8 Summary

This chapter has focused on few selected topics regarding SSI and dynamic behavior of single piles and pile groups. Numerical, experimental and field observations have been presented and discussed.

A review of previous experimental work dealing with pile foundations (single piles and pile groups) in clay and multilayered soil profiles has been done and shows that the available database is still relatively small and that there are still many configurations that need to be tested in centrifuge, specially those configurations that are closer to real foundation structures found in earthquake prone locations (e.g., end-bearing piles embedded in a weak soil layer).

The question of the numerical methods available for the study of dynamic soil-structure interaction of deep foundations have also been addressed. The classical approaches are introduced and confronted to more recent approaches such as SSI macroelements. The advantages and disadvantages of each method are discussed. It is observed that there is still a lack of practical engineering design methods capable of taking into account the principal features controlling the dynamic response of a pile group foundation, e.g., pile group effects and their variation with loading frequency (pile-soil-pile interaction) and nonlinear behavior.

These issues are addressed in the following chapters.



## Chapter 3

# Experimental work

### 3.1 Introduction

The behavior of soils depends on the history and on the level of stress to which they are subjected. Reproducing the same state of stress is thus a necessary condition to simulate, at the level of the reduced scale model, the real behavior of the real structure in full size (prototype). Centrifuge modeling makes it possible by increasing the body forces applied to the small-scale model. When the additional conditions of similarity are respected in the tests, the results can be directly extrapolated from the model to the prototype scale applying the corresponding scaling factors. An introduction to the principles of centrifuge modeling is given in Appendix A. Other interesting references describing centrifuge modeling are for example [60, 206, 56].

This chapter presents a series of dynamic centrifuge tests conducted on single piles and pile groups configurations under seismic and sinusoidal base shakings.

### 3.2 Dynamic centrifuge experimental set-up and program

#### 3.2.1 Centrifuge tests set-up

A total of nine centrifuge tests were performed in this study (Table 3.1). Two feasibility tests to verify the pile installation procedure and the fabrication and setup of the multilayer soil profile. Two static tests to study the response of a single pile under lateral monotonic and cyclic loading. And five dynamic tests which consist in two tests on the response of a single pile without mass at the pile head, one test with a single pile with a mass at the top and two pile group tests with two different superstructures. Figure 3.1 presents the different model configurations used in the dynamic centrifuge tests.

All centrifuge experiments were performed on the 5.5 m radius centrifuge at Université Gustave Eiffel<sup>1</sup> [40] under 50g acceleration. Dynamic tests were performed with an equivalent shear beam (ESB) container [234, 205, 56] with internal dimensions of 800 mm  $\times$  340 mm  $\times$  416 mm ( $l \times w \times h$ ), which corresponds at 50g to a soil column height of 20.8 m. The loading is applied at the base of the container using an embedded earthquake simulator [30].

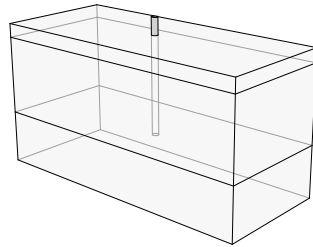
The use of an ESB container and a shaker has important advantages. The equivalent shear beam allows the soil column to deform in shear in a way close to the theoretical case of a soil column subjected to vertical propagating shear waves. Applying the loading at the base of the soil profile allows to effectively take into account kinematic and inertial effects in the loading of the different parts of the system. It is important to note that a pile under earthquake loading is likely to behave differently from the same pile under dynamic loading applied directly at its head. In the latter case, the soil acts as a passive resistor while in seismic events the soil is applying load to

---

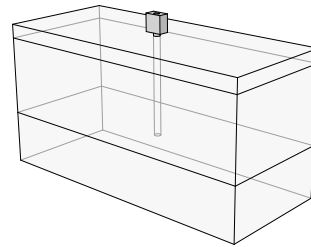
<sup>1</sup>On 1 January 2020, IFSTTAR research institute along with UPEM university, EAVT school of architecture and three engineering schools (EIVP, ENSG and ESIEE Paris) became the Université Gustave Eiffel. IFSTTAR research institute was created in 2011 as a result from the merger of The French National Institute for Transport and Safety Research (INRETS) and the French Central Laboratory of Roads and Bridges (LCPC).

**Table 3.1:** Experimental program

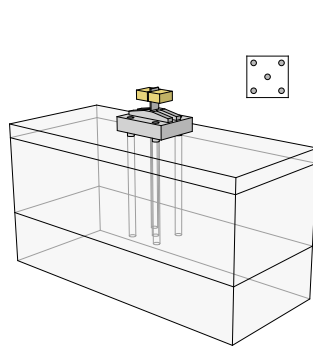
ID	Type	Description
C00	Feasibility	Pile installation test at 1g
C01	Feasibility	Fabrication and instrumentation setup for a multilayer profile for dynamic test
C02	Static	Floating piles under pile head loading
C03	Static	End-bearing piles under pile head loading
C04	Dynamic	Single pile without mass (kinematic loading)
C05	Dynamic	Repeatability test of C04
C06	Dynamic	Single pile with cap mass (kinematic and inertial loading)
C07	Dynamic	Pile group with short superstructure
C08	Dynamic	Pile group with slender superstructure



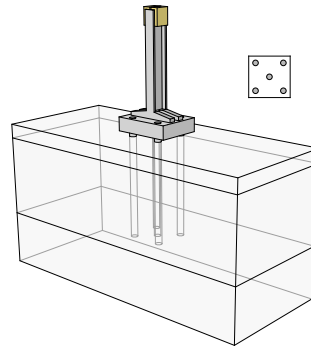
(a) Single pile without mass



(b) Single pile with mass at the top



(c) Pile group with short superstructure



(d) Pile group with tall superstructure

**Figure 3.1:** Model configurations used in the dynamic centrifuge tests

the foundation. This kinematic loading (i.e., pile loading by means of imposed soil displacements) can be important for soft soil profiles and in the case of stratified soil profiles alternating soft and stiff soil layers. In addition, radiation damping is potentially different for both loading cases [228, 10]. It should be noted however that centrifuge tests are not able to correctly reproduce radiation damping which represents one of its main disadvantages.

The case of a single pile without mass at its top (Fig. 3.1a) is aimed to **investigate the performance of single piles under pure kinematic interaction**. The comparison of these tests with the test conducted on a single pile with a mass at the top (Fig. 3.1b) aims to **study the influence of kinematic and inertial interaction in the response of the pile**. A tubular aluminium pile instrumented with strain gauges along the inner side of the pile shaft is used in these tests to record bending moments and axial load along the pile.

In the case of the two dynamic tests conducted with a pile group, the same pile group is used, only the superstructure is changed from one test to another (Figs. 3.1c-d). The objective is to **compare the response of the system with different slenderness ratios of the supported structure**. In addition, the comparison of the response of the piles to that recorded in the case of the tests conducted on single piles without a mass at the top (pure kinematic interaction case) **gives some insight into the importance of kinematic and inertial interactions on the response of the system**. The group of piles used in these two tests consists of five piles with a minimum distance between axes of 3.54 diameters. Three of these piles are instrumented with strain gauges. The layout and the distribution of the piles is indicated in Section 3.2.5.

A dynamic centrifuge test is composed of four elements: the soil column, the pile foundation, the superstructure and the base shaking. They are presented hereafter. The layout of the conducted tests as well as some additional informations are given in Appendix B.

### 3.2.2 Characteristics of the soils used in the tests

A sandy soil and a clayey soil are used in the tests. The clay used is Speswhite kaolin. Clays are low permeability materials which are characterized by a long consolidation time during model preparation. Speswhite kaolin is known to have a relatively high permeability thus reducing the duration of consolidation. It is, therefore, a commonly used material in the preparation of laboratory setups, specially centrifuge tests with a cohesive soil profile [60]. Several experimental studies conducted in the past in the Université Gustave Eiffel centrifuge used this material (e.g., [4, 14]). A physical and mechanical characterization of this material was carried out by Khemakhem [104]. Its main properties are summarized in Table 3.2.

**Table 3.2:** Properties of Speswhite kaolin clay (Khemakhem [104])

Symbol	Material properties	Value
$\gamma_s$	Unit weight of the grains	$26.5 \text{ kN/m}^3$
$w_P$	Plastic limit	30 %
$w_L$	Liquid limit	55 %
$I_P$	Plasticity index	25 %
$C_c$	Compression index	0.33
$C_s$	Recompression index	0.06

The sand used in the tests is Hostun sand HN31 which is a fine and uniform sand with angular to sub-angular grain shape. It has a medium diameter  $D_{50} = 0.35 \text{ mm}$ , and a coefficient of uniformity  $C_u = 1.57$  [15, 16, 17]. As can be seen from the grain size distribution curve in Figure 3.2 it is a uniform graded medium sand. Various measured material properties are listed in Table 3.3. It should be noted that this sand is one of the most used reference materials in many research studies (eg., [124, 58, 8, 210, 211]).



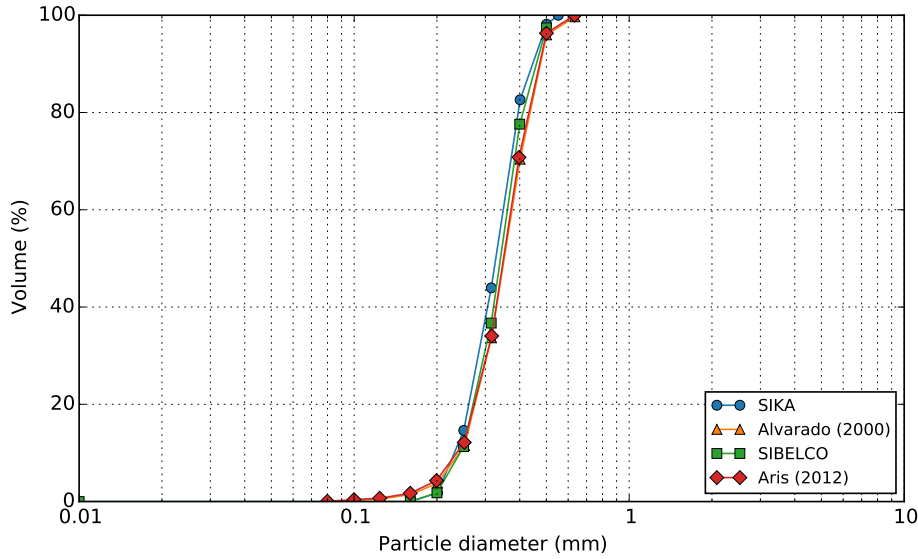


**Figure 3.2:** Grain size distribution of Hostun HN31 sand (data from [15, 8])

**Table 3.3:** Properties of Hostun HN31 sand (Benahmed [15])

Symbol	Material properties	Value
$d_{50}$	Average grain size	0.35 mm
$C_u$	Coefficient of uniformity	1.57
$e_{min}$	Minimum void ratio	0.656
$e_{max}$	Maximum void ratio	1
$\gamma_s$	Unit weight of the grains	26 kN/m <sup>3</sup>
$\gamma_{d,min}$	Minimum dry unit weight	13.047 kN/m <sup>3</sup>
$\gamma_{d,max}$	Maximum dry unit weight	15.696 kN/m <sup>3</sup>

### 3.2.3 Soil profile

The soil profile consists of three horizontal layers of saturated Hostun HN31 sand (bottom), over-consolidated Speswhite kaolin clay (middle) and "dry" Hostun HN31 sand (top). The use of dense sand layer at the bottom allows to reproduce a very common configuration in earthquake prone areas with soft soils at the surface where end-bearing piles are systematically used to transfer loads to a more firm stratum. The choice of using a dense sand layer at the top of the soil profile was done to avoid gap formation between the soil and the pile at shallow depths. In addition, the presence of a top layer of dense sand prevents the clay layer to dry at its surface which would cause an important increase of shear strength profile at shallows depths due to the presence of capillary suction forces. Moreover, this configuration is similar to configurations that are usually found on site because very often a layer of granular material is found on the surface. The theoretical profiles of soil density, effective stress and the overconsolidation ratio are given in Figure 3.3.

The preparation of the soil profile comprises several steps. First, the sand layer at the bottom is air pluviated at 1g gravity level with an automatic hopper system [204]. The relative density  $D_r$  was controlled to be 81%. The main characteristics of the sand at installation are summarized in Table 3.4. The sand layer at the bottom of the container was vacuum saturated with water to avoid desaturation at the bottom of the clay layer and liquefaction of the sand layer (due to scaling laws the simulated prototype has thus an hydraulic conductivity 50 times higher than at the prototype scale for the same sand).

The overconsolidated Speswhite kaolin formation is prepared in three layers and subjected to 160 kPa preloading pressure under 1g gravity field. The number and the thickness of the clay

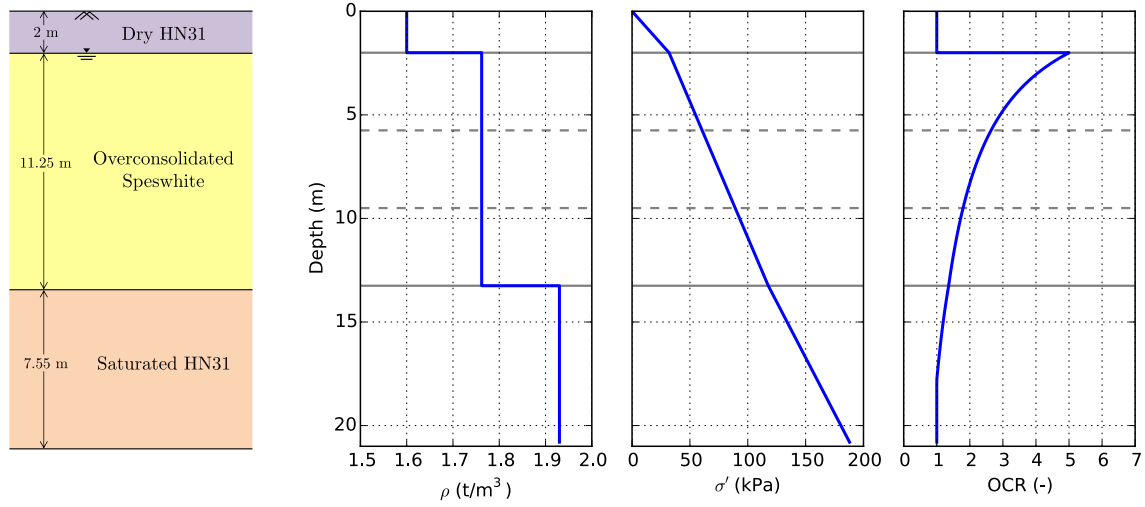


**Figure 3.3:** Theoretical profiles of soil density, effective stress and overconsolidation ratio for the soil profile used in the centrifuge tests

**Table 3.4:** Characteristics of Hostun sand HN31 at installation

Symbol	Description	Value
$I_D$	Relative density	0.81
$\gamma_d$	Unit weight of dry soil	$15.113 \text{ kN/m}^3$
$e$	Void ratio	0.721

layers was chosen according to the consolidation pressure that is applied, the dimensions of the container and the total amount of time needed for consolidation. The overconsolidation ratio  $OCR$  is obtained as the ratio between the preconsolidation stress  $\sigma'_c$  applied at 1g and the effective stress at 50g  $\sigma'_{v,50g}$ :

$$OCR = \frac{\sigma'_c}{\sigma'_{v,50g}} \quad (3.1)$$

The  $OCR$  values in the middle of the three clay layers are 1.55, 2.13 and 3.42 respectively, from bottom to the top of the clay formation (Fig. 3.3). For each one of the clay layers a clay slurry with a target water content of 75% is prepared mixing clay powder with water to facilitate its installation in the ESB container (Fig. 3.4a). The main characteristics of the clay at installation are summarized in Table 3.5. The new clay layer is subjected to the 160 kPa preloading pressure using a hydraulic cylinder under 1g gravity field (Fig. 3.4b). As soon as the consolidation of this new layer is completed, a new layer of clay is poured on it and the same process of consolidation is repeated two more times. It should be noted that prior to the installation of a new clay layer sensors are installed at the top of the already consolidated layer (Fig. 3.4c).

**Table 3.5:** Characteristics of Speswhite kaolinite at installation

Symbol	Description	Value
$\sigma'_v$	Preconsolidation pressure	$160 \text{ kPa}$
$w$	Water content (desired)	75%
$e_0$	Initial void ratio (clay slurry)	1.988

Once the overconsolidated speswhite formation is correctly installed and consolidated in the ESB container, the soil profile is unloaded and the dense Hostun HN31 sand layer on top is air

pluviated. The relative density is controlled to be also 81% for this layer. The soil profile is left 4 days at rest for the swelling process to stabilize [104]. The corresponding single piles or pile groups are installed at 1g before loading the container in the centrifuge. More details about the installation method of piles and pile groups are given in §3.2.6.

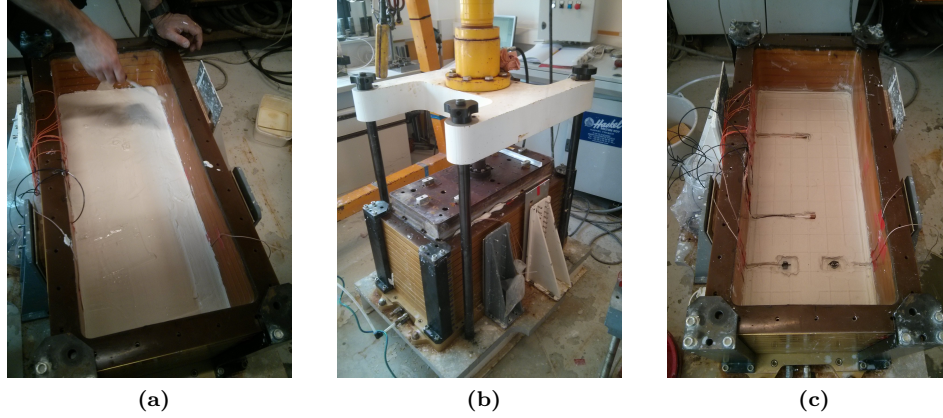


**Figure 3.4:** Preparation steps of a clay layer: (a) installation of the clay slurry in the ESB container, (b) application of preloading pressure using a hydraulic cylinder and (c) installation of sensors prior to the installation of a new clay layer

The soil profile is subjected to four 1-50-1g cycles (increase of the centrifuge acceleration up to 50g, 5 minutes spin at 50g and descent to 1g). The application of these cycles is based on the work of Khemakhem [104] who observed that the evolution of undrained shear stress profile in the first meters of kaolin soil profile was faster than when spinning at 50g without going back to 1g. Several comparison tests conducted by this author showed that the use of four 1-50-1g cycles was enough to get a relative constant undrained shear strength soil profile in clay and that the application of additional cycles conducted to small variations of the undrained shear stress profile. Given that the above-mentioned tests were also conducted at Université Gustave Eiffel centrifuge, this recommendation was also done by the laboratory technical staff. In addition, the application of 1-50-1g cycles has also practical advantages, allowing checking of all the setup (e.g., verification of electrical connections of instrumentation) and the installation/removal of the CPT measurement equipment which, given the centrifuge shaker characteristics, cannot be in place when the shaker is running.

After these series of 1-50-1g cycles, the soil profile was subjected to a stabilization phase at 50g of 2 hours before the application of dynamic loads that are applied one after the other, keeping enough time between two inputs to allow pore pressure build-up induced by base shaking to dissipate.

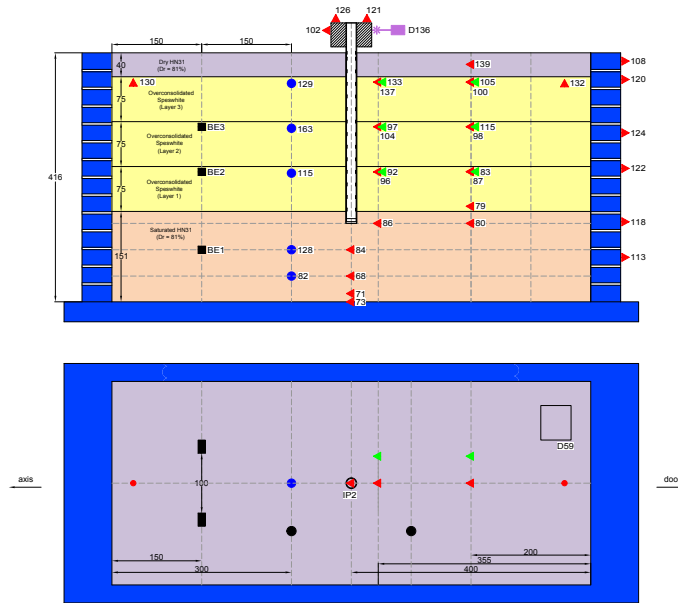
Several choices regarding the soil profile that is used in the tests and its fabrication merit further explanation. The first question concerns the use of water as pore fluid instead of a fluid with higher viscosity. As pointed out by Kutter [113], the time scale factor conflict between diffusion (consolidation) and dynamics phenomena is only important when both time scales are of the same order. The effect of time scale conflict is thus negligible for saturated clay that will not consolidate significantly during the base shaking. Banerjee [10] also pointed out the difficulties to replace water by another pore fluid when working with clay. Problems to consolidate the soil profile appear with much longer consolidation time and, depending on the viscous fluid that is used, the clay-water chemistry can also be modified which may affect to some extent the soil behavior. The laboratory tests conducted by the author on the behavior of Malaysian kaolin clay suggested that the rate-dependent viscous damping of the soil is likely to be much smaller than the hysteretic strain-dependent damping. The study conducted by Mortezaie [147] shows a similar trend for Speswhite kaolin clay. The dense sand layer at the bottom of the soil profile is also saturated with water to avoid desaturation at the bottom of the clay layer. Given the construction process of the

soil profile it is technically impossible to use a pore fluid different than the one used for clay. Due to scaling laws the diffusion scale factor is thus not correctly reproduced and the pore pressure increment dissipation is in this case 50 times faster than at the prototype scale for the same sand. This implies that the diffusion phenomenon (consolidation) is much important during the shaking but at the same time it limits the risk of liquefaction. Given that this layer acts as the bearing layer for the piles, avoiding liquefaction problems is not only convenient but necessary to correctly simulate the behavior of prototype models with piles embedded in dense, non liquefiable, soils.

The second question that needs to be discussed is the evolution of the soil profile at 50g, specially in the case of the clay layer. The undrained cohesion in the clay increases with time when the centrifuge acceleration is kept constant at 50g. In fact, as pointed out by Khemakhem [104], under 50g centrifuge acceleration the soil profile doesn't stop to evolve as a consequence of two opposed mechanisms: the settlement due to the increase of the own weight and the expansion due to the reduction of the suction and rebalancing of the interstitial pressures. Therefore, to ensure that the same soil profile is found in the different tests at the beginning of the base shakings, all tests are carried out after the same stabilization time at 50g (2 hours) to limit the evolution of undrained cohesion with time.

### 3.2.4 Instrumentation

The conducted dynamic tests were highly instrumented in number and in the type of instrumentation: accelerometers, pore pressure transducers, bender elements, laser sensors and instrumented piles. Figure 3.5 shows the layout with the location of the different measurement devices in one of the tests.



out of order during the tests due to an excessive differential settlement between the cable and the sensor body and to short circuits caused by ingress of water. In order to overcome these problems, a review of the installation method and waterproofing of accelerometers installed in the soil profile was needed. Similar problems have also been reported in the literature (e.g., [10]).

Pore pressure transducers were installed in all the dynamic tests but the recordings should be treated and interpreted very carefully because it is not sure that the sensors remained fully saturated during their installation in the soil profile. In addition to this, several problems have already been identified in the literature regarding pore pressure measurements in clay. The arching effect of the clay around the pore pressure transducers reported by Kutter *et al.* [112] along with the very short response time needed introduce additional difficulties to the interpretation of this kind of recordings [228, 11]. However, the pore water pressure generation in the clay layer is expected to be small [223].

Three pairs of bender elements are installed in the soil profile at 6 m, 9.75 m and 15.6 m depths at the prototype scale (two inside the clay layer formation and the third pair in the saturated dense sand layer at the bottom). They allow the calculation of the shear wave velocity of the soil for very low values of distortion.

Instrumented aluminium tubular piles closed at their bottom were used in the tests. They are equipped with 14 equally spaced half-bridge strain gauges along the inner side of the pile shaft in order to measure bending moment (see Fig. C.5). The uppermost strain gauge are located at the soil surface level. Axial forces in the pile are measured by means of two additional half-bridge strain gauges placed near the tip of the pile and at the level of soil surface. Regarding its flexural rigidity the pile is representative of a reinforced concrete prototype pile of almost 1 m of external diameter. The properties of the piles are given in Table 3.6. Details about the installation method are given in §3.2.6.

**Table 3.6:** Properties of the instrumented piles

Property	Hollow aluminium (model scale 50g)	Reinforced concrete (prototype scale 1g)
Embedded length	285 mm	14.25 m
External diameter	18 mm	0.977 m
Internal diameter	16 mm	-
Length	335 mm	16.75 m
Young modulus	74 GPa	20 GPa
Flexural rigidity	$1.43 \times 10^{-4} \text{ MNm}^2$	$8.95 \times 10^2 \text{ MNm}^2$
Yield moment	$5.27 \times 10^{-5} \text{ MNm}$	6.59 MNm

Accelerometers and laser sensors were also installed to monitor the behavior of the pile head, the pile cap and the superstructure. The measurements from the high speed laser used to monitor the response of some of the system parts are also used to verify the displacements calculated by double integration using the acceleration records.

### 3.2.5 Properties of the single pile cap, the pile group cap and the superstructures

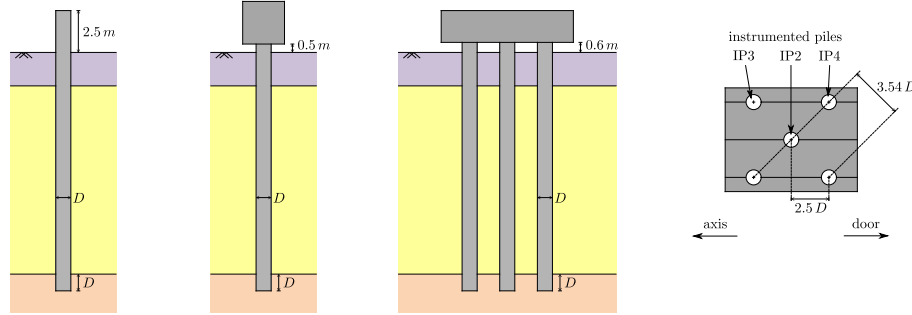
Several are the additional components used in some of the dynamic tests. They are introduced and described in this section.

The mass at the top of the single pile in the dynamic test C06 is reproduced by means of a single aluminium cap that is attached to the pile using several bolts. The properties of this cap are given in Table 3.7. To avoid soil-cap interaction, the pile cap stands at a certain distance above the ground surface. This gap is of 10 mm at model scale (0.5 m at prototype scale) (Fig. 3.6).

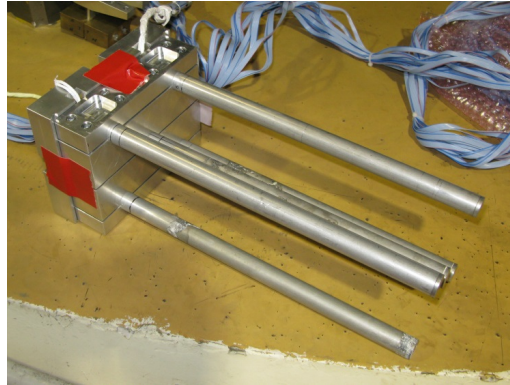
Piles in the pile group used in tests C07 and C08 are rigidly connected together through a stiff pile cap made of aluminium alloy. The pile cap is divided in four pieces connected by means of bolts strategically placed to ensure the same amount of tightening and thus the same rotational

**Table 3.7:** Characteristics of the mass at the top of the single pile

Property	Model scale 50g	Prototype scale 1g
Pile cap dimensions ( $l \times w \times h$ )	50 mm $\times$ 30 mm $\times$ 51 mm	2.5 m $\times$ 1.5 m $\times$ 25.5 m
Total mass	189 g	23.625 t

**Figure 3.6:** Detail of spacings, gap, mass at the top of the single pile (C06 test), pile group cap and distribution of piles in pile group (C07 and C08 tests)

restraint conditions for all piles in the pile group. Figure 3.7 shows the assembly of piles and the pile group cap prior to their installation in the container. Table 3.8 summarizes the main properties of this cap. The distribution of the piles in the pile group is indicated in Figure 3.6.

**Figure 3.7:** Assembly of piles and pile group cap

As in the case of the mass installed at the top of the single pile in C06 tests, the pile cap is kept 12 mm above the ground surface at model scale (0.6 m at prototype scale). This configuration differs to recent pile group tests conducted in clay soils that model a pile group with the pile cap in contact or embedded at the soil surface, i.e., [10, 11, 12, 238]. Due to the friction between the soil and the cap, the lateral resistance of the pile can be significant making it impossible to distinguish the part of the foundation-cap response that is due to the action of piles and that generated by cap-soil interaction.

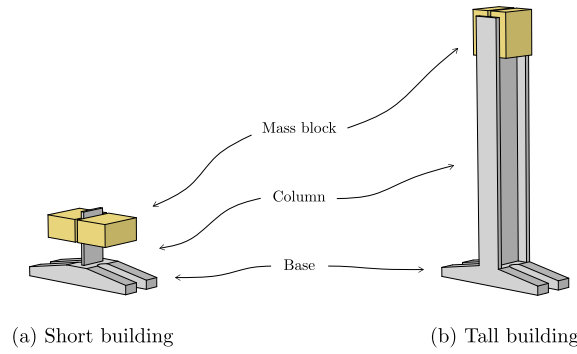
In order to study the influence of the position of the gravity center on the response of structures supported by the pile group foundation, two types of superstructures with different slenderness ratios are used in C07 and C08 tests: a short and a tall building, respectively. The superstructures are simple and they can be assimilated to single degree-of-freedom systems (Fig. 3.8). The design criteria was that (1) both superstructures should have similar mass in order to transmit to the soil similar levels of stresses under static conditions and (2) they should have the same resonant frequency with fixed base condition while having a different slenderness ratio. The fixed-base frequency of the superstructures was chosen to be 1.5 Hz at prototype scale. The fundamental



**Table 3.8:** Characteristics of the pile group cap

Property	Model scale 50g	Prototype scale 1g
Pile cap dimensions ( $l \times w \times h$ )	$158\text{ mm} \times 124\text{ mm} \times 38\text{ mm}$	$7.9\text{ m} \times 6.2\text{ m} \times 1.9\text{ m}$
Cap mass	$1.56\text{ kg}$	$195\text{ t}$

fixed-base frequency of the superstructures was measured and corresponds to 1.54 Hz in the case of the short building and to 1.5 Hz in the case of the tallest one. Some of their characteristics are summarized in Table 3.9. The installation of the superstructures takes place once the pile-group is already installed in the soil profile. The connection between the superstructure and the pile-group cap is done using bolts.

**Figure 3.8:** Superstructures used in the experiments**Table 3.9:** Characteristics of the superstructures

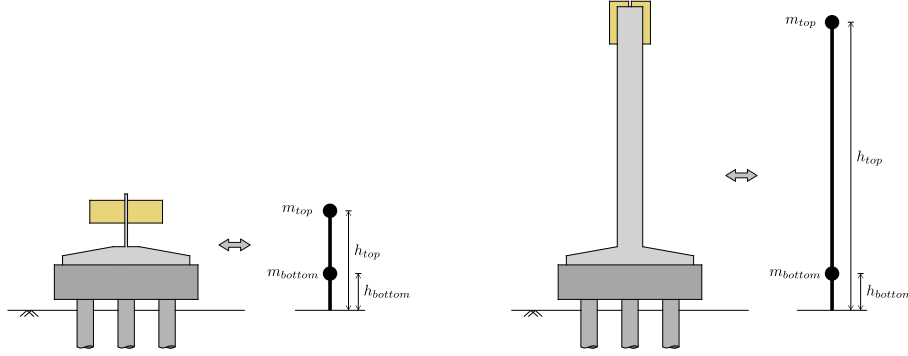
Property	Short superstructure		Tall superstructure	
	Model scale	Prototype scale	Model scale	Prototype scale
Mass block atop	$0.8\text{ kg}$	$100\text{ t}$	$0.7\text{ kg}$	$87.5\text{ t}$
Column + base mass	$0.292\text{ kg}$	$36.5\text{ t}$	$0.532\text{ kg}$	$66.5\text{ t}$
Total mass	$1.092\text{ kg}$	$136.5\text{ t}$	$1.232\text{ kg}$	$154\text{ t}$
Measured fixed-base frequency	$77\text{ Hz}$	$1.54\text{ Hz}$	$75\text{ Hz}$	$1.5\text{ Hz}$

The cap-superstructure system can be idealized as a two degree-of-freedom structure (Fig. 3.9). Following the redistribution of the mass suggested in [117] between the top and the bottom mass of the 2 DOF equivalent system, the characteristics listed in Table 3.10 are found. The top mass of the equivalent system accounts for the mass of the block atop of each one of the superstructures plus 23% of the column mass. The bottom mass takes into account the rest 77% of the column mass and the mass of the pile group cap. The heights  $h_{top}$  and  $h_{bottom}$  are given from the ground surface.

More information about the pile group cap and the superstructures used in these tests is given in Appendix C.

### 3.2.6 Installation of single piles and pile groups

Different techniques are used in practice to install piles. They are classified into two groups depending on whether there is displacement of the surrounding soil or not (pile driving vs boring methods). In the case of centrifuge modeling, it is possible to install the piles in-flight either

**Figure 3.9:** Cap-superstructure equivalent 2DOF models**Table 3.10:** Characteristics of the cap-superstructure equivalent 2DOF models (at prototype scale)

Property	Short superstructure	Tall superstructure
Top mass $m_{top}$	107.5 t	102 t
Bottom mass $m_{bottom}$	224 t	247 t
Height $h_{top}$	5.35 m	15.7 m
Height $h_{bottom}$	1.45 m	1.45 m
Slenderness ratio ( $h_{top}/B$ )	1.2	3.5

$B$  corresponds to the distance axis-to-axis between the piles in the outer part of the pile group, i.e.,  $B = 5D$

by driving them slowly with an hydraulic actuator or using a dropping hammer. This method is recommended for studies on the behavior of displacement piles, particularly when axial forces are important, because the stresses in the surrounding soil are correctly simulated during the installation [104]. However, the installation of piles in-flight is not yet possible for dynamic studies because of several practical limitations, e.g., there is no place left to install the devices for pile installation once the shaker and the ESB container are in the machine and it would be complicated to ensure that the instrumentation cables in the piles are not cut out by the hydraulic actuator or the dropping hammer.

The installation of the piles at 1g is therefore the only possibility in this case. Installing the piles by boring at 1g (to reproduce non-displacement piles) is not possible without complications due to the presence of the sand layer on the surface. In addition, the use of pre-augered pile holes may result in air pockets trapped at the tip of the piles [11].

In order to limit the complexity of the installation method, but also to ensure the reproducibility of the assembly, the single piles and the pile groups were installed at 1g gravity level using a hydraulic actuator (Fig. 3.10). A low driving speed of 0.1 mm/s was used to allow dissipation of pore pressure in the surrounding soil. The piles are embedded one diameter in the saturated sand layer. Piles used in this study are thus end-bearing piles. Regarding the question of the installation of the pile groups, it should be noted that the piles along with the cap were assembled prior to their installation in the soil profile. All the piles in the pile group are therefore pushed into the soil at the same time.

The installation of the model piles at 1g does not accurately model the effects of the pile installation method on the soil behavior. Wang *et al.* [223] pointed out that a pile driven at 1g probably acts more like a drilled shaft than a driven prototype pile, in terms of the lateral stress state around the pile. In the case of granular soils, the study conducted by Dyson and Randolph [54] showed a certain influence of the installation mode at shallow depths and that diminishes with depth. However, Remaud [180] found small differences between piles installed at 1g and in-flight in terms of lateral response. This observation was also confirmed by Rakotonindrianna [178]. In the



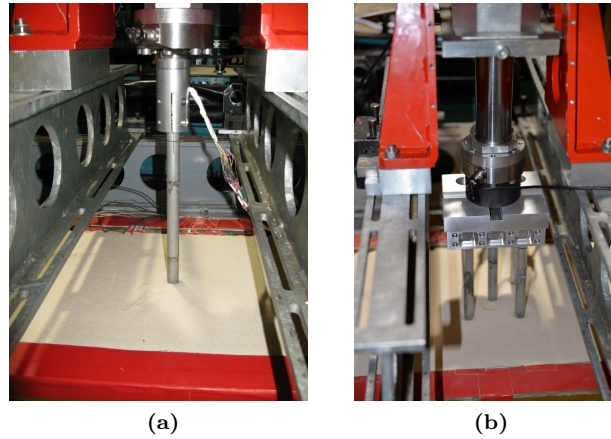


**Figure 3.10:** Pile installation at 1g: (a) single pile and (b) pile group

case of clay soils, Craig [41] showed that driving piles at 1g instead of in-flight had little impact on the bearing capacity and on the behavior of pile foundations. This is explained by the fact that the volume change in clays during pile driving is small compared to sands and thus the effect of excess pore water pressures generated during pile driving is, therefore, minimal [198].

The installation method used in this study has been tested in the feasibility tests, driving two test piles at 1g. CPT measurements were made at 4 and 10 diameters from the pile. These measures showed no significant disturbance in the vicinity of the piles due to their installation. The comparison of CPT measurements made before and after the pile installation indicate the absence of a significant increase in the value of  $C_u$  in the soil in the proximity of the piles. This finding is interesting particularly when dealing with pile groups though no real information is available about the stress state of the soil in between the piles of the pile group.

### 3.2.7 Input signals

A series of 14 base shakings has been employed in the tests. Two types of input have been selected: sines with tapered parts and real broadband earthquake ground motions – Landers 1992 (Lucern Valley station) and Northridge 1994 (Tarzana station) records. Figure 3.11 presents the time and frequency representations of the real earthquake ground motions and of one of the applied sines with tapered parts.

Several limitations need to be respected when selecting and designing the input signals to be used with the shaker at Université Gustave Eiffel laboratory [30]. The frequency content of the signal must be limited within the working frequency range of the shaker, which corresponds at 50g (at the prototype scale) to a frequency from 1 Hz to 4 Hz in the case of sinusoidal signals; and from 0.4 Hz to 7 Hz for a real earthquake input. In addition, the maximum displacement, velocity and acceleration of the shaker is set to  $\pm 5\text{ mm}$ ,  $1\text{ m/s}$  and 50% of the g-level, at model scale, respectively. In order to be in the capacity range of the shaker earthquake signals have been filtered outside the frequency range of 0.4-6 Hz.

The two main objectives behind the use of real broadband earthquakes are the determination of the response frequencies of the soil column and of the soil-pile-superstructure system (using mostly the low intensity inputs) and to analyze the performance of single piles and pile groups when subjected to multi-frequency base shaking. The main objectives of the tests using the sinusoidal signals are to highlight the effect of the input frequency and of its amplitude on the performance of single piles and pile groups. In order to accomplish this task several frequencies are used, 1 Hz, 1.8 Hz, 2.4 Hz and 3.2 Hz. They are expected to cover a broad range at each side of the fundamental response frequency of the soil column (estimated numerically from an elastic model at about 2.62 Hz). Strictly speaking, a parametric study on the effect of frequency is not feasible due to the interconnection between the parameters that define a sinusoidal input. In this study

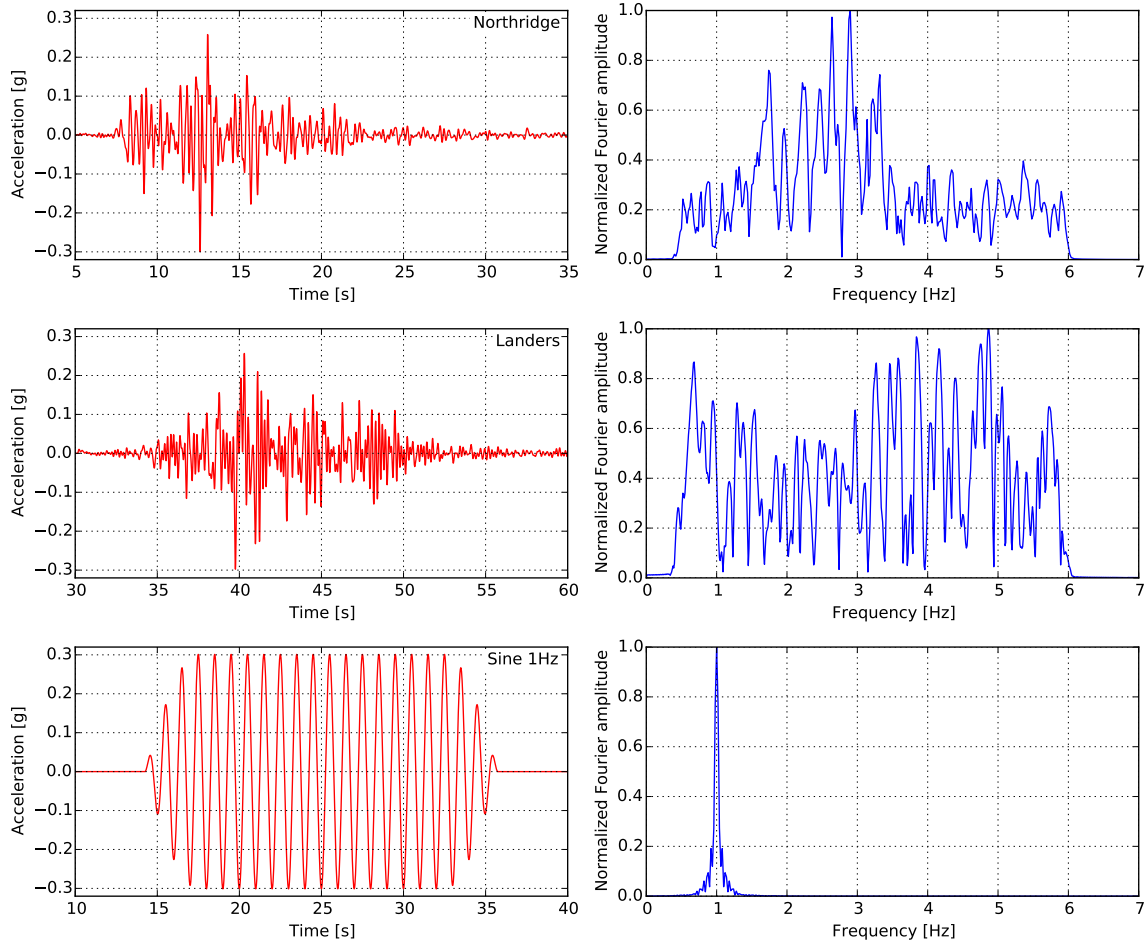


**Figure 3.11:** Time and frequency representations of the real earthquake ground motions and of the 1Hz sine base shakings

the choice is made to keep the number of cycles and the PGA constant. This choice implies that the PGV,  $I_A$  and the duration are not the same.

Scaling of earthquake signals in terms of  $\text{PGA}^2$  (peak ground acceleration) was performed by applying linear scale factors to the acceleration-time history of the motion. The characteristics of these signals are given in Table 3.11 (PGA and PGV: peak ground acceleration and velocity,  $I_A$ : Arias Intensity).

It is found that there is not yet a consensus in the scientific literature as to the ideal parameter to estimate the intensity of a seismic motion. Some authors consider that the most suitable is the Arias Intensity while others highlight the PGV or the PGD for strong earthquakes and the PGA for weak earthquakes [9].

The following criterion was applied in the choice of the order of application of the seismic inputs: earthquake ground motions are applied before the sines (the sinusoidal signals are generally more destructive) and in increasing order of the Arias Intensity (two weak and two strong earthquake ground motions). Then the sines are applied in an order which is a function of the difference between the frequency of the signal and the response frequency of the soil column (estimated numerically from an elastic model at about 2.62 Hz). Two weak seismic motions are applied at the end to compare the response of the system before and after strong excitations. Each base shaking was separated by sufficient time for dissipation of any shaking-induced excess pore water pressure.

It should be noted that the sine 1 Hz 0.3g base shaking was only applied for the two first

<sup>2</sup>In this case, the PGA corresponds to the maximum acceleration applied at the level of the shaking table, that is the base of the soil column.

**Table 3.11:** Characteristics of the reference input signals (prototype scale)

#	Input	PGA (g)	PGV (m/s)	$I_A$ (m/s)	Duration (s)
1	Northridge	0.05	0.037	0.025	11.163
2	Landers	0.05	0.051	0.031	11.505
3	Northridge	0.3	0.220	0.897	11.163
4	Landers	0.3	0.306	1.109	11.505
5	Sine 1 Hz	0.1	0.157	1.417	16.348
6	Sine 3.2 Hz	0.1	0.049	0.443	5.112
7	Sine 1.8 Hz	0.1	0.087	0.787	9.089
8	Sine 2.4 Hz	0.1	0.065	0.588	6.808
9	Sine 1 Hz	0.3	0.470	12.760	16.348
10	Sine 3.2 Hz	0.3	0.146	3.986	5.112
11	Sine 1.8 Hz	0.3	0.261	7.087	9.089
12	Sine 2.4 Hz	0.3	0.195	5.295	6.808
13	Northridge	0.05	0.037	0.025	11.163
14	Landers	0.05	0.051	0.031	11.505

dynamic tests conducted on a single pile without mass at the top (C04 and C05). An important amplification phenomenon was observed in those tests that resulted in excessive bending moments in the pile (up to 28% of the yield moment of the pile section which was estimated at 6.59 MNm). In order to avoid damage of the instrumented piles, particularly in the case of C06 test, it was decided not to apply this base shaking to the following dynamic tests (C06 to C08).

### 3.3 Repeatability of the tests

To avoid confusion in scales and dimensions, all the experimental results in this and the following sections are given using prototype scale units (unless otherwise indicated).

Given the complexity of fabrication of the soil profile it is essential to verify that the procedure of reconstitution of the soil profile enables to reproduce a soil profile with similar characteristics. Several tests have been performed in order to address this point. In addition, the response of the tested systems depends also on the seismic input. Consequently, prior to analyze and to compare the results of different tests it is also convenient to evaluate the repeatability and the quality of the seismic input applied by the shaker at the base of the container. Both issues are addressed in this section.

#### 3.3.1 CPT profile

To ensure that the properties of the soil profile in the tests are the same, in-flight cone penetration testing (CPT) is used. Several CPT tests were performed at the arrival to 50g. The undrained strength of Speswhite kaolin clay layer is calculated from the tip resistance using the following empirical correlation [60]:

$$C_u = q_c/18.5 \quad (3.2)$$

The undrained strength profiles from different tests are compared in Figure 3.12. Note that the given profiles are only valid for the clay layer because the coarse-grained layer behavior cannot be interpreted in terms of total stresses and attributing an undrained strength to them is meaningless. It is observed that the undrained shear strength increases with depth from an approximate value of 22 kPa at the top of the clay layer to an average value of 40 kPa at the bottom.

Results show a **low dispersion of the profile for the first meters of the clay layer**. This is important in the presence of inertial interaction effects. The soil at shallow depths being

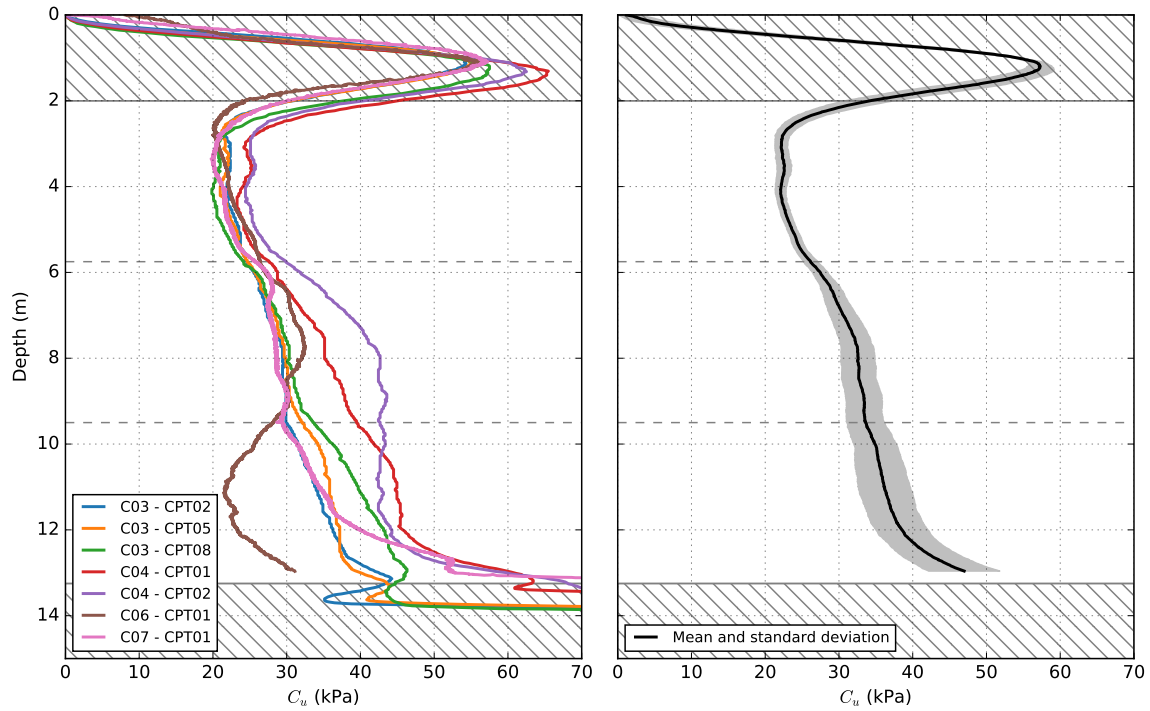


Figure 3.12: CPT tests at arrival to 50g

subjected to a less important state of confinement, the failure characteristics of these soils impact more strongly on the response of the system under high load levels (there is more potential to develop plastic deformations).

**In the lower part of the clay layer however, some discrepancies are observed** between the results from different tests, specially for C04 and C06 tests. This may be explained by some differences between the tests. It was observed that the elapsed time between the unloading of the container and the CPT measurement has no significant result on the measurement. The same applies to the cumulated time at 50g prior to the measurement. However, **a certain correlation has been observed between the number of 1g-50g-1g cycles done prior to the CPT measurement.** In the case of C04 test, due to several problems with the recording device it was necessary to spin-up and down the centrifuge several additional times in order to detect the origin of the problem. These extra 1g-50g-1g cycles seem to have had an impact the CPT measures in the case of C04 test. Some additional data about the differences between the CPT measurements is given in Appendix D.1.

For the C06 test, a different CPT device has been used. It should be noted that the recorded data was in this case too noisy (a correction has been applied to the curve in the plot) which may indicate some problems in the measurement. In addition, the soil at the bottom of the clay layer is close to a saturated sand. Even if the clay layer has been consolidated after installation, some questions could be asked about the chemical equilibrium between the water in the clay and that in the sand.

**The undrained shear strength profile can be used as a first estimate of the maximum acceleration that can be transmitted to the soil surface by the soil profile [191, 166].** Let's consider free-field conditions and a vertically propagating shear wave. In this case, the maximum shear stress  $\tau_{max}$  at a depth  $h$  can be estimated using:

$$\tau_{max} = \rho h a_{max} \quad (3.3)$$

In which  $\rho$  is the mass density and  $a_{max}$  is the maximum horizontal acceleration at the ground surface. As the shear stress reaches the undrained shear strength of clay at some point of the clay

layer, the soil yields and thus it is not able to transmit the input accelerations, which results in a deamplification of the signal at shallower depths of the soil profile.

Let's consider in what follows an average undrained shear strength profile increasing linearly from 22 kPa at the top of the clay layer to a value of 40 kPa at the bottom and a mass density  $\rho = 1.762 \text{ t/m}^3$ . The profiles of maximum shear stress given by Equation (3.3) for several values of the maximum acceleration at the soil surface are compared to the undrained strength profile in Figure 3.13. From this comparison, **it can be deduced that the soil layer would not be able to transmit an acceleration higher than 0.175g to the soil surface, otherwise the clay layer is expected to fail under excessive shear stress** and thus plays a fuse role in the response of the system. This result is confirmed in the analysis of the soil column response (see §3.4.1).

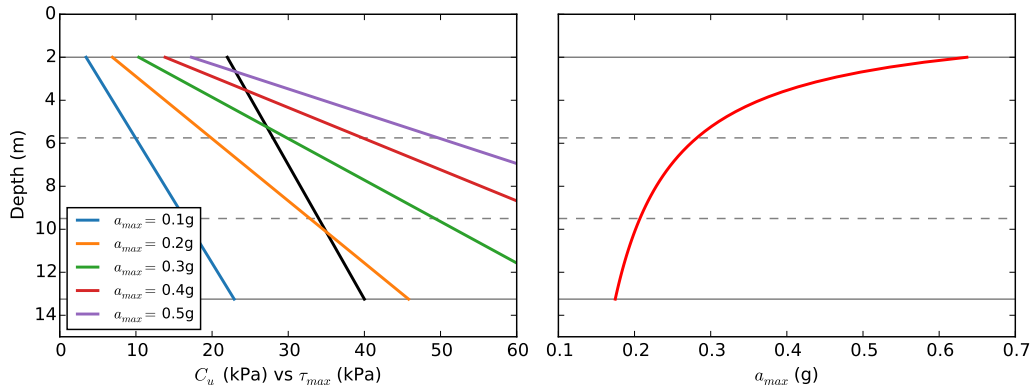


**Figure 3.13:** Comparison of undrained shear stress profile to theoretical estimation of maximum shear stress and maximum acceleration at the soil surface depending on the localization of the shear failure in the clay layer

It should be noted however that this formula is only valid when dealing with constant soil profiles under free-field conditions. The presence of a dense sand layer at the top of the soil profile, the variation of the undrained shear strength of clay with depth and the use of a flexible shear beam container (which is not able to fully reproduce exact free-field conditions) may have an important effect on the result. Nevertheless, it can be used as a first estimate of the order of magnitude of the maximum acceleration that can be transmitted to the soil profile by the soil profile.

### 3.3.2 Shear wave velocity profile

The maximum shear modulus  $G_{max}$  profile at small-strain level is a key parameter for geotechnical problems. It is common to calculate the  $G_{max}$  profile using the values of the shear wave velocity at different soil layers. This is done in centrifuge tests either by using the time delay (cross-correlation) of the signals between pairs of accelerometers in the soil when subjected to very low intensity shaking (i.e., the material behavior remains in the elastic or in the near elastic range) or by using bender element measurements.

The bender element system used at Université Gustave Eiffel has been developed based on the one presented by Brandenburg *et al.* [21]. The experimental set up enables the determination of the shear wave velocity at 3 different depths based on the travel time measurement between the transmitter and the receiver of each pair of bender elements. The ambient vibrations during spinning of the centrifuge that come from the dither of the shaker need to be reduced by digital filtering and signal stacking in order to improve the signal to noise ratio. The first arrival method is used to identify the traveling time (Mitaritonna *et al.* [144]).

The shear wave velocities for the “virgin state” are obtained from measurements performed just before the first base shaking at 6 m, 9.75 m and 15.6 m depths. The obtained values are compared to a theoretical profile in Figure 3.14. The formula proposed by Hardin & Drnevich [85] is used to estimate the maximum shear modulus profile:

$$G_{max} = 625 \frac{OCR^k}{0.3 + 0.7e^2} \sqrt{p_a \sigma'_m} \quad (3.4)$$

where  $OCR$  is the overconsolidation ratio,  $\sigma'_m$  is the mean effective stress and  $e$  is the void ratio. The value of  $k$  depends on the plasticity index. The shear wave velocity can be determined from the following equation:

$$V_s = \sqrt{G_{max}/\rho} \quad (3.5)$$

Using the density of dry soil for the "dry" HN31 sand layer at the top ( $\rho_d = 1.6 t/m^3$ ) and the density of saturated soil for the clay ( $\rho_{sat} = 1.76 t/m^3$ ) and the dense HN31 sand layer ( $\rho_{sat} = 1.93 t/m^3$ ) at the bottom of the soil profile.

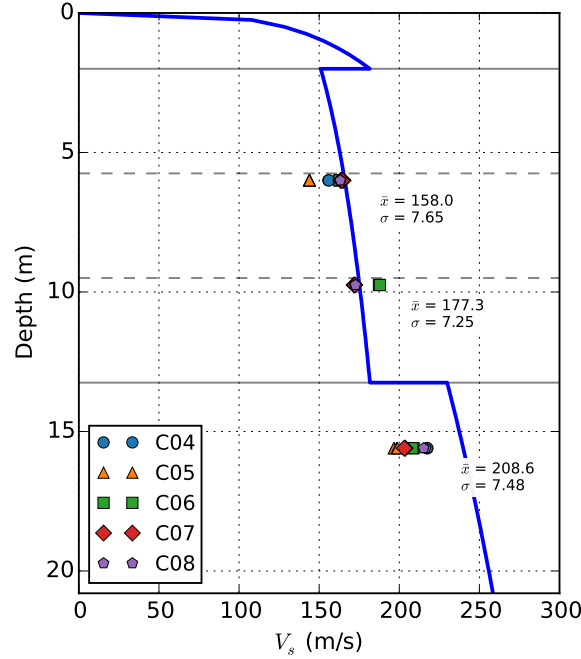


**Figure 3.14:** Small-strain shear wave velocity estimated from bender element measurements compared to the Hardin & Drnevich [85] empirical formulation

The average values of shear wave velocity are 158, 177 and 208 m/s at 6, 9.75 and 15.6 m depths respectively. Variation of data with respect to the average value for each level remains low for all tests with a maximum difference of 8.9% found in the upper level of bender elements in clay in the case of C05 tests. The small deviations in results suggest a **good reproducibility of the shear wave velocity in the initial state**.

The theoretical formula predicts reasonably well the shear wave velocity values in clay. However a slight overestimation is detected for sand. It can be concluded that there is **good agreement between experimental results and the theoretical expression in the case of clay**.

### 3.3.3 Water content profile

Samples of soil profiles were extracted at the end of C03, C04 and C05 tests to measure the water content profile. **An average value of 43.76% was measured in clay** (Fig. 3.15). Differences between tests in terms of average value of water content remain lower than 3.6% in the case of clay. The total unit weight is calculated using the following relation for saturated soils:

$$\gamma = \frac{\gamma_s + e\gamma_w}{1 + e} \quad (3.6)$$

where:

$$e = w_{sat} \frac{\gamma_s}{\gamma_w} \quad (3.7)$$

The void ratio of the clay after consolidation can be calculated from the Equation (3.7) and the water content measurements taken after the C03, C04 and C05 tests (it is assumed that the clay is perfectly saturated). **A void index  $e = 1.166$  is obtained. This value can then be used as input for numerical simulations.** Regarding the saturated unit weight of the clay  $\gamma_{sat}$ :

$$\gamma_{sat} = \frac{\gamma_s + e\gamma_w}{1 + e} = \frac{26.5 + 1.166 \times 10}{1 + 1.166} = 17.62 \text{ kN/m}^3 \quad (3.8)$$

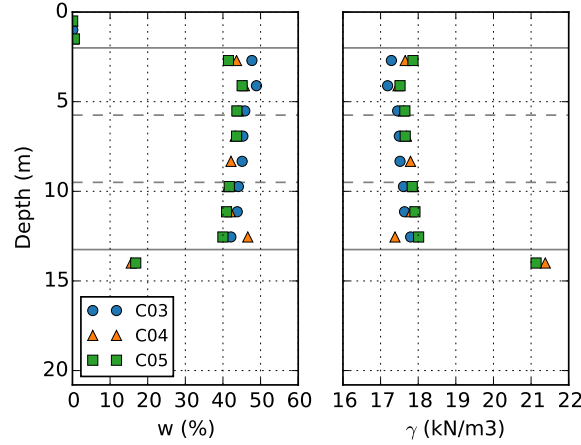


Figure 3.15: Water content profile

### 3.3.4 Quality of the input signal

A good repeatability has been observed when comparing the different inputs for different tests at the same time, both in the time and in the frequency domain. An example of one of these comparisons is shown in Figure 3.16 for Landers 0.3g PGA earthquake input. The frequency content of the seismic events remain almost the same in the frequency range of the shaker (between 0.4 and 6 Hz at the prototype scale for 50g).

A quantitative estimation of the input quality and reproducibility is done through the analysis of peak ground acceleration and velocity, the Arias intensity and the significant duration of the recorded signals. The comparison in terms of relative difference with respect to the mean value gives a good estimation of the variability between tests. The average value and the maximum relative difference calculated for each one of the inputs is given in Table 3.12.

In terms of PGA and PGV, the maximum relative differences are respectively 10.8% and 7.1%. Regarding the Arias intensity, the maximum relative difference of 21.3% is obtained for Northridge 0.3g PGA earthquake input for C04 test. When this input is not taken into account however, the relative difference in terms of Arias intensity remains lower than 13.7%.

Consequently, based on the aforementioned analysis it can be concluded that **the reproducibility of the inputs applied at the base of the container in this series of tests is good enough to allow comparison of the results of the different tests.**



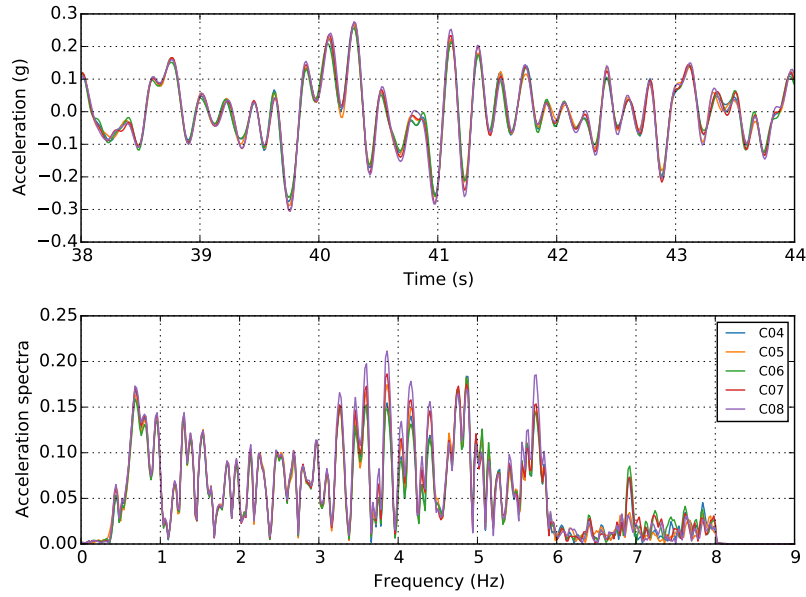


**Figure 3.16:** Repeatability of the input signal: (a) time and (b) frequency representations of the acceleration measured on the table for Landers 0.3g PGA earthquake input

**Table 3.12:** Quantitative estimation of the input quality: average values and maximum value of relative difference of each test with respect to the average value (in brackets)

#	Input	PGA (g)	PGV (m/s)	$I_A$ (m/s)	Significant duration (s)
1	Northridge	0.047 (10.8%)	0.030 (4.1%)	0.018 ( 7.9%)	8.960 (10.6%)
2	Landers	0.053 ( 6.9%)	0.037 (7.0%)	0.026 (10.1%)	10.007 ( 2.8%)
3	Northridge	0.335 ( 3.3%)	0.197 (6.6%)	1.060 (21.3%)	10.115 (13.5%)
4	Landers	0.288 ( 8.6%)	0.253 (4.1%)	1.404 (13.7%)	11.018 ( 2.4%)
5	Sine 1 Hz	0.096 ( 3.0%)	0.134 (2.4%)	1.200 ( 5.0%)	16.797 ( 0.3%)
6	Sine 3.2 Hz	0.107 ( 5.4%)	0.052 (5.5%)	0.452 (11.6%)	5.032 ( 1.2%)
7	Sine 1.8 Hz	0.100 ( 5.6%)	0.087 (3.6%)	0.724 ( 5.5%)	9.255 ( 0.4%)
8	Sine 2.4 Hz	0.109 ( 5.8%)	0.069 (4.3%)	0.608 ( 5.0%)	6.780 ( 0.8%)
9	Sine 1 Hz	0.322 ( 0.1%)	0.432 (0.5%)	12.248 ( 0.0%)	16.321 ( 0.1%)
10	Sine 3.2 Hz	0.303 ( 7.0%)	0.145 (7.1%)	3.738 (12.2%)	5.115 ( 0.7%)
11	Sine 1.8 Hz	0.310 ( 2.5%)	0.254 (3.3%)	6.596 ( 7.2%)	9.062 ( 0.4%)
12	Sine 2.4 Hz	0.361 ( 1.3%)	0.208 (5.1%)	6.029 ( 5.8%)	6.953 ( 0.6%)
13	Northridge	0.046 ( 3.0%)	0.030 (3.3%)	0.019 (11.0%)	8.887 ( 6.2%)
14	Landers	0.054 ( 8.2%)	0.038 (7.1%)	0.026 (13.2%)	10.103 ( 6.5%)



## 3.4 Free-field site response

### 3.4.1 Soil response

Prior to the analysis of the foundation response, the first step is to analyze the response of the soil profile during each base shaking. This is even more important when dealing with deep foundations because the deformation of the soil has a direct impact over the entire length of the piles (kinematic interaction effects). **This analysis is therefore fundamental to understand the development of nonlinearities in the tests that impact the response of the foundation and/or the structure.**

In these series of tests, free-field test has not been performed to obtain a “reference” free-field. However, the response of the “free-field” soil column was recorded at a certain distance from the foundation and the extremities of the soil container to limit as much as possible any interaction (see for example Figure 3.5).

The “free-field” accelerations recorded at different depths of the soil column used in C05 test (single pile without mass at the pile head) are presented in Figure 3.17 for Landers seismic motions with peak base accelerations (PBA) of 0.05g and 0.3g (reference, not measured PBA values). A band-pass filter has been applied (frequency range 0.01-12 Hz at the prototype scale) to the acceleration records in order to wipe out the “noise” in the signal at high frequency due to the shaker’s servo valves actuators which makes it difficult to observe the record especially in the case of low intensity base shakings. A first observation of this data shows that **in the case of the low intensity seismic motion the peak acceleration is amplified at the ground surface, while it is attenuated during strong earthquake motion.** It is noted that in the latter case, **the attenuation takes place in the clay layer** which experiences nonlinear behavior as a result of high strains. At higher acceleration levels, the lower stiffness and nonlinearity of soft clay prevent it from developing peak accelerations as large as those during lower acceleration levels. Similar results are found for the rest of dynamic tests.

Figure 3.18 presents the acceleration response spectra for 5% damping at the base (dotted lines) and at the top (solid line) of the soil profile for the low intensity and high intensity seismic motions and for the five conducted dynamic tests (C04 to C08). In this case the acceleration records are used without previous filtering to calculate the response spectra. The mean and the standard deviation of the respective acceleration response spectra for each one of the base shakings are also presented. These results allow a first observation of the evolution of the response of the system and its dependency on frequency and on loading intensity. The calculated response spectra are found to be close between the different tests, showing the same trends in terms of amplified frequency ranges and with only slight differences in terms of amplitude. This finding highlights the good reproducibility of the soil container and reinforces the possibility of direct comparison of the results from different tests.

The spectral amplification factors, defined as the ratio of the acceleration response spectrum at the top to that at the base of the soil profile, have been calculated using the mean response spectra and are presented in Figure 3.19. In the case of the two weak seismic motions with a PGA of 0.05g, the site experiences amplification for nearly all the frequencies with a maximum spectral amplification ratio between 4 and 4.5 in the frequency range from 1.8 to 2.5 Hz. It can be observed that increasing the intensity of the loadings (from a PGA of 0.05g for weak earthquake motions to 0.3g in the case of strong ones) has an impact in the response of the system through all the frequencies. There is a shift of the amplification zone to low frequencies and **all the frequencies higher than 2 Hz are systematically deamplified in the case of strong seismic motions due to the development of nonlinearities in the soil profile.**

Figure 3.20 gives the average value of peak ground acceleration at the base and at the top of the soil profile for all the dynamic tests (C04 to C08). An amplification phenomenon is observed in the case of low intensity earthquake motions applied at the beginning and at the end of the tests (amplification ratio higher than unity). For the rest of the base shakings the peak ground acceleration recorded at the surface of the soil profile is always lower than that recorded at its base (except for the 1 Hz 0.1g sine base shaking). A deamplification of the signal between the base and

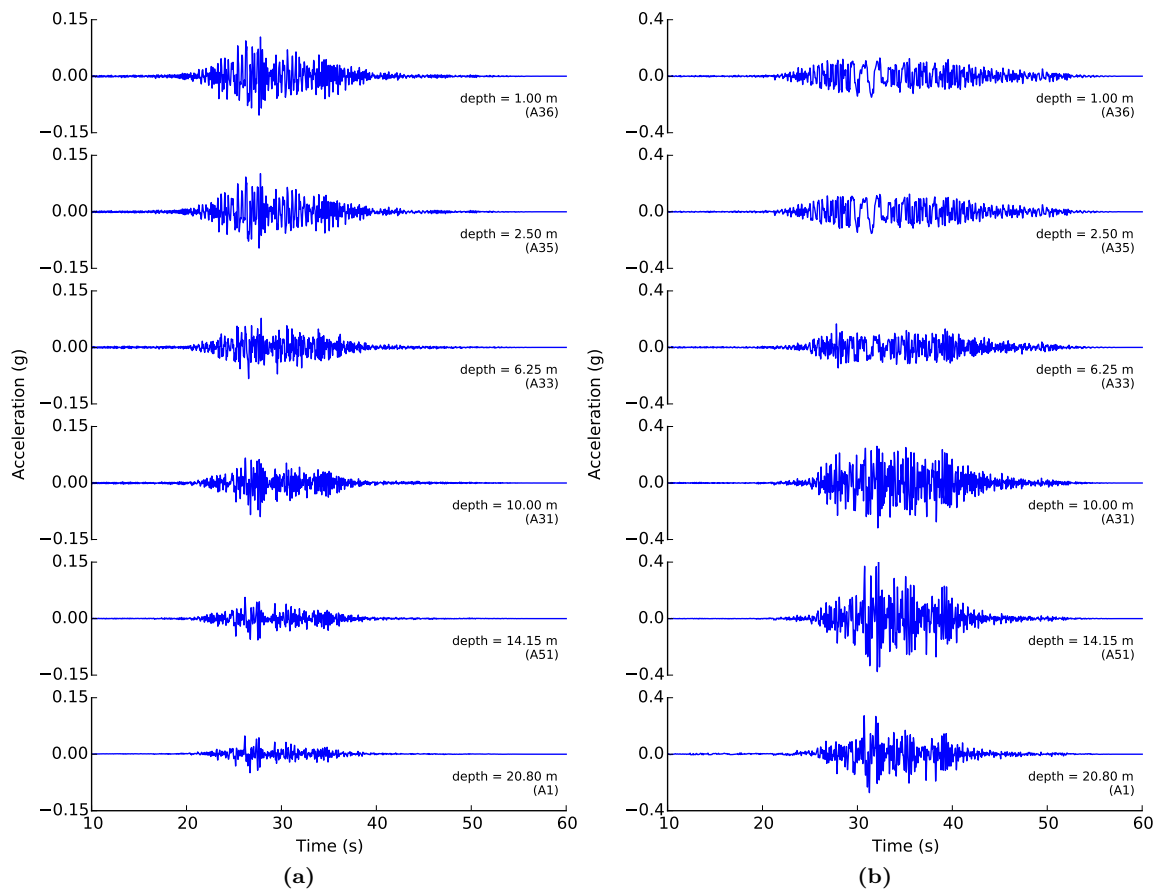


**Figure 3.17:** Time representation of the horizontal acceleration measured at different depths during the C05 test, during (a) 0.05g and (b) 0.3g PGA Landers earthquake motions

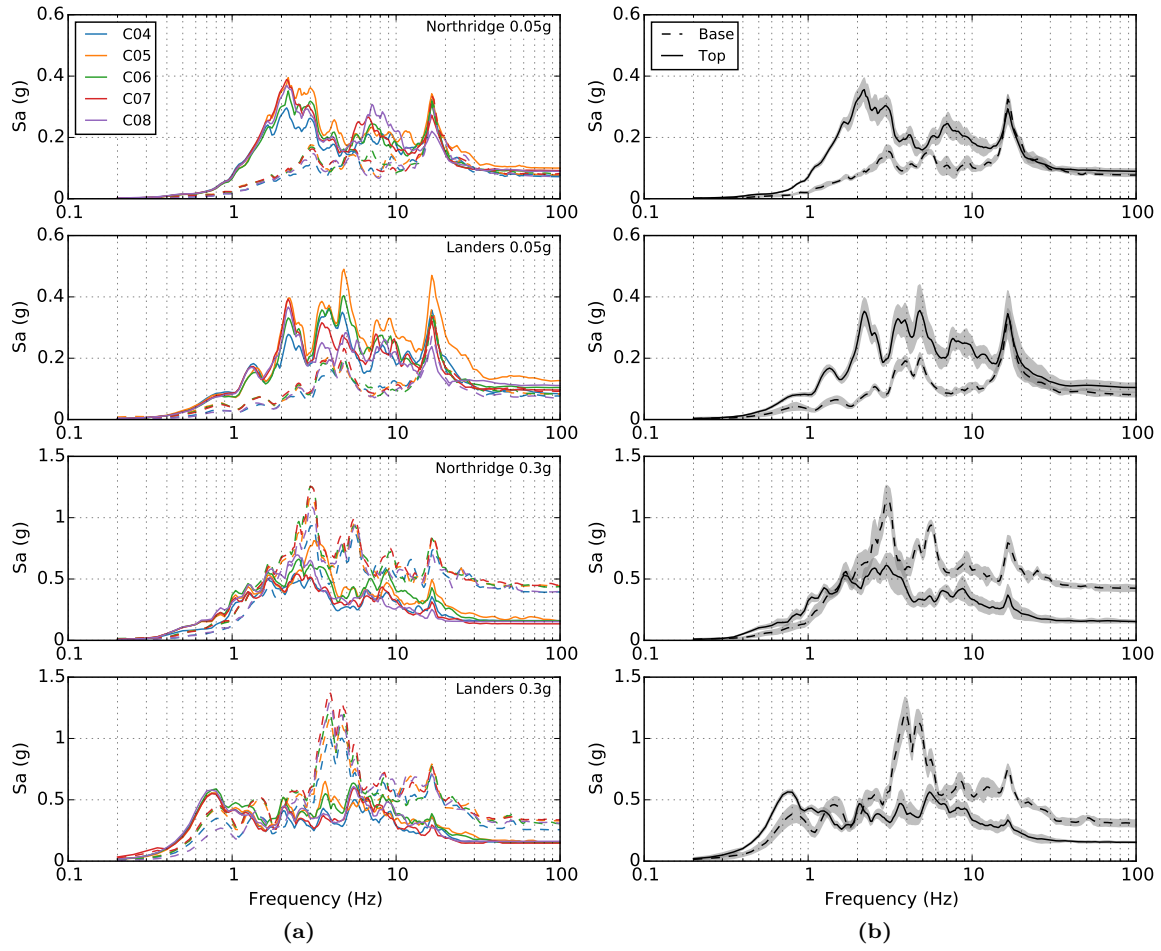


**Figure 3.18:** (a) Acceleration response spectra (damping 5%) at the bottom (dotted line) and the top (solid line) of the soil column for every test and base shaking, (b) mean and standard deviation of response spectra from different tests for each base shaking

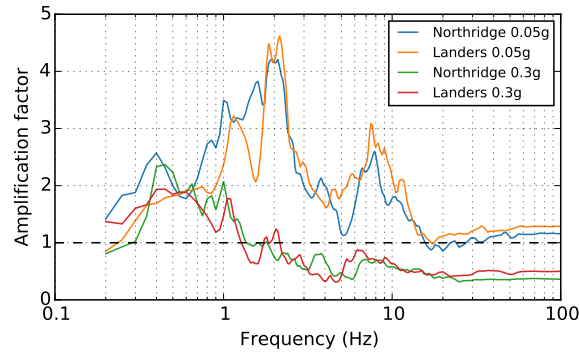


**Figure 3.19:** Amplification factors for the soil column using acceleration response spectra (5% damping) given in Figure 3.18 at the bottom and at the top of the soil column

the top of the soil column takes place. This is no doubt due to the nonlinearities that develop in the soil. Looking closely at the results for sinusoidal base shakings at 0.3g, it is clear that there is a frequency dependence of the response, with peak acceleration values that decrease with increasing values of loading frequency. Finally, it is interesting to compare the results obtained for the weak seismic motions applied at the end of the test with those applied at the beginning. A decrease in soil surface peak acceleration is observed which results also in a decrease of the amplification ratio. This degradation of the soil profile response may indicate a certain degradation due to the accumulation of nonlinearities.

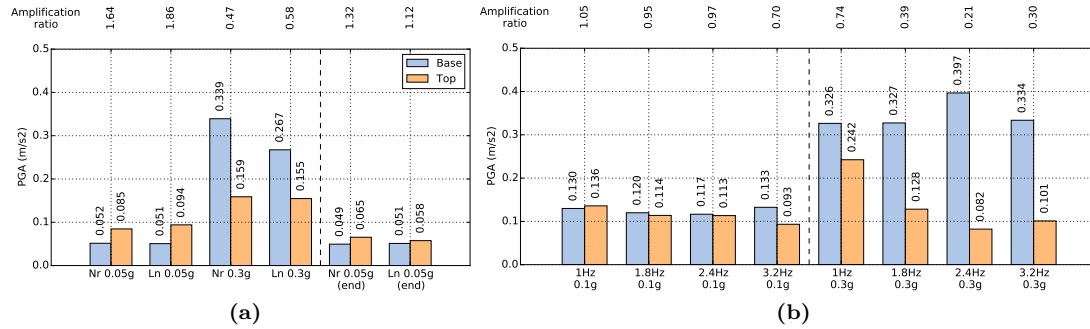


**Figure 3.20:** Average peak ground acceleration recorded at the bottom and at the top of the soil profile: (a) under seismic excitations and (b) sinusoidal base shakings

The average value of peak ground displacement at the base and at the top of the soil profile is given in Figure 3.21. Given the limitation of the acceleration sensors, only the dynamic part of the signal is available. That is, no information about the residual displacement at the end of each one of the base shakings can be obtained from the double integration of the acceleration records.

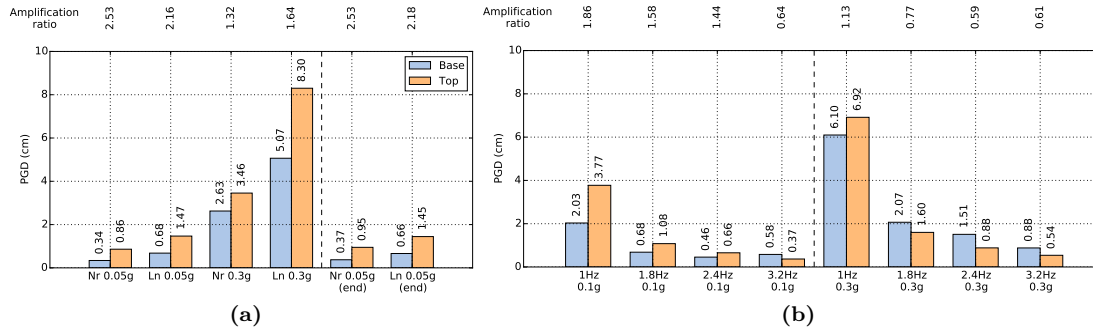


**Figure 3.21:** Average peak ground displacement at the bottom and at the top of the soil profile: (a) under seismic excitations and (b) sinusoidal base shakings

Regarding the results for earthquake base shakings, it is observed that Landers record induces more displacements in the soil profile than Northridge earthquake motion for the same intensity level. It is interesting to note that the amplification ratio between the base and the top displacements is higher in the case of Northridge earthquake for low intensity base shakings and the opposite for strong earthquakes. The analysis of the sinusoidal inputs shows that the displacements in the system (and of the corresponding amplification ratios) decrease with the increase of the loading frequency. The same trend is observed for inputs at 0.1g and 0.3g. Given these results, it is expected that base shakings with important low frequency content to have a more important impact in the response of the system in terms of maximum bending moment in piles.

### 3.4.2 Frequency analysis

A transfer function analysis between the acceleration recordings at the top and at the base of the soil column was conducted on the results from all the dynamic tests. In order to improve readability of the transfer functions, a smoothing process was done using a moving-median in order to wipe out the pics of the curves.<sup>3</sup> However, it should be noticed that even with the smoothing process of the transfer functions the response frequency could not be well identified. Two main reasons explain this, the development of nonlinearity in the soil profile (specially in the case of strong earthquake motions) and the fact that the soil profile is composed of several layers which adds additional complexity to the interpretation of the results due to wave reflections at the interfaces between layers and different amplification/deamplification trends of certain frequency ranges in different parts of the soil profile.

To obtain a better insight into the response of the system and simplify the analysis, the transfer function between the bottom and the top of each soil layer was then studied. This type of analysis was intended to highlight the effects of each one of the soil layers in the overall response and to estimate their fundamental response frequency. In the case of the dense sand layer at the bottom of the soil profile, no significant modification of the signal is observed. On the other hand, in the case of the clay layer, an evolution of the response is observed and the results repeat, in the overall, the same trends as those from the transfer function between the bottom and the top of the soil profile, which suggests that **the response of the soil profile is controlled to an important extent by the clay layer.**

The results also suggested a certain evolution of the response of the clay layer during small seismic motions and a much more important evolution during strong ones. However the fundamental frequency response could not be identified from the transfer function. In the following, the analysis focuses on the response of the clay layer, particularly its response under very low strains, and on the evolution of the response when the clay layer is submitted to earthquake loadings.

Given the evolution in the response of the clay layer during the loading, a time-frequency analysis is conducted by means of time-frequency transfer function between the accelerations recorded at the base and at the top of the clay layer. This type of analysis allows to identify the evolution of the response of the system with time. Examples of this analysis conducted with acceleration recordings from low intensity and strong earthquake motions during C08 test are respectively given in Figures 3.22 and 3.23. It is interesting to observe in these analysis that **there is an evolution of the transfer function with time, even in the case of low intensity seismic motions.**

The analysis of the time-frequency transfer functions that are found just before each one of the applied base shakings gives information about the response of the soil profile under very low distortion (the model is excited by very-low amplitude random vibrations due mainly to the shaker). It is observed for all tests and applied earthquake motions (low and strong ones) **that the response frequency of the clay layer before the earthquake is around 2.6 Hz.** This finding is consistent with the results from the numerical model conducted using low strain shear wave velocity profile given in Figure 3.3.2 (used to estimate the response frequency of the soil profile to be of 2.6 Hz, see Section 4.4.2) and thus with bender element results presented in §3.3.2. Therefore, it can be concluded that the response frequency obtained from **the frequency analysis is very satisfactory and consistent with the bender element measurements and with the theoretical expression in the case of the clay layer.**

Another interesting analysis concerns the time frequency analysis of the transfer function found during the low amplitude seismic motions (Figure 3.22). **In the case of Northridge 0.05g seismic motion an average response frequency of 2 Hz is found. For Landers 0.05g seismic motion the response frequency is about 2.2 Hz.** These results highlight a decrease of the shear modulus of the soil even during the low intensity earthquake motions due to the level of distortion that is reached. The problem can no longer be considered as a pure elastic case. This can be translated in terms of a decrease of the low strain shear modulus  $G_{max}$  using the following formula:

<sup>3</sup>A moving median is better than a moving average for some applications because it is less sensitive to outliers, specially when those outliers are a very short spike (preferably shorter than the median/average sample size).

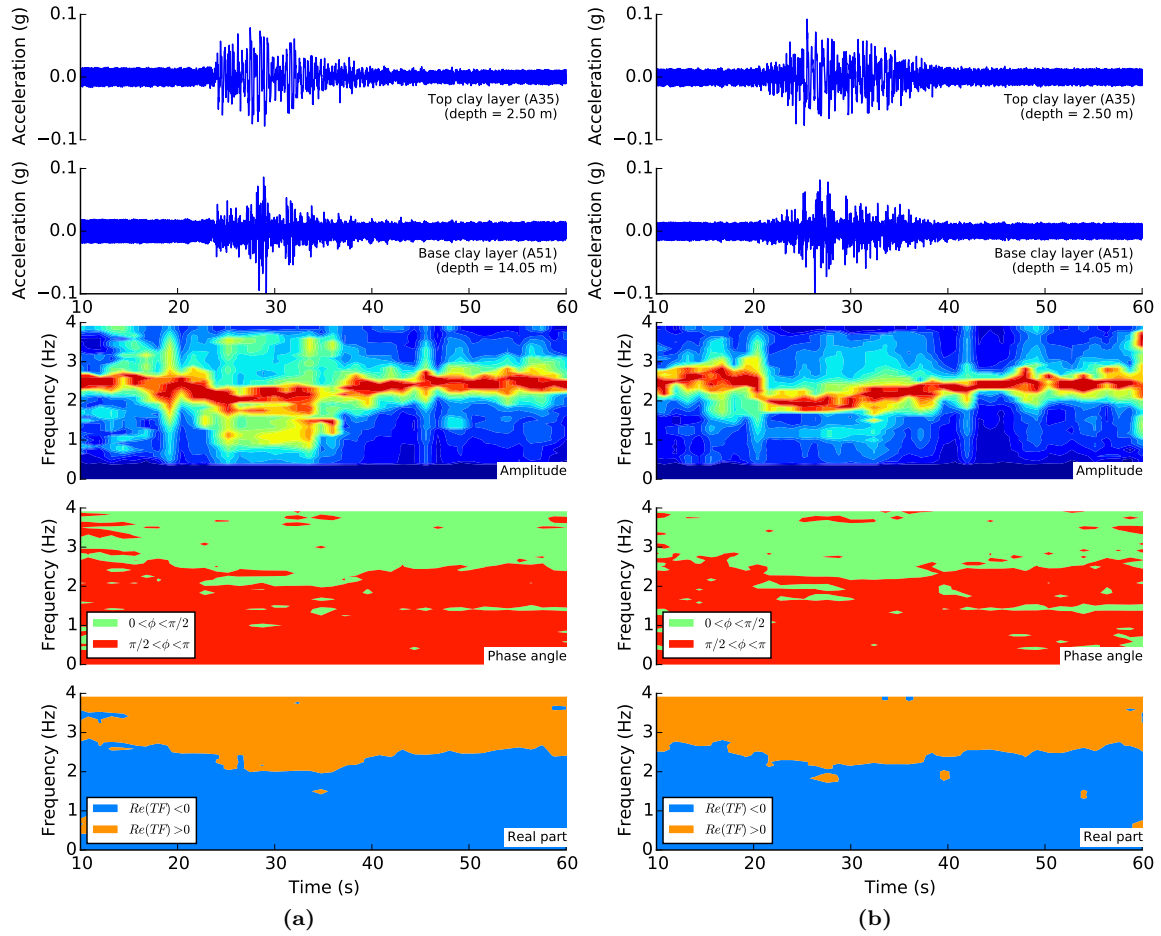


**Figure 3.22:** Time-frequency transfer function between the base and the top of the clay layer recorded during the 0.05g PGA earthquake motions in C08 test: (a) Northridge and (b) Landers

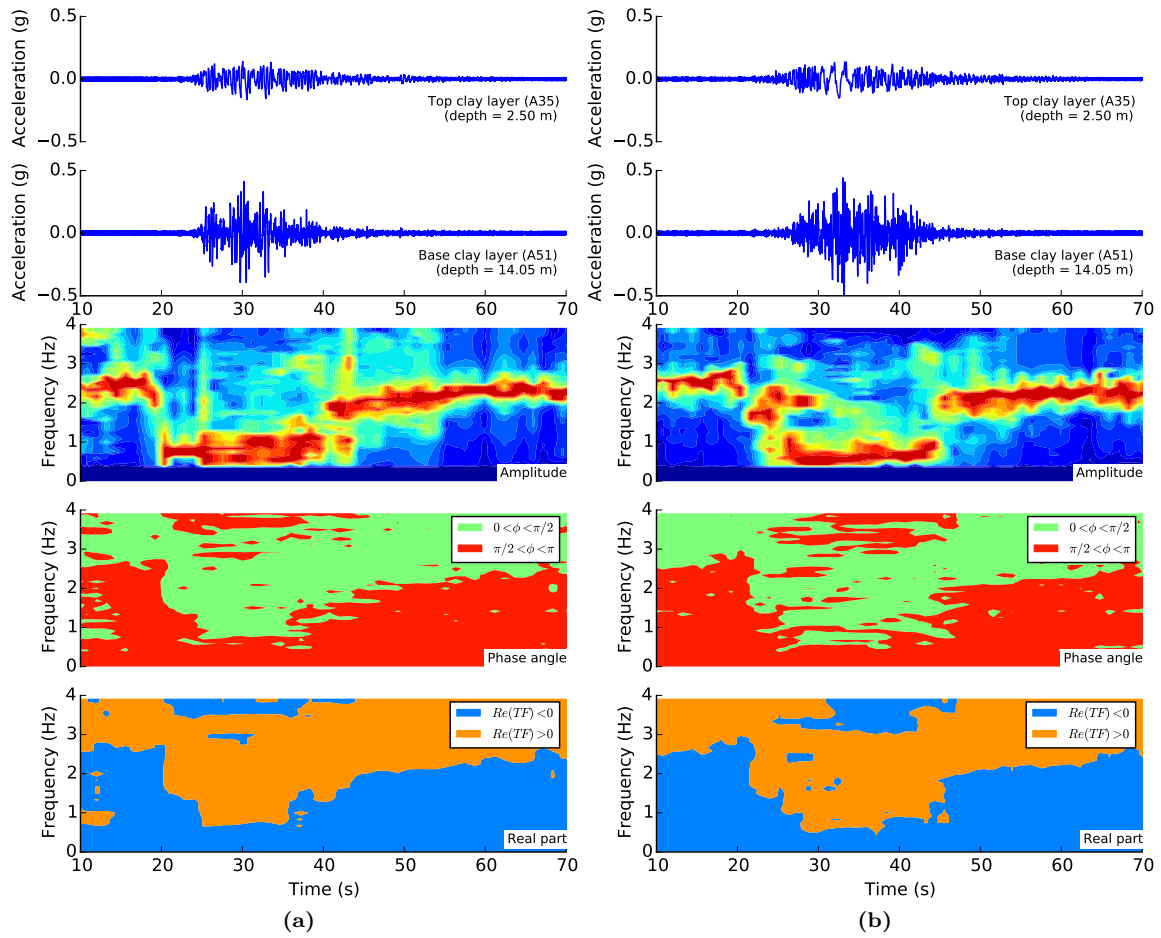


**Figure 3.23:** Time-frequency transfer function between the base and the top of the clay layer recorded during the 0.3g PGA earthquake motions in C08 test: (a) Northridge and (b) Landers



$$G \approx G_{max} \left( \frac{f}{f_{max}} \right)^2 \quad (3.9)$$

With  $f_{max}$  the response frequency at low strain and  $f$  the response frequency detected during the strong shaking phase during the earthquake. **For this particular case it is found that  $G = 0.6G_{max}$  for Northridge 0.05g seismic motion and  $G = 0.7G_{max}$  for Landers 0.05g.**

This difference in terms of shear modulus degradation may be explained by the fact that the Northridge seismic motion is more energy rich in the frequency range from 1 to 3 Hz (Fig. 3.11) which may be responsible of more distortion than in the case of the Landers seismic motion and therefore of a greater degradation of the shear modulus of the soil during the earthquake.

The same analysis is applied this time to the strong seismic motions (e.g., Fig. 3.23). In both earthquakes (Northridge and Landers) and for all the dynamic tests a response frequency between 0.6 and 0.7 Hz is observed. In other words, there is a 2 Hz decrease in frequency compared to the initial state of the soil profile. This corresponds to a shear modulus of about 5%  $G_{max}$ , which constitutes a huge degradation.

It should be noticed that the ESB container has a response frequency at 1g between 32 and 37 Hz that corresponds to a frequency range of 0.64-0.74 Hz at 50g (prototype scale) and therefore this may explain this sharp decrease. **Under strong loadings it is possible that the container controls the response of the system.**

From the above results, it is clear that there is nonlinearity in the system even in the case of weak seismic motions. It is interesting to note however that nonlinearity in the case of weak earthquake motions remains limited allowing thus a direct comparison of the results to those of an equivalent linear numerical model of 1D wave propagation (e.g., Shake [189, 94], see Section 4.4.3). In the case of strong seismic motions, the container may play an important role in the response. In order to compare the results obtained in the tests, the numerical model should incorporate somehow the influence of the container in the response of the soil profile.

### 3.4.3 Boundary effects

As shown in the previous section, there might be some influence of the ESB container on the response of the system when subjected to strong seismic motions. In order to verify that the soil column and the rings of the ESB container are moving in unison during shaking, the first step was to perform a visual (qualitative) comparison of several recordings at the same level of the soil and of the container. This comparison, conducted directly using acceleration and displacement time histories (obtained by double integration of acceleration records) showed that for the weak earthquake motions with a PGA of 0.05g, the response is practically the same in the soil column and on the corresponding container ring. In the case of strong earthquake motions at 0.3g a slight time delay is observed between the response of the soil and that of the container (e.g., in Fig. 3.24). A similar observation is done for sine loadings at 0.1g, with a slight to moderate time delay depending on the loading frequency. Finally, the time delay observed in sine loadings at 0.3g is found to be more important than for the previous loadings. It should be noted that the case for which the time delay appears to be the most important is for the sine loadings at 1 Hz.

These trends have been confirmed by the cross-correlation between acceleration and displacement time histories in the soil and at the corresponding container ring. It is interesting to note that the time delay that is found for a particular shaking is consistent between the different tests which allows to conclude for this study that, when boundary effects are present, they remain close from one test to another allowing thus direct comparison between the results from different tests.

This type of analysis is often absent in most of the experimental works concerning pile foundations in flexible containers. One of the rare examples is found in Wilson [228], which conducted a similar verification and observed that horizontal acceleration and displacement time histories were nearly identical between the soil and the container ring for low shaking levels. The test included a layered soil profile with an important soft clay layer.



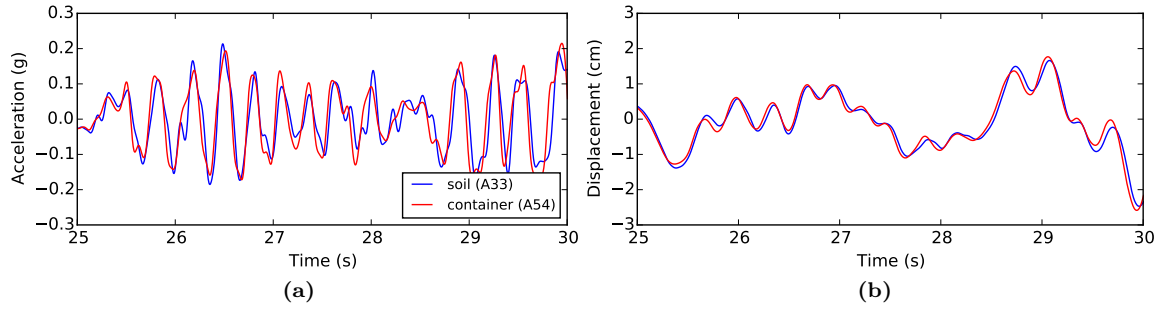


**Figure 3.24:** Comparison of the records at the soil ( $z = 6.25\text{ m}$ ) and at the corresponding container ring during the 0.3g PGA Northridge earthquake motion: (a) acceleration time history and (b) displacement time history (doubled integrated from acceleration records)

A final note to be added regarding boundary effects is that, when comparing these results to numerical models (e.g., non-linear finite element models), particular attention should be done to this aspect, especially in the case of sine loadings with high amplitude.

### 3.5 Definitions and calculation of certain results

Prior to the analysis of the response of the piles and the superstructures that are used in the dynamic tests, several definitions are introduced to help to the understanding of the analysis and the data that is available given the instrumentation and the configurations that have been tested.

#### 3.5.1 Identification of the piles used in the tests

All the tests conducted on the response of a single pile (with or without a mass at its head) have been conducted with the same instrumented pile, named IP2.

In the case of the two tests conducted on the response of a pile group, three instrumented piles have been used. They are named IP2, IP3 and IP4. The instrumented pile IP2 is placed at the center of the pile group and the two other are installed in the same side of the pile group. Their distribution is given in Fig. 3.25.

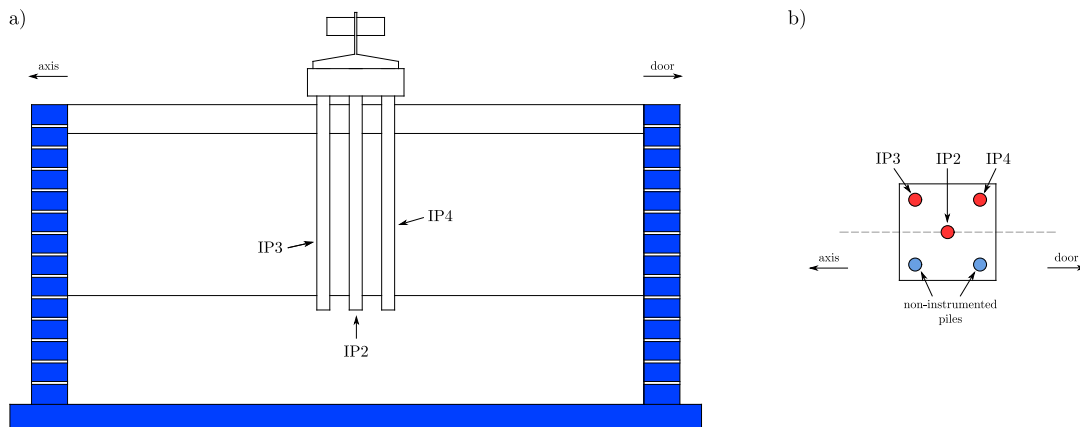


**Figure 3.25:** Identification and location of the piles used in the dynamic centrifuge tests with a pile group (C07 and C08): (a) lateral and (b) top view

It should be noticed that the piles are always oriented in the same way from one test to another. This ensures that the recordings from different tests can be compared directly even before the

application of the corresponding conversion factors (from electrical signal to the corresponding physical measure).

### 3.5.2 Dynamic, total and residual bending moment

The bending moment recorded with the instrumented piles is analyzed in the following sections. Figure 3.26 introduces the definition of several bending moment values than can be studied and compared. In the case of maximum moment envelopes, the maximum value of the moment that is reached during a given earthquake is compared. To obtain the moment variation that corresponds to each input, the signal offset is subtracted at the beginning of each recording. This ensures that the maximum moment value that is used in the comparison is not affected by any accumulated residual moments from the previous base shakings applied to the model.

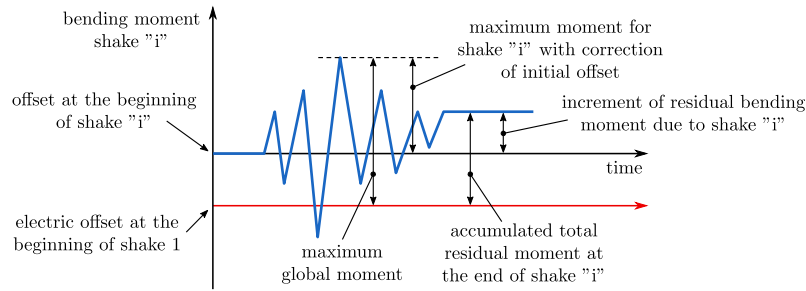


**Figure 3.26:** Definition of several bending moment values

Regarding the residual moment in the pile, they are the result of permanent lateral displacements along the pile due to the permanent deformation of the soil, the influence of the superstructure (when installed) and the impossibility of the pile to deform exactly as the embedding soil. The residual bending moment induced by each one of the base shakings can be measured as the difference between the bending moment at the beginning and at the end of the earthquake (see Fig. 3.26).

Due to a problem with the recording equipment, the moment measurements made in the first meters of the piles in the case of C04 and C05 tests, as well as on the entire length of the pile for the C06 test could record only the dynamic part of the bending moment. The recordings from these test make it impossible to determine the residual moment induced by each one of the base shakings and the evolution of the accumulated value for the aforementioned parts of the piles.

### 3.5.3 Bending moment at the pile tip

The tip of the piles is embedded of one diameter in the dense sand layer at the bottom of the soil profile. Because of this, and due to the stiffness contrast between the sand and the clay layers, strong moments due to kinematic effects can take place. Moreover, as reported in the literature review, efforts from kinematic interaction between the pile and the soil can become significant in the case of stratified soils, specially in the proximity of interfaces between soil layers with different stiffnesses. Therefore, the maximum value of the recorded moment near the pile tip is studied and compared between the different tests. In addition, the residual bending moments at this location are also studied and discussed (when available).

### 3.5.4 Horizontal displacement (translation) and rotation (rocking) of the pile cap

The response of the pile head, of the pile cap and of the superstructures has been captured by means of several accelerometers and laser sensors, as shown in Fig. 3.27.

The displacement histories can be obtained by double integration of the acceleration records. It should be noted that due to the limitations of the accelerometers used in the tests, the displacements

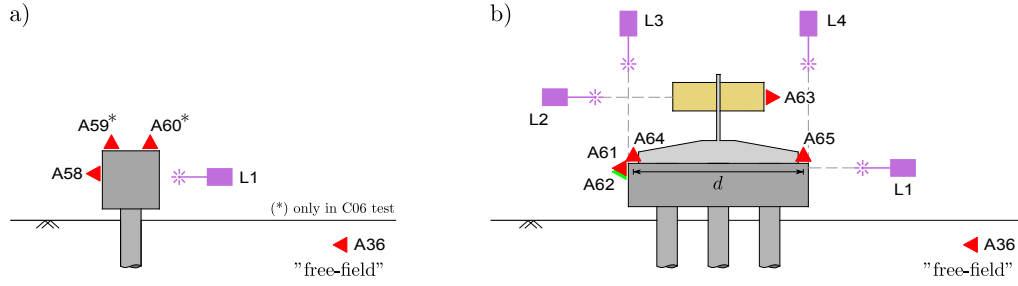


**Figure 3.27:** Illustration of the instrumentation of the pile cap and of the superstructure: (a) single pile tests (C04, C05 and C06) and (b) pile group tests (C07 and C08)

and the rotations that are calculated by double integration of the acceleration records represent only the dynamic part of the response. Therefore, they are not able to capture the residual part of the response.

The relative displacement of the pile cap with respect to the soil surface can be obtained from the differences between the displacement at the level of the pile cap and that in the soil column, near the soil surface (accelerometer sensor denoted as "free-field" in Fig. 3.27).

Given that the pile cap used in the tests is considered very rigid, its rotation  $\theta_{cap}$  can be calculated by using the following equation:

$$\theta_{cap} \approx \tan(\theta_{cap}) = \frac{u_{A65} - u_{A64}}{d}$$

Where  $u_{A65}$  and  $u_{A64}$  are the displacement histories calculated from the acceleration records from the corresponding accelerometers presented in Fig. 3.27-b. The same equation applies to the displacement records from laser devices using the corresponding horizontal separation between them.

Regarding the calculation of the rotation of the pile cap in C07 and C08 tests, several elements need to be kept in mind. In C07 test, accelerograms and laser measurements are available. However, the measurement from one of the laser sensors is very noisy and it is possible that this measurement is not very accurate (at least that is the observation that comes out when the recordings are compared to the measurements from the other laser sensor in the test). Consequently, the rotation is calculated directly from the displacement histories obtained by double integration of the acceleration records. In this case only the dynamic part of the rotation is thus correctly captured. For C08 test no acceleration measurements are available to calculate the rotation of the pile cap. Only the lasers sensors worked well (except for the Northridge 0.05g base shaking where there was some interference in the measurement of one of the laser sensors). The calculation of the rotation of the pile cap is done in this case using directly the displacement measurements from the laser sensors. Care should be taken when comparing the calculated rotation values for C07 test to those calculated for C08 test.

### 3.5.5 Horizontal force and overturning moment at the base of the structure

The calculation of the horizontal force (base shear) and rocking moment at the level of the soil surface can either be calculated from the inertia forces generated by the mass of the superstructure or from the base resistance forces (Fig. 3.28).

Regarding the measurement of the axial forces at the head of the piles it should be noted that the gauges used to measure the axial forces are not compensated in temperature. As a result, only the dynamic part of the response could be captured.

It is to be noticed that given the symmetry of the system and because measurements are available for one side of the outer piles only, it is assumed that their response is the same in the case of non-instrumented piles. The horizontal force and the overturning moment can thus be calculated using the following formulae:

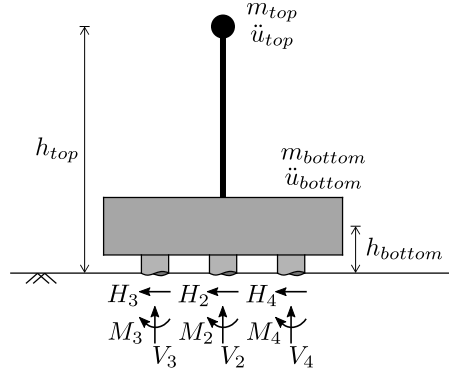


**Figure 3.28:** Schema of forces at the interface between the structure and the soil

$$H_{inertial} = m_{top} \ddot{u}_{top} + m_{bottom} \ddot{u}_{bottom} \quad (3.10)$$

$$H_{base} = -H_2 - H_3 - H_4 \quad (3.11)$$

$$M_{inertial} = m_{top} \ddot{u}_{top} h_{top} + m_{bottom} \ddot{u}_{bottom} h_{bottom} \quad (3.12)$$

$$M_{base} = M_2 + 2(M_3 + M_4) + 2.5D(2V_3 - 2V_4) \quad (3.13)$$

Where  $H_{inertial}$  and  $M_{inertial}$  correspond to the values obtained from inertial forces,  $H_{base}$  and  $M_{base}$  are the corresponding values calculated from the forces and the moments in the pile at the soil surface.

Since at every time instant the system must verify the dynamic equilibrium, the shear force and the overturning moment calculated from inertial forces should be identical to those values calculated from the measurements at the piles.

## 3.6 Performance of single piles under seismic loading

### 3.6.1 Frequency analysis

The analysis is carried out by means of a time-frequency transfer function between the acceleration records near the soil surface and at the pile cap/head. This type of analysis makes it possible to study the evolution of the response of the system over time, especially in the case of strong seismic motions where significant nonlinearities are present and can directly influence the behavior of the system (e.g., Fig. 3.29).

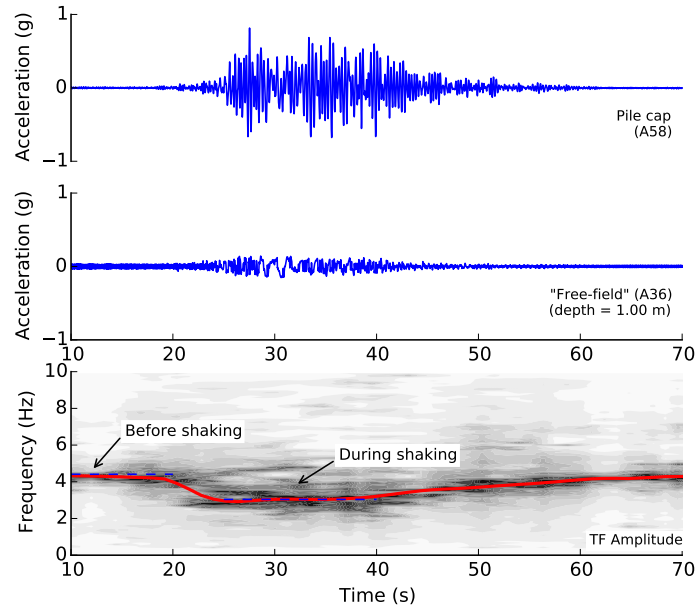


**Figure 3.29:** Time-frequency transfer function between the soil surface ( $z = 1\text{ m}$ ) and the pile cap in C06 test under Landers 0.3g seismic motion

A "classical" transfer function returns the response frequency corresponding to the strong phase of the solicitation. That type of analysis works correctly when nonlinearities in the system remain limited. However, when significant nonlinearities are present, the analysis becomes more complicated and the identification of the fundamental response frequency of the system can, under certain conditions, become an impossible task. In contrast, the time-frequency transfer function analysis allows identification of the fundamental response frequency of the system under very low loads either before or after the main shaking, i.e., the quasi-elastic response of the problem (from very low amplitude vibrations induced by the shaker).

The results corresponding to the C06 test (single pile configuration with a lumped mass at the pile head) are given in Figure 3.30. At very low deformation (measures before shakings) the fundamental response frequency of the system is identified at about 4.41 Hz for all shots. The time-frequency analyses show an evolution of the response frequency of the system with time (e.g., Fig. 3.29) and a direct influence of the loading amplitude on that variation. Thus, for weak earthquake motions at 0.05g a decrease of up to  $-0.98\text{ Hz}$  is observed. In the case of strong earthquake motions with a PGA of 0.3g, a more important evolution is observed with a maximum decrease of the response frequency of  $-1.45\text{ Hz}$  experienced for Northridge earthquake.

In the case of the dynamic tests conducted on a single pile with no head mass (C04 and C05), the transfer function between the soil surface and the head of the pile is not very clear and it is thus difficult to identify the response frequencies of the system. From this analysis a response frequency of the system is expected to be in the frequency range from 12.5 Hz to 13.5 Hz (in the case of weak earthquake motions). In order to increase the readability of the transfer functions for this particular configuration, it would be necessary to have a greater number of measurements (corresponding to

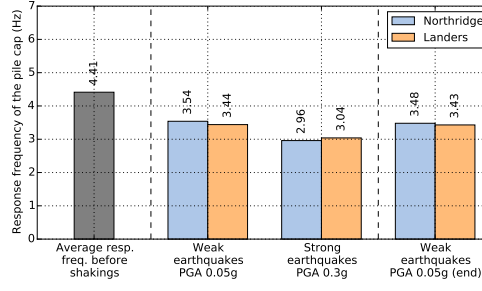


**Figure 3.30:** Frequency response of the pile cap in C06 test

weak earthquakes shakings). This would allow a post-processing by signal stacking so as to put forward the global trend of the answer and to remove as much as possible part of the noise in the transfer function.

### 3.6.2 Pile head response

The maximum acceleration recorded at the pile head in the dynamic tests conducted on single piles is given in Figure 3.31. The first observation is that the response of the C06 test is systematically greater than that for the cases without mass at the pile head (except for the sine 1 Hz 0.1g input, for which the response for all the tests is relatively close).

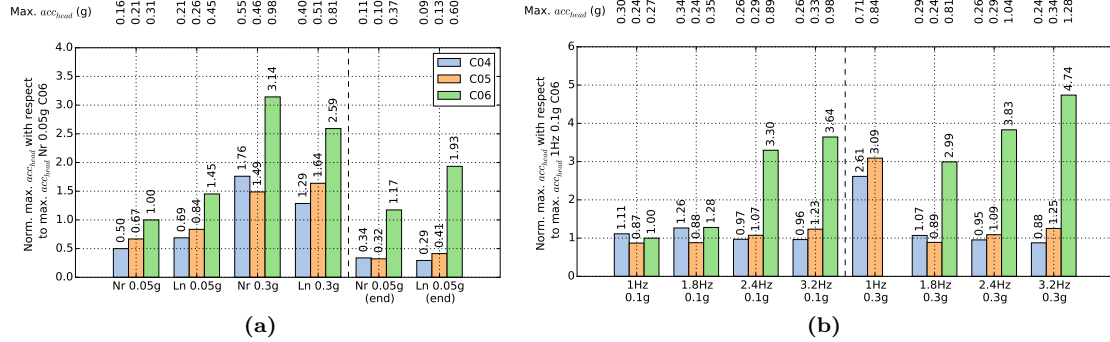


**Figure 3.31:** Normalized maximum acceleration of the pile head/cap: (a) under seismic excitations and (b) sinusoidal base shakings

#### 3.6.2.1 Pile with mass at the pile head

A closer analysis of the results from C06 test reveals several interesting observations. For weak earthquake motions, the maximum acceleration is greater in the case of the Landers earthquake. The response frequency of the pile has been estimated at about 3.44-3.54 Hz and the Landers earthquake is more energy efficient in this frequency range compared to Northridge (see Fig. 3.18).

In the case of strong earthquake motions, the trend is reversed, with greater maximum acceleration when the system is subjected to the Northridge earthquake. In this case it is the Northridge earthquake motion that is more energetic in the system's response frequency range (estimated at 2.96-3.04 Hz during the strong earthquake phase) compared to the Landers earthquake (see Fig. 3.18).

The comparison between the weak seismic motions applied at the end of the tests and those applied at the beginning shows an increase in the maximum acceleration at the head of the pile with an increase of 17.4% in the case of the Northridge earthquake and 33.1% in the case of Landers. This increase is also observed in the maximum moment profiles (see following section), especially in the upper part of the pile which is directly affected by the inertial effects.

The analysis of the system response when subjected to sinusoidal base shakings is also interesting. In the case of the 0.1g sine input and the 1 Hz and 1.8 Hz frequencies, the system response is in the same order of magnitude as the response that is obtained for the configurations with a single pile without mass at the pile head. For 2.4 Hz and 3.2 Hz frequencies, however, the value of the maximum acceleration increases significantly. This observation is in agreement with the response frequencies reported in Fig. 3.30. In the case of sinusoidal base shakings with a PGA of 0.3g, the maximum acceleration increases when the loading frequency is increased.

It should be noticed that because of the simple configuration tested in the C06 test, it is straightforward to calculate the maximum bending moment at the soil surface by multiplying the acceleration recorded at the pile head by the mass of the pile cap and the height of this mass with respect to the soil surface. Therefore, the same trend that has been observed on the maximum acceleration results apply for the maximum bending moment at the soil surface (inertial bending moment). This is confirmed by the bending moment recordings made by the strain gauges in the instrumented pile located at the same level. These data are discussed in the next section.

### 3.6.2.2 Pile without mass at the pile head

The analysis of the results corresponding to the tests on a single pile without mass at the pile head (C04 and C5) allows us to observe that the results of the two tests follow the same trends and that their value remains globally in the same order of magnitude. Some differences are noticed however, especially for strong earthquake motions at 0.3g and sine base shakings. These differences can be explained in part by the presence of noise in the measurements at the pile head which may impact the determination of the maximum acceleration. Indeed, the system does not have a mass at the pile head that by means of inertial forces could smooth the recorded response. The response frequency of the system is in this case estimated to be in the frequency range from 12.5 Hz to 13.5 Hz which makes it more sensitive to suffer the effects of high frequencies in the loading. On the other hand, differences were also observed in the maximum bending moment profiles that are studied in the next section. A slight modification of the response of the soil column between the two tests may also cause a variation of the maximum acceleration recorded at the pile head (and respectively of its bending moment profile as a function of time).

It is interesting to analyze the results corresponding to sinusoidal base shakings. For sines at 0.1g the response at the pile head in terms of maximum acceleration remains relatively constant for the different loading frequencies. The same observation is made in the case of sines at 0.3g and for the loading frequencies 1.8, 2.4 and 3.2 Hz. The response is very similar and in addition it remains in the same order of magnitude as the response obtained for a PGA of 0.1g. For the 1 Hz 0.3g sine, however, the response increases significantly. It is possible that the large energy of this base input results in the developping of important nonlinearity and thus a strong decrease of the response frequency of the soil column. A resonance problem may take place in this case.

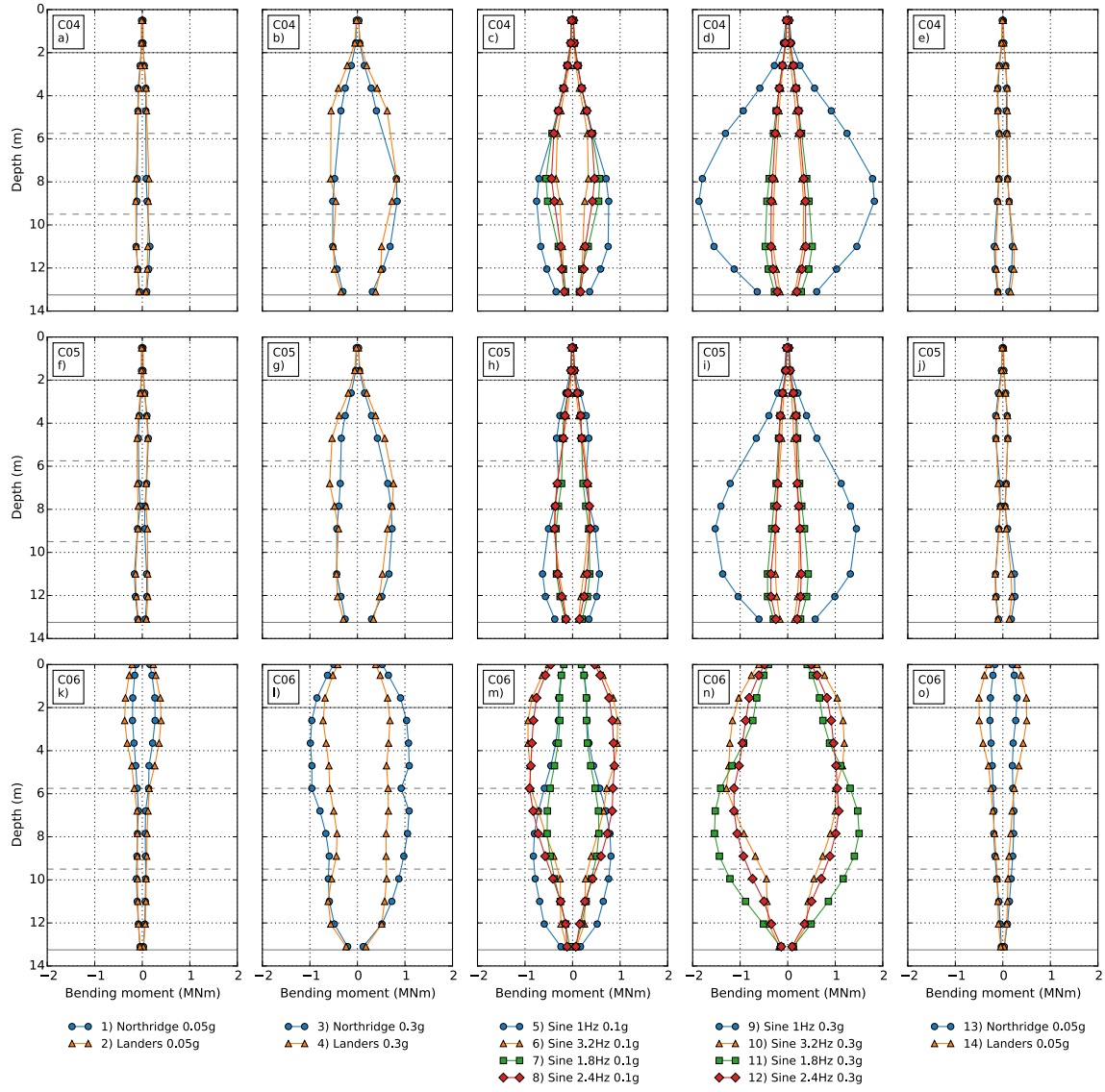
### 3.6.3 Maximum bending moments

Figure 3.32 shows the envelope curves of the maximum bending moments measured in the pile for every dynamic loading in C04, C05 and C06 tests (top, middle and bottom row respectively). Results are grouped according to PGA level and motion type, and ordered from left to right according to the input order as given in Table 3.11.

First the pure kinematic interaction cases, C04 and C05 tests are analyzed and compared. Then, the results from C06 tests which in addition to the instrumented pile was also equipped with a single mass at the top of the pile introducing thus an inertial effect on the response. Finally, results from both cases are compared to study the impact of inertial and kinematic interaction effects on the response of the system.

#### 3.6.3.1 Pure kinematic interaction

Results from C04 and C05 correspond to a pure kinematic interaction case. In addition, the C05 test is a reproducibility test of C04 which makes it also interesting to analyze the possible



**Figure 3.32:** Measured maximum bending moments: (a-e) results from C04 test, (f-j) from C05 and (k-o) from C06 test



differences between both cases. The maximum bending moment values recorded in the pile and the depth at which they are found are summarized in Figs. 3.33 and 3.34, respectively.

With the exception of the 1 Hz sine input, good reproducibility is observed between C04 and C05 tests results. The maximum bending moments are in the same order of magnitude and the envelope profiles have the same overall form. Except for the weak earthquake motions applied at the beginning of the tests, the response in terms of maximum bending moment is found to be slightly higher in C04 test.

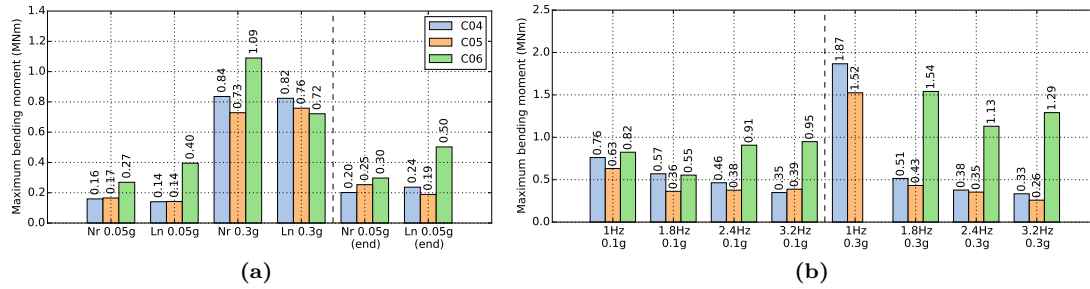


**Figure 3.33:** Maximum bending moment value recorded in the pile: (a) under seismic excitations and (b) sinusoidal base shakings

For both tests the maximum bending moment has been recorded during the 1 Hz 0.3g base shaking. The maximum value for the C04 and C05 tests were measured in the clay at a depth of 8.9 m and are respectively 1.87 MNm and 1.52 MNm. The difference represents a decrease of 18.7% between C04 and C05. It should be noted that a bending moment of 1.87 MNm represents 28% of the yield moment of the pile section. This finding highlights **the importance of considering kinematic interaction effects when designing piles, specially in the case of layered soil profiles with poor soil layers.**

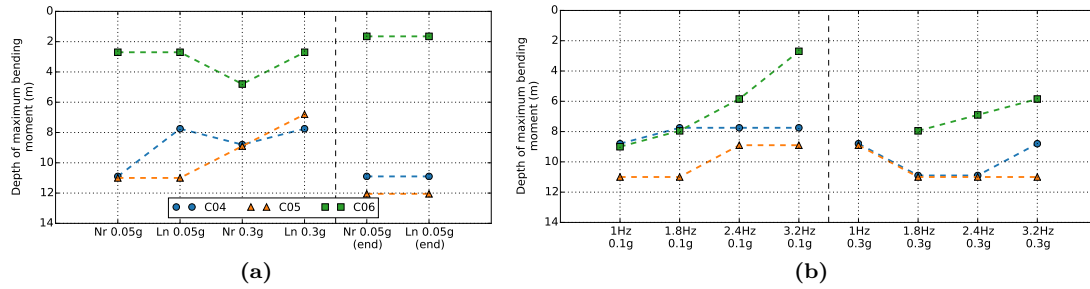


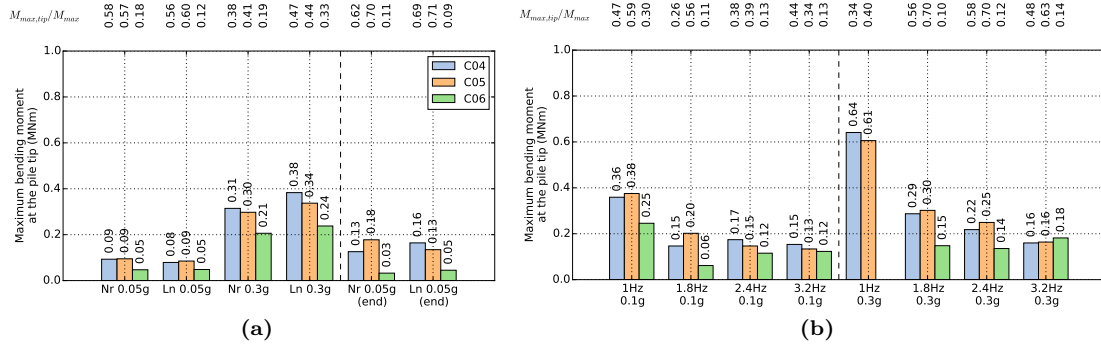
**Figure 3.34:** Depth of recorded maximum bending moment: (a) under seismic excitations and (b) sinusoidal base shakings

The analysis of sinusoidal base shaking cases shows that for the same PGA the maximum bending moment increased when the frequency went from 3.2 to 1 Hz (Fig. 3.32c, d, i, and Fig. 3.33). This evolution can be the effect of a resonance phenomenon of the soil column when the input frequency is in the vicinity of the response of the column in its state of distortion. Despite the fact that the distance between two successive accelerometers located in the same vertical array of accelerometers does not enable a precise determination of the strain level, it can be supposed, based on the previous analysis of the response frequency evolution of the soil, that non negligible nonlinear behavior took place including a decay of the response frequency of the soil column and in certain cases up to a state for which the container can have an influence.

For 1 Hz sine excitation, an important amplification of the response is observed between 0.1g and 0.3g shakings (maximum increase of 146%). On the contrary, results for 1.8 Hz, 2.4 Hz and 3.2 Hz are almost identical for 0.1g and 0.3g levels of PGA. It can be concluded that the effect of

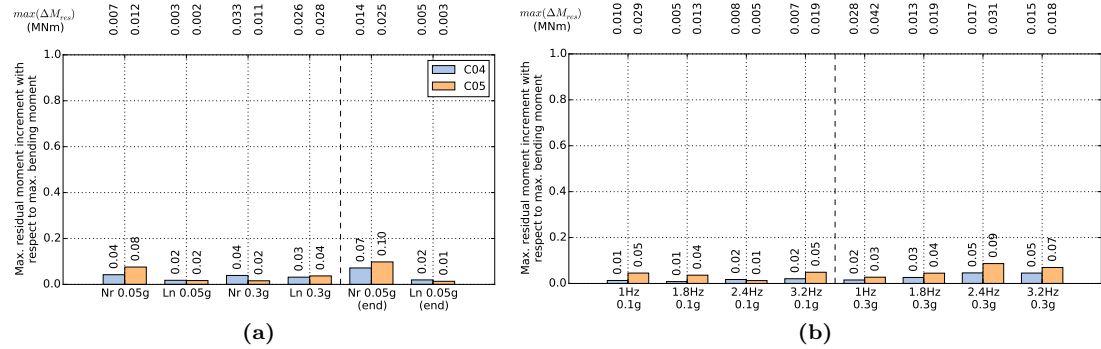
frequency on the maximum moment depends on the level of PGA and that this relation is highly non-linear, with almost no impact for frequencies 1.8 Hz to 3.2 Hz.

Near the pile tip, the bending moments were measured in the vicinity of the clay-sand interface. The results for C04 and C05 tests are given in Figure 3.35. The first observation is that **bending moments due to the pile tip embedment in dense sand are not negligible**. The maximum values are found for the 1 Hz sinusoidal base shaking (0.64 MNm for C04 and 0.61 MNm for C05). When this value is compared to the maximum bending moment recorded in the pile during the same base shaking, a maximum moment up to 70% of the maximum moment (in average) is found in the case of weak earthquake motions applied at the end of both tests.



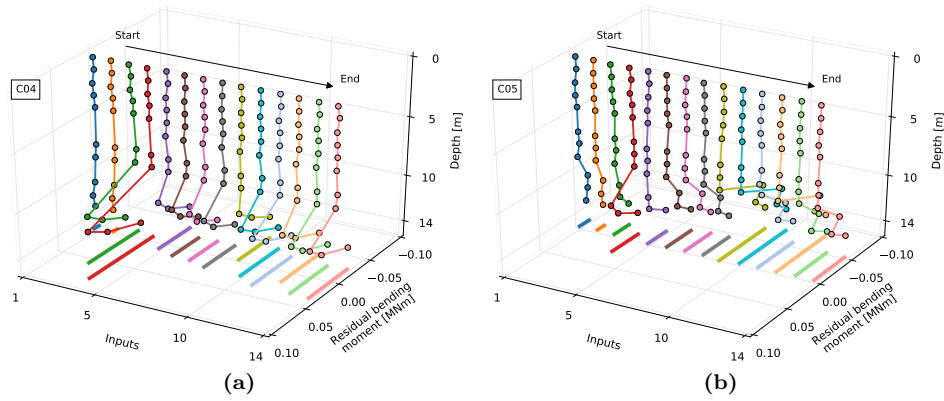
**Figure 3.35:** Maximum bending moment recorded near the pile tip: (a) under seismic excitations and (b) sinusoidal base shakings

The maximum residual bending moment increment induced by each one of the inputs is presented in Figure 3.36. It can be observed that the residual bending moment increments remain limited in comparison to the maximum bending moment for all the inputs, with a maximum ratio of 10%.



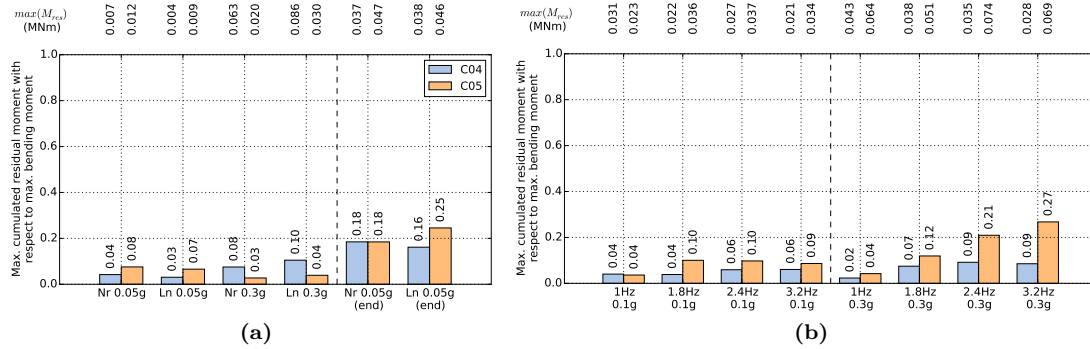
**Figure 3.36:** Maximum residual bending moment increment in C04 and C05 tests: (a) under seismic excitations and (b) sinusoidal base shakings

Figure 3.37 presents the evolution of the accumulated residual bending moment, defined as the bending moment at the end of each shaking minus the initial electric offset at the beginning of the first input, for C04 and C05 tests. It should be noticed that due to a bad configuration of the recording device, only the strain gauges located between 9 m depth and the tip of the pile captured correctly the residual bending moment in the pile. It is observed in Fig. 3.37 that the sign of the incremental residual moment has an impact on the evolution of accumulated residual bending moment. In some cases the incremental residual moment would increase the accumulated residual moment from previous base shakings whereas in other cases it would decrease cumulated values (opposite signs).



**Figure 3.37:** Evolution of accumulated residual bending moment during all 14 base shakings: (a) C04 test and (b) C05 test

The maximum value of accumulated residual bending moment at the end of each input is compared to the maximum bending moment recorded for that input in Fig. 3.38. A maximum ratio of 27% is found for 0.3g 3.2 Hz sine input in C05 test.



**Figure 3.38:** Maximum accumulated residual bending moment in C04 and C05 tests: (a) under seismic excitations and (b) sinusoidal base shakings

### 3.6.3.2 Kinematic and inertial interaction

The maximum bending moment envelopes recorded in C06 test are also given in Figure 3.32. As previously indicated, the sine 1 Hz 0.3g base shaking was not applied in this test.

When the response of the pile under earthquake loadings is analyzed, an interesting observation can be made. While the responses for Landers and Northridge earthquakes are very close in the case of C04 and C05 tests (pure kinematic interaction), this is no longer valid in the case of the C06 test (with inertial interaction) where the response differs between the two earthquakes for the same level of PGA with a stronger response of the Landers earthquake at 0.05g and for Northridge at 0.3g.

These differences can be explained from the analysis of the frequency content of the applied base shakings (see Fig. 3.18) and the frequency analysis of the soil and of the foundation conducted in previous sections. As already highlighted, for low seismic motions (PGA of 0.05g) the Landers earthquake is more energy rich compared to Northridge earthquake in the frequency range corresponding to the estimated response frequency of the system, that is the range 3.44-3.54 Hz. For strong seismic motions the opposite tendency is observed. With these elements in mind it

is straightforward to conclude that the response of the system in terms of bending moment is intimately related in this case to the inertial component (for the considered base shaking).

Having more energy “injected” into the system, this results in a larger development of nonlinearities. A larger development of nonlinearities results in both larger deformations of the soil profile and larger nonlinearities at the interface between the soil and the pile. In the continuity of this observation it is found that the envelope of maximum bending moment is more important for the earthquake that is more energy rich in the response frequency range of the soil column for the corresponding loading amplitude level. In other words, for low seismic motions the maximum bending moment recorded for Landers is more important and for strong seismic motions it corresponds to Northridge earthquake. The comparison of the weak earthquake motions applied at the end of the test to those applied at the beginning shows an increase of the response. This may be explained by the accumulation of nonlinearities in the upper part of the pile (which controls the inertial response of the system).

Looking closely to the results due to sine base shakings at 0.1g PGA (Fig. 3.32m), some interesting observations can be made. Two different zones are identified, the first one in the upper part of the pile up to a depth of 6 meters and the second one from 8 meters depth to the pile tip. In the shallower zone, inputs at 1 Hz and 1.8 Hz show the same overall form with bending moment values that are in the same order of magnitude. In the case of 2.4 Hz and 3.2 Hz sine inputs, they also have a similar shape with slightly higher values of 3.2 Hz sine input. In the case of the second zone identified in the response of the pile, the 1.8 Hz, 2.4 Hz and 3.2 Hz sine inputs have the same overall shape while the response for 1 Hz is much more important. Finally, it is observed that the location of maximum bending moment in the case of sine 0.1g PGA inputs is not always found at the same depth. In the case of 1 Hz input it is located in the lower part of the pile, for 1.8 Hz it is found in the middle part of the pile between 7 and 8 m depth, and in the case of 2.4 Hz and 3.2 Hz in the upper part of the pile.

The analysis of 0.3g PGA base shakings (Fig. 3.32n) shows also some interesting results. Again, two different zones are observed. In the upper part of the pile, up to a depth of around 4 m, the bending moment envelope increases with frequency where in the lower part of the pile, from a depth of about 6 m, the bending moment envelope decreases with frequency.

The evolution from 0.1g to 0.3g PGA is also interesting. In the case of 1.8 Hz base shaking the bending moment envelope has the same overall form with a maximum value located approximately at the same depth. The maximum bending moment increases in this case of about 178% from 0.1g to 0.3g PGA signal (with values of 0.55 MNm and 1.54 MNm respectively). In the case of 2.4 Hz sine input, there is a slight increase of bending moment in the first 4 meters of the pile and a much bigger increase at depths between 6 to 12 meters. Finally, for 3.2 Hz input, the same overall form is found, with a more or less constant increase of bending moment through all the pile length.

It is interesting to note that the depth at which maximum bending moment is recorded for all sinusoidal tests also changes with frequency, decreasing its value for increasing values of frequency. The same trend is observed for 0.1g and 0.3g PGA inputs.

The bending moment near the pile tip are in this case less important than for C04 and C05 tests. A maximum value of 0.25 MNm is recorded for sine 1 Hz 0.1g base shaking which represents 30% of the maximum bending moment that is recorded in the pile.

The observation of the results in Figure 3.35 shows that the response at the pile tip in the case of C06 is almost systematically lower than the same response obtained for C04 and C05 tests. It is possible to imagine that the inertial effects in the system has played some role in this result or that the conditions of the pile at its tip differ slightly between these three tests.

As noted earlier, a configuration problem of the recording device results in the impossibility to exploit the post-earthquake residual moment information for this test.

### 3.6.3.3 Comparison of kinematic and inertial effects

A first attempt to analyze the importance of kinematic and inertial interaction effects on the bending moment profile response can be made by comparing the envelopes obtained in the case

of pure kinematic interaction tests (C04 and C05) to those from the case case where inertial interaction is also present (C06), see Figure 3.39.

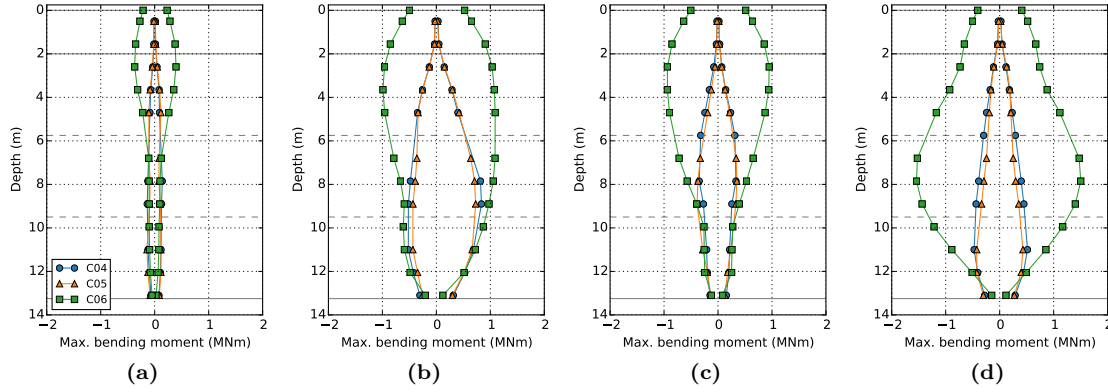


**Figure 3.39:** Comparison of maximum bending moments results from single pile tests without mass at the pile head (C04 and C05) and with a lumped mass at the pile head (C06): under (a) Landers 0.05g earthquake motion, (b) Northridge 0.3g earthquake motion, (c) 3.2 Hz 0.1g sinusoidal base shaking and (d) 1.8 Hz 0.3g sine

A first comparison of these curves makes it possible to conclude that **the inertial interaction plays an important role on the response of the upper part of the pile, up to a depth that depends on the type and the intensity of the loading**. In the case of weak earthquake motions applied at the beginning (with a PGA of 0.05g), the inertial interaction effects modify the response in the first 6 meters of the pile. This value increases up to 10 m when the strong earthquake motions are applied. The same observation is found when comparing sinusoidal inputs at a PGA of 0.1g. Finally, in the case of strong sinusoidal loadings with a PGA of 0.3g, the influence of inertial loading gets up to a depth of 12 m. For depths higher than those aforementioned, the response of the pile is judged close to that recorded in C04 and C05 tests. This observation allows to conclude that from that value of depth on, the response of the pile is essentially controlled by kinematic interaction.

### 3.6.4 Evolution of bending moments with time and frequency content

The previous analyses have focused on the maximum value of the response and the maximum bending moment envelopes. In this section the study would focus on the time evolution of the bending moment and also on the frequency content of the recordings along the pile length.

An example of this type of analysis is given in Fig. 3.40 for the case of a single pile with a mass at the pile head (C06 test) subjected to Landers 0.3g PGA seismic motion. The evolution of the normalized bending moment as well as the frequency analysis of the recordings along the pile depth are presented. The accelerations recorded at the level of the dense sand layer beneath the pile (at a depth of 19.55 m) along with the accelerations corresponding to the pile are also given for comparison.

It is interesting to observe in Fig. 3.40b that **the maximum response of the bending moment at different depths of the pile does not take place simultaneously**. With regard to the frequency analysis given in Fig. 3.40c, it is interesting to note that the response of the pile can be separated in two distinct zones in which the pile response is controlled by different frequency ranges. In the upper part of the pile and up to a depth of about 8 m the response of the pile is controlled by the frequency range from 2.8 to 3.6 Hz approximately. As indicated in Section 3.6.1, the response frequency of the pile cap for this level of loading is estimated in the to be in the frequency range from 2.96 to 3.04 Hz. This observation confirms the importance of inertial effects on the response of the pile in its first meters.

In the lower part of the pile, for depths beyond 8 m, the response is controlled by the frequency

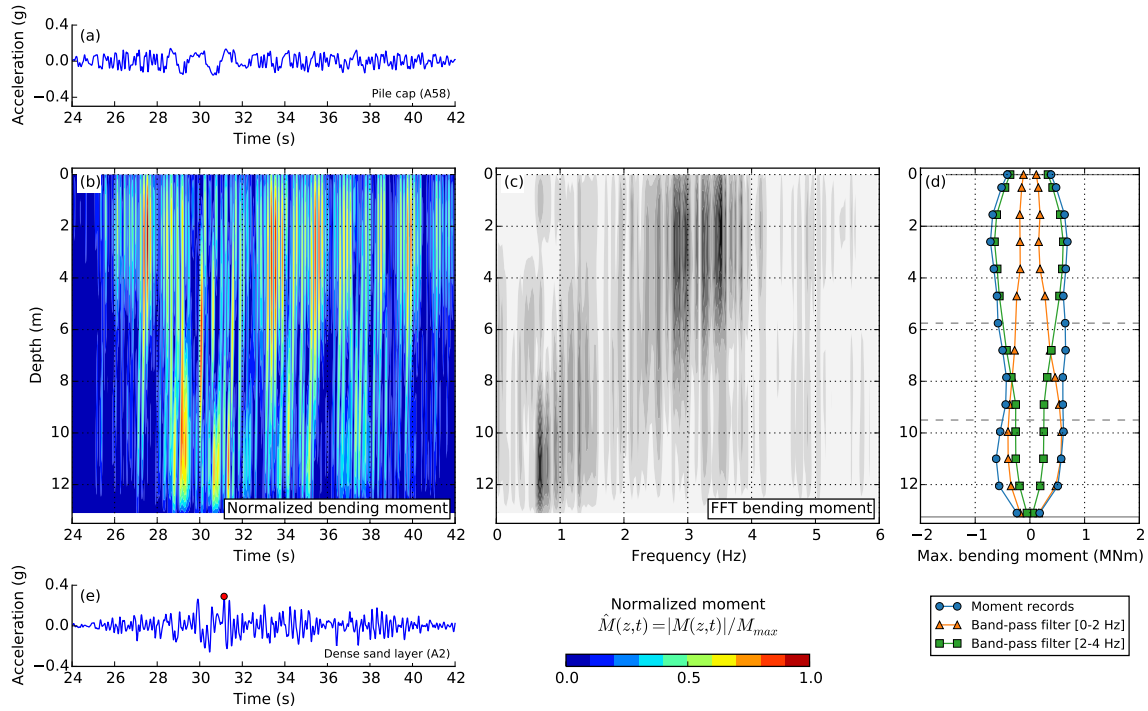


**Figure 3.40:** Time evolution and frequency analysis of the normalized bending moment in the instrumented pile used in C06 test (single pile with a mass at the pile head) under Landers 0.3g seismic motion. The accelerations recorded in the dense sand layer under the pile (at a depth of 19.55 m) and the pile cap are also presented

range from 0.6 to 0.8 Hz. This frequency range is consistent with the observed response frequency range for the soil profile (between 0.6 and 0.7 Hz, see Section 3.4.2).

A different way of visualizing the importance of the frequency content on the response of the system at different depths of the pile is to filter the moment records with a band-pass filter using the limits of the identified frequency ranges, i.e., between 0 and 2 Hz and between 2 and 4 Hz. The results in terms of maximum bending moment envelope are compared in Fig. 3.40d to the maximum moment envelope obtained directly from the unfiltered moment records. The same observations are made, with a response of the top of the pile controlled by the frequency range around the response frequencies of the pile cap (therefore essentially inertial interaction effects) and a response at the bottom of the pile controlled mainly by the frequency range corresponding to the fundamental response frequency of the soil profile (kinematic interaction effects).



## 3.7 Performance of pile groups under seismic loading

### 3.7.1 Frequency analysis

The analysis is carried out by taking into account the minimum value of the response frequency obtained by means of a time-frequency transfer function between the soil surface and the pile cap or the top mass of the structures (e.g., Fig. 3.41).

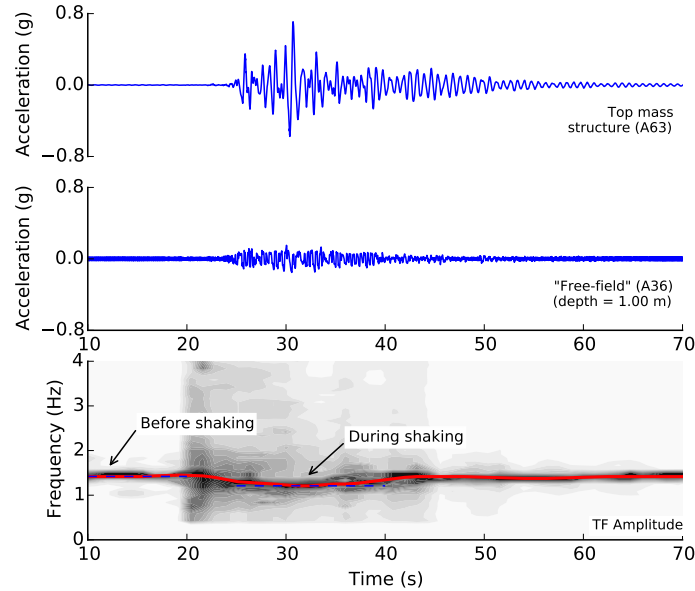


**Figure 3.41:** Time-frequency transfer function between the soil surface ( $z = 1$  m) and the mass at the top of the structure in C08 test under Northridge 0.3g earthquake motion

The estimated fundamental response frequencies for the test with a short structure (C07 test) are given in Figure 3.42. Figure 3.43 presents the corresponding results for the test with a slender structure (C08 test). The results are grouped by loading intensity and the application order of the different earthquakes.

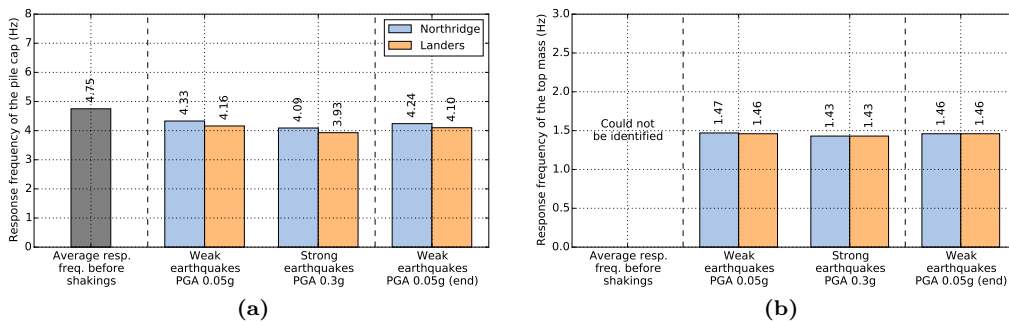


**Figure 3.42:** Frequency response of (a) the pile cap and (b) the top mass of the short structure in C07 test

#### 3.7.1.1 Pile cap

When the results from both tests are compared, the first observation is that the superstructure that is used in the test affects the response frequency of the pile cap, with a higher value of the response frequency of the pile cap when the slender structure is used. The same observation was

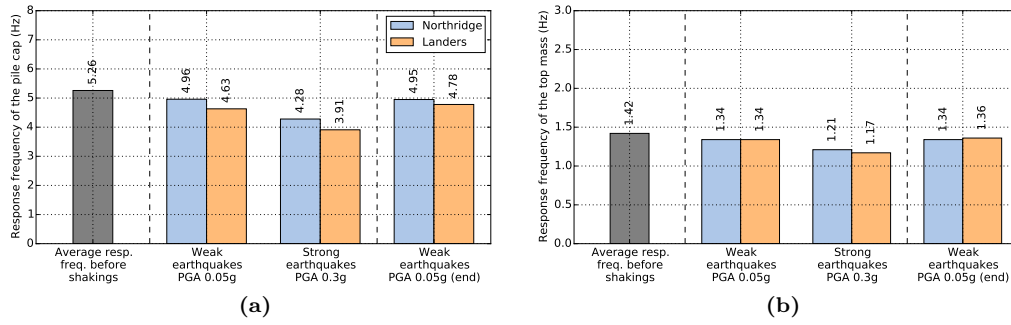


**Figure 3.43:** Frequency response of (a) the pile cap and (b) the top mass of the tall structure in C08 test

made in the case of the study conducted with a 1x2 pile group in a homogeneous Fontainebleau sand profile [117], with a response frequency of the pile cap that increased with the slenderness of the superstructure.

The response frequency of the pile cap in both tests changes with the intensity of the loading with a decrease in frequency that can reach 0.82 Hz in the case of C07 test and 1.35 Hz in the case of C08 test. In addition, it should be noted that the comparison of the results from the pile group tests to those from the test conducted on a single pile with a mass at the pile head (C06 test) shows that the single pile is more affected by the loading intensity (maximum decrease in response frequency of 1.45 Hz).

### 3.7.1.2 Top mass of the structure

As indicated in the previous sections, the response frequency of the buildings on fixed base conditions was measured and corresponds to 1.54 Hz in the case of the short building and 1.5 Hz in the case of the high building. As expected, their response frequency decreases as a result of the soil-foundation-structure interaction (Figs. 3.42b and 3.43b).

In the case of the short superstructure there is almost no effect of the type of earthquake and of the PGA for the input tested. The frequency response of the tall superstructure is more sensitive to the level of base shaking while the type of earthquake has a limited effect.

### 3.7.1.3 Summary

In view of the results it is concluded that **the response frequency of the pile cap is significantly affected by the intensity of the loading and of the nonlinearities that develop in the soil. The type of superstructure that is used has a significant influence on the decrease of the response frequency of the pile cap with a more pronounced effect in the case of the slender superstructure.** On the other hand, with regard to the response frequency of the superstructure, the results show that it is very little affected with a decrease of the response frequency that remains lower than 0.25 Hz in all cases.

In addition, an interesting observation was made during the analysis of the time-frequency transfer functions (e.g., Fig. 3.41), for both the pile cap and the top mass of the structure. The response frequency observed after the strong shaking phase of the earthquakes progressively returns to the response frequency of the system observed before the application of the input, and this for all the applied base shakings.

## 3.7.2 Response of the pile cap

The lateral response of the pile cap used in pile group tests (C07 and C08) is investigated. In this section, the influence of the superstructure slenderness and of the characteristics of the base shakings are analyzed. The response of the pile cap is evaluated in terms of maximum acceleration,



displacement and rotation. The results are shown in Figs. 3.44, 3.45 and 3.46, respectively. Two types of results are analyzed, those corresponding to the system under seismic loading and those corresponding to sinusoidal loadings.

### 3.7.2.1 Maximum acceleration

Under all the applied earthquake loadings the response of the pile cap in terms of maximum acceleration is from 18% to 25% higher when the pile group supports a short building, with the only exception of 0.3g Landers seismic motion for which this trend is reversed (Fig. 3.44).

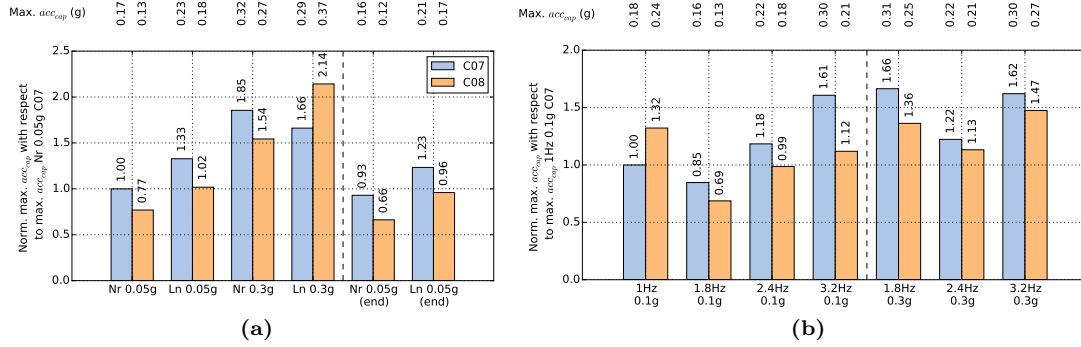


**Figure 3.44:** Normalized maximum acceleration of the pile cap: (a) under seismic excitations and (b) sinusoidal base shakings

It is interesting to note that in the case of the slender superstructure, the response of the system is always more important for the two Landers earthquake motions applied (PGA of 0.05g and 0.3g). On the other hand, in the case of the short building under strong seismic motions, the answer is stronger in the case of the Northridge earthquake which can be explained by the difference in the response frequency between the models (foundation + structure) used in the tests and a decrease of the energy content of the 0.3g Northridge earthquake beyond 4 Hz.

Concerning the two small earthquake motions applied at the end of the tests, the results compare to those from the small earthquake motions applied at the beginning of the tests and show only a slight reduction of the acceleration. The system's response is only slightly affected by the previous base shakings, which justifies the use of the same container with a series of base shakings.

When subjected to sinusoidal base shakings, the maximum acceleration is also higher when a short building is supported. The only exception is for the 1 Hz 0.1g sine that shows a higher maximum acceleration value when a tall building is supported. As it would be introduced later (Section 3.7.5), in this case a particular behaviour of the system was observed with a response that evolves from cycle to cycle. Leaving this particular case aside, an evolution of the response in terms of maximum acceleration depending on the loading frequency is observed.

### 3.7.2.2 Maximum relative displacement

Under weak seismic motions, the maximum relative displacement between the soil surface and the cap of the pile group remains in the same order of magnitude for the two earthquakes and the two tests (Fig. 3.45). It is observed that the maximum relative displacement is largely influenced by the base shaking amplitude regardless of the earthquake and the building. This increase is more important in the case of the tall building, the result of which is very probably influenced by the greater slenderness of the superstructure in that test. The comparison of the response for the weak seismic motions applied before and after the strong ones confirm the analysis based on the acceleration that the system response is only slightly influenced by previous base shakings.

The analysis of the results of the system subjected to sinusoidal solicitations at a PGA of 0.3g shows a decrease of the system response with the increase of the loading frequency.

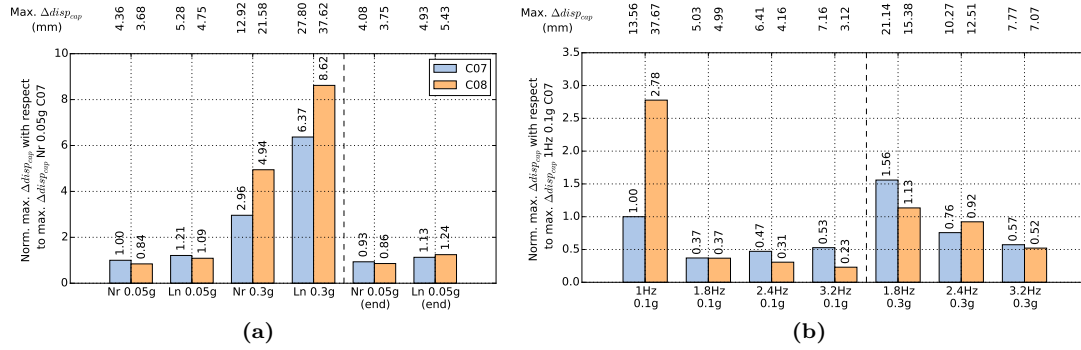


**Figure 3.45:** Normalized maximum displacement difference between the pile cap and the soil surface: (a) under seismic excitations and (b) sinusoidal base shakings

### 3.7.2.3 Maximum rotation

Under earthquake loading, the rotation of the pile cap is systematically higher when a slender superstructure is supported instead of a short building (Fig. 3.46). As expected the rotation increases also with the loading intensity. Regarding the weak seismic motions applied at the end and at the beginning of the test, once again there is no noticeable evolution of the response.

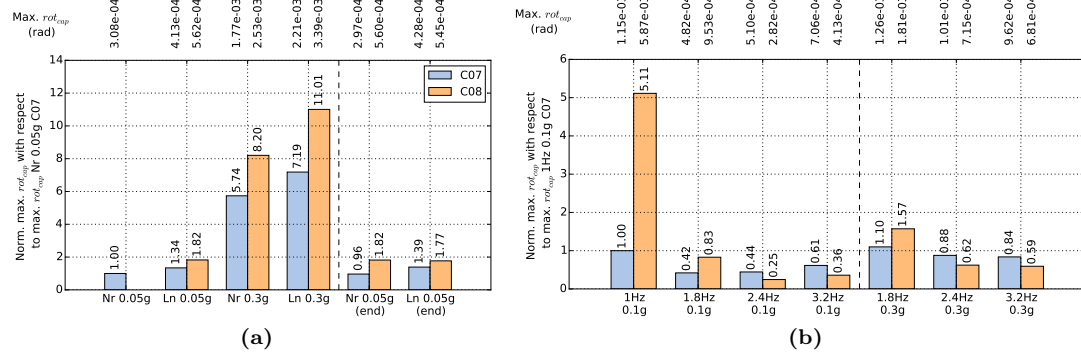


**Figure 3.46:** Normalized maximum rotation of the pile cap: (a) under seismic excitations and (b) sinusoidal base shakings

In the case of sinusoidal base shakings, it is found that the response is more important at low frequencies, i.e., 1 Hz and 1.8 Hz when a slender structure is supported. On the contrary for 2.4 Hz and 3.2 Hz sine loadings, the rotation is larger when a short building is supported. However for this test configuration the rotation remains small in all the cases (lower than  $5.87 \times 10^{-3}$  rad).

It should be noticed that the important amplification of the rotation that is found for 0.1g 1 Hz sine input in the case of the tall building is the result of the evolution of the system response through time. This particular case is studied in more detail in terms of bending moment in Section 3.7.5.

### 3.7.3 Shear force and overturning moment at the base of the superstructure

#### 3.7.3.1 Shear forces

The results in terms of maximum shear forces calculated at the base of the superstructure (see § 3.5.5) are given in Figure 3.47.

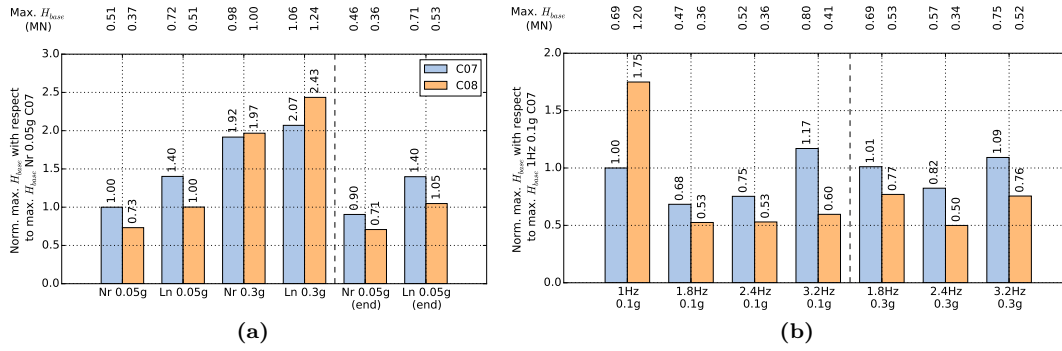


**Figure 3.47:** Normalized maximum base shear force: (a) under seismic excitations and (b) sinusoidal base shakings

Between the weak and the strong seismic motions the PGA of the base shaking is increased by 6 while the base shear force increases in a maximum ratio of 2.7. This observation is a clear indication that **the development of nonlinearities in the soil profile plays an important fuse role which results in a significant decrease of the loadings that are effectively applied at the base of the structure.**

It can also be observed that the response recorded when a short building is supported is more important for weak seismic motions. On the contrary, for strong seismic motions the response of the slender building configuration becomes either similar or more important than that for the short one.

In general terms, the same trends already observed during the analysis of the maximum accelerations at the pile cap are also found here. This is understood by the fact that the pile cap used in both tests is quite massive in comparison to the superstructures and thus, an important component of the inertial forces in the system is due to the vibration of the pile cap.

Under sinusoidal base shakings, shear forces are more important when a short structure is supported except for the 1 Hz 0.1g sine loading which requires a more detailed study (see for example Section 3.7.5).

#### 3.7.3.2 Overturning moment

As expected, the overturning moment when a tall building is supported is much higher than that recorded for the short one (Fig. 3.48). Compared to the increase of the PGA between the weak and strong earthquake motions that is multiplied by 6, the maximum overturning moment is multiplied by 2.57 to 2.8 times. This confirms the results obtained in terms of shear forces and the **beneficial effect of nonlinearity in the soil.**

For sinusoidal loadings, it is observed that the loading frequency has a direct impact on the overturning moment calculated at the base of the slender structure. The maximum overturning moment decreases with the increase of frequency. In addition, up to 2.4 Hz the slender case shows higher values of the overturning moment, while at 3.2 Hz the short structure experiences higher rocking moment values.

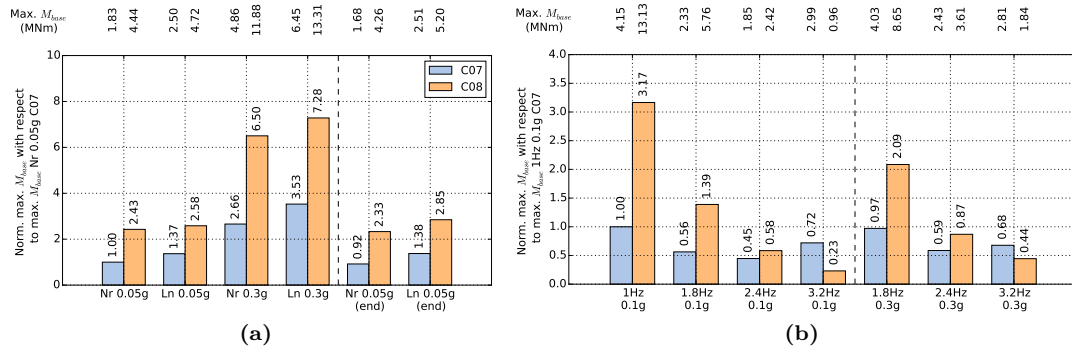


**Figure 3.48:** Normalized maximum overturning moment: (a) under seismic excitations and (b) sinusoidal base shakings

### 3.7.4 Maximum bending moments

The envelope curves of the maximum bending moments recorded in the center pile of the pile group (IP2) for C07 and C08 tests are given in Figure 3.49. Results are grouped according to PGA level and motion type, and ordered from left to right according to the input order as given in Table 3.11.

In what follows these results are analyzed. First the results from both tests are directly compared to highlight the impact of the slenderness of the superstructure in the response in terms of maximum bending moment profiles. Then, the results are compared to those from C04 test conducted on the response of a single pile without mass at its head (that is a pure kinematic interaction case). This comparison allows to study the impact of inertial and kinematic interaction effects on the response of the system.

#### 3.7.4.1 Results from pile group configurations

**Except for the 1 Hz 0.1g sine base shaking, the height of the superstructure gravity center does not have a noticeable effect on the overall shape of the envelope curve of the maximum bending moment.** For small earthquake loading the profiles are found to be almost identical. Some punctual differences appear in the case of strong seismic motions with slightly higher values when a slender superstructure is supported. In the case of sinusoidal base shakings, the slenderness of the superstructure only induces slight differences. In general, differences are concentrated in the upper part of the pile corresponding approximately to the first 6 meters of the pile.

The only case where the superstructure slenderness seems to play an important role in the response of the system is observed for the 1 Hz 0.1g sine input. The envelopes of maximum bending moments are totally different from one test to another. A more detailed analysis is given in Section 3.7.5.

The proximity between the results from both tests is also observed in terms of the maximum bending moment (Fig. 3.50). For all the base shakings the values remain fairly close between the two tests. Whether it is a tall or short superstructure that is supported the maximum bending moment is always located at the soil surface. In the case of sinusoidal base shakings, except for 1 Hz 0.1g sine input, two main zones are identified on the envelope curve of the maximum bending moment. The first one corresponds to the upper part of the pile up to a depth of approximately 6 m, and the second part concerns the lower part of the pile, from a depth of 6 m to the tip of the pile.

Three instrumented piles were used in the tests but only the results from the center pile of the pile group (IP2 pile) are presented and analyzed in this section. Indeed, this is justified by the fact that the response of the three instrumented piles in terms of maximum bending moment envelopes was found very close in both tests and for all the applied base shakings. The maximum difference is in all cases lower than 20% of the maximum bending moment recorded for each input. Figure 3.51

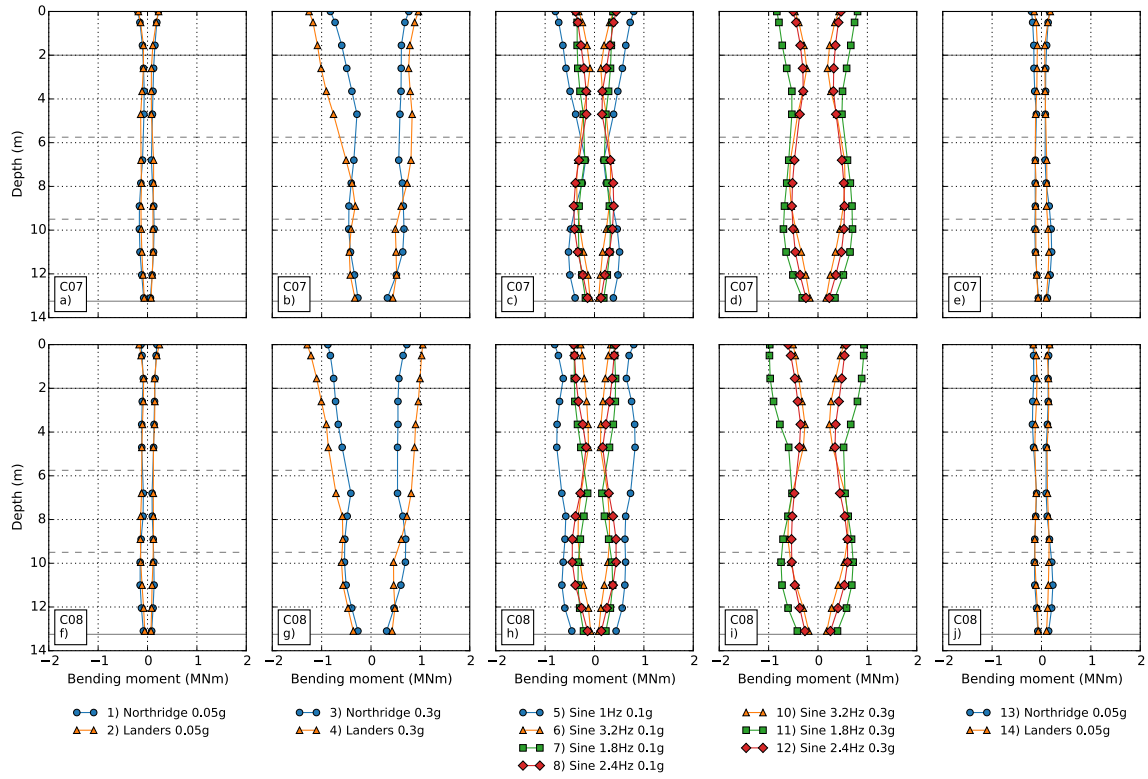


**Figure 3.49:** Measured maximum bending moments in the central pile of the pile group: (a-e) pile group a short superstructure (C07 test) and (f-j) pile group with a tall superstructure (C08 test)

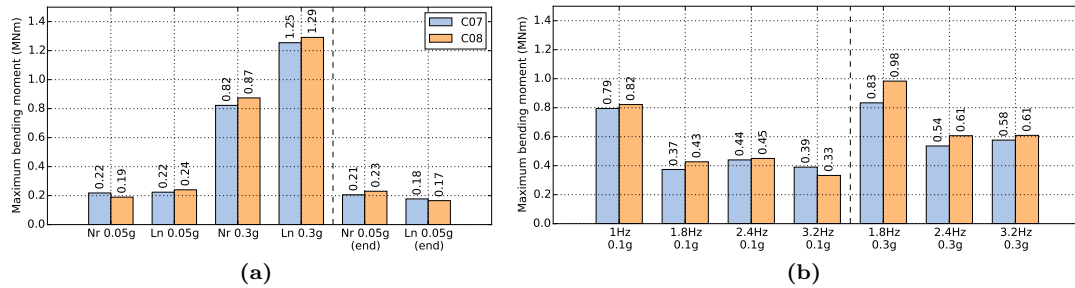


**Figure 3.50:** Maximum bending moment measured in central pile (IP2) in both pile group tests: (a) under seismic excitations and (b) sinusoidal base shakings

shows the comparison of the maximum bending moment envelopes of the three instrumented piles for some of the base shakings.

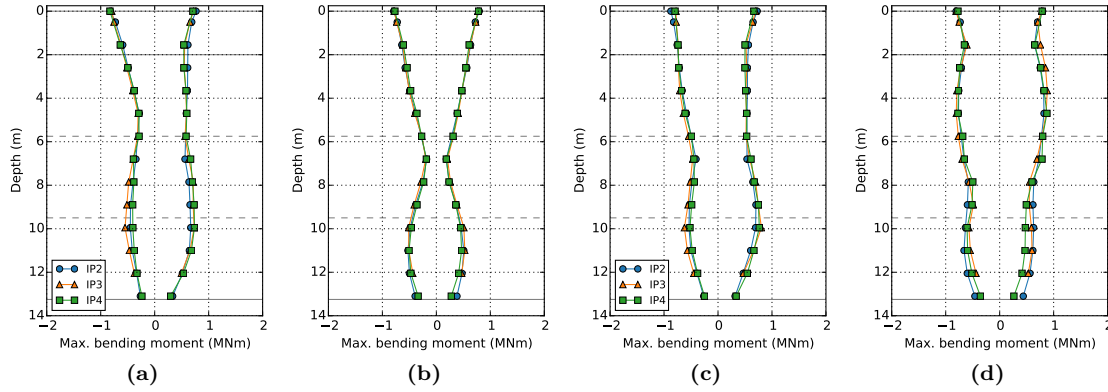


**Figure 3.51:** Comparison of maximum bending moment envelopes of the three instrumented piles in the pile group: for the short superstructure configuration (C07 test) under (a) Northridge 0.3g earthquake motion and (b) 1 Hz 0.1g sine input and for the tall superstructure configuration (C08 test) under (c) Northridge 0.3g earthquake motion and (d) 1 Hz 0.1g sine input

Figure 3.52 shows the maximum bending moment measured in the vicinity of the clay-sand interface near the pile tip. Similar values are found for both tests and they are not negligible. The maximum values are found for Landers 0.3g earthquake and 1 Hz 0.1g sine base shakings (0.44 MNm for C07 and 0.46 MNm for C08). When compared to the maximum bending moment recorded in the pile during the same base shaking, an average maximum ratio of about 60% is found in the case of weak seismic motions applied at the end of both tests. When compared to the same values found in single pile tests under pure kinematic interaction conditions (C04 and C05 tests, see Fig. 3.35), the same overall trends and order of magnitude are found.

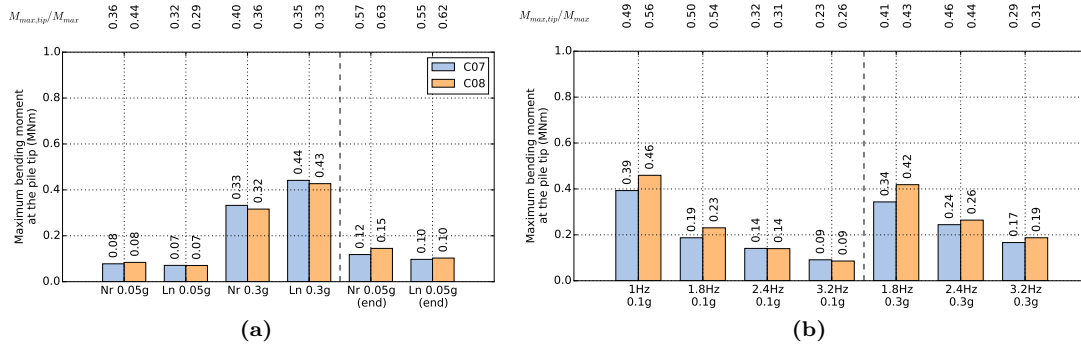


**Figure 3.52:** Maximum bending moment recorded near the pile tip of the central pile (IP2): (a) under seismic excitations and (b) sinusoidal base shakings

In the case of pile group configurations, the residual bending moment increments remain limited in comparison to the maximum bending moment for all the cases, with a maximum ratio of 6% (Fig. 3.53).

The evolution of the accumulated residual bending moment is presented in Figure 3.54. It is observed that unlike the single pile configurations, there is no change in the sign of the residual bending moment increments and therefore the accumulated residual moment either increases or stays the same after every base shaking.

Figure 3.55 compares the maximum value of the accumulated residual moment to the maximum bending moment recorded in each input. It is observed that the accumulated residual bending

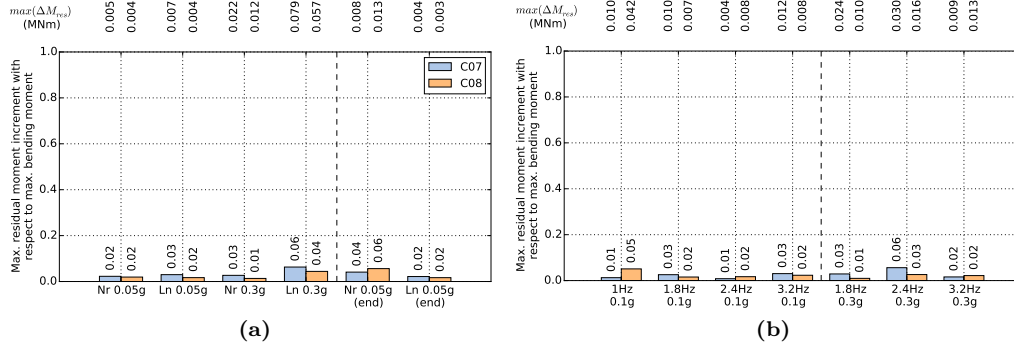


**Figure 3.53:** Maximum residual bending moment increment in C07 and C08 tests: (a) under seismic excitations and (b) sinusoidal base shakings

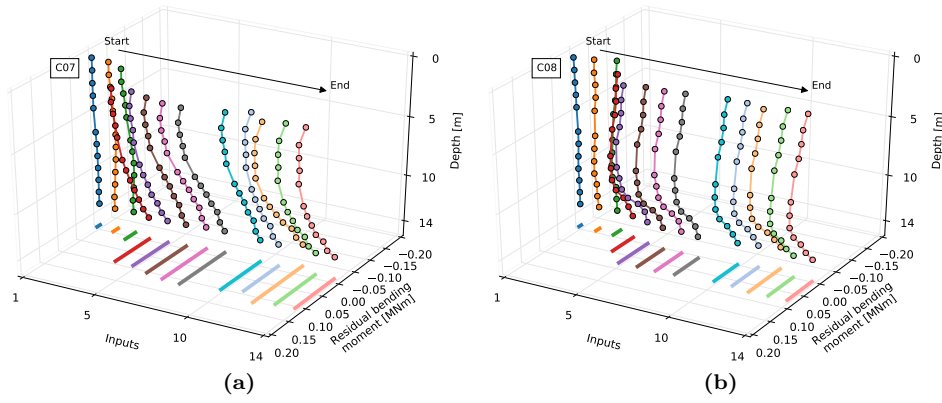


**Figure 3.54:** Evolution of the accumulated residual bending moment during all 14 base shakings: (a) C07 test and (b) C08 test

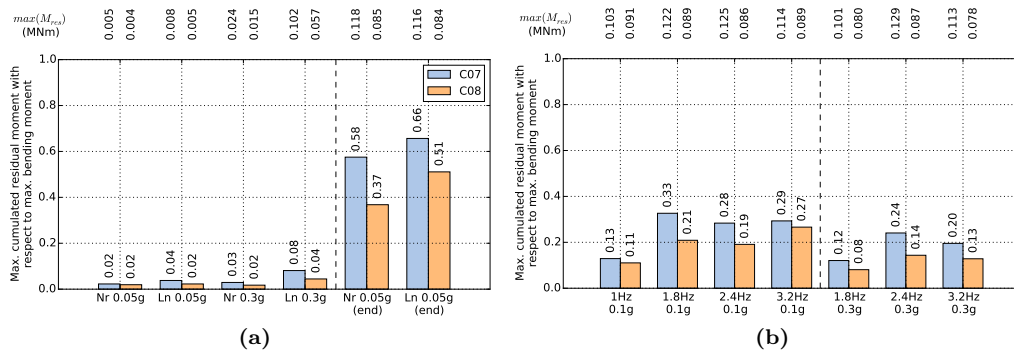


**Figure 3.55:** Maximum accumulated residual bending moment in C07 and C08 tests: (a) under seismic excitations and (b) sinusoidal base shakings



moment is not negligible, specially at the end of the base shakings series when weak signals are used after strong ones.

### 3.7.4.2 Inertial vs. kinematic interaction

The envelope curves of the maximum bending moment recorded in the center pile of the pile group (IP2 pile) are compared in Figure 3.56 to the envelopes from the C04 test, consisted of a single pile without mass at the pile head in the same soil profile and subjected to the same inputs (see §3.6). To avoid making the text more cumbersome, the comparison in the Figure 3.56 is limited to four selected cases. This comparison is a first attempt to analyze the importance of the kinematic and inertial interaction effects on the bending moment profile response. Indeed, the differences on the response in the present case are due to the presence of a mass but also to the pile group effect which influences the kinematic interaction and also introduces rotational restraint at the pile head compared to the case of a single pile with a mass at the pile head.

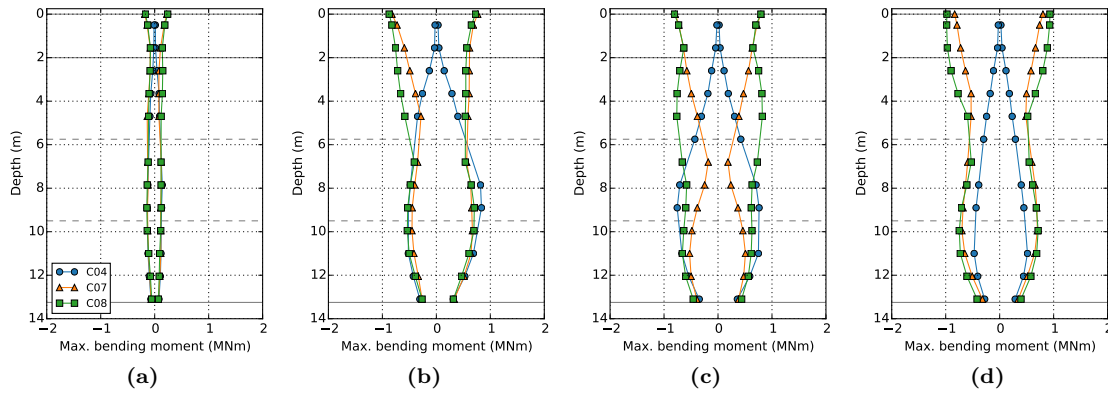


**Figure 3.56:** Comparison of maximum bending moments results from a single pile test (C04) and pile group tests (C07 and C08): under (a) Landers 0.05g earthquake motion, (b) Northridge 0.3g earthquake motion, (c) 1 Hz 0.1g sinusoidal base shaking and (d) 1.8 Hz 0.3g sine

In the case of the seismic motions, the same shape of the maximum bending moment profile is found from the pile tip up to a depth of about 4 m for weak earthquake motion (e.g., Fig. 3.56a), and up to a depth of 7 m for the strong one (e.g., Fig. 3.56b). Therefore, **the response in the lower part of the pile is essentially controlled by the kinematic interaction due to the embedment of the piles tip of one diameter in the dense sand layer. The response at the upper part of the piles is influenced by inertial interaction effects.**

In the case of sinusoidal base shakings, a close response is found for the three test only from a depth beyond 11 m. For base shakings at a PGA of 0.1g, a completely different shape of the response is normally found for the the different tests. The differences are not only in amplitude but also in terms of overall shape (e.g., Fig. 3.56c). When it comes to the analysis of the 0.3g PGA sine inputs, two different zones are identified. A first zone wich generally extends from a depth of around 4-5 m to 11 m where the bending envelopes have the same shape but those corresponding to the pile group cases are higher in amplitude with respect to C04 test. An a second zone, in the first 4 to 5 meters of the pile were the bending moments are modified in an important way by the inertial interaction forces and moments transmitted to the pile foundation by the superstructure (e.g., Fig. 3.56d). These findings indicate that inertial interaction effects play an important role in the pile response in the first 11 m.

The comparison of these observations to those obtained from the analysis of single pile tests results (see §3.6.3.3) reveals that for the same loading, inertial effects on the response of the piles seems to be reduced in depth in the pile group configurations with respect to the single pile with a mass at the pile head case. However, this observation must be treated with caution because there



the boundary conditions at the pile head are different and the pile-head mass used in C06 test is not equivalent to the mass in the pile group tests divided by the number of piles.

### 3.7.5 Evolution of bending moment with time

So far the analysis of bending moment results have been performed in terms of maximum values and envelope profiles. In this section, the evolution of bending moments with time is studied. In the following analysis, the residual bending moment induced by previous base shakings is not considered (the offset at the beginning of each input has been removed).

An example of this analysis is given in Figures 3.57 and 3.58 for the 0.3g PGA Northridge earthquake and the C07 and C08 tests, respectively. Results are given for two instrumented piles in the group, the IP2 pile in the center and the IP3 pile in the outer part of the pile group (see Fig. 3.25). To improve visibility, the moment history is normalized with the maximum bending moment recorded in both piles. The acceleration recorded in the dense sand layer under the pile group (at a depth of 19.55 m and 18.05 m in the case of C07 and C08 tests respectively), along with the accelerations corresponding to the pile cap and the structure are also given for comparison.

It is interesting to observe that the maximum bending moment recorded at depths higher than 6 m (part of the pile that is essentially controlled by kinematic interaction, see Section 3.7.4.2) and those recorded at the top of the piles (controlled by the inertial loading from the superstructure) do not take place simultaneously in time. This confirms the observations made in the literature and several design codes concerning kinematic and inertial type moments that do not necessarily take place at the same moment of time. The same observation was made for all the applied base shakings.

An additional observation concerning the results in Figures 3.57 and 3.58 is that the bending moments are similar from one test to another and only slight differences appear around 4 m depth, which corresponds to the part of the pile influenced by inertial loading and thus reflects the difference in terms of overturning moment between both tests (see Fig. 3.48).

A very interesting result is found for 1 Hz 0.1g sinusoidal inputs where the response of the tall structure configuration (C08 test) shows an important evolution of the bending moment with time. The same analysis is conducted and the time evolution of the normalized bending moment in piles and the envelope of maximum bending moment for these inputs are presented in Figures 3.59 and 3.60.

Regarding the maximum bending moment in the lower part of the pile, the response of both tests is similar during the first cycles. For the configuration with a short building, it is observed that the maximum bending moment profile stabilizes after the first four cycles. In the lower part of the pile, the maximum moment remains stable both in value (maximum value of 0.53 MNm recorded in IP3 pile) and in depth (around 11 m). On the contrary, with the slender superstructure there is a sharp evolution of the moment profile over time. The maximum moment that is initially recorded in the lower part of the pile evolves in amplitude with the cycles. The depth at which the maximum bending moment is recorded also changes with the cycles, from a depth of about 11 m to 4 m when the maximum moment is recorded (0.88 MNm in IP3 pile).

The response of the system for this particular case can be explained by the interaction between the kinematic and inertial effects. The amplitude of the response in the upper part of the piles degrades the surrounding soil and thus the soil reaction. Due to a greater slenderness ratio, the configuration with a tall structure develops a higher overturning moment and thus additional degradation of the soil due to inertial loading. The decrease of the soil reaction is accompanied with an increase of the displacements, the rotations and the bending moment in the upper part of the pile which, as already observed, is essentially controlled by the inertial loadings at the pile head. At the same time, the diminution of the reaction in the upper part of the pile has an influence on the kinematic bending moment. The soil reaction in the upper part of the pile being smaller, the pile is able to better accommodate kinematic deformations induced by the pile tip embedment in the dense sand layer at the bottom of the soil profile. As a consequence, the bending moment in the lower part of the pile is reduced as shown in Fig. 3.61, where the evolution of the maximum bending moment envelope for IP2 pile at different time ranges is presented.

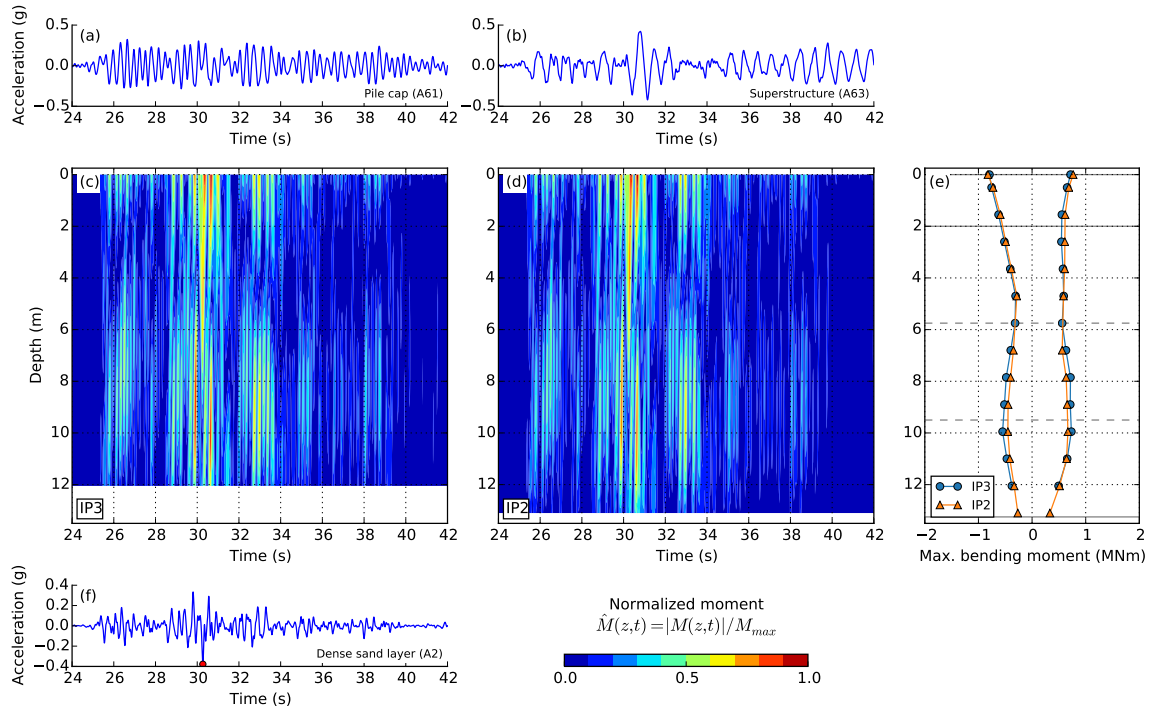


**Figure 3.57:** Time evolution of the normalized bending moment and envelope of the maximum bending moment in two of the instrumented piles (IP2 and IP3) in short superstructure configuration (C07 test) under Northridge 0.3g earthquake. The accelerations recorded in the dense sand layer under the pile group (at a depth of 19.55 m), the pile cap and the superstructure are also presented

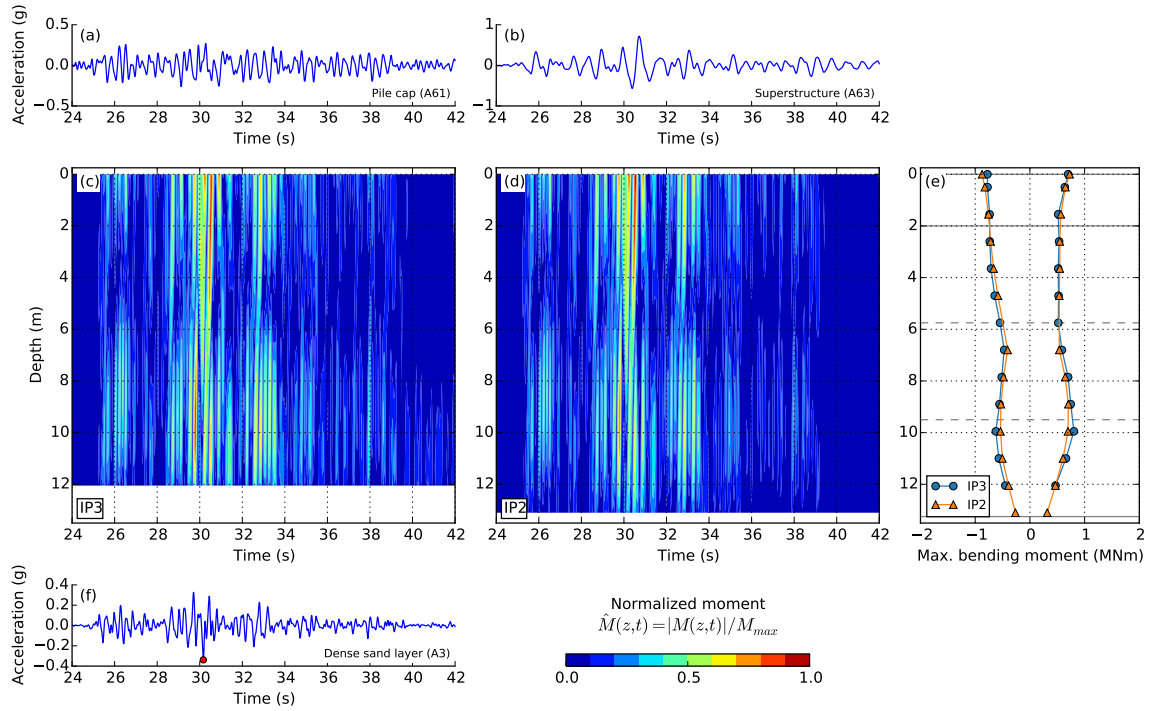


**Figure 3.58:** Time evolution of the normalized bending moment and envelope of the maximum bending moment in two of the instrumented piles (IP2 and IP3) in tall superstructure configuration (C08 test) under Northridge 0.3g earthquake. The accelerations recorded in the dense sand layer under the pile group (at a depth of 18.05 m), the pile cap and the superstructure are also presented

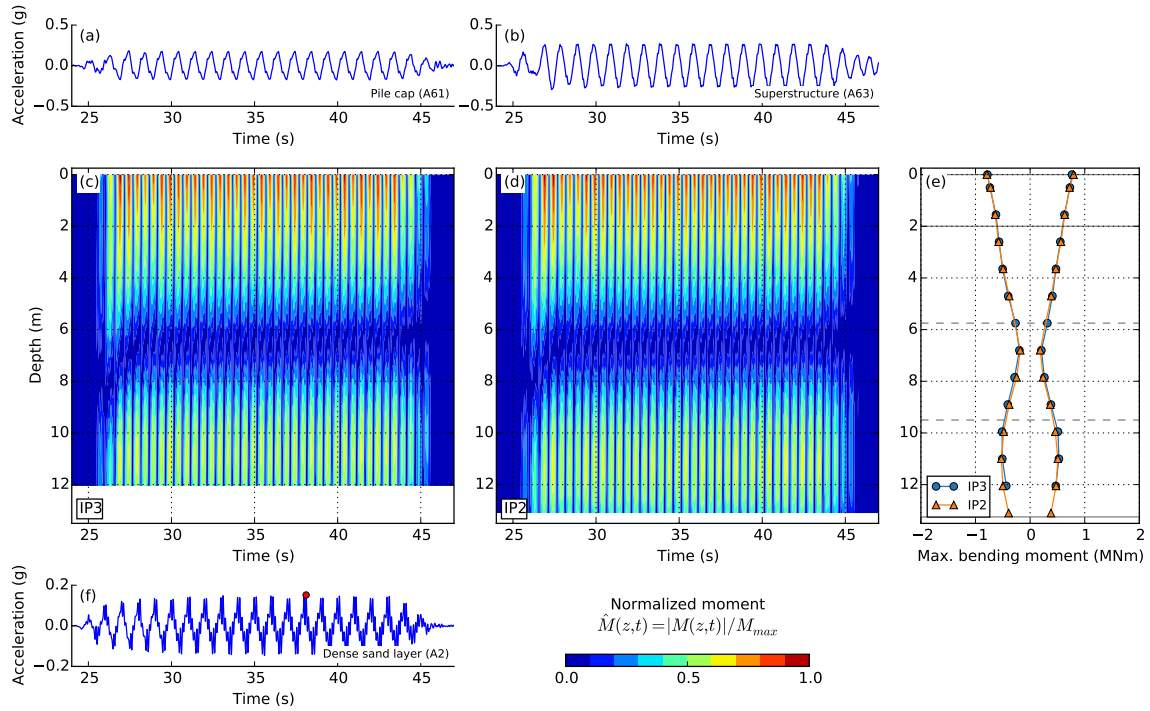


**Figure 3.59:** Time evolution of the normalized bending moment and envelope of the maximum bending moment in two of the instrumented piles (IP2 and IP3) short superstructure configuration (C07 test) under Sine 1 Hz 0.1g base shaking. The accelerations recorded in the dense sand layer under the pile group (at a depth of 19.55 m), the pile cap and the superstructure are also presented

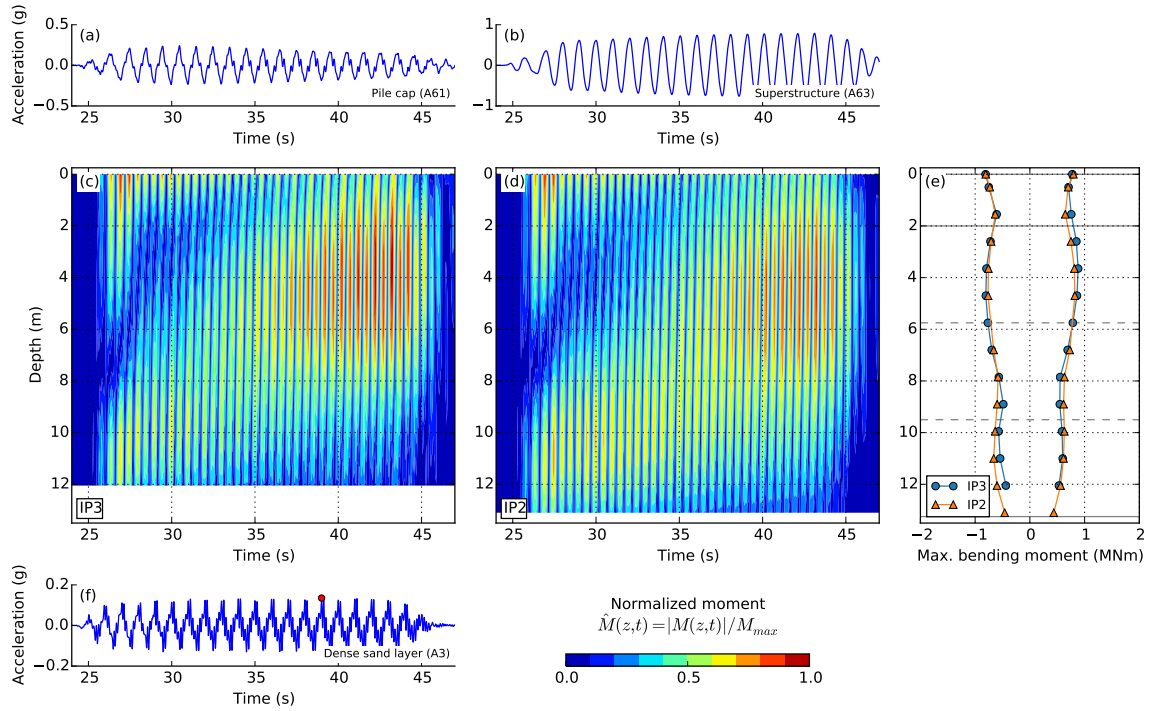


**Figure 3.60:** Time evolution of the normalized bending moment and envelope of the maximum bending moment in two of the instrumented piles (IP2 and IP3) in tall superstructure configuration (C08 test) under Sine 1 Hz 0.1g base shaking. The accelerations recorded in the dense sand layer under the pile group (at a depth of 18.05 m), the pile cap and the superstructure are also presented

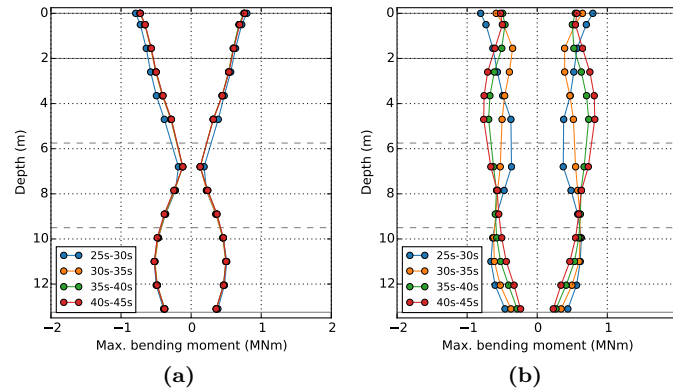


**Figure 3.61:** Maximum bending moment envelopes at different time periods for (a) short superstructure (C07 test) and (b) tall superstructure (C08 test) configurations under Sine 1 Hz 0.1g base shaking

The results from the analysis conducted in this section confirm that **the response of the system in terms of maximum bending moment depends on the type of loading, its intensity and frequency content but also the characteristics of the superstructure which in this case is essentially the slenderness ratio.**

The difference in the response between C07 and C08 tests for the 1 Hz Sine signal is related to the difference in terms of slenderness ratio between the two superstructures and therefore the presence of a higher rotational component in the response of C08 test that amplifies the response of the piles in their upper part and influences the reaction of the surrounding soil. In addition, it can be concluded that **the interactions of inertial or kinematic origin can be brought to interact together and may result in a complex evolution of the response of the system with time under certain configurations.**

### 3.8 Summary

Dynamic centrifuge tests were conducted to study the behavior of end-bearing single pile and pile group configurations in a layered soil profile and subjected to seismic and sinusoidal base shakings. The details of the conducted tests were presented in this chapter along with several relevant results regarding the response of the soil profile, the foundations and the superstructures.

Regarding the **response of the soil profile**, several interesting observations should be highlighted:

- Despite the complexity in the fabrication of the soil profile, the variation of shear wave velocity with respect to the average value remains low for all of the tests with a maximum decrease of 8.9%, which proves a satisfactory repeatability of the soil profile. This allows a direct comparison of the results from one test to another;
- The peak acceleration at the ground surface was amplified during low-amplitude earthquake loadings, while it was attenuated during high amplitude base motions which is a clear indication of nonlinear behavior of the soil profile. Increasing the peak base acceleration increased the degradation of the shear modulus and thus decreasing at the same time the fundamental frequency response of the soil profile;
- Under strong base shaking the clay layer is responsible of most of the attenuation of the signal. This layer experiences nonlinear behavior as a result of high strain levels and controls to an important extent the response of the soil profile.

The analysis conducted on the **response of the piles** both from the single pile and the pile group tests allows to draw the following conclusions:

- The response of the system in terms of maximum bending moment depends on the type of loading, the intensity, the frequency content and the conditions at the pile head;
- The maximum responses of the bending moment at different depths of the pile do not take place simultaneously;
- Kinematic and inertial interaction effects are both important and need to be considered when piled foundations are being used. Kinematic interaction effects may become important in the case of layered soil profiles (as in the present case), when important differences of stiffness between soil layers are present (i.e., bending moments due to the pile tip embedment in dense sand are found in this case not negligible). Special care needs to be addressed to cases where there are important amplification effects which may conduct to bending moments high enough to endanger the integrity of the pile;
- The comparison of the results from single pile tests with and without mass at the pile head allows to observe that the inertial interaction plays an important role on the response of the upper part of the pile, up to a depth that depends on the type (i.e., frequency content) and the intensity of the loading;
- The response of the pile is controlled in its upper part by a frequency range around the fundamental response frequencies of the foundation and at the lower part of the pile by the frequency range that corresponds to the fundamental response frequency of the soil profile;
- The interactions of inertial and kinematic origin can be brought to interfere with each other and may result in a complex evolution of the response of the system under certain configurations.

In terms of the **response of the superstructures**, it is observed that the development of nonlinearities in the soil plays an important role which results in a significant decrease of the loadings that are effectively applied at the base of the structure (both in terms of shear force and overturning moment). The beneficial effect of nonlinearity in the soil is thus highlighted.

## Chapter 4

# Numerical work

### 4.1 Introduction

Finite element modelling is nowadays the most used numerical method to solve SSI problems in academia but also in design offices. When the problem is solved in the time domain it is possible to take into account various nonlinear phenomena (e.g., anelastic material behavior, gapping, sliding...). In the case of deep foundations, the method allows considering the effects of pile-soil-pile interaction, the influence of the frequency and of the intensity of the loading on the foundation response.

Two different approaches are followed in this chapter, a simplified one using the so called equivalent linear elastic model and a more complex approach based on nonlinear finite element analysis with suitable inelastic constitutive models [80]. The equivalent linear elastic approach is commonly used in engineering practice to solve SSI problems, either in a direct way or by means of a superposition scheme, as introduced in Section 2.5. The results from both approaches are compared to recorded data from centrifuge tests in order to assess the performance and limitations of each method.

### 4.2 Nonlinear soil response

#### 4.2.1 Behaviour of soils under cyclic and dynamic loading

Soils are multiphase materials composed of a solid skeleton of soil particles and voids which may be filled with water or air, depending on the soil saturation degree. For simplicity reasons, several constitutive models consider the soils either dry or completely saturated with water [38].

In the latter case, it is also generally assumed that the seismic loading is sufficiently short in time for the soils to remain in an undrained situation (except for coarse sands and gravels), i.e., the increment of pore pressure generated by the seismic loading does not have time to dissipate before the end of the seismic event. This is an important aspect of the dynamic behavior of the soils compared to static conditions [64, 65]. This hypothesis affects the soil deformability, since the water present in the voids prevents volumetric deformations, while the soil strength is considered constant and equal to that available immediately before the earthquake (in the absence of cyclic degradation and susceptibility to liquefaction).

In practice, the undrained strength is often described by considering a failure criterion independent of the effective stress, for example using the Mohr-Coulomb failure criterion with a zero friction angle and a cohesion equal to either the undrained cohesion  $C_u$  for a clay-like soil or the undrained cyclic resistance  $\tau_{cyc}$  for a fully saturated sand-like soil [24]. In other words, when working with completely saturated soils, imposed cyclic stresses and results are usually expressed in terms of total stress. Since the behavior of the soil is governed by the effective stress, only the constitutive laws defined in terms of the effective stresses are capable to determine the tendency to the variation of volume of the soil which is translated, in undrained or partially drained behavior,



to a variation of the pore pressure and therefore the effective stresses. Most SSI analysis consider only the deviatoric behavior of soil and are often conducted in terms of total stresses, thus neglecting the volumetric changes since their simulation require advanced soil models. This approach is no longer valid for partially saturated soils or complex drainage conditions [166, 38].

#### 4.2.1.1 The Mohr-Coulomb failure criterion

The Mohr-Coulomb criterion is widely used in geotechnical applications to take into account (at least in a simplified manner) the inelastic behavior of soils. The criterion assumes that the yield function is governed by the maximum shear stress. Under drained conditions, the Mohr-Coulomb criterion reads:

$$\tau_f = c' + \sigma'_n \tan(\phi') \quad (4.1)$$

where  $\tau_f$  is the maximum possible shear stress in an arbitrary plane,  $c'$  the cohesion,  $\sigma'_n$  the normal effective stress and  $\phi'$  the angle of internal friction or friction angle. The cohesion and friction angle are usually noted  $c'$  and  $\phi'$  respectively in order to point out the use of effective stresses. The criterion is illustrated using the Mohr's circle in Figure 4.1a. It is interesting to observe how increasing the effective confining pressure increases the shear strength.

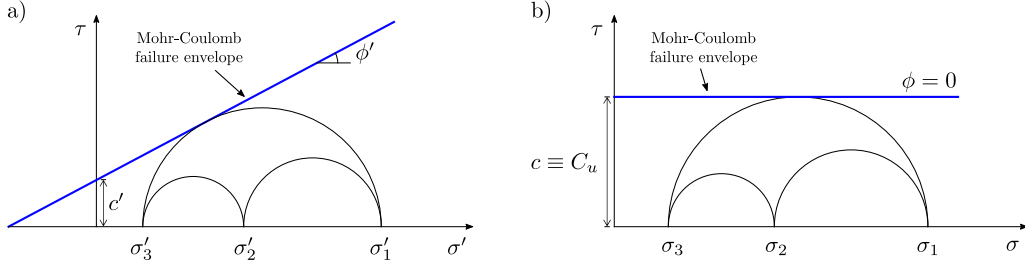


**Figure 4.1:** Mohr-Coulomb criterion for (a) drained conditions and (b) undrained conditions

Under undrained conditions and as already mentioned, the Mohr-Coulomb criterion is often written using total stresses:

$$\tau_f = c + \sigma_n \tan(\phi) \quad (4.2)$$

Furthermore, the friction term is often neglected ( $\phi = 0^\circ$ ) [217] and the Mohr-Coulomb criterion reduces to the Tresca-criterion:

$$\tau_f = C_u \quad (4.3)$$

with  $C_u$  the undrained cohesion. The Mohr-Coulomb criterion for the undrained case is given in Fig. 4.1b.

#### 4.2.1.2 Dilatancy

A fundamental aspect of soil behavior is dilatancy, which is the tendency of soils to change volume when subjected to shear. Under drained conditions, soils increase in volume if they are initially dense or overconsolidated (OC), or contract if they are initially loose or normally consolidated (NC). When no drainage is possible (i.e., most saturated soils under seismic loading), volumetric changes are no free to occur leading to important pore water pressure changes [38].

Dilatancy is measured with the dilation angle  $\psi$ , which controls the amount of plastic volumetric strain developed during yielding. It should be recalled that this is not a general property of soils but a material constant of a specific elastic-perfectly plastic soil model, namely the non-associative Mohr-Coulomb model. A value of  $\psi = 0^\circ$  corresponds to no volume change, which is common for clay soils [217]. For sand, the dilation angle  $\psi$  is dependent on the friction angle  $\phi$  and it can be estimated as  $\psi = \phi - 30^\circ$  [194]. This practical recipe is however too simplistic and cannot be

considered of general validity but it is of some use in simulations made with the elastic-perfectly plastic Mohr-Coulomb model to guess a reasonable value to be adopted for  $\psi$  (assumed constant).

#### 4.2.1.3 Low-strain shear modulus

One important parameter that needs to be taken into account in SSI problems is the low-strain shear modulus,  $G_{max}$  (sometimes also noted  $G_0$ ). It is connected to the shear wave velocity  $V_{s,max} = \sqrt{G_{max}/\rho}$ , where  $\rho$  is the soil mass density. Experimental data suggests that  $G_{max}$ , for all types of soils (granular and cohesive), depends on the soil density (expressed through the relative density  $D_r$  or the void ratio  $e$ ), the current stress state and the stress history (expressed by the overconsolidation ratio, OCR) [221]. In addition, it is also found that the frequency (or the rate of loading) has not practical effect on  $G_{max}$ , i.e., meaning that the soil is basically not a viscous but rather a hysteretic material [68].

A common expression of  $G_{max}$ , that includes the effects of soil plasticity and of the overconsolidation ratio (OCR), is given by Hardin and co-workers [84, 85, 83]:

$$G_{max} = 625 \frac{OCR^k}{0.3 + 0.7e^2} \sqrt{p_a \sigma'_m} \quad (4.4)$$

where  $\sigma'_m = (\sigma'_1 + \sigma'_2 + \sigma'_3)/3$  is the effective mean normal stress,  $p_a$  the atmospheric pressure ( $\sim 100 \text{ kPa}$ ); and  $e$  the void ratio. The value of  $k$  depends on the plasticity index,  $I_P$ , according to Table 4.1.

**Table 4.1:** Exponent  $k$  (after Hardin & Drnevich [85])

$I_P$ (%)	$k$
0	0.00
20	0.18
40	0.30
60	0.41
80	0.48
$\geq 100$	0.50

#### 4.2.1.4 Shear modulus and damping ratio

In most site response analyses and SSI applications the seismic motion is modeled by means of a vertically propagating shear wave. Under these conditions, a soil element at a depth  $h$  is subjected to the idealized cyclic loading presented in Figure 4.2 where  $K_0$  is the coefficient of lateral earth pressure at rest ( $\sim 0.5$  for normally consolidated soils and even higher than 1 in the case of heavily overconsolidated soils) [166].

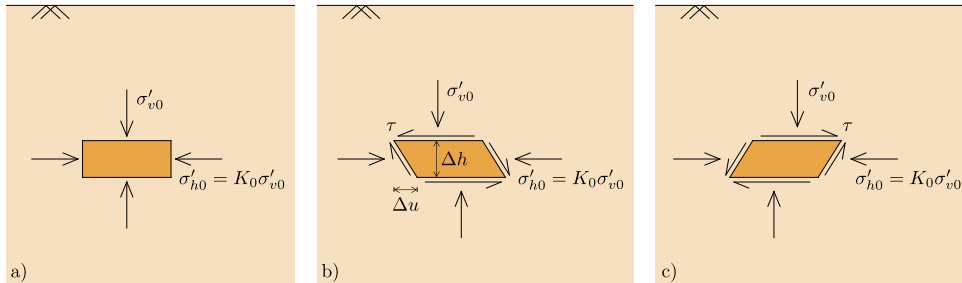


**Figure 4.2:** Idealized cyclic loading sequence (after [166])

A shear stress  $\tau$  is applied to the faces of the soil element which undergoes a simple shear deformation given as (considering no volume change):



$$\gamma = \frac{\Delta u}{\Delta h} \quad (4.5)$$

For a closed cycle, the response of the soil is characterized by an hysteresis loop whose area and inclination depend on the amplitude of the deformation (Fig. 4.3).

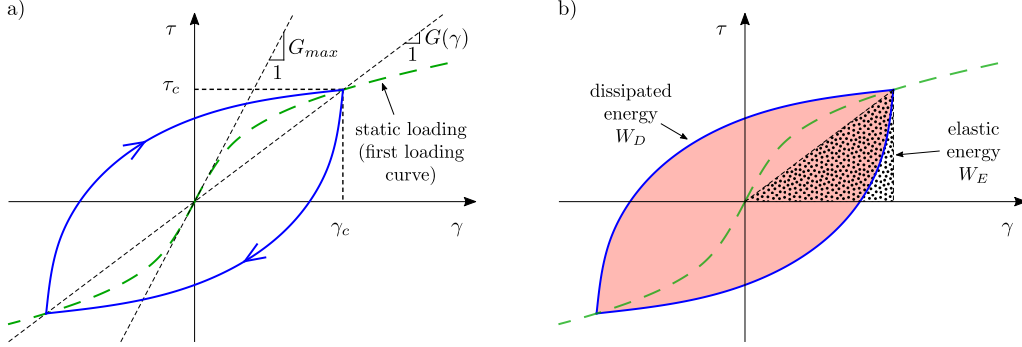


**Figure 4.3:** Cyclic behaviour of soil. Definition of (a) secant shear modulus and (b) hysteretic damping of a cycle using stress-strain curves (modified from [166, 64, 65])

Two parameters are usually used to describe this loop: the secant shear modulus and the damping ratio [166]. The secant shear modulus  $G(\gamma)$  corresponds to the slope of the line connecting the tips of the loop:

$$G(\gamma) = \frac{\tau_c}{\gamma_c} \quad (4.6)$$

The damping ratio  $\beta(\gamma)$  represents the energy dissipated by the material during a hysteretic cycle:

$$\beta(\gamma) = \frac{W_D}{4\pi W_E} = \frac{1}{2\pi} \frac{W_D}{G(\gamma)\gamma_c^2} \quad (4.7)$$

where  $W_E$  is the maximum elastic strain energy and  $W_D$  the area of the hysteretic loop which equals the dissipated energy during a cycle. Experimental evidence shows that the area of the hysteresis loop is not affected by the loading rate [166, 38].

The nonlinear character of the soil response implies a dependence of the shear modulus and of the damping ratio on the shear strain amplitude (Fig. 4.4). This dependence is commonly represented by means of shear modulus degradation curves (sometimes normalized with the value of the maximum shear modulus, i.e.,  $G(\gamma)/G_{max}$ ) and damping curves.

The shear modulus decreases with the level of distortion. Similarly, the damping ratio also varies with the amplitude of the cyclic strain, generally increasing in value when shear strain increases. Modulus degradation and damping curves are thus inversely correlated.

In addition to the cyclic shear strain, the factors that affect the most these curves are the confining pressure and the plasticity index. A higher confining pressure leads to a more linear behavior, with less stiffness degradation and less hysteretic damping [97]. A higher plasticity index also leads to the same result [221]. More specifically, in the case of clays, degradation of the shear modulus generally takes place at larger shear strain levels than in sands. The more plastic is the clay the later appears the shear modulus degradation, thus very plastic clays have an elastic response over a larger range of deformations compared to lower plasticity clays [24]. Other parameters such as the *OCR*, the loading frequency and the number of cycles have a smaller effect on both  $G(\gamma)/G_{max}$  and  $\beta(\gamma)$  curves [64, 38, 65].

An hyperbolic model is usually adopted to illustrate the shear modulus reduction with strain, as in the following equation:

$$\frac{G}{G_{max}} = \frac{1}{1 + \gamma/\gamma_r} \quad (4.8)$$

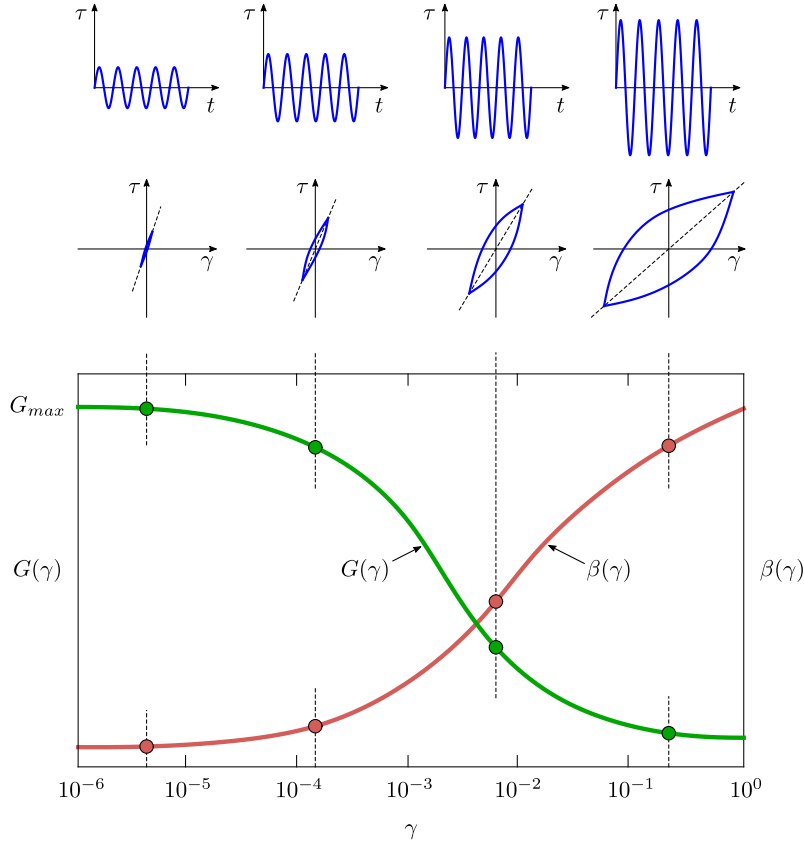


**Figure 4.4:** Soil cyclic response and corresponding shear modulus and hysteretic damping with strain (modified from [64, 65])

where  $\gamma_r$  is a reference strain corresponding, in this case, to a modulus reduction of  $G/G_{max} = 0.5$  [45, 237]. In the model proposed by Hardin & Drnevich [85], however, the reference strain is defined as  $\gamma_r = \tau_{max}/G_{max}$ .

For very small strains ( $\gamma_c < 10^{-5}$ ), soil behaves as quasi-elastic linear material with little hysteretic damping. At very small cyclic strains the soil microstructure practically does not change. There are no noticeable cyclic degradation and permanent cyclic pore water pressure changes (when fully saturated soils are considered). In the small to moderately large strain range ( $10^{-5} < \gamma_c < 10^{-3}$ ) the hysteretic behavior gains importance, with shear modulus and damping ratio depending on the level of shear strains. In general, if shear strains are higher than  $\gamma_c = 10^{-4}$  to  $10^{-3}$  (depending on the type of soil that is considered), volumetric effects and significant irrecoverable strains appear in the response. Linear hysteretic models are incapable to model this phenomenon and more advanced soil models should be used [64, 65].

Following a similar reasoning, Dobry *et al.* [52] introduced the cyclic threshold shear strain concept that distinguishes two different domains of cyclic soil behavior [220, 110, 148]. The volumetric threshold shear strain,  $\gamma_{tv}$ , corresponds to the initiation of gross sliding which results in permanent particle reorientation (i.e., volume change: dilation/contraction) when the element is sheared. The linear cyclic threshold shear strain,  $\gamma_{tl}$ , corresponds to the value of strain until which the theory of viscoelasticity is valid. Both threshold shear strains increase with increasing plasticity index [220]. A rough definition of these strains limits depending on the plasticity index is presented in Figure 4.5.

For a detailed review of the soil cyclic behavior and the different cyclic threshold shear strains defined in the literature, the reader is referred for example to Mortezaie and Vucetic [148].

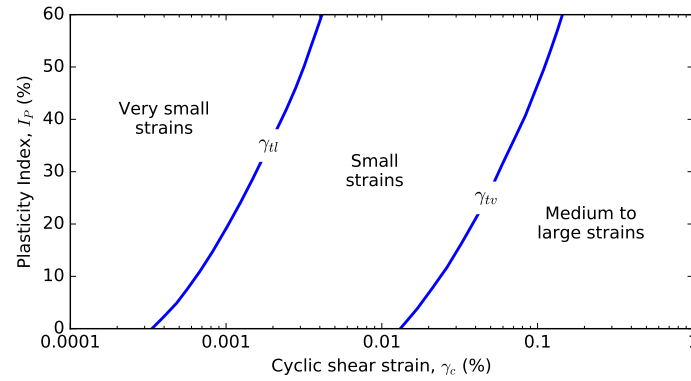


**Figure 4.5:** Threshold values for cyclic shear strains: volumetric threshold shear strain,  $\gamma_{tv}$ , and linear cyclic threshold shear strain,  $\gamma_{tl}$  (after [220])

#### 4.2.2 Dynamic properties of Hostun HN31 sand and Speswhite kaolinite

The strain-dependent shear modulus and the damping ratio are two of the most common parameters considered in the conventional characterization of the cyclic behavior of soils. These parameters are widely used for the seismic analysis of soil deposits with the so-called equivalent linear model and for one-dimensional wave propagation analysis (e.g., [190]).

Laboratory tests on specimens (e.g., triaxial cyclic, cyclic direct simple shear, resonant column tests) are often used to estimate the dynamic properties of soils. Centrifuge tests have also been used as an alternative option (e.g., [22, 118, 117]). Due to the characteristics of the soil profile used in this study, a dynamic characterization of the soils using centrifuge data could not be conducted. Some of the numerical simulations described later in this chapter use therefore data available in literature and presented herein.

Laboratory results from resonant column and cyclic triaxial tests on HN31 Hostun sand reported by Tsinidis *et al.* [211] (including data from Pistolas *et al.* [171]) are presented in Figure 4.6. Nappa *et al.* [153] evaluated the equivalent shear modulus and damping ratio of HN31 using data from centrifuge tests. These values are also shown for comparison.

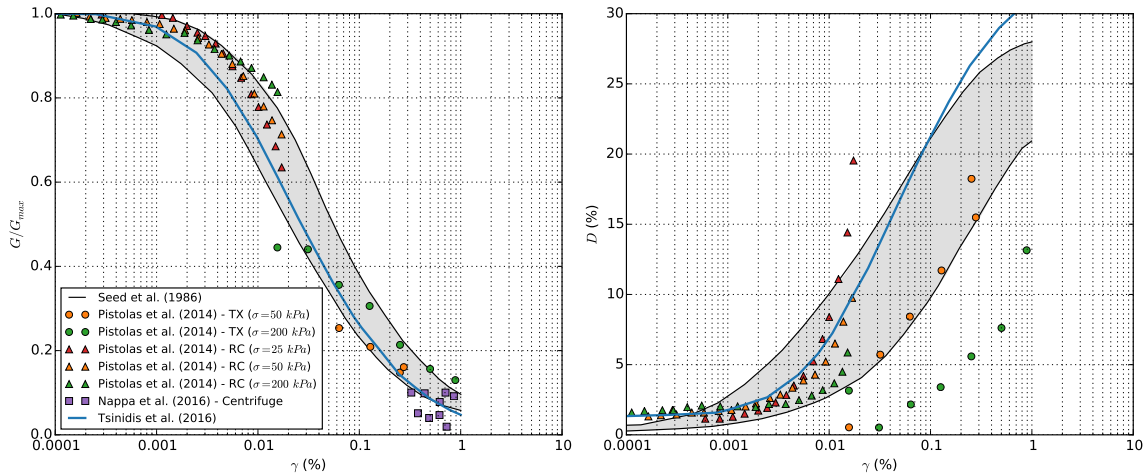


**Figure 4.6:** Secant shear modulus reduction and damping ratio curves for Hostun HN31 sand (data from [171, 211, 153])

The secant shear modulus reduction and damping ratio curves for Speswhite kaolinite are presented in Figure 4.7. The curves given by Wang & Siu [224, 225] are considered as the reference

curves for the numerical simulations conducted in the present chapter. Results from the study conducted by Banerjee [10] on Maylasian kaolin clay are also reported for comparison. The author found that at small shear strains up to about 0.01%, the kaolin clay response is approximately linear, with a constant modulus usually denoted as  $G_{max}$ . Between 0.01% and 1% shear strain, there is a rapid reduction of the shear modulus up to about 10% of  $G_{max}$ . Moreover, there exists a threshold strain around 0.137% below which cyclic stiffness degradation does not take place.

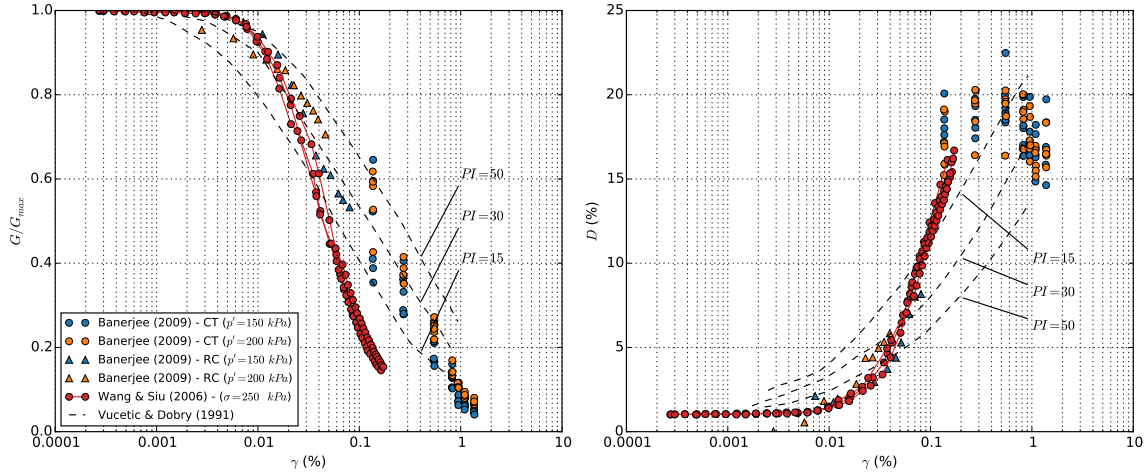


**Figure 4.7:** Secant shear modulus reduction and damping ratio curves for Speswhite kaolinite (data from [10, 224, 225])

Mortezaie [147, 148] conducted cyclic strain-controlled tests on Speswhite kaolinite clay. Under moderate to large cyclic shear strains, a cyclic degradation of stiffness and permanent pore water pressure changes were observed. The author reports two different threshold shear strains: the threshold shear strain for cyclic degradation,  $\gamma_{td}$ , below which there is practically no cyclic degradation; and the threshold shear strain for cyclic pore water pressure generation,  $\gamma_{tp}$ , below which there is practically no permanent cyclic pore water pressure change. For a NC kaolinite clay under a vertical consolidation stress of about 220 kPa, the following average values of threshold shear strains are found:  $\gamma_{td} = 0.012\%$  and  $\gamma_{tp} = 0.03\%$ . For an OC kaolinite clay with  $OCR = 4$ ,  $\gamma_{td}$  is of 0.013 and  $\gamma_{tp} = 0.0165\%$ .

This finding is interesting and allows to conclude that in the presence of cyclic shear strains higher than 0.03% cyclic degradation of the kaolinite may take place along with some pore water pressure generation. However, this degradation is expected to be limited for values of cyclic shear strain lower than 0.1%. Due to the short duration of the seismic loading and the low permeability of clayey soils, pore water pressure build-up would not start to dissipate before the end of the applied loading.

In both the aforementioned studies, the modulus and the damping ratio of kaolinite clay were found to be frequency independent, that is independent of the strain rate.

### 4.3 Hypoplastic constitutive laws

*Nota: following the literature on hypoplasticity and for practical reasons a different notation is used in this section.*

#### 4.3.1 Introduction

A constitutive law is a mathematical relationship between the stress tensor  $\sigma$ , the strain tensor  $\epsilon$  and their increment rates (and eventually other state variables). Sometimes time is also taken into account in the formulation of constitutive laws, however, this is almost never the case for

soil materials under seismic loading (the cyclic response of the soil is assumed to be frequency independent, as observed in laboratory tests) [166, 64, 65]. The soil response is generally nonlinear with the apparition of irreversible deformations even under relatively low loading levels. When submitted to a monotonic load there is not a "pure" elastic initial phase and stiffness degradation takes place all the way along the loading path [135].

There exist a large number of constitutive laws to model the inelastic behavior of soils, following different formulations and levels of complexity [49, 80]. It is also interesting to note that most of the constitutive models in the literature are formulated using the following assumptions: the mechanical problem is limited to linearized kinematics (small-strain formulation), the soil is considered fully saturated (thus the principle of effective stress applies) and the soil behavior is considered rate-independent [200, 201].

Numerous examples of classifications of constitutive laws are available in the literature using different criteria such as the algebraic structure, the predictive capabilities or the considered state variables to cite some examples (e.g., [199, 135]). A brief overview of the so-called incremental nonlinearity classification approach is introduced hereafter. For a detailed exposition of this approach the reader is referred to [135].

Within the concept of incremental nonlinearity, **elastic models** are denoted as incrementally linear. Their main characteristic is that the material response is reversible upon loading path reversal, that is, no residual strains are experienced upon a loading/unloading cycle obtained from a full load reversal [200]. They are defined by a stiffness tensor  $\mathcal{M}$  independent of the loading direction  $\vec{D}$ . That is, the constitutive equation in incremental form reads:

$$\dot{T} = \mathcal{M}(T, q) : D \quad (4.9)$$

with  $\dot{T}$  the stress rate tensor and  $D$  the strain rate tensor.

If the the stiffness tensor  $\mathcal{M}$  is constant, the model is denoted as linear. If it depends on the stress  $T$  and additional state variables  $q$  the elastic model is denoted as nonlinear elastic. Further distinctions can be introduced depending on the internal structure and the definition of the stiffness tensor (e.g., linear elasticity, hyperelasticity, hypoelasticity) [135].

Experimental observations of soil behavior show, however, that elastic models are unable to satisfactorily describe several fundamental aspects of their response. The soil behavior is not only nonlinear, but also irreversible, with accumulation of permanent strains when subjected to closed stress cycles. In addition, when soils approach failure, they tend to experience volumetric deformations under shearing (contractant or dilatant behavior) and strains increments are non-coaxial with applied stress increments [200].

Experiments show also that the ultimate failure conditions for soils are generally independent of the previous loading history, that is the state of the material at failure can be characterized solely in terms of stress. Classical plasticity theory, also referred as **elastic perfectly plastic model**, is thus constructed to predict soil failure conditions only (no internal variables). In other words the behavior inside the yield surface is considered elastic and only once that surface is reached will the plastic flow develop according to the plastic potential surface and the flow rule [38]. The general rate equation of elastoplastic models is:

$$\dot{T} = \mathcal{M}(T, q, \vec{D}) : D \quad (4.10)$$

The stiffness tensor attains in this case two different values depending on the loading direction  $\vec{D}$ ; the elastoplastic stiffness tensor  $\mathcal{M}^{ep}$  in elastoplastic loading and the elastic stiffness tensor  $\mathcal{M}^e$  in elastic unloading. Since there are two options for the value of  $\mathcal{M}$ , the elastoplastic model is denoted as incrementally bilinear. The elastoplastic models can further be classified into different subcategories depending on the properties of the yield surface and on the way the elastoplastic tensor is calculated [135].

Elastoplasticity presents two major improvements with respect to elasticity, i.e., irreversibility of deformation (with the developing of plastic strains) and a stress envelope (a stress limit condition is introduced in the formulation). It is able to capture phenomena as nonlinearity and dilatancy (though the quality depends on the sophistication of the formulation). Elastoplasticity

uses geometrical concept of surfaces in stress space (usually) with yield surface and plastic potential. Finally the approach followed in elastoplastic formulations is of the inductive type, reasoning from the particular to the general [87].

Nevertheless, as stated before, the behavior of soils is strongly nonlinear well before the failure surface is attained. Therefore, both linear and perfectly plastic models are insufficient to describe their response. To achieve a better representation, isotropic and kinematic hardening laws are often adopted that allow the yield surface to evolve by changing its size, shape and position in stress space according to the loading state [38].

Another option is to use hypoplasticity which is a particular type of bounding surface plasticity model with a vanishing elastic domain. Compared to elastoplastic models this formulation can provide a more smooth numerical response [44, 13]. The general rate equation of the **hypoplastic model** reads:

$$\dot{\mathbf{T}} = \mathcal{L} : \mathbf{D} + \mathbf{N} \|\mathbf{D}\| \quad (4.11)$$

The first part of the equation  $\mathcal{L} : \mathbf{D}$  is equivalent to the elastic model. The second term  $\mathbf{N} \|\mathbf{D}\|$ , is a second-order tensor that is independent of  $\dot{\mathbf{D}}$  (for the given  $\|\mathbf{D}\|$ ). Therefore, this term applies a translation of the response envelope in the stress state. This allows the model to predict different stiffness in different loading directions. The hypoplastic model is denoted as incrementally nonlinear and is capable of predicting irreversibility and non-linearity of the soil behavior even inside the asymptotic state boundary surface [135].

Hypoplasticity keeps most of the improvements of elastoplastic models as irreversibility of deformation (incremental nonlinearity). Stresses are bounded and other phenomena of the soil response can be also captured (e.g., dilatancy). Hypoplastic models respond to a deductive approach to the problem, reasoning from the general to the particular [87].

The hypoplastic constitutive laws proposed by von Wolffersdorff [219] for sand and by Mašín [129] for clay are used in this study to reproduce numerically the nonlinear behavior of the soils used in the centrifuge experiments presented in the previous chapter. A brief overview of both formulations is introduced in the next two sections with emphasis on explaining the parameters of both models, their meaning and the calibration procedure. The readers are referred in both cases to several references that introduce and explain the models in much more detail (i.e., [106, 219, 154, 86, 129, 133, 80, 134, 107, 135]).

### 4.3.2 Hypoplastic constitutive law for granular soils

The hypoplastic model developed by von Wolffersdorff [219] is often considered as a reference hypoplastic model for granular materials. It is used in this study to model the Hostun HN31 sand.

This model is based on the Drucker-Prager elastoplastic law with the Matsuoka-Nakai failure criterion [137]. The basic form of the hypoplastic model is provided in Equation (4.11). The initial value  $\mathcal{L}^e$  of the second constitutive tensor  $\mathcal{L}$  depends on the bulk modulus  $K$  and the shear modulus  $G_{max}$  in the elastic range. It has the following form (the Lamé coefficient  $\mu = G_{max}$  according to Hooke's law):

$$\mathcal{L}^e = \begin{bmatrix} K + 4\mu/3 & K - 2\mu/3 & K - 2\mu/3 & 0 & 0 & 0 \\ K - 2\mu/3 & K + 4\mu/3 & K - 2\mu/3 & 0 & 0 & 0 \\ K - 2\mu/3 & K - 2\mu/3 & K + 4\mu/3 & 0 & 0 & 0 \\ 0 & 0 & 0 & \mu & 0 & 0 \\ 0 & 0 & 0 & 0 & \mu & 0 \\ 0 & 0 & 0 & 0 & 0 & \mu \end{bmatrix} \quad (4.12)$$

For a frictional material like sand,  $G_{max}$  is influenced by the mean effective confining pressure  $p$  and the void ratio  $e$  [85].

von Wolffersdorff [219] extended the basic form of the hypoplastic model incorporating the predefined limit state surface of Matsuoka and Nakai [137]. The second order constitutive tensor  $\mathcal{L}$  is defined as:

$$\mathcal{L} = f_s \frac{1}{\hat{\mathbf{T}} : \hat{\mathbf{T}}} \left( F^2 \mathcal{I} + a^2 \hat{\mathbf{T}} \otimes \hat{\mathbf{T}} \right) \quad (4.13)$$

and the fourth-order constitutive tensor  $\mathbf{N}$  is given as:

$$\mathbf{N} = f_s f_d \frac{aF}{\hat{\mathbf{T}} : \hat{\mathbf{T}}} \left( \hat{\mathbf{T}} + \hat{\mathbf{T}}^* \right) \quad (4.14)$$

where  $\mathcal{I}$  is the fourth-order identity tensor,  $\mathcal{I}$  the identity matrix,  $\hat{\mathbf{T}} = \mathbf{T}/\text{tr}\mathbf{T}$  and  $\hat{\mathbf{T}}^* = \hat{\mathbf{T}} - \mathcal{I}/3$  the deviator part of the normalized stresses. The coefficient  $a$  is defined by:

$$a = \frac{\sqrt{3}(3 - \sin\varphi_c)}{2\sqrt{2} \sin\varphi_c} \quad (4.15)$$

The Matsuoka-Nakai failure condition is introduced into the model as:

$$F = \sqrt{\frac{1}{8} \tan^2\psi + \frac{2 - \tan^2\psi}{2 + \sqrt{2} \tan\psi \cos 3\theta}} - \frac{1}{2\sqrt{2}} \tan\psi \quad (4.16)$$

with:

$$\tan\psi = \sqrt{3} \left\| \hat{\mathbf{T}}^* \right\| \quad \cos 3\theta = -\sqrt{6} \frac{\text{tr} \left( \hat{\mathbf{T}}^* \cdot \hat{\mathbf{T}}^* \cdot \hat{\mathbf{T}}^* \right)}{\left[ \hat{\mathbf{T}}^* : \hat{\mathbf{T}}^* \right]^{3/2}} \quad (4.17)$$

The scalar factors  $f_s$  (barotropy factor) and  $f_d$  (pyknotropy factor) take into account the influence of mean pressure and density:

$$f_s = \frac{h_s}{n} \left( \frac{e_i}{e} \right)^\beta \frac{1 + e_i}{e} \left( \frac{-\text{tr}\mathbf{T}}{h_s} \right)^{1-n} \left[ 3 + a^2 - a\sqrt{3} \left( \frac{e_{i0} - e_{d0}}{e_{c0} - e_{d0}} \right)^\alpha \right]^{-1} \quad (4.18)$$

$$f_d = \left( \frac{e - e_d}{e_c - e_d} \right)^\alpha \quad (4.19)$$

The characteristic void ratios  $e_i$ ,  $e_c$  and  $e_d$  decrease with the mean pressure according to the relation (Fig. 4.8a):

$$\frac{e_i}{e_{i0}} = \frac{e_c}{e_{c0}} = \frac{e_d}{e_{d0}} = \exp \left[ - \left( \frac{-\text{tr}\mathbf{T}}{h_s} \right)^n \right] \quad (4.20)$$

The basic formulation of the model requires thus eight material parameters:  $\varphi_c$ ,  $h_s$ ,  $n$ ,  $e_{d0}$ ,  $e_{c0}$ ,  $e_{i0}$ ,  $\alpha$  and  $\beta$ . The parameter  $\varphi_c$  corresponds to the critical state friction angle. It can be measured from the angle of repose or using shear tests.  $h_s$  is the so-called granulate hardness (not to be confused with the hardness of single grains) and is used in the model as a reference pressure. The constant  $n$  describes the sensibility of a grain skeleton to a change in pressure. These two parameters control the shape of the limiting void ratio curves and of any normal compression line followed in asymptotic compression. It is recommended to use oedometric test results performed on loose soil samples for their calibration instead of direct regression of experimental data.  $e_{d0}$ ,  $e_{c0}$  and  $e_{i0}$  are reference void ratios specifying positions of limiting void ratio curves (Fig. 4.8a). The parameter  $e_{c0}$  controls the position of the critical state line in the  $p$  vs  $e$  plane. It is best calibrated using undrained triaxial shear tests.  $e_{i0}$  controls the position of the theoretical isotropic normal compression line and  $e_{d0}$  of the minimum void ratio curve. The empirical formulae  $e_{i0} \approx 1.2e_{c0}$  and  $e_{d0} \approx 0.5e_{c0}$  can be used as a first approximation. Finally, the parameter  $\alpha$  controls the peak friction angle (Fig. 4.8b) and  $\beta$  controls both the bulk and the shear stiffness of the hypoplastic formulation (Fig. 4.8c). Both parameters are often calibrated by trial-and-error procedure using drained triaxial tests on densely compacted soil samples.

Reference values of these parameters for Hostun sand are given in Table 4.2. More details about the calibration procedure and the physical meaning of these parameters are given in [219, 86, 130, 135].



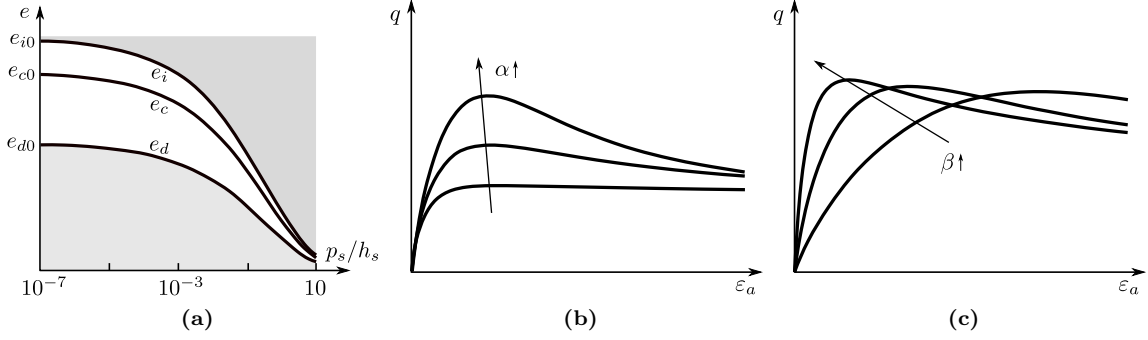


**Figure 4.8:** Hypoplastic constitutive law for granular materials: (a) pressure-dependent limiting void ratios (after Herle and Gudehus [86]), (b) influence of the parameter  $\alpha$  and (c) of the parameter  $\beta$  on the stress-strain curve from triaxial test simulations

**Table 4.2:** Parameters of the hypoplastic model for sands [219] calibrated for Hostun sand [86]

$\varphi_c$	$h_s$	$n$	$e_{d0}$	$e_{c0}$	$e_{i0}$	$\alpha$	$\beta$
$31^\circ$	1e6 kPa	0.29	0.61	0.96	1.09	0.13	2

### 4.3.3 Hypoplastic constitutive law for cohesive soils

The hypoplastic law developed by Mařín [129] for clays is based on an explicit asymptotic state bounding surface approach. It is used in this study to model the behavior of the Speswhite kaolin.

The general expression of the hypoplastic model with explicit incorporation of the asymptotic state boundary surface reads [135]:

$$\dot{\mathbf{T}} = f_s (\mathcal{L} : \mathbf{D} + f_d \mathbf{N} \|\mathbf{D}\|) \quad (4.21)$$

The tensor  $\mathcal{L}$  is represented by an isotropic elasticity:

$$\mathcal{L} = \mathcal{J} + \frac{\nu_{pp}}{1 - 2\nu_{pp}} \mathcal{I} \otimes \mathcal{I} \quad (4.22)$$

where the parameter  $\nu_{pp}$  controls the proportion of bulk and shear stiffness. In practice,  $\nu_{pp}$  regulates the shear stiffness (for a given bulk stiffness). Bulk stiffness on the other hand is controlled by the parameters  $\lambda^*$  and  $\kappa^*$ .

The fourth-order tensor  $\mathbf{N}$  is calculated as:

$$\mathbf{N} = -\frac{\mathcal{A} : \mathbf{d}}{f_s f_d^A} \quad (4.23)$$

with:

$$\mathcal{A} = f_s \mathcal{L} + \frac{\mathbf{T}}{\lambda^*} \otimes \mathcal{I} \quad (4.24)$$

The barotropy factor  $f_s$  is formulated to ensure that the slope of the isotropic unloading line starting from the isotropic normally consolidated state is controlled by the parameter  $\kappa^*$ , it is expressed as:

$$f_s = \frac{3p}{2} \left( \frac{1}{\lambda^*} + \frac{1}{\kappa^*} \right) \frac{1 - 2\nu_{pp}}{1 + \nu_{pp}} \quad (4.25)$$

The pyknotropy factor  $f_d$  is given by:

$$f_d = \left( \frac{2p}{p_e^*} \right)^{\alpha_f} = \left( \frac{2}{OCR} \right) \quad (4.26)$$



Hvorslev's equivalent pressure  $p_e^*$  is defined:

$$p_e^* = p_r \exp \left[ \frac{N - \ln(1 + e)}{\lambda^*} \right] \quad (4.27)$$

where  $p_r$  is a reference stress of 1 kPa, and the variable  $OCR = p_e^*/p$ , with  $p = -I_1/3$ .

The exponent  $\alpha_f$  controls the irreversibility of the deformation inside the asymptotic state boundary surface, and reads:

$$\alpha_f = \frac{\ln \left[ \frac{\lambda^* - \kappa^*}{\lambda^* + \kappa^*} \left( \frac{3 + a_f^2}{a_f \sqrt{3}} \right) \right]}{\ln 2} \quad (4.28)$$

where  $a_f$  is expressed as:

$$a_f = \frac{\sqrt{3}(3 - \sin \varphi_c)}{2\sqrt{2}\sin \varphi_c} \quad (4.29)$$

The factor  $f_d^A$  is the limiting value of  $f_d$  at the asymptotic state boundary surface.  $f_d^A$  is defined as:

$$f_d^A = 2^{\alpha_f} (1 - F_m)^{\alpha_f/\omega} \quad (4.30)$$

The parameter  $\omega$  is calculated:

$$\omega = -\frac{\ln(\cos^2 \varphi_c)}{\ln 2} + 0.3(F_m - \sin^2 \varphi_c) \quad (4.31)$$

$F_m$  is the Matsuoka-Nakai factor, which may be seen as an equivalent to the mobilized friction angle  $\varphi_m$  (with  $F_m = \sin^2 \varphi_m$ ) corresponding to the Matsuoka-Nakai failure criterion [137]:

$$F_m = \frac{9I_3 + I_1 I_2}{I_3 + I_1 I_2} \quad (4.32)$$

with the stress invariants:

$$I_1 = \text{tr} \mathbf{T} \quad I_2 = \frac{1}{2} [\mathbf{T} : \mathbf{T} - (I_1)^2] \quad I_3 = \det \mathbf{T} \quad (4.33)$$

The asymptotic strain rate direction  $\mathbf{d}$  is expressed as:

$$\mathbf{d} = \frac{\mathbf{d}^A}{\|\mathbf{d}^A\|} \quad (4.34)$$

where  $\mathbf{d}^A$  is defined as:

$$\mathbf{d}^A = -\hat{\mathbf{T}}^* + \mathcal{I} \left[ \frac{2}{3} - \frac{\cos 3\theta + 1}{4} F_m^{1/4} \right] \frac{F_m^{\xi/2} - \sin^\xi \varphi_c}{1 - \sin^\xi \varphi_c} \quad (4.35)$$

$\cos 3\theta$  is defined in Eq. (4.17) and  $\xi$  controls the ratio of the volumetric strain to the shear strain:

$$\xi = 1.7 + 3.9 \sin^2 \varphi_c \quad (4.36)$$

The basic form of the model requires five material parameters:  $\varphi_c$ ,  $N$ ,  $\lambda^*$ ,  $\kappa^*$  and  $\nu_{pp}$ . These parameters are equivalent (but not identical) to the parameters of the Modified Cam-clay model.  $\varphi_c$  is the critical state friction angle, parameters  $N$  and  $\lambda^*$  control the position and slope of the isotropic normal compression line in the  $\ln p$  vs  $\ln(1 + e)$  plane.  $\kappa^*$  controls the slope of the isotropic unloading line (Fig. 4.9a). Unlike the Modified Cam-clay model, the slope of the unloading line is not constant in the  $\ln p$  vs  $\ln(1 + e)$  plane, it varies with the overconsolidation ratio. The parameter  $\nu_{pp}$  controls the shear stiffness (Fig. 4.9b), an increase of its value decreases the shear modulus, and it is also related to the evolution of excess pore water pressure under undrained conditions.

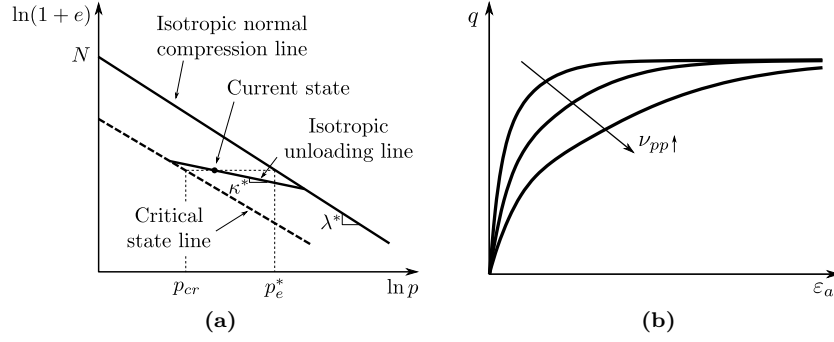


**Figure 4.9:** Hypoplastic constitutive law for cohesive materials: (a) definition of parameters  $N$ ,  $\lambda^*$  and  $\kappa^*$  (after Mašin [133]) and (b) influence of the parameter  $\nu_{pp}$  on the stress-strain curve from an undrained triaxial test simulation

To calibrate the parameters, two experiments are at least necessary. An isotropic or oedometric compression test to calibrate  $N$ ,  $\lambda^*$  and  $\kappa^*$ , and an undrained triaxial shear test for  $\varphi_c$  and  $\nu_{pp}$ . Reference values of these parameters for kaolin clay are given in Table 4.3. The model and the calibration procedures are extensively described in [129, 134, 130, 135].

**Table 4.3:** Parameters of the hypoplastic model for clay [129, 135] calibrated for Kaolin clay [130]

$\varphi_c$	$\lambda^*$	$\kappa^*$	$N$	$\nu_{pp}$
$27.5^\circ$	0.065	0.01	0.918	0.35

#### 4.3.4 Cyclic loading (intergranular strain)

The basic hypoplastic formulation does not allow to realistically reproduce the behavior under cyclic loading because an excessive accumulation of strains or stress (ratcheting) takes place for low amplitude loading cycles (Fig. 4.10).

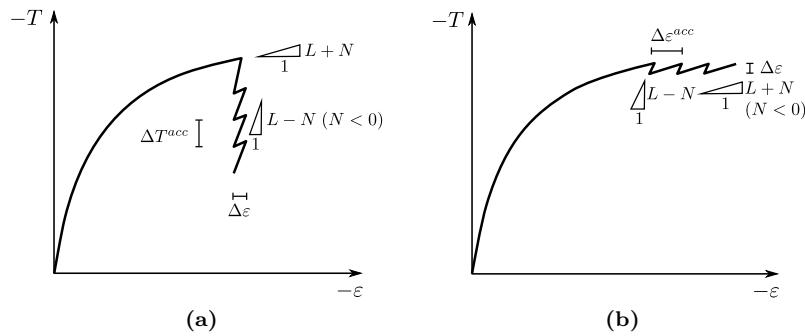


**Figure 4.10:** Excessive stress (a) and strain (b) accumulation during stress and strain cycles, respectively (after Niemunis and Herle [154])

In order to overcome this limitation, the so-called intergranular strain concept proposed by Niemunis & Herle [154] is adopted, which introduces an additional state variable  $\delta$  that represents in a idealized way the interlayer deformation between the different grains. The evolution rate of the intergranular strain is defined as follows:

$$\dot{\delta} = \begin{cases} (\mathcal{I} - \hat{\delta}\hat{\delta}\rho^{\beta_r}) : \mathbf{D} & (\hat{\delta} : \mathbf{D} > 0) \\ \mathbf{D} & (\hat{\delta} : \mathbf{D} \leq 0) \end{cases} \quad (4.37)$$

where  $\rho = \|\delta\|/R$  is the normalized magnitude of the intergranular strain  $\delta$  ( $\rho \in [0, 1]$ ),  $\beta_r$  and  $R$  are constants,  $\mathcal{I}$  is the fourth-order identity tensor and  $\hat{\delta}$  is direction for intergranular strain given as:

$$\hat{\delta} = \begin{cases} \delta/\|\delta\| & (\delta \neq 0) \\ \mathbf{0} & (\delta = 0) \end{cases} \quad (4.38)$$

Introducing the concept of intergranular strain the general rate equation of the hypoplastic model (Eq. (4.11)) is rewritten as [154]:

$$\dot{\mathbf{T}} = \mathcal{M} : \mathbf{D} \quad (4.39)$$

with  $\mathcal{M}$  a fourth-order tangent stiffness material tensor calculated from the hypoplastic tensors  $\mathcal{L}$  and  $\mathbf{N}$  using the following interpolation function:

$$\mathcal{M} = [\rho^\chi m_T + (1 - \rho^\chi) m_R] \mathcal{L} + \begin{cases} \rho^\chi (1 - m_T) \mathcal{L} : \hat{\delta}\hat{\delta} + \rho^\chi \mathbf{N} \hat{\delta} & (\hat{\delta} : \mathbf{D} > 0) \\ \rho^\chi (m_R - m_T) \mathcal{L} : \hat{\delta}\hat{\delta} & (\hat{\delta} : \mathbf{D} \leq 0) \end{cases} \quad (4.40)$$

where  $\chi$ ,  $m_T$  and  $m_R$  are constants. The tensor  $\mathcal{L}$  is modified to ensure that at  $\rho = 0$  ( $\mathcal{M} = m_R \mathcal{L}$ ) the initial stiffness  $\mathcal{L}^e$  is retrieved:

$$\mathcal{L} = \frac{\mathcal{L}^e}{m_R} \quad (4.41)$$

The constitutive law for sands requires in this case five additional material parameters:  $m_R$ ,  $m_T$ ,  $R$ ,  $\beta_r$  and  $\chi$ . The parameters  $m_R$  and  $m_T$  control the initial (very-small-strain) shear modulus upon 180° and 90° strain path reversal respectively (i.e., unloading and neutral loading phases). The size of the elastic range (in the strain space) is controlled by the parameter  $R$ .  $\beta_r$  and  $\chi$  parameters control the rate of degradation of the stiffness with strain.

In the case of the hypoplastic constitutive law for clays, the parameter  $m_R$  is replaced by  $A_g$  and  $n_g$ , and the parameter  $m_T$  by  $m_{rat}$ .  $R$ ,  $\beta_r$  and  $\chi$  are directly used in the formulation.

It should be noted that as of today, not many rigorously calibrated sets of parameters of the intergranular strain concept are available in the literature [135]. In most cases, a numerical calibration based on experimental laboratory results is required. A simplified calibration procedure of the intergranular strain concept parameters is proposed by Mašin [130] as a first approach. Consider  $R = 10^{-4}$  and  $\chi = 1$  as material independent constants, calibrate  $m_R$  ( $A_g$  and  $n_g$  for the clay model) using Bender element measurements, use  $m_T \approx 0.7m_R$  ( $m_{rat} \approx 0.7$  for the clay model) and finally control the cyclic behavior of the model using the parameter  $\beta_r$ . It is preferable to use cyclic loading tests for this calibration. When no data is available, the calibration can be conducted fitting the stiffness degradation curve.

### 4.3.5 Calibration of hypoplastic parameters for HN31 sand

The parameters of the hypoplastic constitutive models are calibrated in this and the following section for the HN31 sand and the Speswhite kaolin using laboratory test data available in the literature. Table 4.4 summarizes the ranges of values of interest for the calibration.

#### 4.3.5.1 Monotonic response

The parameters controlling the monotonic response of the hypoplastic constitutive law for the HN31 sand are calibrated using monotonic triaxial tests [15].

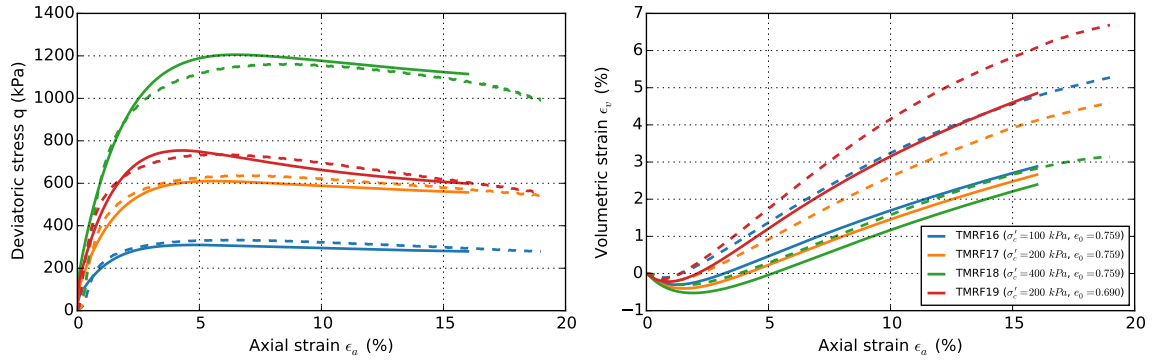
A first calibration of the parameters  $\varphi_c$ ,  $h_s$ ,  $n$ ,  $e_{d0}$ ,  $e_{c0}$ ,  $e_{i0}$ ,  $\alpha$  and  $\beta$  was conducted through the use of an iterative algorithm and a trial and error scheme. However, this calibration strategy

**Table 4.4:** Ranges of values of interest for the calibration of the hypoplastic constitutive laws parameters using laboratory test results for the HN31 sand and the Speswhite kaolin

Layer	$\sigma'$ [kPa]	OCR [-]	$I_D$ [-]
Dry HN31	0 – 32	-	0.81
Speswhite kaolinite	32 – 118	1.36 – 5	-
Saturated HN31	118 – 188	-	0.81

was soon deemed unproductive. The use of multi-objective optimization algorithms within the multidisciplinary design optimization software modeFRONTIER [57] was also tested but barely improved the results, probably because of the optimization criteria that were not the most suitable for this problem and because of the large number of parameters to calibrate at the same time. Indeed, as stated by Mařín [135], direct calibration of the whole set of parameters of the hypoplastic law using triaxial test results is usually unsuccessful. It is recommended to use the parameters that are proposed in the literature and that have been duly calibrated using more convenient tests (e.g., oedometric tests). Adjustments to these parameters may be done afterwards in order to improve the response of the numerical model.

In the following, the set of parameters proposed by Herle & Gudehus [86] for the HN31 sand (see Table 4.2) are used. Slight modifications have been made in order to better reproduce the experimental results of [15]. Different confining pressures  $\sigma'_c$  and void ratios  $e_0$  are used. Figure 4.11 shows the comparison between the numerical (solid curves) and experimental (dashed curves) results. It can be observed that the hypoplastic law for sands captures well the behavior of Hostun sand. The parameters used in the numerical simulation are given in Table 4.5.

**Figure 4.11:** Drained triaxial compression tests on HN31 sand, simulation (solid curves) vs. experiments (dashed curves) [15]**Table 4.5:** Best-estimate calibrated parameters of the hypoplastic model to reproduce the response of HN31 Hostun sand

$\varphi_c$	$h_s$	$n$	$e_{d0}$	$e_{c0}$	$e_{i0}$	$\alpha$	$\beta$	$m_R$	$m_T$	$R$	$\beta_r$	$\chi$
32°	1e6 kPa	0.29	0.61	0.96	1.09	0.13	2.4	7.35	5.15	3e-5	0.1	0.9

#### 4.3.5.2 Cyclic response

The parameters that control the cyclic response of the hypoplastic law (intergranular strain part) are calibrated in order to reproduce the cyclic response and more particularly the shear modulus degradation and damping curves with the strain amplitude. The simplified procedure proposed by Mařín [130] is used (with some slight differences). Several iterative calibration steps are conducted

in order to adjust each one of the parameters until a good response is achieved (two parameters are modified at each iteration while the others are kept constant). Alternating the different parameters a convergence is attained after few iterations. The parameters found at the end of the calibration are given in Table 4.5. The shear modulus degradation and damping curves calculated using a single element model are compared to those found in the literature in Figure 4.12. A good agreement is observed between the simulation and the theoretical curves.

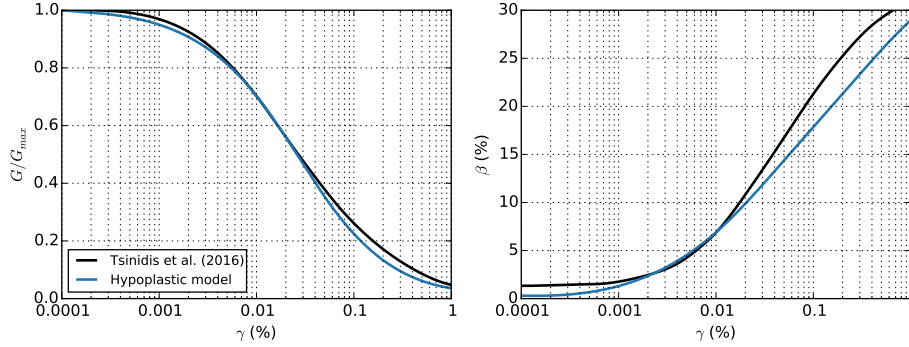


**Figure 4.12:** Secant shear modulus reduction and damping curves for Hostun HN31, comparison between the experimental and the numerical results with the hypoplastic constitutive law

It should be noted however that differences appear in the material damping for small and large strains, where the hypoplastic model underestimates damping. In the first case, the hypoplastic model may lead to amplification problems with respect to an equivalent linear elastic model with viscous damping. It will then be necessary to add an additional damping source into the resolution in order to model the correct amount of damping (e.g., by introducing a certain numerical damping in the numerical resolution algorithm).

#### 4.3.5.3 Remark on the undrained case

The parameters presented so far allow to reproduce the monotonic and cyclic response of the dry HN31 sand layer placed at the top of the soil profile. In theory, using the same model parameters with a pore water bulk modulus  $K_w = 2.2e6 \text{ kPa}$  it should be possible to reproduce also the undrained behavior of the soil. However, this was not the case, as shown in Figure 4.13, where the response of the numerical model is compared to the undrained cyclic triaxial test results of [15]. An excessive pore pressure build-up is observed and numerical calculations stop after one cycle because of numerical instability.

This finding doesn't mean that the hypoplastic law is not able to reproduce the undrained response of the saturated sand but that using the same parameters for the drained and the undrained case is not sufficient. Examples of successful use of the hypoplastic constitutive law for sands under undrained conditions can be found in the literature, for example in [88]. Recent works of Wegener [226] and Wegener & Herle [227] show that it is possible to reduce the ratcheting effects for low amplitude cycles and thus improve the model response in undrained conditions by replacing the exponent  $\chi$  in the term  $\rho^\chi \mathbf{N} \hat{\delta}$  of Equation (4.40) with an independent constant  $\theta \gg \chi$ .

In the following, given that the analysis of the experimental results showed that the degradation of the response of the saturated dense sand layer at the bottom of the soil profile was negligible, especially when compared to the clay layer, a simple elastic-perfectly plastic law with a Mohr-Coulomb criterion is adopted.

### 4.3.6 Calibration of hypoplastic parameters for Speswhite kaolin clay

#### 4.3.6.1 Monotonic response

The parameters of the basic formulation of the hypoplastic constitutive law for clays are calibrated using monotonic triaxial test data [149]. As for the sand, it is recommended to start the calibration

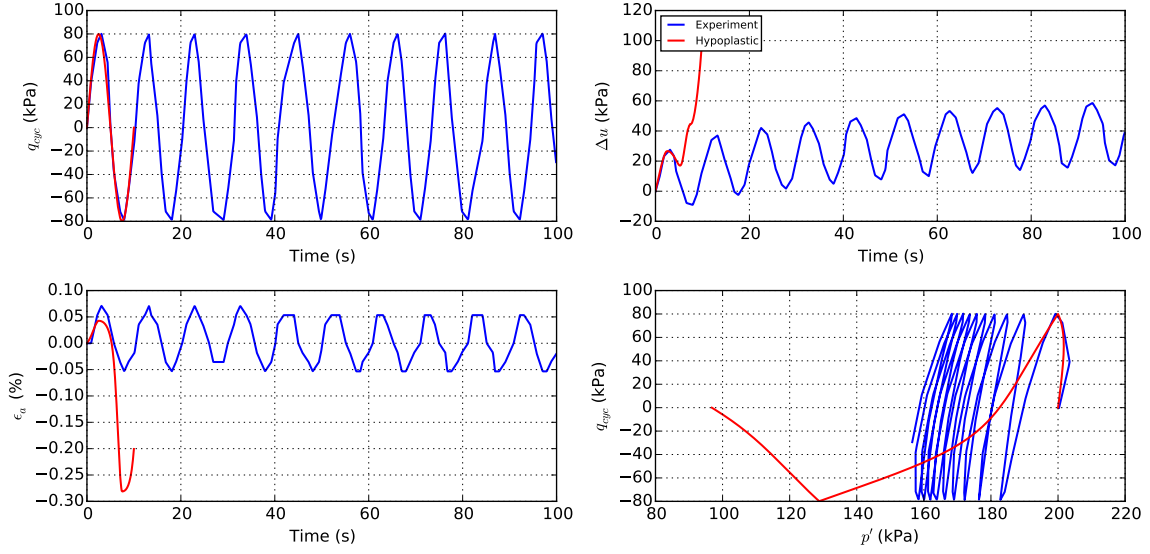


**Figure 4.13:** Undrained triaxial cyclic tests on HN31 sand, simulation using the hypoplastic model vs. experiments from [15]

using the parameters already available in the literature for Speswhite kaolin and then adjust them, if necessary, in order to better reproduce the experimental results. The parameters provided by [89] are used hereafter as the starting point. Figure 4.14 shows the comparison between the experimental and the numerical results. The calibrated parameters are given in Table 4.6.

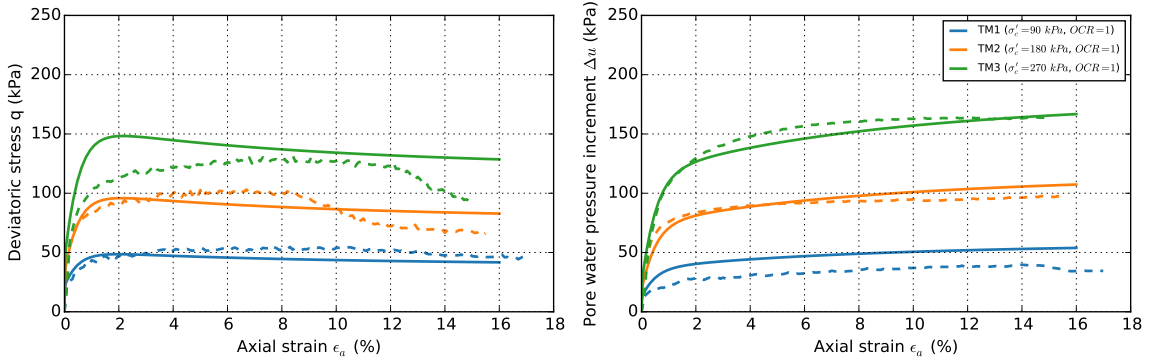


**Figure 4.14:** Undrained triaxial compression tests on Speswhite kaolinite ( $OCR = 1$ ), simulation (solid curves) vs. experiments (dashed curves) [149]

**Table 4.6:** Best-estimate calibrated parameters of the hypoplastic model to reproduce the response of Speswhite kaolin clay

$\varphi_c$	$\lambda^*$	$\kappa^*$	$N$	$\nu_{pp}$	$\alpha_G$	$R$	$\beta_r$	$\chi$	$A_g$	$n_g$	$m_{rat}$
22°	0.114	0.028	1.35	0.1	2	5e-5	0.4	3	2000	0.65	0.7

#### 4.3.6.2 Cyclic response

To calibrate the cyclic response of the model, the results of cyclic direct simple shear (CDSS) tests [147] and the shear modulus degradation and damping curves [224, 225] are used. The calibrated parameters are given in Table 4.6. Figure 4.15 compares the results from the numerical model of a cyclic direct simple shear test with the experimental results. A good agreement can be observed.

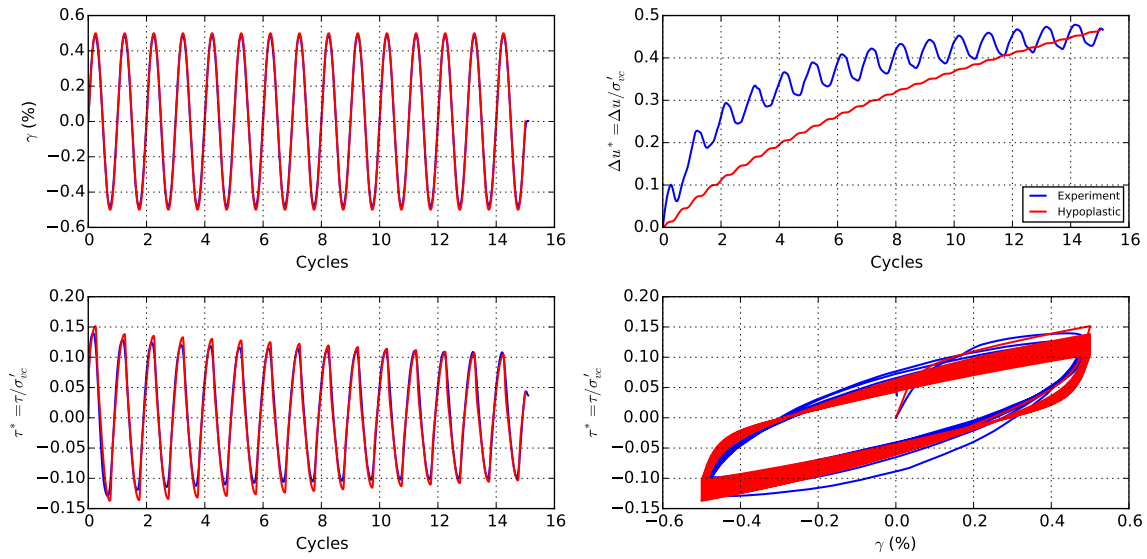


**Figure 4.15:** Cyclic direct simple shear test on Speswhite kaolinite ( $\sigma'_c = 220 \text{ kPa}$ ,  $e = 1.26$ ,  $OCR = 1$ ,  $w = 47.5\%$ ,  $\gamma_c = 0.5\%$ ,  $f = 0.001 \text{ Hz}$ ), simulation vs. experiments [147]

Regarding the shear modulus degradation and damping curves with strain amplitude, the comparison between the numerical model and the experiment results is shown in Figure 4.16. It is observed that the numerical model is not able to reproduce realistically the damping curve, particularly for high strains.

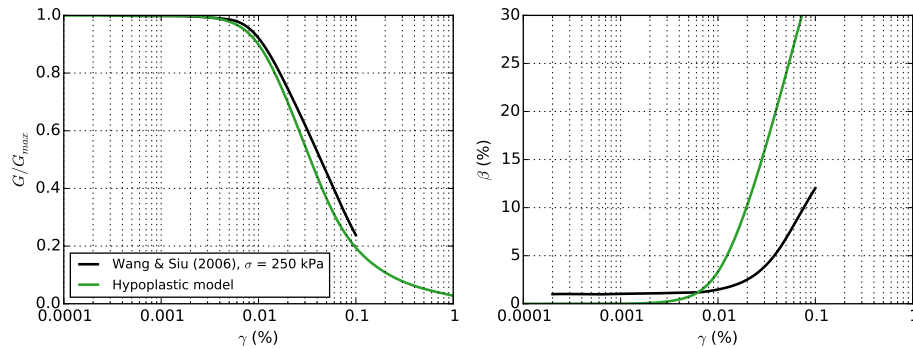


**Figure 4.16:** Secant shear modulus reduction and damping curves for Speswhite kaolin, comparison between the experimental and the numerical results with the hypoplastic constitutive law

## 4.4 Free field ground response

The dynamic response of the soil profile used in the centrifuge tests is studied in this section for several levels of load intensity, namely:

- The quasi-elastic response of the soil profile (when subjected to vibrations of very low amplitude such as the “noise” due to the shaker’s servo valves actuators);
- The response of the soil profile subjected to a weak seismic motion of  $0.05g \text{ PGA}^1$ ;
- The response of the soil profile to a strong seismic motion with a  $\text{PGA}$  of  $0.3g$ .

<sup>1</sup>Peak Ground Acceleration of the signal applied at the base of the soil profile

#### 4.4.1 Soil profile used in dynamic centrifuge tests

The soil profile used in the dynamic centrifuge tests, the soil density, the effective stress and the overconsolidation ratio profiles are presented in Figure 4.17. The maximum shear modulus, Poisson ratio and shear wave velocity profiles are presented in Figure 4.18. A Poisson ratio of 0.3 is considered for the dry dense HN31 sand layer at the top and 0.45 for the other soil layers.

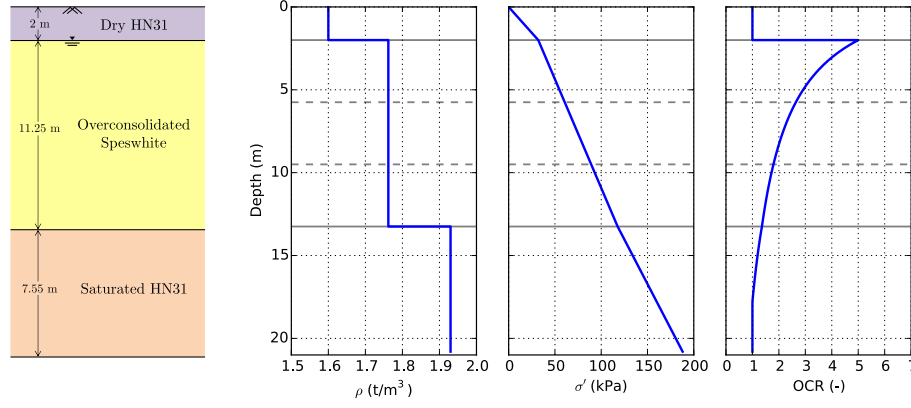


**Figure 4.17:** (a) Soil density, (b) effective stress and (c) overconsolidation ratio profiles for the soil profile used in dynamic centrifuge tests

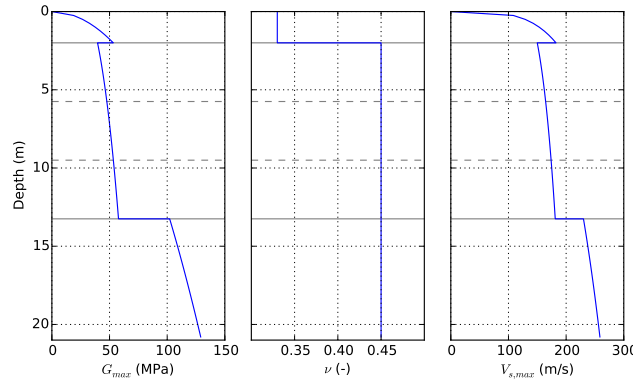


**Figure 4.18:** (a) Maximum shear modulus, (b) Poisson ratio and (c) shear wave velocity profiles for the soil profile used in dynamic centrifuge tests

The formula proposed by Hardin & Drnevich [85] is used to estimate the maximum shear modulus profile:

$$G_{max} = 625 \frac{OCR^k}{0.3 + 0.7e^2} \sqrt{p_a \sigma'_m} \quad (4.42)$$

where  $OCR$  is the overconsolidation ratio,  $\sigma'_m$  is the mean effective stress,  $p_a$  is the atmospheric pressure ( $\sim 100 \text{ kPa}$ ), and  $e$  is the void ratio (0.721 for the HN31 sand and 1.166 for the Speswhite kaolin). The value of  $k$  depends on the plasticity index (0 for HN31 sand and 0.21 for the Speswhite kaolin ( $I_P = 25\%$ )).

The shear wave velocity is determined from the following equation:

$$V_s = \sqrt{\frac{G_{max}}{\rho}} \quad (4.43)$$



#### 4.4.2 Response at very low amplitude strains (elastic response)

The modal response of the elastic soil profile corresponding to very low amplitude distortions (linear elastic range at the beginning of the degradation curves) is estimated using a finite element model of the soil column in Abaqus [193] and the soil profile characteristics presented in the previous section. The finite element model consists of a simple soil column of 8-node solid brick elements with an average size of 0.5 m. The boundary conditions of the model reproduce the same boundary conditions encountered in a free-field soil column [239], i.e., the lateral boundaries of the soil column are tied to each other such as to experience the same lateral deformation.

Three eigenmodes are identified in the frequency range 0-10 Hz; two lateral translation response modes at 2.61 Hz and 7.06 Hz and a pumping mode (translation response mode along vertical axis) at 8.6 Hz. Figure 4.19 illustrates the effective mass ratio mobilized by the two lateral translation response modes as well as their modal deformation shapes. The response frequencies corresponding to elastic shear modulus with a variation of  $\pm 20\%$  are also reported in Fig. 4.19 (grey ranges) to highlight the impact of this parameter on the soil profile response. The fundamental response frequency of the soil column, found at 2.61 Hz, is coherent with the experimental findings presented in Chapter 3.

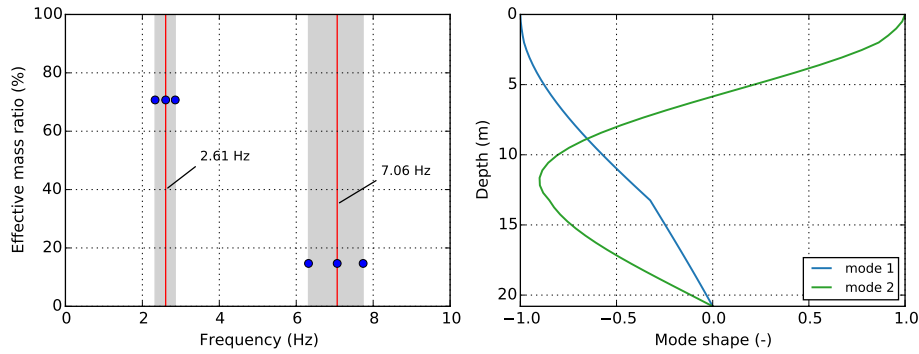


**Figure 4.19:** Eigenfrequencies, effective mass ratio and modal deformation shapes of to the elastic soil profile corresponding to very low amplitude strains

#### 4.4.3 Response under weak seismic motions

The equivalent linear method is used to study the response of the soil profile under weak seismic motions. In order to apply this method, it is necessary to define first the strain-compatible soil characteristics (i.e., shear modulus  $G$  and material damping  $\beta$ ). For this purpose, an iterative one-dimensional wave propagation analysis is performed with the software SHAKE [189, 94]. The nonlinear behavior of the soil is taken into account using the secant shear modulus reduction  $G/G_{max}(\gamma)$  and damping ratio  $\beta(\gamma)$  curves presented in Figure 4.20.

The accelerations recorded at the base of the container for all the dynamic tests are used as acceleration input at the base of the soil column. The strain-compatible equivalent linear elastic soil profiles are calculated for Northridge alone, Landers alone and for all the conducted simulations. The mean profiles calculated for each configuration are presented in Figure 4.21. It is observed that the attained strains are already at the limit of the applicability range of the equivalent linear method, with approximately 0.04% at the bottom of the clay layer (the equivalent linear method is applicable in the low strain range with values between  $10^{-6}$  and  $10^{-4}$ ). It is also interesting to observe that, for this particular case, the maximum strains at the bottom of the clay layer are of the same order of magnitude as the “threshold shear strains” indicated by Mortezaie [147, 148] for the Speswhite kaolin clay.

The Northridge earthquake motion induces more important strains in the clay layer than the Landers earthquake, and therefore a greater degradation of the soil profile characteristics. This observation is consistent with the experimental observations corresponding to weak seismic motions.

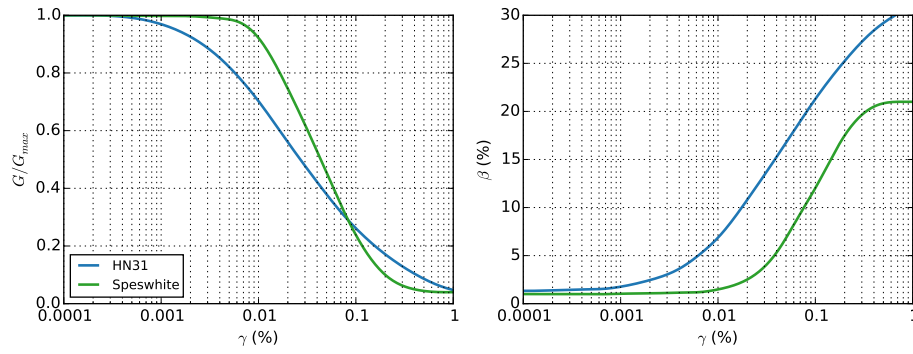


**Figure 4.20:** Secant shear modulus reduction and damping ratio curves used for Hostun HN31 sand and Speswhite kaolinite in the 1D wave propagation analysis

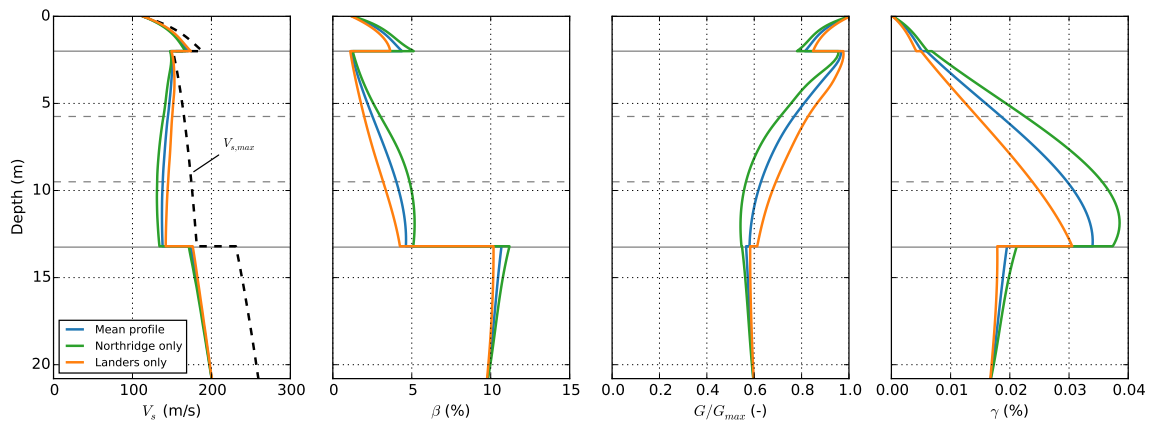


**Figure 4.21:** Strain-compatible soil profiles under low intensity seismic motions (PGA 0.05g)

The modal analysis of the strain-compatible soil profiles presented in Figure 4.21 is conducted with the same finite element model used in the previous section and the software Abaqus [193]. The results are presented in Figure 4.22. The fundamental lateral response mode has now a frequency of about 2.04 Hz. There is therefore a decrease in the response frequency of approximately 0.6 Hz which is in the same order of magnitude as the observations from experimental recordings.

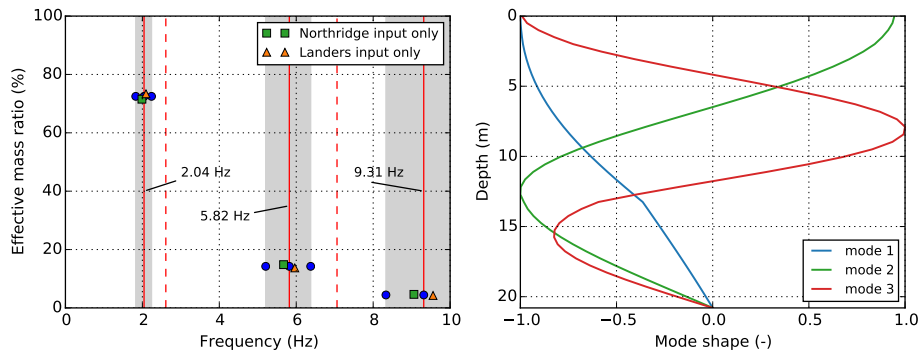


**Figure 4.22:** Eigenfrequencies, effective mass ratio and modal deformation shapes of the strain-compatible equivalent linear soil profiles under low intensity seismic motions (PGA 0.05g)

The transient dynamic response of the soil profile is then studied with the equivalent linear model and a nonlinear model using the hypoplastic constitutive laws for sand and clay presented in the preceding sections. The acceleration time histories calculated at different locations of the soil

profile using the two models are compared with the experimental records in Figure 4.23, in terms of acceleration time histories and 5% response spectra. In general, the response of the system is reproduced rather satisfactorily by both numerical models.

#### 4.4.4 Response under strong seismic motions

The same analysis is conducted in this section for the soil profile under strong seismic motions. It should be noted that the equivalent linear approach is also used but is in this case far from its validity range of application. The results are given for comparison purposes in order to quantify the error committed when this approach is used instead of a more advanced soil model.

The strain-compatible soil profiles are obtained from the one-dimensional wave propagation analysis. They are presented in Fig. 4.24. As expected, very important strain values are attained with a maximum value of about 1% at the bottom of the clay layer (keep in mind that the low strain range corresponds to values between 0.0001% to 0.01%). It is interesting to observe that the Landers earthquake induces more degradation than the Northridge signal. This is consistent with the experimental observations corresponding to strong earthquake motions.

Most of the degradation of the soil column takes place in the clay layer which plays a kind of fuse role. It is therefore clear that the response of the system subjected to strong loading is essentially controlled by the clay layer. Being able to model correctly its nonlinear behavior seems thus essential in order to reproduce numerically the response of the whole system.

As before, a modal analysis of the strain-compatible soil profiles is conducted and presented in Figure 4.25. Surprisingly, despite the fact that the approach is outside of its validity range, the fundamental response frequency of the degraded soil column is found at about 0.7 Hz which is close to the experimental results.

The results of the transient dynamic analysis with the equivalent linear profile and with the hypoplastic constitutive laws are compared with the experimental results (Fig. 4.26). The response of the hypoplastic model is very satisfactory in terms of acceleration and the 5% response spectrum. Regarding the equivalent linear model, larger differences appear with significant deamplifications of certain frequency ranges and at some parts of the clay layer. Nevertheless, results are satisfactory near the surface of the soil column.

### 4.5 Dynamic soil-structure interaction

In this section, several finite element simulations with the hypoplastic constitutive laws are used to reproduce dynamic soil-structure interaction problems under real earthquake motions. The equivalent linear approach is also adopted for comparison purposes. The results are compared with the experimental results and the observed trends are analyzed.

#### 4.5.1 Finite element model

The finite element meshes are presented in Fig. 4.27. They correspond to the four different configurations tested in the experimental tests, that is, single pile without mass, single pile with mass at the top, pile group with a short superstructure and a pile group with a tall superstructure. Taking advantage of the symmetry of the problem only half of the soil-pile system is modeled. Only the mesh corresponding to the soil and the piles is shown. The pile cap mass in C06 test is introduced by means of a lumped mass. The pile group cap and the superstructures in C07 and C08 test are modeled with beams, lumped masses and kinematic constraints to reproduce the infinitely rigid pile cap (see Fig. 3.9). The finite element code Abaqus is used for the numerical simulations [193].

The soil and the piles are modelled using 3D solid elements (C3D8R). The piles have an embedded length  $L = 14.25\text{ m}$ , a diameter  $D = 0.9\text{ m}$  and their behavior is assumed to be linear elastic with a Young's modulus  $E = 2.779\text{e}4\text{ MPa}$  and a Poisson's ratio  $\nu = 0.2$ . This allows to reproduce a pile of equivalent characteristics to that used in the centrifuge experiments (the piles

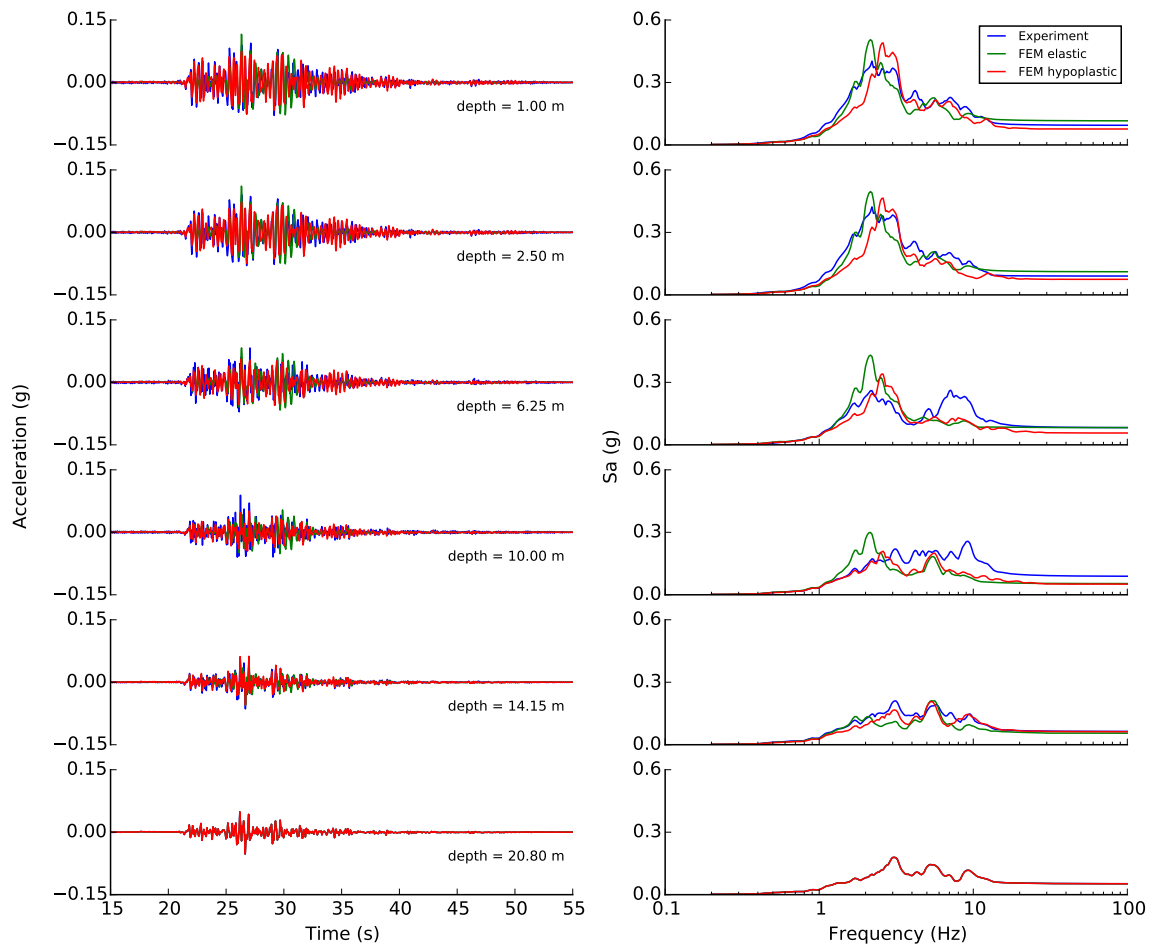


**Figure 4.23:** Free-field ground response under low intensity earthquake motion (Northridge 0.05g), acceleration time-history (left) and response spectra at 5% damping (right) at different depths of the soil profile, experimental records vs. numerical simulations (the equivalent linear model (FEM elastic) and the hypoplastic constitutive law (FEM hypoplastic))

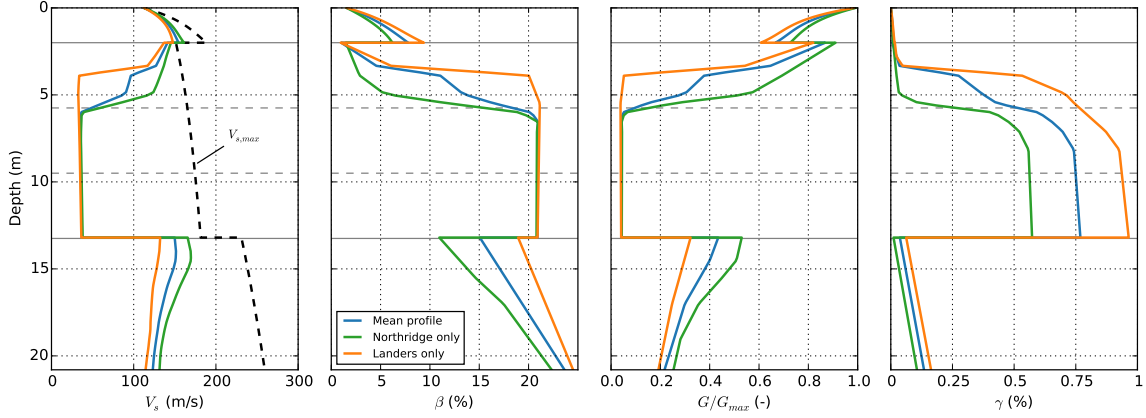


**Figure 4.24:** Strain-compatible soil profiles under strong intensity seismic motions (PGA 0.3g)

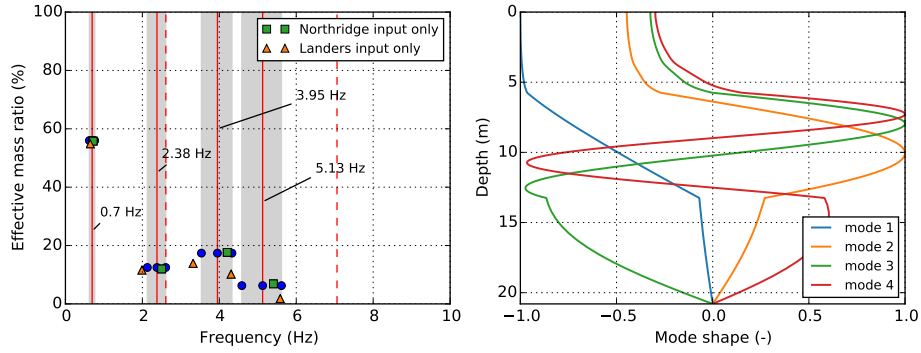


**Figure 4.25:** Eigenfrequencies, effective mass ratio and modal deformation shapes of the strain-compatible equivalent linear soil profiles under strong intensity seismic motions (PGA 0.3g)

in the numerical models have therefore the same flexural rigidity  $EI = 895 \text{ MNm}^2$  as the piles used in experiments at prototype scale).

The nonlinear response of the soil is modeled using the hypoplastic laws for sand and clay presented in the previous sections and the corresponding parameters given in Tables 4.5 and 4.6 for HN31 sand and Speswhite kaolin, respectively. Due to the problems found for the calibration of HN31 under undrained conditions, the soil layer at the bottom of the soil profile is modeled with an elastic-perfectly plastic law using the Mohr-Coulomb criterion. Strain-compatible values of the Young modulus of the soil are used.

The nodes at each side of the numerical model are tied together in order to have the same lateral displacements in X-direction along the soil profile (this makes it possible to reproduce boundary conditions similar to those of the ESB container). Nodal displacements are also restricted in Y-direction. As already mentioned in the analysis of the experimental results, the response frequency of the ESB container and that of the soil profile under strong earthquake loading are very close. The container can therefore influence the response of the soil profile. In order to take this into account, the container is also modeled by adding a network of beams with distributed mass and stiffness. In order to keep the numerical cost to a reasonably level, the nodes of the elements representing the container are directly connected to the nodes of the soil.

The interaction between the pile and the soil is modeled using zero-thickness contact elements that allow relative shear displacements and separation between the soil and the pile. The tangential behavior adopts a classical Coulomb model where the tangential frictional stress is taken proportional to the normal stress. The model requires two parameters, i.e., the interface friction coefficient  $\mu$  and the limiting relative soil pile movement  $\gamma_{lim}$ . A penalty algorithm is adopted for the contact behavior. The contact behavior between the pile and the HN31 sand is considered

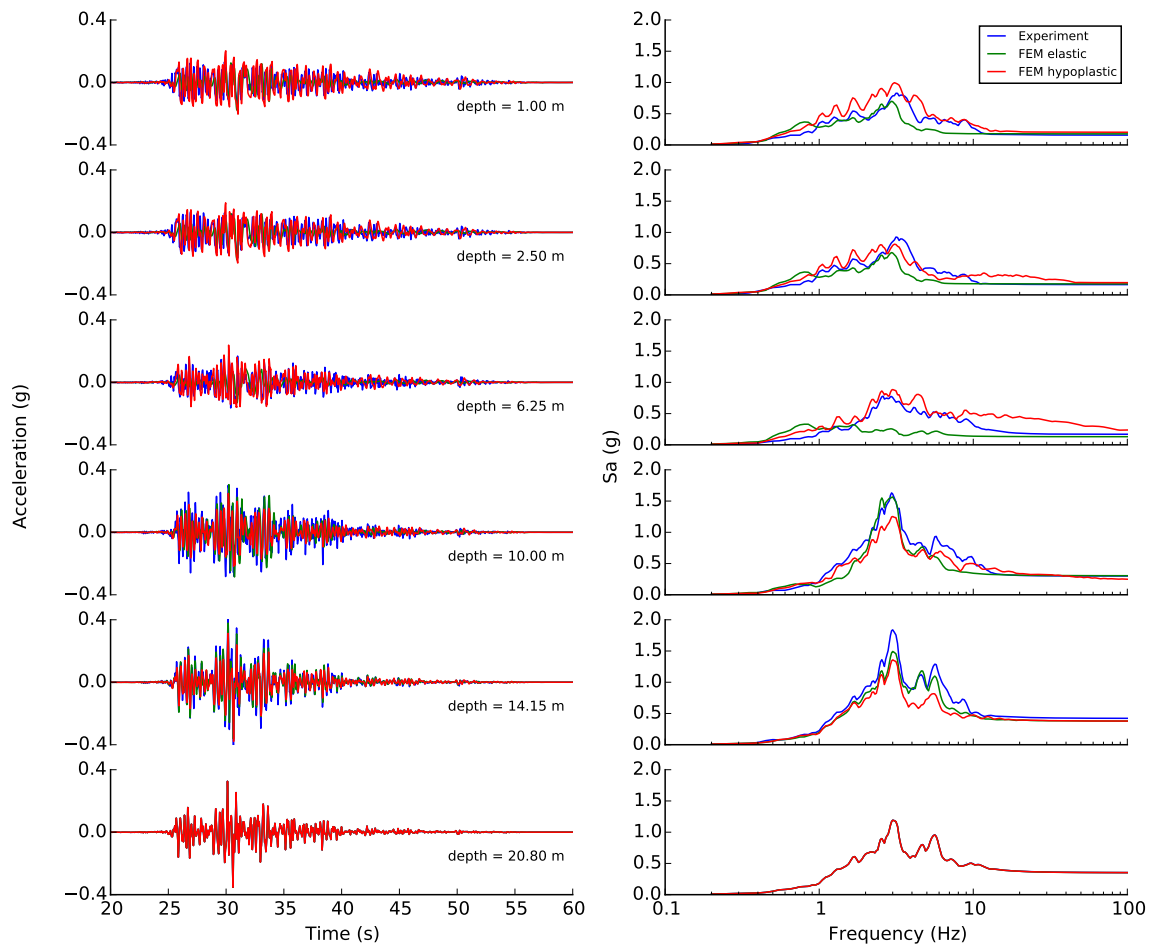


**Figure 4.26:** Free-field ground response under strong earthquake motion (Northridge 0.3g), acceleration time-history (left) and response spectra at 5% damping (right) at different depths of the soil profile, experimental records vs. numerical simulations (the equivalent linear model (FEM elastic) and the hypoplastic constitutive law (FEM hypoplastic))

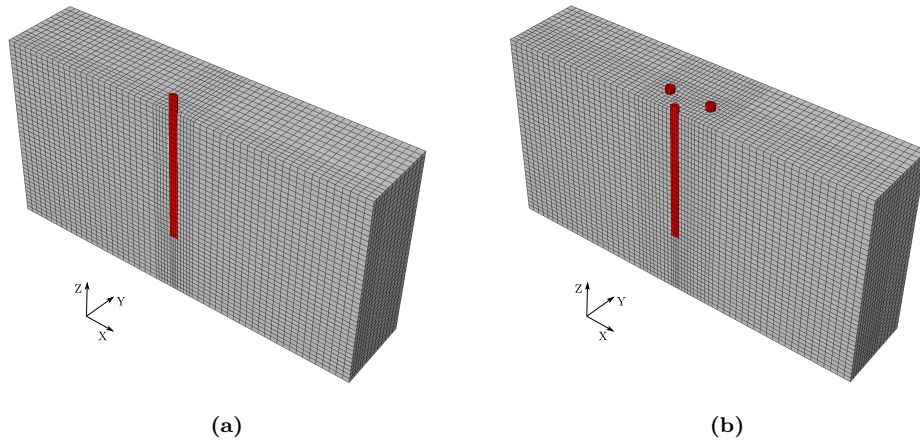


**Figure 4.27:** Finite element mesh for (a) single pile tests (C04, C05 and C06) and (b) pile group tests (C07 and C08) (only the mesh corresponding to the soil and the piles is shown)

using a friction coefficient  $\mu = \tan(\phi_c)$ , with a critical friction angle  $\phi_c = 35^\circ$  [15]. For the contact between the pile and the Speswhite kaolin the parameters  $\mu = 0.3$  and  $\gamma_{lim} = 5 \text{ mm}$  are adopted [89].

Finally, the seismic loading is applied at the base of the finite element model by means of an imposed acceleration time history. The signals effectively applied by the shaker during the tests (recorded by means of an accelerometer attached to the base of the container) are used in the simulations.

#### 4.5.2 Results

Several experimental dynamic tests are simulated hereafter with the equivalent linear approach (FEM elastic) and the nonlinear finite element model with the hypoplastic constitutive laws (FEM hypoplastic). Results of the Northridge earthquake 0.05g and 0.3g PGA tests are shown in Figs. 4.28, 4.29, 4.30 and 4.31 in terms of maximum bending moment envelopes.

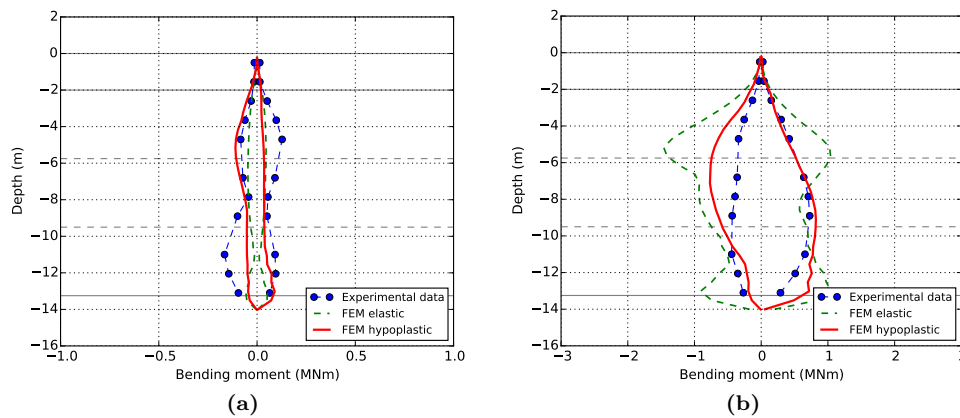


**Figure 4.28:** Comparison of maximum bending moment profiles of a single pile (C05 test), experimental vs numerical results: (a) Northridge 0.05g and (b) Northridge 0.3g earthquake

The equivalent linear model underestimates the maximum moment over the entire length of the pile for weak earthquake loading. Furthermore, the bending moment near the pile-head induced by



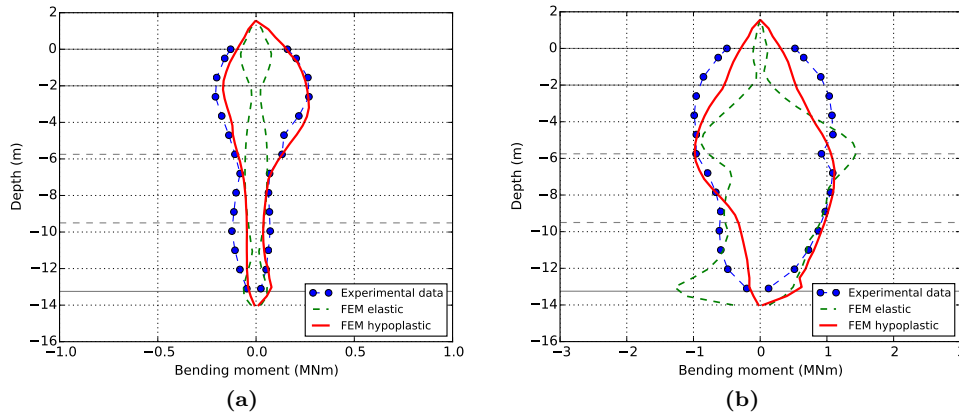


**Figure 4.29:** Comparison of maximum bending moment profiles of a single pile with a mass at its head (C06 test), experimental vs numerical results: (a) Northridge 0.05g and (b) Northridge 0.3g earthquake

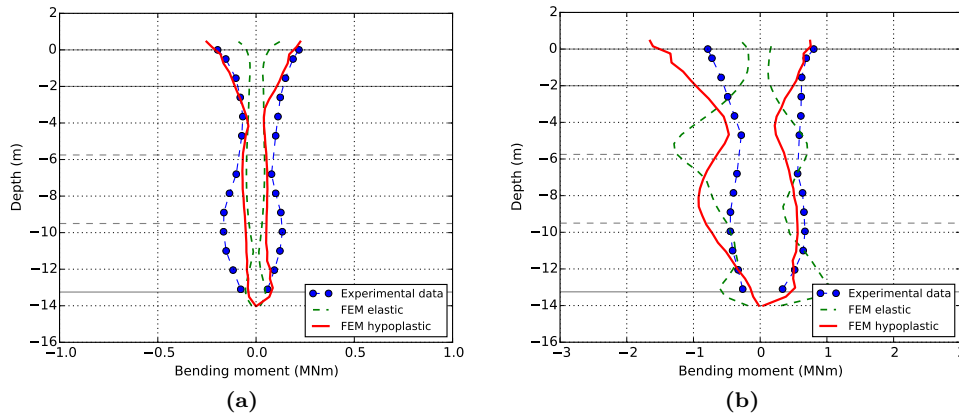


**Figure 4.30:** Comparison of maximum bending moment profiles of the central pile in the pile group with a short superstructure (C07 test), experimental vs numerical results: (a) Northridge 0.05g and (b) Northridge 0.3g earthquake

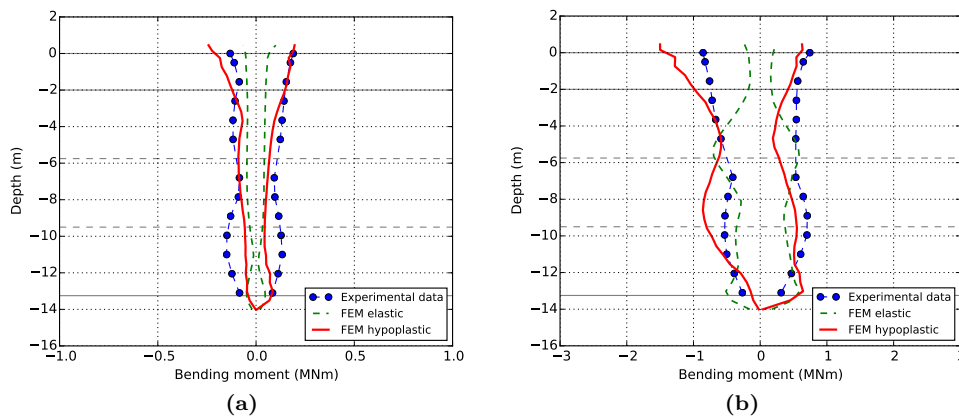


**Figure 4.31:** Comparison of maximum bending moment profiles of the central pile in the pile group with a tall superstructure (C08 test), experimental vs numerical results: (a) Northridge 0.05g and (b) Northridge 0.3g earthquake



inertial interaction (Figs. 4.29 to 4.31) is systematically underestimated for all cases and levels of seismic loading. The maximum bending moments are located near the interfaces of the soil layers presenting a significant stiffness contrast. This is consistent with the literature regarding studies with linear elastic models and harmonic loadings. Nevertheless, peaks exist in the numerical response that are not present in the experimental results because nonlinearity in the surrounding soil and at the pile-soil interface is not correctly taken into account. It should be noted however that in this case, the approach is used either at its limit of applicability (case of weak earthquake motions) or completely outside of the applicability range (case of strong earthquake motions).

The finite element model with the hypoplastic constitutive law is able to predict the overall shape of the maximum bending moment profiles for weak and strong seismic loadings. However, some localized differences are observed in the results. Under low amplitude seismic loading the model underestimates the kinematic type moment at the bottom of the piles. On the other hand, the model reproduces very satisfactorily the moments of inertial type in the upper part. An overestimation of the bending moment at the top of the piles appears in the case of pile group tests (C07 and C08) subjected to strong earthquake motions.

After the comparison of the response of the numerical models with the experimental results in terms of maximum bending moment profiles which has highlighted the interest of introducing nonlinearity in the calculation to obtain more realistic moment profiles, the question to be answered is if the hypoplastic model is also capable to reproduce a complex evolution of the system's response over time. In order to verify this question the finite element model with the hypoplastic constitutive laws is used to reproduce the behavior of the tall superstructure supported by a pile group (C08 test) submitted to a 1 Hz 0.1g Sine base shaking. The results of the simulation are compared with the experiments in Figure 4.32. The numerical and experimental results show an evolution of the location and intensity of the maximum bending moment with time. Some slight differences in amplitude exist but in general the finite element model with the hypoplastic constitutive laws is capable of capturing the evolution of the system's response.

## 4.6 Summary

The equivalent linear method has proved to be a very interesting and practical approach for estimating the acceleration and response frequency of the soil column. Nevertheless, it must be said that this observation is probably not valid for other soil profile configurations and the reader is reminded that the use of the method outside its validity range is generally to be avoided. On the other hand, the model seems not adapted to the calculation of the loads in the piles as it is observed from the comparison of the maximum bending moment envelopes to those from experiments. The model leads sometimes to very important underestimations of the bending moment (i.e., the inertial bending moment at the head of the piles) or localized overestimations in the presence of marked stiffness contrast in the soil profile (i.e., "fictitious" stiffness contrasts that may be present in an equivalent linear soil profile).

The use of hypoplastic models for sand and for clay allows to realistically reproduce the response of the system. In this study a satisfactory agreement is found between the results from nonlinear hypoplastic model and experimental results. However, minor localized differences are observed. Under low amplitude loading the model underestimates the kinematic bending moments in the lower part of the pile, while under high amplitude loading, the model overestimates the inertial bending moments at the head of the piles (related to an important development of nonlinearity near the pile head).

The main drawback of the hypoplastic models is that they require the calibration of an important number of parameters. As of today, the database of calibrated hypoplastic parameters for different soils is still small, and often only the monotonic loading parameters are available. Hypoplastic models are therefore mostly used in academia. The amount of necessary experimental tests data to calibrate and validate the parameters for a given material remains so important that it quickly becomes prohibitive for customary design applications.

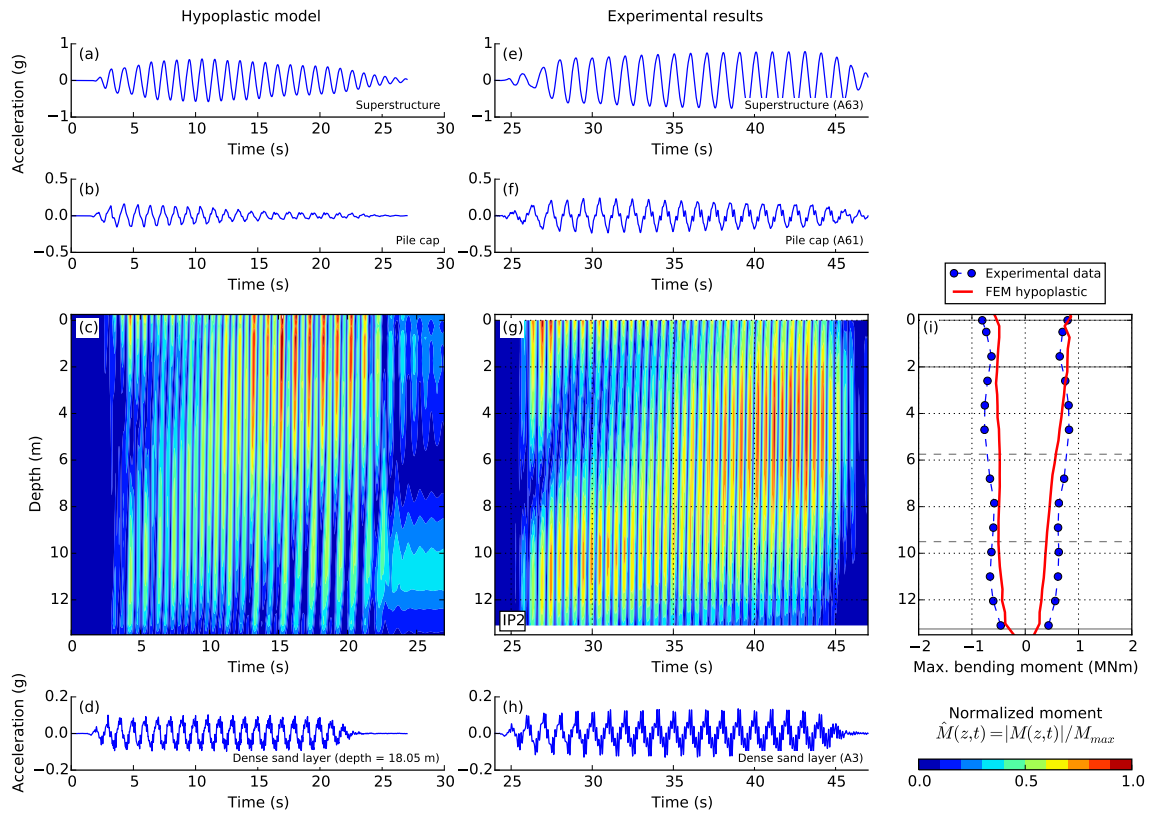


**Figure 4.32:** Time evolution of the normalized bending moment and the envelope of the maximum bending moment in the center pile of the pile group with a tall superstructure (C08 test) subjected to a Sine 1 Hz 0.1g loading. Accelerations in the dense sand layer under the pile group, at the pile cap and at the top of the superstructure are also presented. Numerical (finite element model with the hypoplastic constitutive laws) vs. experimental results

Taking into account nonlinearity in the model, both in the soil but also at the pile-soil interface, gives results closer to reality. This conclusion is drawn in the present study with the hypoplastic model but could be extended to other more “engineering” oriented methods such as the p-y approach, which is often used in engineering practice for the design and verification of piled foundations.

## Chapter 5

# Macroelement

### 5.1 Introduction

The dynamic response of a structure supported by deep foundations is a complex Soil-Structure Interaction (SSI) problem that requires the use of adapted computational methods. Group effects (pile-soil-pile interaction) are important in the case of piled foundations. In addition, they are strongly frequency dependent even for small groups of piles [101].

Traditionally, the design of deep foundations under seismic loadings is carried out by means of conservative methods that aim to assure zero damage of the foundation that therefore remains linear elastic. This approach was justified due to the lack of information about the dynamic non-linear behavior of foundations and the lack of suitable numerical tools. Such limitations become however more and more obsolete as an important number of experimental and numerical results are now available as well as new design methods [169]. In addition, modern design codes as the Eurocode 8 [1] recognize the effect of SSI and of the nonlinear energy dissipation that can be important in the case of strong earthquakes.

In Section 2.5, a bibliographic review introducing the different calculation methods available to take into account SSI in the case of pile foundations is presented. One of them is the macroelement concept, a simplified approach for simulating the multidirectional non-linear soil-foundation response. In this chapter, more details about the macroelement approach are given, with a more in-depth description of its features and commonly assumed hypotheses. The formulation of a new macroelement for pile groups is introduced. The proposed macroelement is finally calibrated and validated using finite element results.

### 5.2 Macroelement model for pile groups

The macroelement can be seen as a multidirectional nonlinear spring that makes possible to concentrate in a single point the overall multidirectional response of the soil and the foundation. It has a 2D or 3D law, described in terms of generalized forces and displacements, decreasing thus dramatically the necessary computational time. Taking into account the nonlinearities and the coupling between the degrees of freedom constitutes the main contribution of this approach. Being a macro-scale numerical tool, one of the inherent particularities and limitations of a macroelement is that it is constructed and calibrated for a specific soil foundation configuration. However, once calibrated and the limits of its applicability clearly defined, it can be intensively used for parametric studies with a reduced computational cost which makes this approach an excellent tool for seismic performance-based design.

The first macroelements were developed for shallow foundations (e.g., [160, 42, 27, 78, 29, 76, 187] among various authors). The extension to deep foundations is more recent and is limited to the case of single piles or 1x2 pile groups in a homogeneous soil profile (i.e., [38, 39, 117, 122, 123]). More details are given in Section 2.5.4.

Piles are more usually installed in groups, rather than as single piles. Furthermore, a pile group

must be considered as a composite block of piles and soil and not as a multiple set of single piles as piles interact with each other under static loading. This behavior may be accentuated when dynamic loadings are considered as group effects are found to be strongly frequency dependent even for small groups of piles [101].

The existing macroelements for deep foundations have several limitations that do not allow to reproduce (at least in an explicit way) the pile group response under static and dynamic loadings (i.e., they do not include the effects of the pile-soil-pile interaction, its variation with loading frequency and the radiation damping). A modular approach to the problem is proposed, using single pile macroelements, interaction factors and/or advanced rheological models (Fig. 5.1). Nonlinearities are concentrated at the soil-pile interface and are modeled using single pile macroelements at the location of each pile. A rigid pile cap is considered with all the piles connected to the control node of the pile group using rigid links. The pile-soil-pile interaction (group effect) is taken into account by means of interaction factors and radiation damping is also considered.

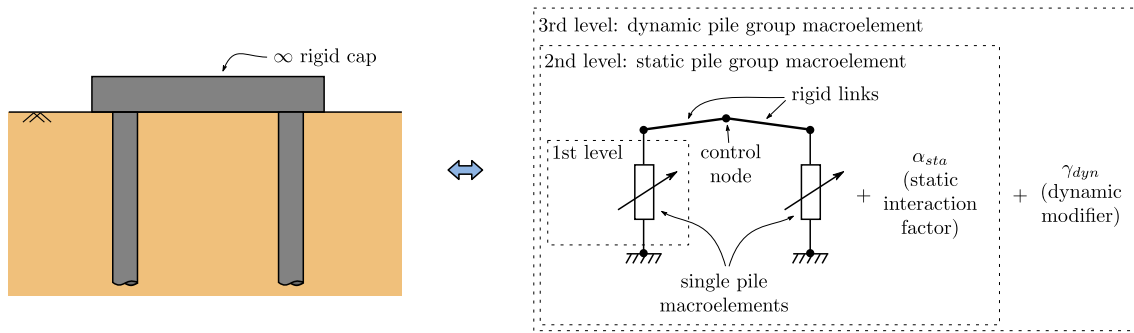


**Figure 5.1:** Modular macroelement concept for a pile group

The proposed modular macroelement concept allows to treat the different aspects controlling the response of a pile group in three levels, that is:

- first level: a macroelement model for a single pile is adopted to reproduce the nonlinear static response of each one of the piles;
- second level: static group effects (pile-soil-pile interactions) are considered introducing static interaction factors to reproduce the nonlinear static response of a pile group;
- third level: frequency effects and radiation damping are introduced using dynamic interaction factors or advanced rheological models.

Several are the advantages of this modular approach as it allows modeling virtually any pile group distribution, decoupling the phenomena related to the behavior of a single pile and of a pile group, reducing numerical calibration costs (each level follows its own calibration strategy) while offering a simplified modeling tool that allows fast changes in the geometrical distribution of the piles within the group. The main limitation of the approach is that the piles are considered connected with an infinitely rigid base slab.

The details of the three different levels of the macroelement are described in the following sections.

### 5.2.1 1<sup>st</sup> level: single pile macroelement model

The formulation of the single pile macroelement proposed by Li [117] is used in the present study. It is based on the theory of hypoplasticity and follows the scheme proposed by Salciarini and Tamagnini [187] in their hypoplastic shallow foundation macroelement. In this section a short presentation is given of the single pile macroelement that is used as the base of the proposed pile group macroelement. For simplicity and in the interest of the presentation, the basic form of the formulation is presented first. This form is suitable for monotonic (not cyclic) loadings. The internal displacement feature, based on the "intergranular strain" concept by Niemunis & Herle

[154], is introduced afterwards to extend the model to cyclic loading. A detailed formulation of the macroelement can be found in [117, 122]. The reader is also referred to [202] for more details about the implementation and the resolution of a macroelement in the framework of the hypoplasticity.

The mechanical response of the pile in the macroelement approach is described by a constitutive equation that links the force and the displacement vectors at the pile head, named  $\mathbf{t}$  and  $\mathbf{u}$  respectively, (Fig. 5.2):

$$\mathbf{t} = \{V, H, M\}^T \quad (5.1)$$

$$\mathbf{u} = \{w, u, \theta\}^T \quad (5.2)$$

It should be noted that the formulation of the single pile macroelement follows the sign convention used in geotechnics, that is  $V > 0$  for compression and  $V < 0$  for traction at the head of the pile (Fig. 5.2a-b). A transformation matrix is applied to the tangent stiffness matrix, the displacement and the internal force vectors of the macroelement in order to pass from the geotechnical to the structural engineering sign convention used in most finite element softwares ( $V < 0$  for compression), (Fig. 5.2c-d).

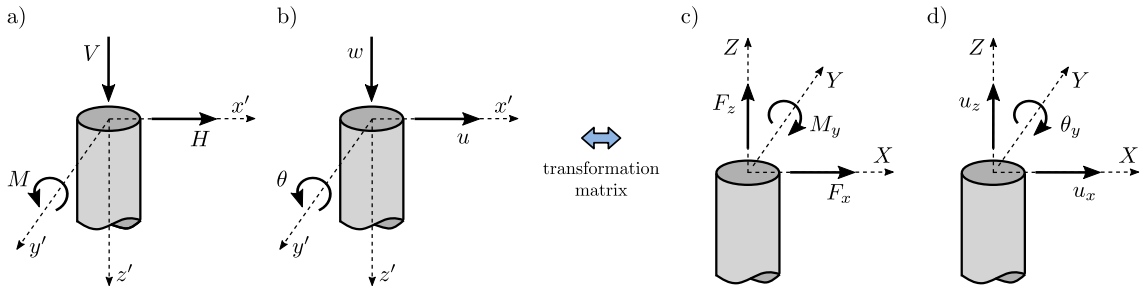


**Figure 5.2:** Notation adopted for (a) forces and (b) displacement components at pile head in local coordinate system and the corresponding values, respectively (c) and (d), in global coordinate system (only the 2D case is illustrated)

In order to reproduce nonlinearity, irreversibility and loading dependence, the constitutive equation is formulated in incremental form:

$$\dot{\mathbf{t}} = \mathcal{K}(\mathbf{t}, \boldsymbol{\eta}) \dot{\mathbf{u}} \quad (5.3)$$

$$\mathcal{K} = \mathcal{L}(\mathbf{t}) + \mathbf{N}(\mathbf{t}) \boldsymbol{\eta}^T \quad (5.4)$$

$$\boldsymbol{\eta} = \dot{\mathbf{u}} / \|\dot{\mathbf{u}}\| \quad (5.5)$$

where  $\mathcal{K}$  is the tangent stiffness matrix and  $\boldsymbol{\eta}$  is the direction of the velocity. Different from elastoplasticity, the deformation velocity  $\dot{\mathbf{u}}$  is not decomposed into reversible and irreversible parts and the tangent stiffness  $\mathcal{K}(\mathbf{t}, \boldsymbol{\eta})$  varies continuously with the direction of  $\boldsymbol{\eta}$ . This property is known as incremental nonlinearity [203] and plays an important role in modeling the irreversible behavior [187].

In the above equations, the matrix  $\mathcal{L}$  is related to the elastic stiffness matrix  $\mathcal{K}^e$  of the system upon full displacement reversal (pseudo-elastic stiffness) by the relation:

$$\mathcal{L} = \frac{1}{m_R} \mathcal{K}^e \quad (5.6)$$

with  $m_R$  a model constant. The elastic stiffness matrix is written:

$$\mathcal{K}^e = \begin{bmatrix} k_v & 0 & 0 \\ 0 & k_h & k_{hm} \\ 0 & k_{hm} & k_m \end{bmatrix} \quad (5.7)$$

where  $k_v$ ,  $k_h$ ,  $k_m$  and  $k_{hm}$  are respectively the vertical, horizontal, rotational and coupled horizontal-rotational elastic stiffness at the pile head.

The constitutive vector  $\mathbf{N}$  accounts for the nonlinearity developed in the macroelement. It can be expressed as:

$$\mathbf{N}(\mathbf{t}) = -Y(\mathbf{t})\mathcal{L}\mathbf{m}(\mathbf{t}) \quad (5.8)$$

In this equation, the scalar function  $Y(\mathbf{t}) \in [0, 1]$  accounts for the degree of nonlinearity, as it depends on the distance from the current stress state to the final yield surface (failure criterion). When  $Y(\mathbf{t}) = 1$  the failure criterion is reached. Its value decreases with increasing distance. It is defined by the following expression:

$$Y(\mathbf{t}) = \xi^\kappa$$

where  $\xi \in [0, 1]$  stands for the normalized measure of the distance and  $\kappa$  is a model constant that controls the hardening behavior of the macroelement.

The unit vector  $\mathbf{m}(\mathbf{t})$  defines the direction of the macroelement velocity at failure (plastic flow direction) and is defined as:

$$\mathbf{m}(\mathbf{t}) = \left( \frac{\dot{\mathbf{u}}}{\|\dot{\mathbf{u}}\|} \right)_f = \boldsymbol{\eta}_f \quad (5.9)$$

An associative plastic flow rule in the generalized loading space is adopted in the present formulation. The vector  $\mathbf{m}(\mathbf{t})$  for states on the failure surface can be evaluated as follows:

$$\mathbf{m}_f = \frac{\partial F / \partial \mathbf{t}}{\|\partial F / \partial \mathbf{t}\|} \quad (5.10)$$

where  $F$  is the failure surface, defined analytically from the bearing capacity of a single pile. For a single vertical pile, Li *et al.* [121, 122] proposed the following failure surface:

$$\begin{aligned} F(\mathbf{t}) = & \left( \frac{H}{H_0} \right)^2 + \left( \frac{M}{M_0} \right)^2 - 1.5 \left( \frac{H}{H_0} \right) \left( \frac{M}{M_0} \right) \\ & + \left\{ \mathcal{H}(V) \left( \frac{V}{V_{c0}} \right)^2 + \mathcal{H}(-V) \left( \frac{V}{V_{t0}} \right)^2 \right\} - 1 = 0 \end{aligned} \quad (5.11)$$

where  $\mathcal{H}(x)$  is the Heaviside step function, defined by:

$$\mathcal{H}(x) = \begin{cases} 0 & (x \leq 0) \\ 1 & (x > 0) \end{cases} \quad (5.12)$$

The scalar quantities  $H_0$ ,  $M_0$ ,  $V_{c0}$  and  $V_{t0}$  correspond to the horizontal, bending, vertical in compression and vertical in traction bearing capacities of the pile, respectively (Fig. 5.3).

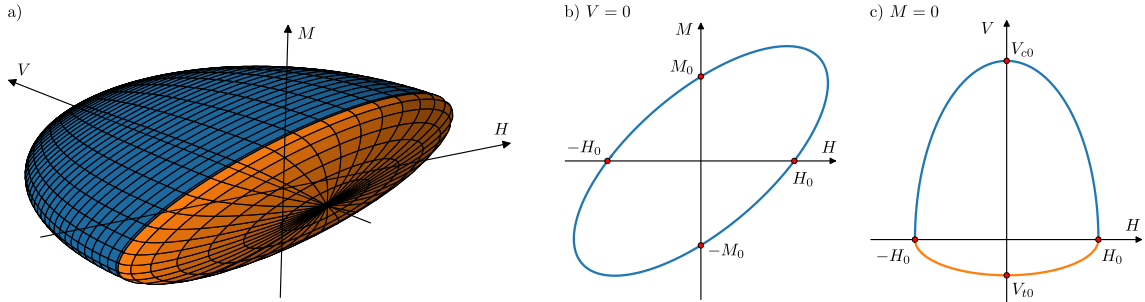


**Figure 5.3:** Failure surface of a single vertical pile (after [121, 117, 122, 123])

In the present formulation it is assumed that the loading surface  $f(\mathbf{t})$  is homothetic to the failure surface, but of smaller size. A direct result of this assumption is that for each loading state  $\mathbf{t}$  inside the failure surface, an image state  $\mathbf{t}^*$  can be defined on the failure surface by a simple projection from the origin of the loading space. Using the measure of the distance  $\xi$  both states are linked by:

$$\mathbf{t}^* = \frac{1}{\xi} \mathbf{t} \quad (5.13)$$

The scalar multiplier  $\xi$  is obtained by imposing the condition  $F(\mathbf{t}^*) = 0$ . For the failure surface in Eq. (5.11) the following closed form expression is found:

$$\xi = \sqrt{\left(\frac{H}{H_0}\right)^2 + \left(\frac{M}{M_0}\right)^2 - 1.5 \left(\frac{H}{H_0}\right) \left(\frac{M}{M_0}\right) + \left\{ \mathcal{H}(V) \left(\frac{V}{V_{c0}}\right)^2 + \mathcal{H}(-V) \left(\frac{V}{V_{t0}}\right)^2 \right\}} \quad (5.14)$$

The loading surface reads:

$$\begin{aligned} f(\mathbf{t}) = & \left(\frac{H}{\xi H_0}\right)^2 + \left(\frac{M}{\xi M_0}\right)^2 - 1.5 \left(\frac{H}{\xi H_0}\right) \left(\frac{M}{\xi M_0}\right) \\ & + \left\{ \mathcal{H}(V) \left(\frac{V}{\xi V_{c0}}\right)^2 + \mathcal{H}(-V) \left(\frac{V}{\xi V_{t0}}\right)^2 \right\} - 1 = 0 \end{aligned} \quad (5.15)$$

A 2D projection of the loading and failure surfaces in the loading space is given in Fig. 5.4. This geometrical interpretation suggests that, for all the admissible loading states, the vector  $\mathbf{m}$  can be defined as the unit gradient to the loading surface, that is:

$$\mathbf{m}(\mathbf{t}) = \frac{\partial f / \partial \mathbf{t}}{\|\partial f / \partial \mathbf{t}\|} \quad (5.16)$$

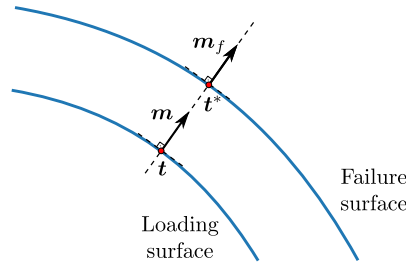


**Figure 5.4:** Direction of plastic flow  $\mathbf{m}(\mathbf{t})$

The constitutive Eq. (5.3) is suitable for monotonic loading. The current loading state being the only state variable, such formulation is however unable to distinguish loading states characterized by the same value of  $\mathbf{t}$  but different load paths which makes it unsuitable to reproduce cyclic loading conditions. In order to do this, a new variable is introduced that keeps track of the previous displacement. This variable, named internal displacement  $\delta$ , is inspired on the "intergranular strain" tensor introduced by Niemunis & Herle [154] in the context of continuum hypoplasticity and was first introduced in the context of hypoplastic macroelements by Salciarini & Tamagnini [187]. With the incorporation of the additional state variable, the constitutive equation of the macroelement takes the form:

$$\dot{\mathbf{t}} = \mathcal{K}(\mathbf{t}, \boldsymbol{\eta}, \delta) \dot{\mathbf{u}} \quad (5.17)$$

The evolution rate of the internal displacement  $\dot{\delta}$  is defined as:



$$\dot{\boldsymbol{\delta}} \begin{cases} (\mathcal{I} - \rho^{\beta_r} \boldsymbol{\eta}_\delta \boldsymbol{\eta}_\delta^T) \dot{\mathbf{u}} & (\boldsymbol{\eta}_\delta \cdot \boldsymbol{\eta} > 0) \\ \dot{\mathbf{u}} & (\boldsymbol{\eta}_\delta \cdot \boldsymbol{\eta} \leq 0) \end{cases} \quad (5.18)$$

where  $\mathcal{I}$  is the 3x3 identity matrix and  $\beta_r$  is a constant of the model. The quantity  $\boldsymbol{\eta}_\delta$  provides the direction of the internal displacement vector  $\boldsymbol{\delta}$ :

$$\boldsymbol{\eta}_\delta = \begin{cases} \boldsymbol{\delta} / \|\boldsymbol{\delta}\| & (\|\boldsymbol{\delta}\| > 0) \\ 0 & (\|\boldsymbol{\delta}\| = 0) \end{cases} \quad (5.19)$$

The scalar variable  $\rho \in [0, 1]$  provides the normalized measure of the magnitude of the internal displacement vector. It is defined as  $\rho = \|\boldsymbol{\delta}\| / R$ , where  $R$  is another constant of the model.

From Eq. (5.18) it can be deduced that for sufficiently long monotonic displacement paths ( $\boldsymbol{\eta} \simeq \text{const}$ ,  $\rho = 1$ ),  $\boldsymbol{\eta}_\delta = \boldsymbol{\eta}$  and  $\dot{\boldsymbol{\delta}} = \mathbf{0}$ , i.e.,  $\boldsymbol{\delta}$  is constant and tangent to the displacement trajectory. When a sharp change in the displacement path direction occurs ( $\boldsymbol{\eta} \cdot \boldsymbol{\eta}_\delta < 0$ ),  $\dot{\boldsymbol{\delta}} = \dot{\mathbf{u}}$  and the internal displacement changes its direction to adapt to the new loading path [123].

Finally the constitutive equation of the hypoplastic model becomes:

$$\boldsymbol{\kappa} = [\rho^\chi m_T + (1 - \rho^\chi) m_R] \boldsymbol{\mathcal{L}} + \begin{cases} \rho^\chi (1 - m_T) (\boldsymbol{\mathcal{L}} \boldsymbol{\eta}_\delta) \boldsymbol{\eta}_\delta^T + \rho^\chi \mathbf{N} \boldsymbol{\eta}_\delta & (\boldsymbol{\eta}_\delta \cdot \boldsymbol{\eta} > 0) \\ \rho^\chi (m_R - m_T) (\boldsymbol{\mathcal{L}} \boldsymbol{\eta}_\delta) \boldsymbol{\eta}_\delta^T & (\boldsymbol{\eta}_\delta \cdot \boldsymbol{\eta} \leq 0) \end{cases} \quad (5.20)$$

where  $\chi$ ,  $m_T$  and  $m_R$  are constants.

From the comparison of the tangential stiffness matrix in the basic form of the hypoplastic macroelement model (Eq. (5.3)) to the one using the internal displacement vector (Eq. (5.20)), it is observed that both the linear and nonlinear parts of the constitutive relationship are modified in order to reproduce cyclic loadings.

The parameters of the hypoplastic macroelement for a single pile used in this study are summarized in Table 5.1.

**Table 5.1:** Parameters of the hypoplastic macroelement for a single pile [117, 122]

Parameter	Description	Related behavior
$k_h$	Horizontal stiffness	Low deformation response with elastic stiffness
$k_m$	Rotational stiffness	
$k_{hm}$	Coupled translation-rotation stiffness	
$k_v$	Vertical stiffness	
$H_0$	Horizontal bearing capacity	Failure criterion with the bearing capacity of a single pile
$M_0$	Bending bearing capacity	
$V_{c0}$	Axial bearing capacity (compression)	
$V_{t0}$	Axial bearing capacity (traction)	
$\kappa$	Hardening parameter controlling stiffness degradation	Evolution of the yield surface
$m_R$	Stiffness at load reversal point	Cyclic behavior
$m_T$	Stiffness when neutral loading	
$R$	Range of linearity	
$\beta_r$	Rate of evolution of intergranular strain	
$\chi$	Transition of stiffness	

It is interesting to note that for some practical applications it is possible to bypass the need to use a full finite element model to calibrate some of these parameters. The stiffness parameters  $k_h$ ,  $k_m$ ,  $k_{hm}$  and  $k_v$  can be evaluated using analytical formulae from the literature (e.g., [61, 68, 1]) or Winkler-type models (i.e., elastic p-y and t-z models). Regarding the scalar quantities  $H_0$ ,

$M_0$  and  $V_0$  that correspond to the horizontal, bending and vertical bending capacities of the pile, respectively, they can also be evaluated using empirical formulae (e.g., [141, 140, 139]) or nonlinear Winkler-type models (i.e., nonlinear p-y and t-z models).

### 5.2.2 2<sup>nd</sup> level: static pile group macroelement model

In the modular approach presented here, each pile is modeled by the single pile hypoplastic macroelement presented in the previous section. The top node of each single pile macroelement is linked to the control node of the pile group by means of rigid links. The control node of the pile group connects the foundation to the supported superstructure. The second level in the scheme in Fig. 5.1 summarizes this approach. It is designed to answer two questions; the possibility to take into account different geometries of the pile group (different pile distributions) and to incorporate group effects (pile-soil-pile interaction) under static loadings.

#### 5.2.2.1 Static condensation

The first question is addressed considering that a rigid cap connects the different pile heads and applying a static condensation. All the single pile macroelements as well as the rigid links are condensed in a single discrete element, the pile group macroelement (Fig. 5.5).

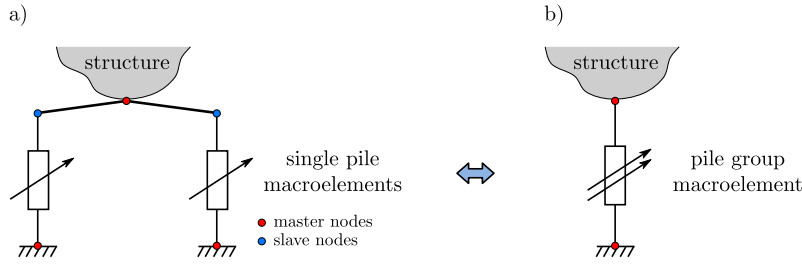


**Figure 5.5:** Static condensation of the pile group foundation system

The static condensation makes possible to reduce the number of unknowns of the finite element model [25]. The degrees of freedom of the initial model are separated into master degrees of freedom, for which the displacements/rotations are known (i.e., control node of the pile group and blocked nodes at the base of each macroelement), and internal degrees of freedom (or slave nodes) that are calculated inside the pile group macroelement.

Let  $\mathbf{K}_F$  be the matrix of the pile group foundation (assembly of the individual single pile macroelements and the rigid links connecting the head of the piles to the control node).  $\mathbf{K}_F$  is therefore a  $6(2N + 1) \times 6(2N + 1)$  matrix (each node has 6 degrees of freedom),  $N$  being the number of piles in the pile group and the 6 additional degrees of freedom of the control node. The foundation stiffness matrix can be separated into sub-matrices according to the distinction between master and slave nodes (Fig. 5.5a) as follows:

$$\mathbf{K}_F = \begin{bmatrix} \mathbf{K}_{ss} & \mathbf{K}_{sm} \\ \mathbf{K}_{ms} & \mathbf{K}_{mm} \end{bmatrix} \quad (5.21)$$

The equilibrium equation of the system in incremental form reads:

$$\begin{bmatrix} \mathbf{K}_{ss} & \mathbf{K}_{sm} \\ \mathbf{K}_{ms} & \mathbf{K}_{mm} \end{bmatrix} \begin{Bmatrix} \Delta \mathbf{u}_s \\ \Delta \mathbf{u}_m \end{Bmatrix} = \begin{Bmatrix} \Delta \mathbf{F}_s \\ \Delta \mathbf{F}_m \end{Bmatrix} \quad (5.22)$$

Taking into account the equilibrium conditions at the internal degrees of freedom makes it possible to write a linear dependence relationship between the internal (slave) and external (master) displacement increments:

$$\Delta \mathbf{u}_s = \mathbf{K}_{ss}^{-1} \Delta \mathbf{F}_s - \mathbf{K}_{ss}^{-1} \mathbf{K}_{sm} \Delta \mathbf{u}_m \quad (5.23)$$

The system in Eq. (5.22) is thus equivalent to the following condensed system:

$$\mathbf{K}_{MG} \Delta \mathbf{u}_m = \Delta \mathbf{F}_{MG} \quad (5.24)$$

with:

$$\mathbf{K}_{MG} = \mathbf{K}_{mm} - \mathbf{K}_{sm}^T \mathbf{K}_{ss}^{-1} \mathbf{K}_{sm} \quad (5.25)$$

$$\Delta \mathbf{F}_{MG} = \Delta \mathbf{F}_m - \mathbf{K}_{sm}^T \mathbf{K}_{ss}^{-1} \Delta \mathbf{F}_s \quad (5.26)$$

$\mathbf{K}_{MG}$  is the tangent stiffness matrix and  $\Delta \mathbf{F}_{MG}$  the internal force increment vector of the pile group macroelement (Fig. 5.5b). Finally, the internal force vector is calculated using its value at the beginning of the resolution step  $j$  and its increment:

$$\mathbf{F}_{MG}^{(j+1)} = \mathbf{F}_{MG}^{(j)} + \Delta \mathbf{F}_{MG}^{(j+1)} \quad (5.27)$$

The static condensation makes thus possible to obtain a pile group macroelement that allows to take into account any virtual configuration of pile group (each pile is represented by a single pile macroelement positioned at the desired location). It is therefore possible to omit to modify the global mesh file for each simulation, an interesting feature for the performance based design of a foundation system. The diagram in Figure 5.6 indicates the steps followed at each Newton-Raphson iteration to calculate the new tangent stiffness matrix and the internal force vector of the pile group macroelement (no static or dynamic group effects are yet considered).

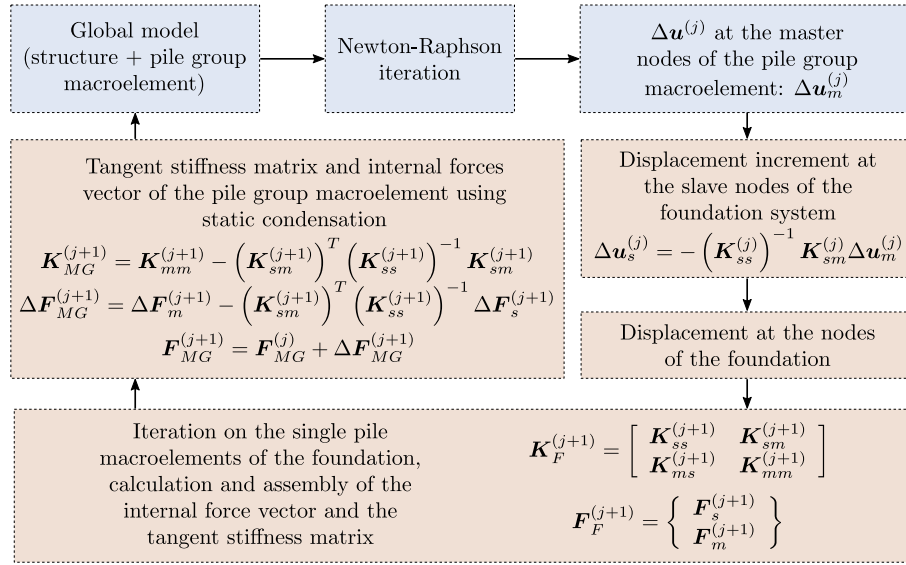


**Figure 5.6:** Resolution scheme for the pile group macroelement at each Newton-Raphson iteration (without static or dynamic group effects)

### 5.2.2.2 Static group effect

In order to take into account the static group effect (pile-soil-pile interaction), the interaction factor approach is adopted hereafter [172, 173, 101, 51]. To better illustrate the implementation and for the sake of simplicity, let's consider first only one degree of freedom per pile head (the extension to the general case is straightforward). In view of a nonlinear resolution, the formulation is developed in incremental form.

The interaction factor  $\alpha_{ij}$  between the piles  $i$  and  $j$  is defined, in incremental form, as the ratio of the displacement increment of the pile  $i$  due to the pile  $j$ , named  $\Delta u_{ij}$ , and the displacement increment of the pile  $j$  alone,  $\Delta u_{jj}$ :

$$\alpha_{ij} = \frac{\Delta u_{ij}}{\Delta u_{jj}} \quad (5.28)$$

The total displacement increment of the pile  $i$ ,  $\Delta u_i$ , is calculated as the sum of its displacement increment alone  $\Delta u_{ii}$  and the additional displacement increment due to the displacement of the surrounding piles thanks to the superposition formula:

$$\Delta u_i = \Delta u_{ii} + \sum_{j \neq i}^N \Delta u_{ij} = \Delta u_{ii} + \sum_{j \neq i}^N \alpha_{ij} \Delta u_{jj} \quad (5.29)$$

For a pile group foundation consisting of  $N$  piles, Equation (5.29) can be written in matrix form as follows:

$$\begin{Bmatrix} \Delta u_1 \\ \Delta u_2 \\ \vdots \\ \Delta u_N \end{Bmatrix} = \begin{bmatrix} 1 & \alpha_{12} & \cdots & \alpha_{1N} \\ \alpha_{21} & 1 & \cdots & \alpha_{2N} \\ \vdots & \vdots & \ddots & \vdots \\ \alpha_{N1} & \alpha_{N2} & \cdots & 1 \end{bmatrix} \begin{Bmatrix} \Delta u_{11} \\ \Delta u_{22} \\ \vdots \\ \Delta u_{NN} \end{Bmatrix} \Rightarrow \begin{Bmatrix} \Delta u_1 \\ \Delta u_2 \\ \vdots \\ \Delta u_N \end{Bmatrix} = \mathbf{A} \begin{Bmatrix} \Delta u_{11} \\ \Delta u_{22} \\ \vdots \\ \Delta u_{NN} \end{Bmatrix} \quad (5.30)$$

where  $\mathbf{A}$  is the interaction matrix:

$$\mathbf{A} = \begin{bmatrix} 1 & \alpha_{12} & \cdots & \alpha_{1N} \\ \alpha_{21} & 1 & \cdots & \alpha_{2N} \\ \vdots & \vdots & \ddots & \vdots \\ \alpha_{N1} & \alpha_{N2} & \cdots & 1 \end{bmatrix} \quad (5.31)$$

For the case where there is no interaction between the piles, that is  $\{\Delta u_1, \Delta u_2, \dots, \Delta u_N\}^T \equiv \{\Delta u_{11}, \Delta u_{22}, \dots, \Delta u_{NN}\}^T$  the interaction matrix  $\mathbf{A}$  becomes the identity matrix.

The displacement increment of a single pile alone is given as:

$$\Delta u_{ii} = \frac{\Delta F_i}{K_i} \quad (5.32)$$

with  $\Delta F_i$  the force increment applied at the head of the pile  $i$  and  $K_i$  the tangent stiffness of the pile alone. If  $\Delta \mathbf{F} = \{\Delta F_1, \Delta F_2, \dots, \Delta F_N\}^T$  the vector of the force increments applied at the head of the piles, we have:

$$\begin{Bmatrix} \Delta F_1 \\ \Delta F_2 \\ \vdots \\ \Delta F_N \end{Bmatrix} = \begin{bmatrix} K_1 & 0 & \cdots & 0 \\ 0 & K_2 & \cdots & 0 \\ \vdots & \vdots & \ddots & \vdots \\ 0 & 0 & \cdots & K_N \end{bmatrix} \begin{Bmatrix} \Delta u_{11} \\ \Delta u_{22} \\ \vdots \\ \Delta u_{NN} \end{Bmatrix} \Rightarrow \begin{Bmatrix} \Delta u_{11} \\ \Delta u_{22} \\ \vdots \\ \Delta u_{NN} \end{Bmatrix} = \mathbf{K}^{-1} \Delta \mathbf{F} \quad (5.33)$$

where  $\mathbf{K}$  is the tangent stiffness matrix of the pile group found by performing the assembly of the tangent stiffness matrices of all the piles without considering the connections at their heads nor the pile-soil-pile interaction.

Equation (5.30) therefore becomes:

$$\begin{Bmatrix} \Delta u_1 \\ \Delta u_2 \\ \vdots \\ \Delta u_N \end{Bmatrix} = \mathbf{A} \mathbf{K}^{-1} \begin{Bmatrix} \Delta F_1 \\ \Delta F_2 \\ \vdots \\ \Delta F_N \end{Bmatrix} \Rightarrow \begin{Bmatrix} \Delta F_1 \\ \Delta F_2 \\ \vdots \\ \Delta F_N \end{Bmatrix} = \mathbf{K} \mathbf{A}^{-1} \begin{Bmatrix} \Delta u_1 \\ \Delta u_2 \\ \vdots \\ \Delta u_N \end{Bmatrix} \Rightarrow \begin{Bmatrix} \Delta F_1 \\ \Delta F_2 \\ \vdots \\ \Delta F_N \end{Bmatrix} = \mathbf{K}^* \begin{Bmatrix} \Delta u_1 \\ \Delta u_2 \\ \vdots \\ \Delta u_N \end{Bmatrix} \quad (5.34)$$

with  $\mathbf{K}^*$  the tangent stiffness matrix of the system considering the group effect (pile-soil-pile interaction):

$$\mathbf{K}^* = \mathbf{K} \mathbf{A}^{-1} \quad (5.35)$$

In the above formulas, single degree of freedom piles were studied. A more realistic response is of course found considering the coupling between lateral (horizontal) displacements and rotations, see Fig. 5.7.

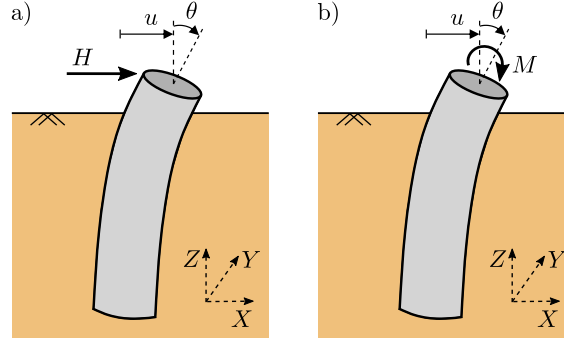


**Figure 5.7:** Single pile response under (a) lateral loading and (b) moment

The equation linking the the forces/moments with the displacements/rotations at the head of a single pile is written in an incremental form:

$$\begin{Bmatrix} \Delta F \\ \Delta M \end{Bmatrix} = \begin{bmatrix} k_h & -k_{hm} \\ -k_{hm} & k_m \end{bmatrix} \begin{Bmatrix} \Delta u \\ \Delta \theta \end{Bmatrix} \quad (5.36)$$

Consider now the coupling between lateral displacements and rotations in a pile group with two piles. Equations (5.30) and (5.33) become:

$$\begin{Bmatrix} \Delta u_1 \\ \Delta \theta_1 \\ \Delta u_2 \\ \Delta \theta_2 \end{Bmatrix} = \begin{bmatrix} 1 & 0 & \alpha_h^{12} & \alpha_{hm}^{12} \\ 0 & 1 & \alpha_h^{12} & \alpha_m^{12} \\ \alpha_h^{21} & \alpha_{hm}^{21} & 1 & 0 \\ \alpha_{hm}^{21} & \alpha_m^{21} & 0 & 1 \end{bmatrix} \begin{Bmatrix} \Delta u_{11} \\ \Delta \theta_{11} \\ \Delta u_{22} \\ \Delta \theta_{22} \end{Bmatrix} \quad (5.37)$$

$$\begin{Bmatrix} \Delta F_1 \\ \Delta M_1 \\ \Delta F_2 \\ \Delta M_2 \end{Bmatrix} = \begin{bmatrix} k_h^1 & k_{hm}^1 & 0 & 0 \\ k_{hm}^1 & k_m^1 & 0 & 0 \\ 0 & 0 & k_h^2 & k_{hm}^2 \\ 0 & 0 & k_{hm}^2 & k_m^2 \end{bmatrix} \begin{Bmatrix} \Delta u_{11} \\ \Delta \theta_{11} \\ \Delta u_{22} \\ \Delta \theta_{22} \end{Bmatrix} \quad (5.38)$$

It is obvious that the form of the equations remains unchanged and the same reasoning can be applied to obtain the stiffness matrix of the system taking into account the pile-soil-pile interaction:

$$\begin{Bmatrix} \Delta F_1 \\ \Delta M_1 \\ \Delta F_2 \\ \Delta M_2 \end{Bmatrix} = \begin{bmatrix} k_h^1 & k_{hm}^1 & 0 & 0 \\ k_{hm}^1 & k_m^1 & 0 & 0 \\ 0 & 0 & k_h^2 & k_{hm}^2 \\ 0 & 0 & k_{hm}^2 & k_m^2 \end{bmatrix} \begin{bmatrix} 1 & 0 & \alpha_h^{12} & \alpha_{hm}^{12} \\ 0 & 1 & \alpha_h^{12} & \alpha_m^{12} \\ \alpha_h^{21} & \alpha_{hm}^{21} & 1 & 0 \\ \alpha_{hm}^{21} & \alpha_m^{21} & 0 & 1 \end{bmatrix}^{-1} \begin{Bmatrix} \Delta u_1 \\ \Delta \theta_1 \\ \Delta u_2 \\ \Delta \theta_2 \end{Bmatrix} \quad (5.39)$$

It should be noted however that in most practical cases, the interaction factors applied to the rotation  $\alpha_m$  and to the displacement/rotation couplings  $\alpha_{hm}$  are neglected.

The **static interaction factors** can be obtained from analytical formulas and charts (e.g., [51, 68, 127, 67, 170, 150, 24]) valid for simple soil profiles (e.g., constant soil profile). For more complex configurations (e.g., particular stratigraphy) they can be evaluated numerically using for example the finite element method (see Fig. 5.8).

For two floating piles in a homogeneous soil profile, the following analytical formulae can be used to calculate the static interaction factors [67]:

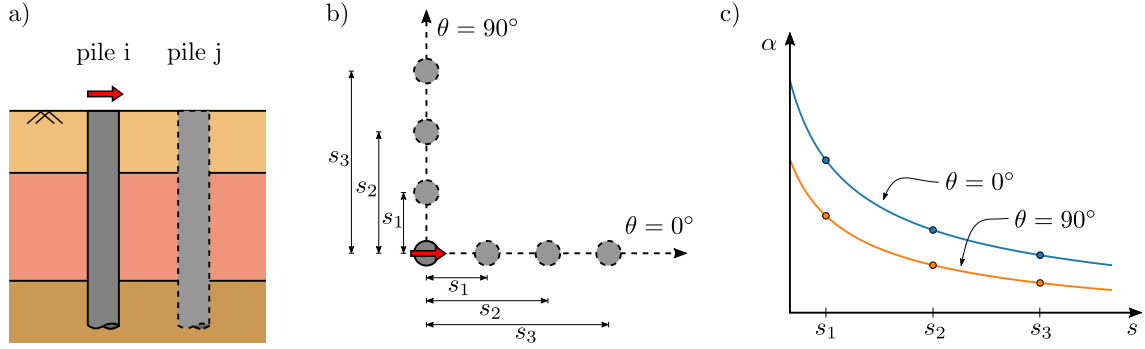


**Figure 5.8:** Example of numerical calculation procedure of static interaction factors, for different values of pile spacing  $s$  and angle  $\theta$  between the loading direction and the plane defined by the axis of both piles

$$\alpha_v \approx \frac{1}{\sqrt{2}} \left( \frac{s}{d} \right)^{-\frac{1}{2}} \quad (5.40)$$

$$\alpha_h(\theta) \approx \alpha_h(0^\circ) \cos^2 \theta + \alpha_h(90^\circ) \sin^2 \theta \quad (5.41)$$

$$\alpha_h(0^\circ) \approx \frac{1}{\sqrt{2}} \left( \frac{s}{d} \right)^{-\frac{1}{2}} \quad (5.42)$$

$$\alpha_h(90^\circ) \approx \frac{3}{4} \alpha_v \quad (5.43)$$

$$\alpha_m \approx \alpha_{hm} \approx 0 \quad (5.44)$$

where  $\alpha_v$  and  $\alpha_h$  are the vertical and horizontal interaction factors,  $\alpha_m$  and  $\alpha_{hm}$  the rotation and coupled displacement/rotation interaction factors (these last two terms are often neglected),  $s/d$  the ratio between the distance (axis to axis)  $s$  and the diameter  $d$  of the piles and  $\theta$  the angle between the loading direction and the vertical plane that is defined by the axis of both piles.

### 5.2.2.3 Combining static condensation and static group effect

Static condensation and static interaction factors can be effectively combined together in the formulation of the pile group macroelement. The Algorithm 1 resumes the different steps followed inside the static pile group macroelement for every Newton-Raphson iteration.

Preliminary calculations (before dynamic resolution)

- Assembly of the stiffness matrix of rigid links connecting the head of the piles to the control node  $\mathbf{K}_{rigid}$
- Assembly of the interaction matrix  $\mathbf{A}$

Newton-Raphson iteration  $j$ :  $\Delta \mathbf{u}^{(j)}$

Displacement increment at the master nodes of the pile group macroelement:  $\Delta \mathbf{u}_m^{(j)}$

Displacement increment at the slave nodes inside the pile group macroelement:

$$\Delta \mathbf{u}_s^{(j)} = - \left( \mathbf{K}_{ss}^{(j)} \right)^{-1} \mathbf{K}_{sm}^{(j)} \Delta \mathbf{u}_m^{(j)}$$

Displacement increment at the head of the piles:  $\Delta \mathbf{u}_i^{(j)} \equiv \Delta \mathbf{u}_s^{(j)}$

Displacement increment due to the deformation of each one of the piles in the system alone:  $\Delta \mathbf{u}_{ii}^{(j)} = \mathbf{A}^{-1} \Delta \mathbf{u}_i^{(j)}$

Iterate on the single pile macroelements, calculation and assembly of  $\mathbf{K}^{(j+1)}$  and  $\mathbf{F}^{(j+1)}$ , assemblies of the tangent stiffness matrices and internal forces vectors of the single pile macroelements

Application of static interaction factors:  $\mathbf{K}^* = \mathbf{K} \mathbf{A}^{-1}$

Tangent stiffness matrix of the foundation:  $\mathbf{K}_F^{(j+1)} = (\mathbf{K}^*)^{(j+1)} + \mathbf{K}_{rigid}$

Static condensation:

$$\begin{aligned} \mathbf{K}_F^{(j+1)} &= \begin{bmatrix} \mathbf{K}_{ss}^{(j+1)} & \mathbf{K}_{sm}^{(j+1)} \\ \mathbf{K}_{ms}^{(j+1)} & \mathbf{K}_{mm}^{(j+1)} \end{bmatrix} & \Delta \mathbf{F}_F^{(j+1)} &= \begin{Bmatrix} \Delta \mathbf{F}_s^{(j+1)} \\ \Delta \mathbf{F}_m^{(j+1)} \end{Bmatrix} \\ \mathbf{K}_{MG}^{(j+1)} &= \mathbf{K}_{mm}^{(j+1)} - \left( \mathbf{K}_{sm}^{(j+1)} \right)^T \left( \mathbf{K}_{ss}^{(j+1)} \right)^{-1} \mathbf{K}_{sm}^{(j+1)} \\ \Delta \mathbf{F}_{MG}^{(j+1)} &= \Delta \mathbf{F}_m^{(j+1)} - \left( \mathbf{K}_{sm}^{(j+1)} \right)^T \left( \mathbf{K}_{ss}^{(j+1)} \right)^{-1} \Delta \mathbf{F}_s^{(j+1)} \\ \mathbf{F}_{MG}^{(j+1)} &= \mathbf{F}_{MG}^{(j)} + \Delta \mathbf{F}_{MG}^{(j+1)} \end{aligned}$$

The tangent stiffness matrix  $\mathbf{K}_{MG}^{(j+1)}$  and the internal force vector  $\mathbf{F}_{MG}^{(j+1)}$  of the pile group macroelement are returned to the main code to perform the global equilibrium

Newton-Raphson iteration

**Algorithm 1:** Resolution scheme followed by the static pile group macroelement ( $2^{nd}$  level) at each Newton-Raphson iteration taking into account static group effects

### 5.2.3 3<sup>rd</sup> level: dynamic pile group macroelement model

Three configurations (namely configuration 2a, 2b and 2c, see Figure 5.9) are proposed hereafter in order for the pile group macroelement to take into account frequency effects and radiation damping.

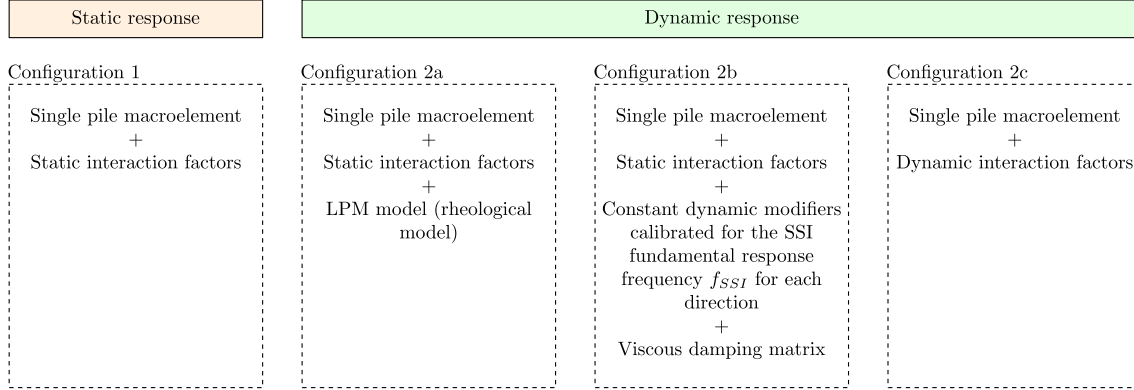


**Figure 5.9:** Configurations of the pile group macroelement for the resolution of static and dynamic problems

#### 5.2.3.1 Configuration 2a

The impedance functions of a given foundation are generally frequency-dependent, specially in the case of layered soil profiles, complex foundation configurations, pile groups, etc. [101, 68, 185, 186]. They can be easily applied in the frequency domain but these type of studies are restricted to elastic problems. When the inelastic behavior of the structure needs to be considered, as for example in performance based design, transient resolution schemes are however necessary.

It is possible to account for the variation of the impedance function with frequency in a transient dynamic analysis using simple rheological models, also known as lumped parameter models (LPM). In general, LPMs consist of springs, dashpots, and masses having frequency independent coefficients (e.g., [231, 47, 230, 233, 185] to cite some examples). Figure 5.10 presents two well known LPM models available in the literature. The parameters of the various elements in the LPM models are calibrated by an optimization method to reproduce as closest as possible the variation of the impedance function with frequency [222]. The advantage of LPM models is that they can be directly applied to linear and nonlinear dynamic analyses in the time domain. Furthermore, the use of a rheological model allows to bypass the trial and error approach required for the proper choice of the foundation stiffnesses when a set of independent constant springs and viscous dashpots are used at the base of the structure to represent SSI [167, 186].

By combining the static pile group macroelement introduced in the previous section with a LPM model, it is possible to introduce a frequency dependent behavior. Let's consider for example the LPM model presented in Fig. 5.11a. This model is capable of reproducing the elastic frequency-dependent response of a given foundation (using the corresponding set of calibrated parameters). The proposed configuration 2a consists in replacing the linear elastic spring indicated in Fig. 5.11a by the pile group macroelement, Fig. 5.11b. The modified model is thus able to reproduce a quasi-linear dynamic response at low amplitude loadings and a nonlinear dynamic response under more important loadings.

The LPM model in Fig. 5.11a has two types of components connected in parallel. A base component which aims to reproduce the response of the system at zero frequency and several additional components that allow to adjust the variation of the response with the frequency, see Figure 5.12.

The response of the model at zero frequency is controlled by the stiffness term of the base component, i.e., the elastic spring. The modified model proposed in Fig. 5.11b can be therefore used for static and dynamic calculations. To do this, the additional components cannot include springs connecting directly both ends of the model. Given that all the components are connected in



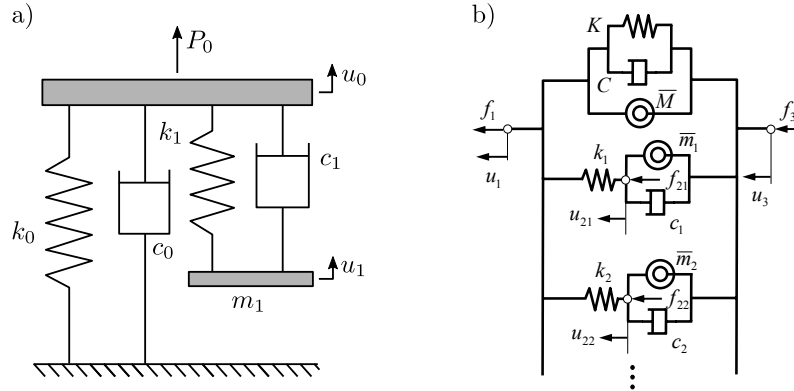


**Figure 5.10:** Example of LPM models: (a) five-parameter discrete model proposed by De Barros and Luco [47] and (b) generalized Type II model with gyromass elements proposed by Saitoh [185]

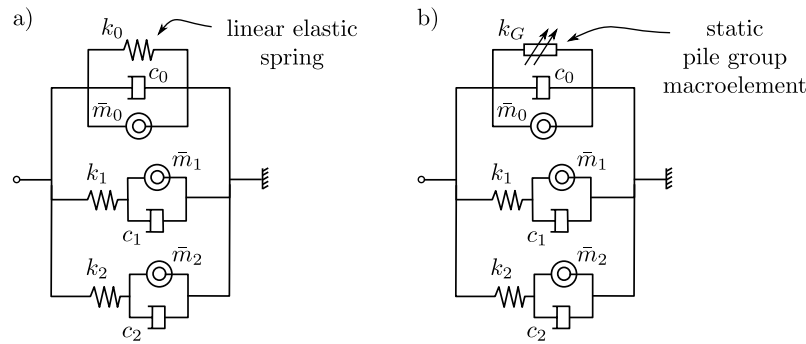


**Figure 5.11:** Introduction of frequency effects and radiation damping in the pile-group macroelement: (a) elastic frequency-dependent rheological model proposed by Saitoh [185] (b) frequency-dependent pile-group macroelement model by combination of the static pile group macroelement with a LPM model

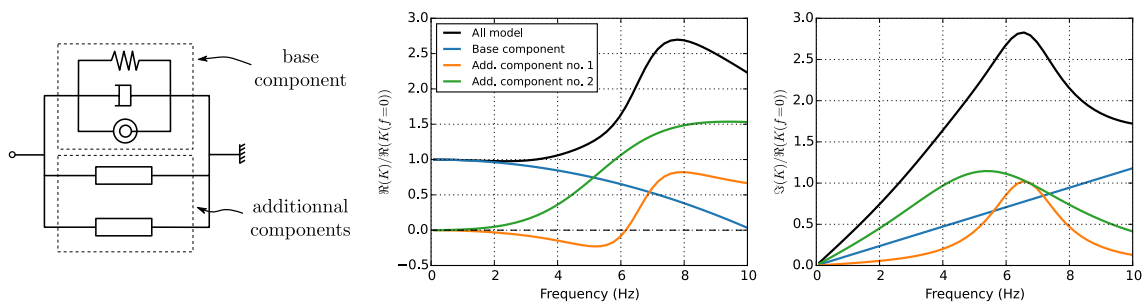


**Figure 5.12:** Components of the rheological model used in the dynamic pile group macroelement and their influence on the impedance function

parallel, the impedance function of the model is equivalent to the sum of the impedance functions of each component alone.

The rheological model proposed by Saitoh [185] is used in the present work to construct the dynamic pile macroelement. Other LPM models can of course be used, provided that the interaction between the different parts of the model (specially the stiffness at zero frequency) are clearly identified. This is important when calibrating the model parameters.

The configuration 2a of the dynamic pile group macroelement is able to reproduce the frequency effect and the radiation damping on the response of the system. Its main disadvantage however is that it necessitates to calibrate the parameters of the LPM model in order to reproduce the corresponding impedance function. This task is often done via trial and error calibration. With the development of sophisticated optimization methods such as neural networks, genetic algorithms, etc., this task might become less laborious. This possibility however has not been explored in this thesis. A SSI problem using the configuration 2a macroelement for pile groups is presented in Section 5.3.

### 5.2.3.2 Configuration 2b

A simplified alternative solution to the use of LPM models is to use constant springs and dashpots whose parameters are adjusted using a specific frequency of the system. The most common choice is to use the fundamental SSI frequency of the soil-foundation-superstructure system (this is in fact common practice in today's design practice, particularly when multimode spectral analysis are conducted using the substructuring method, see Section 2.5). Other options are to use the static stiffness and the initial slope of the imaginary part of the impedance function, the stiffness at the fundamental frequency of the structural system and the secant of the imaginary part of the impedance function at that frequency or the stiffness and the corresponding damping at the dominant frequency of the input motion. It is worth noting that among these three options, the third one is found to give closer results to those obtained using a complete LPM model [186].

Within the framework of the modular macroelement concept this results in the condensation of the second and third levels presented in Fig. 5.1 into a single step. The static interaction factors are modified with constant dynamic modifiers (one per direction) that are numerically calibrated in order to match the effective stiffness of the pile group macroelement at low deformation to that indicated by the dynamic impedance functions at the selected frequency (e.g., the fundamental SSI frequency of the structure):

$$\alpha_X^{dyn} = \gamma_X \times \alpha_X^{sta} \quad \alpha_Y^{dyn} = \gamma_Y \times \alpha_Y^{sta} \quad \alpha_Z^{dyn} = \gamma_Z \times \alpha_Z^{sta} \quad (5.45)$$

where  $\alpha_X^{sta}$ ,  $\alpha_Y^{sta}$  and  $\alpha_Z^{sta}$  are the static interaction factors,  $\gamma_X$ ,  $\gamma_Y$  and  $\gamma_Z$  the constant dynamic modifiers and  $\alpha_X^{dyn}$ ,  $\alpha_Y^{dyn}$  and  $\alpha_Z^{dyn}$  the modified interaction factors that are effectively applied to the stiffness matrix of the pile group.

The radiation damping is directly modeled using a viscous damping matrix whose terms are obtained using the values of the impedance functions corresponding to the selected frequency of the system for each direction.

A SSI problem using the configuration 2b macroelement for pile groups is presented in Chapter 6.

### 5.2.3.3 Configuration 2c

The third configuration consists in using dynamic interaction factors to model the frequency-dependent pile-soil-pile interactions (group and frequency effects). For the case of two floating piles in a homogeneous soil profile for example, the following analytical formulae can be used to calculate the dynamic interaction factors [67]:

$$\alpha_v \approx \frac{1}{\sqrt{2}} \left( \frac{s}{d} \right)^{-\frac{1}{2}} \exp \left( \frac{-\beta \omega s}{V_s} \right) \exp \left( \frac{-i \omega s}{V_s} \right) \quad (5.46)$$

$$\alpha_h(\theta) \approx \alpha_h(0^\circ) \cos^2 \theta + \alpha_h(90^\circ) \sin^2 \theta \quad (5.47)$$

$$\alpha_h(0^\circ) \approx \frac{1}{\sqrt{2}} \left(\frac{s}{d}\right)^{-\frac{1}{2}} \exp\left(\frac{-\beta\omega s}{V_{La}}\right) \exp\left(\frac{-i\omega s}{V_{La}}\right) \quad (5.48)$$

$$\alpha_h(90^\circ) \approx \frac{3}{4}\alpha_v \quad (5.49)$$

$$\alpha_m \approx \alpha_{hm} \approx 0 \quad (5.50)$$

where  $\alpha_v$  and  $\alpha_h$  are the vertical and the horizontal interaction factors, respectively.  $\alpha_m$  and  $\alpha_{hm}$  are the interaction factors that apply to the rotation and the coupled displacement/rotation terms of the stiffness matrix respectively (these two terms are often neglected).  $s/d$  is the ratio between the spacing (axis to axis) and the diameter of the piles and  $\theta$  is the angle between the loading direction and the vertical plane that is defined by the pile axis. The characteristics of the soil are introduced by means of its shear wave velocity  $V_s$ , the so-called Lysmer analogue wave velocity  $V_{La} = \frac{3.4V_s}{\pi(1-\nu)}$  and the hysteretic damping ratio  $\beta$ . To introduce these dynamic interaction factors, the same approach followed for the static interaction factors can be used. The only difference is that in this case the operations are done with complex values.

Several limitations of this approach are nevertheless to be considered. Interaction factors are evaluated for a pair of piles assuming transparent intermediate piles. In other words, the attenuating phenomena of wave interference are not reproduced by this model which can lead to an overestimation of the interaction when the number of piles is important or their spacing is reduced. However, studies conducted by several authors (e.g., [101, 188, 182]) have demonstrated that the results of this approximation are, indeed, in very good agreement with more rigorous dynamic solutions [51].

Most of the analytical formulae for dynamic interaction factors available in the literature are given for simple soil profiles. When more complex configurations need to be taken into account (e.g., multilayer soil profile), it is possible to calculate these interaction factors  $\alpha(\omega, s, \theta)$  using a numerical model with two piles for different loading frequencies, pile spacing and loading directions (see Fig. 5.8). The boundary element approach using specialized software (e.g., SASSI [126, 165] and MISS3D [35, 36]) is suitable for this task.

### 5.3 Validation of the pile group macroelement

In this section, a nonlinear dynamic SSI case study is analysed with the pile group macroelement (configuration 2a) and the numerical results are compared to a 3D nonlinear finite element analysis. First, the calibration procedure of the pile group macroelement components is detailed and then validation follows.

#### 5.3.1 Calibration

In order to calibrate and validate the performance of the pile group macroelement (configuration 2a), the response of a 2x2 pile group in a constant modulus soil profile is studied (Fig. 5.13).

The 2x2 pile group is composed of reinforced concrete piles of 1 m in diameter and 15 m in length embedded in a homogeneous cohesive soil profile. The spacing between the axes of the piles is equal to 5 diameters and a rigid weightless cap connects all the piles at their head. The behavior of the soil is modeled with an elastic-perfectly plastic law using Mohr-Coulomb's criterion, Young's modulus  $E_s = 20 \text{ MPa}$ , Poisson's ratio  $\nu = 0.4$ , mass density  $\rho_s = 1.75 \text{ t/m}^3$ , viscous damping  $\beta = 5\%$  and cohesion  $c = 20 \text{ kPa}$ . The behavior of the piles is assumed to be linear elastic.

It should be noted that the foundation and the soil profile have the same non-dimensional ratios as those used in the analytical study by Kaynia and Kausel [101], a study often cited as an example of a pile group SSI study using a linear viscoelastic model and the boundary element method (resolution in the frequency domain). This choice allows to compare the proposed approach with traditional methods limited to elastic cases and then to study the case where nonlinearity is taken into account.

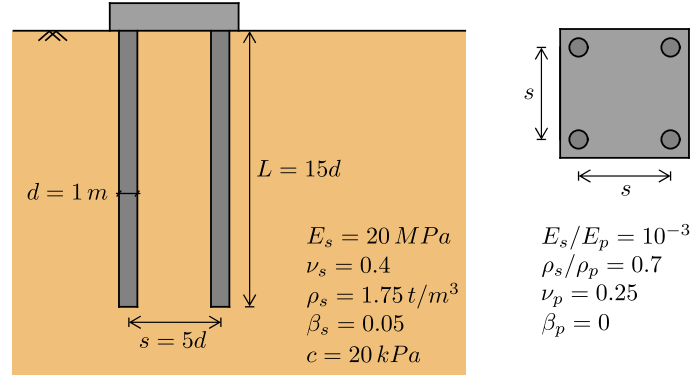


**Figure 5.13:** Case study for the calibration and the validation of the pile group macroelement (configuration 2a): a 2x2 pile group in a constant modulus soil profile

### 5.3.1.1 Calibration: response of a single pile (1<sup>st</sup> level)

The first step is to calibrate the parameters of the single pile macroelement in order to reproduce the static nonlinear response of a single pile. A nonlinear finite element model with a single pile is used for the calibration.

The terms of the elastic stiffness matrix at the pile head ( $k_h$ ,  $k_m$ ,  $k_{hm}$  and  $k_v$ ) are determined with the finite element model by imposing small displacements or rotations at the pile-head and evaluating the corresponding reactions, as illustrated in Figure 5.14. The following values are found:  $k_h = 8.69 \times 10^4 \text{ kN/m}$ ,  $k_m = 4.5 \times 10^5 \text{ kNm/rads}$ ,  $k_{hm} = 1.27 \times 10^5 \text{ kN/rad}$  and  $k_v = 2.25 \times 10^5 \text{ kN/m}$ .

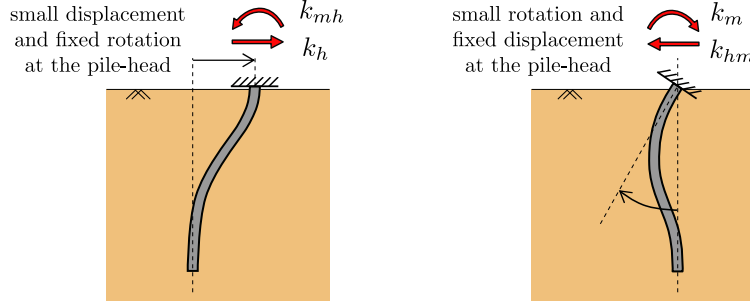


**Figure 5.14:** Calculation of the pile-head elastic stiffness matrix terms

The finite element model is then used to calculate the bearing capacity of the single pile. The following definitions are used: the lateral bearing capacity  $H_0$  corresponds to the horizontal reaction for an imposed lateral displacement  $u_0$  equal to one diameter at the pile-head. The same applies to the axial bearing capacity of the pile  $V_0$  for a vertical displacement  $w_0$  at the pile-head. The rotational bearing capacity is the moment reaction  $M_0$  corresponding to a rotation angle  $\theta_0$  at the pile head, equal to the angle at the pile head for an imposed lateral displacement  $u_0$ . Figure 5.15 presents the results of the relevant simulations. The following values are found:  $H_0 = 2.22 \times 10^3 \text{ kN}$ ,  $M_0 = 1.42 \times 10^4 \text{ kNm}$  and  $V_0 = 2.45 \times 10^3 \text{ kN}$ .

It should be noted that in previous studies (e.g., [121, 117]) the failure criterion was defined at the numerical divergence of the simulation. The fact of defining the failure condition at the pile head (bearing capacity) according to the criterion previously mentioned, limits the computational time and removes a certain arbitrariness that may appear in the computation (e.g., numerical divergence may not be reached at the same time for two different resolution algorithms, different convergence criterion, etc.). On the other hand, the size of the failure criterion is now smaller and the parameters controlling the evolution of nonlinearity are slightly different (i.e., the parameter  $\kappa$  that controls the transition from linear to fully nonlinear behavior).

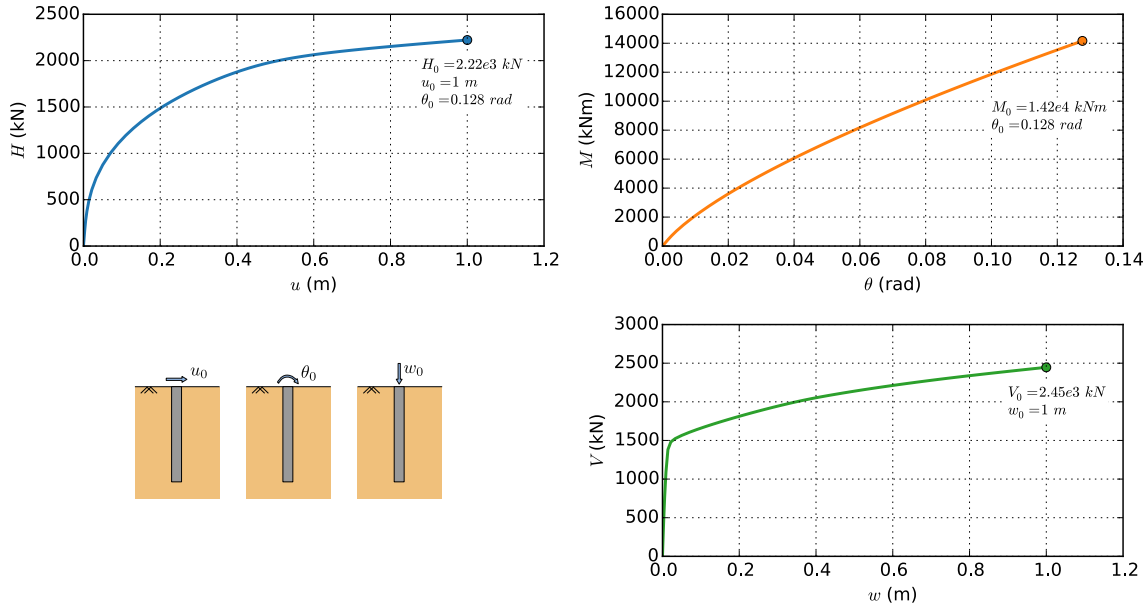


**Figure 5.15:** Calculation of the bearing capacity of the single pile

The parameters controlling the evolution of the yield surface and the cyclic behavior of the single pile macroelement need also to be calibrated. The response of the pile subjected to a monotonic lateral loading allows calibration of the hardening parameter  $\kappa$  that controls the degree of nonlinearity (i.e., the way the current loading state approaches the final failure state). The comparison between the results from the finite element model and from the single pile macroelement is presented in Figure 5.16.

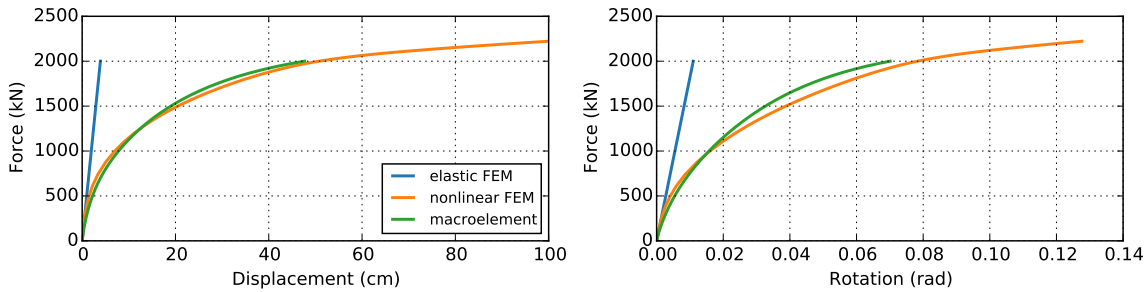


**Figure 5.16:** Monotonic lateral loading of a single pile: elastic FEM vs nonlinear FEM vs single pile macroelement results

The parameters controlling the cyclic response of the single pile macroelement are calibrated by direct comparison of the cyclic response of the pile using the finite element model. Figure 5.17 presents this comparison for two amplitude levels of the loading.

It can be observed that the macroelement model is able to reproduce the response at the pile head in translation and in rotation for different levels of loading. The calibrated parameters are given in Table 5.2.

### 5.3.1.2 Calibration: static response of the pile group (2<sup>nd</sup> level)

In order to reproduce the static response of the pile group, the static interaction factors given in Equations (5.40) to (5.44) are used.

The static response of the pile group macroelement is compared to that of the finite element model in Figs. 5.18 (monotonic lateral loading) and 5.19 (cyclic lateral loading). The performance

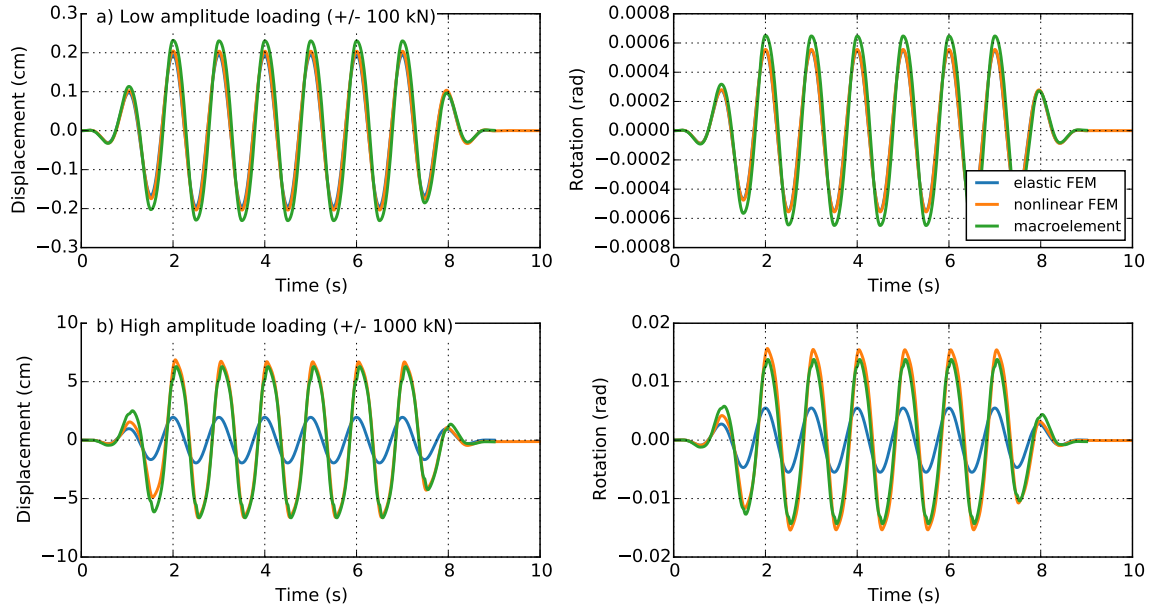


**Figure 5.17:** Lateral cyclic loading of a single pile: elastic FEM vs nonlinear FEM vs single pile macroelement results

**Table 5.2:** Calibrated parameters for the single pile macroelement

Parameter	Value	Description and related behavior
$k_h$	$8.69 \times 10^4 \text{ kN/m}$	Low deformation response (elastic stiffness)
$k_m$	$4.5 \times 10^5 \text{ kNm/rads}$	
$k_{hm}$	$1.27 \times 10^5 \text{ kN/rad}$	
$k_v$	$2.25 \times 10^5 \text{ kN/m}$	
$H_0$	$2.22 \times 10^3 \text{ kN}$	Failure criterion (bearing capacity of a single pile)
$M_0$	$1.42 \times 10^4 \text{ kNm}$	
$V_0$	$2.45 \times 10^3 \text{ kN}$	
$\kappa$	0.4	Evolution of the yield surface
$m_R$	2.25	Cyclic behavior
$m_T$	2	
$R$	$6 \times 10^{-3}$	
$\beta_r$	0.3	
$\chi$	0.4	

of the macroelement is very satisfactory. Calculations for other load levels (results are not shown here) confirm also the ability of the macroelement to reproduce the static response of the pile group.

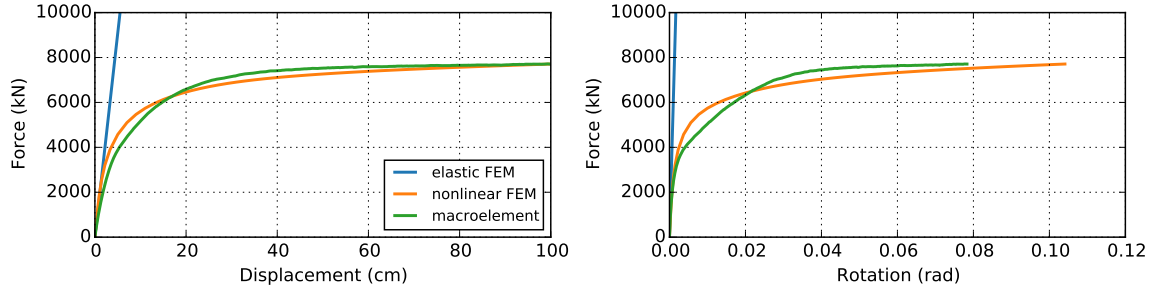


**Figure 5.18:** Monotonic lateral loading of the 2x2 pile group: elastic FEM vs nonlinear FEM vs static pile group macroelement

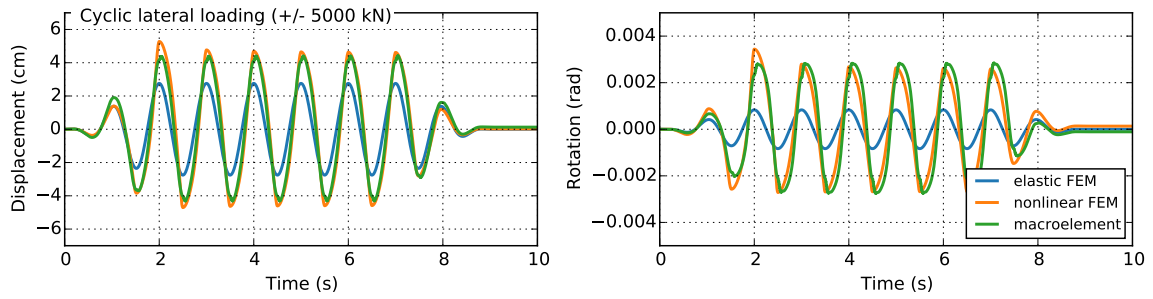


**Figure 5.19:** Lateral cyclic loading of the 2x2 pile group: elastic FEM vs nonlinear FEM vs static pile group macroelement results

### 5.3.1.3 Calibration: introduction of frequency effects and radiation damping (3<sup>rd</sup> level)

The next step is to introduce the frequency effects and radiation damping into the model. The LPM Type II model proposed by Saitoh [185] is modified and introduced in the pile group macroelement to replicate the dynamic behavior of the foundation (see Section 5.2.3.1). The calibrated parameters of the LPM model that allow to reproduce the lateral dynamic response of the 2x2 pile group for this particular case are provided by Saitoh and summarized in Table 5.3.

**Table 5.3:** Calibrated parameters of the LPM model inside the pile group macroelement to reproduce the dynamic lateral translation response of the 2x2 pile group (adapted from [185])

	Coefficient	Value
	$\gamma_0$	1.2
	$\mu_0$	1
	$\beta_1$	0.4
	$\gamma_1$	0.6
	$\mu_1$	2.3
	$\beta_2$	1.2
	$\gamma_2$	1.8
	$\mu_2$	2.5

Figure 5.20 compares the lateral translation dynamic impedance function, real and imaginary parts, of the 2x2 pile group foundation calculated using the boundary element approach and the

software SASSI [126, 165], the rigorous solutions given by Kaynia [103] and the results from the LPM Type II model proposed by Saitoh [185]. It can be observed that the calibrated LPM model reproduces correctly the dynamic impedance.

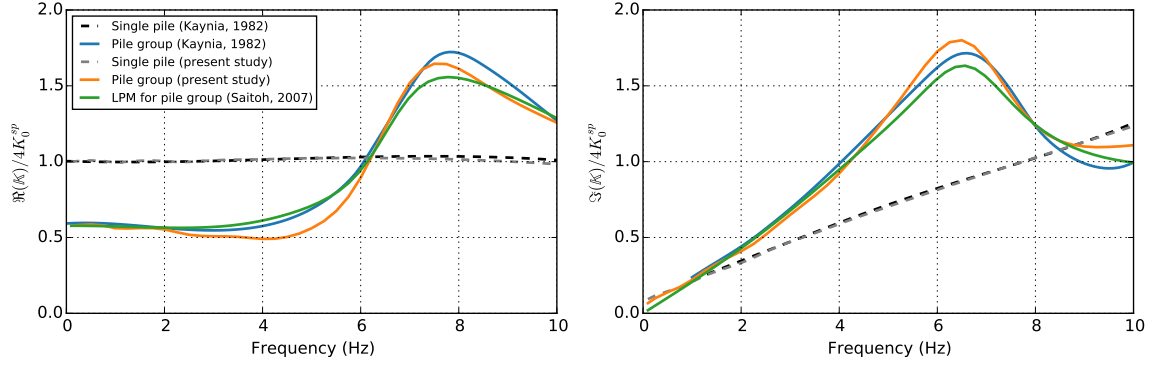


**Figure 5.20:** Lateral translation dynamic impedance function of the 2x2 pile group: numerical results using the boundary element approach and the software SASSI [126, 165] vs. the rigorous solution given by Kaynia [103] vs. the response given by the LPM Type II model proposed by Saitoh [185]

In order to validate the performance of the dynamic pile group macroelement (3<sup>rd</sup> level), two lateral dynamic loadings at 1 Hz and 5 Hz are applied at the control node. A Newmark direct implicit integration scheme is used to solve the dynamic equilibrium equation and the results are presented in Fig. 5.21.

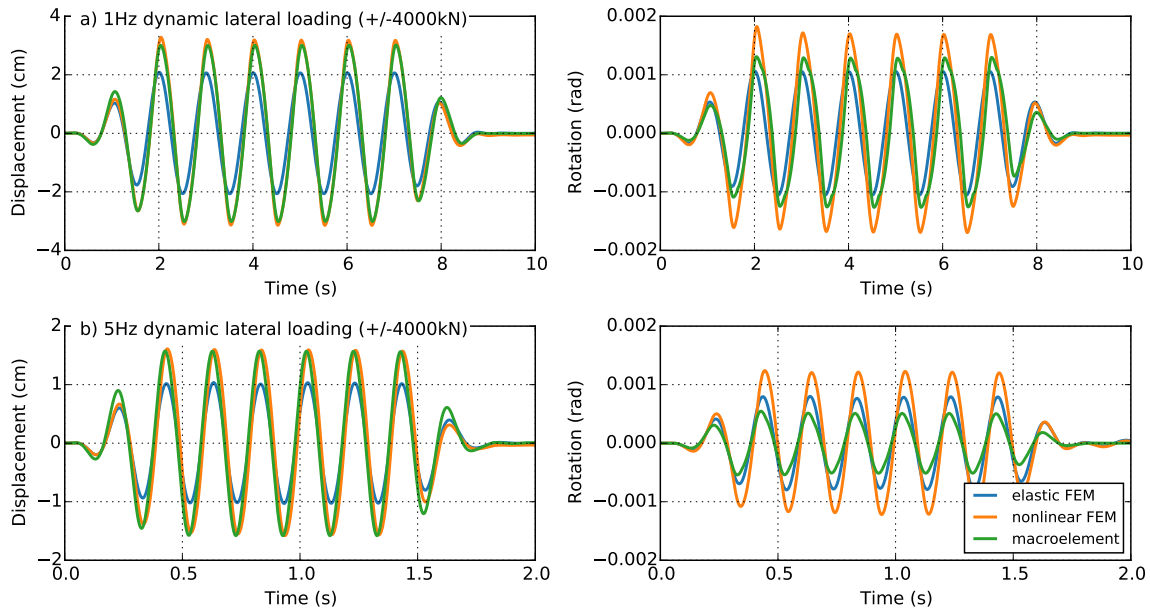


**Figure 5.21:** Lateral response of the 2x2 pile group under dynamic loading: (a) 1 Hz sine and (b) 5 Hz sine loadings: elastic FEM vs nonlinear FEM vs dynamic pile group macroelement

It is found that the proposed pile group macroelement is capable of correctly reproducing the dynamic lateral response of the pile group, especially in displacement. The model however underestimates the rotation for high levels of loading. This can be important in the case of slender structures where a finer calibration of the macroelement for the rocking response could be required.



### 5.3.2 Validation on a SSI nonlinear seismic problem

The nonlinear seismic response of a superstructure supported by the 2x2 pile group foundation is studied in this section. The superstructure is modeled using an inverted pendulum whose fixed-base frequency is set at 2 Hz and has a damping ratio of 5%. The behavior of the piles and of the superstructure is assumed to be linear elastic. The foundation and the structure are shown in Fig. 5.22.

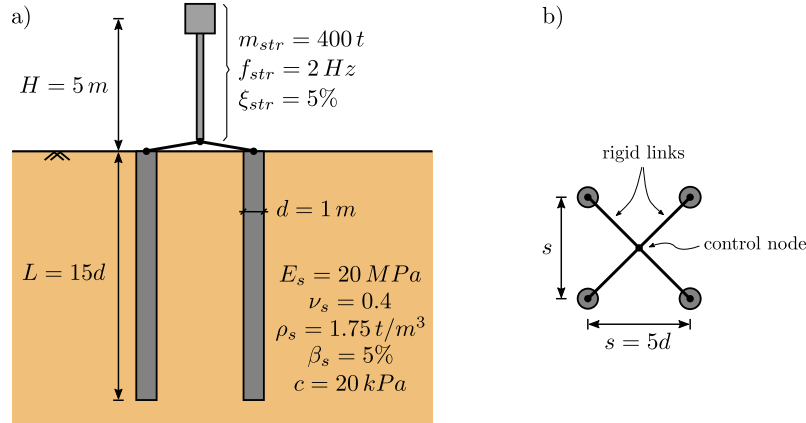


**Figure 5.22:** SSI nonlinear seismic problem: (a) cross section view and (b) plan view of the foundation

The calibrated pile group macroelement in the previous section is used to reproduce the seismic nonlinear SSI. Two real broadband earthquake motions are used, scaled to a maximum acceleration of 0.4g: Northridge 1994 (Tarzana station) and Landers 1992 (Lucern Valley station). The results are compared with a 3D nonlinear finite element model. Loading is applied at the ground surface in the finite element model and at the base for the macroelement.

The horizontal accelerations and displacements of the superstructure using the 3D finite element model and the pile group macroelement are presented in Fig. 5.23. Results confirm the ability of the new macroelement to reproduce nonlinear SSI problems and the dynamic behavior of the pile group.

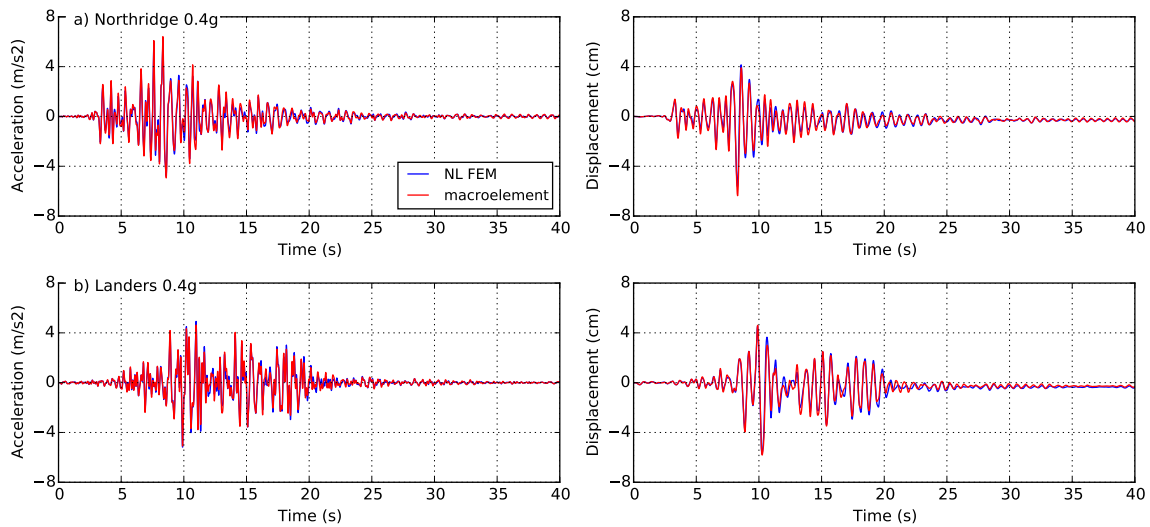


**Figure 5.23:** Acceleration and displacement of the superstructure: nonlinear FEM vs. pile group macroelement

Once the performance of the dynamic pile group macroelement has been confirmed, it can be used in intensive parametric calculations. The following application is concerned with the calculation of the lateral displacement of the superstructure (maximum value during earthquake and residual value after the earthquake) and the maximum rocking moment at the level of the pile cap as a function of the PGA of the signal. The results of this parametric study are presented in Figure 5.24 and compared to linear and nonlinear finite element results.

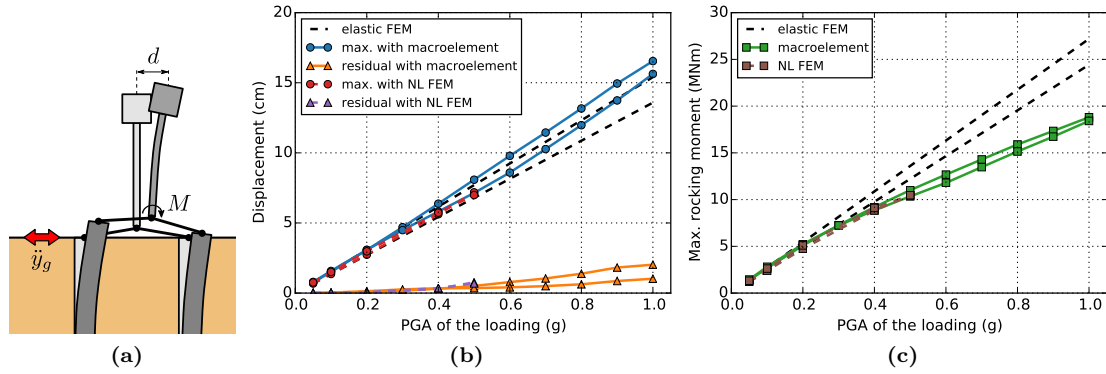


**Figure 5.24:** Simple parametric study: (a) nonlinear SSI seismic problem, (b) lateral displacement of the superstructure (maximum and residual values) and (c) maximum rocking moment. Results from linear and nonlinear FEM and dynamic pile group macroelement models

For low levels of acceleration (quasi-elastic response), the results of the three models (macroelement, elastic FEM and nonlinear FEM) converge. The first differences between the linear and the nonlinear approaches appear from an acceleration of 0.2g. The nonlinear finite element model and the macroelement provide similar results in terms of lateral displacement (maximum and residual values) and maximum rocking moment and this for different PGAs.

The simple example presented here highlights the advantages of the macroelement such as being able to perform parametric studies (at a very low numerical cost) allowing a more sophisticated design of the foundations, with the possibility to check whether or not a certain displacement criteria is met. Taking into account nonlinearities leads, in most cases, to a reduction of the seismic loading that reaches the superstructure (compared to that calculated with a conventional linear approach) and thus allows to optimize the design of the foundation and the structure.

## 5.4 Additional notes

Several alternatives to the approach described in the previous sections have been tested or at least imagined during the development of the pile group macroelement. They are reported hereafter in view of future studies on the macroelement approach for pile groups.

### 5.4.1 Response of a single pile

A single pile macroelement is adopted in the present work as the constituent element of the pile group macroelement. It makes possible to introduce in the model the static (monotonic or cyclic) nonlinear response of each of the piles in the pile group. Another possibility would be to model the response at the head of the piles by means of Winkler-type models (with nonlinear p-y/t-z springs or discrete nonlinear rheological elements). From the point of view of the formulation it is possible to introduce this type of models in the modular approach presented in the preceding sections (Fig. 5.25).

The advantage of this approach is that it is closer to the numerical methods used in design practice for the verification and design of piles and that it gives direct access to the load distributions

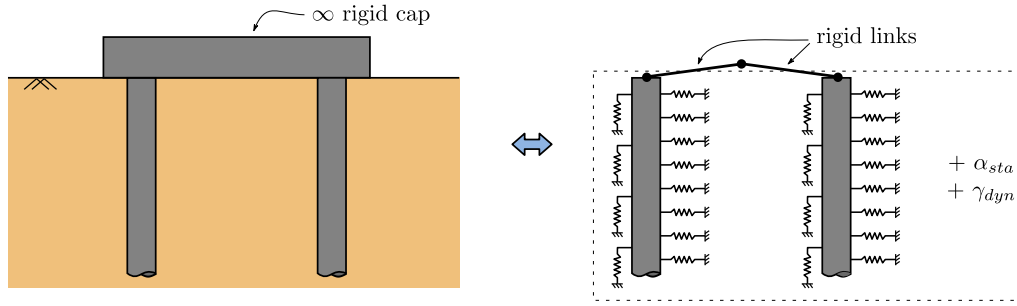


**Figure 5.25:** Modular approach using Winkler-type models as the constitutive model of the pile group macroelement

along the piles. In addition, it allows the use of advanced constitutive models for the pile-soil interface behavior (e.g., [71, 214, 215]). This approach has however several disadvantages, as the numerical model to be solved would be in this case heavier (the number of degrees of freedom considered in the simulation increases rapidly with the number and length of the piles) and the quality of the prediction depends to an important extent on the quality of the data available for the selection of p-y curves, pile-soil interface laws, etc.

#### 5.4.2 Failure surface

The failure surface proposed by Li *et al.* [117, 121, 122] is used in the present work. Other analytical failure surface expressions exist in the literature for different types of soils and soil profiles (e.g., [38, 69, 72]) and can be used in the presented approach with only small modifications of the formulation. A comparative study on the performance and the adequacy of the different failure surfaces could give valuable informations in view of a future generalization of the macroelement approach for customary pile foundation design.

#### 5.4.3 Group effects

The modular macroelement concept introduced in the previous sections relies on the use of a single pile macroelement per pile in the pile group and interaction factors to account for the static and/or dynamic group effect. A different strategy was suggested in [117] to reproduce group effects. The idea is to use a single pile macroelement to represent the pile group and a constant group factor that modifies the loading and the failure surfaces depending on the number and spacing of the piles.

This approach seems to work well when dealing with static problems [212] and also dynamic problems when group effects are found to be independent of the loading frequency [176]. It should be noted that the study conducted by Tu [212] shows that the model gives even better results when the elastic stiffness of the macroelement is also modified in relation to the group factor used to modify the loading and the failure surfaces.

Studies conducted so far have involved only small groups of piles. Further studies are thus necessary in order to identify the validity domain of the approach.

Another strategy, also tested during the present work, consists in simulating group effects by means of a dynamic interaction factor applied directly to the elastic stiffness matrix of the single pile macroelement presented in Section 5.2.1. In this approach, each pile is also simulated with a single pile macroelement and all piles are connected to the control node of the pile group considering rigid links. The dynamic interaction factor for each direction of interest is either calculated and updated at each time step of the transient dynamic analysis or calibrated numerically from full 3D-FEM analysis [177].

The dynamic interaction factor  $\alpha$  is directly applied to the translation component  $k_h$  of the macroelement elastic stiffness matrix. The formulae giving the stiffness at the head of a pile

embedded in a semi-infinite homogeneous elastic medium can be used as a first approximation in order to find its contribution to the other degrees of freedom:

$$k_h = E_s l_0 \quad (5.51)$$

$$k_{hm} = -\frac{1}{2} E_s l_0^2 \quad (5.52)$$

$$k_m = \frac{1}{2} E_s l_0^3 \quad (5.53)$$

$$l_0 = \sqrt[4]{\frac{4EI}{E_s}} \quad (5.54)$$

where  $l_0$  is the transfer length and  $EI$  the flexural rigidity of the pile. After the application of the interaction factor  $\alpha$ , the translation stiffness term becomes:

$$k_h^* = \alpha k_h \quad (5.55)$$

From the above equations the interaction factor  $\alpha$  can be interpreted as a reduction factor that is indirectly applied to the soil reaction module  $E_s$ . Using the Equation (5.51) the new soil reaction module can be calculated:

$$E_s^* = \alpha^{4/3} E_s \quad (5.56)$$

The substitution of this new soil reaction module in Equations (5.52) and (5.53) gives:

$$k_{hm}^* = \alpha^{2/3} k_{hm} \quad (5.57)$$

$$k_m^* = \alpha^{1/3} k_m \quad (5.58)$$

Finally, the elastic stiffness matrix controlling the lateral response at the pile head becomes:

$$\mathbf{K} = \begin{bmatrix} \alpha k_h & \alpha^{2/3} k_{hm} \\ \alpha^{2/3} k_{hm} & \alpha^{1/3} k_m \end{bmatrix} \quad (5.59)$$

A similar reasoning can be applied to the translation stiffness term in the vertical direction.

The numerical application presented in [177] explores the possibilities of this approach using a constant dynamic interaction factor back-calibrated using finite element models. The comparison with non-linear finite element simulations shows a good performance of the model, especially in the case of low amplitude loadings with limited non-linearity. Several differences were found regarding the rotational response of the system at high amplitude loadings.

Despite the fact that this approach remains simple and computationally efficient, several disadvantages are highlighted. A numerical calibration using finite element models is needed. In addition, the model has no viscous damping nor mass terms. It is therefore able to reproduce the correct amplitude of the response (if the effective stiffness of the foundation system is correctly captured by the interaction factor) but does not take into account the phase shift between the loading and the response of the foundation. This question may be important if the system to be studied is sensitive to high frequencies.

#### 5.4.4 Flexible pile cap

The pile group macroelement presented in the previous sections considers a rigid pile cap connecting the piles in the pile group. However, the same concept can also be applied to the case of a pile group connected by a flexible pile cap with slight changes (Fig. 5.26). Since the interaction coefficients do not take into account the boundary conditions at the head of the piles, the same equations can be applied. The treatment of the static case doesn't present any particular problem, the second

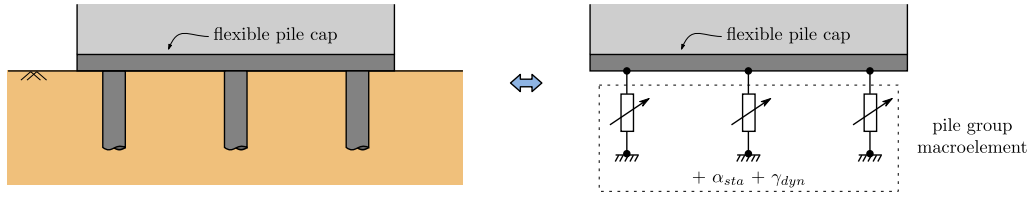


**Figure 5.26:** Application of the modular macroelement concept for a pile group in the case of a flexible pile cap

level of the modular macroelement concept can be applied directly as described in the preceding sections.

In the case of a dynamic analysis, given that the pile cap is now flexible, the dynamic impedance function calculated at the control node of the pile group doesn't represent completely the dynamic response of the system (the rigid block hypothesis no longer applies in this case). It is therefore not possible to take into account the frequency dependence of the system response with an associated rheological model as proposed in the third level of the modular macroelement concept (configuration 2a). Nevertheless, it is possible to use configurations 2b and 2c of the pile group macroelement, setting the values of the dynamic constants modifiers, in the first case, or the dynamic interaction factors, in the latter, for a specific frequency of the system (e.g., the fundamental SSI frequency of the structure).

Several are the advantages of introducing the macroelement in the study of the response of a structure with a flexible pile cap. In addition to those presented in the previous sections, it allows also to take into account the true stiffness of the pile cap and thus to better model the boundary conditions at the head of the piles. This case, in between the two extreme configurations usually considered in pile design (blocked and free rotation at the pile head), may result in the optimisation of the reinforcement steel that is needed at the pile head as well as at the level of the raft.

#### 5.4.5 Radiation damping

Radiation, or geometric, damping is an important phenomenon that needs to be taken into account in the study of dynamic soil-structure interaction problems. It represents in most cases an important source of energy dissipation and thus plays a beneficial role in the overall dynamic response of the system. The way radiation damping is introduced in the model is therefore an important question that is however not always studied carefully.

In the present work it is proposed to consider radiation damping by means of a viscous dashpot in parallel with the pile group macroelement. Despite its simplicity, this way of introducing radiation damping into the model is far from ideal because the use of viscous dashpots in parallel with a hysteretic element can provide a mechanism for unrealistically large forces to be transmitted around the hysteretic element through the viscous dashpot [223, 78, 76]. In order to avoid this problem, the linear viscous dashpot should only be placed in parallel with the linear components of the hysteretic element, and in series with the nonlinear ones. In the framework of macroelement modeling, this means that radiation damping should be applied only to the elements representing the far-field whose behavior is considered linear elastic.

The pile group introduced in this work does not explicitly distinguish the near-field from the far-field. It is therefore not possible to just apply the radiation damping to the far-field elements, however several simple strategies could be considered to improve the model in further research and applications:

- to directly reduce the viscous damping depending on the loading intensity, the importance class of the building, the level of nonlinearity attained during the simulation (by a trial and error procedure), etc.;
- to modify the characteristics of the viscous dashpot in real time during the simulation depending of the evolution of the nonlinearity in the macroelement (i.e., the distance between

the loading surface and the failure surface). Physically, this choice could be justified by the development of local nonlinearities near the foundation and at the soil-foundation interface (e.g., gaping in the case of cohesive soils) that will impact the way the system is able to dissipate energy. For instance, when a gap is formed between the soil and the foundation this may result in a softening of the response of the foundation that may turn beneficial for the superstructure in terms of reduction of the seismic loadings that are effectively transmitted to the structure, however the separation between soil and the foundation may conduct to a wave trapping phenomenon making difficult for the system to dissipate energy through the soil.



## Chapter 6

# Application to a real project

### 6.1 Introduction

In this chapter, a study of the seismic response of a real structure is performed. Three different approaches are used and compared, namely, the analysis of the fixed-base structure, the analysis of the structure taking into account SSI by means of a set of elastic dynamic impedances and finally the analysis using a pile-group macroelement introduced in the previous chapter at the base of the structure to model nonlinear SSI. The problem studied, the characteristics of the structure as well as the assumptions used in the calculation are first presented. A set of real earthquake records are used in the analysis to carry out a parametric study. Several quantities are drawn from this study in order to estimate the behavior of the structure under seismic loading. The results are then analyzed and the contributions of the macroelement approach are discussed.

### 6.2 The Atlantic Bridge (Panama)

The Atlantic Bridge (also known as the third bridge over the Panama Canal) is a cable-stayed, dual 2-lane, concrete roadway bridge with a length of 1050 meters (2820 m taking into account the access viaducts to the main bridge). The bridge has a main span of 530 m, pylons 212.5 m high, and a vertical navigation clearance of 75 meters. It is located 3 kilometers north of the Gatun Locks, near the city of Colón, Panama. It now allows vehicles to cross the Panama Canal on the Atlantic side, regardless of the operation of the locks. The Atlantic Bridge is today the world's longest concrete cable-stayed bridge [218, 195]. Figure 6.1 presents the general schematic elevation view of the main bridge. Note that the foundation configuration and the soil profile represented in the figure differ from those in real project.

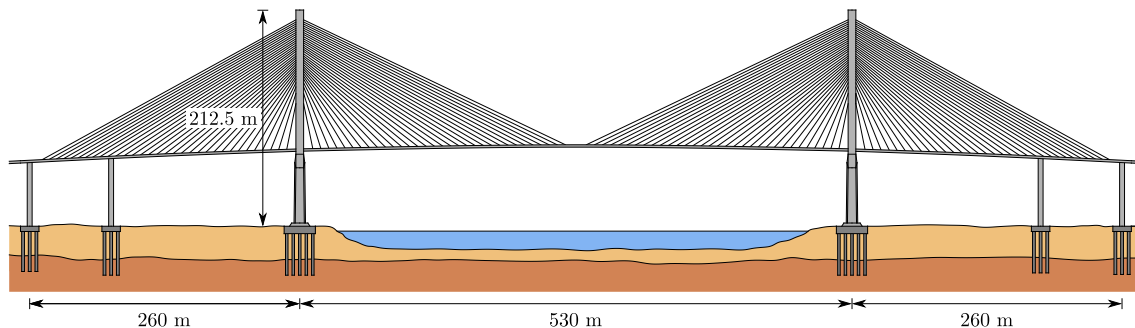


**Figure 6.1:** Elevation view of the Atlantic Bridge (also known as the third bridge over the Panama Canal), a cable-stayed bridge with a main span of 530 meters (note that the foundation configuration and the soil profile used in this study differ from those in real project)



### 6.2.1 Model used in the present study

The analysis conducted in this numerical application focuses on the lateral response of the pylon. Instead of studying the full cable-stayed bridge, which is numerically expensive, a simplified model of the pylon is used in this study. The cable-system strongly coerces the pylon in the longitudinal direction whereas it causes a negligible effect along the transverse axis (unless the cable planes are significantly inclined as may be the case with short span bridges). Therefore a cantilever-like model of the pylon can be used as a first approximation of pure transverse pylon response [37].

The structure is entirely modeled using beam elements and lumped masses are distributed along the pylon anchorages to represent the tributary mass of the deck and the cable-system. Figure 6.2 presents a front view of the pylon and the corresponding finite element model. The response of the pylon in the longitudinal direction of the bridge is not studied in this case, therefore all degrees of freedom in the longitudinal direction are fixed and only displacements in Y and Z direction and rotations around the X axis of the bridge are allowed.

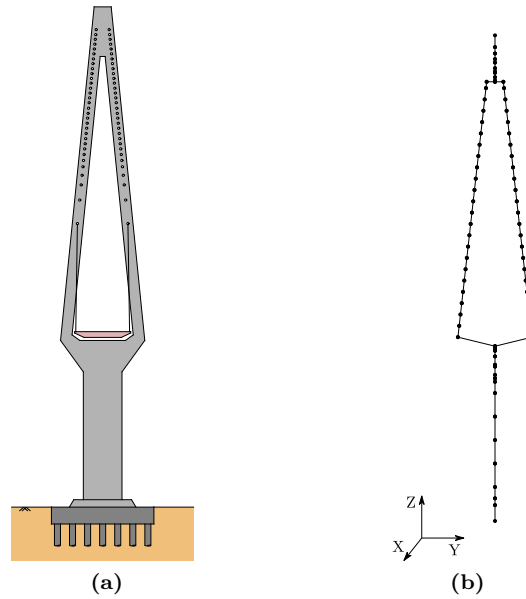


**Figure 6.2:** Front view of the main pylon considered in this study: (a) schematic view and (b) finite element model of the structure

The pylon is made of reinforced concrete and it is assumed that its response is linear elastic during the seismic response. It should be noted that in customary design pylons are intended to remain in the elastic range, which is advisable since they assume the main part of the global structure resistance [37]. A Young's modulus  $E = 4.15e4 MPa$ , a Poisson's ratio  $\nu = 0.3$ , and a density  $\rho = 2.62 t/m^3$  are considered in the calculations.

Despite the fact that energy dissipation is a key issue in any dynamic analysis it is still a misshandled phenomenon and the simulation of the specific sources of damping is often avoided in engineering practice. Instead the use of simple viscous damping through constant factors  $\xi$ , provided by relevant design codes, is adopted in the calculation of conventional bridges and structures. Cable-stayed bridges present low damping, with usual values of the fraction of the critical damping  $\xi$  in the 2-4% range [37]. In the present study a 2% damping is considered for the global structure. It is introduced in the dynamic resolution using Rayleigh's damping theory [34].

Three types of boundary conditions at the base of the structure are considered. The first one, corresponding to the fixed-base approach, all the degrees of freedom at the base of the structure are directly fixed. In the second one, a conventional SSI approach, the compliance (i.e., deformability) of both the foundation and the soil is introduced in the model by means of elastic stiffness matrices corresponding to the dynamic impedance functions. Finally, in the third approach, a pile group macroelement is used.

### 6.2.2 Foundation

*Disclaimer: the foundation configuration and the soil profile used in this study differ from those in the real project.*

The pylon is supported by a 5x7 pile group of reinforced concrete, end-bearing piles of 2.5 m in diameter and 40 m in length. The piles are embedded in a two-layered soil profile, with a 25 m thick soft clay layer at the surface (Fig. 6.3). The behavior of the clay layer is modeled with an elastic-perfectly plastic law using Mohr-Coulomb criterion, with shear wave velocity  $V_s = 100 \text{ m/s}$ , Poisson's ratio  $\nu = 0.45$ , density  $\rho = 1.75 \text{ t/m}^3$ , viscous damping  $\beta = 10\%$  and a cohesion  $c = 50 \text{ kPa}$ . The bedrock is modeled as a linear isotropic elastic material with a shear wave velocity  $V_s$  of  $800 \text{ m/s}$ , a Poisson's ratio  $\nu = 0.4$ , density  $\rho = 2 \text{ t/m}^3$  and a viscous damping  $\beta$  of  $2\%$ . The behavior of the piles is assumed to be elastic with a Young's modulus of  $2e4 \text{ MPa}$ ,  $\nu = 0.2$  and  $\rho = 2.5 \text{ t/m}^3$ .

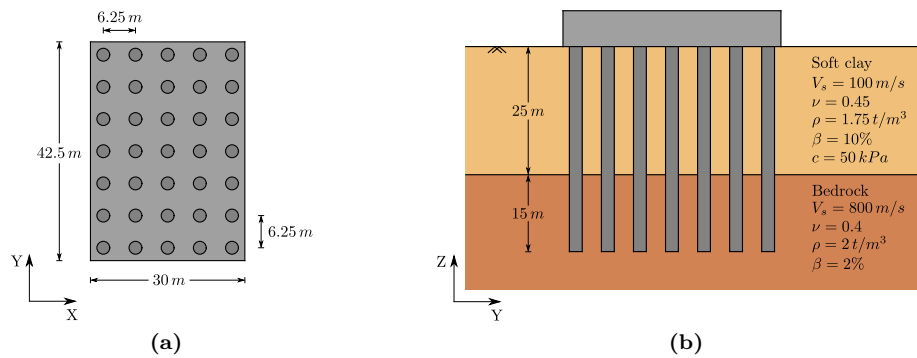


**Figure 6.3:** Foundation detail: (a) plan view and (b) cross section view of the foundation and the soil profile (note that the foundation configuration and the soil profile used in this study differ from those in the real project)

The dynamic impedance functions of the foundation are calculated using the boundary element approach with the software SASSI [126, 165]. A finite element model of the foundation, piles and soil is used, with the piles modeled as elastic beam elements at their exact location and the soil as horizontal layers. The piles are connected at their head by an infinitely stiff, massless cap.

The results of the impedance analysis consist of complex frequency dependent matrices  $\mathcal{K}(\omega)$ , each term representing values of the foundation stiffness (spring) and damping (dashpot) for a given foundation degree of freedom. The real part of each term represents the stiffness and the imaginary part, which denotes a phase shift between the force and the displacement, is related to the overall damping  $\xi$  that includes both radiation and material damping:

$$\xi(\omega) = \frac{Im(\mathcal{K}(\omega))}{2Re(\mathcal{K}(\omega))} \quad (6.1)$$

It is common practice to bound its value by at most 30% so as not to consider excessive damping in the model which falls on the unsafe side. The dynamic impedances calculated for the pile group are presented in Figure 6.4.

### 6.2.3 Modal analysis

The study of the vibration modes of a structure is an essential step prior to conducting any dynamic analysis. Valuable information about the dynamic behavior of the structure is obtained from this analysis and allows to find out if there are any elements in the model with inappropriate dynamic behavior prior to the time-consuming seismic calculations. In addition, when SSI is also introduced into the model, the variation of the vibration modes of the structure on fixed-base to those considering SSI allows to have a better understanding about how the structure-foundation-soil system interacts when it is subjected to dynamic loadings.

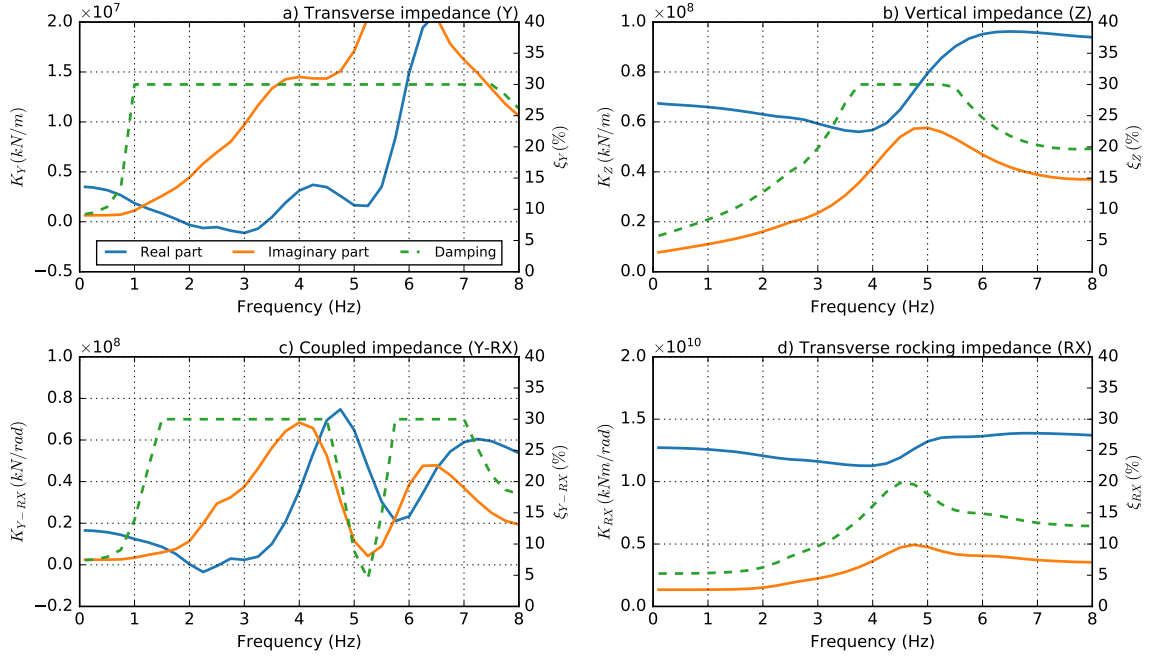


**Figure 6.4:** Dynamic impedances at the center of the pile group

The fundamental vibration modes corresponding to the structure on fixed-base are presented in Figure 6.5. Only the fundamental vibration modes with an effective modal mass ratio higher than 5% are represented. Indeed, the eigenmodes with a greater effective modal mass ratio contribute more importantly to the global response of the structure (it can be interpreted as the part of the total mass responding to the earthquake in each mode) [34]. The effective modal mass  $\tilde{m}_j$  for each direction and mode is calculated using:

$$\tilde{m}_j = \frac{(\phi_j^T \mathbf{M} \mathbf{\Delta})^2}{\phi_j^T \mathbf{M} \phi_j} \quad (6.2)$$

where  $\phi_j$  is the eigenvector corresponding to the mode  $j$ ,  $\mathbf{M}$  the mass matrix and  $\mathbf{\Delta}$  a vector that indicates the degrees of freedom that are concerned for each direction. The ratio between this quantity and the total mass of the structure  $M_T$  corresponds to the effective modal mass ratio  $\eta_j = \tilde{m}_j / M_T$ . Figure 6.7 presents the evolution of the cumulative effective modal mass ratio with frequency. As expected, the firsts vibration modes concentrate most of the contribution in the global seismic response of the structure.

It should be noted that under fixed-base conditions, a significant part of the structure mass is blocked. This mass corresponds to the pile cap and the first meters of the pylon which in this particular case are massive and account up to 39% of the total mass. In other words the cumulative effective mass ratio cannot be higher than 61% when considering fixed-base conditions.

SSI is introduced at the base of the model by means of elastic springs that correspond to the real part of the impedance function for a given frequency. With the dynamic impedances calculated in the previous section, the modal analysis of the structure taking into account SSI is carried out and iterations are performed, updating the SSI springs until good agreement is obtained between the assumed values and the SSI frequencies of vibration of the soil-foundation-structure system.

Figure 6.6 presents the fundamental vibration modes of the structure taking into account SSI. The evolution of the cumulative effective modal mass ratio with frequency for this case is also given in Fig. 6.7. In this case, in contrast to fixed-base model, more than 90% of the structure total mass is effectively mobilized in the first modes. The fundamental SSI mode in Y-direction is found at 0.96 Hz and the corresponding mode in Z-direction at a frequency of 7.22 Hz.

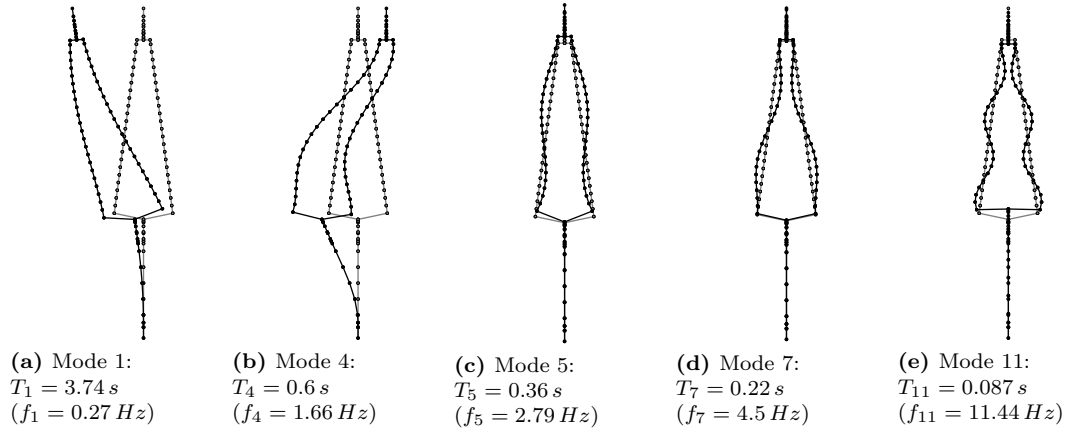


**Figure 6.5:** First vibration modes of the structure on fixed-base conditions with an effective mass ratio higher than 5%

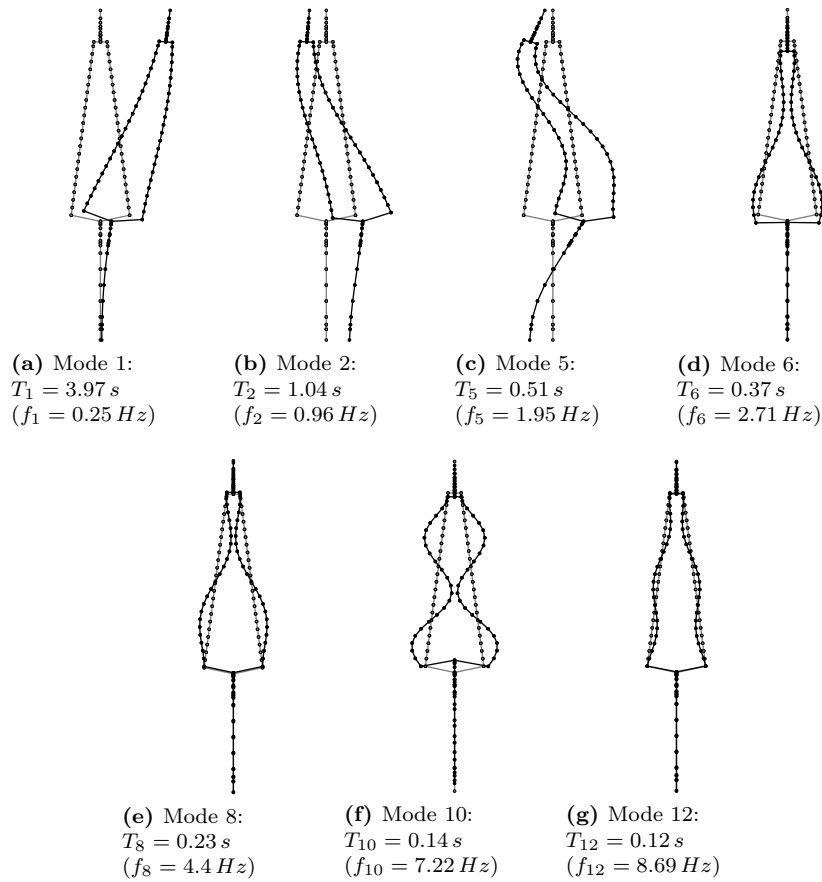


**Figure 6.6:** First vibration modes of the structure considering SSI and with an effective mass ratio higher than 5%

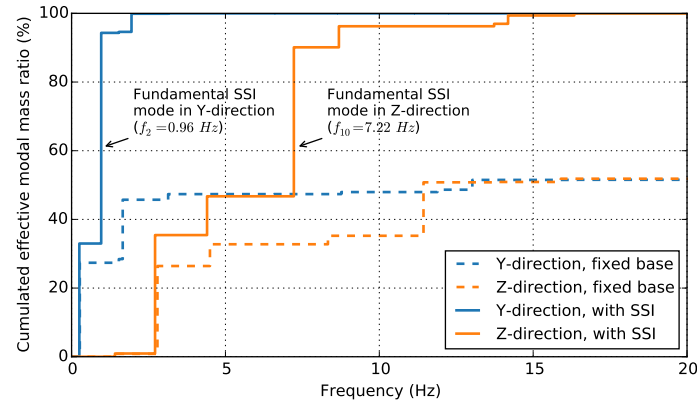


**Figure 6.7:** Evolution of the cumulative effective modal mass ratio with frequency

### 6.2.4 Calibration of pile group macroelement parameters

The pile-group macroelement introduced in the previous chapter is used in this study to introduce non-linear SSI at the base of the pylon. Prior to the used of this element in the calculations it is necessary to calibrate its parameters.

#### 6.2.4.1 Response of a single pile

The non-linear static response of a single pile is reproduced using the single pile macroelement presented in the previous chapter. A non-linear finite element model with a single pile is used to calibrate its parameters. The same calibration procedure introduced in Section 5.3.1.1 is followed:

1. The elastic stiffness terms at the pile head ( $k_h$ ,  $k_m$ ,  $k_{hm}$  and  $k_v$ ) are calculated from finite element model by imposing small displacements or rotations at the pile-head and evaluating the corresponding reactions;
2. The bearing capacity of a single pile ( $H_0$ ,  $M_0$  and  $V_0$ ) are determined using the following "failure" criteria. The lateral bearing capacity  $H_0$  corresponds to the horizontal reaction that is calculated for an imposed lateral displacement of one diameter at the pile-head. The same applies to the axial bearing capacity of the pile  $V_0$ . The rotation angle at the pile head that corresponds to the lateral bearing capacity is taken as the failure rotation and applied to the pile-head. The corresponding moment reaction is used as the rotational bearing capacity of the pile  $M_0$ ;
3. The hardening parameter  $\kappa$  by comparison of the response of the pile subjected to a monotonic lateral loading between the finite element model and the single pile macroelement;
4. Finally, the parameters controlling the cyclic response of the single pile macroelement ( $m_R$ ,  $m_T$ ,  $R$ ,  $\beta_r$  and  $\chi$ ) are calibrated using trial and error by direct comparison of the cyclic response of both models. Three different intensity levels of loading are used in the calibration to ensure that the model is able to reproduce the response under quasi-linear conditions, moderate and important nonlinearities.

Table 6.1 presents the parameters of the single pile macroelement that allow reproducing the non-linear static response of a 2.5 m in diameter, reinforced concrete, end-bearing single pile embedded in the two-layer soil profile considered in this study.

#### 6.2.4.2 Group effects (static and dynamic)

To integrate the group effect (pile-soil-pile interaction) and its variation with frequency, a simple strategy based on static interaction factors is used. For that, the interaction factors given in [67] are modified, taking only the part corresponding to zero frequency loading and adding the

**Table 6.1:** Calibrated parameters for the single pile hypoplastic macroelement

Parameter	Value	Description and related behavior
$k_h$	$3.084 \times 10^5 \text{ kN/m}$	Low deformation response (elastic stiffness)
$k_m$	$9.503 \times 10^6 \text{ kNm/rads}$	
$k_{hm}$	$1.155 \times 10^6 \text{ kN/rad}$	
$k_v$	$3.237 \times 10^6 \text{ kN/m}$	
$H_0$	$3.278 \times 10^4 \text{ kN}$	Failure criterion (bearing capacity of a single pile)
$M_0$	$3.918 \times 10^5 \text{ kNm}$	
$V_0$	$7.791 \times 10^6 \text{ kN}$	
$\kappa$	0.08	Evolution of the yield surface
$m_R$	1.25	Cyclic behavior
$m_T$	2	
$R$	$6 \times 10^{-3}$	
$\beta_r$	0.15	
$\chi$	1.2	

modifiers  $\gamma_Y$  and  $\gamma_Z$  (one per direction). These numerical calibrated modifiers allow to match the effective stiffness of the pile group macroelement at low deformation to that indicated by the dynamic impedance functions for the corresponding SSI frequencies. In other words, the levels II and III of the pile-group macroelement presented in the preceding chapter are condensed here and treated in a single step. The corresponding formulas are:

$$\alpha_v \approx \gamma_Z \times \left( \frac{1}{\sqrt{2}} \left( \frac{s}{d} \right)^{-\frac{1}{2}} \right) \quad (6.3)$$

$$\alpha_h(\theta) \approx \gamma_Y \times (\alpha_h(0^\circ) \cos^2 \theta + \alpha_h(90^\circ) \sin^2 \theta) \quad (6.4)$$

$$\alpha_h(0^\circ) \approx \frac{1}{\sqrt{2}} \left( \frac{s}{d} \right)^{-\frac{1}{2}} \quad (6.5)$$

$$\alpha_h(90^\circ) \approx \frac{3}{4} \alpha_v \quad (6.6)$$

Where  $\alpha_v$  and  $\alpha_h$  are the vertical and horizontal interaction factors, respectively, accounting for SSI dynamic effects.  $s/d$  is the ratio between the spacing (axis to axis) and the diameter of the piles and  $\theta$  is the angle between the loading direction and the vertical plane that is defined by the axis of both piles.

The use of this strategy to incorporate group and frequency effects into the model is justified by several reasons:

- The fundamental response modes of the structure are found for a relatively narrow range of frequencies (particularly those controlling transverse response of the structure). Adjusting the stiffness of the macroelement using the fundamental SSI frequency of the soil-foundation-superstructure provides a reasonably close result to that of the model using a complete LPM model approach (see for example [186]);
- The soil profile considered in this application is not a homogeneous soil profile (case treated by the analytical formulas) and differences appear already at zero frequency. The modifiers introduced in the interaction factor formulae allow thus to correct this difference along with the differences corresponding to the frequency effect;
- Avoids the calibration step of a LPM model, which may be interesting in view of applications to current engineering practice.

The modifiers are numerically calibrated so as to obtain, at the control node of the pile-group, the desired stiffness, i.e., the elastic stiffness of the foundation used in SSI simulations. The calibration procedure is based on a trial and error approach applying very low displacements at the control node of the pile-group macroelement and modifying the value of the modifiers until the correct stiffness is reproduced. Convergence is attained within a few iterations. The following interaction factors modifiers have been calibrated:  $\gamma_Y = 0.59$  and  $\gamma_Z = 0.02$ .

### 6.2.4.3 Damping

The radiation damping of the foundation is directly modeled using a viscous damping matrix whose terms are obtained using the values of the dynamic impedance function presented in Section 6.2.2 corresponding to the SSI frequencies of the system in Y and Z-directions:

$$\mathbf{C}_{foundation} = \begin{pmatrix} C_Y & C_{Y-RX} & 0 \\ C_{Y-RX} & C_{RX} & 0 \\ 0 & 0 & C_Z \end{pmatrix} \quad (6.7)$$

The following numerical values are used in the simulations:  $C_Y = 1.758 \times 10^5 \text{ kNs/m}$ ,  $C_{Y-RX} = 5.494 \times 10^5 \text{ kNs/rad}$ ,  $C_{RX} = 2.21 \times 10^8 \text{ kNms/rad}$  and  $C_Z = 8.373 \times 10^5 \text{ kNs/m}$ .

## 6.3 Incremental dynamic analysis (IDA)

An incremental dynamic analysis (IDA) is a parametric analysis method allowing a complete characterization of the nonlinear response of a structure. Its methodology consists of computing the nonlinear structural seismic response to one or more ground motions, each scaled to multiple levels of intensity. The result of this incremental analysis, for each record, is a curve providing the evolution of a given damage measure (DM) or engineering demand parameter (EDP) versus an intensity measure (IM). A statistical treatment of the results is usually undertaken in order to provide meaningful information on the overall response of the structure. This type of analysis, sometimes also referred as "dynamic pushover", is commonly considered the most precise way to obtain an accurate insight of the nonlinear response of a structure under large ground motion excitations [213, 37, 38, 169].

Conducting IDAs requires performing sets of nonlinear dynamic calculations for different records and intensity levels, and sometimes a parametrization of some of the structure characteristics. Despite the improvements in computer capabilities in performing nonlinear dynamic calculations, using full nonlinear finite element models remains a computationally expensive approach. However, new efficient nonlinear simulation methods are now available to perform such studies, allowing to model the nonlinear response of the system at a reduced computational cost (e.g., multifiber beams, SSI macroelements, etc) [169]. Examples of the application of SSI macroelements in the context of IDAs may be found in [168, 38, 39, 169].

In this section a suite of earthquake records is presented and employed to perform an incremental dynamic analysis of the pylon supported by the pile group macroelement. The results of this analysis are compared to those from the fixed-base approach and from the conventional SSI approach using elastic stiffness matrices.

### 6.3.1 Seismic loading

A set of 14 real earthquake records is employed in this study. They are selected for a small interval of relatively large earthquake moment magnitudes,  $M_W = 6.5$  to 7, with moderate distances ranging from 15 to 35 km, and for sites with  $V_{s,30} \leq 200 \text{ m/s}$ . The unscaled signals are presented in Figure 6.8 and Table 6.2 gives general information and some of their characteristics.

In this application, the signals are applied directly as foundation input motions at the base of the structure. The kinematic interaction between the piles and the surrounding ground and its effects on the foundation input motions are thus not considered in this study. Given that the main objective of this application is to compare the results from three different analysis approaches

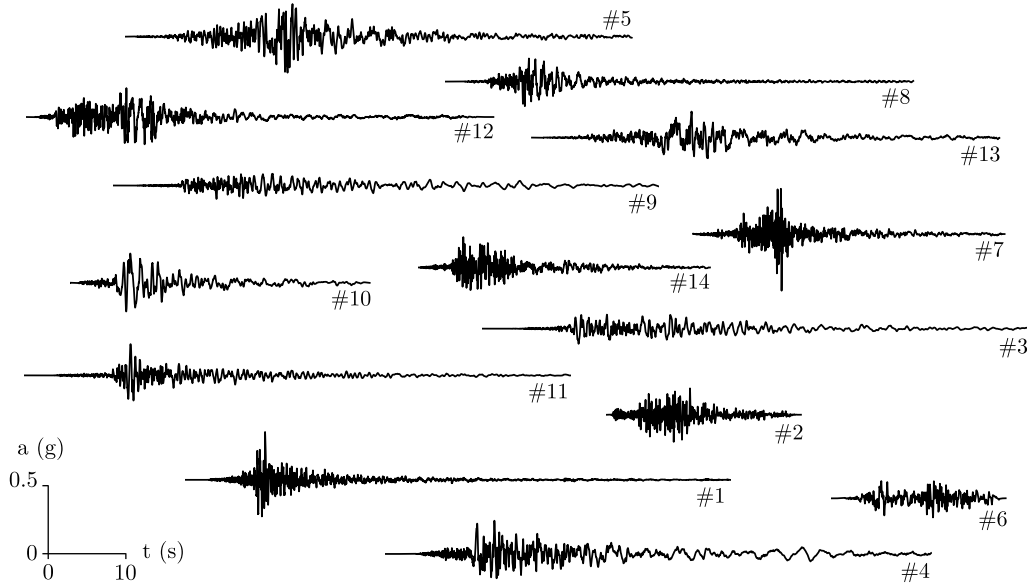


**Figure 6.8:** Real earthquake records used for analysis of the bridge pylon (data from the PEER Strong Motion Database [32])

for the same input data and that the structure's response is controlled by low frequencies, this simplification is judged acceptable. In fact, as presented in Section 2.6.2.1, several studies in the literature have found that the pile-cap follows globally the movement of the soil at low frequencies whereas high frequencies are systematically filtered.

### 6.3.2 Intensity measure and engineering demand parameters

A damage measure (DM) or engineering demand parameter (EDP), also known as structural state variables, is a non-negative scalar that characterizes the additional response of the system due to a prescribed seismic loading. It corresponds to an observable quantity that is part of, or can be deduced from, the output of the corresponding non-linear dynamic analysis [213]. Several state variables are of interest in this study, namely:

- The maximum and residual displacement at the pile cap and at the top of the pylon;
- The maximum and residual rotation at the pile cap;
- The maximum absolute acceleration at the pile cap and at the top of the pylon;
- And the maximum shear and rocking moment at the base of the pylon.

The selection of a suitable set of state variables depends on the characteristics of the structure to be analyzed. Typically, structures such as the one studied here must fulfill several displacement criteria, i.e., a maximum relative displacement between two adjacent pylons or the maximum acceptable rotation of the foundation that guarantees the equilibrium of the structure. Residual deformations are also important in performance-based design and allow to verify that the serviceability criteria of the structure are met over its life span.

Finally, the maximum shear and rocking moment at the base of the structure are clear indicators of the seismic demand that is transmitted to the foundations by the inertial loading of the superstructure. A significant decrease of the inertial loads may allow a more rational design of the foundation particularly for massive structures whose foundations are traditionally oversized. In addition, as already demonstrated by several authors in the recent years (e.g., [6, 66]) overdesign of foundations doesn't always means a safer structure.

Several intensity measures (IM) may be used in an IDA study, such as the peak ground acceleration (PGA), the peak ground velocity (PGV), the cumulative absolute velocity (CAV), the



**Table 6.2:** General information and characteristics of the real earthquake records used for the analysis of the bridge pylon: component ( $\varphi$ ), average shear wave velocity in the upper 30 m of the soil profile ( $V_{s,30}$ ), moment magnitude ( $M_W$ ), closest distance to fault rupture ( $R_{rup}$ ), peak ground acceleration (PGA), peak ground velocity (PGV), Arias Intensity ( $I_A$ ) and significant duration (data from the PEER Strong Motion Database [32])

#	Earthquake	Year	Station	NGA Number	$\varphi$	$V_{s,30}$ (m/s)	$M_W$	$R_{rup}$ (km)	PGA (g)	PGV (cm/s)	$I_A$ (m/s)	Significant duration (s)
1	Niigata (Japan)	2004	NIG022	4212	000	193	6.6	18.0	0.349	20.598	0.795	13.02
2	Northridge (USA)	1994	Pacific Palisades - Sunset	1049	280	191	6.7	24.1	0.198	13.929	0.659	10.29
3	Chuetsu-oki (Japan)	2007	NIG014	5260	000	128	6.8	27.1	0.111	18.591	0.587	38.21
4	Iwate (Japan)	2008	MYG006	5665	000	147	6.9	30.4	0.243	35.106	1.474	43.32
5	Darfield (New Zealand)	2010	Christchurch Resthaven	6959	090	141	7.0	19.5	0.261	62.144	1.800	24.75
6	Superstition Hills (USA)	1987	Salton Sea Wildlife Refuge	726	315	191	6.5	25.9	0.140	18.114	0.358	12.98
7	Imperial Valley (USA)	1979	El Centro Array 2, Keystone Rd.	-	230	189	6.5	15.3	0.427	27.068	1.003	11.74
8	Tottori (Japan)	2000	SMN002	3934	090	139	6.6	16.6	0.179	21.949	0.581	13.98
9	Niigata (Japan)	2004	NIG014	4204	090	128	6.6	28.4	0.098	14.798	0.508	54.72
10	Loma Prieta (USA)	1989	Hollister City Hall	777	180	199	6.9	27.6	0.214	44.956	1.061	13.62
11	Chuetsu-oki (Japan)	2007	NIG025	5271	090	135	6.8	28.6	0.228	27.194	0.722	23.37
12	Superstition Hills (USA)	1987	Westmorland Fire Sta	728	180	194	6.5	13.0	0.211	32.349	1.198	19.21
13	Darfield (New Zealand)	2010	Christchurch Botanical Gardens	6887	270	187	7.0	18.1	0.189	60.607	0.856	23.14
14	Imperial Valley (USA)	1979	El Centro Array 3, Pine Union School	178	230	163	6.5	12.9	0.215	35.474	0.682	14.15

$\xi = 5\%$  damped spectral acceleration at the structure's first-mode period ( $S_a(T_1, 5\%)$ ), etc [213]. However, as already indicated in the previous chapters, there is not yet a consensus in the scientific literature as to the ideal parameter to estimate the intensity of an earthquake motion. In this application PGA is used as intensity measure. A total of 13 PGA values ranging from 0.05g to 3g are considered for each record.

### 6.3.3 Results: IDA curves and impact of SSI on the response

The IDA results for all records are presented in Figures 6.9, 6.10 and 6.11. Every circle represents the result from a time history analysis conducted for a given record and intensity level. The lines represent the evolution of the median value of the result for increasing values of PGA, and the 16%-84% fractile range is indicated in gray. In addition, to facilitate interpretation of the results, the median value of the results from fixed-base and elastic SSI approaches are also presented in the graphs in the form of dashed lines.

The median and quartiles are used in this analysis instead of the mean and standard deviation to avoid extreme outliers that, given the reduced record set used in the calculations, would have an important impact on the mean value.

Figure 6.9 presents the response, in terms of maximum absolute acceleration at the pile cap and at the top of the pylon. It is clear from these results that SSI plays an important role in the reduction of the maximum absolute acceleration that is experienced, especially at the top of the pylon where an important reduction of acceleration takes already place between the fixed-base approach and the SSI approach on elastic springs. Adding nonlinearity in this case by means of the pile-group macroelement collaborates in the reduction of the acceleration maximum value, especially at the level of the pile cap.

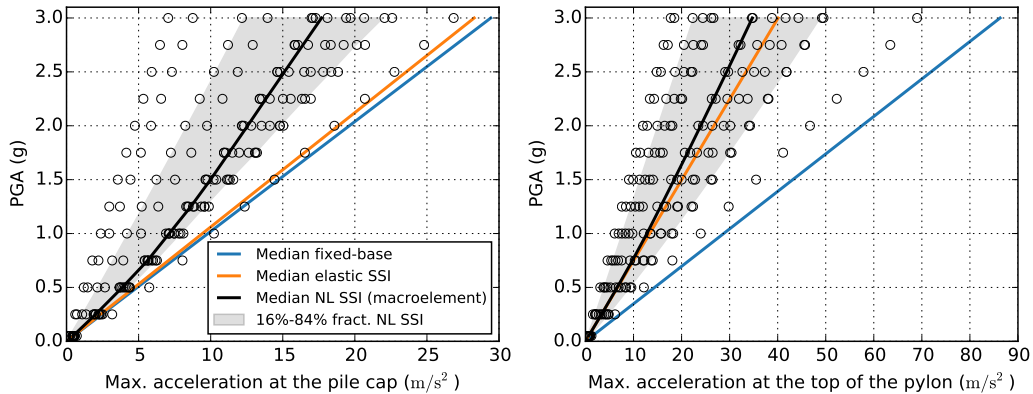


**Figure 6.9:** IDA curves: maximum absolute acceleration at the pile cap and at the top of the pylon

The results regarding the maximum shear force and moment reactions at the base of the pylon follow the same trend (Fig. 6.10). The structure response being essentially controlled by the first two translation modes presented in the modal analysis, a reduction in the absolute acceleration value results in an important reduction of inertial forces and moments and thus to the reactions transmitted to the foundation at the base of the pylon. This effect becomes more important with increasing loading intensity and highlights the importance of taking into account SSI effects in the design. The beneficial rôle of nonlinearity is clearly observed in these results.

Figure 6.11 presents the results in terms of maximum and residual relative displacements (with respect to free-field displacement) at the pile cap and at the top of the pylon, and maximum and residual rotation of the pile cap.

Regarding the displacements and rotations at the pile cap, it is obvious that taking into account nonlinear SSI always implies an increase in the residual displacement and rotation that are assumed to be zero in the fixed-base approach and linear elastic SSI. The results in terms of maximum response show that taking into account nonlinearity in the SSI model has no significant impact

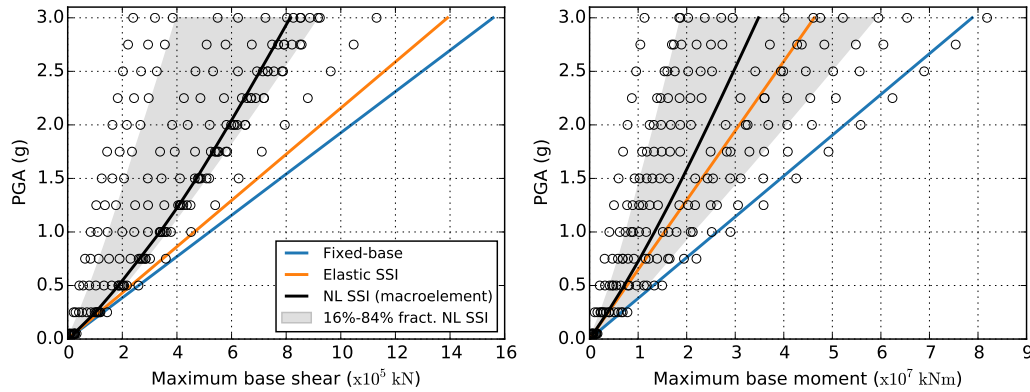


**Figure 6.10:** IDA curves: maximum base shear and moment

and the responses are very close to those corresponding to the elastic SSI case for this particular application. Concerning the residual displacement of the pile cap, it is only for values of the PGA greater than 0.5g that residual displacements start to be observed, with an almost linear increase in value between PGA values of 1.25g and 3g.

In terms of maximum displacements at the top of the pylon, it is found that SSI has a very limited impact on this value and that the median of the results using the three different supports are very close. However, taking into account SSI effects often results in an important increase of the displacements at the top of the structure. This result may be explained for this particular application by the important flexibility of the structure alone and its low damping. The residual displacement at the top of the pylon, which is the result of the addition of the residual displacement and rotation of the cap is limited and represents less than 4% of the maximum top displacement attained during the analysis.

The direct observation of the IDA curves allows to realize the importance of SSI effects on the response of the system for different engineering demand parameters. In order to quantify its impact, the variation ratio of the median values between the fixed-base results and those corresponding to linear and nonlinear SSI approaches is calculated. The results are presented in Figures 6.12, 6.13 and 6.14.

Important decrease ratios are observed in terms of maximum acceleration and reactions at the base of the structure when SSI is considered in the analysis. In all cases, nonlinearity further extends the impact of elastic SSI effects specially at the level of the pile cap. Furthermore, the contribution of nonlinear SSI increases in these cases with the intensity of the loading.

The evolution of the variation ratio of maximum displacements at the top of the pylon is interesting in this case (Fig. 6.14). A slight decrease of the maximum displacements is observed when linear SSI is introduced. When nonlinearity is considered in the SSI model, the maximum displacements at the top of the pylon further decrease with the intensity of the loading.

## 6.4 Additional comments

The dynamic response of a cable-stayed bridge is a complex dynamic problem. Due to their great flexibility and consequent long fundamental vibration periods (thus associated with low spectral acceleration), these structures present in principle a good seismic behavior. However, this important flexibility added to the relative light weight and associated low damping of some of its components causes large amplitude oscillations when they are excited by an earthquake or any other dynamic action. Due to the complexity and the inherent couplings between the different parts of the bridge, the dynamic analysis using a complete 3D finite element model (including the deck, the cables and the pylons) is still a delicate and numerically expensive analysis that requires an important level of expertise in order to correctly model the different parts of the system. In addition, both the dynamic and static responses of cable-stayed bridges may present relevant

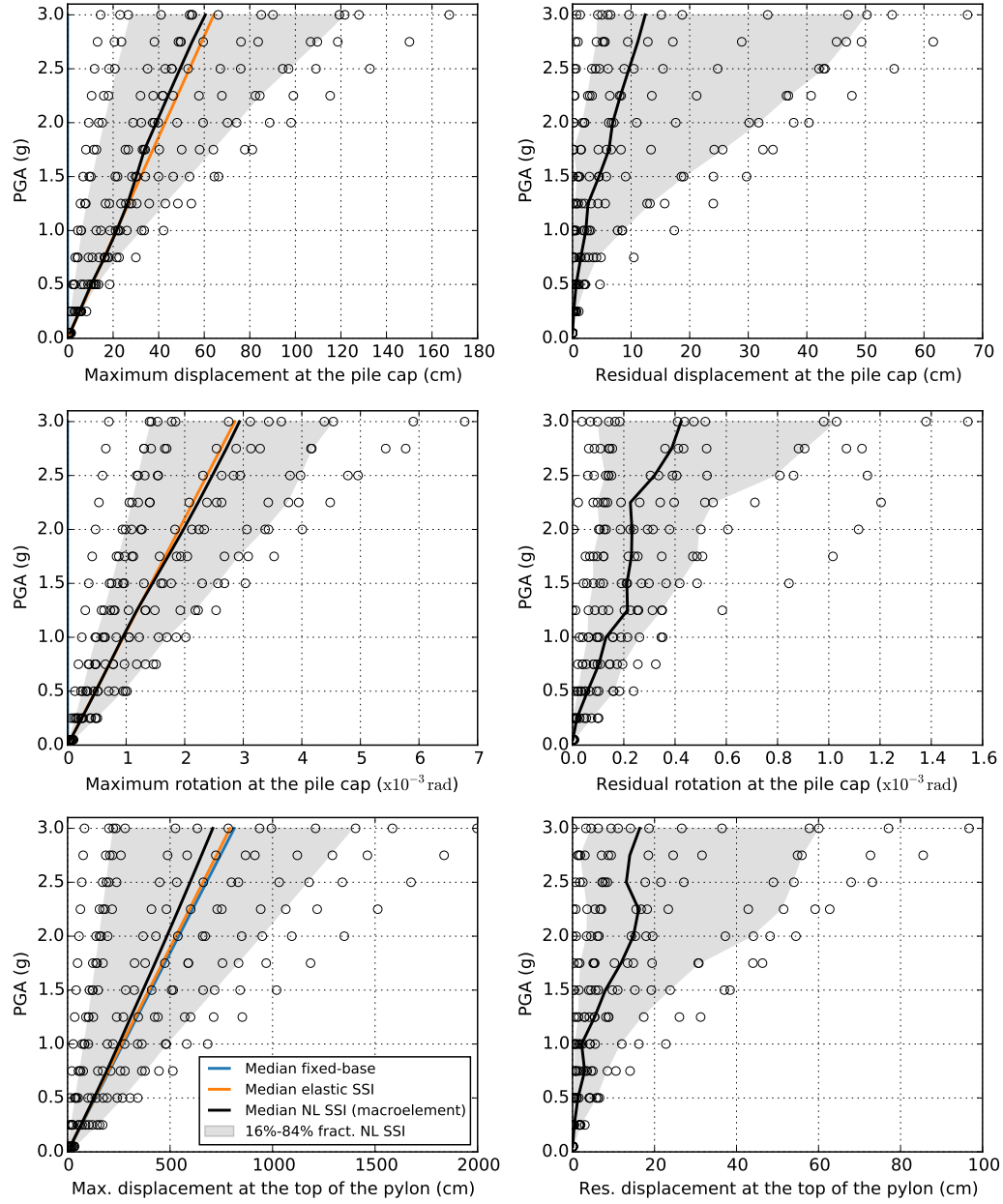


**Figure 6.11:** IDA curves: maximum and residual relative displacement (with respect to free-field displacement) at the pile cap and at the top of the pylon, and maximum and residual rotation of the pile cap

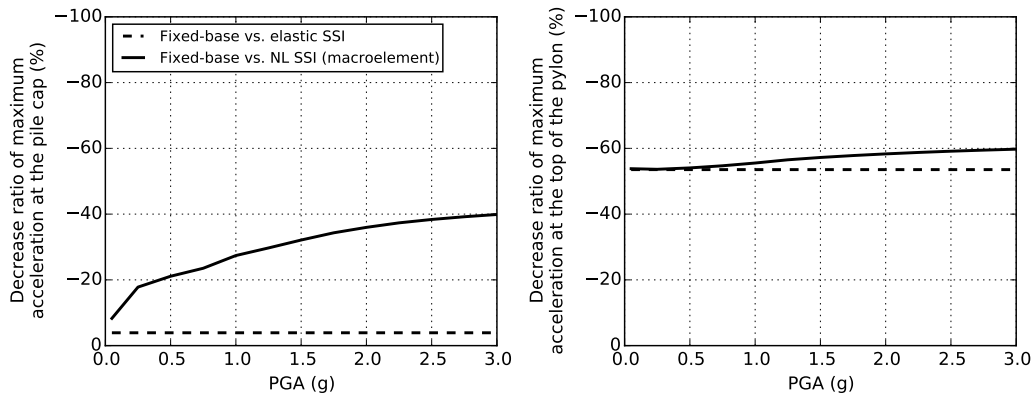


**Figure 6.12:** Impact of SSI in terms of maximum absolute acceleration at the pile cap and at the pylon top

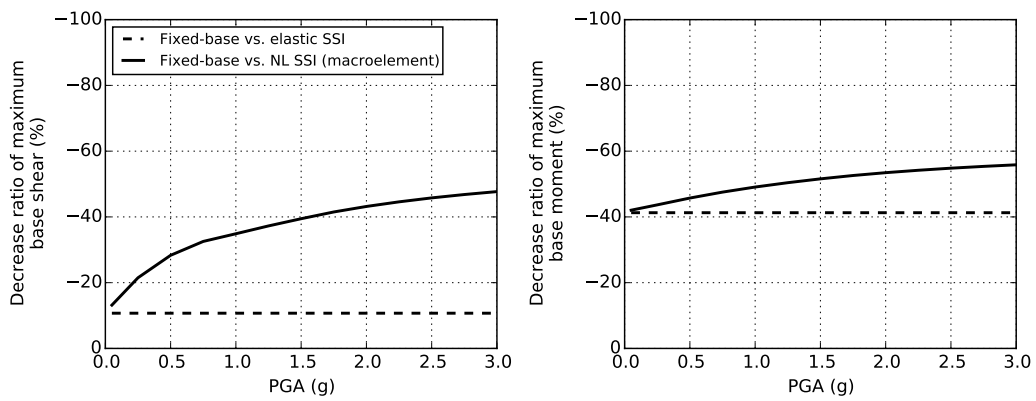


**Figure 6.13:** Impact of SSI in terms of maximum base shear and moment

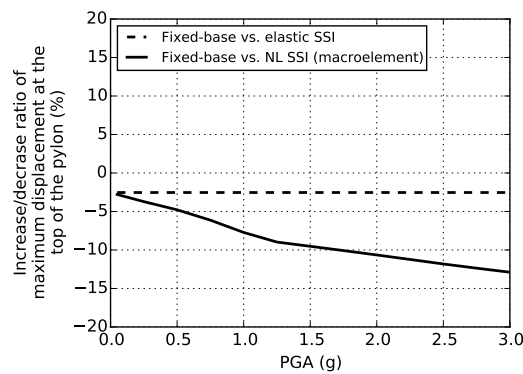


**Figure 6.14:** Impact of SSI in terms of maximum displacement at the pylon top

material and geometric nonlinearities (e.g.,  $P - \Delta$  effects) [37].

In the present study a simplified model of the pylon was used, with the tributary mass of the deck and the cable-system directly attached to the pylon as concentrated masses. The model used in the calculation is therefore not able to reproduce the response modes that correspond to those parts of the bridge, namely: pure vertical deck modes, pure torsional deck modes, transverse deck modes and cable-structure interaction (which accounts for the transferred energy between local cable and global modes). However, it is usually considered that cable-structure interaction plays a beneficial role in the seismic response of cable-stayed bridges and thus neglecting its effects on the pylon may be acceptable for some design steps of the structure and when the interest is focused on the overall response of the structure. For a complete characterization of the nonlinear response of the bridge a full 3D nonlinear model of the structure should be considered. The impact of the development of nonlinearity at different levels of the structure may result in a redistribution of the loading in the structure.

It should be noted that many of the IDAs studies conducted so far on cable-stayed bridges focus on the response of the structure alone and neglect (or treat in a very simplified manner) the effects of SSI on the system's response in terms of stiffness and additional damping. As it has been highlighted in this application, SSI effects may result in an important modification of some of the engineering demand values of interest (see for example results in terms of maximum base shear and moment). These effects are already present when SSI is accounted for using the conventional approach using elastic stiffness and damping matrices, and they are further enhanced when non-linearity is introduced. The use of the macroelement approach allows to consider the evolution of the foundation/soil system from the initial elastic range up to the nonlinearity level imposed by the seismic demand. Moreover, it allows to estimate the residual deformations of the system which is an important advantage of employing this approach [38].

## 6.5 Summary

The seismic response of the pylon of a cable-stayed bridge was studied through multi-IDA analysis considering a set of 14 different earthquake records. The results for three different support conditions were compared, namely: fixed-base approach, SSI approach using elastic stiffness matrices and nonlinear SSI approach using the pile group macroelement.

A simple statistical treatment of the results showed that, in terms of the median values of the response indicators, the maximum base shear and moments are reduced by taking into account SSI effects and this reduction is further enhanced when nonlinearity at the soil foundation is taken into account by means of the pile-group macroelement. In terms of maximum displacements at the top of the pylon, it is found that SSI has a very limited impact on this value. This may be explained by the important flexibility of the structure alone and the low damping values. In addition, due to the important vertical stiffness of the piles, the rocking response of the structure when taking into account SSI effects in the calculation is limited.

The performance of the pile-group macroelement was confirmed by these analyses, in terms of computational time required and accuracy. It should be noted that the number of time-history analyses performed could hardly be accomplished, at a reasonable cost, using only full 3D finite element models. The use of a SSI macroelement requires instead only a minor computational effort which allows structural design to move a step forward into a probabilistic treatment of SSI problems within a complete performance-based earthquake engineering (PBEE) framework.

As a final remark, it should be pointed out that the numerical application presented in this chapter, though complete and rich of useful insights on the effects of SSI in a practical application, remains simple. Several enhancements are suggested for further applications: using a full 3D model of the bridge, adding nonlinearity in the bridge elements and using a larger set of accelerograms (or several sets of records compatible with different earthquakes scenarios). Future work would explore these possibilities.



## Chapter 7

# Conclusions and perspectives

### 7.1 Conclusions

In this Ph.D dissertation, the behavior of single piles and pile groups under seismic loading has been studied using both dynamic centrifuge experiments and finite element simulations. The study is completed by the development of a new macroelement for pile groups under seismic loading. The main contributions and conclusions of the present work are summarized below:

A relatively broad **literature review** has been conducted focusing on a few selected topics about Soil-Structure Interaction and the dynamic behavior of pile foundations. The post-earthquake observations show the important role played by the foundations in the overall performance of several buildings and highlight the importance of considering SSI effects on the design of structures and foundations. A review of the previous experimental centrifuge works dealing with pile foundations (single piles and pile groups) in clay and multilayered soils shows that the available database is not yet sufficiently exhaustive and that there are still many configurations that need to be investigated, particularly those closer to real configurations found in earthquake prone locations (e.g., end-bearing piles embedded in a weak soil layer). The review of existing numerical methods to study SSI problems of structures supported by pile foundations reveals that there is still need for adapted computational tools in order to make this type of studies affordable in current engineering practice.

A large number of numerical and analytical studies on the dynamic response of single piles and pile groups are available in the literature. Their most important findings may be summarized in the following points:

- The response of a soil-pile system to dynamic loading depends on the characteristics of the loading and the dynamic properties of the system itself (e.g., its stiffness, mass, inelastic properties, damping);
- Kinematic interaction and radiation damping usually dominate the system response under low levels of the seismic loading;
- For moderate to high levels of the seismic loading, inertial interaction effects become preponderant. In addition, under high levels of loading, inelasticity exerts generally an important influence on the dynamic characteristics of the system. As nonlinearity develops (soil nonlinearity at high strain, pile separation (gapping), slippage and friction), the system period lengthens and the damping is also modified;
- Finally, it is found that group effects are important for inertial interactions but negligible for kinematic ones. Group effects (pile-soil-pile interaction) can modify in a substantial way the response of the system through the different frequencies of the loading.

**Dynamic centrifuge tests** have been carried out with a multilayered soil profile, considering several different configurations and a series of earthquakes and sinusoidal base shakings. Despite



the complexity in its fabrication, a good repeatability of the soil profile has been observed. Several interesting observations are done in these tests:

- The response of the soil profile is controlled by the clay layer, specially under high amplitude loading where an important degradation of the shear modulus takes place in this layer;
- The response of the system in terms of maximum bending moment depends on the type of loading, the intensity, the frequency content and the conditions at the pile head;
- The maximum bending moments in different parts of the piles are not reached at the same time during the loading. This confirms previous observations in the literature and the importance of doing an appropriate combination of kinematic and inertial loads in the design of piles;
- Kinematic and inertial interactions effects are both important in the tested configurations and need to be considered when pile foundations are used. Special care needs to be given to kinematic interaction effects in the case of layered soil profiles with important differences in stiffness between soil layers, specially when some of the layers exhibits an important degradation of its response;
- Under certain configurations inertial and kinematic interaction effects can be brought to interact together and may result in a complex evolution of the system response with time.

**Nonlinear finite element calculations** have also been performed and compared to experimental results to investigate the ability of current numerical models to satisfactorily reproduce the nonlinear response of foundations. The equivalent linear elastic approach, commonly used nowadays in design practice for the resolution of SSI problems, is also used and compared to experimental and full nonlinear simulations to better understand its limits and to quantify its range of applicability.

The interest of the full nonlinear approach has been confirmed particularly when important strain levels are mobilized in the soil. The use of advanced nonlinear constitutive laws such as the hypoplastic models for sand and for clay allows to reproduce in a close way the response of the system, with a satisfactory agreement between the results from numerical calculations and those from centrifuge experiments. However it should be noted that the main drawback of this approach is the cumbersome calibration process of the model parameters (and thus the need of detailed laboratory test data) and the high computational cost of the finite element simulations. This two disadvantages make this approach prohibitive to use in customary design applications.

The equivalent linear method has proved to be a very interesting and practical approach for estimating the acceleration and the response frequency of the soil column. The results given by this approach remain close to the experimental results in terms of orders of magnitude and allow to reproduce in a satisfactory way the same tendencies of the response of the tested configuration. Nevertheless, it must be said that this observation is probably not valid for other configurations and care should be taken specially for cases under high amplitude loading. Regarding the calculation of the loads in the piles it is observed that this model is not adequate and leads in some cases to a very important underestimation of the bending moment (i.e., the inertial bending moment at the head of the piles) as well as to a localized overestimation of the bending moment in the presence of marked stiffness contrast in the soil profile (i.e., “fictitious” stiffness contrasts that may be present in the equivalent linear soil profile).

A **novel macroelement for pile groups** under static (monotonic and cyclic) and seismic loading has been developed and numerically validated. It allows taking into account the group effects and their variation with the loading frequency (pile-soil-pile interaction) as well as the nonlinearity developed in the system. Comparison between the macroelement predictions and numerical full nonlinear 3D finite element simulations indicates that the macroelement is capable of reproducing the response of the foundation under different loading conditions. The required calculation time is much smaller than that of a classical finite element model and therefore is an adapted tool for capacity design, framework of performance based design.

To highlight the performance and the possibilities of the macroelement approach in customary design, the developed macroelement model for pile groups is used to perform the Incremental Dynamic Analysis (IDA) of a cable-stayed bridge pylon.

## 7.2 Perspectives

Future work could be focused on the following aspects:

### 7.2.1 Experimental part

1. The large number of sensors used in the tests made it possible to collect a large number of data records. Some results have been subjected to a detailed analysis and discussed in the present dissertation but there are still several recordings that need to be analyzed more thoroughly. Future work is expected to treat these results and therefore to complete the observations that have been made to date;
2. Test of new configurations to increase the existing database: comparing several pile spacings, different pile distributions, soil profiles (type of soil and stratigraphy) and superstructures;
3. Further investigate the evolution of the system response with the development of nonlinearity and the loading frequency, testing a larger set of loading frequencies and intensities.

### 7.2.2 Numerical part

1. Due to the inherent limitations of dynamic centrifuge tests, numerical models with adapted constitutive models could be used to study more complex configurations;
2. Calculation of the failure surface of the foundation (or part of the foundation) could be undertaken using specific tools to conduct limit analysis without the limitations of conventional finite element analysis;
3. The analysis of the capabilities of the available numerical models to reproduce the response of pile foundations should be continued. In addition, new methods and approaches adapted to current engineering design practice should be explored in order to reproduce the foundations behavior at a reduced cost.

### 7.2.3 Macroelement

1. The macroelement model for pile groups proposed in this study uses the single pile macroelement developed by Li and coworkers [117, 122, 123] to model the response of each single pile in the pile group. The same failure surface proposed in the original formulation is used without modifications. Future work may focus on this issue in order to develop and/or validate different failure surfaces depending on the type of soil or stratigraphy that is being modeled. One possibility could be to develop an equivalent model with a multisurface criterion formulated within the framework of elastoplasticity;
2. Another important topic that has not been addressed yet in a detailed way in the available macroelements models to date is the radiation damping and how it is included in the macroelement formulation. Given the importance of damping in the overall response of any system, this topic should be investigated in detail in future work;
3. The question of pile-soil-pile interaction coefficients taking into account the level of loading should be addressed in future research. A series of charts could be proposed for typical configurations in order to improve the performance of the macroelement approach introduced in this dissertation;

4. In the continuation of some of the reasonings behind the development of the proposed macroelement, a similar approach could be imagined for the case of rigid inclusions. The macroelement would be equipped in that case with a fuse allowing to reproduce the filtering effect of the mattress between the reinforced soil and the supported structures;
5. From an engineering point of view, the generalization of SSI macroelements in customary design would need the definition of a series of charts or analytical formulae allowing to calculate easily some of the parameters of the proposed models for typical configurations. The addition of some of these new discrete elements inside some of the most common finite element programs would allow the engineers to conduct more advanced studies at a reduced numerical cost. In the case of the pile group macroelement proposed here it would be possible to take into account in the structural model nonlinear SSI effects;
6. The proposed pile group macroelement could be used to evaluate the effects of soil-structure interactions under seismic loading in combination to recent developments allowing to take into account the nonlinear response of the structure elements (e.g., multifiber Timoshenko beams [108, 138, 19, 18] or nonlinear constitutive models for cracked reinforced concrete panels [91, 90] to cite some examples). Examples of successful combination of the macroelement approach with multifiber Timoshenko beams are found in [77, 76, 75].

# Bibliography

- [1] NF EN 1998-5 - Eurocode 8 - Partie 5 - Fondations, ouvrages de soutènement et aspects géotechniques, sep 2005.
- [2] Soil-structure interaction for building structures. Technical Report NIST GCR 12-917-21, National Institute of Standards and Technology, 2012.
- [3] Y. Abboud. *Développement d'un macroélément pour l'étude des fondations superficielles sous charge sismique*. PhD thesis, Université Paris-Est, 2017.
- [4] Y. Akou. *Etude expérimentale et modélisation de l'élargissement des remblais sur sols compressibles*. PhD thesis, Ecole Nationale des Ponts et Chaussées, 1995.
- [5] A. Anandarajah, H. Rashidi, and K. Arulanandan. Elasto-plastic finite element analyses of a soil-structure system under earthquake excitations. *Computers and Geotechnics*, 17:301–325, 1995.
- [6] I. Anastasopoulos, G. Gazetas, M. Loli, M. Apostolou, and N. Gerolymos. Soil failure can be used for seismic protection of structures. *Bulletin of Earthquake Engineering*, 8(2):309–326, aug 2009.
- [7] G. Anoyatis, R. D. Laora, A. Mandolini, and G. Mylonakis. Kinematic response of single piles for different boundary conditions: Analytical solutions and normalization schemes. *Soil Dynamics and Earthquake Engineering*, 44:183–195, jan 2013.
- [8] M. Aris. *Investigations expérimentales des effets de la microstructure sur le comportement des milieux granulaires et sur l'instabilité de liquéfaction*. PhD thesis, Université d'Aix-Marseille, 2012.
- [9] S. Auclair and J. Rey. Corrélation indicateur de mouvement du sol / intensité. vers l'acquisition conjointe de données instrumentales et macrosismiques. Technical Report BRGM/RP-57785-FR, BRGM, December 2009.
- [10] S. Banerjee. *Centrifuge and numerical modelling of soft clay-pile-raft foundations subjected to seismic shaking*. PhD thesis, National University of Singapore, 2009.
- [11] S. Banerjee, S. Goh, and F. Lee. Earthquake-induced bending moment in fixed-head piles in soft clay. *Géotechnique*, 64(6):431–446, 2014.
- [12] S. Banerjee, M. Joy, and D. Sarkar. Parametric study and centrifuge-test verification for amplification and bending moment of clay-pile system subject to earthquakes. *Geotechnical and Geological Engineering*, pages 1–10, 2016.
- [13] J. P. Bardet. Hypoplastic model for sands. *Journal of Engineering Mechanics*, 116(9):1973–1994, sep 1990.
- [14] G. Baudouin. *Sols renforcés par inclusions rigides: modélisation physique en centrifugeuse de remblais et de dallage*. PhD thesis, Université de Nantes, 2010.

- [15] N. Benahmed. *Comportement mécanique d'un sable sous cisaillement monotone et cyclique*. PhD thesis, Ecole Nationale des Ponts et Chaussées, 2001.
- [16] N. Benahmed, J. Canou, and J.-C. Dupla. Structure initiale et propriétés de liquéfaction statique d'un sable. *Comptes Rendus Mécanique*, 332(11):887–894, nov 2004.
- [17] N. Benahmed, J. Canou, and J.-C. Dupla. Propriétés de liquéfaction et structure des sables lâches. In *7ème Colloque National AFPS 2007*, 2007.
- [18] I. Bitar, N. Benkemoun, P. Kotronis, and S. Grange. A multifiber timoshenko beam with embedded discontinuities. *Engineering Fracture Mechanics*, 214:339–364, jun 2019.
- [19] I. Bitar, S. Grange, P. Kotronis, and N. Benkemoun. A comparison of displacement-based timoshenko multi-fiber beams finite element formulations and elasto-plastic applications. *European Journal of Environmental and Civil Engineering*, 22(4):464–490, jul 2016.
- [20] R. W. Boulanger, C. J. Curras, B. L. Kutter, D. W. Wilson, and A. Abghari. Seismic soil-pile-structure interaction experiments and analyses. *Journal of Geotechnical and Geoenvironmental Engineering*, 125(9):750–759, 1999.
- [21] S. Brandenberg, S. Choi, B. Kutter, D. Wilson, and J. Santamarina. A bender element system for measuring shear wave velocities in centrifuge models. In *Physical Modelling in Geotechnics - 6th ICPMG*, 2006.
- [22] A. J. Brennan, N. I. Thusyanthan, and S. P. G. Madabhushi. Evaluation of shear modulus and damping in dynamic centrifuge tests. *Journal of Geotechnical and Geoenvironmental Engineering*, 131(12):1488–1497, dec 2005.
- [23] S. Brûlé and F. Cuira. Bases de l'interaction sol-structure sous séisme - principes généraux et effets inertiels. *Techniques de l'Ingénieur*, (ref. article : c251), 2017. fre.
- [24] S. Brûlé and F. Cuira. *Pratique de l'interaction sol-structure sous séisme*. AFNOR Editions, 2018.
- [25] J. Campedelli. *Modélisation globale statique des systèmes mécaniques hyperstatiques pré-chargés*. PhD thesis, Lyon, INSA, 2002.
- [26] S. Carbonari, M. Morici, F. Dezi, and G. Leoni. A lumped parameter model for time-domain inertial soil-structure interaction analysis of structures on pile foundations. *Earthquake Engineering & Structural Dynamics*, 47(11):2147–2171, jun 2018.
- [27] C. Chatzigogos. *Comportement sismique des fondations superficielles: Vers la prise en compte d'un critère de performance dans la conception*. PhD thesis, Ecole Polytechnique, 2007.
- [28] C. Chatzigogos, A. Pecker, and J. Salençon. A macro-element for dynamic soil-structure interaction analyses of shallow foundations. In *4th International Conference on Earthquake Geotechnical Engineering*, number 1387, June 2007.
- [29] C. Chatzigogos, A. Pecker, and J. Salençon. Macroelement modeling of shallow foundations. *Soil Dynamics and Earthquake Engineering*, 29(5):765–781, 2009.
- [30] J. L. Chazelas, S. Escoffier, J. Garnier, L. Thorel, and G. Rault. Original technologies for proven performances for the new LCPC earthquake simulator. *Bulletin of Earthquake Engineering*, 6(4):723–728, oct 2008.
- [31] N. Chenaf. *Interaction inertielle et interaction cinématique sol - pieu*. PhD thesis, Ecole Centrale de Nantes, 2007.
- [32] B. Chiou, R. Darragh, N. Gregor, and W. Silva. NGA project strong-motion database. *Earthquake Spectra*, 24(1):23–44, feb 2008.

- [33] A. K. Chopra. *Dynamics of structures - Theory and applications to earthquake engineering*. Pearson, 3rd edition edition, 2007.
- [34] R. W. Clough and J. Penzien. *Dynamics of structures*. Computers & Structures, 3rd edition, 2003.
- [35] D. Clouteau. *Propagation d'ondes dans des milieux hétérogènes - application à la tenue des ouvrages sous séismes*. PhD thesis, Ecole Centrale Paris, 1990.
- [36] D. Clouteau and D. Aubry. Miss 6.4: Manuel scientifique. version 1.2. Technical report, Ecole Centrale Paris, 2005.
- [37] A. Cámara Casado. *Seismic behaviour of cable-stayed bridges: design, analysis and seismic devices*. PhD thesis, Universidad Politécnica de Madrid, 2011.
- [38] A. Correia. *A pile-head macro-element approach to seismic design of monoshaft-supported bridges*. PhD thesis, Università degli Studi di Pavia, 2011.
- [39] A. Correia, A. Pecker, S. Kramer, and R. Pinho. Nonlinear pile-head macro-element model: SSI effects on the seismic response of a monoshaft-supported bridge. In *15 WCEE, Lisboa 2012*, 2012.
- [40] J. Corté and J. Garnier. A centrifuge for research in geotechnics. *Bulletin Liaison Laboratoire Ponts et Chaussées*, (145):128, 1986.
- [41] W. Craig. Modeling pile installation in centrifuge experiments. In *Proc., 11th Int. Conf. on Soil Mechanics and Foundation Engineering*, pages 1101–1104, 1985.
- [42] C. Cremer, A. Pecker, and L. Davenne. Cyclic macro-element for soil-structure interaction: material and geometrical non-linearities. *International Journal for Numerical and Analytical Methods in Geomechanics*, 25(13):1257–1284, 2001.
- [43] C. J. Curras, R. W. Boulanger, B. L. Kutter, and D. W. Wilson. Dynamic experiments and analyses of a pile-group-supported structure. *Journal of Geotechnical and Geoenvironmental Engineering*, 127(7):585–596, July 2001.
- [44] Y. F. Dafalias. Bounding surface plasticity. i: Mathematical foundation and hypoplasticity. *Journal of Engineering Mechanics*, 112(9):966–987, sep 1986.
- [45] M. B. Darendeli. *Development of a new family of normalized modulus reduction and material damping curves*. PhD thesis, The University of Texas at Austin, Texas, USA, 2001.
- [46] S. R. Dash, L. Govindaraju, and S. Bhattacharya. A case study of damages of the Kandla Port and Customs Office tower supported on a mat-pile foundation in liquefied soils under the 2001 Bhuj earthquake. *Soil Dynamics and Earthquake Engineering*, 29(2):333–346, feb 2009.
- [47] F. C. P. De Barros and J. E. Luco. Discrete models for vertical vibrations of surface and embedded foundations. *Earthquake Engineering & Structural Dynamics*, 19(2):289–303, feb 1990.
- [48] L. de Sanctis, R. di Laora, N. Caterino, G. Maddaloni, S. Aversa, A. Mandolini, and A. Occhiuzzi. Effect of the filtering action exerted by piles on the seismic response of rc frame buildings. *Bulletin of Earthquake Engineering*, 13(11):3259–3275, May 2015.
- [49] C. S. Desai and H. J. Siriwardane. *Constitutive laws for engineering materials with emphasis on geologic materials*. Number BOOK. Prentice-Hall, 1984.
- [50] F. Dezi, S. Carbonari, and G. Leoni. Kinematic bending moments in pile foundations. *Soil Dynamics and Earthquake Engineering*, 30(3):119–132, mar 2010.

- [51] R. Dobry and G. Gazetas. Simple method for dynamic stiffness and damping of floating pile groups. *Géotechnique*, 38(4):557–574, 1988.
- [52] R. Dobry, R. Ladd, F. Y. Yokel, R. M. Chung, and D. Powell. *Prediction of pore water pressure buildup and liquefaction of sands during earthquakes by the cyclic strain method*, volume 138. National Bureau of Standards Gaithersburg, MD, 1982.
- [53] H. Dou. *Response of pile foundation under simulated earthquake loading*. PhD thesis, The University of British Columbia, 1991.
- [54] G. J. Dyson and M. F. Randolph. Monotonic lateral loading of piles in calcareous sand. *Journal of Geotechnical and Geoenvironmental Engineering*, 127(4):346–352, apr 2001.
- [55] A. S. Elnashai and L. D. Sarno. *Fundamentals of earthquake engineering*. Wiley, 2008.
- [56] S. Escoffier. Centrifuge modelling of foundations subjected to earthquake loadings. In P. Kotronis, C. Tamagnini, and S. Grange, editors, *ALERT Doctoral School: Soil-Structure Interaction*. 2013.
- [57] ESTECO. modeFRONTIER: Multi-objective optimization design environment.
- [58] A. Ezaoui. *Comportement expérimental statique et dynamique des sables et modélisation élasto-visco-plastique anisotrope en petites et moyennes déformations*. PhD thesis, Institut National des Sciences Appliquées de Lyon, 2008.
- [59] K. Fan, G. Gazetas, A. Kaynia, E. Kausel, and S. Ahmad. Kinematic seismic response of single piles and pile groups. *Journal of Geotechnical Engineering*, 117(12):1860–1879, December 1991.
- [60] J. Garnier. Modèles physiques en géotechnique: Etat des connaissances et avancées récentes. In *Première Conférence Coulomb*. Comité Français de Mécanique des Sols, 2001.
- [61] G. Gazetas. Seismic response of end-bearing single piles. *Soil Dynamics and Earthquake Engineering*, 3(2):82–93, 1984.
- [62] G. Gazetas and R. Dobry. Simple radiation damping model for piles and footings. *Journal of Engineering Mechanics*, 110(6):937–956, 1984.
- [63] G. Gazetas, K. Fan, T. Tazoh, and K. Shimizu. Seismic response of the pile foundation of Ohba-Ohashi bridge. In *Proc. 3rd Intl. Conf. on Case Histories in Geotech. Eng.*, volume 3, pages 1803–1809, St. Louis, 1993.
- [64] G. Gazetas. *Lecture on "Dynamic soil behavior" and "Dynamic soil-structure interaction"*. National Technical University of Athens, Thessaloniki, 1997.
- [65] G. Gazetas. *Lecture on "Soil dynamics"*. Universidad Politécnica de Cataluña, 2012.
- [66] G. Gazetas, I. Anastasopoulos, and E. Garini. Geotechnical design with apparent seismic safety factors well-below 1. *Soil Dynamics and Earthquake Engineering*, 57:37–45, feb 2014.
- [67] G. Gazetas, K. Fan, and A. Kaynia. Dynamic response of pile groups with different configurations. *Soil Dynamics and Earthquake Engineering*, 12:239–257, 1993.
- [68] G. Gazetas. Foundation vibrations. In H.-Y. Fang, editor, *Foundation Engineering Handbook*, chapter 15, pages 553–593. Fang, H-Y., 2nd edition, 1991.
- [69] N. Gerolymos, O. Papakyriakopoulos, and R. Brinkgreve. Macroelement modeling of piles in cohesive soil subjected to combined lateral and axial loading. *Numerical Methods in Geotechnical Engineering*, 2014.
- [70] N. Gerolymos and G. Gazetas. Constitutive model for 1-D cyclic soil behaviour applied to seismic analysis of layered deposits. *Soils and Foundations*, 45(3):147–159, 2005.

- [71] N. Gerolymos and G. Gazetas. Phenomenological model applied to inelastic response of soil-pile interaction systems. *Soils and Foundations*, 45(4):119–132, aug 2005.
- [72] N. Gerolymos, S. Giannakos, and V. Drosos. Generalised failure envelope for laterally loaded piles: analytical formulation, numerical verification and experimental validation. *Géotechnique*, pages 1–20, feb 2019.
- [73] N. Gerolymos and O. Papakyriakopoulos. Macroelement modelling of laterally loaded piles and pile-groups. In *1st International Conference on Natural Hazards & Infrastructure*, Chania, Greece, 2016.
- [74] D. Giardini, G. Grünthal, K. M. Shedlock, and P. Zhang. *International Handbook of Earthquake & Engineering Seismology, International Geophysics Series 81 B*, chapter The GSHAP Global Seismic Hazard Map, pages 1233–1239. Academic Press, Amsterdam, 2003.
- [75] S. Grange, L. Botrugno, P. Kotronis, and C. Tamagnini. The effects of Soil-Structure Interaction on a reinforced concrete viaduct. *Earthquake Engineering & Structural Dynamics*, 40(1):93–105, 2010.
- [76] S. Grange, P. Kotronis, and J. Mazars. A macro-element to simulate dynamic soil-structure interaction. *Engineering Structures*, 31(12):3034–3046, December 2009.
- [77] S. Grange, P. Kotronis, and J. Mazars. Numerical modelling of the seismic behaviour of a 7-story building: NEES benchmark. *Materials and Structures*, 42(10):1433–1442, dec 2008.
- [78] S. Grange. *Modélisation simplifiée 3D de l’interaction sol-structure : application au génie parasismique*. PhD thesis, Institut Polytechnique de Grenoble, 2008.
- [79] S. Grange. Simplified modeling strategies for soil-structure interaction problems: The macroelement concept. In P. Kotronis, C. Tamagnini, and S. Grange, editors, *ALERT Doctoral School: Soil-Structure Interaction*. 2013.
- [80] G. Gudehus, A. Amorosi, A. Gens, I. Herle, D. Kolymbas, D. Mašín, D. M. Wood, A. Niemunis, R. Nova, M. Pastor, C. Tamagnini, and G. Viggiani. The soilmodels.info project. *International Journal for Numerical and Analytical Methods in Geomechanics*, 32(12):1571–1572, aug 2008.
- [81] J. A. Gutierrez and A. K. Chopra. A substructure method for earthquake analysis of structures including structure-soil interaction. *Earthquake Engineering & Structural Dynamics*, 6(1):51–69, jan 1978.
- [82] M. Hamada. Damage to piles by liquefaction-induced ground displacements. In *Proceedings of the 3rd US Conference Lifeline Earthquake Engineering, ASCE*, pages 1172–1181, Los Angeles, 1991.
- [83] B. O. Hardin. The nature of stress-strain behavior for soils. pages 3–90. ASCE, 1978.
- [84] B. O. Hardin and W. L. Black. Vibration modulus of normally consolidated clay. *Journal of the Soil Mechanics and Foundations Division*, 94(2):353–370, 1968.
- [85] B. O. Hardin and V. P. Drnevich. Shear modulus and damping in soils: design equations and curves. *Journal of the Soil Mechanics and Foundations Division*, 98(SM7):667–692, July 1972.
- [86] I. Herle and G. Gudehus. Determination of parameters of a hypoplastic constitutive model from properties of grain assemblies. *Mechanics of Cohesive-frictional Materials*, 4(5):461–486, 1999.
- [87] I. Herle. Hypoplasticity without critical states. In *ALERT Summerschool / Olek Zienkiewicz Course*, Dresden, 2012.



- [88] J. Hleibieh and I. Herle. The performance of a hypoplastic constitutive model in predictions of centrifuge experiments under earthquake conditions. *Soil Dynamics and Earthquake Engineering*, 122:310–317, jul 2019.
- [89] Y. Hong, B. He, L. Wang, Z. Wang, C. Ng, and D. Mašín. Cyclic lateral response and failure mechanisms of semi-rigid pile in soft clay: centrifuge tests and numerical modelling. *Canadian Geotechnical Journal*, 54(6):806–824, 2017.
- [90] M. Huguet, S. Erlicher, P. Kotronis, and F. Voldoire. Stress resultant nonlinear constitutive model for cracked reinforced concrete panels. *Engineering Fracture Mechanics*, 176:375–405, may 2017.
- [91] M. Huguet, F. Voldoire, P. Kotronis, and S. Erlicher. Homogenized global nonlinear constitutive model for rc panels under cyclic loadings. In *11th World Congress on Computational Mechanics (WCCM XI)*. Barcelona, 2014.
- [92] M. N. Hussien, M. Karray, T. Tobita, and S. Iai. Kinematic and inertial forces in pile foundations under seismic loading. *Computers and Geotechnics*, 69:166 – 181, 2015.
- [93] M. N. Hussien, T. Tobita, S. Iai, and K. M. Rollins. Soil-pile separation effect on the performance of a pile group under static and dynamic lateral loads. *Canadian Geotechnical Journal*, 47(11):1234–1246, nov 2010.
- [94] I. M. Idriss and J. I. Sun. *SHAKE91: A computer program for conducting equivalent linear seismic response analyses of horizontally layered soil deposits*. University of California, Davis, November 1992.
- [95] J. Idriss and R. Kennedy. Analysis for soil-structure interaction effects for nuclear power plants. Technical report, Ad Hoc Group on Soil Structure Interaction of the Committee on Nuclear Structures and Materials of the Structural Division of ASCE, 1980.
- [96] M. Ilankatharan. *Centrifuge modeling for soil-pile-bridge systems with numerical simulations accounting for soil-container-shaker interaction*. PhD thesis, University of California, Davis, CA, USA, 2008.
- [97] K. Ishihara. *Soil behavior in earthquake geotechnics*. Clarendon Press, 1996.
- [98] T. Kagawa and L. M. Kraft. Seismic p-y responses of flexible piles. *Journal of the geotechnical engineering division*, 106(8):899–918, August 1980.
- [99] E. Kausel, R. V. Whitman, J. P. Morray, and F. Elsabee. The spring method for embedded foundations. *Nuclear Engineering and Design*, 48(2-3):377–392, aug 1978.
- [100] M. Kavvadas and G. Gazetas. Kinematic seismic response and bending of free-head piles in layered soil. *Géotechnique*, 43(2):207–222, 1993.
- [101] A. M. Kaynia and E. Kausel. Dynamic behavior of pile groups. In *Proc. of Second International Conference on Numerical Method in Offshore Piling*, page 24, 1982.
- [102] A. M. Kaynia and M. Novak. Response of pile foundations to Rayleigh waves and obliquely incident body waves. *Earthquake Engineering & Structural Dynamics*, 21(4):303–318, 1992.
- [103] A. M. Kaynia. *Dynamic stiffness and seismic response of pile groups*. PhD thesis, Massachusetts Institute of Technology, January 1982.
- [104] M. Khemakhem. *Etude expérimentale de la réponse aux charges latérales monotones et cycliques d’un pieu foré dans l’argile*. PhD thesis, Ecole Centrale de Nantes, 2012.
- [105] H. Kishida, Y. Suzuki, and S. Nakai. Behavior of a pile under horizontal cyclic loading. In *Proceedings 11th ICSMFE*, volume 3, pages 1413–16, 1985.

- [106] D. Kolymbas. An outline of hypoplasticity. *Archive of Applied Mechanics*, 61(3):143–151, Mar 1991.
- [107] D. Kolymbas and G. Medicus. Genealogy of hypoplasticity and barodesy. *International Journal for Numerical and Analytical Methods in Geomechanics*, 40(18):2532–2550, jun 2016.
- [108] P. Kotronis and J. Mazars. Simplified modelling strategies to simulate the dynamic behaviour of R/C walls. *Journal of Earthquake Engineering*, 9(2):285–306, March 2005.
- [109] K. Koyamada, Y. Miyamoto, and K. Tokimatsu. Field investigation and analysis study of damaged pile foundation during the 2003 Tokachi-Oki earthquake. In *Seismic performance and simulation of pile foundations in liquefied and laterally spreading ground*. American Society of Civil Engineers, oct 2005.
- [110] S. L. Kramer. *Geotechnical Earthquake Engineering*. Civil engineering and engineering mechanics. Prentice Hall, editor Hall, W. J., 1996.
- [111] A. M. Krishna, A. P. Teja, S. Bhattacharya, and B. Ghosh. Seismic design of pile foundations for different ground conditions. In *15 World Conferences on Earthquake Engineering, Lisboa*, 2012.
- [112] B. Kutter, N. Sathialingam, and L. Herrmann. Effects of arching on response time of miniature pore pressure transducer in clay. *Geotechnical Testing Journal*, 13(3):164–178, 1990.
- [113] B. L. Kutter. Recent advances in centrifuge modeling of seismic shaking. In *Third International Conference on Recent Advances in Geotechnical Earthquake Engineering and Soil Dynamics*. University of Missouri–Rolla, 1995.
- [114] C. G. Lai and M. Martinelli. Soil-structure interaction under earthquake loading: Theoretical framework. In P. Kotronis, C. Tamagnini, and S. Grange, editors, *ALERT Doctoral School: Soil-Structure Interaction*. 2013.
- [115] R. D. Laora and E. Rovithis. Kinematic bending of fixed-head piles in nonhomogeneous soil. *Journal of Geotechnical and Geoenvironmental Engineering*, 141(4):04014126, apr 2015.
- [116] N. Lesgidis, A. Sextos, and O.-S. Kwon. A frequency-dependent and intensity-dependent macroelement for reduced order seismic analysis of soil-structure interacting systems. *Earthquake Engineering & Structural Dynamics*, 47(11):2172–2194, jun 2018.
- [117] Z. Li. *Etude expérimentale et numérique de fondations profondes sous sollicitations sismiques: Pieux verticaux et pieux inclinés*. PhD thesis, Ecole Centrale de Nantes, 2014.
- [118] Z. Li, S. Escoffier, and P. Kotronis. Using centrifuge tests data to identify the dynamic soil properties: application to Fontainebleau sand. *Soil Dynamics and Earthquake Engineering*, 52:77–87, 2013.
- [119] Z. Li, S. Escoffier, and P. Kotronis. Experimental study of the performance of inclined pile foundations under dynamic loadings by centrifuge modeling - earthquake excitations. *Soil Dynamics and Earthquake Engineering*, 2014.
- [120] Z. Li, S. Escoffier, and P. Kotronis. Centrifuge modelling of batter pile foundations under sinusoidal dynamic excitation. *Bulletin of Earthquake Engineering*, 14:673–697, 2015.
- [121] Z. Li, P. Kotronis, and S. Escoffier. Numerical study of the 3D failure envelope of a single pile in sand. *Computers and Geotechnics*, 62:11–26, 2014.
- [122] Z. Li, P. Kotronis, S. Escoffier, and C. Tamagnini. A hypoplastic macroelement for single vertical piles in sand subject to three-dimensional loading conditions. *Acta Geotechnica*, 11(2):373–390, sep 2016.

- [123] Z. Li, P. Kotronis, S. Escoffier, and C. Tamagnini. A hypoplastic macroelement formulation for single batter piles in sand. *International Journal for Numerical and Analytical Methods in Geomechanics*, may 2018.
- [124] Y. Lins and T. Schanz. Determination of hydro-mechanical properties of sand. In *Springer Proceedings in Physics*, pages 15–32. Springer-Verlag, 2005.
- [125] J. Lysmer. Analytical procedures in soil dynamics - state of the art. In *ASCE Conference on Soil Dynamics and Earthquake Engineering*, Pasadena, California, 1978.
- [126] J. Lysmer, M. Raissi, F. Tajirian, S. Vahdani, and F. Ostadan. SASSI - A system for analysis of soil-structure interaction. Technical Report 81-02, University of California, Berkeley, 1991. Geotechnical report No. 81-02.
- [127] N. Makris and G. Gazetas. Dynamic pile-soil-pile interaction. Part II: Lateral and seismic response. *Earthquake Engineering and Structural Dynamics*, 21:145–162, 1992.
- [128] N. Makris. Soil-pile interaction during the passage of Rayleigh waves: An analytical solution. *Earthquake Engineering & Structural Dynamics*, 23(2):153–167, feb 1994.
- [129] D. Mašín. A hypoplastic constitutive model for clays. *International Journal for Numerical and Analytical Methods in Geomechanics*, 29(4):311–336, 2005.
- [130] D. Mašín. Hypoplasticity for practical applications - part 4: Determination of material parameters, June 2015. PhD course on hypoplasticity Zhejiang University.
- [131] B. Manna and D. K. Baidya. Nonlinear dynamic response of piles under horizontal excitation. *Journal of Geotechnical and Geoenvironmental Engineering*, 136(12):1600–1609, dec 2010.
- [132] M. Martinelli and C. Tamagnini. Modeling SSI on piled foundations: the effects of kinematic interaction. In P. Kotronis, C. Tamagnini, and S. Grange, editors, *ALERT Doctoral School: Soil-Structure Interaction*. 2013.
- [133] D. Mašín. *Hypoplastic models for fine-grained soils*. PhD thesis, Charles University, Prague, September 2006.
- [134] D. Mašín. *Development and applications of hypoplastic constitutive models*. Habilitation thesis, Charles University in Prague, December 2009. Dissertation submitted for habilitation.
- [135] D. Mašín. *Modelling of Soil Behaviour with Hypoplasticity*. Springer International Publishing, 2019.
- [136] H. Matlock, S. H. Foo, and L. M. Bryant. Simulation of lateral pile behavior under earthquake motion. In *Proceedings of the ASCE Geotechnical Engineering Division Specialty Conference, June 19-21, 1978, Pasadena, California.*, volume I, June 1978.
- [137] H. Matsuoka and T. Nakai. Stress-deformation and strength characteristics of soil under three different principal stresses. 1974(232):59–70, 1974.
- [138] J. Mazars, P. Kotronis, F. Ragueneau, and G. Casaux. Using multifiber beams to account for shear and torsion. *Computer Methods in Applied Mechanics and Engineering*, 195(52):7264–7281, November 2006.
- [139] G. G. Meyerhof and D. P. Ghosh. Ultimate capacity of flexible piles under eccentric and inclined loads. *Canadian Geotechnical Journal*, 26(1):34–42, feb 1989.
- [140] G. G. Meyerhof, V. V. R. N. Sastry, and A. S. Yalcin. Lateral resistance and deflection of flexible piles. *Canadian Geotechnical Journal*, 25(3):511–522, aug 1988.
- [141] G. G. Meyerhof, A. S. Yalcin, and S. K. Mathur. Ultimate pile capacity for eccentric inclined load. *Journal of Geotechnical Engineering*, 109(3):408–423, mar 1983.

- [142] P. Meymand, M. Reimer, and R. Seed. Large scale shaking table tests of seismic soil-pile interaction in soft clay. In *Proc. 12th World Conf. Earthquake Eng. New Zealand*, volume 5, 2000. paper number 0915.
- [143] P. J. Meymand. *Shaking table scale model tests of non-linear soil-pile-superstructure interaction in soft clay*. PhD thesis, University of California, Berkeley, 1998.
- [144] G. Mitaritonna, A. Amorosi, and F. Cotecchia. Multidirectional bender element measurements in the triaxial cell: equipment set-up and signal interpretation. *RIG Rivista Italiana di Geotecnica*, 44(1):50–69, 2010.
- [145] H. Mizuno. Pile damage during earthquake in japan (1923-1983). *Proceedings of the ASCE Conference on Dynamic Response of Pile Foundations - Experiment, Analysis and Observation*, (11), 1987. Geotechnical Special Publication.
- [146] S. Modak and W. F. Cofer. Determination of rheological parameters of pile foundations for bridges for earthquake analysis. Technical Report WA-RD 406.1, Washington State Transportation Center (TRAC), jul 1997.
- [147] A. R. Mortezaie. *Cyclic threshold strains in clays versus sands and the change of secant shear modulus and pore water pressure at small cyclic strains*. PhD thesis, University of California, 2012.
- [148] A. Mortezaie and M. Vucetic. Threshold shear strains for cyclic degradation and cyclic pore water pressure generation in two clays. *Journal of Geotechnical and Geoenvironmental Engineering*, 142(5):04016007, may 2016.
- [149] R. D. Muhammed. *Etude en chambre d'étalonnage du frottement sol-pieu sous grands nombres de cycles. Application au calcul des fondations dans les sols fins saturés*. PhD thesis, Université Pierre et Marie Curie, 2015.
- [150] G. Mylonakis and G. Gazetas. Lateral vibration and internal forces of grouped piles in layered soil. *Journal of Geotechnical and Geoenvironmental Engineering*, 125(1):16–25, 1999.
- [151] G. Mylonakis, G. Gazetas, N. Gerolymos, and I. Anastasopoulos. *Recent Advances in Applied Mechanics, Honorary Volume for Professor A.N.Kounadis, N.T.U.A.*, chapter Detrimental Role of Soil-Structure Interaction and the Collapse of the 18-Pier Fukae Bridge in Kobe, pages 145–159. 2000.
- [152] M. H. E. Nagggar. Bridging the gap between structural and geotechnical engineers in SSI for performance-based design. In *Special Topics in Earthquake Geotechnical Engineering*, chapter 11, pages 315–351. Springer Netherlands, nov 2011.
- [153] V. Nappa, E. Bilotta, A. Flora, and S. P. G. Madabhushi. Centrifuge modelling of the seismic performance of soft buried barriers. *Bulletin of Earthquake Engineering*, 14(10):2881–2901, apr 2016.
- [154] A. Niemunis and I. Herle. Hypoplastic model for cohesionless soils with elastic strain range. *Mechanics of Cohesive-frictional Materials*, 2(4):279–299, 1997.
- [155] A. Nikolaou, G. Mylonakis, and G. Gazetas. Kinematic bending moments in seismically stressed piles. Technical Report NCEER-95-0022, National Center for Earthquake Engineering Research. Buffalo: State University of New York., 1995.
- [156] S. Nikolaou, G. Mylonakis, G. Gazetas, and T. Tazoh. Kinematic pile bending during earthquakes: analysis and field measurements. *Géotechnique*, 51(5):425–440, jun 2001.
- [157] T. Nogami and M. Novak. Resistance of soil to a horizontally vibrating pile. *Earthquake Engineering & Structural Dynamics*, 5, 1977.

- [158] T. Nogami and K. Konagai. Time domain axial response of dynamically loaded single piles. *Journal of Engineering Mechanics*, 112(11):1241–1252, nov 1986.
- [159] T. Nogami and K. Konagai. Time domain flexural response of dynamically loaded single piles. *Journal of Engineering Mechanics*, 114(9):1512–1525, sep 1988.
- [160] R. Nova and L. Montrasio. Settlements of shallow foundations on sand. *Géotechnique*, 41(2):243–256, 1991.
- [161] M. Novak. Piles under dynamic loads. In *Second International Conference on Recent Advances In Geotechnical Earthquake Engineering and Soil Dynamics*, 1991.
- [162] M. Novak. *Pile-soil-pile interaction under small and large displacements*. 1993.
- [163] A. Ohira, T. Tazoh, K. Dewa, K. Shimizu, and M. Shimada. Observations of earthquake response behaviors of foundation piles for road bridge. In *Proc. 8th World Conf. Earthquake Eng.*, volume 3, pages 577–584, San Francisco, 1984.
- [164] T. Ohta, S. Uchiyama, M. Niwa, and K. Ueno. Earthquake response characteristics of structure with pile foundation on soft subsoil layer and its simulation analysis. In *Proceedings of the 7th World Conference on Earthquake Engineering*, volume 3, 1980.
- [165] F. Ostadan and N. Deng. *SASSI2010 - Theoretical manual - A system for analysis of soil-structure interaction*, version 1.0 edition, May 2012.
- [166] A. Pecker. *Dynamique des Sols*. Presses de l'Ecole Nationale des Ponts et Chaussées, Paris, France, 1984.
- [167] A. Pecker. *Dynamique des Structures et des Ouvrages*. Ecole des Ponts ParisTech, Paris, France, 2011 edition, 2011.
- [168] A. Pecker and C. T. Chatzigogos. Non linear soil structure interaction: impact on the seismic response of structures. In *Earthquake Engineering in Europe*, pages 79–103. Springer, 2010.
- [169] A. Pecker, R. Paolucci, C. Chatzigogos, A. A. Correia, and R. Figini. The role of non-linear dynamic soil-foundation interaction on the seismic response of structures. In S. ISS-MGE, editor, *Second International Conference on Performance Based Design in Earthquake Geotechnical Engineering*, May 2012.
- [170] M. J. Pender. Aseismic pile foundation design analysis. *Bulletin of the New Zealand National Society for Earthquake Engineering*, 26(1), March 1993.
- [171] G. A. Pistolas, A. Tsinaris, A. Anastasiadis, and K. Pitilakis. Undrained dynamic properties of hostun sand. In *Proceedings of the 7th Greek geotechnics conference*, Athens, 2014.
- [172] H. G. Poulos. Analysis of the settlement of pile groups. *Géotechnique*, 18(4):449–471, dec 1968.
- [173] H. G. Poulos and E. H. Davis. *Pile foundation: Analysis and design*. 1980.
- [174] H. G. Poulos. Tall building foundations: design methods and applications. *Innovative Infrastructure Solutions*, 1(1), jun 2016.
- [175] H. G. Poulos. *Tall buildings foundation design*. CRC Press, 2017.
- [176] J. Pérez-Herreros, F. Cuira, P. Kotronis, and S. Escoffier. Apports de l'interaction sol structure dans le dimensionnement des groupes de pieux sous séisme. In *Journées Nationales de Géotechnique et de Géologie de l'Ingénieur - Champs-sur-Marne*, 2018.
- [177] J. Pérez-Herreros, P. Kotronis, S. Escoffier, and F. Cuira. A macroelement for dynamic soil-structure interaction analysis of pile-group foundations. In *7th International Conference on Earthquake Geotechnical Engineering*, pages 4267–4274. Associazione Geotecnica Italiana, 2019.

- [178] J. Rakotonindriana. *Comportement des pieux et des groupes de pieux sous chargement latéral cyclique*. PhD thesis, Ecole Nationale des Ponts et Chaussées, 2009.
- [179] H. Rashidi. *Centrifuge and theoretical study of the earthquake soil-pile-structure interaction of structures founded on clays*. PhD thesis, University of California, Davis, 1993.
- [180] D. Remaud. *Pieux sous charges laterales: Etude expérimentale de l'effet de groupe*. PhD thesis, Ecole Centrale de Nantes, 1999.
- [181] H. Ritchie and M. Roser. Natural disasters. *Our World in Data*, 2019. <https://ourworldindata.org/natural-disasters>.
- [182] J. M. Roesset. Dynamic stiffness of pile groups. In *Analysis and design of pile foundations*, pages 263–286. ASCE, 1984.
- [183] K. M. Rollins, J. D. Lane, and T. M. Gerber. Measured and computed lateral response of a pile group in sand. *Journal of Geotechnical and Geoenvironmental Engineering*, 131(1):103–114, jan 2005.
- [184] N. M. Sa'don. *Full scale static and dynamic lateral loading of a single pile*. PhD thesis, The University of Auckland, January 2012.
- [185] M. Saitoh. Simple model of frequency-dependent impedance functions in soil-structure interaction using frequency-independent elements. *Journal of Engineering Mechanics*, 133(10):1101–1114, 2007.
- [186] M. Saitoh. On the performance of lumped parameter models with gyro-mass elements for the impedance function of a pile-group supporting a single-degree-of-freedom system. *Earthquake Engng Struct. Dyn.*, 41(4):623–641, jul 2011.
- [187] D. Salciarini and C. Tamagnini. A hypoplastic macroelement model for shallow foundations under monotonic and cyclic loads. *Acta Geotechnica*, 4(3):163–176, 2009.
- [188] I. Sanchez-Salinero. Dynamic stiffness of pile groups: approximate solutions. Technical report, University of Texas at Austin, 1983. Geotechnical Engineering Report GR83-5.
- [189] P. B. Schnabel, J. Lysmer, and H. B. Seed. Shake a computer program for earthquake response analysis of horizontally layered sites. Technical report, Earthquake Engineering Research Center, University of California, Berkeley, 1972. Report No. UCB/EERC-70/10.
- [190] H. B. Seed and I. M. Idriss. Soil moduli and damping factors for dynamic response analyses. Technical Report EERC 70-10, Earthquake Engineering Research Center, University of California, Berkeley, 1970.
- [191] H. B. Seed and I. M. Idriss. Simplified procedure for evaluating soil liquefaction potential. *Journal of Soil Mechanics & Foundations Division*, 97(SM9), 1971.
- [192] R. B. Seed, S. E. Dickenson, M. F. Riemer, J. D. Bray, N. Sitar, J. K. Mitchell, I. M. Idriss, R. E. Kayen, A. L. Kropp, L. F. Harder, and M. S. Power. Preliminary report on the principal geotechnical aspects of the October 17, 1989 Loma Prieta earthquake. Technical Report UCB/EERC-90/05, Earthquake Engineering Research Center, University of California, 1990.
- [193] Simulia. *ABAQUS/Standard User's Manual, Version 6.14*, 2014.
- [194] N. Strömblad. Modelling of soil and structure interaction subsea. Master's thesis, Chalmers University of Technology, 2014.
- [195] Structurae. Atlantic Bridge, 2019. Accessed August 10 at URL <https://structurae.net/en/structures/atlantic-bridge>.
- [196] U. G. Survey. Earthquake facts and statistics, 2019. Accessed April 29 at URL <https://earthquake.usgs.gov/earthquakes/browse/stats.php>.

- [197] A. Taghavi, K. Muraleetharan, G. Miller, and A. Cerato. Centrifuge modeling of laterally loaded pile groups in improved soft clay. *Journal of Geotechnical and Geoenvironmental Engineering*, 142(4):04015099, 2016.
- [198] A. Taghavi, K. K. Muraleetharan, and G. A. Miller. Nonlinear seismic behavior of pile groups in cement-improved soft clay. *Soil Dynamics and Earthquake Engineering*, 99:189–202, aug 2017.
- [199] C. Tamagnini and G. Viggiani. Constitutive modelling for rate-independent soils: a review. *Revue Française de Génie Civil*, 6:933–974, 2002.
- [200] C. Tamagnini. Elasticity and perfect plasticity. In *ALERT Olek Zienkiewicz School*, Dresden, 2012.
- [201] C. Tamagnini. Strain-hardening plasticity. In *ALERT Olek Zienkiewicz School*, Dresden, 2012.
- [202] C. Tamagnini, D. Salciarini, and R. Ragni. Implementation of a 6-dof hypoplastic macroelement in a finite element code. 2013.
- [203] C. Tamagnini, G. Viggiani, and R. Chambon. A review of two different approaches to hypoplasticity. In *Constitutive modelling of granular materials*, pages 107–145. Springer, 2000.
- [204] O. Ternet. *Reconstitution and characterization of the sand samples. Application to the tests out of the centrifuge and calibration chamber*. PhD thesis, Université de Caen, 1999.
- [205] B. Teymur and S. P. G. Madabhushi. Experimental study of boundary effects in dynamic centrifuge modelling. *Géotechnique*, 53(7):655–663, sep 2003.
- [206] L. Thorel. Centrifuge modelling of foundations subjected to cyclic loading. In P. Kotronis, C. Tamagnini, and S. Grange, editors, *ALERT Doctoral School: Soil-Structure Interaction*. 2013.
- [207] K. Tokimatsu, H. Mizuno, and M. Kakurai. Building damage associated with geotechnical problems. *Soils and foundations*, 36(Special):219–234, 1996.
- [208] K. Tokimatsu, H. Suzuki, and M. Sato. Effects of inertial and kinematic interaction on seismic behavior of pile with embedded foundation. *Soil Dynamics and Earthquake Engineering*, 25(7):753 – 762, 2005. 11th International Conference on Soil Dynamics and Earthquake Engineering (ICSDEE): Part 1.
- [209] A. M. Trochanis, J. Bielak, and P. Christiano. Simplified model for analysis of one or two piles. *Journal of Geotechnical Engineering*, 117(3):448–466, mar 1991.
- [210] G. Tsinidis, K. Pitilakis, G. Madabhushi, and C. Heron. Dynamic response of flexible square tunnels: centrifuge testing and validation of existing design methodologies. *Géotechnique*, 65(5):401–417, may 2015.
- [211] G. Tsinidis, K. Pitilakis, and G. Madabhushi. On the dynamic response of square tunnels in sand. *Engineering Structures*, 125:419–437, oct 2016.
- [212] D. Tu. Numerically study on pile group effect using hypoplastic macroelement. Master’s thesis, Ecole Centrale de Nantes, 2017.
- [213] D. Vamvatsikos and C. A. Cornell. Incremental dynamic analysis. *Earthquake Engineering and Structural Dynamics*, 31(3):491–514, 2002.
- [214] Varun. *A non-linear dynamic macroelement for soil structure interaction analysis of piles in liquefiable soils*. PhD thesis, Georgia Institute of Technology, August 2010.

- [215] Varun, D. Assimaki, and A. Shafieezadeh. Soil-pile-structure interaction simulations in liquefiable soils via dynamic macroelement: Formulation and validation. *Soil Dynamics and Earthquake Engineering*, 47:92–107, 2013.
- [216] A. S. Veletsos. Design concepts for dynamics of soil-structure interaction. In P. Güllkan and R. Clough, editors, *Developments in Dynamic Soil-Structure Interaction*, pages 307–325. Kluwer Academic Publishers, 1993.
- [217] A. Verruijt. *Soil Dynamics*. 2008.
- [218] Vinci Construction Grands Projets. Atlantic Bridge, 2019. Accessed August 10 at URL <https://www.vinci-construction-projets.com/en/realisations/atlantic-bridge/>.
- [219] P.-A. von Wolffersdorff. A hypoplastic relation for granular materials with a predefined limit state surface. *Mechanics of Cohesive-frictional Materials*, 1(3):251–271, 1996.
- [220] M. Vucetic. Cyclic threshold shear strains in soils. *Journal of Geotechnical Engineering*, 120(12):2208–2228, dec 1994.
- [221] M. Vucetic and R. Dobry. Effect of soil plasticity on cyclic response. *Journal of Geotechnical Engineering*, 117(1):89–107, jan 1991.
- [222] J. Wang, D. Zhou, W. Liu, and S. Wang. Nested lumped-parameter model for foundation with strongly frequency-dependent impedance. *Journal of Earthquake Engineering*, 20(6):975–991, feb 2016.
- [223] S. Wang, B. L. Kutter, M. J. Chacko, D. W. Wilson, R. W. Boulanger, and A. Abghari. Nonlinear seismic soil-pile structure interaction. *Earthquake Spectra*, 14(2):377–396, may 1998.
- [224] Y. H. Wang and W. K. Siu. Structure characteristics and mechanical properties of kaolinite soils. I. Surface charges and structural characterizations. *Canadian Geotechnical Journal*, 43:587–600, 2006.
- [225] Y. H. Wang and W. K. Siu. Structure characteristics and mechanical properties of kaolinite soils. II. Effects of structure on mechanical properties. *Canadian Geotechnical Journal*, 43:601–617, 2006.
- [226] D. Wegener. *Numerical investigation of permanent soil displacements due to dynamic loading*. PhD thesis, Institut für Geotechnik, Technische Universität Dresden, 2013.
- [227] D. Wegener and I. Herle. Prediction of permanent soil deformations due to cyclic shearing with a hypoplastic constitutive model. *geotechnik*, 37(2):113–122, jun 2014.
- [228] D. W. Wilson. *Soil-pile-superstructure interaction in liquefying sand and soft clay*. PhD thesis, University of California, Davis, September 1998. REPORT NO. UCD/CGM-98/04.
- [229] J. P. Wolf. *Dynamic Soil-Structure Interaction*. Prentice-Hall International Series in Civil Engineering and Engineering Mechanics. Prentice-Hall International, 1985.
- [230] J. P. Wolf. Simple physical models for foundation dynamics. In *Developments in Geotechnical Engineering*, pages 1–70. Elsevier, 1998.
- [231] J. P. Wolf and D. R. Somaini. Approximate dynamic model of embedded foundation in time domain. *Earthquake Engineering & Structural Dynamics*, 14(5):683–703, sep 1986.
- [232] J. P. Wolf and G. A. von Arx. Horizontally travelling waves in a group of piles taking pile-soil-pile interaction into account. *Earthquake Engineering & Structural Dynamics*, 10(2):225–237, 1982.
- [233] W.-H. Wu and W.-H. Lee. Nested lumped-parameter models for foundation vibrations. *Earthquake Engineering & Structural Dynamics*, 33(9):1051–1058, jun 2004.



- [234] X. Zeng and A. N. Schofield. Design and performance of an equivalent-shear-beam container for earthquake centrifuge modelling. *Géotechnique*, 46(1):83–102, mar 1996.
- [235] C. Zhang and J. P. Wolf, editors. *Dynamic Soil-Structure Interaction. Current research in China and Switzerland*. Number 83 in Elsevier Science B.V. Elsevier, 1998.
- [236] F. Zhang, K. Okawa, and M. Kimura. Centrifuge model test on dynamic behavior of group-pile foundation with inclined piles and its numerical simulation. *Frontiers of Architecture and Civil Engineering in China*, 2(3):233–241, Sep 2008.
- [237] J. Zhang, R. D. Andrus, and C. H. Juang. Normalized shear modulus and material damping ratio relationships. *Journal of Geotechnical and Geoenvironmental Engineering*, 131(4):453–464, apr 2005.
- [238] L. Zhang, S. H. Goh, and J. Yi. A centrifuge study of the seismic response of pile - raft systems embedded in soft clay. *Géotechnique*, 67(6):479–490, 2017.
- [239] O. C. Zienkiewicz, N. Bicanic, and F. Q. Shen. *Earthquake Input Definition and the Transmitting Boundary Conditions*, pages 109–138. Springer Vienna, Vienna, 1989.

# Appendix A

## Centrifuge modeling

### A.1 Principles

The physical modeling in centrifuge consists in carrying out tests on reduced models while respecting the conditions of similarity in order to be able to transpose the results obtained on the model to the structure in full size. This technique makes it possible to reproduce, at the level of the reduced model, levels of stress and deformations similar to those found on the real structure [206].

The similarity of behavior between the model and the full-scale structure implies that there are constant relations called scaling factors  $X^*$  ( $X^* = X_m/X_p$ ) between the variables  $X_m$  representing the reduced model and the variables  $X_p$  describing the prototype.

Every physical system must satisfy the equilibrium equations of mechanics, in matrix form:

$$\nabla \cdot \boldsymbol{\sigma} + \mathbf{b} = \rho \ddot{\mathbf{u}} \quad (\text{A.1})$$

Where  $\boldsymbol{\sigma}$  is the Cauchy stress tensor,  $\mathbf{b}$  the vector of body forces,  $\rho$  is the mass density per unit volume and  $\ddot{\mathbf{u}}$  the acceleration vector. The dimensional analysis applied to these equations leads to the following similarity conditions [60] linking the scale factors on the stress ( $\sigma^*$ ), the mass density ( $\rho^*$ ), the components of the gravitational field ( $g^*$ ), the length ( $l^*$ ), the displacements ( $\xi^*$ ) and time ( $t^*$ ):

$$\sigma^* = \rho^* g^* l^* \quad (\text{A.2})$$

$$\xi^* = g^* t^{*2} \quad (\text{A.3})$$

Geotechnical materials such as soil and rock have non-linear mechanical properties that depend on the effective confining stress and stress history to which they are subjected. In order to simulate the real behavior of the structure in full scale it is therefore essential to reproduce the same state of stress in the reduced model which leads to impose the following additional condition:

$$\sigma^* = 1 \quad (\text{A.4})$$

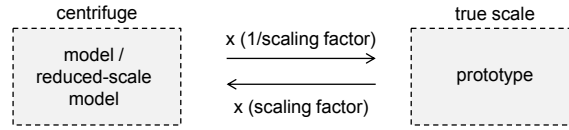
When real soils are used in the reduced model, the similarity condition on the density is imposed:

$$\rho^* = 1 \quad (\text{A.5})$$

The Equation (A.2) becomes:

$$g^* l^* = 1 \quad (\text{A.6})$$

In other words, a  $1/N$  scaled model must be accelerated  $N$  times faster than the gravitational acceleration in order to reproduce the same stresses and deformations as the prototype (Figure A.1). The Table A.1 groups together the scaling factors commonly used in centrifuge modeling.

**Figure A.1:** Scaling factors use scheme**Table A.1:** Scale factors commonly used in geotechnical centrifuge modeling

Physical quantity	Scaling factor	SI unit
Displacement, length	$1/N$	$m$
Velocity	$1$	$m/s$
Acceleration	$N$	$m/s^2$
Mass density	$1$	$kg/m^3$
Mass	$1/N^3$	$kg$
Pressure, stress	$1$	$Pa (N/m^2)$
Deformation	$1$	$-$
Force	$1/N^2$	$N$
Moment	$1/N^3$	$N.m$
Flexural stiffness ( $EI$ )	$1/N^4$	$N.m^2$
Deformation module	$1$	$N/m^2$
Time (dynamic problem)	$1/N$	$s$
Time (diffusion problem)	$1/N^2$	$s$
Frequency	$N$	$Hz (1/s)$
Energy	$1/N^3$	$J$

One of the advantages of this technique is that it makes it possible to take into account the stress gradient with the depth and the effect of the presence of a free surface in the response. These two elements play a very important role in the response of deep foundations.

When the prototype materials (soil and pore fluid) are directly used in the reduced model, a similarity conflict of time scaling factors arises between inertial ( $t^* = 1/N$ ) and diffusion phenomena ( $t^* = 1/N^2$ ).

The use on the model of a fluid  $N$  times more viscous than water is necessary. Another possibility is to conserve the water as fluid in the reduced model and to consider that the simulated prototype has a permeability  $N$  times higher than that of the model [60].

## A.2 Difficulties and/or limitations of dynamic centrifuge tests

Several difficulties may be present when doing experimental dynamic centrifuge tests [228]:

- The repeatability of the model preparation procedures (e.g., reproducing the same soil profile for different testing configurations);
- Technical limitations of the earthquake simulator in terms of amplitude and frequency content of the signal that can be applied, presence of parasite movements in the vertical or the transverse axis;
- It is complicated to model certain sources of damping that are present in a soil-foundation-structure system. Structures are often modeled using simple metal structures (e.g., inverted pendulums) that are able to reproduce the good ratio between stiffness and mass of the prototype but which have low material damping compared to, for example, reinforced concrete

structures. The radiation damping also cannot be reproduced in a correct way given the physical characteristics of the model container and of the shaking table;

- Boundary effects are usually present due to the “imperfections” of the model container which make it impossible to reproduce exactly the free-field boundary conditions, mass and stiffness contrast between container and soil, etc.

Because of the aforementioned limitations, often centrifuge tests are not designed to reproduce a real prototype but rather to provide test data from a carefully designed and well instrumented configuration which can be used as a benchmark to test advanced numerical simulations or to study the impact of a given parameter in the overall response of the soil-foundation-structure system.



## Appendix B

# Experimental program and base shaking signals

### B.1 List of experiments

#### B.1.1 List of experiments by chronological order

**Table B.1:** List of experiments by chronological order

ID	Date	Type	Description
C00	05/08/2016	Feasibility	Pile installation at 1g
C01	10/10/2016	Feasibility	Fabrication and setup of a multilayer profile for dynamic test
C02	29/11/2016	Static	Floating piles under pile head loading
C03	07/03/2017	Static	End-bearing piles under pile head loading
C04	24/04/2017	Dynamic	Single pile
C05	03/08/2017	Dynamic	Repeatability test of C04
C06	29/09/2017	Dynamic	Single pile with mass
C07	28/11/2017	Dynamic	Pile group with short superstructure
C08	12/02/2018	Dynamic	Pile group with slender superstructure

#### B.1.2 Details of experiments

##### **C00 - Feasibility test of pile installation in clay at 1g**

The pile installation procedure of piles at 1g was verified in this feasibility test. The soil profile consist of a 300 mm thick layer of overconsolidated speswhite kaolinite. CPT measurements carried out at several distances from pile have shown that the undrained shear strenght profile is not affected by this installation mode, even for distances between axes equal to three times the diameter of the pile.

##### **C01 - Feasibility test of fabrication and setup of multilayer soil profile for dynamic test**

The objective of this feasibility test was to answer several points of uncertainty that were identified at the start of the project:

- Signal transmission at the interfaces: container-soil and soil-soil (i.e. between saturated sand and clay layers);
- Feasibility of fabrication of a multilayered soil profile with saturated dense sand, overconsolidated clay and dry dense sand;
- Study of the evolution of the soil profile at 50g;
- Study of the boundary effects that may be present.

To this end, the soil profile has been heavily instrumented with accelerometers, pore pressure transducers, settlement sensors and bender elements.

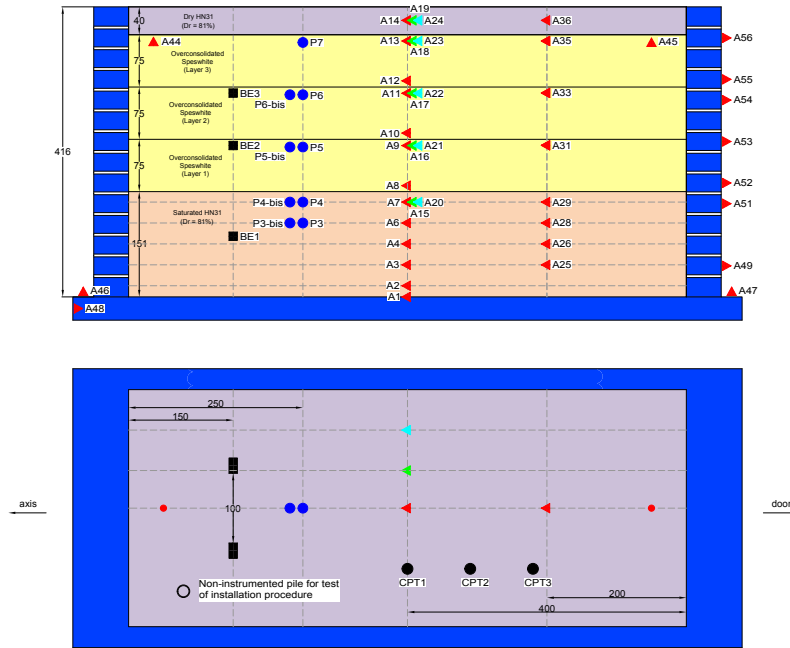


**Figure B.1:** Experimental layout - C01 test

Due to a mistake during the preconsolidation of clay layer at 1g, a very important preconsolidation pressure was applied (600 kPa instead of 160 kPa expected) which do not allow to extend the results to the case finally studied. However this test showed that the installation procedure used in the installation of accelerometers was not satisfying (a large quantity of accelerometers have not worked, in particular those in the clay, because of a differential settlement between the body sensor and the cable). The installation procedure was thus reviewed and improved for the subsequent tests.

C02 - Static test of floating piles under pile head loading

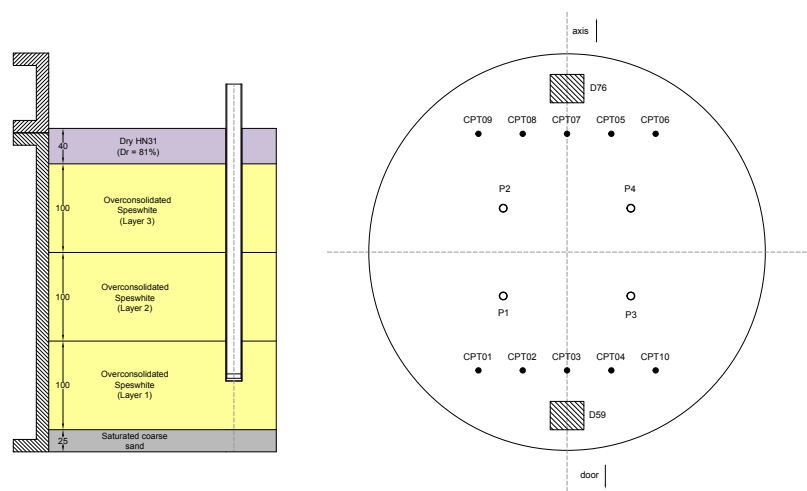


Figure B.2: Experimental layout - C02 test

C03 - Static test of end-bearing piles under pile head loading

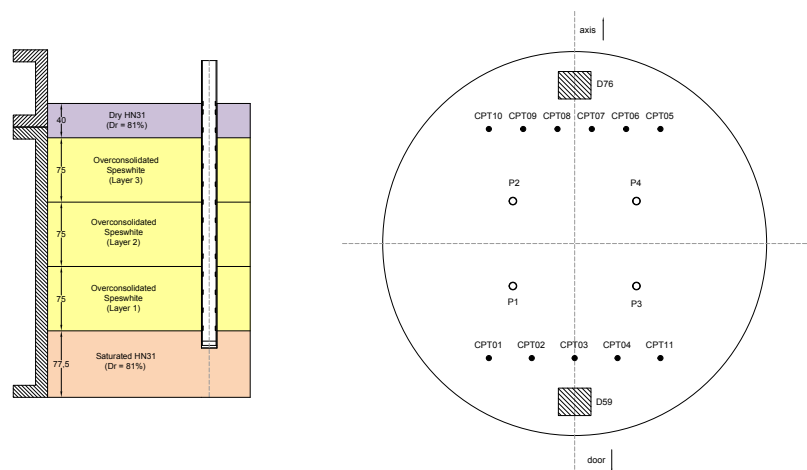


Figure B.3: Experimental layout - C03 test



C04 - Dynamic test of single pile

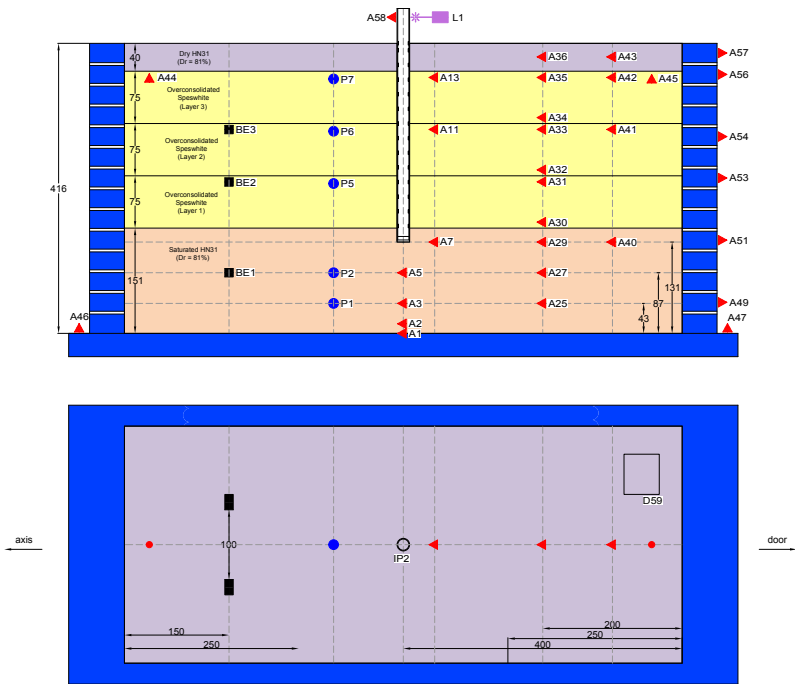


Figure B.4: Experimental layout - C04 test

C05 - Repeatability test of C04

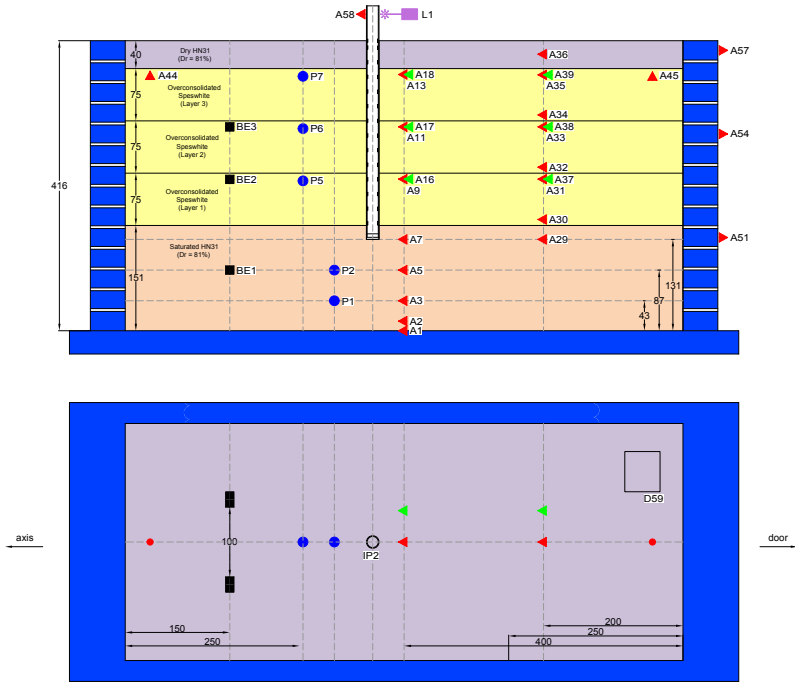


Figure B.5: Experimental layout - C05 test

C06 - Dynamic test of single pile with mass

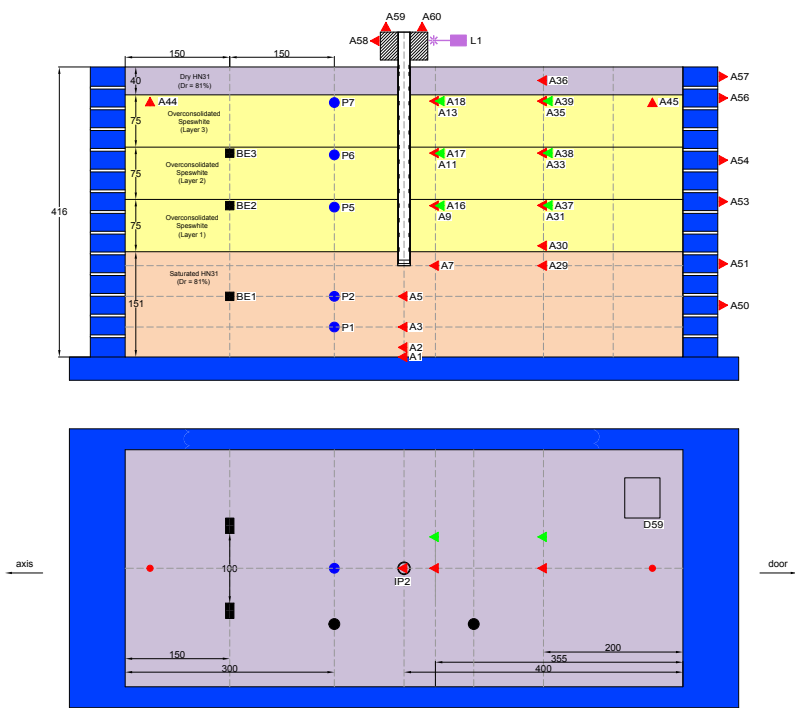
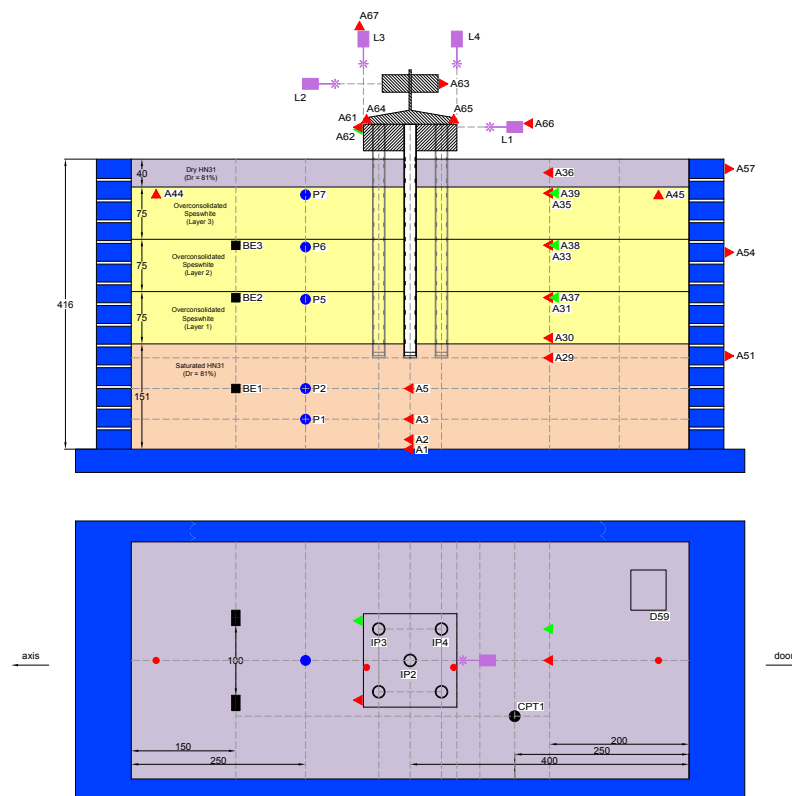
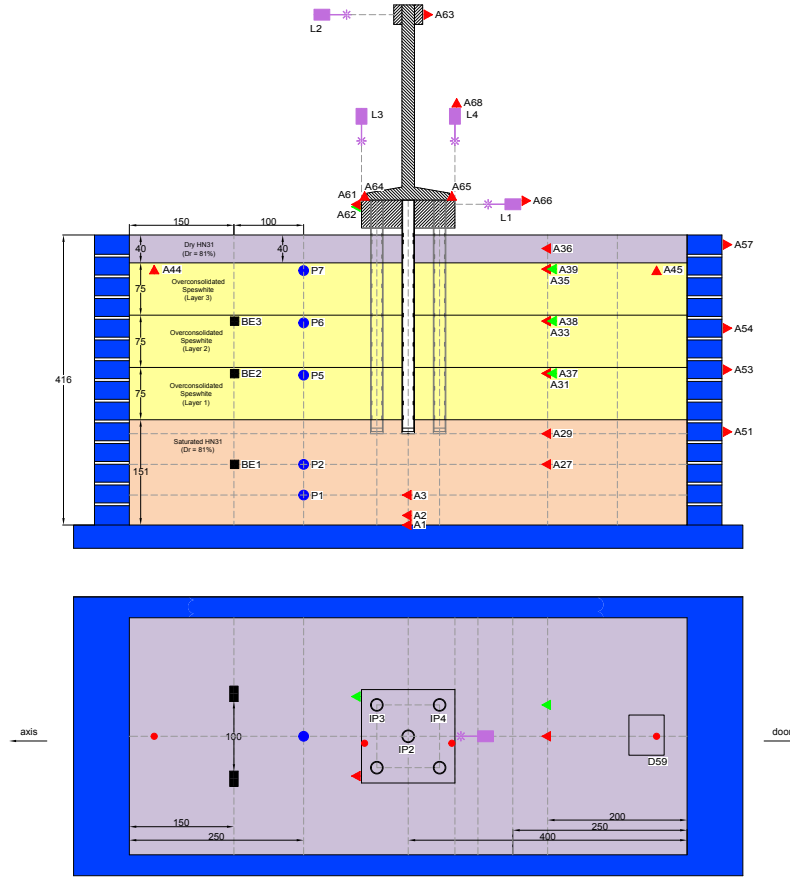


Figure B.6: Experimental layout - C06 test

### C07 - Dynamic test of pile group with short superstructure



**Figure B.7:** Experimental layout - C07 test

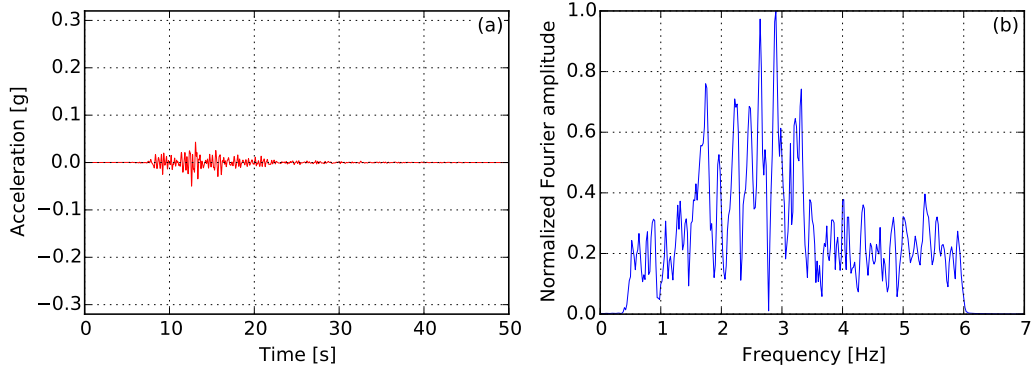
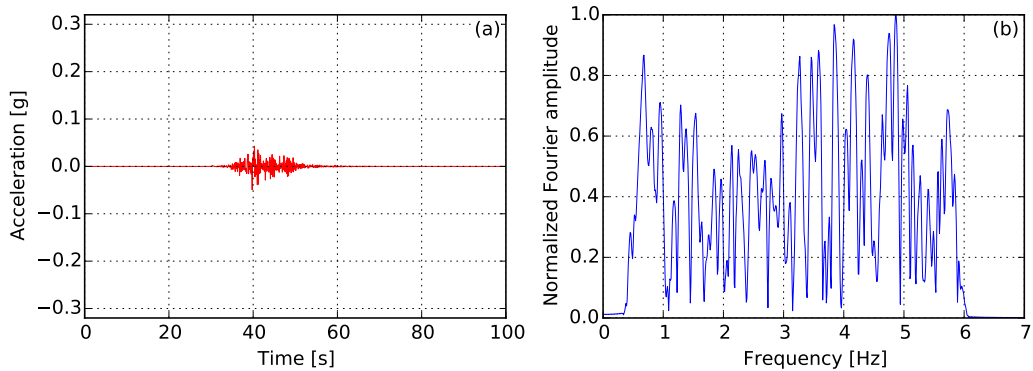
**C08 - Dynamic test of pile group with slender superstructure****Figure B.8:** Experimental layout - C08 test**B.2 Characteristics of the selected inputs**

Two types of inputs have been selected: sines with tapered parts and real broadband earthquakes (Landers 1992 (Lucern Valley station) and Northridge 1994 (Tarzana station) records). In order to be in the capacity range of the shaker [30], earthquake signals have been filtered outside the frequency range of 0.4-6 Hz. The characteristics of these signals are given in Table B.2.

**Table B.2:** Characteristics of the selected inputs (prototype scale): peak ground acceleration (PGA), peak ground velocity (PGV), Arias Intensity ( $I_A$ ) and significant duration

#	Signal	PGA (g)	PGV (m/s)	$I_A$ (m/s)	Significant duration (s)
1	Northridge 0.05g	0.05	0.037	0.025	11.163
2	Landers 0.05g	0.05	0.051	0.031	11.505
3	Northridge 0.3g	0.3	0.22	0.897	11.163
4	Landers 0.3g	0.3	0.306	1.109	11.505
5	Sine 1 Hz 0.1g	0.1	0.157	1.417	16.348
6	Sine 1.8 Hz 0.1g	0.1	0.087	0.787	9.089
7	Sine 2.4 Hz 0.1g	0.1	0.065	0.588	6.808
8	Sine 3.2 Hz 0.1g	0.1	0.049	0.443	5.112
9	Sine 1 Hz 0.3g	0.3	0.47	12.76	16.348
10	Sine 1.8 Hz 0.3g	0.3	0.261	7.087	9.089
11	Sine 2.4 Hz 0.3g	0.3	0.195	5.295	6.808
12	Sine 3.2 Hz 0.3g	0.3	0.146	3.986	5.112

### B.3 Representation of inputs in time and frequency domain

**Figure B.9:** Time (a) and frequency (b) representation of Northridge 0.05g earthquake**Figure B.10:** Time (a) and frequency (b) representation of Landers 0.05g earthquake

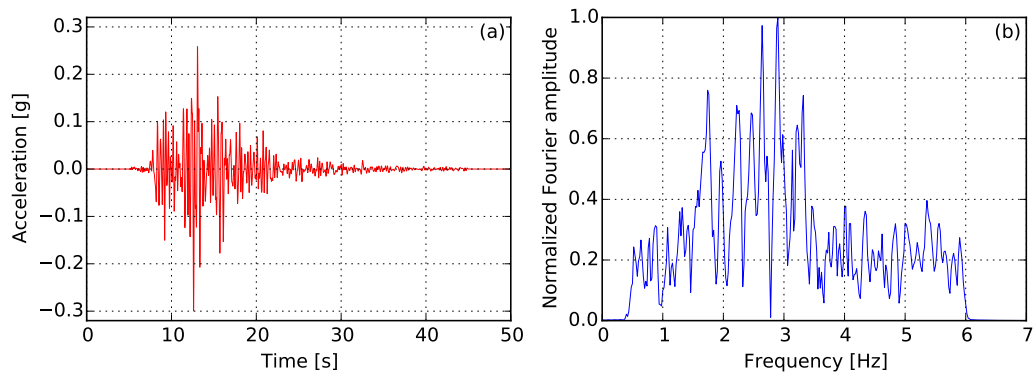


**Figure B.11:** Time (a) and frequency (b) representation of Northridge 0.3g earthquake

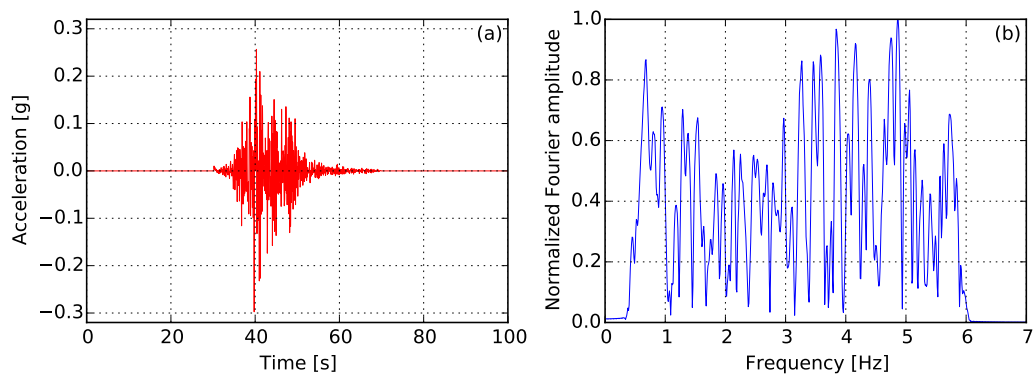


**Figure B.12:** Time (a) and frequency (b) representation of Landers 0.3g earthquake

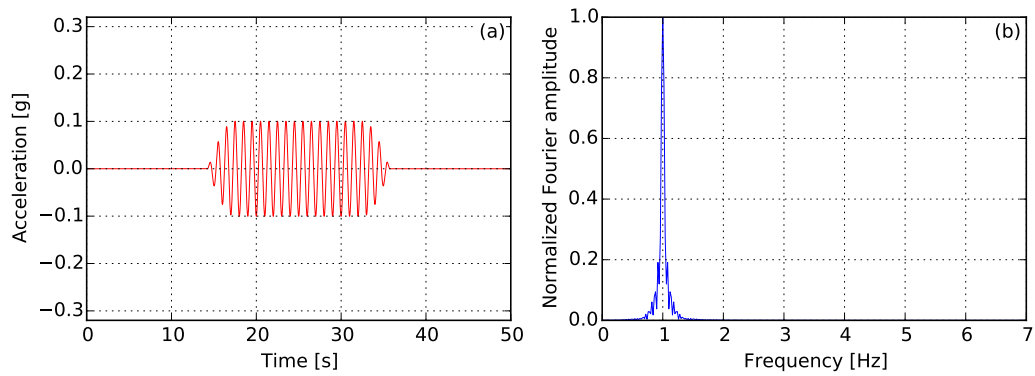


**Figure B.13:** Time (a) and frequency (b) representation of sine 1 Hz 0.1g input

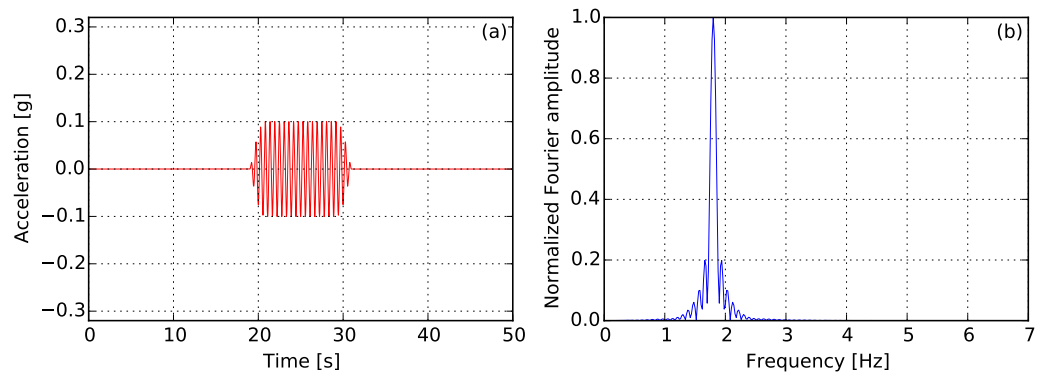


**Figure B.14:** Time (a) and frequency (b) representation of sine 1.8 Hz 0.1g input

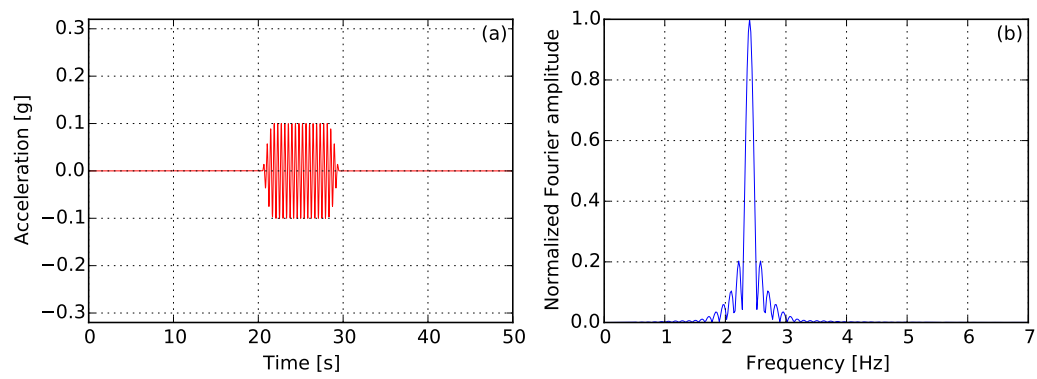


**Figure B.15:** Time (a) and frequency (b) representation of sine 2.4 Hz 0.1g input

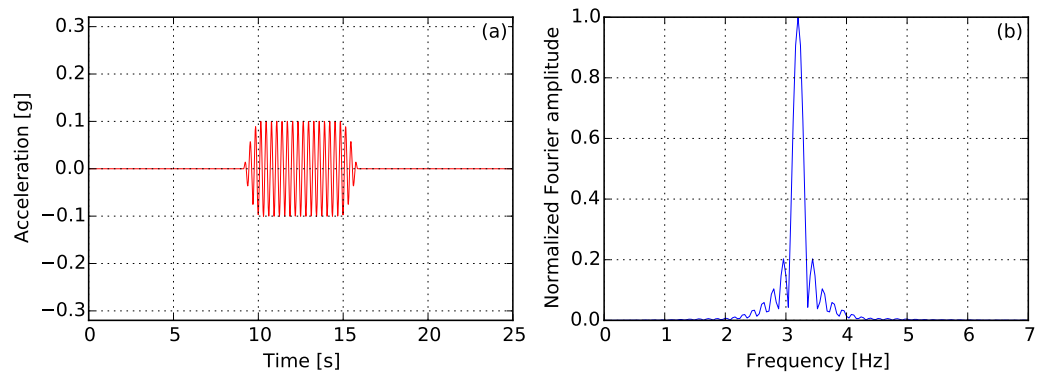


**Figure B.16:** Time (a) and frequency (b) representation of sine 3.2 Hz 0.1g input

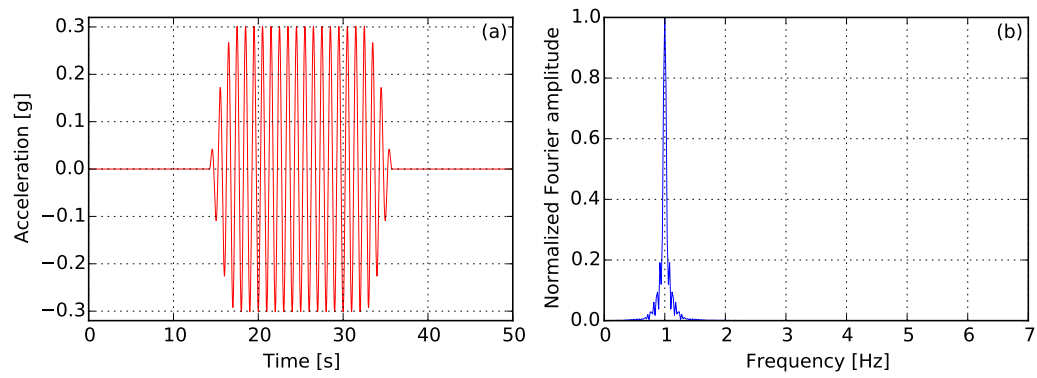


**Figure B.17:** Time (a) and frequency (b) representation of sine 1 Hz 0.3g input

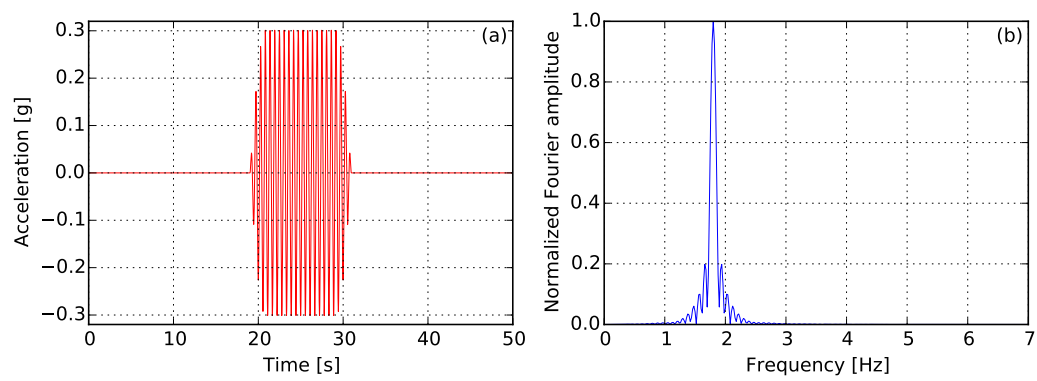


**Figure B.18:** Time (a) and frequency (b) representation of sine 1.8 Hz 0.3g input

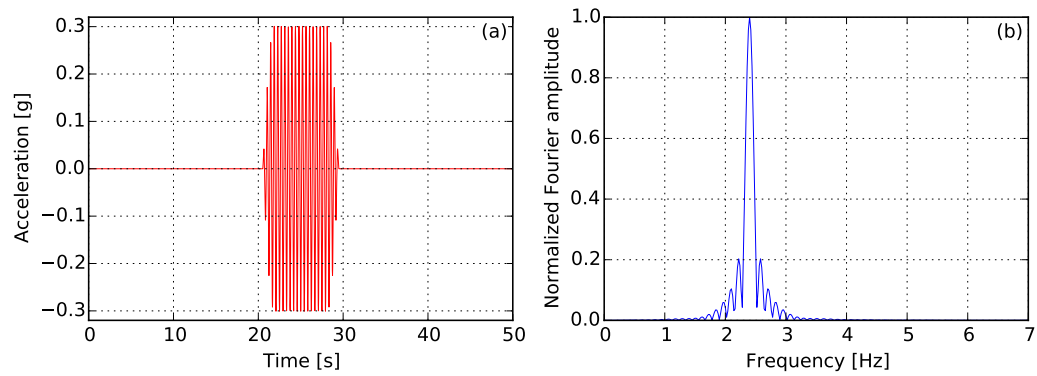


**Figure B.19:** Time (a) and frequency (b) representation of sine 2.4 Hz 0.3g input



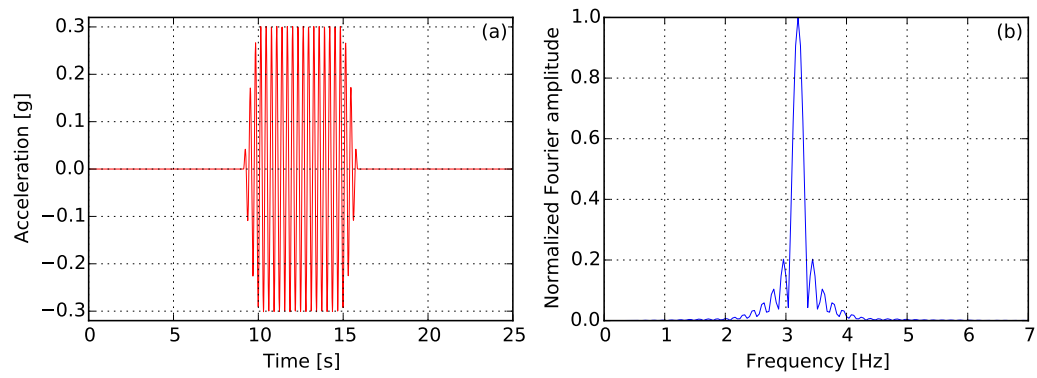


**Figure B.20:** Time (a) and frequency (b) representation of sine 3.2 Hz 0.3g input

## Appendix C

# Instrumentation and equipments

### C.1 Structures

#### C.1.1 Single pile cap

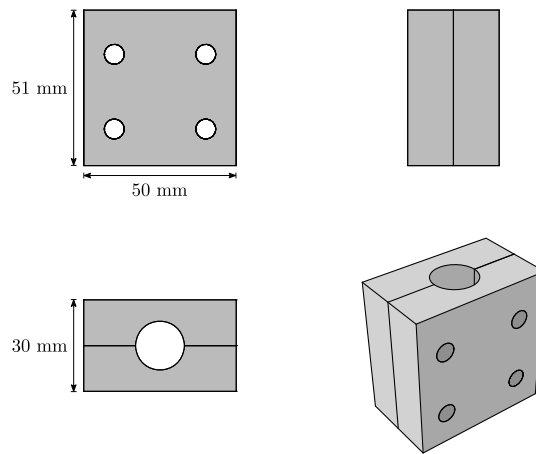


**Figure C.1:** Scheme drawing of the single pile cap (at model scale)

**Table C.1:** Parameters of the single pile cap (at model scale)

Material	Aluminum
Dimensions ( $l \times w \times h$ )	$50\text{ mm} \times 30\text{ mm} \times 51\text{ mm}$
Mass	$0.189\text{ kg}$

C.1.2 Pile group cap

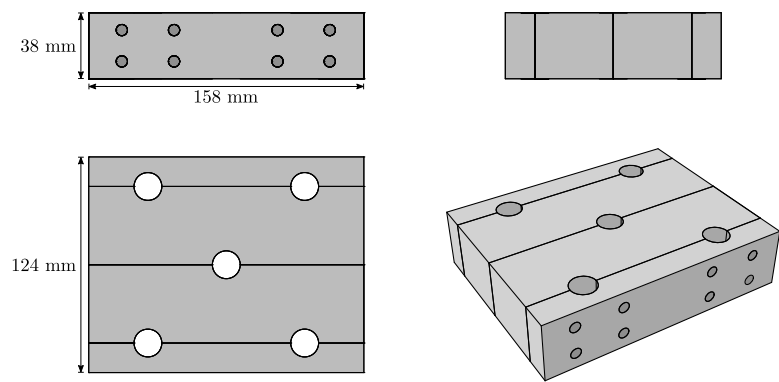


Figure C.2: Scheme drawing of the pile group cap (at model scale)

Table C.2: Parameters of the pile group cap (at model scale)

Material	Aluminum
Dimensions ( $l \times w \times h$ )	$158\text{ mm} \times 124\text{ mm} \times 38\text{ mm}$
Mass	$1.56\text{ kg}$

C.1.3 Short building

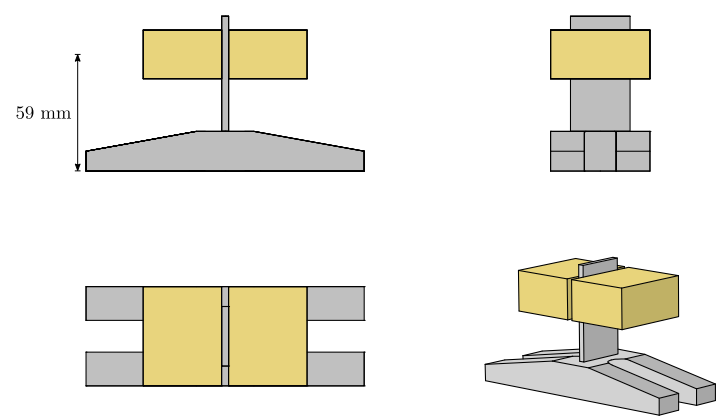


Figure C.3: Scheme drawing of the short building (at model scale)

Table C.3: Parameters of the short building (at model scale)

Property	Mass block at the top	Column + base
Material	Brass	Aluminum
Mass	$0.8\text{ kg}$	$0.292\text{ kg}$
Total mass	$1.092\text{ kg}$	
Height	$59\text{ mm}$	
Measured fixed-base frequency	$77\text{ Hz}$	
Measured damping	$0.35\%$	

C.1.4 Tall building

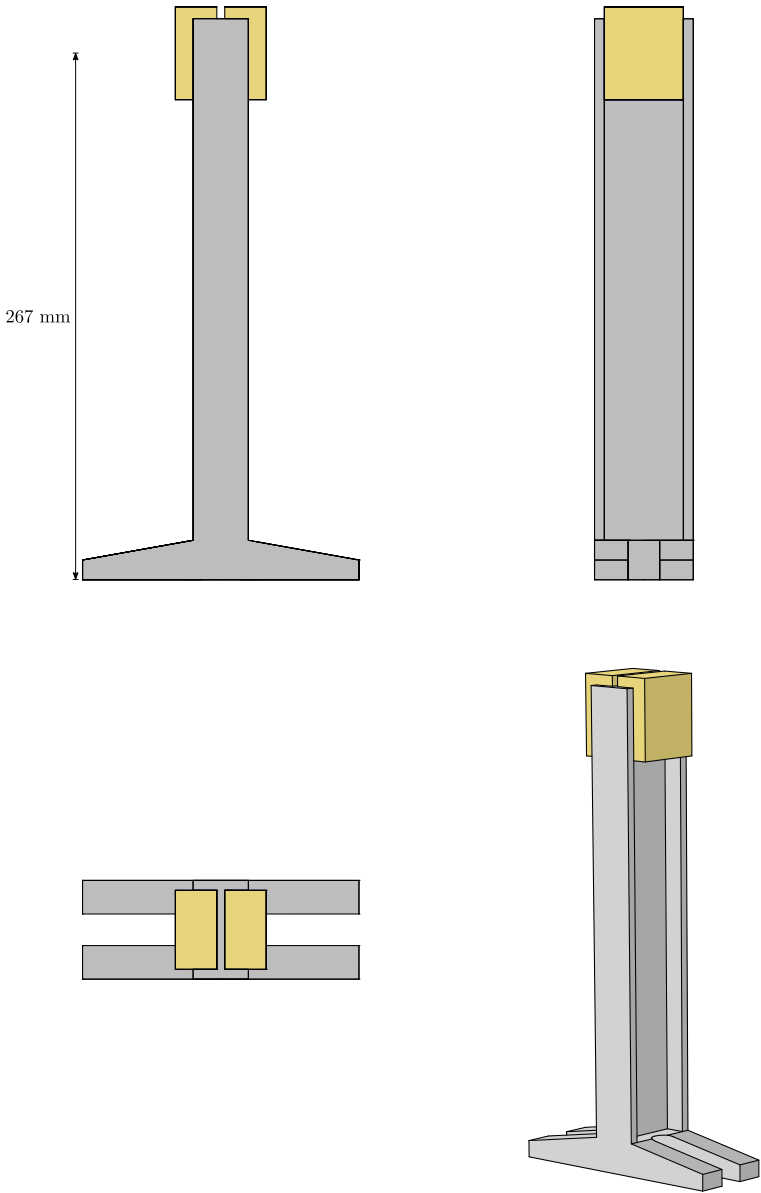
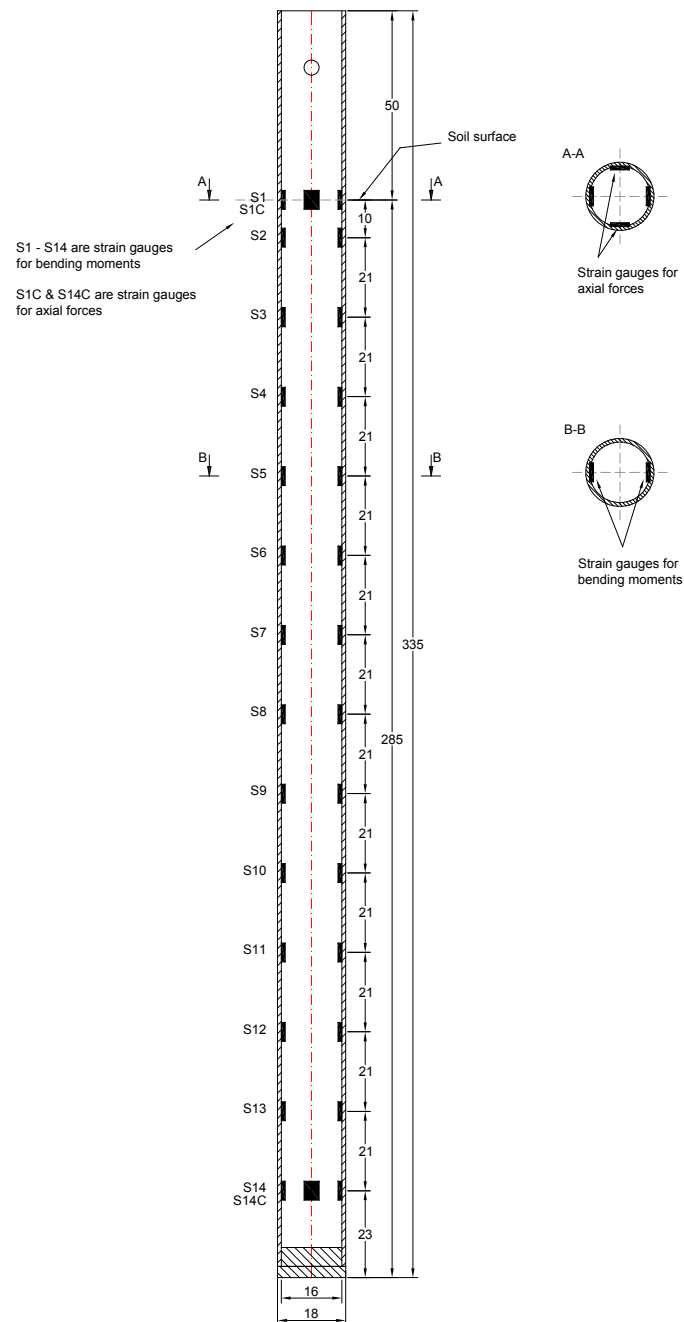


Figure C.4: Scheme drawing of the tall building (at model scale)

Table C.4: Parameters of the tall building (at model scale)

Property	Mass block at the top	Column + base
Material	Brass	Aluminum
Mass	0.7 kg	0.532 kg
Total mass	1.232 kg	
Height	267 mm	
Measured fixed-base frequency	75 Hz	
Measured damping	0.7 %	

## C.2 Instrumented piles



**Figure C.5:** Distribution of strain gauges on instrumented piles (all dimensions are given in mm at model scale)

## Appendix D

# Study of repeatability of experiments

### D.1 CPT profiles

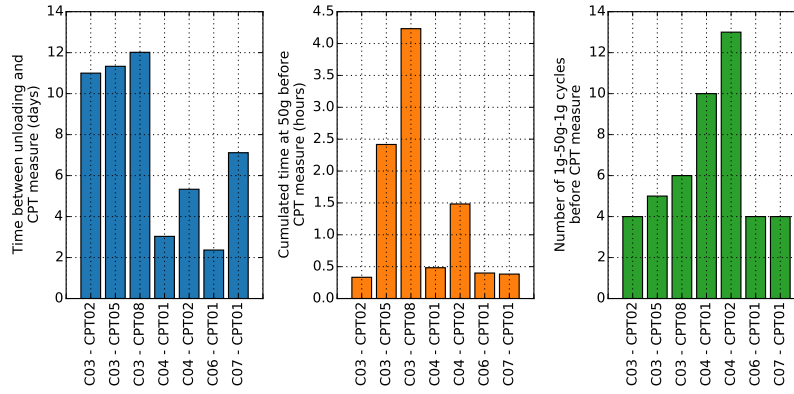


**Figure D.1:** Information about CPT measurements: elapsed time between container unloading and CPT measurement, accumulated time at 50g before CPT measurement and number of 1g-50g-1g cycles before CPT measurement

### D.2 Ground motion parameters

Many parameters have been proposed in the literature to describe strong ground motion in terms of amplitude, frequency content and duration. Because of the complexity of earthquake ground motions, a single parameter is not sufficient to describe accurately all the particularities of the ground motion and several parameters need to be used at the same time [110]. In the following, several ground motion parameters are introduced. They are used through the text to quantify the intensity of the used signals, the repeatability of the conducted tests, etc.

- Peak Ground Acceleration (PGA): it is commonly used to measure the amplitude of a particular ground motion. Earthquakes with higher PGA are usually, but not always, more destructive than those with smaller acceleration peaks.

$$PGA = \max(|\ddot{u}(t)|) \quad (D.1)$$

- Peak Ground Velocity (PGV): given that the velocity is less sensitive to high frequencies than the acceleration (the integration of acceleration has a filtering effect), this parameter is more

suitable for the characterization of the ground motion for intermediate frequencies. The velocity time history shows substantially less high-frequency motion than the acceleration time history. The PGV gives usually a more accurate indication of the potential for damage than PGA in the case of structures that are more susceptible to loadings in the intermediate frequency range (e.g., tall buildings, bridges, etc).

$$PGV = \max(|\dot{u}(t)|) \quad (D.2)$$

- Peak Ground Displacement (PGD): as for the PGV, the PGD is another useful parameter for the characterization of ground motion amplitude. It is much less sensitive to high frequencies than the acceleration time history. The displacement peaks are usually associated with the low-frequency content of an earthquake.

$$PGD = \max(|u(t)|) \quad (D.3)$$

- Arias Intensity ( $I_A$ ): it is obtained by integration over the entire duration of the squared value of acceleration at every time instant. This parameter includes, a priori, the effects of the amplitude and frequency of a strong motion. One of the advantages of Arias Intensity is that it is fairly insensitive to large, high-frequency accelerations.

$$I_A = \frac{\pi}{2g} \int_0^\infty [\ddot{u}(t)]^2 dt \quad (D.4)$$

- Significant duration: it is defined as the interval of time over which a proportion (percentage) of the total Arias Intensity is accumulated (usually the interval between the 5% and the 95% thresholds of  $I_A$  is used). As indicated by Kramer [110], the duration of strong ground motion can have a strong influence on earthquake damage. The number of load or stress reversals that occur during an earthquake have a direct impact on the outcome of many physical processes, such as the degradation of stiffness and strength of certain types of structures and the buildup of porewater pressures in loose, saturated sands. A motion with moderate amplitude but long duration can produce more substantial damage than a short one with higher amplitudes but much less load reversals.

It is found that there is not yet a consensus in the scientific literature as to the ideal parameter to estimate the intensity of a seismic motion. Some authors consider that the most suitable parameter is the Arias Intensity while others highlight the PGV or the PGD for strong earthquakes and the PGA for weak earthquakes. It should be noted that this question, which has attracted the interest of many authors, is still open and the present conclusions seem to guide the analysis towards multicriteria approaches capable of taking into account several indicators at the same time [9].

In addition to the above presented parameters, the frequency content of an earthquake motion is often investigated by means of the Fourier transform or the response spectrum. Indeed, the frequency content of an earthquake motion will strongly influence the effects of that motion. A narrow Fourier amplitude spectrum implies that the motion has a dominant frequency (or period), whereas a broad spectrum corresponds to a motion that contains a variety of frequencies.

For instance, it should be noted that the response spectrum of an earthquake motion is extensively used in earthquake engineering practice, i.e., definition of the seismic loading by means of a set of design spectra. The response spectrum describes the maximum response of single degree of freedom (SDOF) system to a particular input motion as a function of the natural frequency (or natural period) and damping ratio (usually a 5% damping is considered) [110].

## Appendix E

# Numerical resolution of the seismic SSI problem

### E.1 Finite Element Development and Analysis Environment (FEDAE)

A finite element analysis tool has been developed during this PhD study in order to facilitate the development and testing of different pile-group macroelement concepts and resolution strategies. This tool, named FEDAE (Finite Element Development and Analysis Environment), is programmed in Python and Fortran and incorporates linear and nonlinear resolution algorithms for static and dynamic problems (e.g., modal analysis, Newmark, Newton-Raphson, explicit integration scheme, etc.). The organization of the program is presented in Figure E.1.

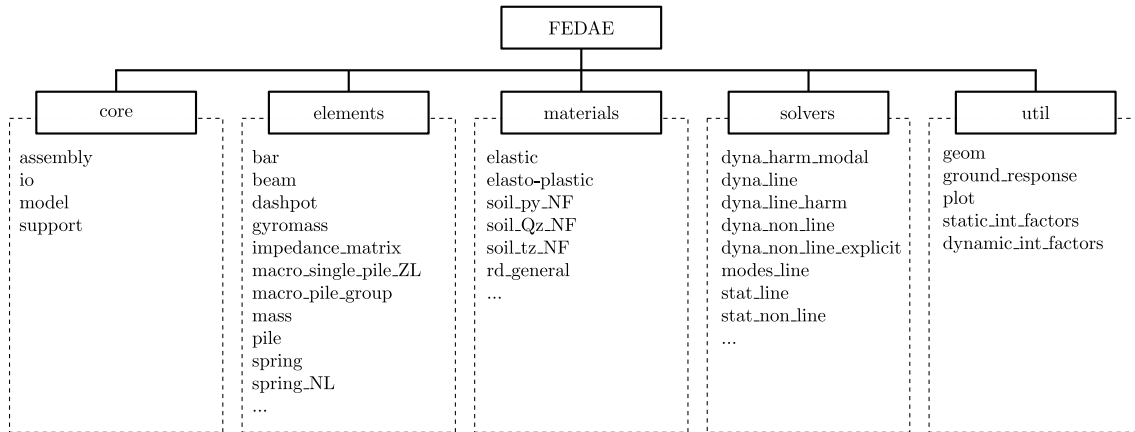


**Figure E.1:** FEDAE function organization

Several reasons motivated this development:

- Total control over the entire code which translates into a higher level of freedom to develop and implement new ideas and concepts;
- Python language allows fast development and validation of new elements, materials and resolution schemes. Critical parts of the code can be compiled in Fortran to speed up the calculation;
- Can benefit of all the third party libraries for data visualization, numerical analysis, etc. available in the Python ecosystem;



- Possibility to run parametric studies using the scripting capabilities of Python.

The following section describes the Newmark/modified Newton-Raphson algorithm for the time integration of a nonlinear system implemented in FEDAE.

## E.2 Transient dynamic analysis of a nonlinear system

The analytical resolution of the equation of motion governing the response of a given system is generally only possible for very simple cases. When the applied loading varies arbitrarily with time or the system has nonlinear behavior, the use of numerical resolution methods is necessary [34, 33, 167].

For an inelastic single degree of freedom system the equation of motion may be written as:

$$m\ddot{u} + c\dot{u} + f_S(u, \dot{u}) = p(t) \quad (\text{E.1})$$

Or in the case of an acceleration  $\ddot{u}_g(t)$  applied at the base of the sytem:

$$m\ddot{u} + c\dot{u} + f_S(u, \dot{u}) = -m\ddot{u}_g(t) \quad (\text{E.2})$$

The displacement and the velocity for  $t = 0$  are the initial conditions to the problem:

$$u_0 = u(0) \quad \dot{u}_0 = \dot{u}(0) \quad (\text{E.3})$$

Note that in Equation (E.2),  $u$ ,  $\dot{u}$  and  $\ddot{u}$  constitute the relative displacement, velocity and acceleration of the nodes of the system with respect to its base (relative reference frame). If necessary, the absolute displacement, velocity and acceleration (with respect to the Galilean reference frame) can be calculated as follows:

$$u_t = u + u_g \quad \dot{u}_t = \dot{u} + \dot{u}_g \quad \ddot{u}_t = \ddot{u} + \ddot{u}_g \quad (\text{E.4})$$

Generally a viscous linear damping is considered. Other forms of damping, including nonlinear damping, can be considered in this formulation but they are rarely used because of the lack of information concerning the damping and more precisely that associated with large amplitude loadings [33].

In a numerical resolution scheme the response of the system is determined at the discrete time instants  $t_i$ . The solution is sought for a system in equilibrium, including inertial and damping forces, in the time interval  $\Delta t$  between two consecutive time instants,  $t_i$  and  $t_{i+1}$ :

$$m\ddot{u}_i + c\dot{u}_i + (f_S)_i = p_i \quad (\text{E.5})$$

$$\Delta t_i = t_{i+1} - t_i \quad (\text{E.6})$$

$$m\ddot{u}_{i+1} + c\dot{u}_{i+1} + (f_S)_{i+1} = p_{i+1} \quad (\text{E.7})$$

With  $(f_S)_i$  the resisting force at time  $t_i$ . For an elastic system it corresponds with the elastic restoring force  $(f_S)_i = ku_i$ . In the case of an inelastic system its value would depend on the prior history of displacement and on the velocity at time  $t_i$ .

The difference between Equations (E.5) and (E.7) makes it possible to write the equation of motion in incremental form:

$$m\Delta\ddot{u}_i + c\Delta\dot{u}_i + (\Delta f_S)_i = \Delta p_i \quad (\text{E.8})$$

### E.2.1 The Newmark method

The Newmark algorithm family is based on the following time-marching scheme:

$$u_{i+1} = u_i + \Delta t \dot{u}_i + \frac{\Delta t^2}{2} ((1 - 2\beta)\ddot{u}_i + 2\beta\ddot{u}_{i+1}) \quad (\text{E.9})$$

$$\dot{u}_{i+1} = \dot{u}_i + \Delta t ((1 - \gamma)\ddot{u}_i + \gamma\ddot{u}_{i+1}) \quad (\text{E.10})$$

The parameters  $\beta$  and  $\gamma$  control the variation of the acceleration during the time increment  $\Delta t$  and the stability and accuracy of the algorithm. The Newmark method is unconditionally stable for  $2\beta \geq \gamma \geq 1/2$ . When  $\gamma = 1/2$  the numerical damping introduced by the algorithm is zero.

Specific choices of these parameters lead to the following integration schemes:

$$\begin{cases} \gamma = 1/2 & \beta = 1/4 & \text{constant mean acceleration} \\ \gamma = 1/2 & \beta = 1/6 & \text{linear acceleration increment} \\ \gamma = 1/2 & \beta = 0 & \text{central difference} \end{cases}$$

Only the constant mean acceleration scheme is unconditionally stable, the other two are stable only if the time step is lower than a critical value.

### E.2.2 Newmark integration algorithm for a nonlinear system

For an inelastic system,  $(\Delta f_S)_i$  in Equation (E.8) corresponds with the increment of the restoring force at time step  $i$ , that is:

$$(\Delta f_S)_i = (k_{sec})_i \Delta u_i \quad (\text{E.11})$$

For a single degree of freedom system, this relation can be represented graphically as shown in Figure E.2. This schema shows that the secant stiffness  $(k_{sec})_i$  can not be determined at the time step  $i$  because the displacement  $u_{i+1}$  has not yet been calculated. When the time step  $\Delta t$  is small enough, the secant stiffness  $(k_{sec})_i$  can be replaced by the tangent stiffness  $(k_{tan})_i$  without committing, a priori, a significant error in the resolution.

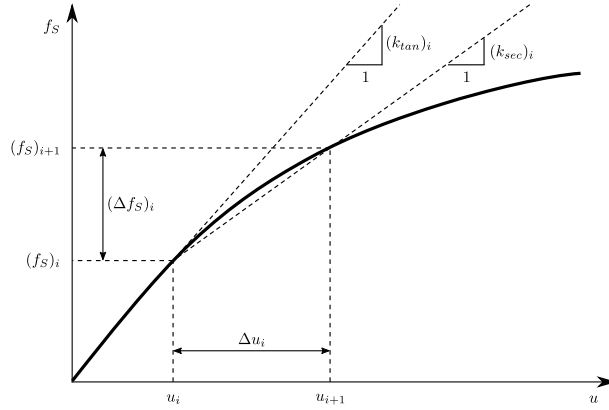


**Figure E.2:** Restoring force in a single degree of freedom system

Equation (E.11) can therefore be written in an approximate way using the tangent stiffness:

$$(\Delta f_S)_i \simeq (k_{tan})_i \Delta u_i \quad (\text{E.12})$$

The incremental form of the equation of motion (E.8) becomes:

$$m\Delta\ddot{u}_i + c\Delta\dot{u}_i + (k_{tan})_i\Delta u_i = \Delta p_i \quad (\text{E.13})$$

Equation (E.13) can be rewritten as:

$$(\hat{k}_{tan})_i \Delta u_i = \Delta \hat{p}_i \quad (\text{E.14})$$

Where the terms  $(\hat{k}_{tan})_i$  and  $\Delta \hat{p}_i$  are calculated respectively:

$$(\hat{k}_{tan})_i = (k_{tan})_i + \frac{\gamma}{\beta \Delta t} c + \frac{1}{\beta \Delta t^2} m \quad (\text{E.15})$$

$$\Delta \hat{p}_i = \Delta p_i + \left( \frac{\gamma}{\beta} c + \frac{1}{\beta \Delta t} m \right) \dot{u}_i + \left( \Delta t \left( \frac{\gamma}{2\beta} - 1 \right) c + \frac{1}{2\beta} m \right) \ddot{u}_i \quad (\text{E.16})$$

In order to reduce the error committed at each time step with the use of the tangent matrix an iterative procedure can be introduced for the calculation of the evolution of the restoring force during the time step. Figure E.3 shows the application of a modified Newton-Raphson iterative scheme in the resolution of the time step  $i$  for a single degree of freedom system.

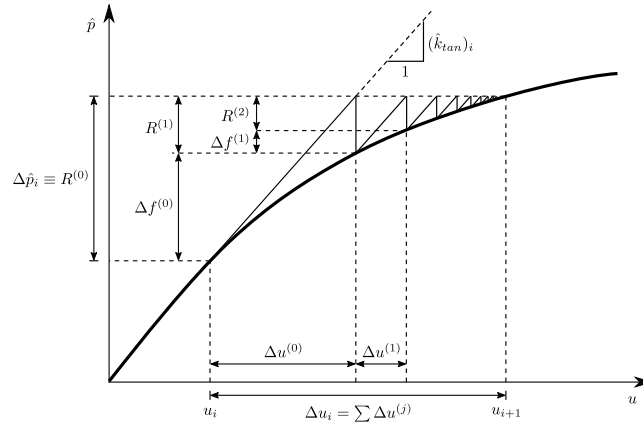


**Figure E.3:** Modified Newton-Raphson iteration

The same principle applies to a more general system. Algorithm 2 combines the modified Newton-Raphson iterative technique with the Newmark's implicit integration scheme to solve the equation motion of a nonlinear system.

Initial conditions:  $\mathbf{u}_0$ ,  $\dot{\mathbf{u}}_0$  and  $\mathbf{p}_0$

Preliminary calculations:

Initial tangent stiffness:  $(\mathbf{K}_{tan})_0$

$$\mathbf{a} = \frac{\gamma}{\beta} \mathbf{C} + \frac{1}{\beta \Delta t} \mathbf{M} \quad \mathbf{b} = \Delta t \left( \frac{\gamma}{2\beta} - 1 \right) \mathbf{C} + \frac{1}{2\beta} \mathbf{M}$$

$i = 0$

**while**  $t_i < t_{end}$  **do**

$$\Delta \hat{\mathbf{p}}_i = \Delta \mathbf{p}_i + \mathbf{a} \dot{\mathbf{u}}_i + \mathbf{b} \ddot{\mathbf{u}}_i$$

$$(\hat{\mathbf{K}}_{tan})_i = (\mathbf{K}_{tan})_i + \frac{\gamma}{\beta \Delta t} \mathbf{C} + \frac{1}{\beta \Delta t^2} \mathbf{M}$$

$$\mathbf{f}_S^{(0)} = (\mathbf{f}_S)_i \quad \mathbf{R}^{(0)} = \Delta \hat{\mathbf{p}}_i$$

$j = 0$

**while**  $\|\mathbf{R}^{(j)}\| > tol$  **do**

$$\Delta \mathbf{u}^{(j)} = \left[ (\hat{\mathbf{K}}_{tan})_i \right]^{-1} \mathbf{R}^{(j)}$$

Iterate on the elements, calculation and assembly of  $\mathbf{f}_S^{(j+1)}$  and  $(\mathbf{K}_{tan})_{i+1}$

$$\Delta \mathbf{f}^{(j)} = \mathbf{f}_S^{(j+1)} - \mathbf{f}_S^{(j)} + \left( (\hat{\mathbf{K}}_{tan})_i - (\mathbf{K}_{tan})_i \right) \Delta \mathbf{u}^{(j)}$$

$$\mathbf{R}^{(j+1)} = \mathbf{R}^{(j)} - \Delta \mathbf{f}^{(j)} \quad \Delta \mathbf{u}_i = \sum \Delta \mathbf{u}^{(j)}$$

$j = j + 1$

**end**

$$\Delta \dot{\mathbf{u}}_i = \frac{\gamma}{\beta \Delta t} \Delta \mathbf{u}_i - \frac{\gamma}{\beta} \dot{\mathbf{u}}_i + \Delta t \left( 1 - \frac{\gamma}{2\beta} \right) \ddot{\mathbf{u}}_i$$

$$\Delta \ddot{\mathbf{u}}_i = \frac{1}{\beta \Delta t^2} \Delta \mathbf{u}_i - \frac{1}{\beta \Delta t} \dot{\mathbf{u}}_i - \frac{1}{2\beta} \ddot{\mathbf{u}}_i$$

$$\mathbf{u}_{i+1} = \mathbf{u}_i + \Delta \mathbf{u}_i \quad \dot{\mathbf{u}}_{i+1} = \dot{\mathbf{u}}_i + \Delta \dot{\mathbf{u}}_i \quad \ddot{\mathbf{u}}_{i+1} = \ddot{\mathbf{u}}_i + \Delta \ddot{\mathbf{u}}_i$$

$$t_{i+1} = t_i + \Delta t_i$$

$$i = i + 1$$

**end**

**Algorithm 2:** Newmark/modified Newton-Raphson algorithm for the time integration of a nonlinear system



## Appendix F

# SSI in current engineering design practice

### F.1 SSI in current design practice

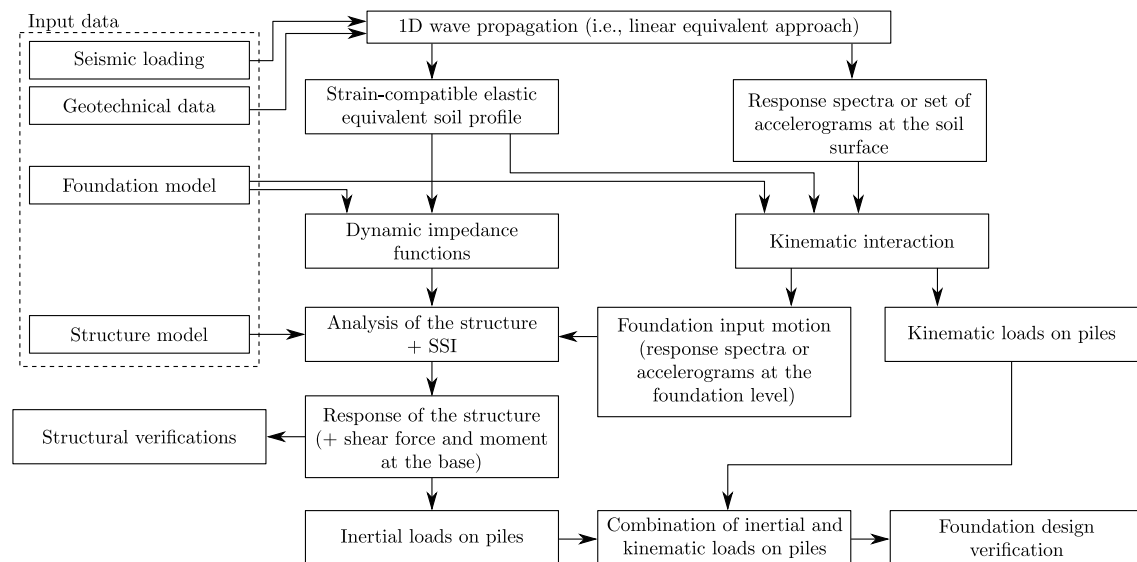


**Figure F.1:** Consideration of SSI in current design of structures under earthquake loading

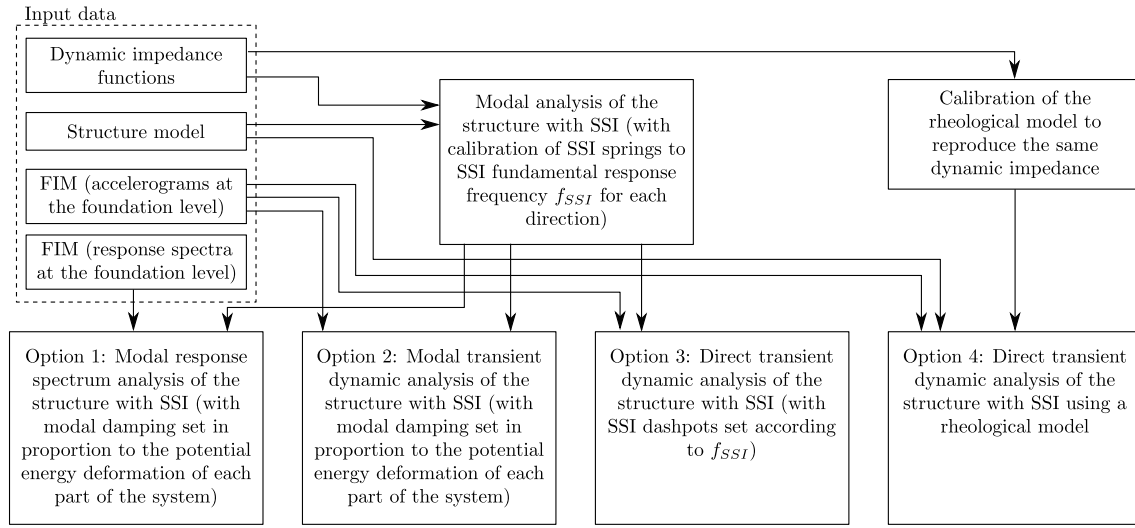


**Figure F.2:** Several possible approaches for the dynamic analysis of a structure taking into account SSI effects

## F.2 Dynamic impedance functions of the pile group used in experimental tests

The dynamic impedance functions of the single pile and the 5 pile group used in the experimental tests are calculated using the boundary element approach and the code SASSI [126, 165]. The equivalent linear soil profiles presented in Sections 4.4.3 and 4.4.4 are used in the calculations.

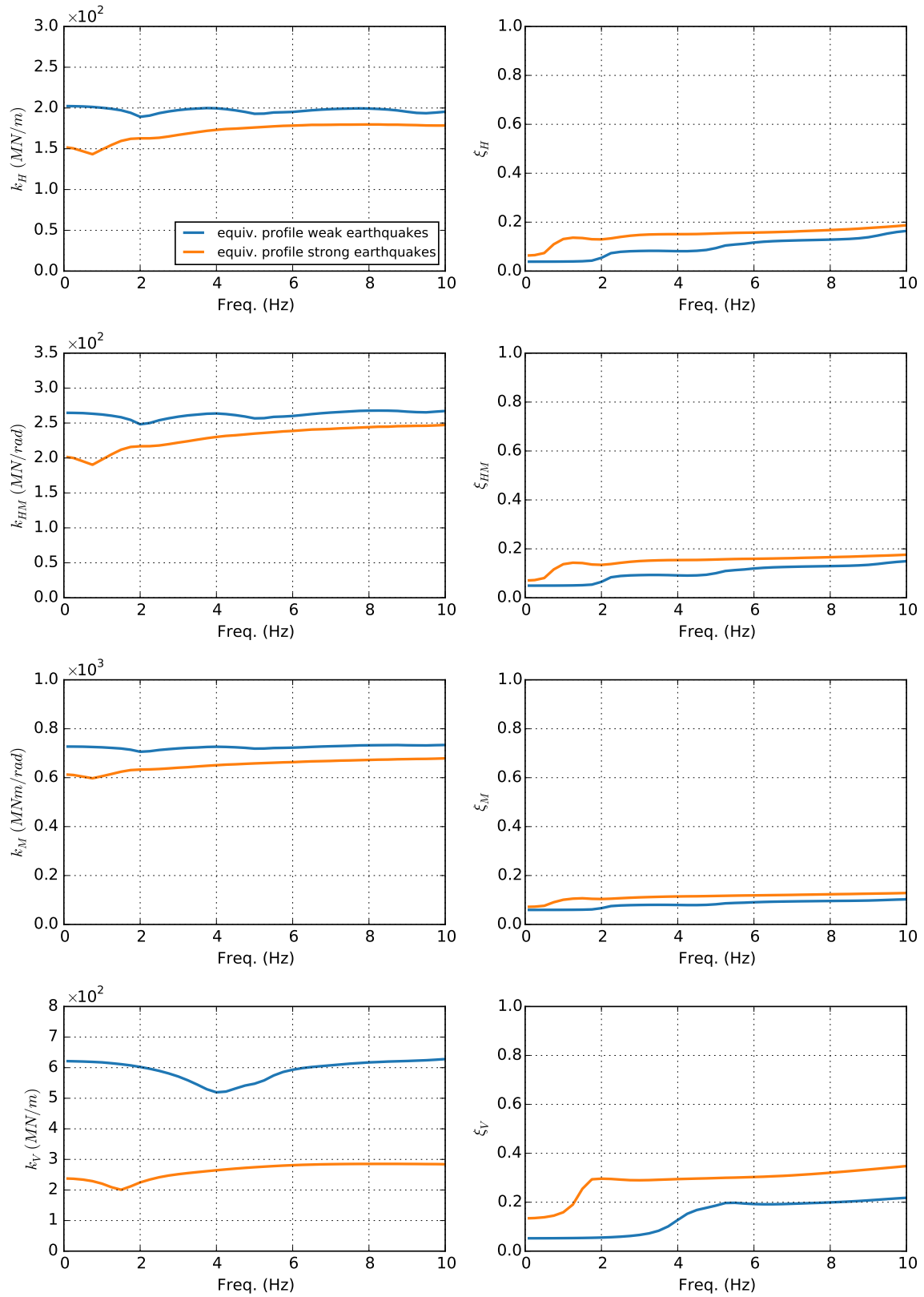


**Figure F.3:** Dynamic stiffnesses and damping ratios for the single pile used in centrifuge tests using the equivalent linear elastic approach



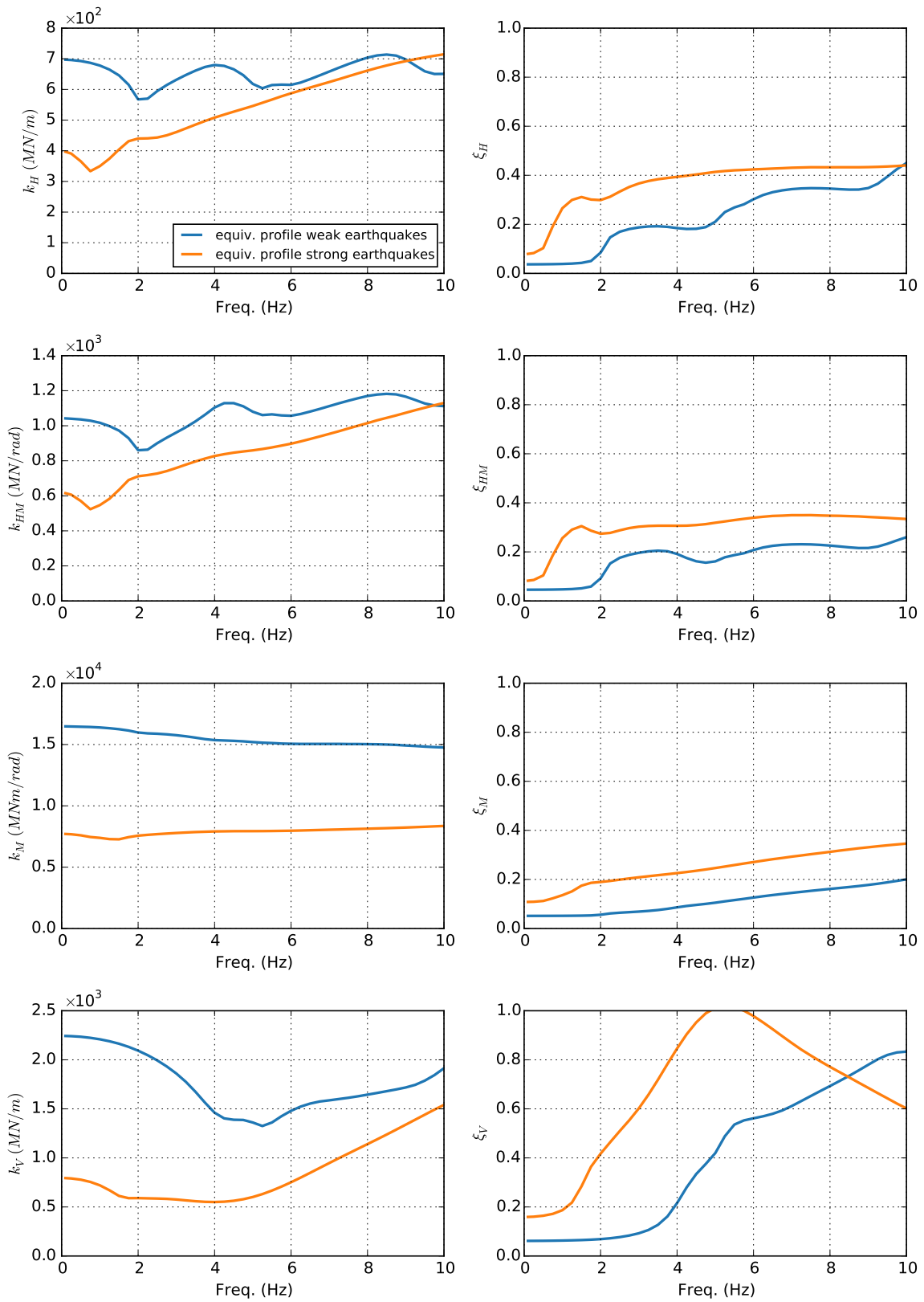


**Figure F.4:** Dynamic stiffnesses and damping ratios of the pile group used in centrifuge tests using an equivalent linear elastic approach



---

## **Titre : Interaction dynamique sol-structure des fondations sur pieux : étude expérimentale et numérique**

**Mots clés :** Interaction Sol-Structure ; groupe de pieux ; chargement sismique ; macroélément ; essais en centrifugeuse

**Résumé :** La réponse dynamique d'une structure supportée par des fondations profondes constitue un problème complexe d'Interaction Sol-Structure (ISS). Sous chargement sismique, les pieux sont soumis à la sollicitation imposée par le sol (interaction cinématique) et aux forces d'inertie transmises par la superstructure (interaction inertielle).

Le dimensionnement des fondations profondes soumises à des sollicitations sismiques est souvent réalisé au moyen de méthodes conservatrices visant à assurer que les fondations ne soient pas endommagées. La plupart de ces méthodes considèrent le comportement de la fondation élastique linéaire et par conséquent la capacité de la fondation à dissiper de l'énergie du fait des mécanismes non-linéaires est négligée. Cette approche était justifiée dans le passé en raison du manque d'informations sur le comportement non-linéaire des fondations et de l'absence d'outils numériques adaptés. De telles limitations deviennent de plus en plus obsolètes, puisqu'un nombre pertinent de résultats expérimentaux et numériques sont maintenant disponibles, ainsi que de nouvelles méthodes de conception (Pecker *et al.* 2012).

Dans cette thèse, le comportement des pieux isolés et des groupes de pieux sous chargement sismique est étudié avec une approche couplant l'expérimental et le numérique. Des essais dynamiques en centrifugeuse sont effectués avec un sol stratifié, plusieurs configurations de fondations et une série de séismes et sollicitations sinusoïdales.

Des calculs non-linéaires aux éléments finis sont également effectués et comparés aux résultats expérimentaux afin d'étudier la capacité des modèles numériques à reproduire de manière satisfaisante la réponse non-linéaire des fondations.

Un nouveau macroélément pour les groupes de pieux sous chargement sismique est proposé et validé numériquement. Le macroélément permet de prendre en compte les effets de groupe et leur variation avec la fréquence de sollicitation (interaction pieu-sol-pieu) ainsi que la non-linéarité développée dans le système. Le nouveau macroélément est enfin utilisé pour effectuer une analyse dynamique incrémentale (IDA) du pylône centrale d'un pont à haubans.

---

## **Title: Dynamic soil-structure interaction of pile foundations: experimental and numerical study**

**Keywords:** Soil-Structure Interaction; pile-group foundation; seismic loading; macroelement; centrifuge modelling

**Abstract:** The dynamic response of a structure supported by pile foundations is a complex Soil-Structure Interaction (SSI) problem. Under earthquake loading, the piles are subjected to loadings due to the deformation imposed by the soil (kinematic interaction) and to the inertial forces transmitted by the superstructure (inertial interaction).

The design of deep foundations under seismic loadings is often carried out by means of conservative methods that aim to assure zero damage of the foundation. Most of these methods consider the behavior of the foundation as linear elastic. As a result, the capability of the foundation to dissipate energy during seismic loading due to nonlinear mechanisms is neglected. This approach was justified in the past due to the lack of information about the nonlinear behavior of foundations and the absence of adapted numerical tools. Such limitations are becoming more and more obsolete, as a relevant number of experimental and numerical results are now available as well as new design methods (Pecker *et al.* 2012).

In this Ph.D, the behavior of single piles and pile groups under seismic loading is studied using both experiments and finite element calculations. Dynamic centrifuge tests are carried out with a multilayered soil profile, several foundation configurations and a series of earthquakes and sinusoidal base shakings.

Nonlinear finite element calculations are also performed and compared to experimental results to investigate the ability of current computational models to satisfactorily reproduce the nonlinear response of foundations.

A novel macroelement for pile group foundations under seismic loading is developed and numerically validated. It allows taking into account the group effects and their variation with the loading frequency (pile-soil-pile interaction) as well as the nonlinearity developed in the system. Finally, the macroelement model for pile groups is used to perform an Incremental Dynamic Analysis (IDA) of the main pylon of a cable-stayed bridge.